# Deformations of Piezoceramic-Composite Actuators

Adel Benhaj Jilani

Dissertation submitted to the Faculty of the
Virginia Polytechnic Institute and State University
in partial fulfillment of the requirements for the degree of

Doctor of Philosophy
in
Engineering Mechanics

Michael W. Hyer, Chair
Muhammad R. Hajj
Scott L. Hendricks
Liviu Librescu
Yuriko Renardy

November 11, 1999
Blacksburg, Virginia

Keywords: Geometric Nonlinearities, Stability, Fiber-Reinforced Composites, Rayleigh-Ritz Method, Thermal Effects, Benders

# Deformations of Piezoceramic-Composite Actuators

Adel Benhaj Jilani

(ABSTRACT)

In the past few years a new class of layered piezoceramic and piezoceramic-composite actuators, known as RAINBOW and GRAPHBOW, respectively, that are capable of achieving 100 times greater out-of-plane displacements than previously available has been developed. Prior to the development of RAINBOW and GRAPHBOW, large stacks of piezoelectric actuators, requiring complicated electronic drive circuits, were necessary to achieve the displacement now possible through the use of a single RAINBOW actuator. The major issues with both RAINBOW and GRAPHBOW are the prediction of their room-temperature shapes after processing, and their deformation response under application of electric field. In this research, methodologies for predicting the manufactured shapes of rectangular and disk-style RAINBOW and GRAPHBOW are developed. All of the predictive analyses developed are based on finding approximate displacement responses that minimize the total potential energy of the devices through the use of variational methods and the Rayleigh-Ritz technique. These analyses are based on classical layered plate theory and assumed the various layers exhibited linear elastic, temperature-independent behavior. Geometric nonlinearities are important and are included in the strain-displacement relations. Stability of the predicted shapes is determined by examining the second variation of the total potential energy. These models are easily modified to account for the deformations induced by actuation of the piezoceramic. The results indicate that for a given set of material properties, rectangular RAINBOW can have critical values of sidelength-to-thickness ratio ($L_x/H$ or $L_y/H$) below which RAINBOW exhibits unique, or single-valued, spherical, or domed, shapes when cooled from the processing temperature to room temperature. For values of sidelength-to-thickness ratio greater than the critical value, to a trifurcation in the temperature-curvature relation, RAINBOW exhibits multiple room-temperature shapes. Two of the shapes are stable and are, in general, near-cylindrical. The third shape is again spherical, but it is unstable. Similarly, disk-style RAINBOW can have critical values of radius-to-thickness ratios ($R/H$) below which RAINBOW exhibits axisymmetric spherical room-temperature shapes. For values of $R/H$ greater than the critical value, disk-style RAINBOW exhibits two stable near-cylindrical shapes and one unstable spherical shape. Moreover, it is found that for the set of

material properties used in this study, the optimal reduced layer thickness would be at 55%, since the maximum change in curvature is achieved under the application of an electric field, while the relationship between the change in curvatures and the electric field is kept very close to being linear. In general, good agreement is found for comparisons between the predicted and manufactured shapes of RAINBOW. A multi-step thermoelastic analysis is developed to model the addition of the fiber-reinforced composite layer to RAINBOW to make GRAPHBOW. Results obtained for rectangular RAINBOW indicate that if the trifurcation temperature in the temperature-curvature relation is lower than the composite cure temperature, then a unique stable GRAPHBOW shape can be obtained. If the RAINBOW trifurcation temperature is above the composite cure temperature, multiple room-temperature GRAPHBOW shapes are obtained and saddle-node bifurcations, or limit points, can be encountered during the cooling to room temperature of [$0^o$/RAINBOW], [RAINBOW/$0^o$], and [$0^o_2$/RAINBOW]. Rectangular [RAINBOW/$0^o$/$90^o$] seems to be less likely to encounter saddle-node bifurcations. Furthermore, the unstable spherical RAINBOW configuration is converted to a stable near-cylindrical configuration. For the case considered of disk-style GRAPHBOW, three stable room-temperature shapes are obtained and the unstable axisymmetric RAINBOW configuration is also converted to a stable near-cylindrical configuration. For both rectangular and disk-style GRAPHBOW, the relationship between the major curvature and the electric field is shown to be very close to being linear. This characteristic would aid any dynamic analysis of RAINBOW or GRAPHBOW.

# Dedication

*To my mother,*

*my father,*

*my brother,*

*and my sisters,*

*whose love and*

*support I cherish*

# Acknowledgments

It is a great pleasure to me to acknowledge those many many people who have influenced my thinking and contributed to my inadequate knowledge. Amongst many I must single out the assistance and guidance given to me by Professor Michael W. Hyer, my advisor, one whose contributions and ideas to this study are deeply appreciated. Thanks are also due to Professors Muhammad Hajj, Scott Hendricks, Liviu Librescu, Saad Ragab, and Yuriko Renardy for their interest in my research and the council and advice given. The author wishes to express his gratitude to Dr. Wallace L. Vaughn from NASA Langley Research Center for his assistance in carrying on the experimental measurements of material properties and the manufacturing of RAINBOW devices.

The present study was made possible by the financial support of the NASA Langley Research Center through grant no. NCC-1-304. The author wishes to express his gratitude for that support.

Special thanks go to Flor Martinez for all the love and support she has given me. Finally, I wish to give my thanks to Loretta Tickle for her help with administrative matters and to my colleagues and friends, Dr. Walter Lacarbonara, Piergiovanni Marzocca, Tom Ochinero, Ilhan Tuzcu, Rakesh Gummalla, and Sean Fahey for their friendship and support.

# Contents

# List of Figures

# List of Tables

# Chapter 1

# Introduction

## 1.1 Introduction

Piezoelectrics are defined to be materials that either generate a charge when subjected to a mechanical stress, or exhibit a dimensional change when a charge is imposed on them. The latter effect is very similar to the dimensional change in a material that accompanies a temperature change. Jaffe *et al.* [1] and Haertling [2] refer to these two modes of behavior of piezoelectric materials as the direct and indirect modes of operation, respectively. These two modes of operation make piezoelectric materials ideal for use in numerous applications. Indeed, these materials have the ability to sense their surroundings and respond as necessary to changes in their environment, and are often referred to as *smart* or *intelligent* materials. The simplest example of a smart material is a bimetallic strip [3] which can be used in a thermostat to control temperature. The principle behind a bimetallic strip thermometer relies on the fact that two different metals expand at different rates as the temperature changes, causing the strip to bend as shown in Figure 1.1, thereby producing out-of-plane displacements. For a positive change of temperature, bending occurs towards the side of the metal with the lower coefficient of thermal expansion. On the other hand, for a negative change of temperature, bending occurs towards the side of the metal with the higher coefficient of thermal expansion. By bonding two different metals together, a simple electric device can be made to control temperature. Referring to Figure 1.2, if the device were being used in an oven, then

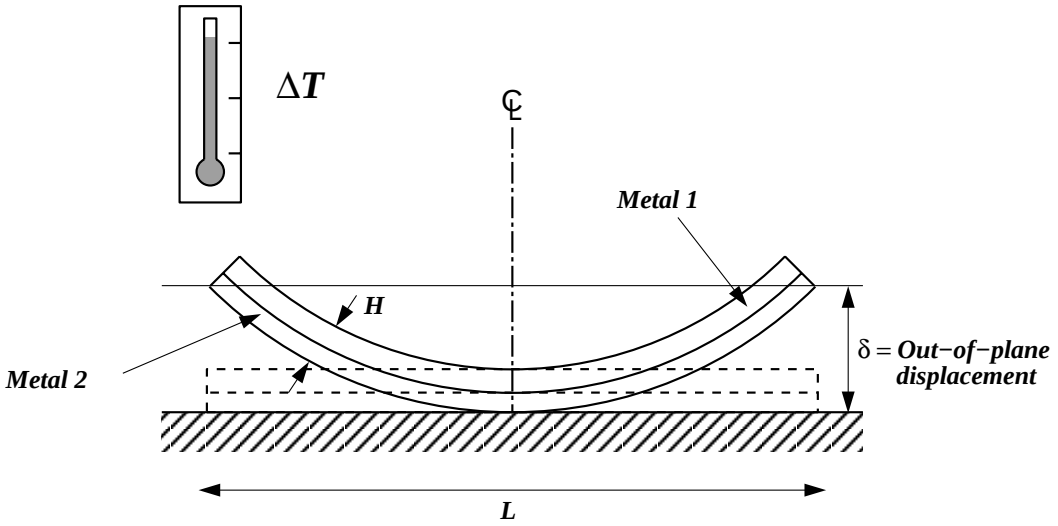


Figure 1.1: Thermal bending of a bimetallic strip (After [3]).

metal 1 would be chosen to expand more than metal 2 to cause the strip to bend downward and away from the electrical contact when the desired temperature is reached, thereby stopping power to the electrodes. In a refrigerator, metal 2 would be chosen to expand more than metal 1 to cause the strip to bend upwards as the temperature rises, making contact so that current would flow, thereby starting a refrigerator pump. On a much wider scale, the use of smart materials in the form of piezoelectric materials includes vibration cancellation and optical positioning in aerospace systems [5, 6, 7], active control of boundary layers along leading edges [8], the suppression of aircraft cabin noise [9], the elimination of panel flutter [10] and tail buffeting [11] in fixed-wing aircraft, and vibration elimination in helicopter rotor blades [12, 13, 14]. In the last fifteen years, the use of piezoelectric ceramic materials as actuators for small ($< 20\mu m$) and precise movement devices has undergone considerable investigation and development [15, 16, 17, 18, 19, 20, 21]. More recently, it has become more evident that these devices are needed in newer applications such as linear motors, cavity pumps, switches, loud speakers, noise canceling devices, variable focus mirrors, laser deflectors, and other devices that require very large out-of-plane displacements ($> 1000\mu m$ (40 mils)) [22]. The direct extensional strain in most piezoelectric ceramic materials is at best a few tenths of one percent [22]. Hence, a means of amplifying this strain is essential to their successful use in these applications that require large out-of-plane displacements.

Lately, a new class of piezoelectric ceramic devices that are capable of achieving 100 times greater

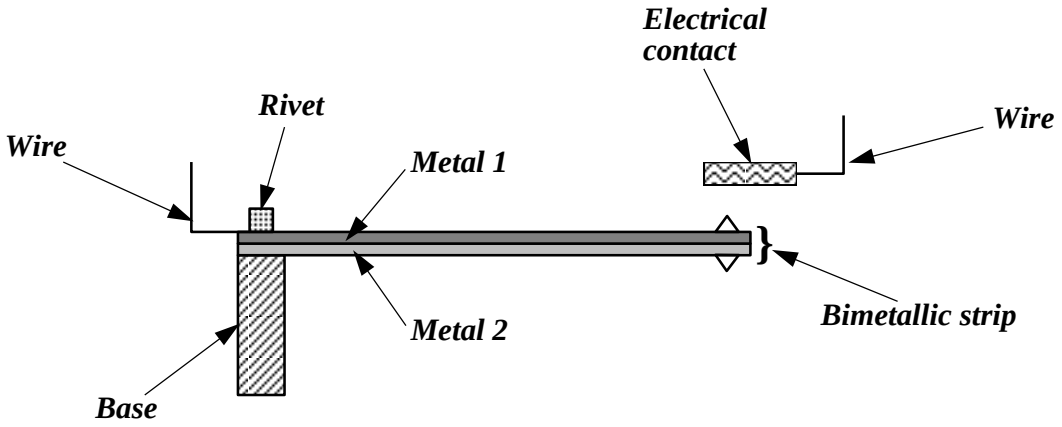


Figure 1.2: A bimetallic strip thermostat (After [4]).

out-of-plane displacements than previously available ($> 1000\mu m$) and sustaining moderate pressures (0.6 MPa (85 psi)) has been developed through cooperative agreement between NASA-Langley Research Center and Clemson University, Clemson, South Carolina [23]. This new type of piezoelectric ceramic device is known as RAINBOW (Reduced And INternally Biased Oxide Wafer) and is commercially available from Aura Ceramics, Inc., Minneapolis, Minnesota [23]. RAINBOW is a fundamental advancement in the area of piezoelectric actuators and affords potential for application in vibration/noise-suppression systems, pointing and positioning devices, speakers and microphones, and fluid transfer pumps. RAINBOW technology received a 1994 R&D 100 Award as one of the year's most significant new products. Prior to the invention of RAINBOW, large stacks of piezoelectric actuators, requiring complicated electronic drive circuits, were necessary to achieve the displacement now possible through the use of a single RAINBOW actuator. In addition to their wider range of strain-stress characteristics than other commercially available lead-zirconate-titanate (PZT) piezoelectrics, RAINBOW actuators have advantages over the conventional ones in terms of simplicity, quick processing, ease of fabrication, surface mountable configuration, low cost [22], and long term reliability, this latter point referring to the fact that delamination may be less of an issue than with actuators made by bonding layers of metal, adhesive, and piezoceramic together.

A RAINBOW actuator is produced by chemically reducing one side of a conventional lead-containing round or rectangular piezoelectric wafer, such as PZT, at an elevated temperature. This process is depicted in Figure 1.3 for a rectangular wafer. In this process, the piezoelectric wafer, which

is on the order of 0.1 to 0.5 mm thick (5–20 mils)and up to 50 mm on a side (2 in.), is placed on graphite block and inserted into a furnace preheated to 975 $^{o}$C [24]. While at high temperature, along the interface between the piezoceramic and the graphite block, oxygen is removed from the piezoelectric wafer, creating a wafer that possesses a primarily metallic lead layer (the chemically reduced, or oxygen-deficient, layer) and an unreduced piezoelectric ceramic layer [24]. The wafer then has bimaterial properties, i.e., differences in thermal expansion coefficients and Young's moduli between the two layers. When cooled to room temperature, because of the difference in the material properties between the reduced and unreduced layers, the RAINBOW device deforms out of the plane of the originally flat wafer, much like the bimetallic strip, creating an internally stressed structure. Figure 1.3(c) shows the cooled shapes observed as a result of this reduction process. The shape can be cylindrical, with the generators of the cylinder oriented in either of two directions, or it can be spherical-, or dome-, like. This latter shape is difficult to identify because of the rectangular geometry. The actual shape observed depends to a large degree on the processing time and dimensions (sidelengths, thickness) of the wafer. Of course processing time determines the thickness of the reduced layer, so the shape actually depends on the relative thicknesses of the reduced and unreduced layers. When electric field is applied through the thickness, creating additional dimensional changes in the piezoelectric ceramic layer, the internally stressed structure exhibits additional out-of-plane displacements which are several orders of magnitude greater than those of the starting piezoelectric material. These are due simply to the bending action of the device. Hence the terminology 'RAINBOW bender'. Round benders are made in a similar fashion, and the shape seems to depend again on wafer dimensions (radius, thickness) and processing time, and the cylinders or dome are the two shapes observed.

A variant of a RAINBOW bender is produced by re-heating a RAINBOW bender to the cure temperature of a graphite-epoxy fiber-reinforced composite material and bonding single or multiple layers of composite material to one side of it. Once the composite layer is added to a RAINBOW actuator and cured, the temperature is returned to room temperature. Additional internal stresses are induced due to the mismatch in material properties between the unreduced ceramic, reduced ceramic, and the composite layer, producing a deformed stress-biased device which can also exhibit large out-of-plane displacements. This new form of material, known as GRAPHBOW, may have advantage over RAINBOW materials in terms of load bearing capacity, resistance to dam-

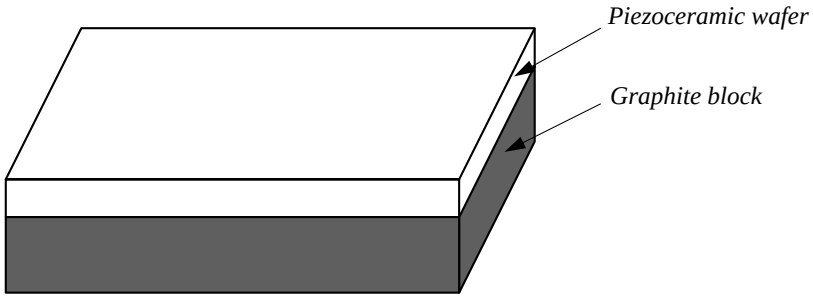


*(a) Piezoceramic wafer and graphite block*

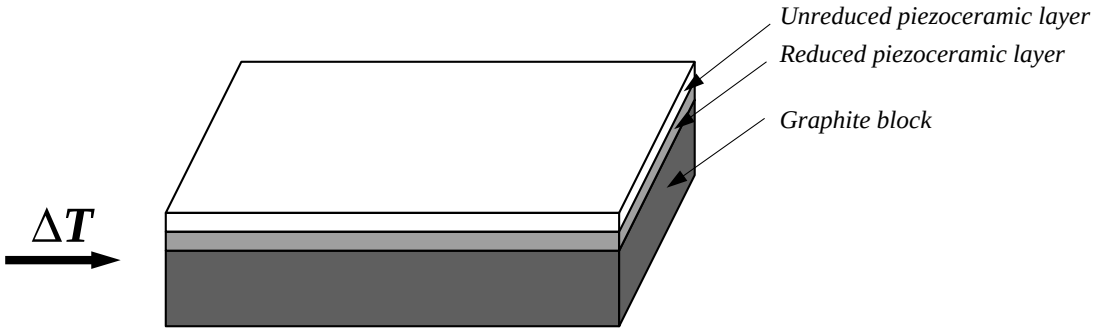


*(b) The result of heating at 975 °C for about 1 hour*

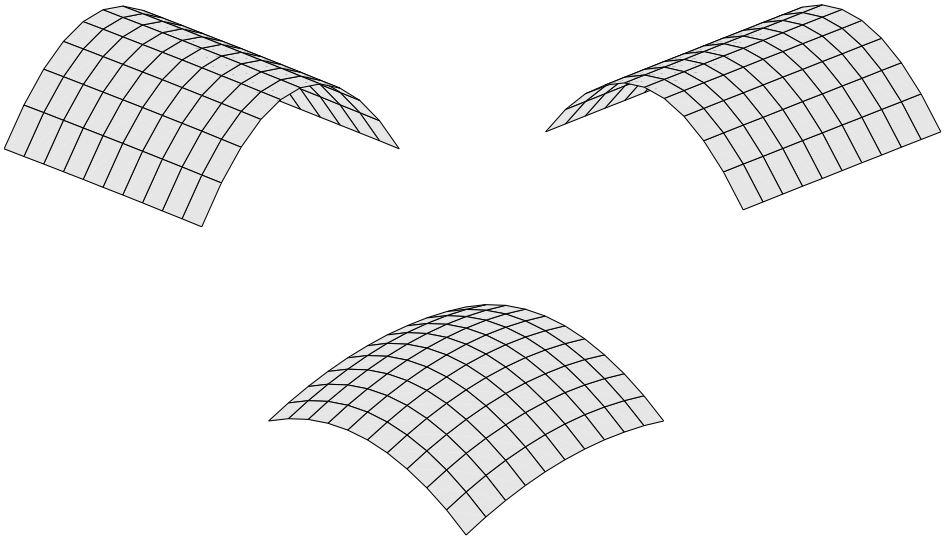

*(c) Possible shapes of wafer cooled to room temperature*

Figure 1.3: Steps for manufacturing RAINBOW actuators.

age, and long-term reliability, since the composite layer acts as a backing and keeps the ceramic layers together in case cracks form in the piezoceramic layers. (Though the words RAINBOW and GRAPHBOW are acronyms, hereafter, for convenience, they will be treated as nouns. The noun can be referring to a material, as with steel, or a device, as with RAINBOW actuators. Furthermore, it will be assumed that the singular and plural forms are the same.)

A major issue with both RAINBOW and GRAPHBOW is the prediction of their room-temperature shapes after processing. With GRAPHBOW, the shape of the RAINBOW is altered upon re-heating and adding other layers of material. With both round and rectangular actuators, as has been mentioned previously, the room-temperature shapes appear to be a function of the dimensions and the thicknesses of the reduced and unreduced layers. A predictive tool to explain this behavior would be quite useful, and it could aid in design. Also at issue is the deformation response when an electric field is used to actuate the material. These deformations are what are used for vibration suppression, positioning, etc. and understanding their nature is of primary importance. Therefore, the research discussed herein has two objectives. The first objective is to develop a methodology for predicting the manufactured shape of RAINBOW and GRAPHBOW. The methodology should be able to accommodate material properties of the reduced and unreduced layers, and composite layers, wafer thickness, wafer radius, for the round devices, and wafer length and width, for the rectangular devices, the thickness of the various layers, and the temperature change. For GRAPHBOW, the temperature to which RAINBOW is re-heated to cure the composite layer is also an important parameter. The second objective is to develop a methodology for predicting the deformations of RAINBOW and GRAPHBOW to actuation of the piezoceramic. Again, the methodology should be able to accommodate all the important geometric and material properties.

In the chapters to follow, a number of predictive analyses are developed. They are all based on finding approximate displacement responses that minimize the total potential energy of the devices. This is done through the use of variational methods. For predicting the manufactured shape, the energy is due to the thermoelastic strain energy generated as the device cools from the processing temperature to its service temperature. For predicting the deformations of the manufactured shape due to actuating the piezoceramic material, additional energy due to the indirect mode of operation of the piezoceramic material is included. Approximate solutions are sought because the problem is

inherently geometrically nonlinear. Generally when cooled from the processing temperature to the service temperature, the out-of-plane deformations are at least several times the thickness of the wafer. This is an indication that geometric nonlinearities can be important and should be included. Inclusion of geometric nonlinearities, or nonlinearities of any kind, greatly complicates the problem and more than likely leads to intractable governing equations which require appropriate solution techniques, such as finite-element or finite-difference approaches, for obtaining numerical results. Hence the approximation is made early on, in the form of a Rayleigh-Ritz approximation to the displacement fields. The Rayleigh-Ritz procedure is aided by the fact that the cooled shape of the devices can be either cylindrical or domed. Such shapes can be represented by well-behaved functions of the spatial coordinates.

Since nonlinearities are being considered, it would not be surprising to have more than one room-temperature shape predicted for a given set of conditions. Linear systems have single unique solutions, but nonlinear systems may have more than one solution. Accordingly, an examination of the stability of the predicted shapes is considered. While minimum states of the total potential energy are being sought, maximums of the energy, which correspond to unstable shapes, may be inadvertently found. This can be determined by studying the stability of the shapes predicted. The study of stability is a direct extension of the use of variational methods. Whereas the shapes that minimize, or maximize, the total potential energy are found by considering the first variation of the total potential energy, stability is studied by examining the second variation.

Though there are a number of similarities among the various analyses presented, the predictive tools for the rectangular devices are based on analyses in a Cartesian coordinate system, while the predictive tools for the round or disk-style devices are based on a polar coordinate system. All analyses are based on classical layered plate theory. All analyses assume the various layers exhibit linear elastic temperature-independent behavior, including the effects of orthotropy. For the fiber-reinforced composite layer added to RAINBOW to make GRAPHBOW, orthotropy is certainly important. However, the piezoceramic wafers might show some signs of orthotropy due to the manner in which they are manufactured [22]. More important, the predictive tools developed can be applied to devices containing metallic layers, such as THUNDER, and metals can display 10-15% orthotropy due to roll forming. Any orthotropy at all will lead to preferred directions of response,

so it must be included from the onset. Moreover, on the global scale RAINBOW is considered to be made of a reduced piezoceramic layer and an unreduced layer; however, on a smaller scale, since the reduction is a diffusion-based process, there is actually a gradient of material properties between the reduced and unreduced layers. If desired, this gradient region can be modeled by introducing one, two, or more additional layers, each with spatially uniform material properties. For that reason, the present theories are made to account for a multi-layered approach.

## 1.2 Road Map to Remaining Chapters

The next chapter discusses the development of the model for rectangular RAINBOW. The assumptions in the model to predict the manufactured shape are discussed, as are the expression for the total potential energy, including thermally-induced strain effects, the stress-strain relations, the strain-displacement relations, the approximate displacement fields of the Rayleigh-Ritz approach, equilibrium, and stability. Then, the additions to the model to include piezoelectric-induced deformations are considered. Numerical results are presented to illustrate the influence of geometry, including the thickness of the reduced layer, on the manufactured shape. Numerical results are also present to illustrate the changes in manufactured shape due to application of an electric field through the thickness of the device.

Chapter 3 considers rectangular GRAPHBOW. Again, the model for predicting its manufactured shape is presented, but the model is more complicated than the model for RAINBOW due to the step of adding the composite layer at the elevated cure temperature of the composite. This requires a multi-step thermoelastic analysis. The influence of adding one or more composite layers on the final manufactured shape is investigated using numerical results. Comparisons with RAINBOW are made.

Chapter 4 again considers RAINBOW, but for disk-style geometries. The basic foundation of the model for predicting the manufactured shape and piezoelectric-induced deformations of disk-style RAINBOW is the same as for rectangular RAINBOW, except the analysis is conducted in polar coordinates. The assumed displacement fields are then functions of the radial and circumferential coordinates instead of rectangular coordinates. The chapter examines the influence of radius-

to-thickness ratio and reduced layer thickness on the manufactured shape. Also, the effect of radius-to-thickness ratio and reduced layer thickness on the piezoelectric induced deformations is considered.

Chapter 5 considers disk-style GRAPHBOW. The model presented in Chapter 4 is extended in a straightforward fashion to accommodate the incorporation of the composite layer at the elevated cure temperature of the composite. Again, a multi-step thermoelastic analysis is used to obtain numerical results for various GRAPHBOW with different composite layer arrangements, and comparisons are made with their RAINBOW counterparts. Finally, in Chapter 6, conclusions of this research work and recommendations for future work are specified.

# Chapter 2

# Rectangular RAINBOW Actuators

## 2.1 Introduction

In this chapter, a discussion of the theory developed to predict the manufacturing and piezoelectric-induced deformation characteristics of rectangular RAINBOW is presented. Discussed are the key assumptions, the stress-strain relations, the strain-displacement relations, including geometric nonlinearities, total potential energy, and variational methods. A discussion of the results predicted by the developed theory, as well as their implications, is given.

## 2.2 Model Definition and Assumptions

Figure 2.1 illustrates the specific problem being considered and defines the $x$-$y$-$z$ coordinate system used for analysis. Figure 2.1 describes the details of the layer numbering scheme. The rectangular actuator is assumed to be made of multiple thin layers of orthotropic materials, and each layer is assumed to be homogeneous. The layers can represent unreduced or reduced piezoceramic material (PZT), or some rule-of-mixtures combination of these two to represent a region of diffusion, and there are assumed to be $N$ layers. In Figure 2.1, the device, which is flat at its reducing temperature, deforms out of plane upon cooling due to the asymmetry of the layer material properties with respect to the device's geometric midsurface. It is assumed that the out-of-plane deflections develop only

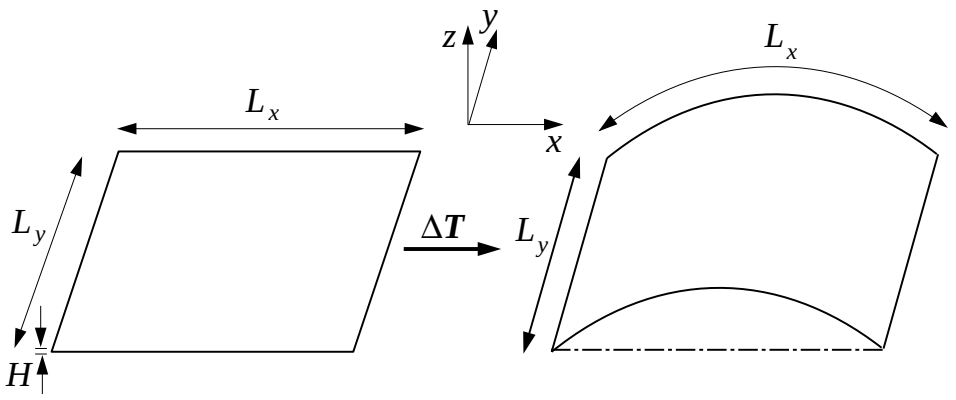


Figure 2.1: Analysis of rectangular RAINBOW in the $x$-$y$-$z$ coordinate system.

because of the differences in the thermo-elastic properties of the individual layers. The deformations are assumed to be reversible and only a function of the temperature difference between states. When flat at the reducing temperature, the device has inplane dimensions $L_x$ by $L_y$ and is of thickness $H$, which is greatly exaggerated in Figure 2.2 for clarity. The location $z$=0 is the geometric midsurface, here taken to be the reference surface. The lower and upper boundaries of layer 1 are located at $z$=$z_o$=$-H/2$ and $z$=$z_1$, the boundaries of layer 2 at $z_1$ and $z_2$, and in general, the boundaries of the $k^{th}$ layer at $z_{k-1}$ and $z_k$. Layer no. 1 is assumed to be at the negative-most $z$ position. Upon cooling from the flat configuration of the reducing temperature, shown in Figure 2.3(a), the actuator deforms into one of the shapes given by Figures 2.3(b), (c), and (d). Of these shapes, it is assumed that the shape observed for any temperature is the shape that minimizes the total potential energy of the device. In an attempt to predict these shape characteristics, classical layered plate theory is extended to include geometric nonlinearities through the von Karman approximation to Green's strain measures. This extended theory is thus based on the following major assumptions:

- the displacements are continuous throughout the layered actuator,
- the Kirchhoff hypothesis, which states that every straight line in the plate that was originally perpendicular to the plate middle surface before deformation remains straight and perpendicular to the deflected middle surface after deformation, is valid,
- the von Karman approximation to Green's strain measures is used,
- the material is linearly elastic, and the thermoelastic properties are independent of tempera-

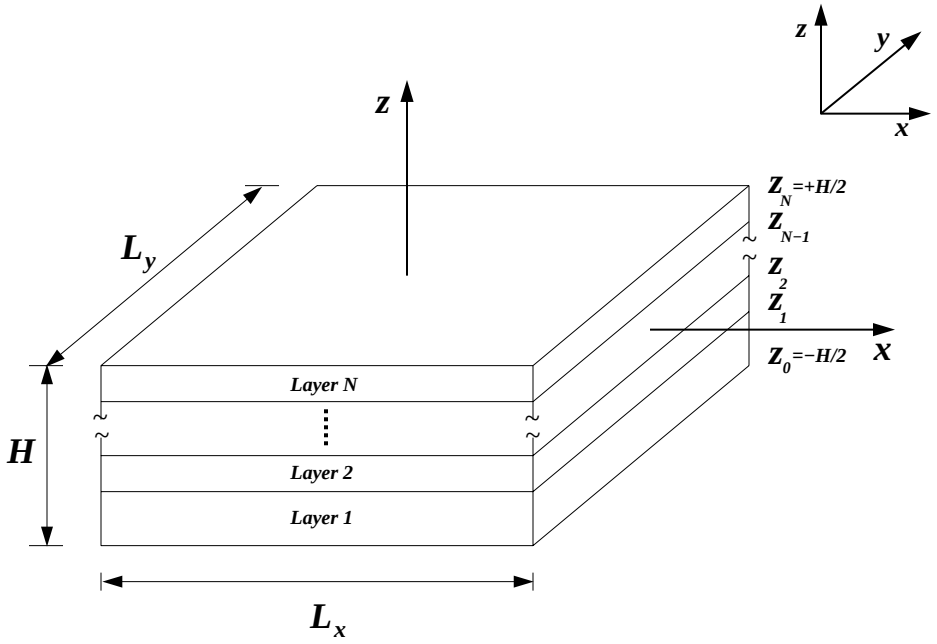


Figure 2.2: Geometry and nomenclature of rectangular RAINBOW considered.

ture,

- the through-the-thickness stresses are small in comparison to the inplane stresses, i.e., the plane-stress assumption is assumed valid, and,
- the temperature changes are assumed to be uniform, i.e., independent of the spatial coordinates.

### 2.2.1 Total Potential Energy

Since it is assumed external tractions are not important during the cooling process, the total potential energy, including the effects of thermal expansion, is given in general form by Fung [25] as

$$\Pi = \int_{Vol} \omega dVol \tag{2.1}$$

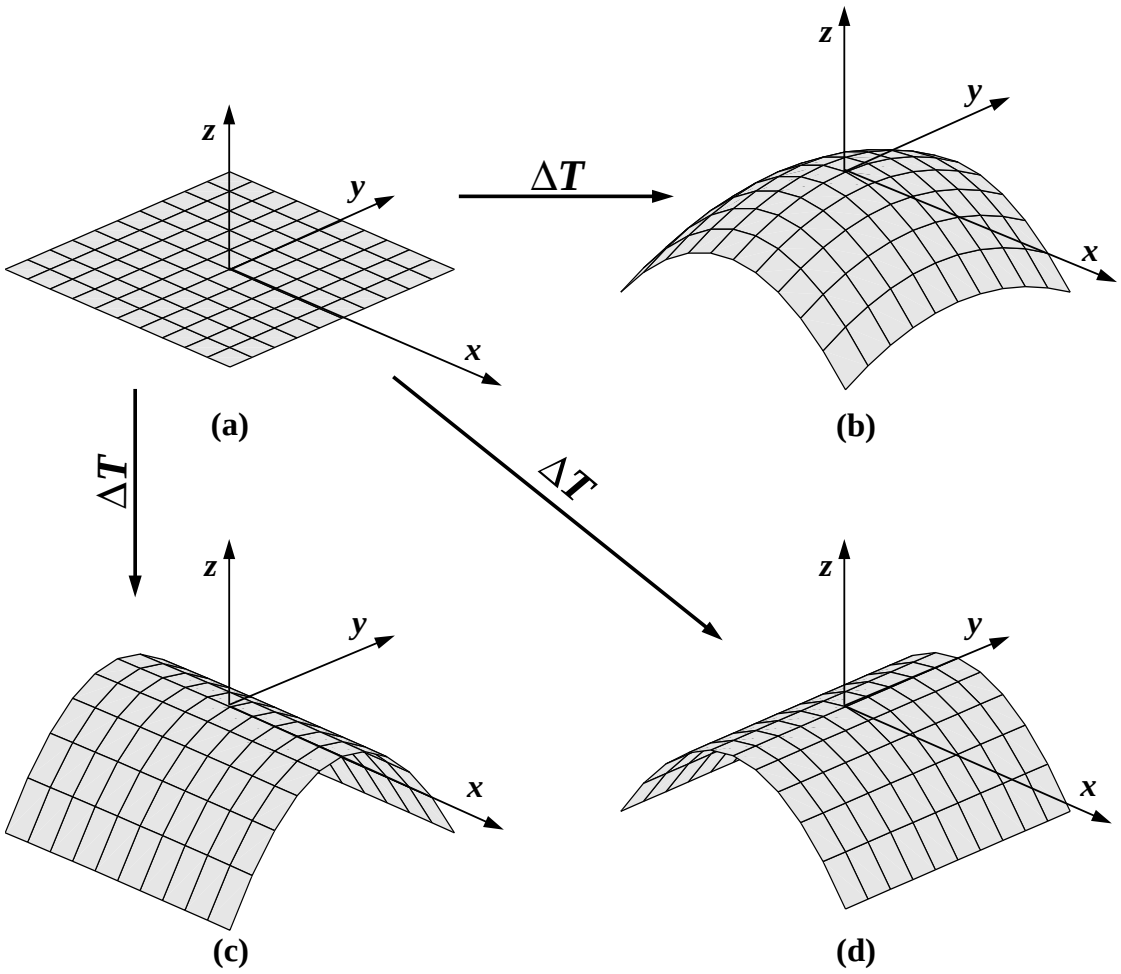


Figure 2.3: RAINBOW shapes: (a) flat at the elevated reducing temperature, (b) a dome, or spherical, shape at room temperature, (c) a cylindrical shape at room temperature, and (d) another cylindrical shape at room temperature.

In this equation

$$\omega = \frac{1}{2} C_{ijkl} \epsilon_{ij} \epsilon_{kl} - \beta_{ij} \epsilon_{ij} \Delta T, \quad i,j,k,l = 1,3 \tag{2.2}$$

where $\omega$ is the strain energy density. The $C_{ijkl}$ are the elastic constants of the material and the $\beta_{ij}$ are coefficients related to the elastic constants and the coefficients of thermal expansion of the material. The $\epsilon_{ij}$ are the strains in the material and $\Delta T$ is the temperature change in the material due to cooling from the reduction temperature. The stress components are

$$\sigma_{ij} = \frac{\partial \omega}{\partial \epsilon_{ij}} = C_{ijkl} \epsilon_{kl} - \sigma_{ij}^T, \quad i,j,k,l = 1,3 \tag{2.3}$$

where

$$\sigma_{ij}^T = \beta_{ij} \Delta T, \quad i,j = 1,3 \tag{2.4}$$

Equation (2.2) can be then rewritten in the form

$$\omega = \frac{1}{2} (\sigma_{ij} - \sigma_{ij}^T) \epsilon_{ij}, \quad i,j = 1,3 \tag{2.5}$$

Enforcing the plane-stress assumption by equating $\sigma_{i3}$=0, $i$=1,3, and changing nomenclature so that $\sigma_{11} = \sigma_x$, $\sigma_{22} = \sigma_y$, $\sigma_{12} = \tau_{xy}$, $\sigma_{11}^T = \sigma_x^T$, $\sigma_{22}^T = \sigma_y^T$, and $\sigma_{12}^T = \tau_{xy}^T$, the total potential energy, $\Pi$, may be rewritten as

$$\Pi = \frac{1}{2} \int_{-\frac{L_x}{2}}^{+\frac{L_x}{2}} \int_{-\frac{L_y}{2}}^{+\frac{L_y}{2}} \int_{-\frac{H}{2}}^{+\frac{H}{2}} ((\sigma_x - \sigma_x^T)\epsilon_x + (\sigma_y - \sigma_y^T)\epsilon_y + (\tau_{xy} - \tau_{xy}^T)\gamma_{xy}) dx\, dy\, dz \tag{2.6}$$

where integration is over the volume of the actuator. The strains in the energy expression are given by the Kirchhoff hypothesis as

$$\begin{aligned} \epsilon_x &= \epsilon_x^o + z\kappa_x^o \\ \epsilon_y &= \epsilon_y^o + z\kappa_y^o \\ \gamma_{xy} &= \gamma_{xy}^o + z\kappa_{xy}^o \end{aligned} \tag{2.7}$$

The quantities $\epsilon_x^o$, $\epsilon_y^o$, $\gamma_{xy}^o$, and $\kappa_x^o$ , $\kappa_y^o$, $\kappa_{xy}^o$ are the reference surface strains and curvatures, respectively. The reference surface quantities are functions of $x$ and $y$. Including the effects of moderate rotations, the reference surface strains are

$$\begin{aligned} \epsilon_x^o &= \frac{\partial u^o}{\partial x} + \frac{1}{2}\beta_x^{o2} \\ \epsilon_y^o &= \frac{\partial v^o}{\partial y} + \frac{1}{2}\beta_y^{o2} \\ \gamma_{xy}^o &= \frac{1}{2}\left(\frac{\partial u^o}{\partial y} + \frac{\partial v^o}{\partial x}\right) + \beta_x^o \beta_y^o \end{aligned} \tag{2.8}$$

where

$$\beta_x^o = -\frac{\partial w^o}{\partial x} \text{ and } \beta_y^o = -\frac{\partial w^o}{\partial y} \tag{2.9}$$

are identified with cross-sectional rotations. The reference surface curvatures are given by

$$\begin{aligned} \kappa_x^o &= \frac{\partial \beta_x^o}{\partial x} = -\frac{\partial^2 w^o}{\partial x^2} \\ \kappa_y^o &= \frac{\partial \beta_y^o}{\partial y} = -\frac{\partial^2 w^o}{\partial y^2} \\ \kappa_{xy}^o &= \frac{\partial \beta_x^o}{\partial y} + \frac{\partial \beta_y^o}{\partial x} = -2\frac{\partial^2 w^o}{\partial x \partial y} \end{aligned} \tag{2.10}$$

The quantities $u^o$, $v^o$, and $w^o$ are the total displacements in the $x$, $y$, and $z$ directions, respectively, of the reference surface.

Equation (2.8) represents the principal departure from classical layered plate theory and includes the usual approximation associated with thin-plate theory when employing the nonlinear geometric effects in the strain-displacement relations. These approximations assume the elongation and shearing strains and the squares of the rotations are the same order of magnitude, but this order is small compared to unity [26, 27].

Because of the plane-stress assumption, the stress-strain relations in Equations (2.3) and (2.5) can

be written as

$$\begin{aligned}
\sigma_x &= \bar{Q}_{11}(\epsilon_x - \alpha_x \Delta T) + \bar{Q}_{12}(\epsilon_y - \alpha_y \Delta T) + \bar{Q}_{16}(\gamma_{xy} - \alpha_{xy} \Delta T) \\
\sigma_y &= \bar{Q}_{12}(\epsilon_x - \alpha_x \Delta T) + \bar{Q}_{22}(\epsilon_y - \alpha_y \Delta T) + \bar{Q}_{26}(\gamma_{xy} - \alpha_{xy} \Delta T) \\
\tau_{xy} &= \bar{Q}_{16}(\epsilon_x - \alpha_x \Delta T) + \bar{Q}_{26}(\epsilon_y - \alpha_y \Delta T) + \bar{Q}_{66}(\gamma_{xy} - \alpha_{xy} \Delta T)
\end{aligned} \tag{2.11}$$

or

$$\begin{aligned}
\sigma_x &= \bar{Q}_{11}\epsilon_x + \bar{Q}_{12}\epsilon_y + \bar{Q}_{16}\gamma_{xy} - \sigma_x^T \\
\sigma_x &= \bar{Q}_{12}\epsilon_x + \bar{Q}_{22}\epsilon_y + \bar{Q}_{26}\gamma_{xy} - \sigma_y^T \\
\tau_{xy} &= \bar{Q}_{16}\epsilon_x + \bar{Q}_{26}\epsilon_y + \bar{Q}_{66}\gamma_{xy} - \tau_{xy}^T
\end{aligned} \tag{2.12}$$

where

$$\begin{aligned}
\sigma_x^T &= (\bar{Q}_{11}\alpha_x + \bar{Q}_{12}\alpha_y + \bar{Q}_{16}\alpha_{xy})\Delta T \\
\sigma_y^T &= (\bar{Q}_{12}\alpha_x + \bar{Q}_{22}\alpha_y + \bar{Q}_{26}\alpha_{xy})\Delta T \\
\tau_{xy}^T &= (\bar{Q}_{16}\alpha_x + \bar{Q}_{26}\alpha_y + \bar{Q}_{66}\alpha_{xy})\Delta T
\end{aligned} \tag{2.13}$$

In the above the $\bar{Q}$'s are the reduced stiffnesses and the $\alpha$'s are the coefficients of thermal expansion in the $x$-$y$ coordinate system. The quantities $\sigma_x^T$, $\sigma_y^T$, and $\tau_x^T$ have the physical interpretation of being the thermally-induced stresses at a point if the device is fully constrained from deformation. All of the material properties in Equations (2.11)–(2.13) are, of course, layer-dependent.

Substituting the strains from Equation (2.7) into the energy expression given by Equation (2.6) leads to

$$\begin{aligned}
\Pi = \frac{1}{2} \int_{-\frac{L_x}{2}}^{+\frac{L_x}{2}} \int_{-\frac{L_y}{2}}^{+\frac{L_y}{2}} \int_{-\frac{H}{2}}^{+\frac{H}{2}} \big\{ &(\sigma_x - \sigma_x^T)(\epsilon_x^o + z\kappa_x^o) + (\sigma_y - \sigma_y^T)(\epsilon_y^o + z\kappa_y^o) \\
&+ (\tau_{xy} - \tau_{xy}^T)(\gamma_{xy}^o + z\kappa_{xy}^o) \big\} \, dx \, dy \, dz
\end{aligned} \tag{2.14}$$

Integrating with respect to $z$, through the thickness, results in

$$\begin{aligned}\Pi &= \frac{1}{2}\int_{-\frac{L_x}{2}}^{+\frac{L_x}{2}}\int_{-\frac{L_y}{2}}^{+\frac{L_y}{2}}\Big\{(N_x-\hat{N}_x^T\Delta T)\epsilon_x^o+(N_y-\hat{N}_y^T\Delta T)\epsilon_y^o+(N_{xy}-\hat{N}_{xy}^T\Delta T)\gamma_{xy}^o \\ &+ (M_x-\hat{M}_x^T\Delta T)\kappa_x^o+(M_y-\hat{M}_y^T\Delta T)\kappa_y^o+(M_{xy}-\hat{M}_{xy}^T\Delta T)\kappa_{xy}^o\Big\}\,dxdy \qquad (2.15)\end{aligned}$$

The quantities $N_x$, $N_y$, $N_{xy}$, $M_x$, $M_y$, and $M_{xy}$ are the force and moment resultants, respectively, and $\hat{N}_x^T$, $\hat{N}_y^T$, $\hat{N}_{xy}^T$, $\hat{M}_x^T$, $\hat{M}_y^T$, and $\hat{M}_{xy}^T$ are the effective inplane unit thermal loads and the effective unit thermal moments, respectively, [28]. These are strictly material properties and will be defined shortly. The force and moment resultants are defined by

$$N_x\equiv\int_{-\frac{H}{2}}^{+\frac{H}{2}}\sigma_x dz = A_{11}\epsilon_x^o+A_{12}\epsilon_y^o+A_{16}\gamma_{xy}^o+B_{11}\kappa_x^o+B_{12}\kappa_y^o+B_{16}\kappa_{xy}^o-\hat{N}_x^T\Delta T \qquad (2.16)$$

$$N_y\equiv\int_{-\frac{H}{2}}^{+\frac{H}{2}}\sigma_y dz = A_{12}\epsilon_x^o+A_{22}\epsilon_y^o+A_{26}\gamma_{xy}^o+B_{12}\kappa_x^o+B_{22}\kappa_y^o+B_{26}\kappa_{xy}^o-\hat{N}_y^T\Delta T \qquad (2.17)$$

$$N_{xy}\equiv\int_{-\frac{H}{2}}^{+\frac{H}{2}}\tau_{xy} dz = A_{16}\epsilon_x^o+A_{26}\epsilon_y^o+A_{66}\gamma_{xy}^o+B_{16}\kappa_x^o+B_{26}\kappa_y^o+B_{66}\kappa_{xy}^o-\hat{N}_{xy}^T\Delta T \qquad (2.18)$$

$$M_x\equiv\int_{-\frac{H}{2}}^{+\frac{H}{2}}z\sigma_x dz = B_{11}\epsilon_x^o+B_{12}\epsilon_y^o+B_{16}\gamma_{xy}^o+D_{11}\kappa_x^o+D_{12}\kappa_y^o+D_{16}\kappa_{xy}^o-\hat{M}_x^T\Delta T \qquad (2.19)$$

$$M_y\equiv\int_{-\frac{H}{2}}^{+\frac{H}{2}}z\sigma_y dz = B_{12}\epsilon_x^o+B_{22}\epsilon_y^o+B_{26}\gamma_{xy}^o+D_{12}\kappa_x^o+D_{22}\kappa_y^o+D_{26}\kappa_{xy}^o-\hat{M}_y^T\Delta T \qquad (2.20)$$

$$M_{xy}\equiv\int_{-\frac{H}{2}}^{+\frac{H}{2}}z\tau_{xy} dz = B_{16}\epsilon_x^o+B_{26}\epsilon_y^o+B_{66}\gamma_{xy}^o+D_{16}\kappa_x^o+D_{26}\kappa_y^o+D_{66}\kappa_{xy}^o-\hat{M}_{xy}^T\Delta T \qquad (2.21)$$

In the above, the $A$'s , $B$'s, and $D$'s have the usual definitions associated with laminates [28]. The effective unit thermal force and moment resultants are defined as [28]

$$\hat{N}_x^T \equiv \int_{-\frac{H}{2}}^{+\frac{H}{2}}\left(\bar{Q}_{11}\alpha_x+\bar{Q}_{12}\alpha_y+\bar{Q}_{16}\alpha_{xy}\right)dz \qquad (2.22)$$

$$\hat{N}_y^T \equiv \int_{-\frac{H}{2}}^{+\frac{H}{2}}\left(\bar{Q}_{12}\alpha_x+\bar{Q}_{22}\alpha_y+\bar{Q}_{26}\alpha_{xy}\right)dz \qquad (2.23)$$

$$\hat{N}_{xy}^T \equiv \int_{-\frac{H}{2}}^{+\frac{H}{2}}\left(\bar{Q}_{16}\alpha_x+\bar{Q}_{26}\alpha_y+\bar{Q}_{66}\alpha_{xy}\right)dz \qquad (2.24)$$

$$\hat{M}_x^T \equiv \int_{-\frac{H}{2}}^{+\frac{H}{2}}\left(\bar{Q}_{11}\alpha_x+\bar{Q}_{12}\alpha_y+\bar{Q}_{16}\alpha_{xy}\right)zdz \qquad (2.25)$$

$$\hat{M}_y^T \equiv \int_{-\frac{H}{2}}^{+\frac{H}{2}} \left(\bar{Q}_{12}\alpha_x + \bar{Q}_{22}\alpha_y + \bar{Q}_{26}\alpha_{xy}\right) z dz \tag{2.26}$$

$$\hat{M}_{xy}^T \equiv \int_{-\frac{H}{2}}^{+\frac{H}{2}} \left(\bar{Q}_{16}\alpha_x + \bar{Q}_{26}\alpha_y + \bar{Q}_{66}\alpha_{xy}\right) z dz \tag{2.27}$$

Since the present work deals with devices made of ceramic layers that are orthotropic in the analysis coordinate system, $\bar{Q}_{16}$, $\bar{Q}_{26}$, and $\alpha_{xy}$ are identically zero. As a result $A_{16}$, $A_{26}$, $B_{16}$, $B_{26}$, $D_{16}$, $D_{26}$, $N_{xy}^T$, and $M_{xy}^T$ are all zero.

### 2.2.2 The Rayleigh-Ritz Approach

The Rayleigh-Ritz approach uses approximate displacement fields which are then substituted into the expressions making up the total potential energy. With the approximate displacement fields, the functional forms are know to within a number of constants. Based on the observed shapes in Figure 2.3, the out-of-plane displacement field, $w^o(x, y)$, can be approximated as

$$w^o(x, y) = \frac{1}{2}(ax^2 + by^2) \tag{2.28}$$

where $a$ and $b$ are to-be-determined constants and represent the curvatures of the device in the $x$ and $y$ directions, respectively. This functional form includes either cylindrical shape or the dome shape. Also, as a result of the shapes shown in Figure 2.3 and the deformed cross-section illustrated schematically in Figure 2.4, the inplane displacements $u^o(x, y)$ and $v^o(x, y)$ are approximated as

$$u^o(x, y) = cx - \frac{a^2x^3}{6} - \frac{abxy^2}{4} \tag{2.29}$$

$$v^o(x, y) = dy - \frac{b^2y^3}{6} - \frac{abx^2y}{4} \tag{2.30}$$

Here $c$ and $d$ are additional to-be-determined constants. The four constants, $a$, $b$, $c$, and $d$, will be determined by minimizing the total potential energy. The approximation to $u^o(x, y)$ is based on the afore-mentioned fact that in deforming from a flat shape at the reduction temperature to any of the shapes in Figures 2.3(b), (c), or (d) at room temperature, most of the $u^o(x, y)$ displacement is due to the device developing curvature in the $x$ direction. However, there is a component of

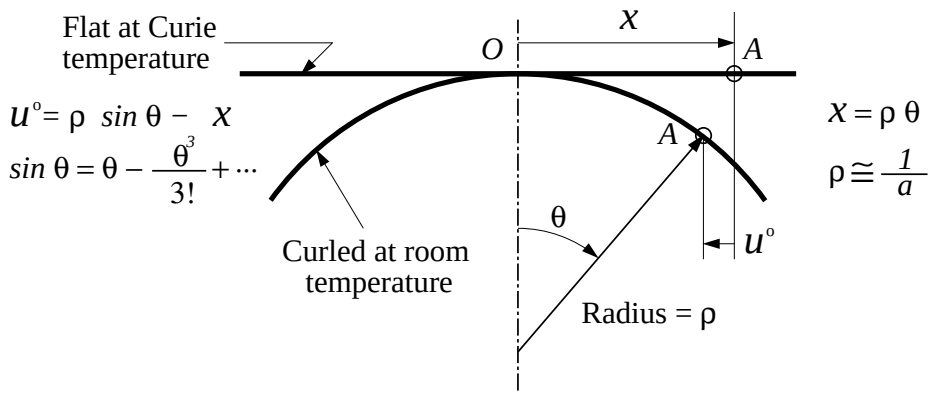


Figure 2.4: Kinematics of a flat device deforming into a cylinder (After [30]).

$u^o(x, y)$ due to inplane thermal strain because of the temperature decrease, and that is represented by the constant $c$. Finally, use is made of the assumption of negligible inplane shear strain. The net result is the functional form given by Equation (2.29). Similar arguments lead to the expression for $v^o(x, y)$ in Equation (2.30). The inplane displacement component approximations are more fully discussed in [29, 30, 31], which consider a related problem.

The expressions for the approximate displacement fields are substituted into the strain-displacement and curvature-displacement relations, Equations (2.8)–(2.10), and these, in turn, are substituted into the expressions for the force and moment resultants Equations (2.16)–(2.21), and into the expression for the total potential energy, Equation (2.15). The integrand of the total potential energy expression is then a function of material properties and geometry, the four constants, and $x$ and $y$. The energy expression is integrated with respect to $x$ and $y$ over the dimensions of the device, i.e., $L_x$ by $L_y$, resulting in a purely algebraic expression for total potential energy involving material properties, geometry, and the four constants. The first and second variations (first and second derivatives, in this case) of the total potential energy are then taken with respect to $a$, $b$, $c$, and $d$. As the first variation must be zero for equilibrium, the result is four nonlinear algebraic equations for $a$, $b$, $c$, and $d$. These are given in Appendix A and they can be solved and numerical results obtained for specific values of material and geometric parameters. Stability is evaluated by checking the positive definiteness of the second variation. Since the problem has been reduced to

an algebraic one, the second variation can be written in the form

$$\delta^2\Pi = \begin{bmatrix} \delta a & \delta b & \delta c & \delta d \end{bmatrix} \begin{bmatrix} C \end{bmatrix} \begin{bmatrix} \delta a \\ \delta b \\ \delta c \\ \delta d \end{bmatrix} \tag{2.31}$$

The matrix $[C]$ is given in Appendix A and the study of stability reduces to examining its eigenvalues. If all eigenvalues are positive, the equilibrium solution is stable, otherwise the equilibrium solution is unstable. All of these mathematical manipulations are accomplished with the aid of the symbolic manipulation package *Mathematica®* [32].

### 2.2.3 Piezoelectric Effects

As the primary uses of RAINBOW involve the application of an electric field through the thickness of the unreduced piezoceramic layer to produce a dilatational strain, which it turns causes a change in the shape of the device, it is of value to use the above model to predict those changes in shape. To that end, the total potential energy of Equation (2.15) is modified to include the effective force and moment resultants produced by the electric-field-induced dilatational strains in the piezoceramic. Since the electric field effects are in addition to the temperature effects discussed in the last section, the expression for strain energy density becomes

$$\omega = \frac{1}{2} C_{ijkl}\epsilon_{ij}\epsilon_{kl} - \beta_{ij}\epsilon_{ij}\Delta T - e_{ijk}\epsilon_{ij}E_k, \quad i,j,k,l = 1,3 \tag{2.32}$$

where $e_{ijk}$ are the piezoelectric moduli and $E_k$ is the component of the electric field vector $\mathbf{E}$ in the $k^{th}$ direction. The stress components for a piezoelectric medium are

$$\sigma_{ij} = \frac{\partial \omega}{\partial \epsilon_{ij}} = C_{ijkl}\epsilon_{kl} - \sigma_{ij}^T - \sigma_{ij}^E, \quad i = 1,3 \tag{2.33}$$

where

$$\sigma_{ij}^E = e_{ijk}E_k, \quad i,j,k = 1,3 \tag{2.34}$$

The electric field vector **E** is derivable from a scalar electric potential $\phi$, namely,

$$E_i = -\frac{\partial \phi}{\partial x_i} \quad i = 1, 3 \tag{2.35}$$

In the present case the electric field will be applied through the thickness, so the only nonzero component of **E** is $E_3 = -\frac{\partial \phi}{\partial x_3} = E_z = -\frac{\partial \phi}{\partial z}$. The voltage $V$ between two points located at $z = z_1$ and $z = z_2$ is related to the potential difference according to

$$V = \phi(z_1) - \phi(z_2) \tag{2.36}$$

Since the formulation considered is for a state of plane stress, for an orthotropic piezoelectric layer the $e_{ijk}$'s of Equation (2.32) can be related to the $\bar{Q}_{11}$, $\bar{Q}_{12}$, and $\bar{Q}_{22}$, and $d_{31}$ and $d_{32}$, the piezoelectric constants in the $x$-$y$-$z$ coordinate system [33]. The following terms are then appended to the total potential energy expression:

$$\hat{N}_x^E E_z \equiv \int_{-\frac{H}{2}}^{+\frac{H}{2}} \left(\bar{Q}_{11} d_{31} + \bar{Q}_{12} d_{32}\right) E_z dz \tag{2.37}$$

$$\hat{N}_y^E E_z \equiv \int_{-\frac{H}{2}}^{+\frac{H}{2}} \left(\bar{Q}_{12} d_{31} + \bar{Q}_{22} d_{32}\right) E_z dz \tag{2.38}$$

$$\hat{M}_x^E E_z \equiv \int_{-\frac{H}{2}}^{+\frac{H}{2}} \left(\bar{Q}_{11} d_{31} + \bar{Q}_{12} d_{32}\right) E_z z dz \tag{2.39}$$

$$\hat{M}_y^E E_z \equiv \int_{-\frac{H}{2}}^{+\frac{H}{2}} \left(\bar{Q}_{12} d_{31} + \bar{Q}_{22} d_{32}\right) E_z z dz \tag{2.40}$$

where $d_{31}E_z$ and $d_{32}E_z$ are the dilatational strains induced in the piezoceramic in the $x$ and $y$ directions, respectively, due to application of electric field in the $z$ direction, $E_z$. The electric field effects are modeled analogously to thermal expansion effects and it is obvious where these terms go in the energy expression of Equation (2.15). It should be noted that the reduced layer contributes nothing to the integrals of Equations (2.37)–(2.40), as it is assumed $d_{31}$ and $d_{32}$ are zero for that layer. It is assumed that the displacements resulting from the temperature change plus the application of the electric field are also approximated by Equations (2.28)-(2.30). The computation of the first variation, and the resulting governing equations, and the second variation,

and the resulting $[C]$ matrix, follow the steps outlined in a previous section. For this portion of the problem the change in the constants $a$, $b$, $c$, and $d$ relative to their values corresponding to room temperature are computed as a function of the electric field strength. This provides a measure of the shape change due to application of the electric field.

## 2.3 Assumption of Isotropic Properties

To a very good first approximation, the piezoceramic material being studied here is isotropic, though in the previous sections assumptions have been made for orthotropic material behavior. Assuming the material properties are isotropic greatly simplifies the equations of Appendix A. Taking advantage of this, to more conveniently examine the influence of RAINBOW geometry and material properties on the room-temperature shapes, the four nonlinear algebraic equations are reduced to two simple nonlinear non-dimensional algebraic equations. This is done by solving Equations (A.3) and (A.4) for $c$ and $d$ in terms of $a$ and $b$, substituting them in Equations (A.1) and (A.2), assuming both piezoceramic layers are isotropic and that their the Poisson's ratios are equal, and by using the following transformations to nondimensional quantities

$$l_x = \frac{L_x}{H},\ l_y = \frac{L_y}{H},\ A = aH,\ B = bH,\ h = \frac{H_r}{H},\ \alpha = \alpha_r - \alpha_o,\ E_{r/o} = \frac{E_r}{E_o} \tag{2.41}$$

where the subscripts "o" and "r" denote unreduced (original) and reduced piezoceramic layers, respectively. Also, the thickness of the reduced layer is given by $H_r$, the $\alpha$'s are coefficients of thermal expansion, and the $E$'s are extensional (Young's) moduli. The two non-dimensional algebraic equations are given by

$$\begin{aligned} &AB^2(l_x^4 + l_y^4)(1 - h + E_{r/o}h)^2 + 1440\Delta T E_{r/o}h\alpha(h-1)(1+\nu)) \\ &+240(1 + h(h^3 - 4h^2 + 6h - 4 - E_{r/o}h^3)(E_{r/o} - 1))(A + B\nu) \end{aligned} \tag{2.42}$$

$$\begin{aligned} &BA^2(l_x^4 + l_y^4)(1 - h + E_{r/o}h)^2 + 1440\Delta T E_{r/o}h\alpha(h-1)(1+\nu)) \\ &+240(1 + h(h^3 - 4h^2 + 6h - 4 - E_{r/o}h^3)(E_{r/o} - 1))(B + A\nu) \end{aligned} \tag{2.43}$$

## 2.4 Numerical Results

To illustrate the results predicted by the theory, consider a rectangular RAINBOW consisting of a reduced (layer no. 1) and an unreduced piezoceramic layer (layer no. 2). The relevant material properties and thicknesses are given in Table 2.1. These material properties data were provided by Dr. W. L. Vaughn of the NASA-Langley Research Center [34]. It was noted in the experiments involving measurement of the coefficient of thermal expansion using a push-rod dilatometer that the coefficients of thermal expansion of the reduced material and the unreduced material did not differ above the Curie temperature, $T_C$=340 $^o$C. Therefore despite the 955 $^o$C temperature difference between the reduction temperature (975 $^o$C) and room temperature (20 $^o$C), only the difference between the Curie and room temperatures is important in producing the shapes at room temperature. A discussion of the measurement of material properties of the reduced and unreduced piezoceramic is provided in section B.1 of Appendix B. Figure 2.5 depicts schematically the problem being considered. Note that the polarity of the unreduced material is indicated. Figures 2.6 and 2.7 illustrate a typical behavior of RAINBOW described by Figure 2.5, Table 2.1, and Equations (2.28)–(2.30), as it is cooled from the Curie temperature of the piezoceramic to room temperature. Specifically, in Figure 2.6 the parameters $a$ and $b$ of Equations (2.28)–(2.30), which represent the curvatures of the device in the $x$ and $y$ directions, respectively, are shown as a function of the temperature, 20 $^o$C corresponding to the room temperature. Figure 2.7 illustrates the actual shape of RAINBOW at a few selected temperatures from Figure 2.6. It is assumed that $L_x$, $L_y$, $H$, and $H_r/H$ are 63.5 mm (2.5 in.), 38.1 mm (1.5 in.), 0.381 mm (15 mils), and 0.35, respectively.

Table 2.1: RAINBOW material properties.

| Properties | Original PZT | Reduced PZT |
|---|---|---|
| Thickness ($\mu m$) | 247.65 | 133.35 |
| $E$ ($GPa$) | 44.4 | 29.9 |
| $\nu$ | 0.377 | 0.381 |
| $\alpha$ ($10^{-6}/^oC$) | 2.13 | 8.41 |
| $d_{31}$ ($10^{-12}m/V$) | -190 | - |
| $d_{32}$ ($10^{-12}m/V$) | -190 | - |

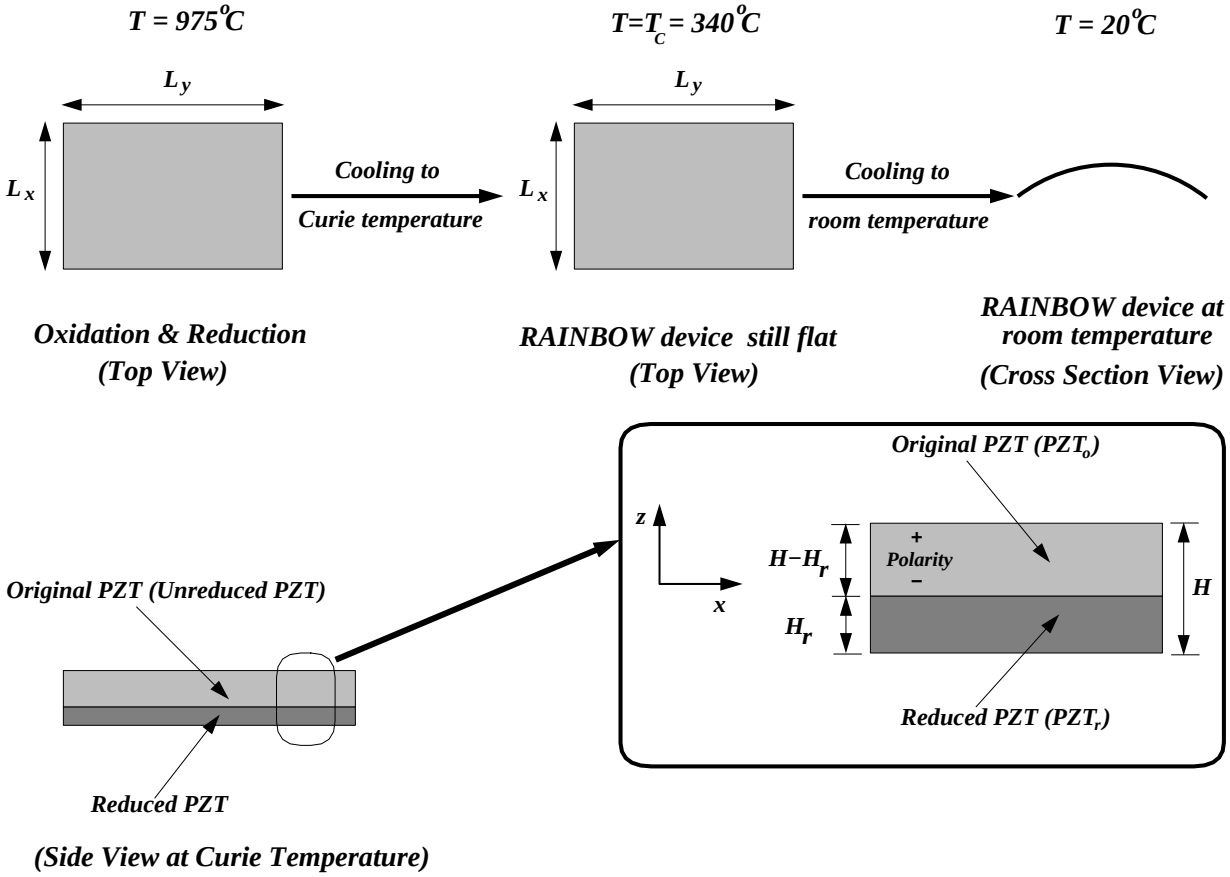


Figure 2.5: Schematic of the rectangular RAINBOW considered.

Referring to Figure 2.6, point A represents RAINBOW flat at its Curie temperature ($a$=$b$=0). As the temperature is reduced, the device develops equal negative curvatures in both the $x$ and $y$ directions. These equal curvatures represent a dome shaped device. As the temperature is reduced further below Curie temperature, the dome becomes deeper and deeper. At a temperature corresponding to point B, the temperature-curvature relationship trifurcates into branches BC, BE, and BD. For this specific device the trifurcation temperature is 267 $^o$C. The trifurcation occurring at point B is referred to as a *supercritical pitchfork static-bifurcation* in the temperature-curvature domain because the branches AB, BC, BD, and BE have the geometry of a pitchfork at point B. Reducing the temperature below the 267 $^o$C level, solution path BC represents a change from the spherical shape to a shape which has more curvature in the $y$ direction and less in the $x$ direction. At room temperature the solution represents a shape that has seventy times the curvature in the $y$ direction as in the $x$ direction. If the curvature in the $x$ direction were zero, the solution would

represent a right circular cylinder. This however, is not quite the case here and the terminology near-cylindrical is used. If instead of following path BC, path BD is followed, the solution represents a shape with more curvature in the $x$ direction and less in the $y$ direction. At room temperature the solution is similar to the solution represented by path BC but with the roles of the curvatures in the $x$ and $y$ directions interchanged. That is, the curvature in the $y$ direction is seventy times the curvature in the $x$ direction. Finally, if path BE is followed through the trifurcation point, the spherical shape deepens even further. A stability analysis reveals the important details of these three paths. Specifically, paths BC and BD represent stable equilibrium shapes, and path BE represents unstable equilibrium shapes. Therefore, the shapes represented by path BE will never be observed. The shapes represented by paths BC and BD will be what is observed when RAINBOW are actually fabricated. In theory, a device with a shape represented by path BC can be changed to the shape represented by path BD by a simple snap-through action. That is, by holding a device when it is in the shape represented by path BC by opposite edges and applying opposite moments, the device can be forced into the shape represented by path BD, and vice versa. This is accomplished by what can be referred to as a snap-through action, i.e., the shape can be force-snapped from one near-cylindrical configuration to the other. A snap-through action occurs because the one near-cylindrical configuration only has to be deformed so far, and it will then dynamically move in a sudden fashion, i.e., snap, to the other configuration. This is related to the storing and subsequent releasing of potential energy. Actually doing this, however, may be an issue because of the brittle nature of the material.

Figure 2.7(a) illustrates the shape of RAINBOW at a temperature just above the trifurcation temperature, point B. The shape is a stable spherical one and note that the two horizontal axes in the sub-figures of Figure 2.7 are the $x$ and $y$ coordinates (origin at the geometric center of the device) divided by the respective side-lengths of the device. The figures reflect, however, the correct aspect ratio of the actuator, i.e., $L_y/L_x$=0.6. Figure 2.7(b) depicts the device at the room-temperature condition corresponding to point C. As can be seen, due to the rectangular geometry of this particular example, the device looks quite cylindrical, with generators in the $x$ direction. Likewise, Figure 2.7(c) depicts the device at the room-temperature condition corresponding to point D. Finally, Figure 2.7(d) shows the unstable spherical shape at room temperature, point E in Figure 2.6. This sphere is deeper than the one of Figure 2.7(a) and it is interesting to note that

the depth of the spherical shape of path ABE is not linear with temperature.

Finite-element analyses, using the commercial code ABAQUS [35], were conducted to simulate the cooling of RAINBOW from Curie temperature to room temperature. Because there are multiple equilibrium configurations, once the trifurcation temperature is reached, ABAQUS must be coaxed to continue on a particular equilibrium path to obtain the different shapes at room temperature. To force ABAQUS to follow a particular path, a slight imperfection in the initial shape of the device was introduced. With slight imperfection, ABAQUS would follow one of the two stable paths, namely, path BC or path BD. Thus, to obtain the room-temperature shapes of RAINBOW considered, two series of finite element calculations were conducted. For each finite element analysis a mesh of 256 8-node-shell elements (S8R5), which allow transverse shear in the element, was used. The RAINBOW was free on the edges, but clamped at the node at the geometric center of the device. A constant temperature change was applied at the nodes. The displacement field and the curvatures $\kappa_x^o$, $\kappa_y^o$ and $\kappa_{xy}^o$ of the device were computed by ABAQUS at every node. It was found that the curvatures are actually not constant over the device surface, the largest deviations from being constant occurring at the edges. In Figure 2.6, the curvatures evaluated by finite element analysis at the node at the geometric center of the device are indicated by the label ABAQUS. In general, good correlations can be observed between the two theories, and thus the curvatures computed by the present theory are good estimates for the average curvatures of RAINBOW. However, it was not possible to exactly determine the trifurcation temperature using ABAQUS, since it was not possible to obtain all of branch BC in Figure 2.6. To overcome this, a temperature increase rather than a temperature decrease was used. However, this resulted in other problems, namely, the fact that when the solution was coaxed to follow the path CB, it would jump to path DB as the heating temperature approached the trifurcation point B. Moreover, it was not possible to coax ABAQUS to follow the unstable path BE. Thus, information about the unstable shape could not be obtained.

### 2.4.1 Effect of Geometry on Room-Temperature Shape

It is of interest to determine the influence of rectangular RAINBOW geometry on the characteristics of the shapes at room temperature. In particular, it is of interest to know how sidelength influences

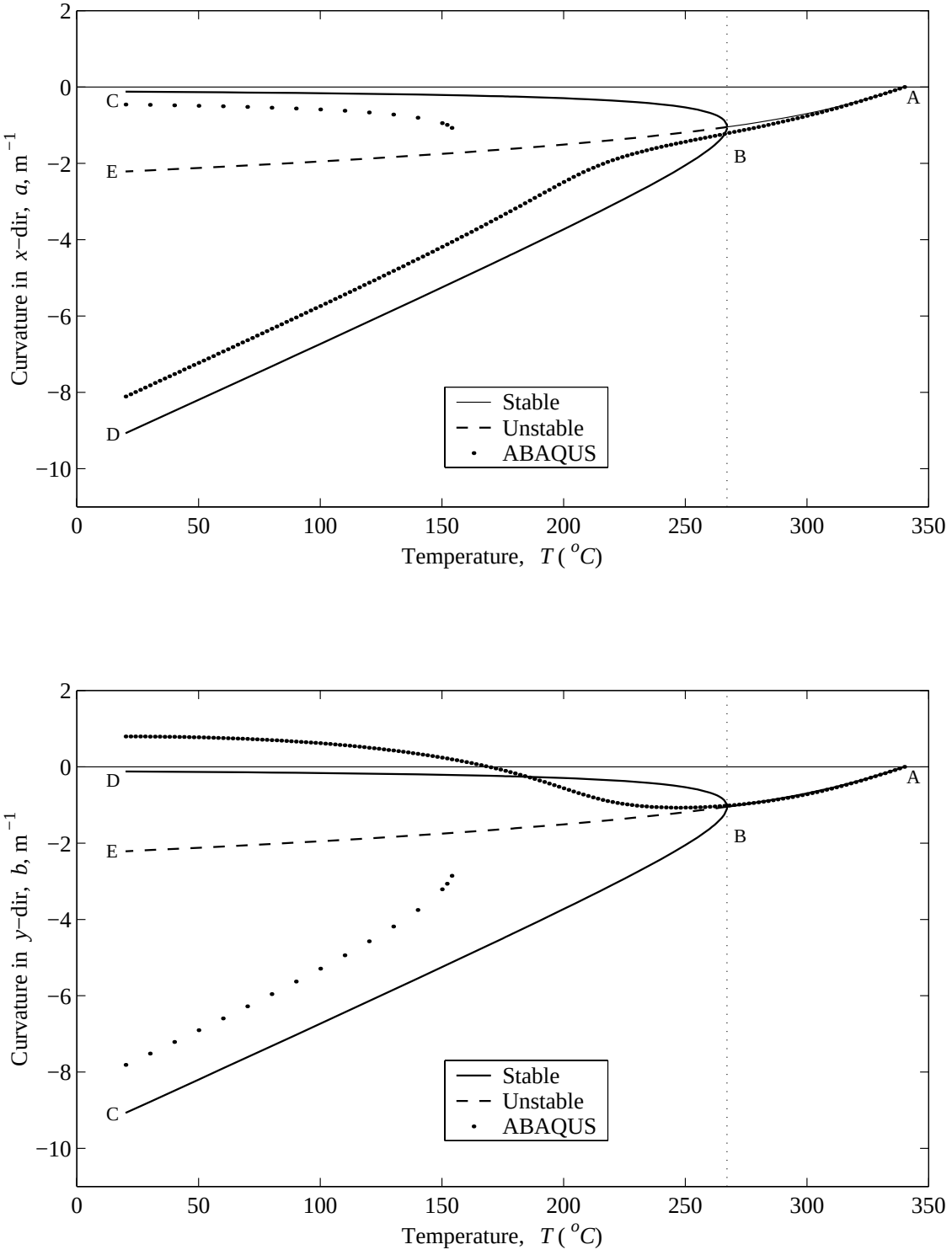


Figure 2.6: Temperature-curvature relation of rectangular RAINBOW ($L_x$=63.5 mm, $L_y$=38.1 mm, $H_r/H$=0.35).

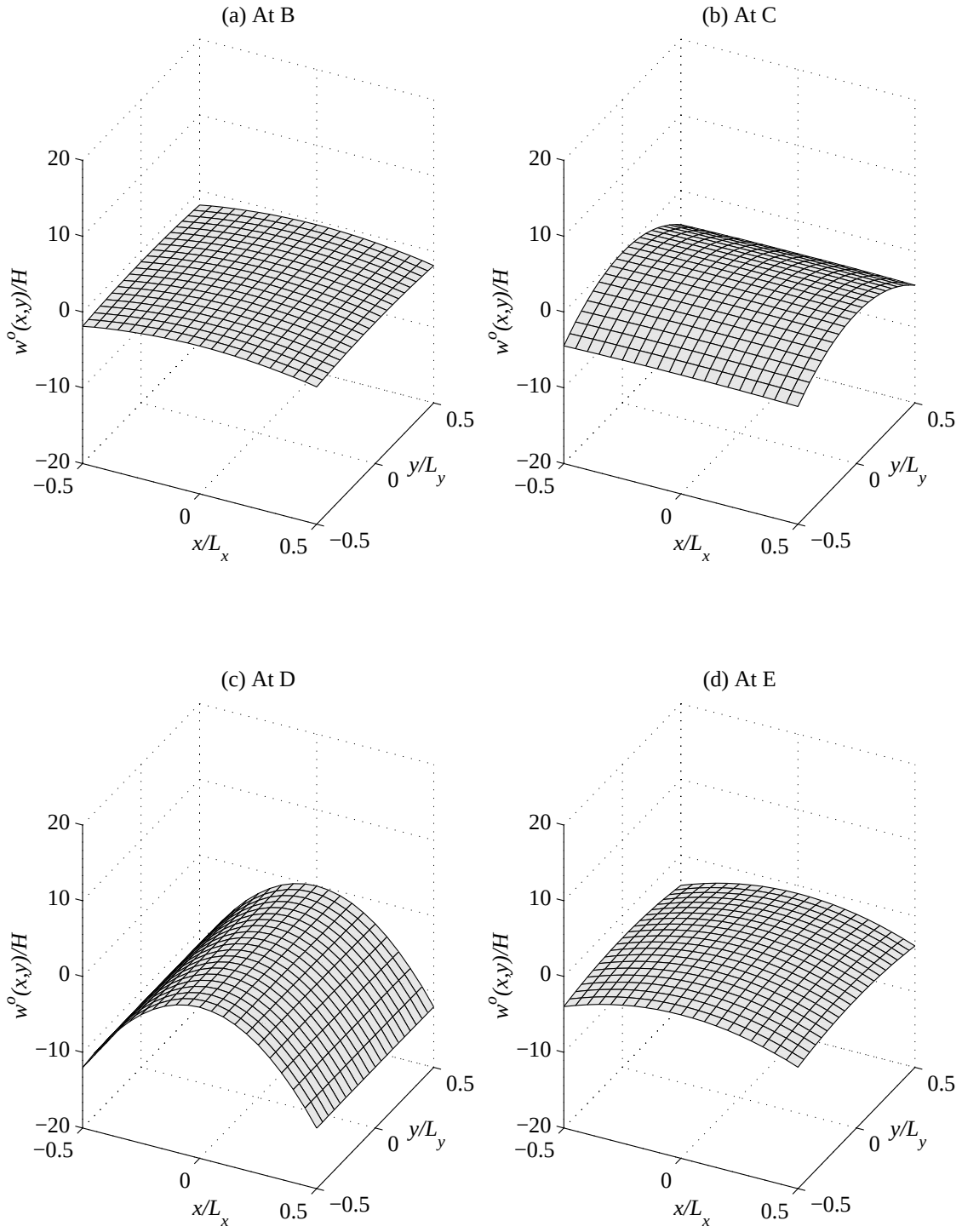


Figure 2.7: Equilibrium shapes of rectangular RAINBOW (refer to Figure 2.6).

the shapes. Though there is a large range of geometries possible, Figures 2.8–2.10 illustrate one of the important features of the dependence of the room-temperature shape on geometry. In these figures the curvatures in the $x$ and $y$ directions at room temperature are plotted as a function of RAINBOW sidelength. For convenience, the axes in Figures 2.8–2.10 have been nondimensionalized by using RAINBOW thickness, $H$, as a scaling parameter. The aspect ratios in Figures 2.8–2.10 are fixed at $L_y/L_x$=1, $L_y/L_x$=1/2, and $L_y/L_x$=1/5, respectively, while the reduced layer thickness to total thickness ratio, $H_r/H$, is kept constant at 0.35. Referring to any of these figures, moving from small (small $L_x/H$) to large RAINBOW, it is seen that the relationship between room-temperature curvatures and sidelength changes from being single-valued to being multiple-valued. For small sidelengths, denoted by the range A′ to B′ in Figures 2.8–2.10, the actuator is predicted to have but one room-temperature shape. That shape is spherical and the shape is stable. At a sidelength corresponding to point B′, the relationship trifurcates into branches B′C′, B′E′ and B′D′. This is interpreted to mean that for sidelengths greater than the value corresponding to point B′, RAINBOW exhibits multiple room-temperature shapes. For sidelengths considerably larger than that corresponding to point B′, one of these shapes is near-cylindrical, with a large curvature in the $x$ direction and practically no curvature in the $y$ direction. The other shape is near-cylindrical but with practically no curvature in the $x$ direction and a large curvature in the $y$ direction. Both of these shapes are stable. When in one near-cylindrical shape RAINBOW can be snapped through to the other near-cylindrical shape. The third shape is spherical and it is unstable. Thus there is a critical sidelength-to-thickness ratio. For the cases considered in Figures 2.8–2.10 the critical values are 69, 81, and 82, respectively. Hence, the larger the aspect ratio $L_y/L_x$, the lower the critical sidelength-to-thickness ratio. However, as the aspect ratio is made smaller and smaller, the critical sidelength-to-thickness ratio seems to converge to the value 82, above which RAINBOW exhibits multiple room-temperature shapes even for a very small aspect ratio ($L_y/L_x \approx$0.01). For RAINBOW with a sidelength-to-thickness ratio just slightly larger than the critical value, the behavior of RAINBOW shapes is somewhat unusual. The two stable shapes are similar in appearance to each other and forcing them from one shape to the other would not require much force. In fact, the shape may change by simple handling of RAINBOW. In some sense, the two shapes are not as far apart as, for example, the two near-cylindrical shapes for the case $L_x/H > 150$ in Figures 2.8–2.10. Moreover, the nondimensional curvatures in the $x$ and $y$ directions tend to be independent of

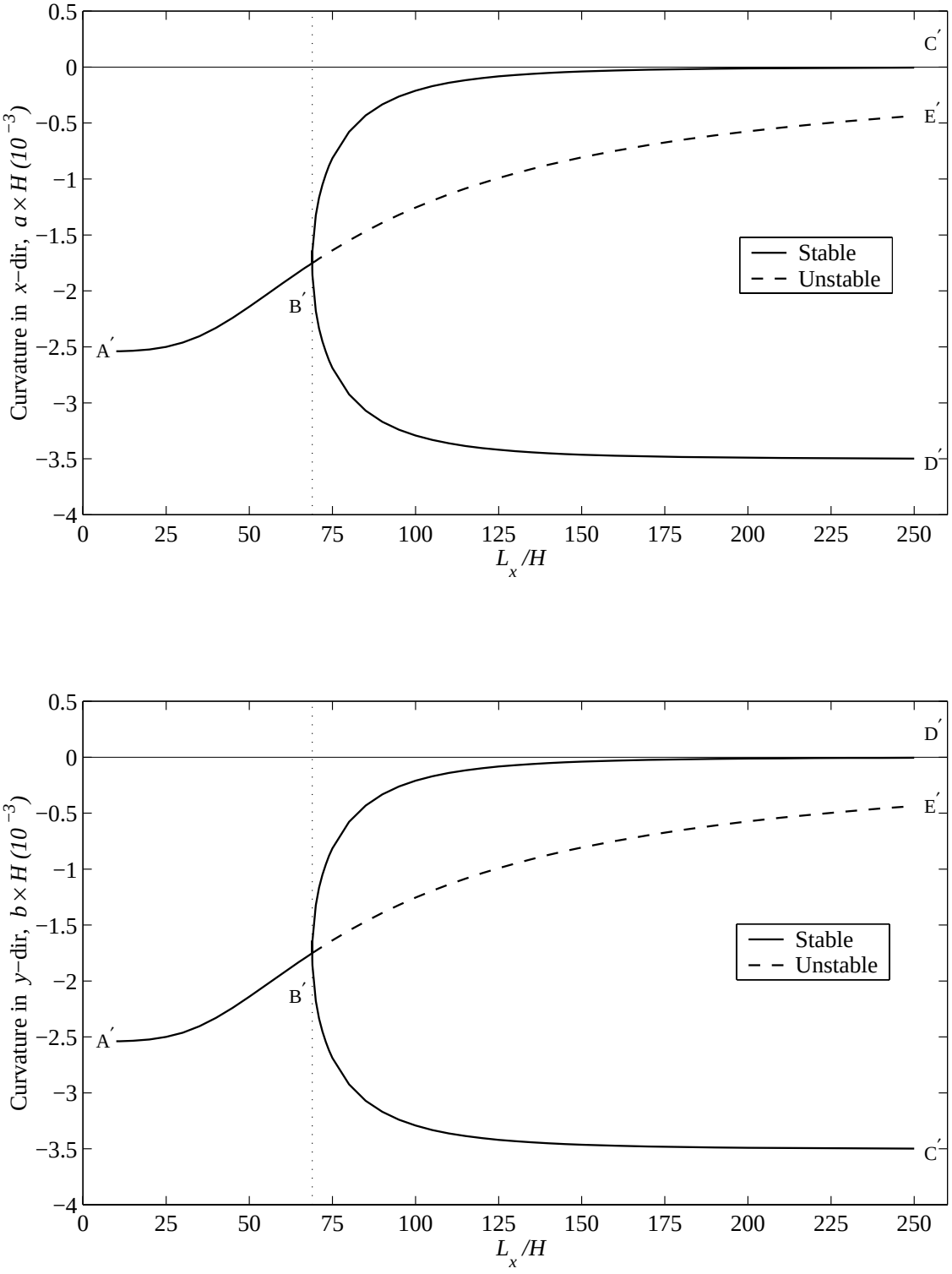


Figure 2.8: Room-temperature shapes of rectangular RAINBOW as a function of geometry ($L_y/L_x$=1, $H_r/H$=0.35).

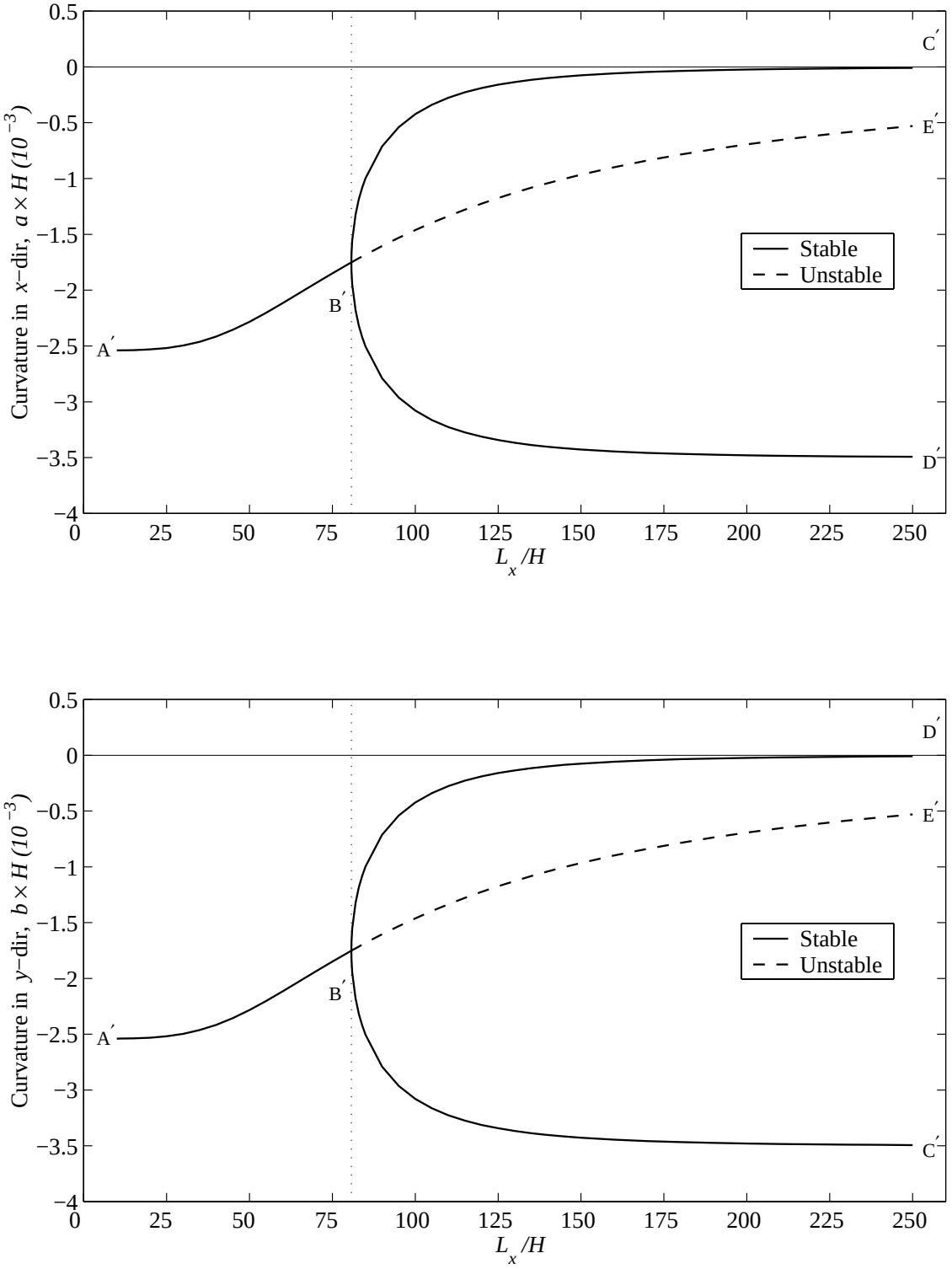


Figure 2.9: Room-temperature shapes of rectangular RAINBOW as a function of geometry ($L_y/L_x$=1/2, $H_r/H$=0.35).

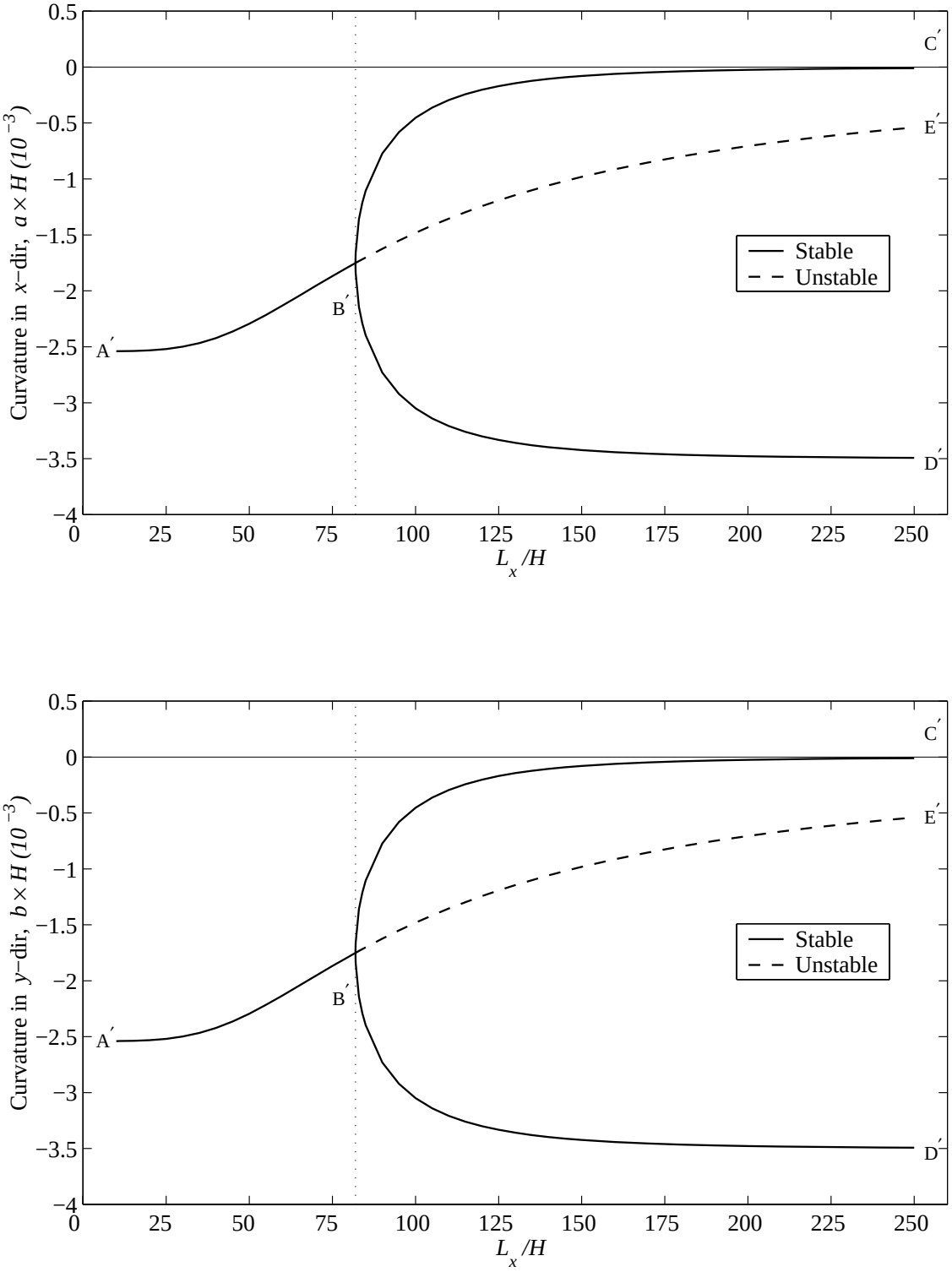


Figure 2.10: Room-temperature shapes of rectangular RAINBOW as a function of geometry ($L_y/L_x$=1/5, $H_r/H$=0.35).

the aspect ratio $L_x/L_y$ for considerably large sidelengths ($L_x/H > 200$). For reference purposes, Figure 2.11 illustrates the behavior of RAINBOW described by Table 2.1, Equations (2.28)–(2.30), and Figure 2.5 with $L_y/L_x$=1, $L_x/H$=100, and $H_r/H$=0.35, as it cooled from the Curie temperature of the piezoceramic to room temperature. Since the value of $L_x/H$ for RAINBOW of Figure 2.11 is 100, a value greater than the critical value $L_x/H$=69, RAINBOW exhibits multiple room-temperature shapes. For this specific RAINBOW the trifurcation temperature corresponding to point B in Figure 2.11 is about 188 $^o$C. This compares with a trifurcation temperature of 267 $^o$C for the device in Figure 2.6, which has an aspect ratio $L_y/L_x$=0.6.

The existence of a critical value of $L_x/H$ could lead to other unusual or unexpected behavior. Unknowingly, RAINBOW may be manufactured that has a geometry very close to the critical value. If two RAINBOW are manufactured with this geometry, they may behave quite differently. Specifically, though the trifurcation point is mathematically exact, manufacturing of RAINBOW is not exact and small variations in material properties, variation in layer thicknesses, nonuniform cooling, and other such realities of manufacturing will no doubt influence the results. The effective sidelength-to-thickness ratio of one RAINBOW may be just slightly less than the critical value, and, due to manufacturing variations, the effective sidelength-to-thickness ratio of the other RAINBOW may be just slightly greater than the critical value. These two 'identical' RAINBOW will not behave the same way.

### 2.4.2 Effect of Reduced Layer Thickness on Room-Temperature Shape

In addition to the effect of geometry on room-temperature shapes, it is of interest to determine the influence of the reduced layer thickness on the characteristics of the shapes of RAINBOW at room temperature. Figures 2.12–2.14 illustrate the most important features of the dependence of the room-temperature shape on reduced layer thickness. In these figures the curvatures in the $x$ and $y$ directions at room temperature are plotted as a function of reduced layer thickness. Again, for convenience, the axes in Figures 2.12–2.14 have been nondimensionalized by using the total thickness, $H$, as a scaling parameter. The aspect ratios in Figures 2.12–2.14 are fixed at $L_y/L_x$=1, $L_y/L_x$=1/2, and $L_y/L_x$=1/5, respectively, while the sidelength-to-thickness ratio, $L_x/H$, is kept constant at 100. In these figures, it is seen that the relationship between reduced layer thickness

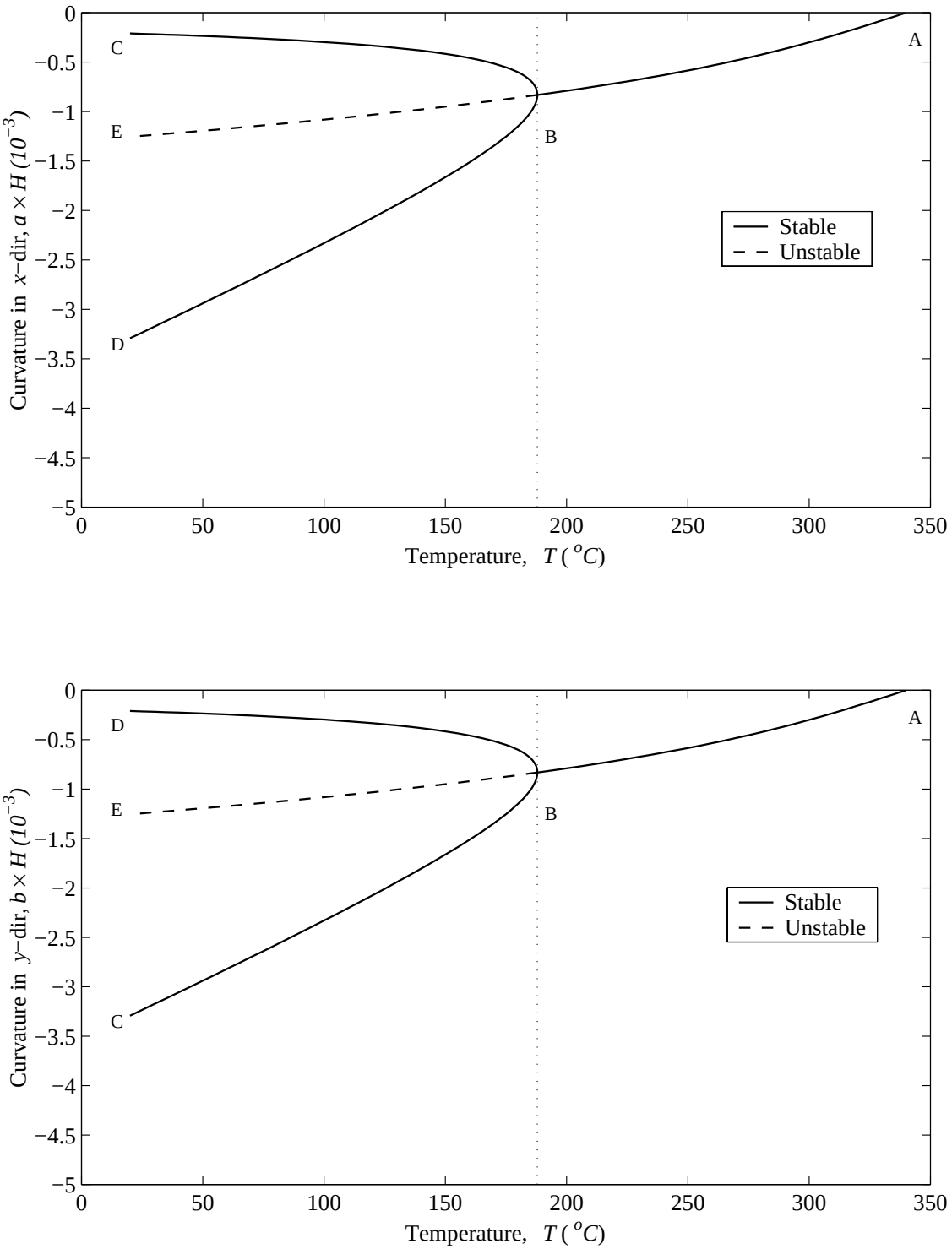


Figure 2.11: Temperature-curvature relation of rectangular RAINBOW ($L_y/L_x$=1, $L_x/H$=100, $H_r/H$=0.35).

and room-temperature curvature changes from being single valued to being multiple valued and again to being single valued as the reduced layer thickness is increased from 0 to 100%. For small reduced layer thickness, denoted by range $A_1$ to $B_1$ in Figures 2.12–2.14, RAINBOW is predicted to have but one room-temperature shape. That shape is spherical and it stable. At a reduced layer thickness corresponding to point $B_1$, the relationship trifurcates into branches $B_1C_1$, $B_1E_1$, and $B_1D_1$. On the other hand, at a reduced layer thickness corresponding to point $B_2$, the relationship changes from being multiple valued to being single valued, as depicted by branch $B_2A_2$. This is interpreted to mean that for reduced layer thickness between the two values corresponding to point $B_1$ and $B_2$, RAINBOW exhibits multiple room-temperature shapes. One of these shapes is near-cylindrical, with a larger curvature in the $x$ direction than in the $y$ direction. The other shape is also near-cylindrical but with a larger curvature in the $y$ direction than in the $x$ direction. The third shape is spherical and it is unstable. For reduced layer thicknesses smaller than the value corresponding to point $B_1$ or greater than the value corresponding to point $B_2$, RAINBOW exhibits one stable spherical room-temperature shape. For the cases considered in Figures 2.12–2.14 the critical values corresponding to point $B_1$ and $B_2$ are 14% and 91%, 20% and 86%, and 21% and 86%, respectively. Hence, the smaller the aspect ratio $L_y/L_x$ is, the larger the critical reduced layer thickness corresponding to point $B_1$ is and the smaller the critical reduced layer thickness corresponding to point $B_2$ is. However, as the aspect ratio is made smaller, the two critical reduced layer thickness values corresponding to points $B_1$ and $B_2$ tend to converge to 21% and 86%, respectively. Hence, for RAINBOW with $L_x/H$=100 and reduced layer thickness between 21% and 86%, these devices will exhibit multiple room-temperature shapes independent of the value of the aspect ratio $L_y/L_x$. Moreover, Figures 2.12–2.14 indicate that at 55% of reduced layer thickness, the maximum major curvature and the minimum minor curvature are achieved. For the sake of comparison of the characteristics of the shapes of RAINBOW at room temperature, the results shown in the previous section in Figures 2.8–2.11 are reproduced using a reduced layer thickness of 55%. These results are depicted in Figures 2.15–2.18. In Figures 2.15–2.17, the critical sidelength-to-thickness ratio $L_x/H$ corresponding to point B′ are 64, 75, and 76.5, respectively. These values are lower than those corresponding to 35% reduced layer thickness. Figure 2.18 indicates that the trifurcation temperature corresponding to point B is 208 $^o$C, 20 $^o$C higher than the one in Figure 2.11.

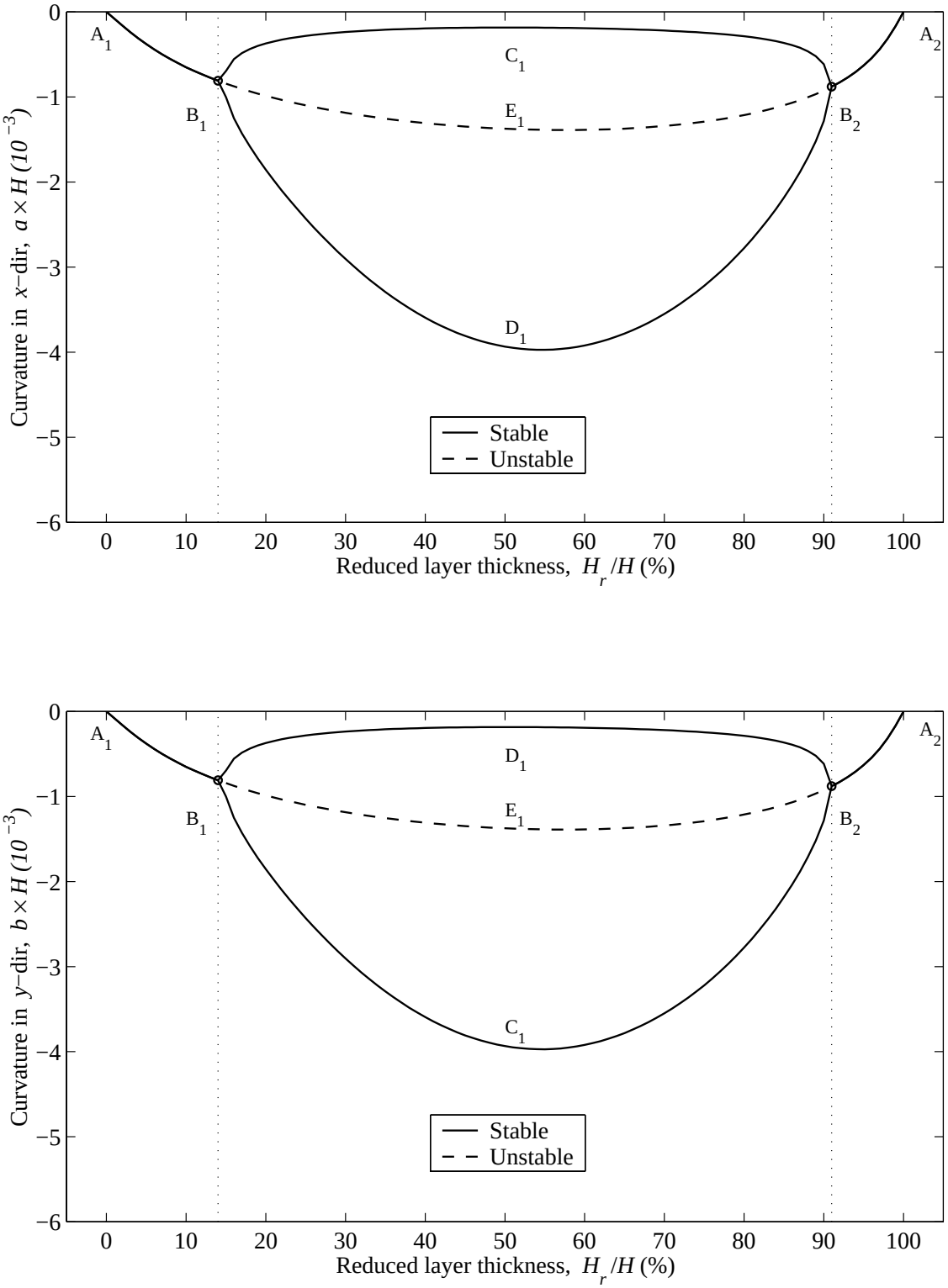


Figure 2.12: Room-temperature shapes of rectangular RAINBOW as a function of reduced layer thickness $H_r/H$ ($L_y/L_x$=1, $L_x/H$=100).

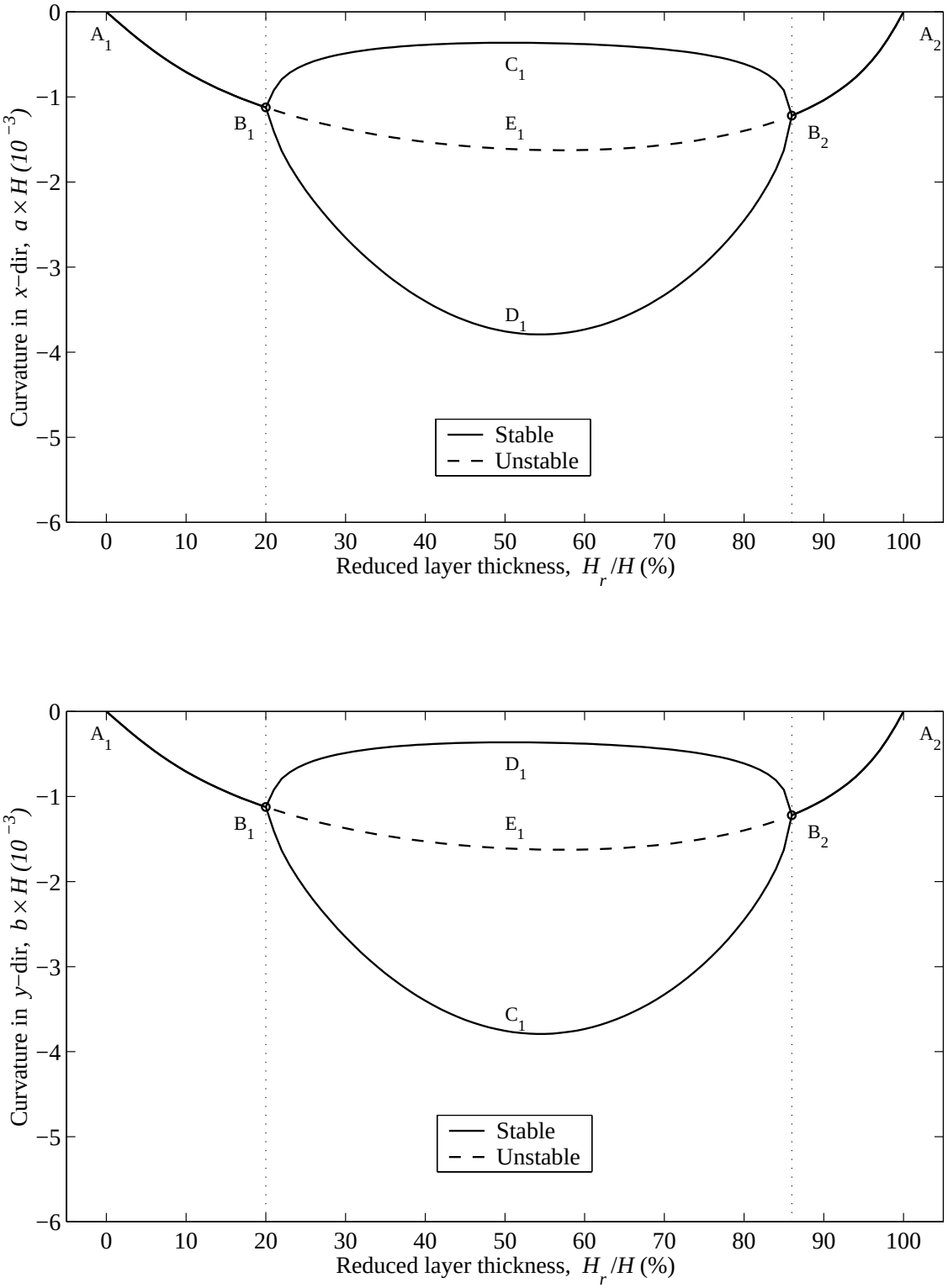


Figure 2.13: Room-temperature shapes of rectangular RAINBOW as a function of reduced layer thickness $H_r/H$ ($L_y/L_x$=1/2, $L_x/H$=100).

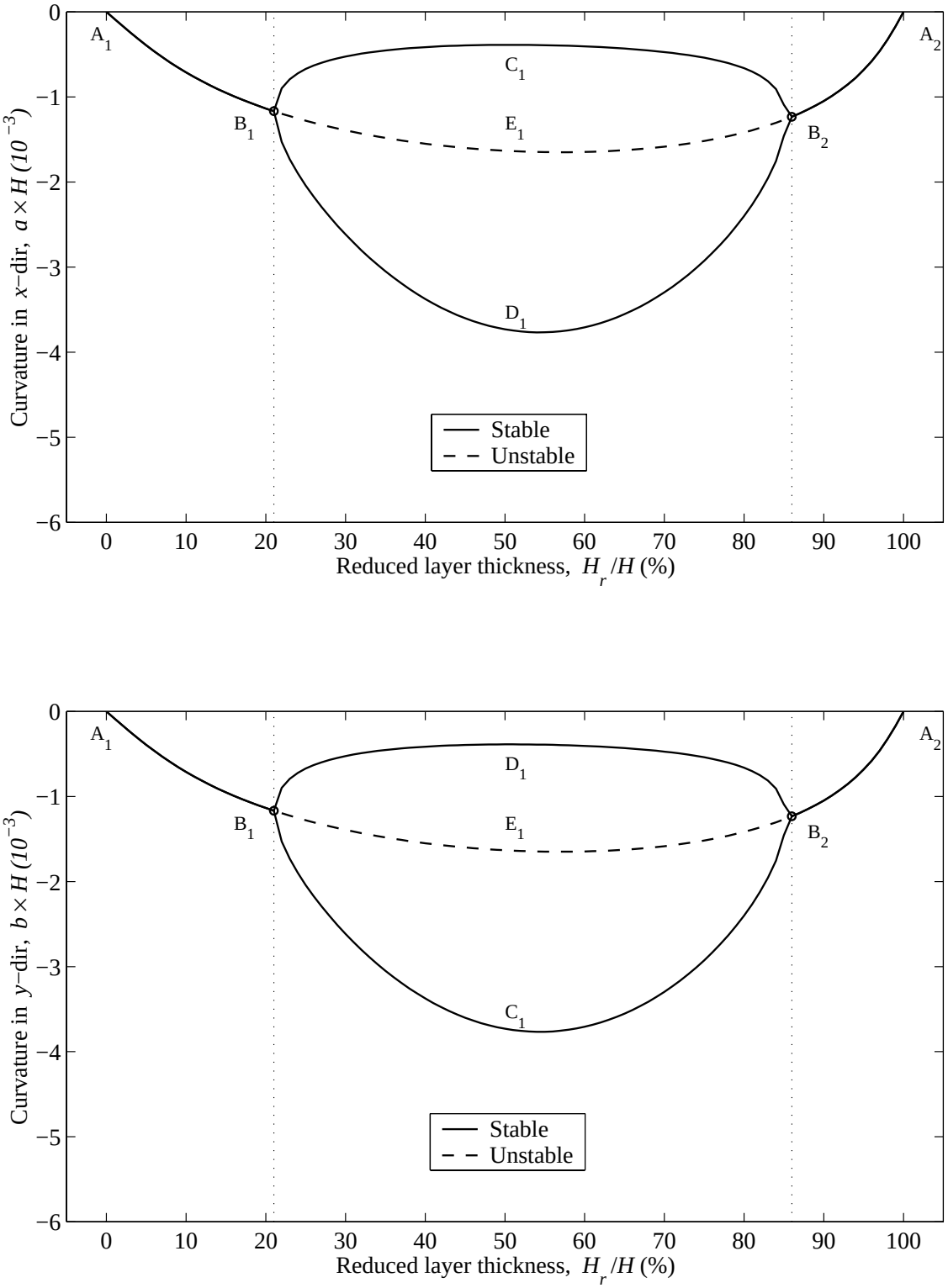


Figure 2.14: Room-temperature shapes of rectangular RAINBOW as a function of reduced layer thickness $H_r/H$ ($L_y/L_x$=1/5, $L_x/H$=100).

The existence of critical values of reduced layer thickness would add more complexity to the unusual and unexpected behavior of RAINBOW. Indeed, during the manufacturing of RAINBOW, a variation in the reduced layer thickness due to nonuniform reduction process will no doubt influence the room-temperature shapes. Two RAINBOW with the same geometry and with reduced layer thicknesses close to a critical value may behave quite differently due to small inconsistencies between the two.

### 2.4.3 Application of an Electric Field

Figure 2.19 illustrates the relationship between the change in curvatures relative to their room-temperature values, $\Delta a$ and $\Delta b$, as a function of the electric field strength for the range $E$=$\pm$1.5 MV/m. It is assumed that RAINBOW is in a shape represented by a large negative curvature in the $x$ direction and a smaller negative curvature in the $y$ direction, point D in Figure 2.11. The polarity of the unreduced piezoceramic material is assumed to be as shown in Figure 2.5 and the sign of $E$ is such that for positive $E$ the potential of the unreduced piezoceramic is higher than the potential of the reduced piezoceramic. A positive $E$ thus produces contraction strains in the unreduced piezoceramic in the $x$ and $y$ directions. Since the reduced layer is composed of the solid products of the reduction reaction, i.e., conductive metallic lead and the oxides of Pb, Zr and Ti which form along with the unreduced material [36], the reduced layer is considered to be a conductor and its piezoelectric coefficients $d_{31}$ and $d_{32}$ are assumed to be zero. The piezoelectric coefficients of the unreduced piezoceramic are given in Table 2.1. As can be seen in Figure 2.19, a reasonable change in the major curvature, $\Delta a$, can be achieved with a moderate field strength. For the case considered, a positive $E$ tends to flatten RAINBOW in the $x$ direction. It should be noted that the relationship between $\Delta a$, the major curvature, and $E$ is very close to being linear, and to a first approximation, the relationship between $\Delta b$, the minor curvature, and $E$ is also linear. The slight nonlinearity in the relation between $\Delta b$ and $E$ may be unimportant since this curvature is smaller in magnitude than $a$. The linearity of the relation between $E$ and $\Delta a$ and $\Delta b$ could be important and considerably simplify other analyses, e.g., analyses of the dynamic behavior of RAINBOW.

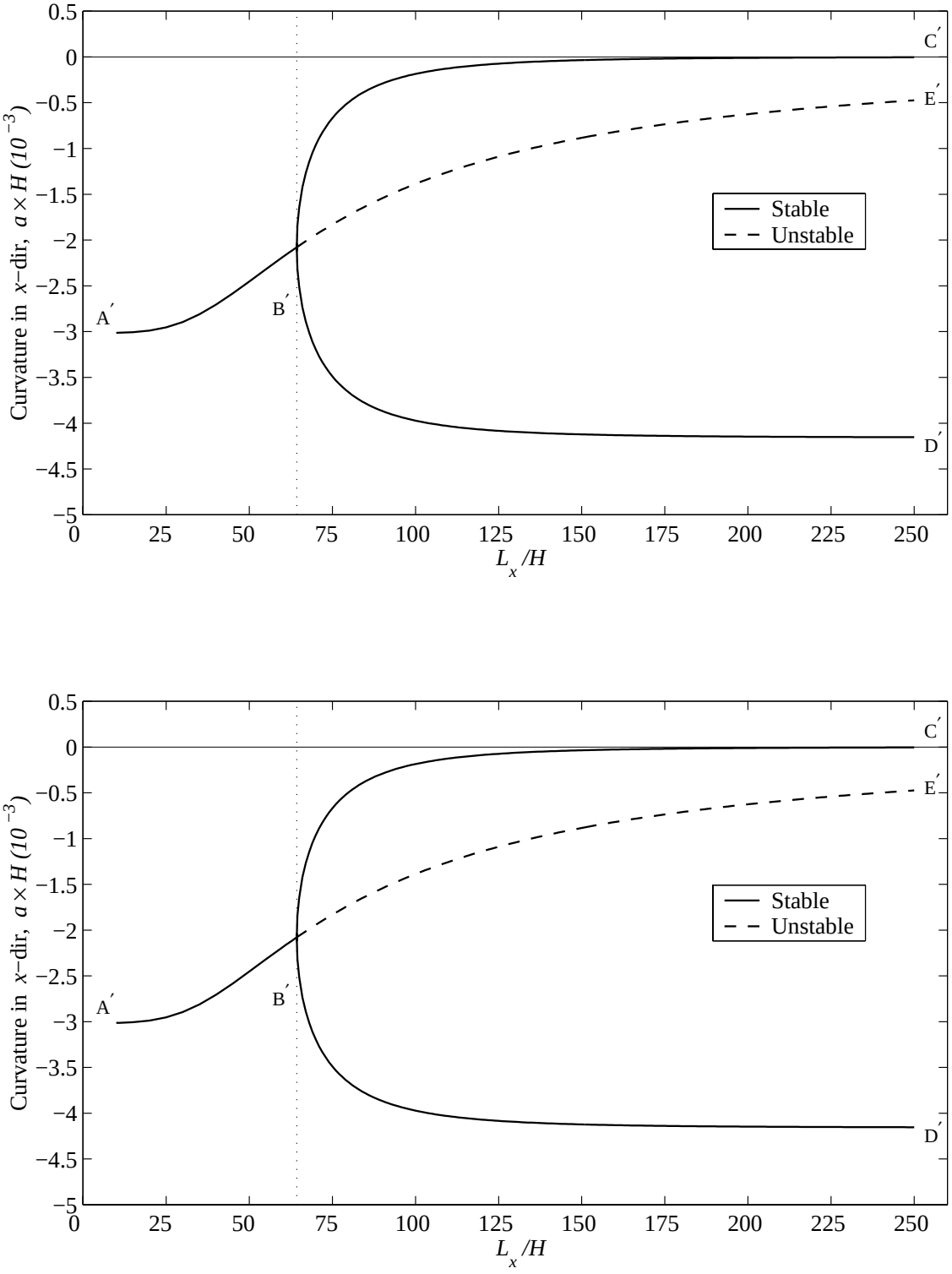


Figure 2.15: Room-temperature shapes of rectangular RAINBOW as a function of geometry ($L_y/L_x$=1, $H_r/H$=0.55) (counterpart to Figure 2.8).

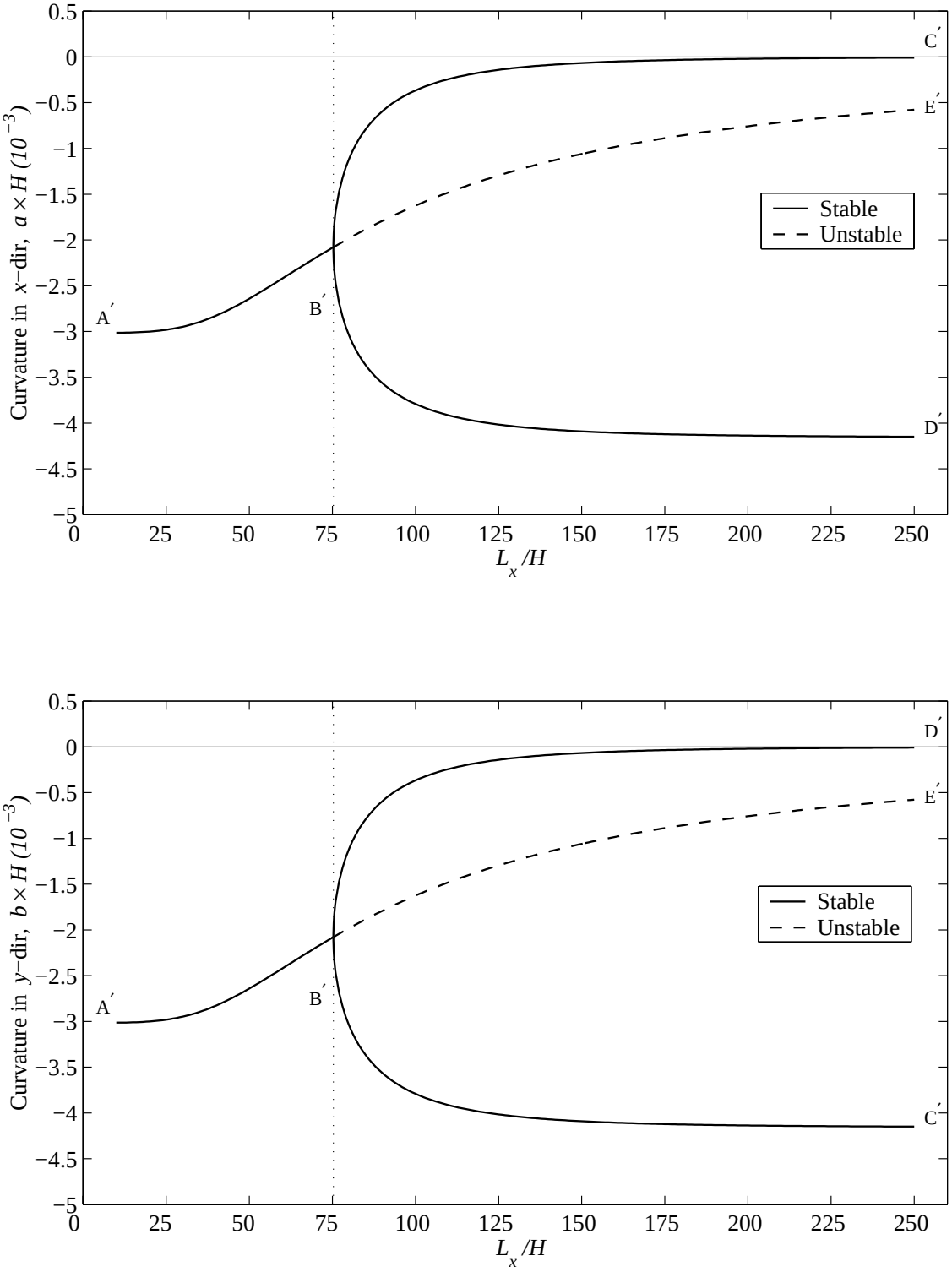


Figure 2.16: Room-temperature shapes of rectangular RAINBOW as a function of geometry ($L_y/L_x$=1/2, $H_r/H$=0.55) (counterpart to Figure 2.9).

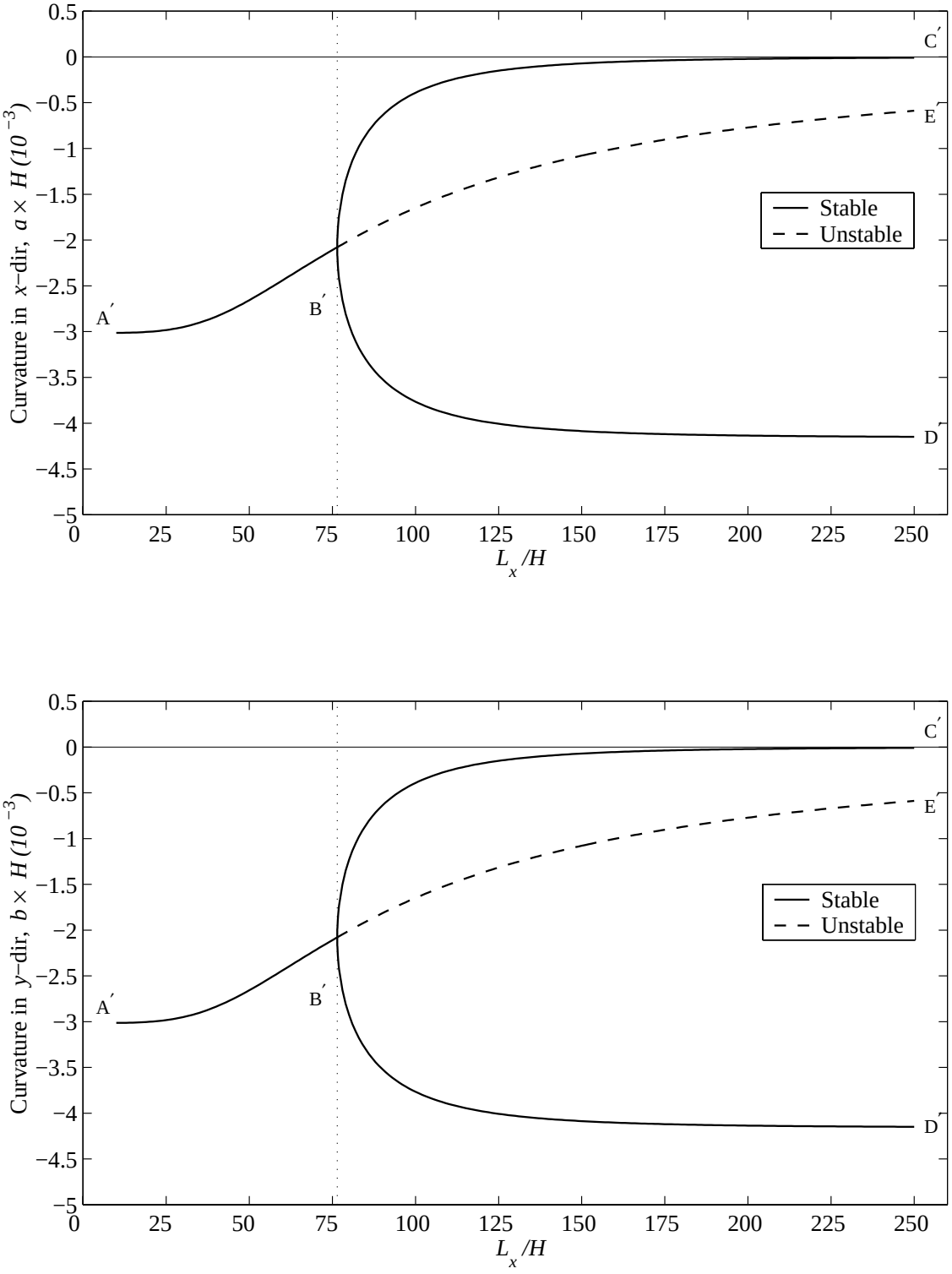


Figure 2.17: Room-temperature shapes of rectangular RAINBOW as a function of geometry ($L_y/L_x$=1/5, $H_r/H$=0.55) (counterpart to Figure 2.10).

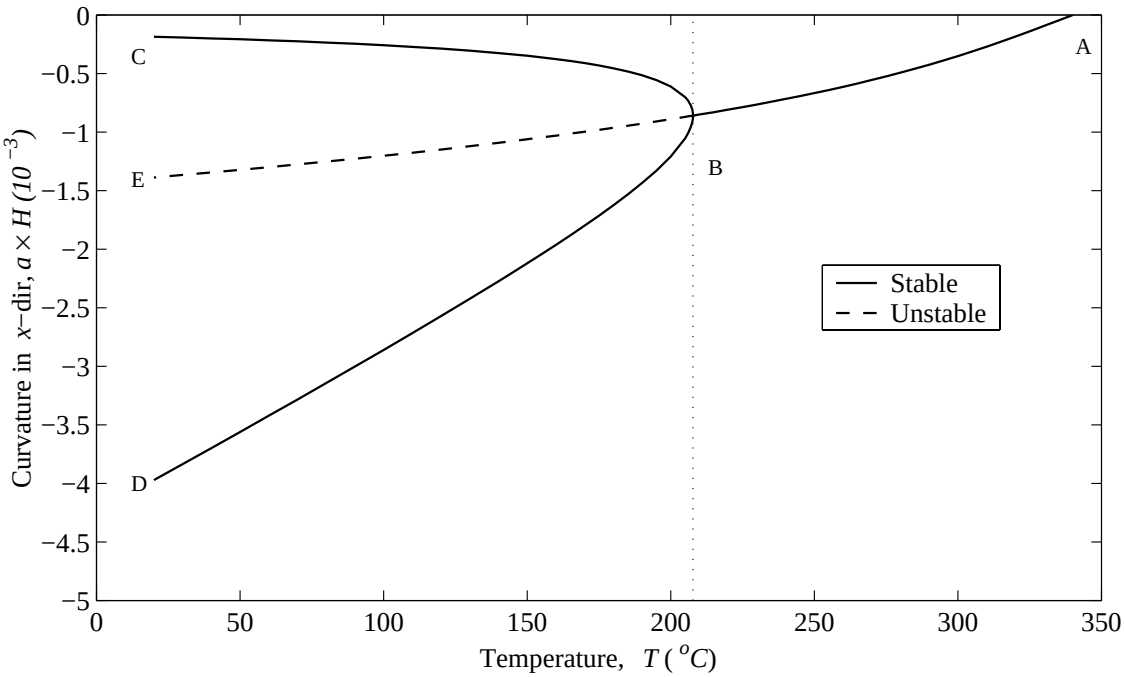


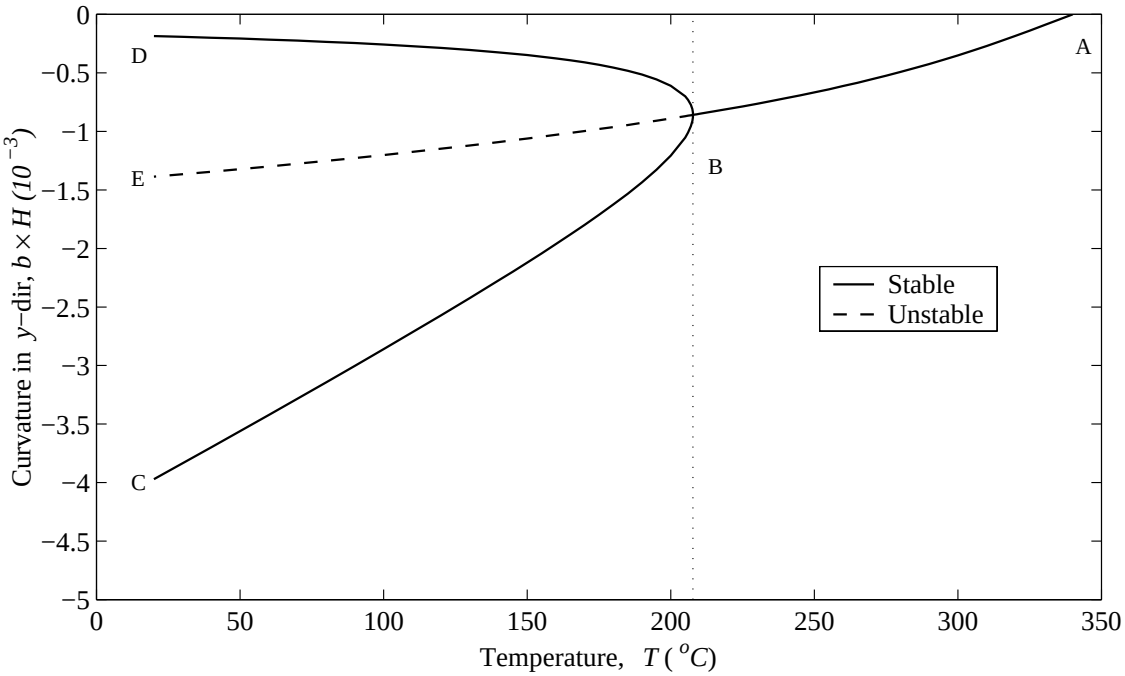


Figure 2.18: Temperature-curvature relation of rectangular RAINBOW ($L_y/L_x$=1, $L_x/H$=100, $H_r/H$=0.55) (counterpart to Figure 2.11).

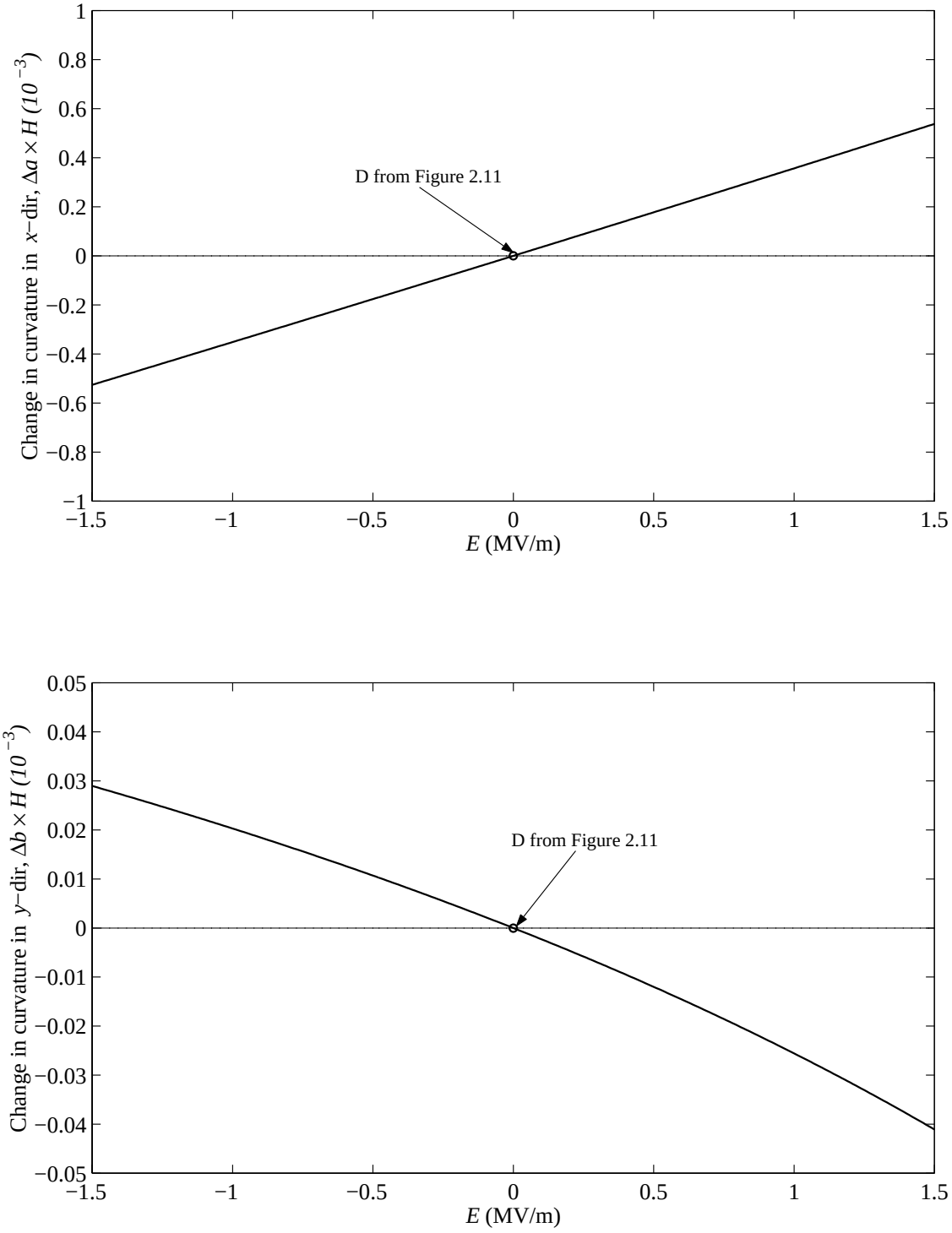


Figure 2.19: Variations of $a$ and $b$ as a function of $E$ ($L_x/H$=100, $L_y/L_x$=1, $H_r/H$=0.35).

#### 2.4.3.1 Effect of Geometry on the Piezoelectric-Induced Deformations

The results shown in Figure 2.19 for the case of Figure 2.11, RAINBOW with $L_x/H$=100, $L_y/L_x$=1, and $H_r/H$=0.35, can change dramatically if another RAINBOW is considered which has a value of $L_x/H$=70, a value closer to the critical value of 69. Consider again Figure 2.8, but as shown in Figure 2.20, this time with two specific values of $L_x/H$ noted. For $L_x/H$=100, the values of $a$ and $b$ are those shown by the points C, D, and E in Figure 2.11. This value of $L_x/H$ is sufficiently removed from the critical value of $L_x/H$=69 and the effect of applying a $E$=± 1.5 MV/m was shown in Figure 2.19. A value of $L_x/H$=70, though, is quite close to the critical value. For this case the values of the room-temperature curves are denoted by C″, D″, and E″, the latter representing an unstable equilibrium shape. If an electric field of $E$=± 1.5 MV/m is applied to RAINBOW with $L_x/H$=70, the results shown in Figure 2.21 are predicted. This figure is more complicated than Figure 2.19 because of the potential for a change in shape due to the applied electric field, and because curvatures rather than the change in curvatures are plotted. If RAINBOW has a room-temperature shape represented by point D″ in Figure 2.21, then a negative $E$ results in an increase in magnitude of curvature $a$ and a decrease in magnitude of curvature $b$. That is, RAINBOW becomes more cylindrical, with a negative curvature in the $x$ direction dominating. If, on the other hand, $E$ is positive, a qualitative change in shape of RAINBOW is possible. Again referring to Figure 2.21, as $E$ increases from zero at point D″, the value of $a$ becomes less negative and the value of $b$ becomes more negative. When the electric field strength reaches a value represented by F″, the two curvatures have equal negative value. The shape is spherical. A further increase in electric field strength to point G″ continues to result in a spherical shape, but one that is somewhat less deep. If at point G″ the electric field strength is decreased, the spherical shape begins to deepen again. At point F″, RAINBOW can follow path F″C″ or F″D″. If RAINBOW follows path F″D″, it will return to the original shape as $E$ approaches zero. If it follows path F″C″, RAINBOW will assume the 'snapped through' room-temperature shape when $E$ approaches zero. Essentially, the application of the electric field has the potential for changing the character of the shape. Obviously, the closer $L_x/H$ is to the critical value, the more readily this can be accomplished with minimal $E$. However, the closer $L_x/H$ is to the critical value, the less distinct are the two room-temperature shapes corresponding to points C″ and D″, i.e., the shapes are not 'far apart'. In the context of

Figure 2.21, the closer $L_x/H$ is to the critical value, the closer points F$''$ is to $E$=0. Of course, if the electric field is applied when RAINBOW has a spherical shape at room temperature, the radius of the sphere can be made to increase or decrease, and RAINBOW could be made to move through the trifurcation point.

#### 2.4.3.2 Effect of Reduced-Layer Thickness on the Piezoelectric-Induced Deformations

It is of interest to determine the influence of the reduced layer thickness on the characteristics of the piezoelectric-induced deformations of RAINBOW at room temperature. Figure 2.22 illustrates the very important features of the dependence of the piezoelectric-induced deformations on reduced layer thickness. In this figure the change in curvatures in the $x$ and $y$ directions at room-temperature are plotted as a function of reduced layer thickness under applied electric fields of 0.25, 0.5, 1.0, and 1.5 MV/m. Again, for convenience, the change in curvatures in Figure 2.22 has been nondimensionalized by using the total thickness, $H$, as a scaling parameter. The aspect ratio and the sidelength-to-thickness ratio of RAINBOW in Figure 2.22 are fixed at 1 and 100, respectively. In this figure, it is seen that the maximum absolute change in the major and minor curvatures, $\Delta a$ and $\Delta b$ in this case, can be achieved when the reduced layer thickness is in the range of 14% to 18% or 88% to 91%, depending on the value of the electric field. However, at 55% of reduced layer thickness a local maximum in $\Delta a$ and a global minimum in absolute value of $\Delta b$ occur. The sudden change in the values of $\Delta a$ and $\Delta b$ in the ranges of 14% to 18% and 88% to 91% of reduced layer thickness is due to the fact that in these ranges a trifurcation in the room-temperature shapes occurs, as shown in Figure 2.12. To further investigate the behavior of the curvatures under applied electric fields, the change in curvatures are plotted in Figure 2.23 as a function of applied electric field for selected values of reduced layer thickness. Figure 2.23 indicates a minor change in the reduced layer thickness within the range of 14% to 18% can considerably change the piezoelectric-induced change in curvatures, as the results corresponding to 14% and 17% of layer thickness are showing. Indeed, in the ranges of 14% to 18% and 88% to 91% of reduced layer thickness, the relationship between the change in curvatures, $\Delta a$ and $\Delta b$, and the electric field, $E$, is nonlinear due to the sudden change in $\Delta a$ and $\Delta b$, as shown in Figure 2.22. Such nonlinearity can considerably complicate the dynamic behavior of RAINBOW. In view of these

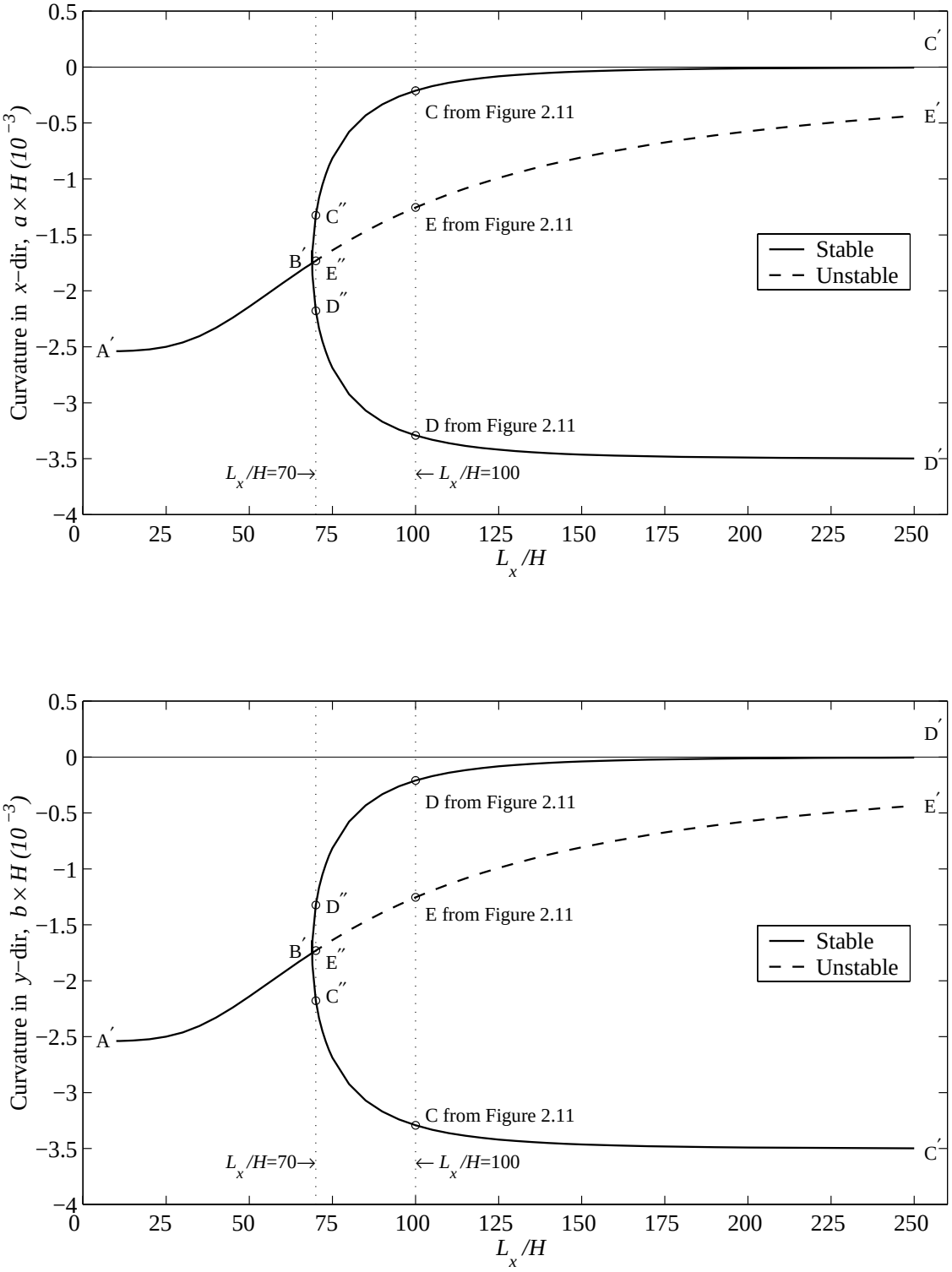


Figure 2.20: Room-temperature shapes of rectangular RAINBOW at two specific geometries ($L_y/L_x$=1, $H_r/H$=0.35).

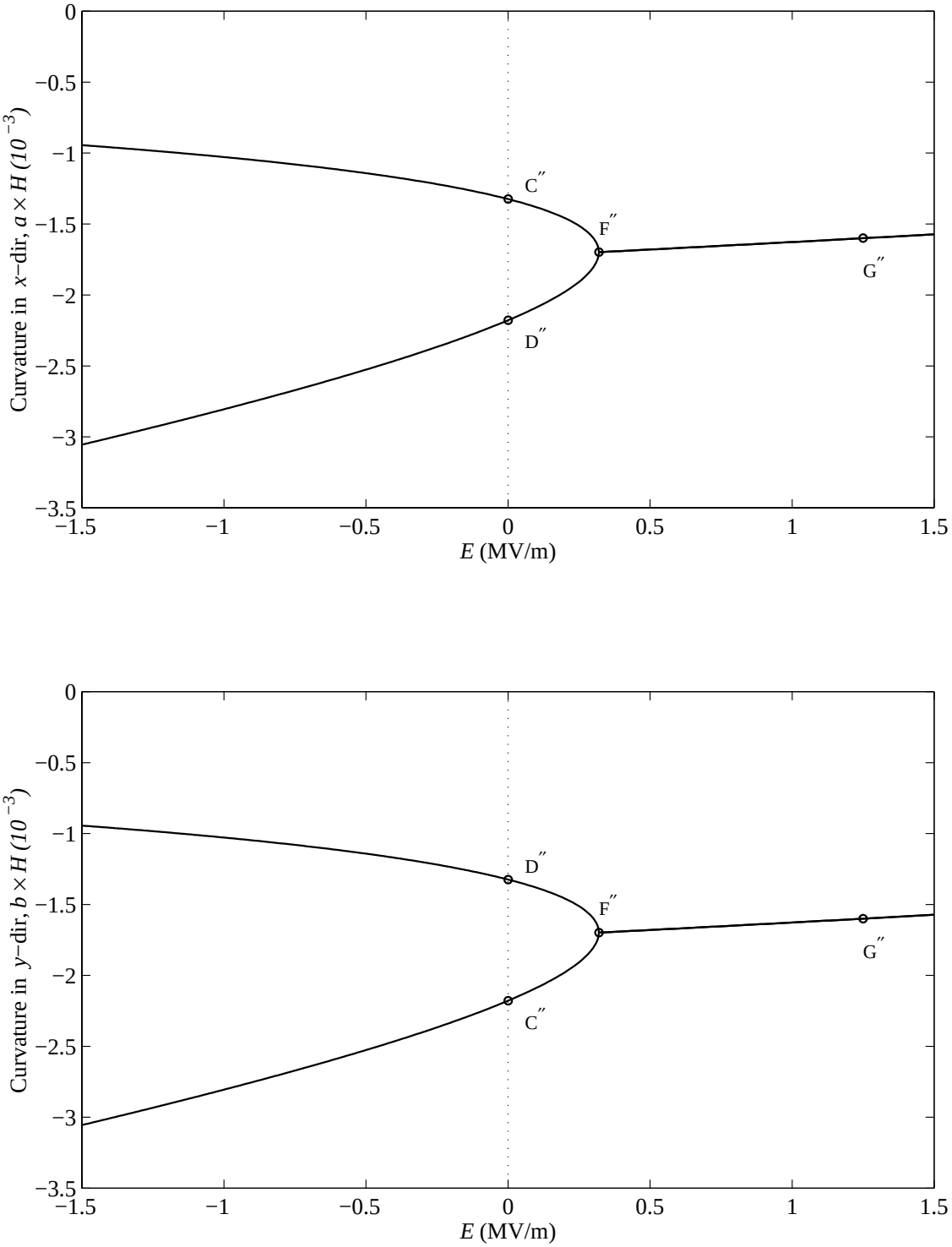


Figure 2.21: Variations of $a$ and $b$ as a function of $E$ ($L_x/H$=70, $L_y/L_x$=1, $H_r/H$=0.35).

observations, the optimal reduced layer thickness would be at 55%, since the maximum change in the major curvature $\Delta a$ is achieved while the relationship between $\Delta a$ and $\Delta b$ and $E$ is still very close to being linear.

## 2.5 Chapter Summary

In this chapter, a model for predicting the room-temperature shapes of rectangular RAINBOW has been developed. The assumptions adopted to develop the model, the expression for the total potential energy, including thermally-induced strain effects, the stress-strain relations, the strain-displacements relations, the approximate displacement fields of the Rayleigh-Ritz approach, equilibrium, and stability were discussed. The model was easily extended to account for piezoelectric-induced deformations. In general, the model presented was shown to have a good agreement with the finite element results obtained using ABAQUS. The present analysis was shown to have several formulative and computational advantages over finite element analysis. These advantages include simplicity of formulation and the relative ease of extending the model to include piezoelectric-induced deformations; in contrast to ABAQUS which requires a three-dimensional analysis to model the piezoelectric-induced deformations. In addition, the formulation of the method is quite straightforward, and the bulk of the computational effort can be completed in much less time than the finite element analysis. The results presented in this chapter indicate that the predicted room-temperature shape for rectangular RAINBOW can be either near-cylindrical or spherical. Furthermore, for a given set of material properties of the reduced and unreduced piezoceramic, there exists a critical value of sidelength-to-thickness ratio ($L_x/H$ or $L_y/H$) below which RAINBOW exhibits spherical shapes when cooled from processing temperature to room temperature. This is interpreted to mean that for values of sidelength-to-thickness ratio greater than the critical value, RAINBOW exhibits multiple room-temperature shapes. Two of the shapes are stable and are in general near-cylindrical. The third shape is spherical and is unstable. The present model is able to predict the three room-temperature shapes simultaneously; on the other hand, ABAQUS has to coaxed to follow each solution. For sidelength-to-thickness ratios larger than the critical value the two stable shapes become near-cylindrical. The existence of a critical value of sidelength-to-thickness ratio suggests that care should be taken when designing rectangular RAIN-

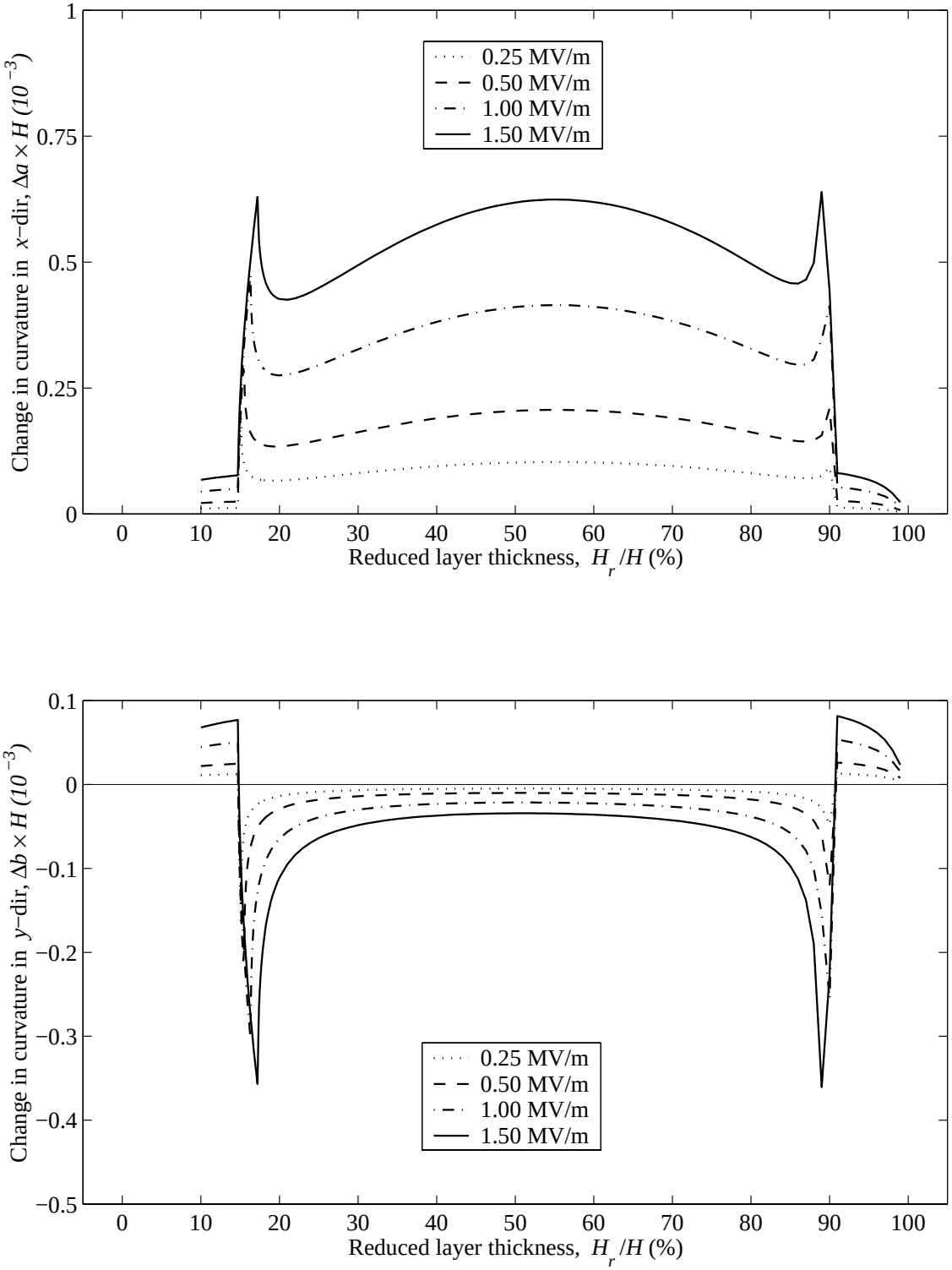


Figure 2.22: Variations of $a$ and $b$ as a function of reduced layer thickness under selected applied electric fields $E$ ($L_x/H$=100, $L_y/L_x$=1).

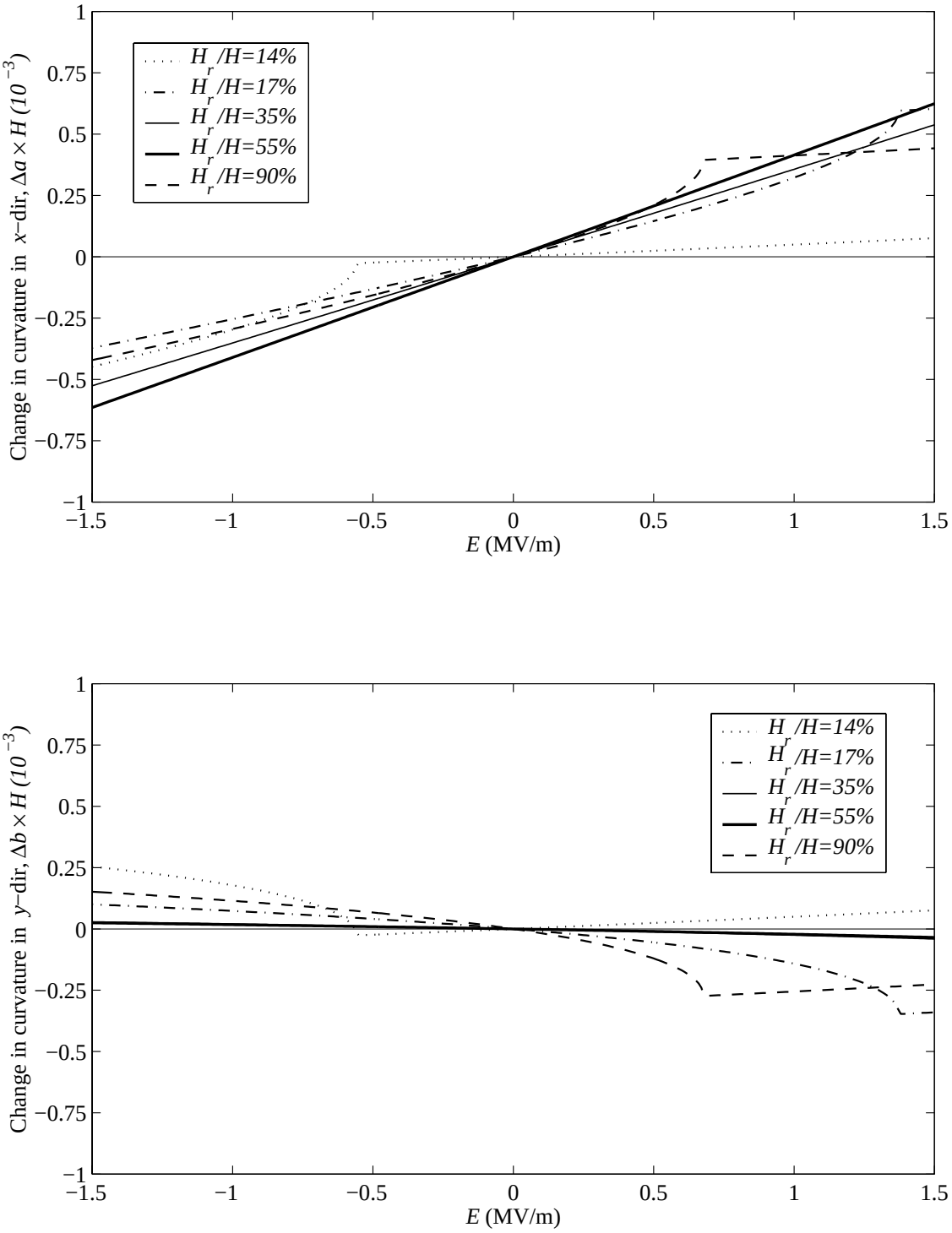


Figure 2.23: Variations of $a$ and $b$ as a function of $E$ for selected reduced layer thicknesses ($L_x/H$=100, $L_y/L_x$=1).

BOW actuators. Indeed, if two RAINBOW are manufactured with a geometry that is very close to the critical value, they may behave quite differently. Specifically, manufacturing irregularities such as small variations in material properties, variation in layer thickness, or nonuniform cooling may shift differently the effective sidelength-to-thickness ratio of both RAINBOW and hence result in two 'identical' RAINBOW which will not behave the same way. Furthermore, the present analysis reveals the existence of two critical values of reduced layer thickness which adds more complexity to the unusual behavior of RAINBOW. Indeed, it shown that for a reduced layer thickness bounded by these two critical values, RAINBOW exhibit two stable near-cylindrical shapes and one unstable spherical shape. However, if the reduced layer thickness is outside the interval bounded by the critical values, RAINBOW exhibit a unique and stable spherical shape. Thus, the variation in the reduced layer thickness due to nonuniform reduction will no doubt influence the room-temperature shapes. The extension of the model to account for piezoelectric-induced deformations shows that the relationship between the change in curvatures and the electric is very close to be linear. This finding is very important since it makes the analysis of the dynamic behavior of RAINBOW much simpler. Moreover, it is shown that the application of the electric field has the potential for changing the character of the shape of RAINBOW with $L_x/H$ close to the critical value i.e., RAINBOW could be made to move through the trifurcation point. It is found that for the set of material properties used in this study, the optimal reduced layer thickness would be at 55%, since the maximum change in curvature is achieved under the application of an electric field, while the relationship between the change in curvatures and the electric field is kept very close to being linear.

To validate the model developed in this chapter, rectangular RAINBOW were manufactured and comparison between the predicted curvatures and the measured curvatures are made. A detailed discussion of the comparison is provided in section B.2.1 of Appendix B. In the next chapter, an extension of the present model is made to simulate a multi-step thermoelastic analysis to predict the room-temperature shapes of rectangular GRAPHBOW, as well as their deformation response under application of electric field. The extended model will be used to investigate the influence of composite layer arrangements on the room-temperature shapes.

# Chapter 3

# Rectangular GRAPHBOW Actuators

## 3.1 Introduction

In this chapter, an extension of the model described in Chapter 2 is developed to predict the manufacturing and piezoelectric-induced deformation characteristics of rectangular GRAPHBOW. The extensions to the model are discussed, and numerical results are presented to illustrate the qualitative and quantitative characteristics of the room-temperature shapes, as well as piezoelectric-induced deformation characteristics, of GRAPHBOW. The influences of adding composite material to RAINBOW are emphasized.

## 3.2 Modeling Definition and Assumptions

Figure 3.1 describes the process used to incorporate one or more thin layers of fiber-reinforced composite onto RAINBOW. Please note the temperature nomenclature. First, RAINBOW is manufactured as described in Chapter 1. It is cooled to room temperature and removed from the reducing chamber. Then, graphite-epoxy fiber-reinforced prepreg material is applied to one side (or perhaps both sides). The RAINBOW actuator with the prepreg applied may then be vacuum bagged for curing the composite in an autoclave, or conceivably, the RAINBOW actuator and prepreg may be put in a hot press for curing. In any case, the temperature is raised to $T^*$, the

curing temperature of the particular prepreg being used, and perhaps vacuum and pressure are applied. These conditions are held for a period of time to cure the composite. After fully cured, the composite's elastic and thermal expansion properties develop, and the composite layer bonds to the ceramic. The now-GRAPHBOW actuator is cooled and any pressure or vacuum released. The room-temperature shape is most likely different than the original RAINBOW shape. Since the incorporation of the composite layers is done at lower temperature than the reduction with carbon, a multi-step thermoelastic analysis is developed to model the addition of the composite layers. As with the analysis of RAINBOW, the analysis is based on the total potential energy approach along with the Rayleigh-Ritz method. All the assumptions in section 2.2 are considered to be valid for GRAPHBOW. Continuity of the displacements through the actuator is tanamount to assuming there is no slippage between the composite layer and the original RAINBOW. Also, it is still assumed that the deformation state is only a function of the temperature of that state. Because of this, the room-temperature shape of GRAPHBOW will be predicted based on the following scenario: RAINBOW is cooled from the Curie temperature of the piezoceramic, $T_C$, to the cure temperature of the composite, $T^*$. It is assumed that the composite layer is bonded stress free at this temperature, and then the RAINBOW/composite material combination is cooled to room temperature. After this, if desired, an electric field is passed through the piezoceramic to cause further deformations.

Figure 3.2 describes the geometry and nomenclature of the problem considered. The first $N$ layers are assumed to be thin layers of orthotropic materials (reduced and unreduced piezoceramic) with thickness, $H$, and the next $M$ layers represent additional layers of fiber-reinforced composite material with thickness $H_c$. Layer positions, locations of the upper and lower boundaries of the $k^{th}$ layer, i.e., $z_k$ and $z_{k-1}$, sidelengths $L_x$ and $L_y$, and the analysis coordinate system are the same as for the RAINBOW analysis.

### 3.2.1 Total Potential Energy

To obtain the expression of the total potential energy of the manufacturing process described in Figure 3.1, the following logic is adopted: The total potential energy of GRAPHBOW at room temperature is equal to the total potential energy due to a temperature change $\Delta T_C$ in the $N +$

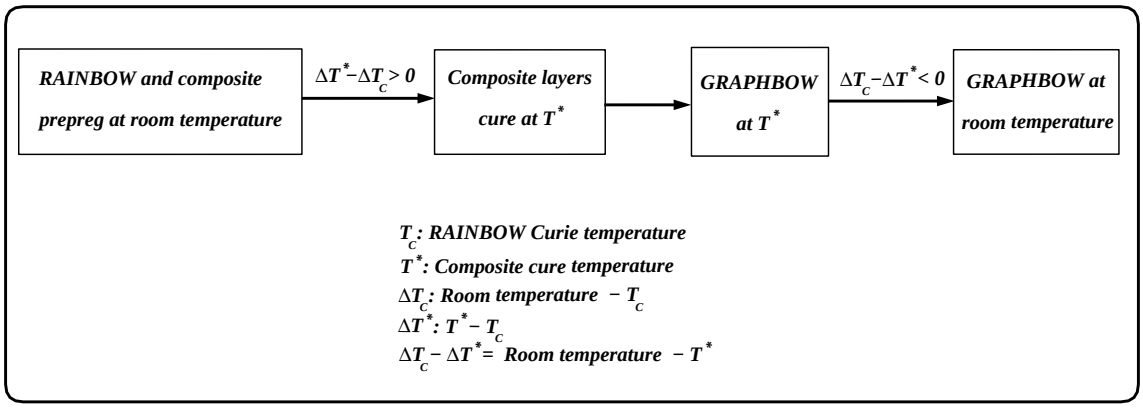


Figure 3.1: Flowchart of the manufacturing process of GRAPHBOW.

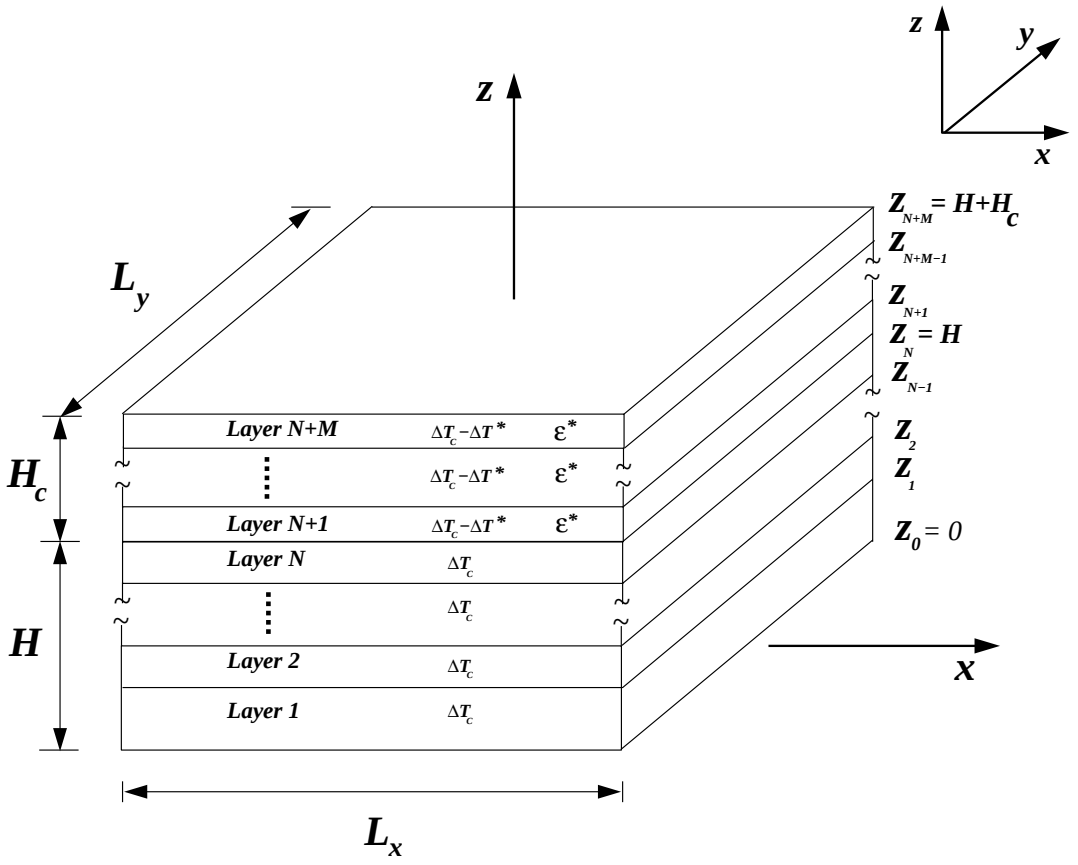


Figure 3.2: Geometry and nomenclature of rectangular GRAPHBOW considered.

$M$ layers (unreduced piezoceramic, reduced piezoceramic, and the composite), minus the total potential energy due to a temperature change $\Delta T^*$ in the composite layers. Alternatively, the total potential energy of the GRAPHBOW actuator at room temperature may be considered the sum of the total potential energy of RAINBOW due to the temperature change from the Curie temperature to the curing temperature, $\Delta T^*$, plus the total potential energy of the RAINBOW/composite material combination due to temperature change from the curing temperature to room temperature, $\Delta T_C - \Delta T^*$. Potential energy is not created in the composite until the temperature is below the cure temperature, $T^*$. With either interpretation, using Equations (2.1)–(2.5) and enforcing the plane-stress assumption, the total potential energy is given by

$$\Pi = \frac{1}{2}\int_{-\frac{L_x}{2}}^{+\frac{L_x}{2}}\int_{-\frac{L_y}{2}}^{+\frac{L_y}{2}}\int_{z_o}^{z_{N+M}} \big\{(\sigma_x - \sigma_x^T)(\epsilon_x^o + z\kappa_x^o) + (\sigma_y - \sigma_y^T)(\epsilon_y^o + z\kappa_y^o) + (\tau_{xy} - \tau_{xy}^T)(\gamma_{xy}^o + z\kappa_{xy}^o)\big\}\, dx\, dy\, dz \tag{3.1}$$

The stress components superscripted with a "$T$" denote the equivalent stresses due to thermal effects. Care must be taken when integrating $\Pi$ through the thickness, since not all layers are present at all temperatures. The strains and curvatures in the energy expression are given by Equations (2.7)–(2.10). The location $z = z_o = 0$ is taken here to be the reference surface of the originally two-layer flat RAINBOW and the quantities $u^o$, $v^o$, and $w^o$ are the total displacements in the $x$, $y$, and $z$ directions, respectively, of the reference surface. Expanding the stresses in Equation (3.1), we obtain the following relations

$$\begin{aligned} \sigma_x &= \bar{Q}_{11}(\epsilon_x - \epsilon_x^T) + \bar{Q}_{12}(\epsilon_y - \epsilon_y^T) \\ \sigma_y &= \bar{Q}_{12}(\epsilon_x - \epsilon_x^T) + \bar{Q}_{22}(\epsilon_y - \epsilon_y^T) \\ \tau_{xy} &= \bar{Q}_{66}(\gamma_{xy} - \gamma_{xy}^T) \end{aligned} \tag{3.2}$$

where $\epsilon_x^T$, $\epsilon_y^T$ and $\gamma_{xy}^T$ are the equivalent strains due to thermal effects and the fact that strains in the composite are nonzero only below the cure temperature. The assumption of material orthotropy in the $x$–$y$ analysis coordinate system is used in Equation (3.2). This means that the composite layers to be added have their fiber aligned either with the $x$- or $y$-directions. Equation (3.2) can

be rewritten as

$$\begin{aligned} \sigma_x &= \bar{Q}_{11}\epsilon_x + \bar{Q}_{12}\epsilon_y - \sigma_x^T \\ \sigma_y &= \bar{Q}_{12}\epsilon_x + \bar{Q}_{22}\epsilon_y - \sigma_y^T \\ \tau_{xy} &= \bar{Q}_{66}\gamma_{xy} - \tau_{xy}^T \end{aligned} \tag{3.3}$$

where

$$\begin{aligned} \sigma_x^T &= \bar{Q}_{11}\epsilon_x^T + \bar{Q}_{12}\epsilon_y^T \\ \sigma_y^T &= \bar{Q}_{12}\epsilon_x^T + \bar{Q}_{22}\epsilon_y^T \\ \tau_{xy}^T &= \bar{Q}_{66}\gamma_{xy}^T \end{aligned} \tag{3.4}$$

Since at room temperature the temperature in the piezoceramic layers is changed by $\Delta T_C$, due to cooling from the Curie temperature, the equivalent strains in the two layers of RAINBOW are given by

$$\begin{aligned} \epsilon_{x(PZT)}^T &= \alpha_x \Delta T_C \\ \epsilon_{y(PZT)}^T &= \alpha_y \Delta T_C \\ \gamma_{xy(PZT)}^T &= \alpha_{xy} \Delta T_C \end{aligned} \tag{3.5}$$

The equivalent strains in the composite layer are defined by

$$\begin{aligned} \epsilon_{x(Composite)}^T &= \alpha_x(\Delta T_C - \Delta T^*) + \epsilon_x^* \\ \epsilon_{y(Composite)}^T &= \alpha_y(\Delta T_C - \Delta T^*) + \epsilon_y^* \\ \gamma_{xy(Composite)}^T &= \alpha_{xy}(\Delta T_C - \Delta T^*) + \gamma_{xy}^* \end{aligned} \tag{3.6}$$

where $\epsilon_x^*$, $\epsilon_y^*$, and $\gamma_{xy}^*$ are the strains computed at temperature $T^*$. Integrating with respect to $z$ through the thickness of GRAPHBOW results in

$$\begin{aligned}\Pi &= \frac{1}{2}\int_{-\frac{L_x}{2}}^{+\frac{L_x}{2}}\int_{-\frac{L_y}{2}}^{+\frac{L_y}{2}}\Big\{(N_x-\hat{N}_x^T\Delta T_C-N_x^*)\epsilon_x^o+(N_y-\hat{N}_y^T\Delta T_C-N_y^*)\epsilon_y^o \\ &+ (N_{xy}-\hat{N}_{xy}^T\Delta T_C-N_{xy}^*)\gamma_{xy}^o+(M_x-\hat{M}_x^T\Delta T_C-M_x^*)\kappa_x^o \\ &+ (M_y-\hat{M}_y^T\Delta T_C-M_y^*)\kappa_y^o+(M_{xy}-\hat{M}_{xy}^T\Delta T_C-M_{xy}^*)\kappa_{xy}^o\Big\}\,dxdy \end{aligned} \tag{3.7}$$

where

$$N_x \equiv \int_0^{H+H_c}\sigma_x dz = A_{11}\epsilon_x^o+A_{12}\epsilon_y^o+B_{11}\kappa_x^o+B_{12}\kappa_y^o-\hat{N}_x^T\Delta T_C-N_x^* \tag{3.8}$$

$$N_y \equiv \int_0^{H+H_c}\sigma_y dz = A_{12}\epsilon_x^o+A_{22}\epsilon_y^o+B_{12}\kappa_x^o+B_{22}\kappa_y^o-\hat{N}_y^T\Delta T_C-N_y^* \tag{3.9}$$

$$N_{xy} \equiv \int_0^{H+H_c}\tau_{xy} dz = A_{66}\gamma_{xy}^o+B_{66}\kappa_{xy}^o-\hat{N}_{xy}^T\Delta T_C-N_{xy}^* \tag{3.10}$$

$$M_x \equiv \int_0^{H+H_c} z\sigma_x dz = B_{11}\epsilon_x^o+B_{12}\epsilon_y^o+D_{11}\kappa_x^o+D_{12}\kappa_y^o-\hat{M}_x^T\Delta T_C-M_x^* \tag{3.11}$$

$$M_y \equiv \int_0^{H+H_c} z\sigma_y dz = B_{12}\epsilon_x^o+B_{22}\epsilon_y^o+D_{12}\kappa_x^o+D_{22}\kappa_y^o-\hat{M}_y^T\Delta T_C-M_y^* \tag{3.12}$$

$$M_{xy} \equiv \int_0^{H+H_c} z\tau_{xy} dz = B_{66}\gamma_{xy}^o+D_{66}\kappa_{xy}^o-\hat{M}_{xy}^T\Delta T_C-M_{xy}^* \tag{3.13}$$

and

$$N_x^* \equiv \int_H^{H+H_c}\sigma_x dz = A_{11}^*\epsilon_x^{o*}+A_{12}^*\epsilon_y^{o*}+B_{11}^*\kappa_x^{o*}+B_{12}^*\kappa_y^{o*}-\hat{N}_x^{T*}\Delta T^* \tag{3.14}$$

$$N_y^* \equiv \int_H^{H+H_c}\sigma_x dz = A_{12}^*\epsilon_x^{o*}+A_{22}^*\epsilon_y^{o*}+B_{12}^*\kappa_x^{o*}+B_{22}^*\kappa_y^{o*}-\hat{N}_y^{T*}\Delta T^* \tag{3.15}$$

$$N_{xy}^* \equiv \int_H^{H+H_c}\tau_{xy} dz = A_{66}^*\gamma_{xy}^{o*}+B_{66}^*\kappa_{xy}^{o*}-\hat{N}_{xy}^{T*}\Delta T^* \tag{3.16}$$

$$M_x^* \equiv \int_{H+H_c}^{H} z\sigma_x dz = B_{11}^*\epsilon_x^{o*}+B_{12}^*\epsilon_y^{o*}+D_{11}^*\kappa_x^{o*}+D_{12}^*\kappa_y^{o*}-\hat{M}_x^{T*}\Delta T^* \tag{3.17}$$

$$M_y^* \equiv \int_H^{H+H_c} z\sigma_x dz = B_{12}^*\epsilon_x^{o*}+B_{22}^*\epsilon_y^{o*}+D_{12}^*\kappa_x^{o*}+D_{22}^*\kappa_y^{o*}-\hat{M}_y^{T*}\Delta T^* \tag{3.18}$$

$$M_{xy}^* \equiv \int_H^{H+H_c} z\tau_{xy} dz = B_{66}^*\gamma_{xy}^{o*}+D_{66}^*\kappa_{xy}^{o*}-\hat{M}_{xy}^{T*}\Delta T^* \tag{3.19}$$

Also, the effective thermal force and moment resultants are defined as

$$\hat{N}_x^T \equiv \int_0^{H+H_c} \left(\bar{Q}_{11}\alpha_x + \bar{Q}_{12}\alpha_y\right) dz \tag{3.20}$$

$$\hat{N}_y^T \equiv \int_0^{H+H_c} \left(\bar{Q}_{12}\alpha_x + \bar{Q}_{22}\alpha_y\right) dz \tag{3.21}$$

$$\hat{N}_{xy}^T \equiv \int_0^{H+H_c} \bar{Q}_{66}\alpha_{xy} dz \tag{3.22}$$

$$\hat{M}_x^T \equiv \int_0^{H+H_c} \left(\bar{Q}_{11}\alpha_x + \bar{Q}_{12}\alpha_y\right) z dz \tag{3.23}$$

$$\hat{M}_y^T \equiv \int_0^{H+H_c} \left(\bar{Q}_{12}\alpha_x + \bar{Q}_{22}\alpha_y\right) z dz \tag{3.24}$$

$$\hat{M}_{xy}^T \equiv \int_0^{H+H_c} \bar{Q}_{66}\alpha_{xy} z dz \tag{3.25}$$

$$\hat{N}_x^{T*} \equiv \int_H^{H+H_c} \left(\bar{Q}_{11}\alpha_x + \bar{Q}_{12}\alpha_y\right) dz \tag{3.26}$$

$$\hat{N}_y^{T*} \equiv \int_H^{H+H_c} \left(\bar{Q}_{12}\alpha_x + \bar{Q}_{22}\alpha_y\right) dz \tag{3.27}$$

$$\hat{N}_{xy}^{T*} \equiv \int_0^{H+H_c} \bar{Q}_{66}\alpha_{xy} dz \tag{3.28}$$

$$\hat{M}_x^{T*} \equiv \int_H^{H+H_c} \left(\bar{Q}_{11}\alpha_x + \bar{Q}_{12}\alpha_y\right) z dz \tag{3.29}$$

$$\hat{M}_y^{T*} \equiv \int_H^{H+H_c} \left(\bar{Q}_{12}\alpha_x + \bar{Q}_{22}\alpha_y\right) z dz \tag{3.30}$$

$$\hat{M}_{xy}^{T*} \equiv \int_0^{H+H_c} \bar{Q}_{66}\alpha_{xy} z dz \tag{3.31}$$

In the above, the $A$'s, $B$'s, $D$'s, $A^*$'s, $B^*$'s, and $D^*$'s have the following definitions

$$A_{ij} = \sum_{k=1}^{N+M} \left(\bar{Q}_{ij}\right)_k (z_k - z_{k-1}) \tag{3.32}$$

$$B_{ij} = \frac{1}{2} \sum_{k=1}^{N+M} \left(\bar{Q}_{ij}\right)_k (z_k^2 - z_{k-1}^2) \tag{3.33}$$

$$D_{ij} = \frac{1}{3} \sum_{k=1}^{N+M} \left(\bar{Q}_{ij}\right)_k (z_k^3 - z_{k-1}^3) \tag{3.34}$$

$$A^*_{ij} = \sum_{k=N}^{N+M} \left(\bar{Q}_{ij}\right)_k (z_k - z_{k-1}) \tag{3.35}$$

$$B^*_{ij} = \frac{1}{2} \sum_{k=N}^{N+M} \left(\bar{Q}_{ij}\right)_k (z_k^2 - z_{k-1}^2) \tag{3.36}$$

$$D^*_{ij} = \frac{1}{3} \sum_{k=N}^{N+M} \left(\bar{Q}_{ij}\right)_k (z_k^3 - z_{k-1}^3) \tag{3.37}$$

Note well the indices on the various summations.

### 3.2.2 The Rayleigh-Ritz Approach

For applying the Rayleigh-Ritz approach, the displacement fields for GRAPHBOW are assumed to have the same functional form as for RAINBOW, i.e., Equations (2.28)–(2.30). Again the values of $a$, $b$, $c$, and $d$ are sought by using the first variation of the total potential energy, and stability is evaluated using the second variation. The procedures are identical to those discussed in Chapter 2.

### 3.2.3 Piezoelectric Effects

To study the deformations due to applying an electric field to the unreduced piezoceramic, the total energy expression of Equation (3.7) is modified to include the effective force and moment resultants produced by the electric-field-induced dilatational strains. Hence, the following terms are appended to the total potential energy expression:

$$\hat{N}^E_x E_z \equiv \int_0^{H+H_c} \left(\bar{Q}_{11} d_{31} + \bar{Q}_{12} d_{32}\right) E_z dz \tag{3.38}$$

$$\hat{N}^E_y E_z \equiv \int_0^{H+H_c} \left(\bar{Q}_{12} d_{31} + \bar{Q}_{22} d_{32}\right) E_z dz \tag{3.39}$$

$$\hat{M}^E_x E_z \equiv \int_0^{H+H_c} \left(\bar{Q}_{11} d_{31} + \bar{Q}_{12} d_{32}\right) E_z z dz \tag{3.40}$$

$$\hat{M}^E_y E_z \equiv \int_0^{H+H_c} \left(\bar{Q}_{12} d_{31} + \bar{Q}_{22} d_{32}\right) E_z z dz \tag{3.41}$$

It should be noted that only the unreduced piezoceramic layer contributes to the integrals of Equations (3.38)–(3.41), as $d_{31}$ and $d_{32}$ are considered to be zero for the reduced layer and the composite. Again, it is assumed that the displacements resulting from the temperature change plus the application of the electric field are approximated by Equations (2.28)-(2.30).

## 3.3 Numerical Results

To illustrate the results predicted by the present theory, consider the rectangular RAINBOW discussed in Chapter 2 with $L_x$ =63.5 mm, $L_x$=38.1 mm, $H$=0.381 mm, $H_r$=0.35. The temperature-curvature relation is shown in Figure 2.6. Assume a single layer of graphite-epoxy composite material is applied to the reduced side of RAINBOW. Assume further that the composite material cures at $T^*$=177 $^o$C. With this arrangement, layer no. 1 is the composite, layer no. 2 is the reduced layer, and layer no. 3 is the unreduced layer. The fibers are aligned with the $x$ direction of the analysis coordinate system, and hence the composite layer is considered a $0^o$ layer. The assumed properties of the composite material are:

$$\begin{aligned} E_1 &= 155.0 \text{ GPa} \\ E_2 &= 12.1 \text{ GPa} \\ G_{12} &= 4.0 \text{ GPa} \\ \nu_{12} &= 0.248 \\ \alpha_1 &= -0.018 \times 10^{-6} \ {}^oC^{-1} \\ \alpha_2 &= 24.3 \times 10^{-6} \ {}^oC^{-1} \\ \text{thickness} &= 0.127 \text{ mm.} \end{aligned}$$

where 1 is the fiber direction.

Figure 3.3 illustrates the behavior of this particular GRAPHBOW, which is assigned the nomenclature [$0^o$/RAINBOW], as it is cooled from the composite cure temperature $T^*$=177 $^o$C to room temperature. For temperatures greater than $T^*$, the results of Figures 2.6 and 2.7 apply. Specifically, in Figure 3.3 the parameters $a$ and $b$ of Equations (2.28)-(2.30), representing the curvatures

of GRAPHBOW in the $x$ and $y$ directions, respectively, are shown as a function of the temperature. Figure 3.4 illustrates GRAPHBOW room-temperature shapes.

Referring to Figure 3.3, the solid and dashed lines correspond to the stable and unstable equilibrium solutions, respectively. At a temperature lower than $T^*$, the temperature-curvature relationship of GRAPHBOW is depicted by branches $C^*C_1$, $E^*E_1$, and $D^*D_1D_2D_3D_4D_5$. The solution paths of branches BC, BD, and BE from RAINBOW in Figure 2.6 are included for direct comparison. Reducing the temperature below $T^*$, solution path $C^*C_1$ represents a near-cylindrical shape which has more curvature in the $y$ direction than it does in the $x$ direction. At room temperature [$0^o$/RAINBOW] has 1230 times the curvature in the y-direction than in the $x$ direction. Compared to RAINBOW, [$0^o$/RAINBOW] has much more curvature in the $y$ direction than in the $x$ direction on this branch, i.e., 1230:1 vs. 70:1.

If path $D^*$ to $D_5$ is followed, then as the temperature is gradually decreased from $T^*$ the curvatures follow the path until the temperature corresponding to point $D_2$ is reached. Here, a jump occurs from the stable branch $D^*D_1D_2$ to the stable branch $D_3D_4D_5$. As the temperature is decreased beyond the temperature corresponding to point $D_2$, the curvatures $a$ and $b$ follow the curve $D_4D_5$. Consequently, as the temperature is slowly decreased, the equilibrium configuration of [$0^o$/RAINBOW] changes continuously except at the critical temperature corresponding to point $D_2$, where it experiences a discontinuous (jump) change. At point $D_2$, a *saddle-node static bifurcation* occurs. Note that point $D_2$ is a point of vertical tangency. Because saddle-node bifurcation points are locations of vertical tangencies, they are called *tangent bifurcations*. Further, because of the geometry at such points, they are called *turning points*. Yet another name for these bifurcation points is *limit points* [37, 38]. Therefore, the saddle-node bifurcation at point $D_2$ is a *discontinuous bifurcation*. At room temperature the solution at point $D_5$ represents [$0^o$/RAINBOW] that has 52 times the curvature in $y$ direction as in the $x$ direction. Alternatively, if [$0^o$/RAINBOW] is heated from the room temperature condition (point $D_5$), the curvatures $a$ and $b$ follow the curve $D_5D_4D_3$. At the temperature corresponding to point $D_3$, a jump occurs from point $D_3$ to point $D_1$. As the temperature is increased beyond the critical temperature corresponding to point $D_3$, the curvatures $a$ and $b$ follow the branch $D_1D^*$. Again, there is a discontinuous bifurcation at the saddle-node bifurcation point $D_3$ at which the curvatures of [$0^o$/RAINBOW] are discontinuous.

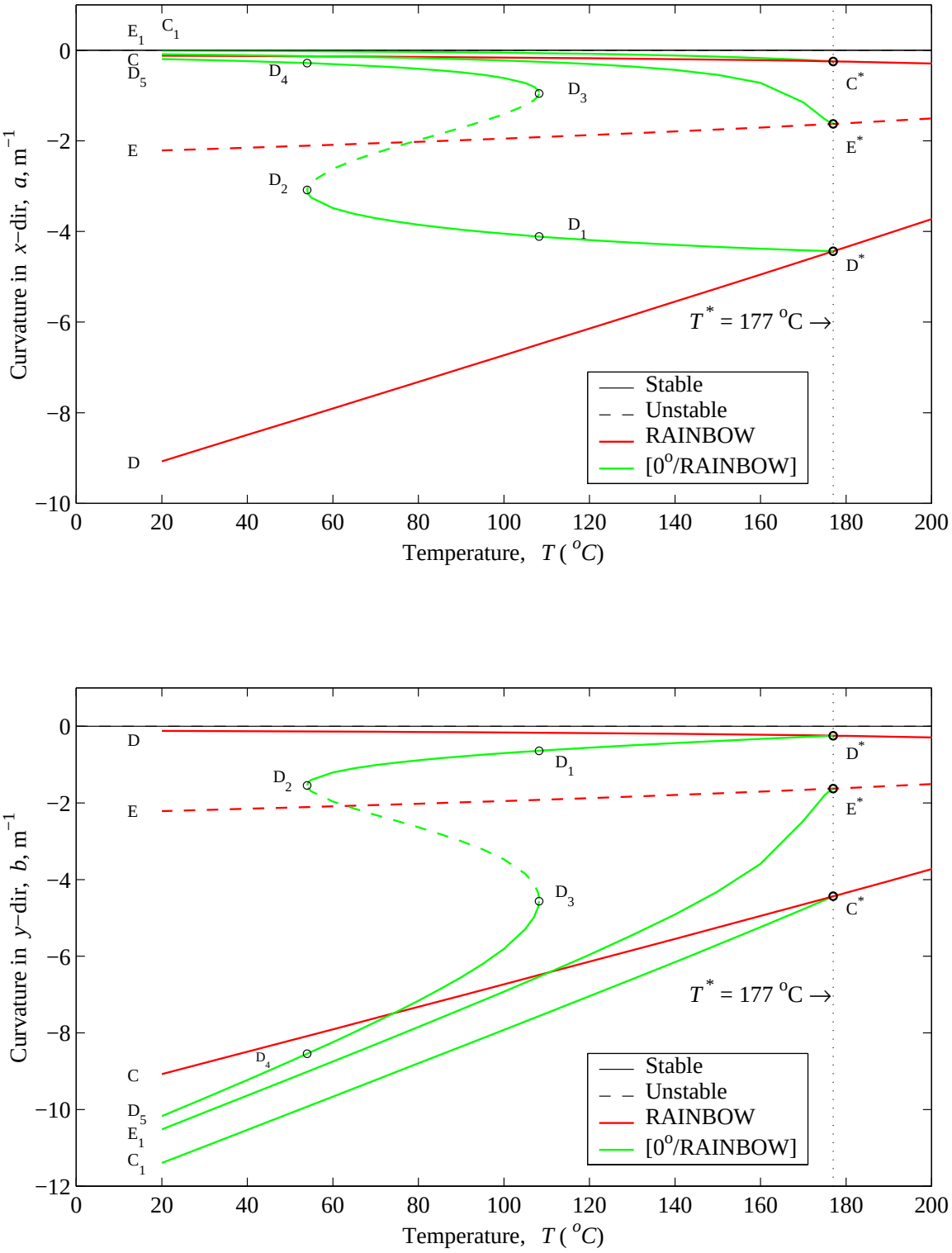


Figure 3.3: Temperature-curvature relation of rectangular [$0^o$/RAINBOW] ($L_x$=63.5 mm, $L_y$=38.1 mm, $H$=0.381 mm, $H_r/H$=0.35).

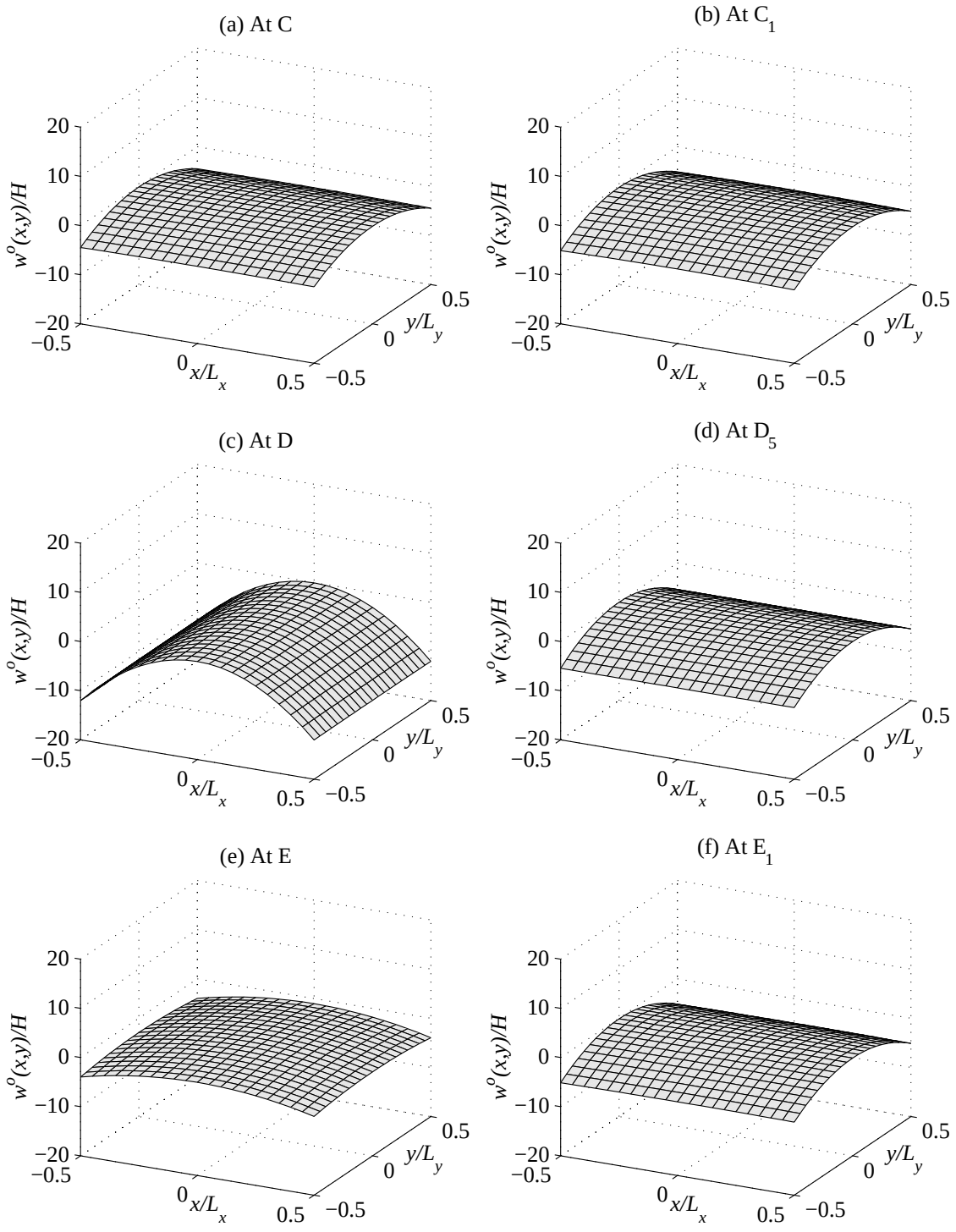


Figure 3.4: Comparison of RAINBOW and [$0^o$/RAINBOW] room-temperature shapes (refer to Figure 3.3).

Note that in the range of temperature between points $D_2$ and $D_3$, the realized deformation response of [$0^o$/RAINBOW] depends on the direction of the temperature change. This phenomenon is called the *hysteresis phenomenon*. In the range of temperature between points $D_2$ and $D_3$, two stable branches of equilibrium solutions, originating from point $D^*$, coexist. Therefore, this interval is referred to as an interval of *bistability* [39]. In the bistability interval, there are two stable and one unstable equilibrium solutions for each value of temperature.

Finally, if path $E^*E_1$ is followed, the unstable spherical shape of RAINBOW at $T^*$ changes to a stable spherical shape once the composite layer is added, and as [$0^o$/RAINBOW] is cooled to room temperature, it changes from the spherical shape to a shape which has more curvature in the $y$ direction and less in the $x$ direction. At room temperature the equilibrium configuration of [$0^o$/RAINBOW] represents a shape that has 1000 times the curvature in the $y$ direction as in the $x$ direction. That is, the room-temperature shape is near-cylindrical and much like the configurations represented by points $C_1$ and $D_5$. In fact, it is quite interesting to note that adding a composite layer with fibers in the $x$ direction leads to three configurations, i.e., $C_1$, $D_5$, and $E_1$, that have very little curvature in the $x$ direction. This is in contrast to the original RAINBOW which can have configurations with a major curvature either in the $y$ direction, i.e., C, or in the $x$ direction, i.e., D. Furthermore, the unstable spherical configuration E for RAINBOW has been "converted" to a stable near-cylindrical configuration $E_1$. None of these configurations can be 'snapped through' to another configuration. These three similar configurations and the "conversion" are illustrated in Figure 3.4.

### 3.3.1 Effect of Geometry and Composite Layer Arrangements on GRAPHBOW Room-Temperature Shape

The representative example described in the previous section has shown that incorporating a single layer of $0^o$ fiber reinforced composite onto the reduced piezoceramic layer of RAINBOW has introduced saddle-node bifurcations in the temperature-curvature relation, resulting in a discontinuous (jump) qualitative change in the features of room-temperature shapes. Such behavior is undesired if GRAPHBOW is to be used as an actuator. On the other hand, the addition of the $0^o$ layer of composite resulted in all three equilibrium configurations being near-cylindrical. Hence, it is of

great interest to investigate the influence of other composite layer arrangements, their position with respect to the two piezoceramic layers (bonded to the unreduced piezoceramic, or bonded to the reduced piezoceramic), and the aspect ratio of the device on the temperature-curvature relation of GRAPHBOW. For that purpose, three cases of different aspect ratios $L_y/L_x$=1/2, 1, 2 and three types of composite layer arrangements $[0^o]$, $[0_2^o]$, $[0^o/90^o]$, are considered. The behavior of these GRAPHBOW designs with $L_y/L_x$=1/2, $L_y/L_x$=1, and $L_y/L_x$=2 is illustrated in Figures 3.5–3.10, Figures 3.11–3.16, and Figures 3.17–3.22, respectively, as they are cooled from the composite cure temperature $T^*$=177 $^o$C to room temperature. Referring to Figures 3.5–3.22, as in past sections, the solid and dashed lines correspond to the stable and unstable solutions, respectively. In these figures, the curvatures in the $x$ and $y$ directions have been nondimensionalized by using the RAINBOW device thickness, $H$, as a scaling parameter.

In Figures 3.5–3.10, at a temperature lower than $T^*$, the temperature-curvature relations of GRAPHBOW are depicted by branches $A^*A_1$. The solution paths of branches BC, BD, and BE from RAINBOW are included. These figures indicate that GRAPHBOW equilibrium solutions are single-valued, the trifurcation that occurred to RAINBOW at temperature corresponding to point B is eliminated, and no saddle-node bifurcations (points of vertical tangencies) are encountered. These figures also indicate the sensitivity of the temperature-curvature relation to GRAPHBOW geometry. The GRAPHBOW of Figure 3.3 had values of $L_x/H$ and $L_y/L_x$ of 167 and 0.6, respectively, and resulted in the rather complicated temperature-curvature relation shown. The GRAPHBOW of Figure 3.5, with $L_x/H$ and $L_y/L_x$ of 100 and 1/2, respectively, results in a much simpler temperature-curvature relation.

In Figures 3.5–3.10, the room-temperature equilibrium solution is indicated by point $A_1$ and the corresponding values of curvatures are tabulated in Table 3.1. In Figure 3.5, a single $0^o$ layer of composite material is bonded to the unreduced side of RAINBOW. With this arrangement, layer no. 1 is the unreduced layer, layer no. 2 is the reduced layer, and layer no. 3 is the composite. At room temperature the equilibrium configuration of [RAINBOW/$0^o$] represents a shape that has 7 times the curvature in the $x$ direction as in the $y$ direction. In Figure 3.6, a single $0^o$ layer of composite material is bonded to the reduced side of RAINBOW such that layer no. 1 is the composite, layer no. 2 is the reduced layer, and layer no. 3 is the unreduced layer. The room-temperature shape

of [$0^o$/RAINBOW] is a cylinder-like shape that has 18 times the curvature in the $y$ direction as in the $x$ direction. Figure 3.7 illustrates the temperature-curvature relation of [RAINBOW/$0^o_2$], where two $0^o$ layers of fiber composite material are bonded to the unreduced side of RAINBOW. With that arrangement, layer no. 1 is the reduced layer, layer no. 2 is the unreduced layer, layer nos. 3 and 4 are the composite. The behavior of GRAPHBOW in this case is similar to the one shown in Figure 3.5, except the fact that the curvature in the $y$ direction becomes positive while the curvature in the $x$ direction is negative, resulting in a slight saddle shape. The ratio of the absolute value of the curvature in the $x$ direction to the curvature in the $y$ direction is 12. Also, it is interesting to note that the branch $A^*A_1$ for $x$ direction curvature in Figure 3.7 is closer to unstable RAINBOW branch BE than in Figure 3.5. The behavior of [$0^o_2$/RAINBOW] shown in Figure 3.8 is not much different than [$0^o$/RAINBOW], shown in Figure 3.6, except the fact that the curvature in the $x$ direction is slightly larger in magnitude. The curvature in the $y$ direction is much the same, resulting in a ratio of the curvature in the $y$ direction to the curvature in the $x$ direction equal to 9 rather than 18. Referring to Figure 3.9, bonding [$0^o/90^o$] layers of fiber-reinforced composite to the unreduced side of RAINBOW results in a shape that that has a ratio of curvature in the $y$ direction to the curvature in the $x$ direction equal to 1.8. This is a shape that is more spherical than cylindrical. It is worth mentioning the fact that branches $A^*A_1$ in Figure 3.9 are close to the unstable RAINBOW branches BE. On the other hand, bonding [$0^o/90^o$] layers of fiber-reinforced composite to the reduced side of RAINBOW results in a shape that has 14 times the curvature in the $x$ direction as in the $y$ direction. Figures 3.5–3.10 indicate that the relationship between the GRAPHBOW curvatures, $a$ and $b$, and the change in temperature is close to being linear. Because of cross-ply construction (fibers in the $x$ and $y$ directions), GRAPHBOW shown in Figures 3.9 and 3.10 might be quite tough and damage tolerant.

Figures 3.11–3.16 illustrate the behavior of GRAPHBOW with $L_y/L_x$=1 as they are cooled from the composite cure temperature $T^*$=177 $^o$C to room temperature. With $L_y/L_x$=1/2, there is a geometric bias. Then adding $0^o$ or [$0^o/90^o$] composite layers adds a material bias. Here there is no geometric bias, since $L_y/L_x$=1. Adding $0^o$ or [$0^o/90^o$] composite layers adds the only bias there is. It is interesting to note that with $L_y/L_x$=1/2, the trifurcation temperature of RAINBOW is lower than the cure temperature of the composite. Thus the temperature-curvature relations for GRAPHBOW in Figures 3.5–3.10 each branched from the single point $A^*$. In contrast, with

$L_y/L_x$=1, the trifurcation temperature of RAINBOW is higher than the cure temperature of the composite, so there are multiple branches to the temperature-curvature relations of GRAPHBOW in Figures 3.11–3.16. At a temperature lower than $T^*$, the temperature-curvature relationship of GRAPHBOW are depicted by branches $C^*C_1$, $E^*E_1$, and $D^*D_1$. The room-temperature equilibrium solutions are indicated by points $C_1$, $D_1$, and $E_1$ in Figures 3.11–3.16 and the corresponding values of curvatures are tabulated in Table 3.2. These figures indicate that bonding composite layers either to the unreduced piezoceramic or to the reduced piezoceramic leads to three stable room-temperature GRAPHBOW configurations without encountering any saddle-node bifurcations during cooling. The unstable RAINBOW branch BE is stabilized and the "converted" stable branch is $E^*E_1$. In Figure 3.11, bonding a $0^o$ composite layer to the unreduced layer of RAINBOW results in three similar room-temperature configurations, i.e., larger curvature in the $x$ direction than in the $y$ direction. These three configurations are all near-cylindrical and curvature ratios corresponding to points $C_1$, $D_1$, and $E_1$ in Figure 3.11 are 6, 13, and 28, respectively. On the other hand, bonding a $0^o$ composite layer to the reduced layer of RAINBOW, as shown in Figure 3.12, results in three similar near-cylindrical room-temperature shapes with larger curvature in the $y$ direction than in the $x$ direction. The curvature ratios corresponding to points $C_1$, $D_1$, and $E_1$ in Figure 3.12 are 42, 21, and 28, respectively. The behavior of [RAINBOW/$0_2^o$] shown in Figure 3.13 is not much different than [RAINBOW/$0^o$], shown in Figure 3.11, except for the fact that the curvatures in the $x$ and $y$ directions are somewhat lower in absolute value. The behavior of [$0_2^o$/RAINBOW] shown in Figure 3.14 is similar to the [$0^o$/RAINBOW], shown in Figure 3.12, except for the fact that [$0_2^o$/RAINBOW] has more curvature in the $x$ direction. Referring to Figures 3.15 and 3.16, the bonding of [$0^o/90^o$] composite layers to the unreduced layer can to result in room-temperature shapes that are more spherical than cylindrical. However, the behavior of [RAINBOW/$0^o/90^o$] shown in Figure 3.16 is not much different than [RAINBOW/$0_2^o$], shown in Figure 3.13. It is interesting to note that in Figure 3.15, the room-temperature equilibrium configuration corresponding to point $D_1$ is a spherical shape with a ratio of the curvature in the $x$ direction to the curvature in the $y$ direction equal to 0.95. This shape is very similar to the unstable RAINBOW shape corresponding to point E. Furthermore, Figure 3.16 shows that branch $E^*E_1$ almost coincides with RAINBOW unstable branch $E^*E$ for the curvature in the $x$ direction. Both Figures 3.15 and 3.16 indicate that the relationship between the change in temperature and GRAPHBOW curvatures is close to being

linear.

Figures 3.17–3.22 illustrate the behavior of the GRAPHBOW devices with aspect ratio $L_y/L_x$=2 as they are cooled from $T^*$ to room temperature. As the temperature is decreased from $T^*$ to room temperature, the temperature-curvature relations of GRAPHBOW are depicted by branches $C^*C_1C_2C_3C_4C_5$, $E_1E_2E^*E_3E_4E_5$, $D^*D_1$ in Figure 3.17, $C^*C_1$, $D^*D_1D_{21}$, $D_3D_{22}$, $D_3D_4$, $E^*E_2E_{31}$, $E_{32}E_4E_5$ in Figure 3.18, $C^*C_1$, $D^*D_1$, $E^*E_1$ in Figures 3.19, 3.21 and 3.22, and $C^*C_1$, $D^*D_1D_{21}$, $D_3D_{22}$, $D_3D_4$, and $E^*E_1$ in Figure 3.20. As can be seen, the temperature-curvature relations are quite complex. The curvatures of the room-temperature equilibrium configurations are tabulated in Table 3.3. The points with subscripts 2 or 3 refer to saddle-node bifurcation points. The points with subscripts 21, 22, and 31, 32 refer to points on branches that are likely to meet at saddle-node points with subscripts 2 and 3, respectively.

Figure 3.17 indicates that bonding a $0^o$ composite layer to the unreduced layer of RAINBOW results in saddle-node bifurcations during cooling if the solutions are originated from $C^*$ or $E^*$. Actually, it interesting to note that at $T^*$ two new equilibrium solutions $E_1$ and $E_3$ are created once the $0^o$ composite layer is added. The solution originating from $D^*$ does not experience any saddle-node bifurcations during cooling. In Figure 3.18, the equilibrium solutions originating from $D^*$ and $E^*$ encounter saddle-node bifurcations, and at room temperature four stable equilibrium configurations and one unstable equilibrium configuration, originating from $D^*$, are obtained. Similar behavior occurs in Figure 3.20 when two $0^o$ composite layers are bonded to the reduced layer of RAINBOW. In Figure 3.19, although saddle-node bifurcations are not encountered, the slope of path $C^*C_1$ is very steep at around $T$=100 $^o$C, indicating that a saddle-node bifurcation (point of vertical tangency) tends to occur. It is interesting to note that for larger GRAPHBOW ($L_y/L_x$=2), the saddle node-bifurcations are likely to occur during the cooling, except for the cases of [RAINBOW/$0^o$/$90^o$] and [$0^o$/$90^o$RAINBOW], where the bonding of [$0^o$/$90^o$] to either the unreduced piezoceramic or to the reduced piezoceramic tends to eliminate the saddle-node bifurcations seen in the other cases. For smaller GRAPHBOW ($L_y/L_x$=1/2 or 1), the saddle-node bifurcations are absent.

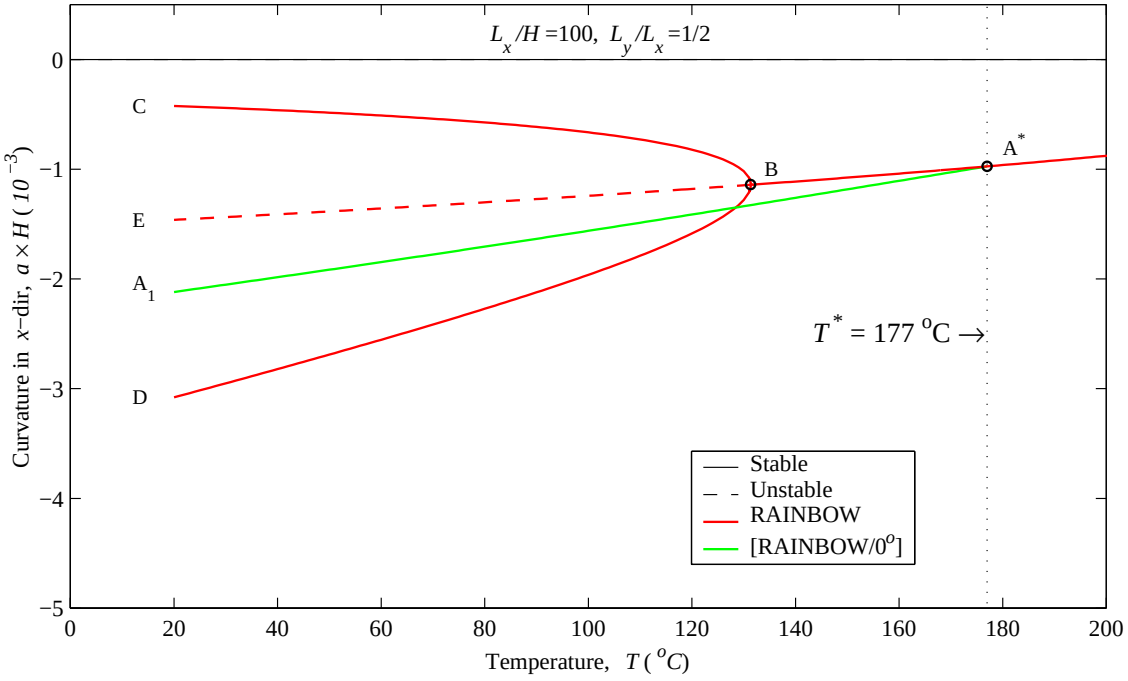


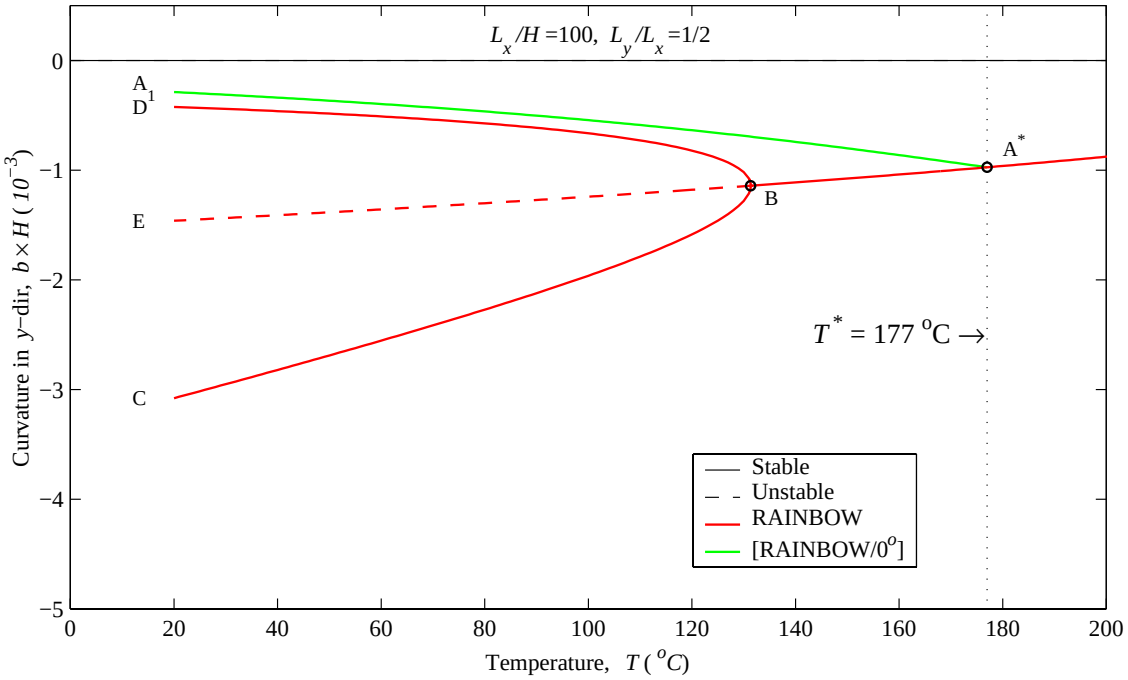


Figure 3.5: Temperature-curvature relation of rectangular [RAINBOW/$0^o$] ($L_y/L_x$=1/2, $L_x/H$=100, $H_r/H$=0.35).

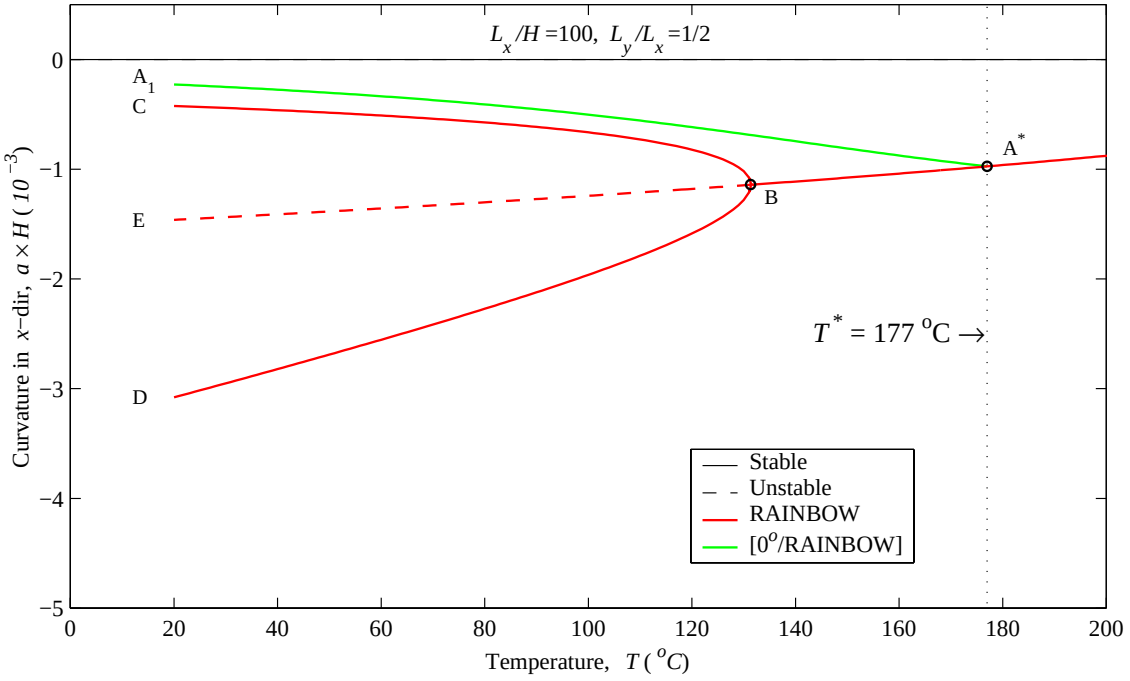


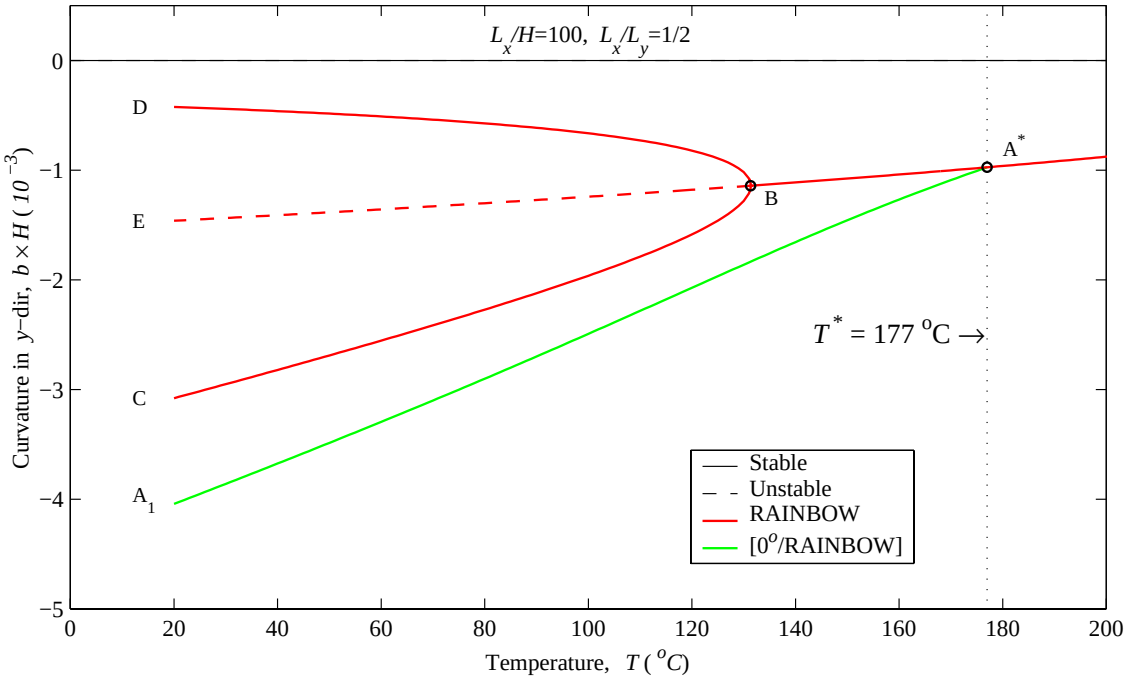


Figure 3.6: Temperature-curvature relation of rectangular [$0^o$/RAINBOW] ($L_y/L_x$=1/2, $L_x/H$=100, $H_r/H$=0.35).

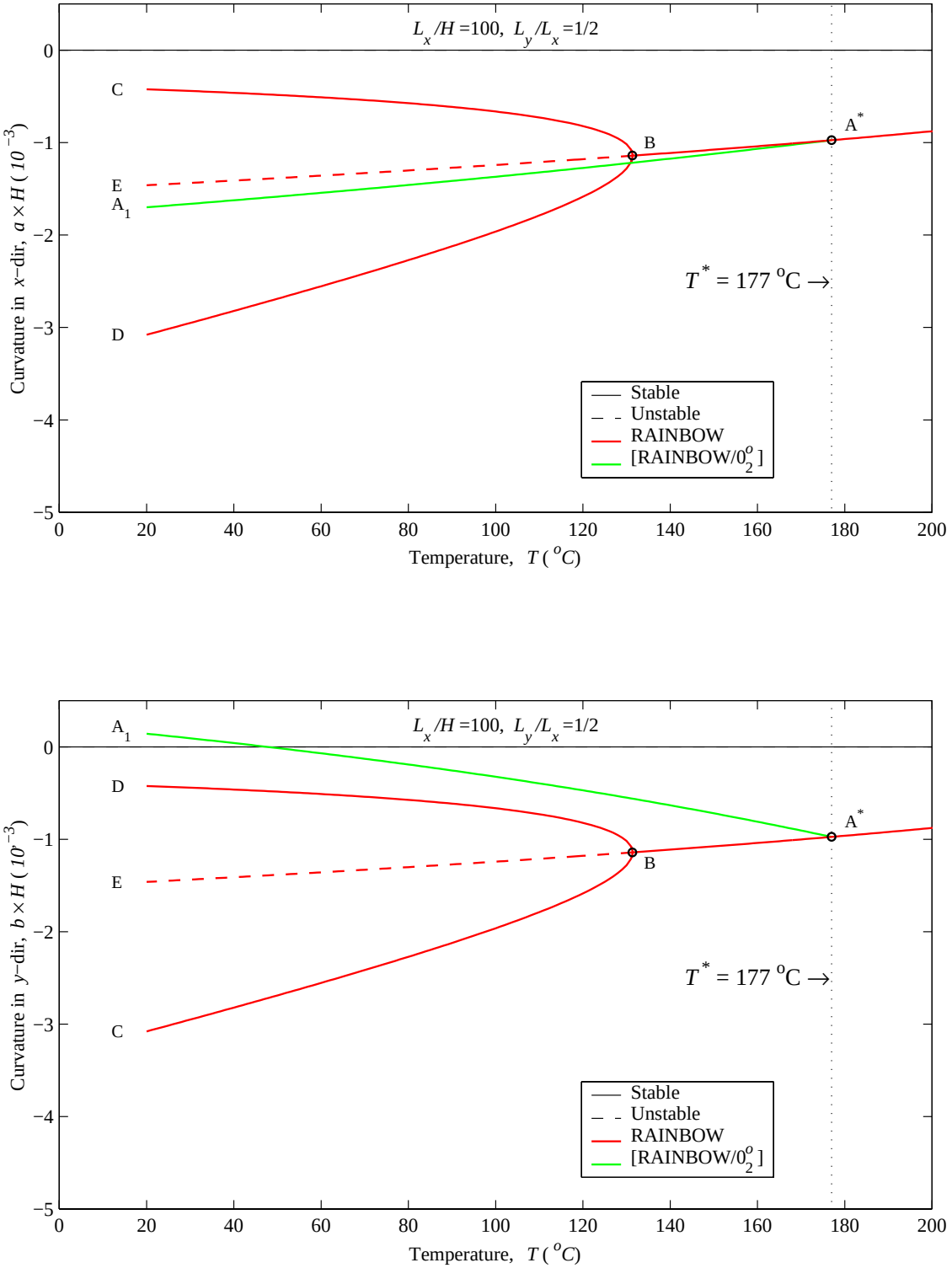


Figure 3.7: Temperature-curvature relation of rectangular [RAINBOW/$0_2^o$] ($L_y/L_x$=1/2, $L_x/H$=100, $H_r/H$=0.35).

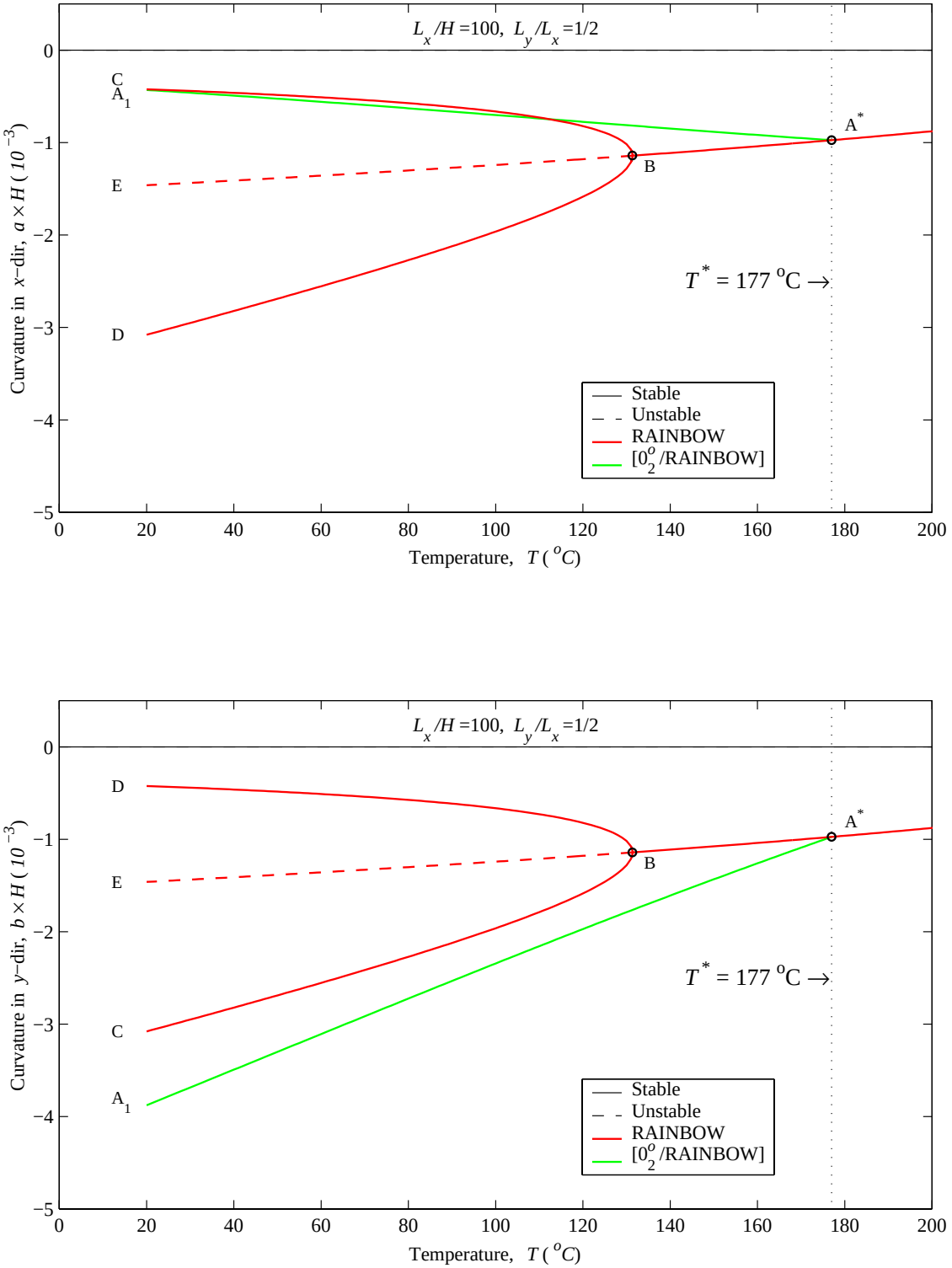


Figure 3.8: Temperature-curvature relation of rectangular [$0_2^o$/RAINBOW] ($L_y/L_x$=1/2, $L_x/H$=100, $H_r/H$=0.35).

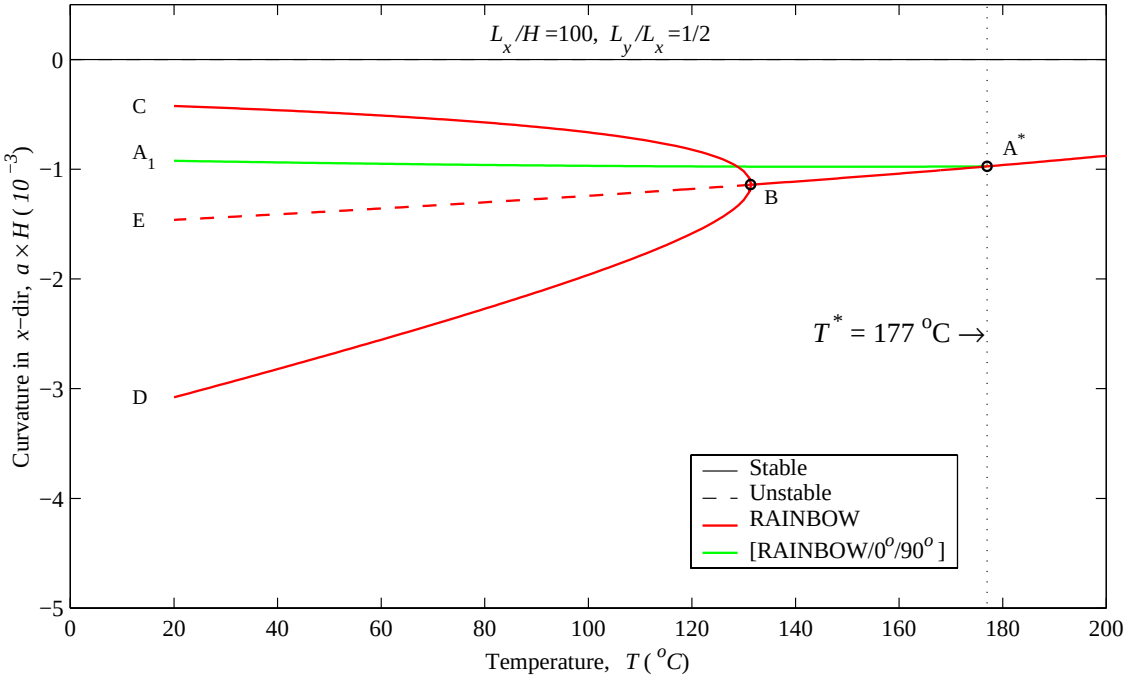


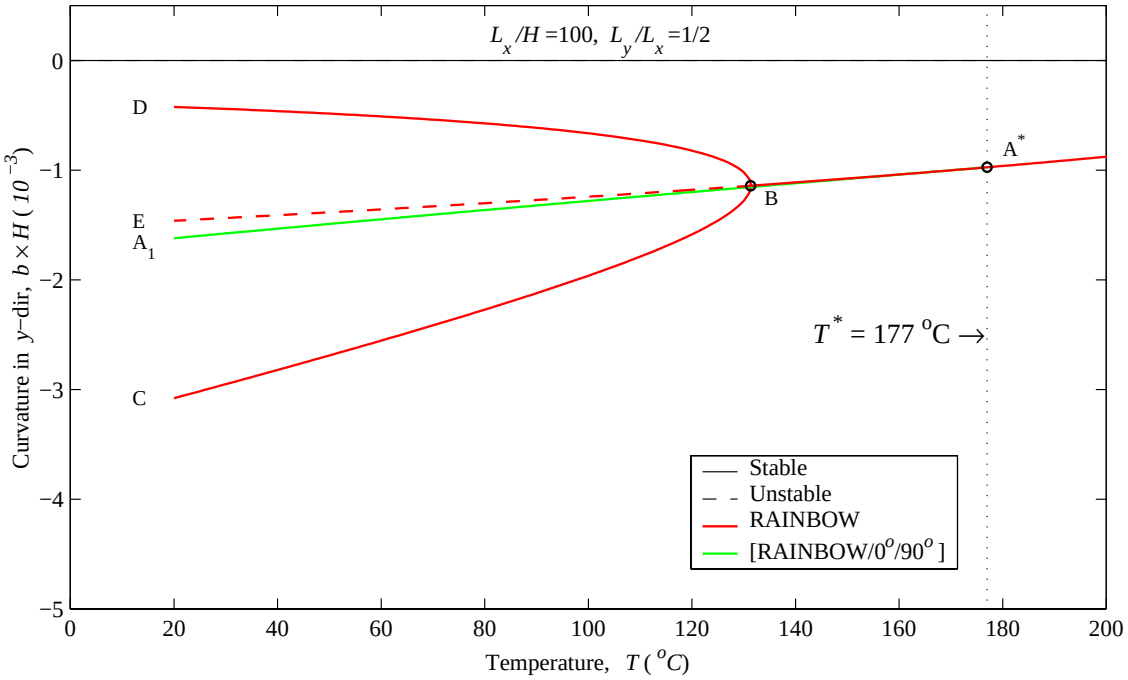


Figure 3.9: Temperature-curvature relation of rectangular [RAINBOW/$0^o$/$90^o$] ($L_y/L_x$=1/2, $L_x/H$=100, $H_r/H$=0.35).

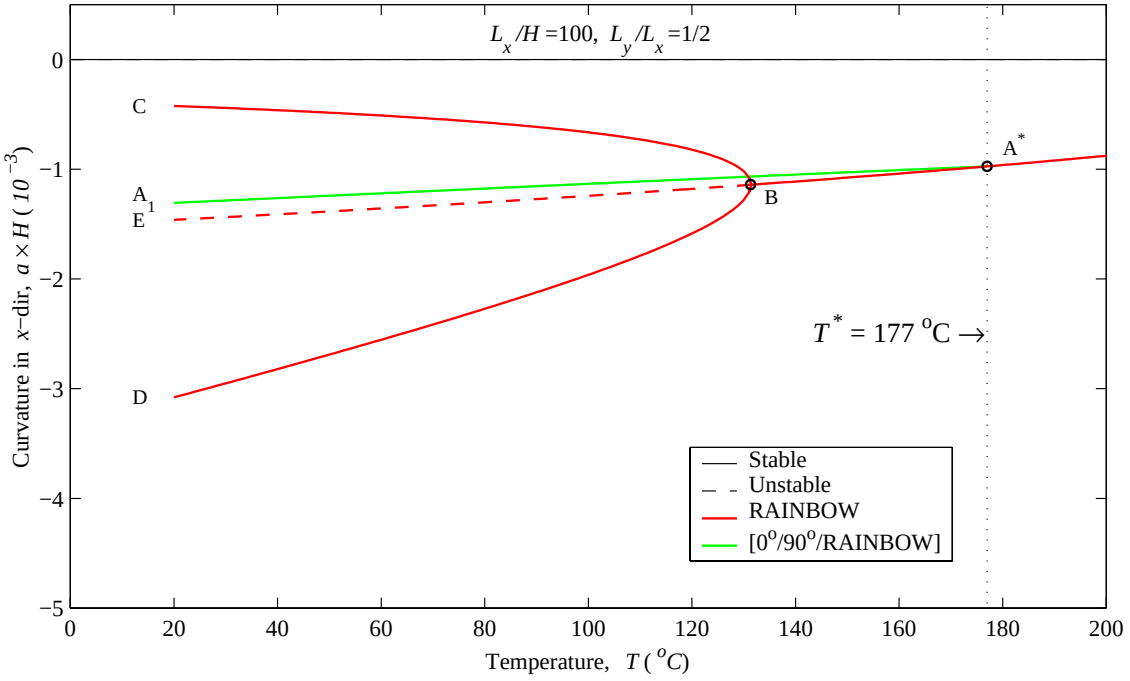


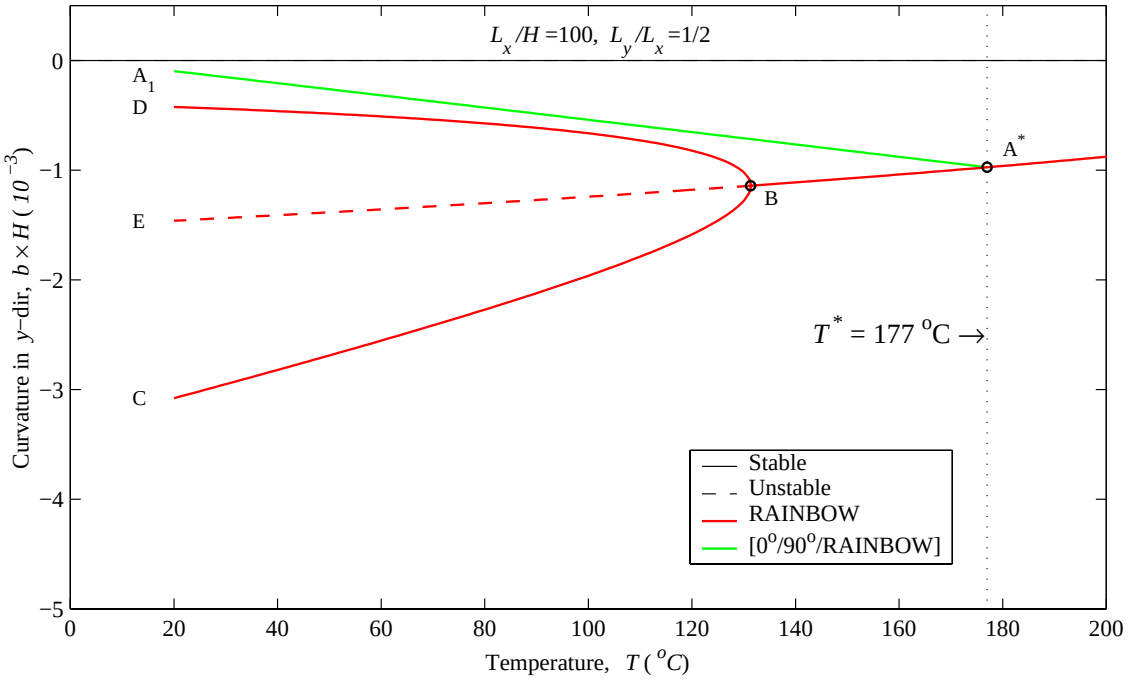


Figure 3.10: Temperature-curvature relation of rectangular [$0^o$/$90^o$/RAINBOW] ($L_y/L_x$=1/2, $L_x/H$=100, $H_r/H$=0.35).

Table 3.1: Room-temperature curvatures of various GRAPHBOW devices with $L_y/L_x$=1/2 (refer to Figures 3.5–3.10).

| Material | Solution originating from $A^*$ | | |
|---|---|---|---|
| | $a \times H$ ($10^{-3}$) | $b \times H$ ($10^{-3}$) | Stability state |
| RAINBOW | -0.4234 | -3.0791 | Stable |
| | -1.4615 | -1.4615 | Unstable |
| | -3.0791 | -0.4234 | Stable |
| [RAINBOW/$0^o$] | -2.1188 | -0.2883 | Stable |
| [$0^o$/RAINBOW] | -0.2277 | -4.0431 | Stable |
| [RAINBOW/$0_2^o$] | -1.7004 | +0.1424 | Stable |
| [$0_2^o$/RAINBOW] | -0.4307 | -3.8777 | Stable |
| [RAINBOW/$0^o$/$90^o$] | -0.9233 | -1.6207 | Stable |
| [$0^o$/$90^o$/RAINBOW] | -1.3068 | -0.0974 | Stable |

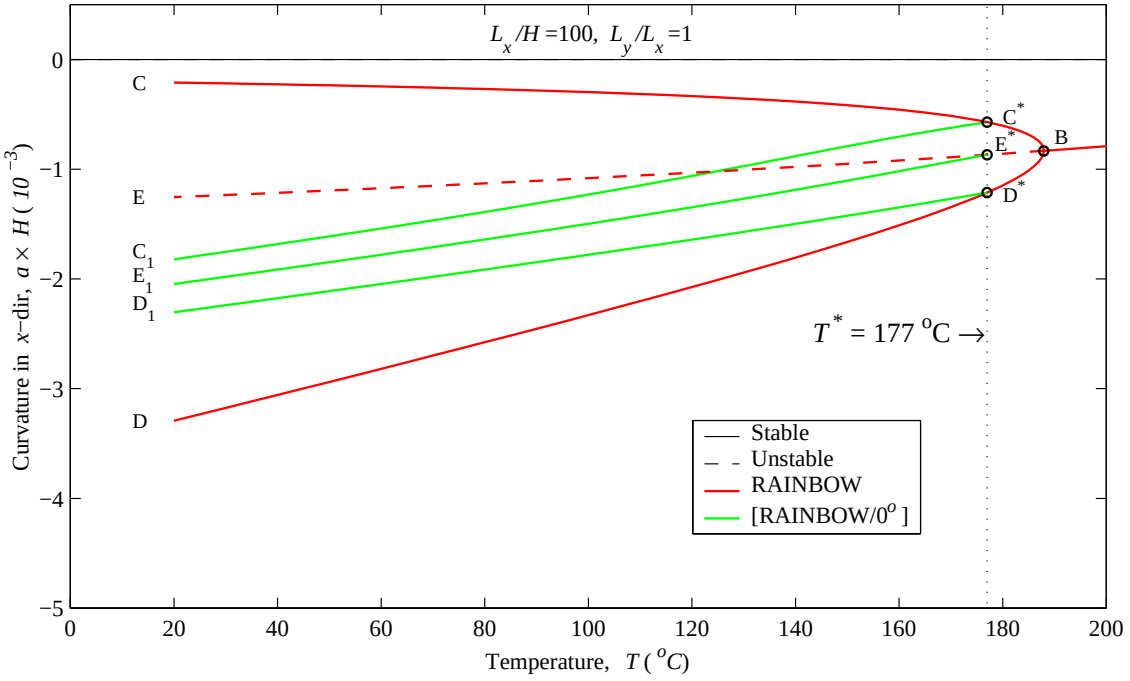


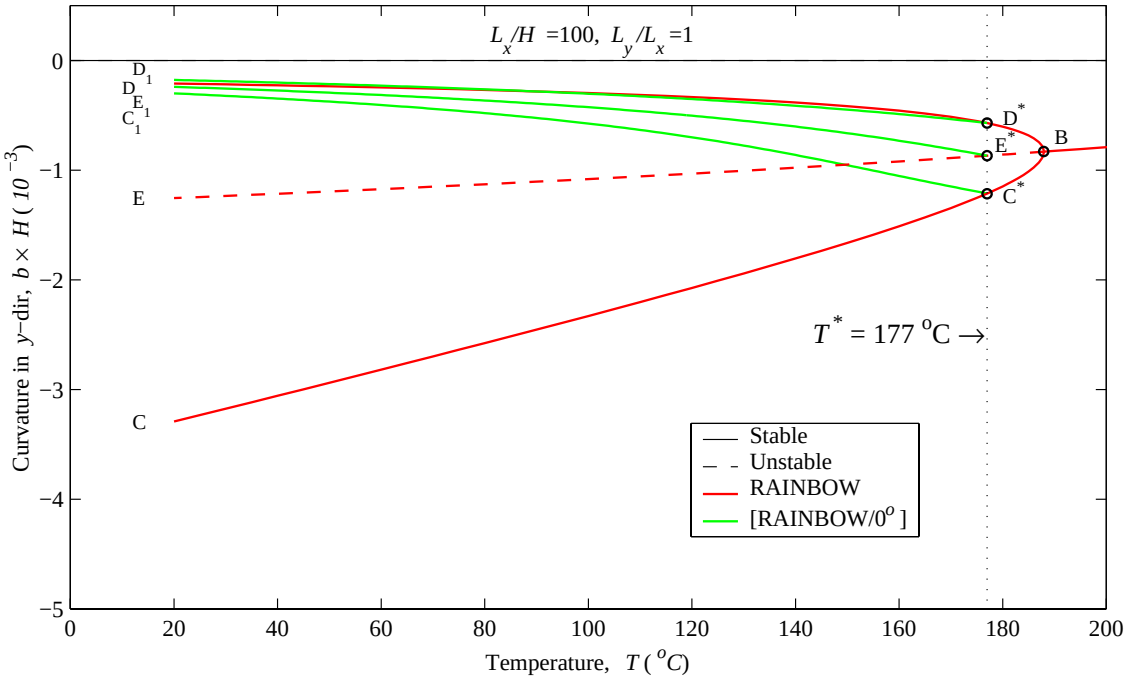


Figure 3.11: Temperature-curvature relation of rectangular [RAINBOW/$0^o$] ($L_y/L_x$=1, $L_x/H$=100, $H_r/H$=0.35).

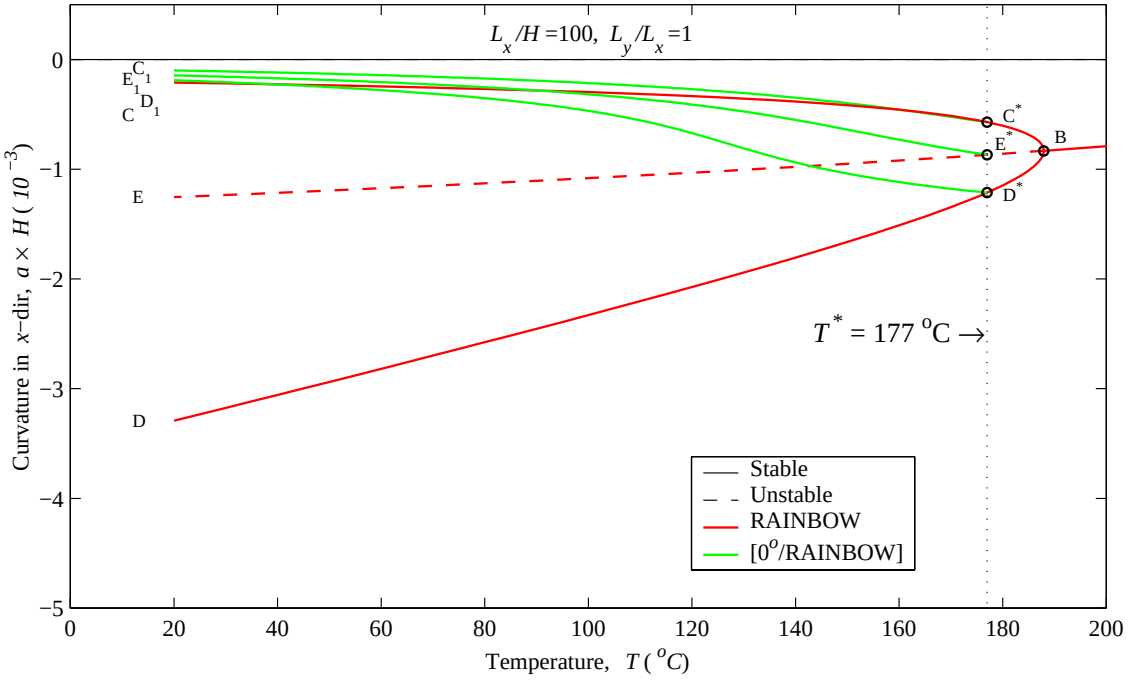


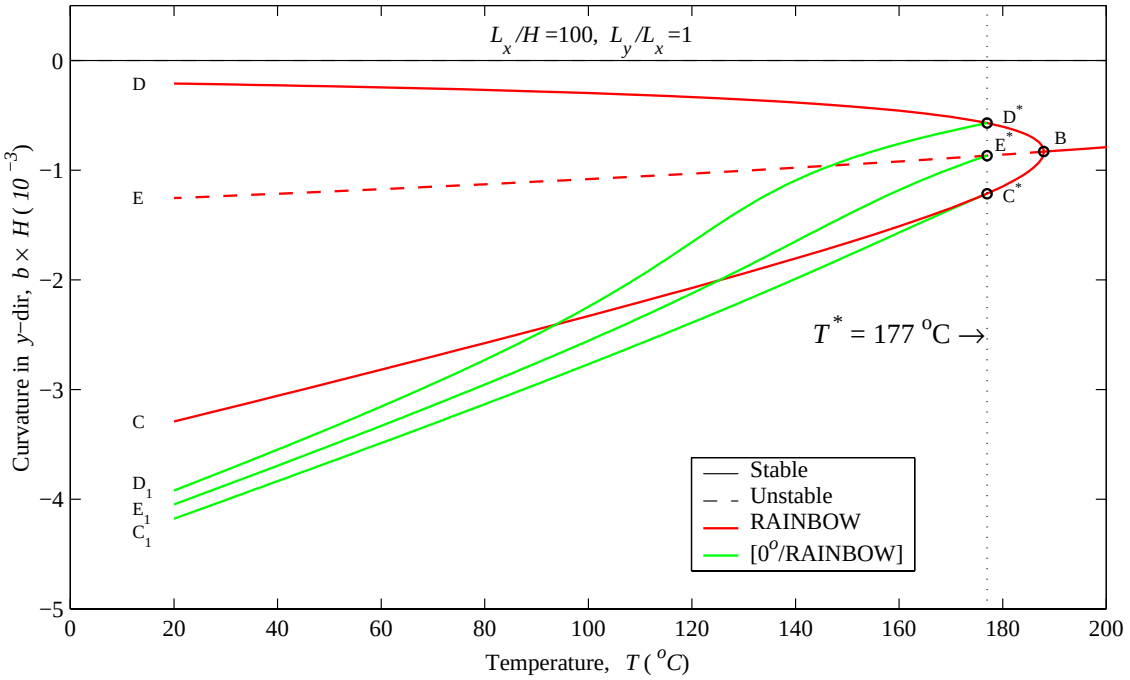


Figure 3.12: Temperature-curvature relation of rectangular [$0^o$/RAINBOW] ($L_y/L_x$=1, $L_x/H$=100, $H_r/H$=0.35).

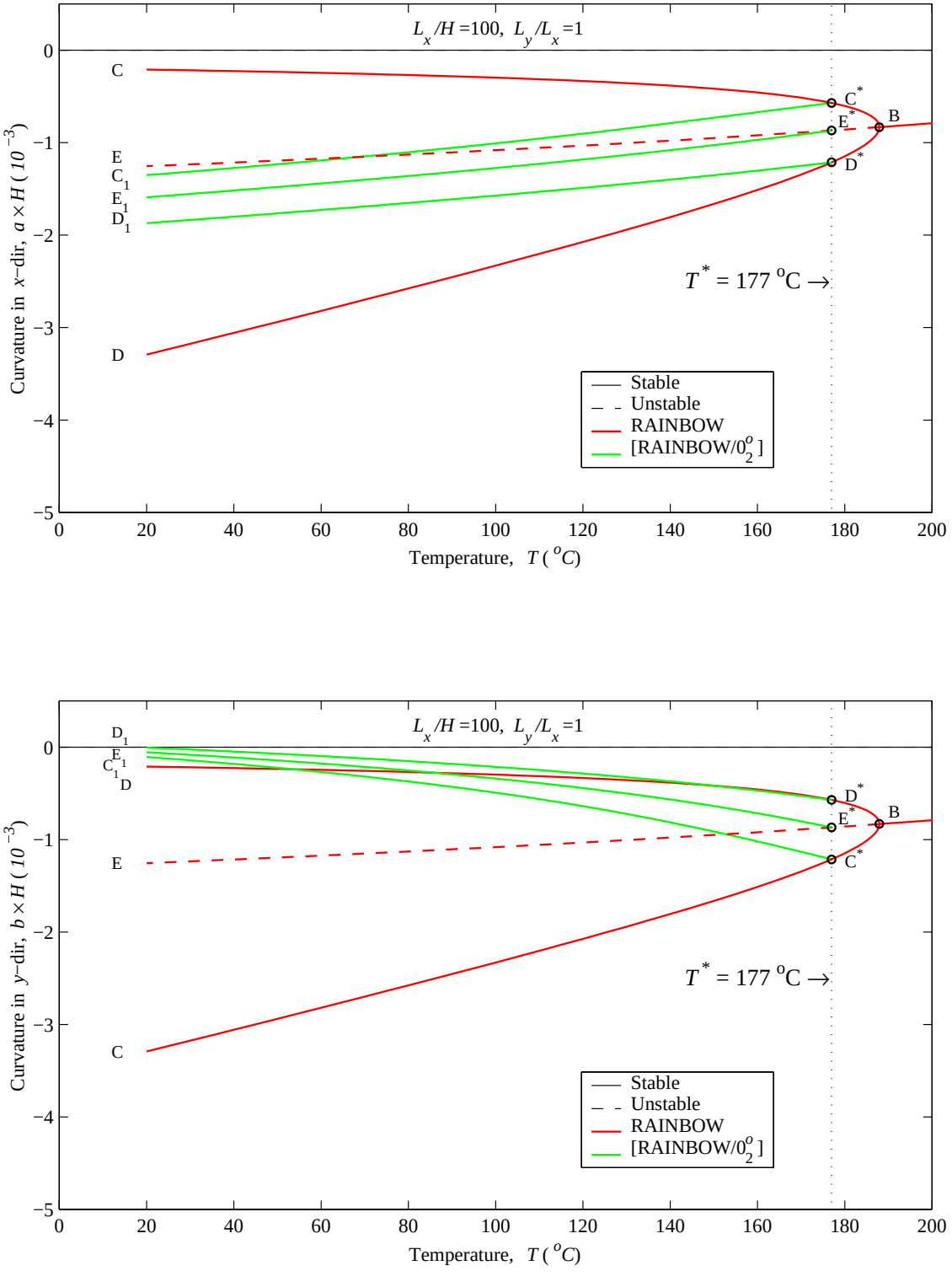


Figure 3.13: Temperature-curvature relation of rectangular [RAINBOW/$0_2^o$] ($L_y/L_x$=1, $L_x/H$=100, $H_r/H$=0.35).

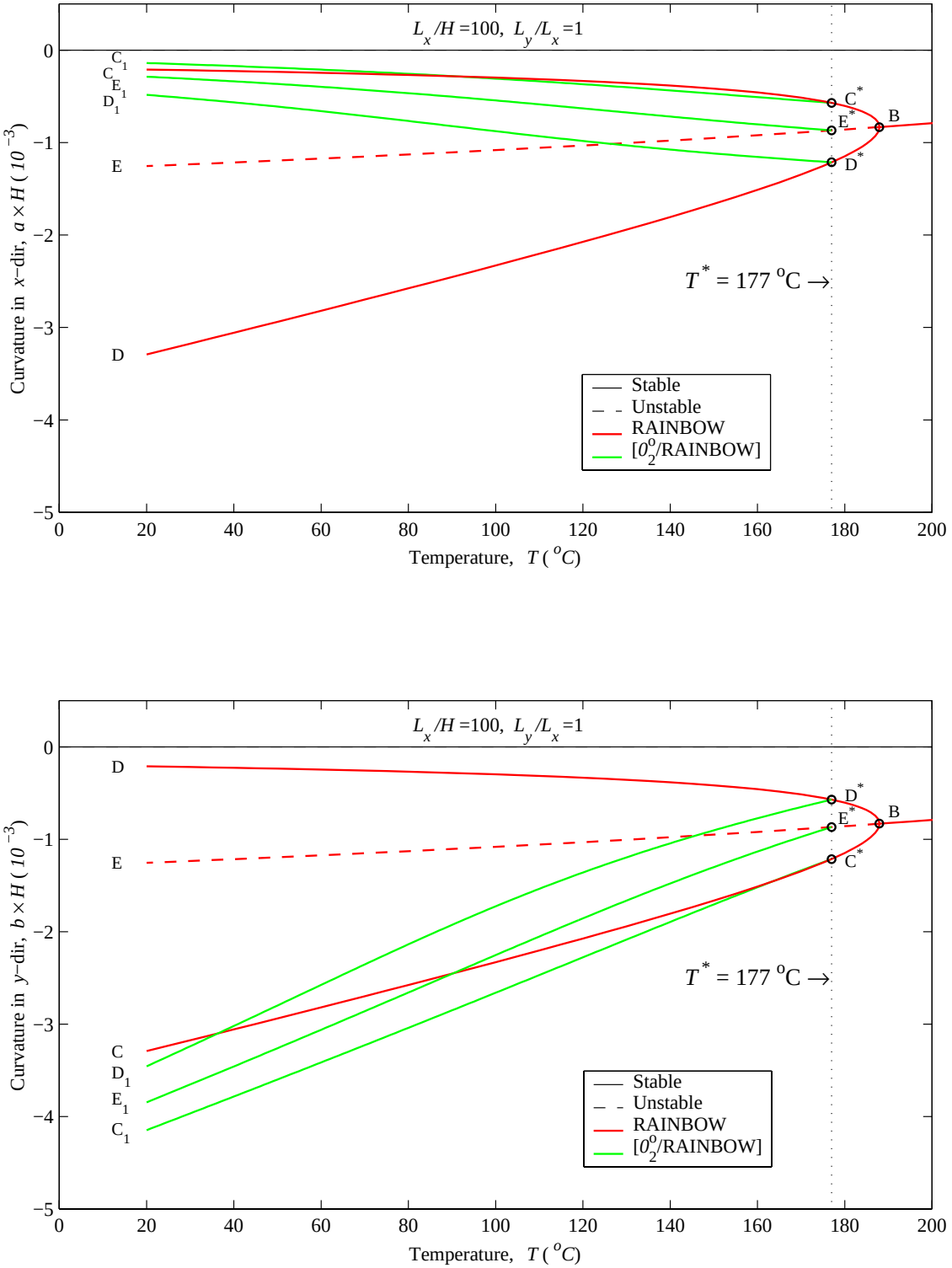


Figure 3.14: Temperature-curvature relation of rectangular [$0^o_2$/RAINBOW] ($L_y/L_x$=1, $L_x/H$=100, $H_r/H$=0.35).

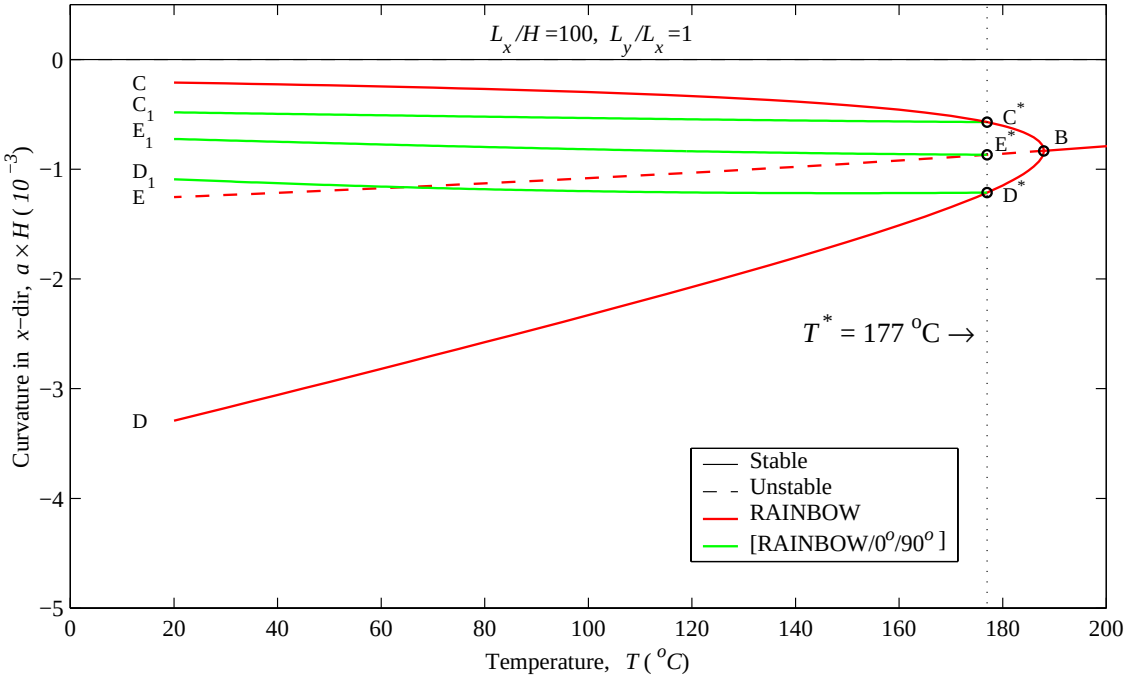


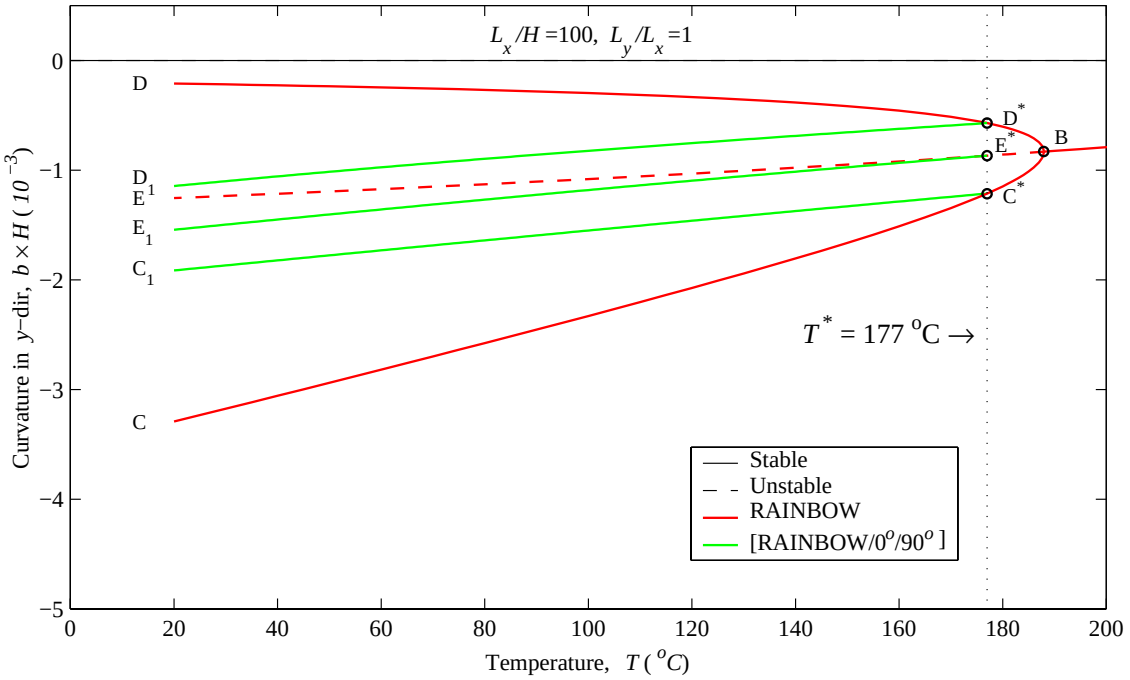


Figure 3.15: Temperature-curvature relation of rectangular [RAINBOW/$0^o$/$90^o$] ($L_y/L_x$=1, $L_x/H$=100, $H_r/H$=0.35).

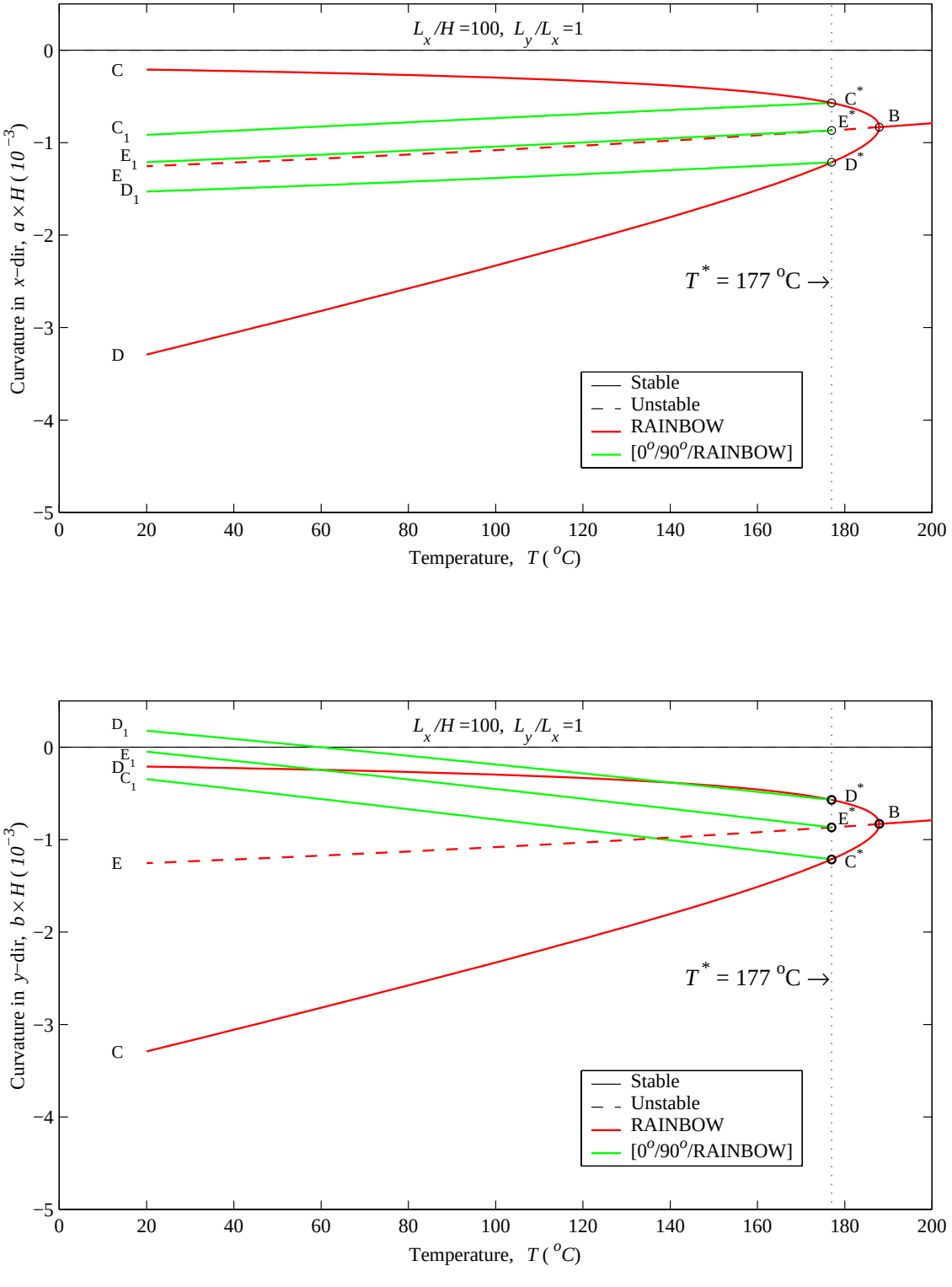


Figure 3.16: Temperature-curvature relation of rectangular [$0^o$/$90^o$/RAINBOW] ($L_y/L_x$=1, $L_x/H$=100, $H_r/H$=0.35).

Table 3.2: Room-temperature curvatures of various GRAPHBOW devices with $L_y/L_x$=1 (refer to Figures 3.11–3.16).

| Material | Solution originating from $C^*$ | | | Solution originating from $D^*$ | | | Solution originating from $E^*$ | | |
|---|---|---|---|---|---|---|---|---|---|
| | $a \times H$ ($10^{-3}$) | $b \times H$ ($10^{-3}$) | Stability state | $a \times H$ ($10^{-3}$) | $b \times H$ ($10^{-3}$) | Stability state | $a \times H$ ($10^{-3}$) | $b \times H$ ($10^{-3}$) | Stability state |
| RAINBOW | -0.2104 | -3.2921 | Stable | -3.2921 | -0.2104 | Stable | -1.2549 | -1.2549 | Unstable |
| [RAINBOW/$0^o$] | -1.8210 | -0.3002 | Stable | -2.3032 | -0.1779 | Stable | -2.0461 | -0.2407 | Stable |
| [$0^o$/RAINBOW] | -0.1000 | -4.1777 | Stable | -0.1898 | -3.9210 | Stable | -0.1445 | -4.0481 | Stable |
| [RAINBOW/$0_2^o$] | -1.3515 | -0.1061 | Stable | -1.8713 | -0.0050 | Stable | -1.5907 | -0.1447 | Stable |
| [$0_2^o$/RAINBOW] | -0.1393 | -4.1474 | Stable | -0.4841 | -3.4569 | Stable | -0.2872 | -3.8467 | Stable |
| [RAINBOW/$0^o$/$90^o$] | -0.4818 | -1.9146 | Stable | -1.0915 | -1.1449 | Stable | -0.7244 | -1.5438 | Stable |
| [$0^o$/$90^o$/RAINBOW] | -0.9157 | -0.3460 | Stable | -1.5289 | +0.1769 | Stable | -1.2111 | -0.0493 | Stable |

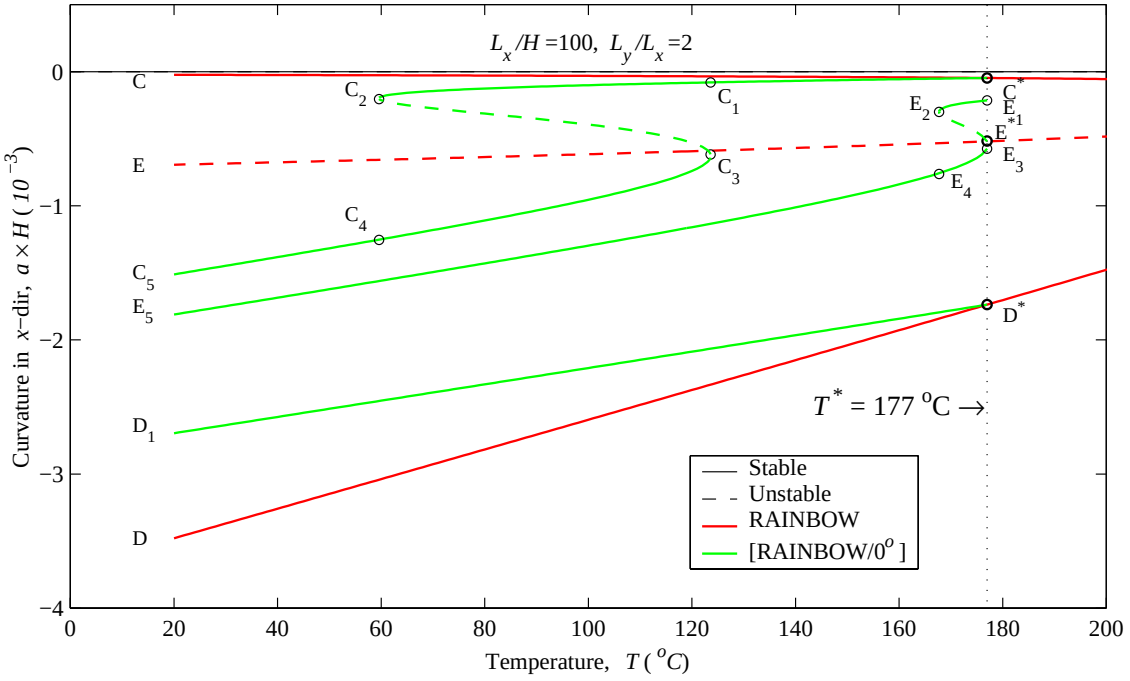


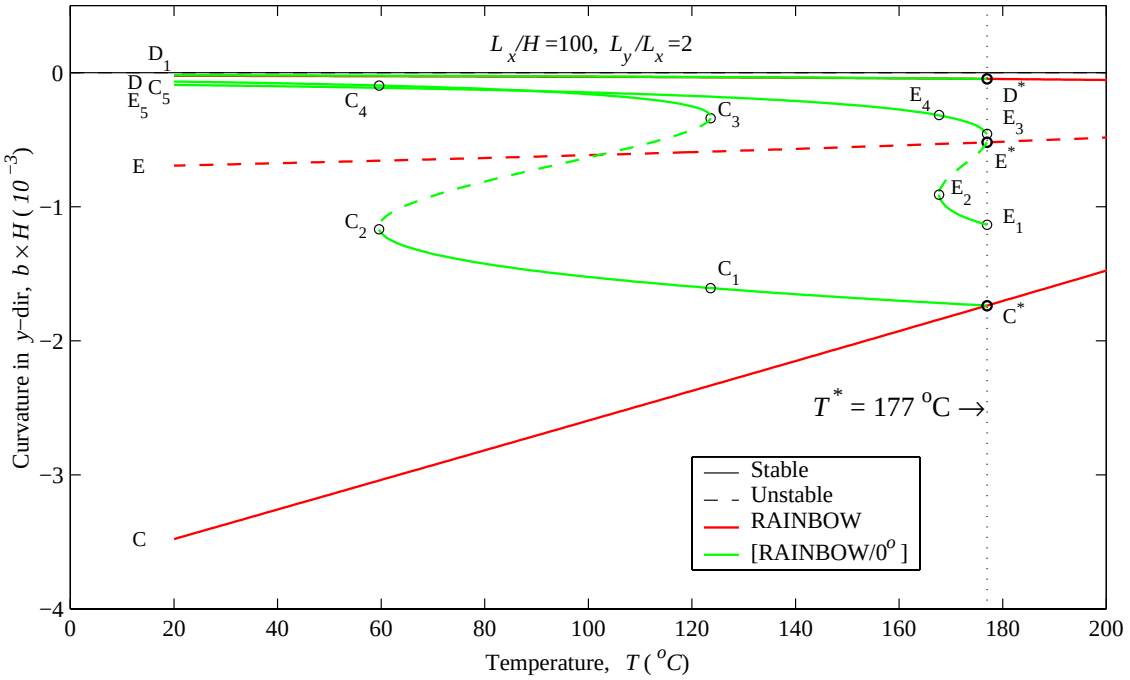


Figure 3.17: Temperature-curvature relation of rectangular [RAINBOW/$0^o$] ($L_y/L_x$=2, $L_x/H$=100, $H_r/H$=0.35).

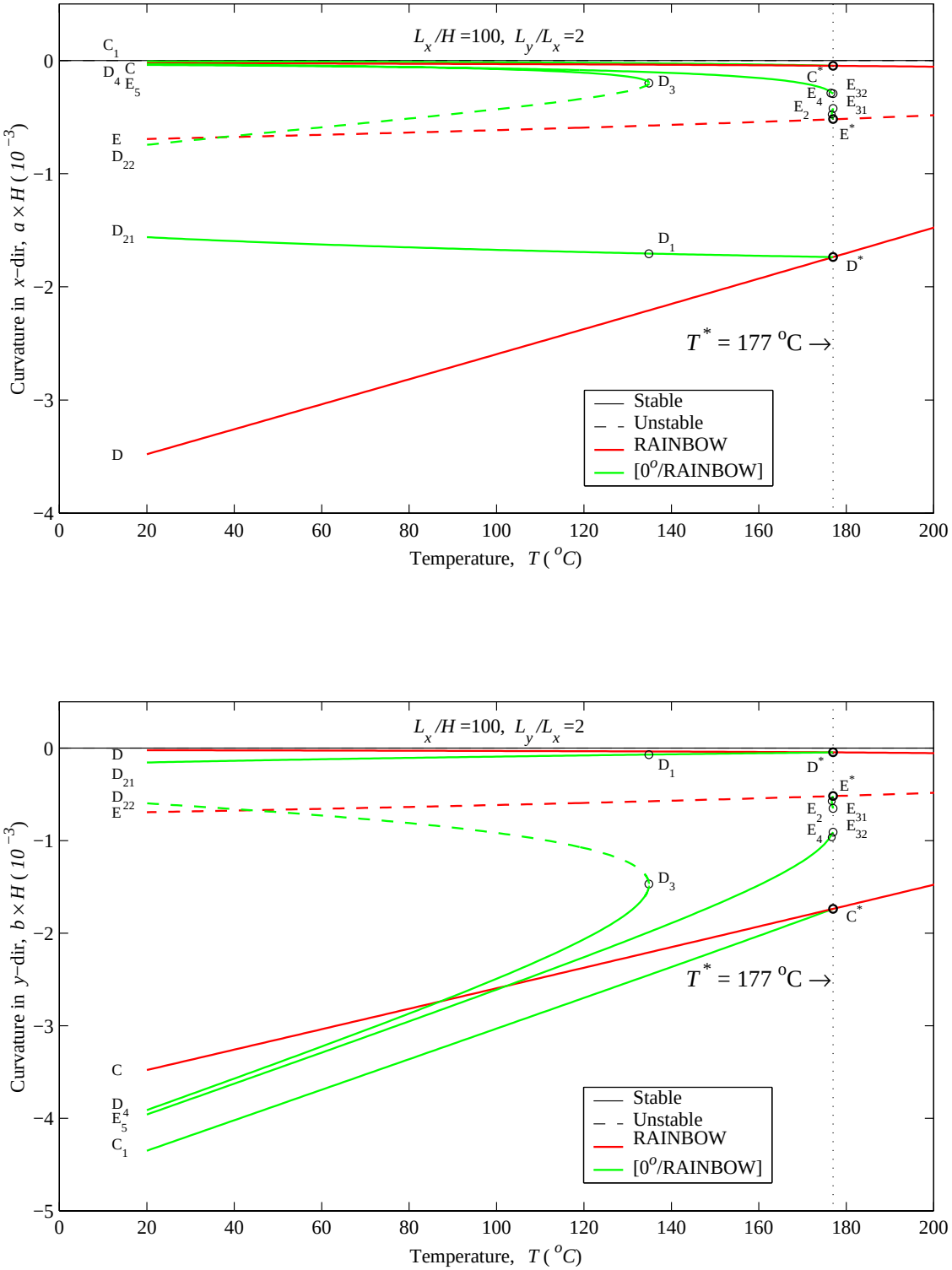


Figure 3.18: Temperature-curvature relation of rectangular [$0^o$/RAINBOW] ($L_y/L_x$=2, $L_x/H$=100, $H_r/H$=0.35).

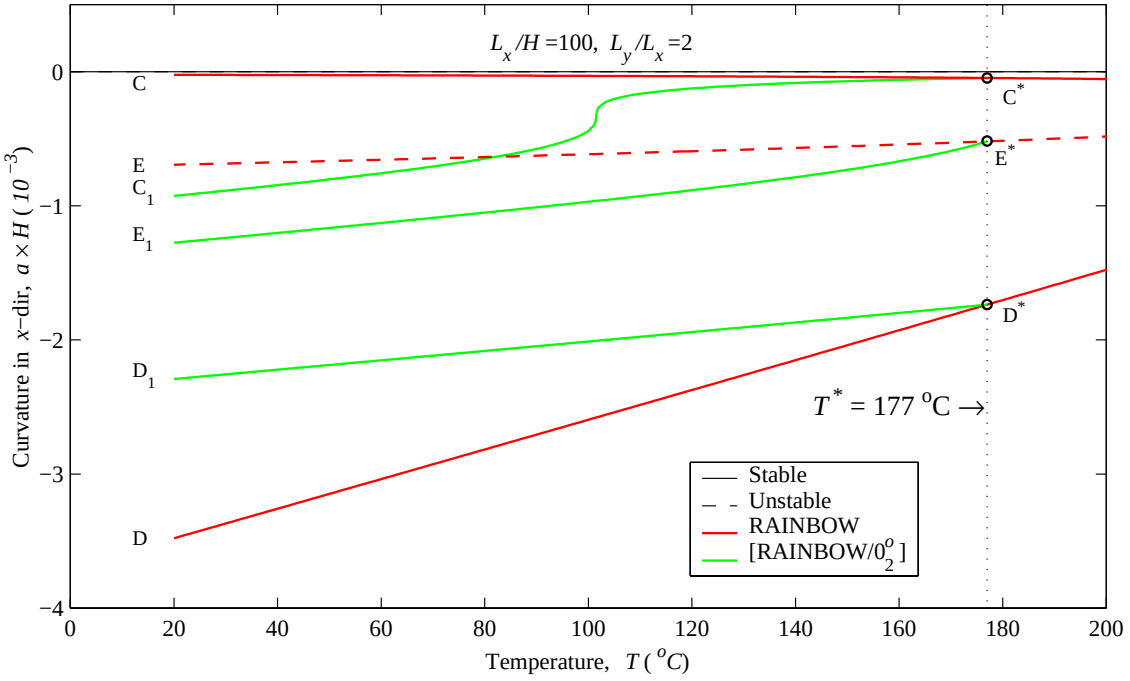


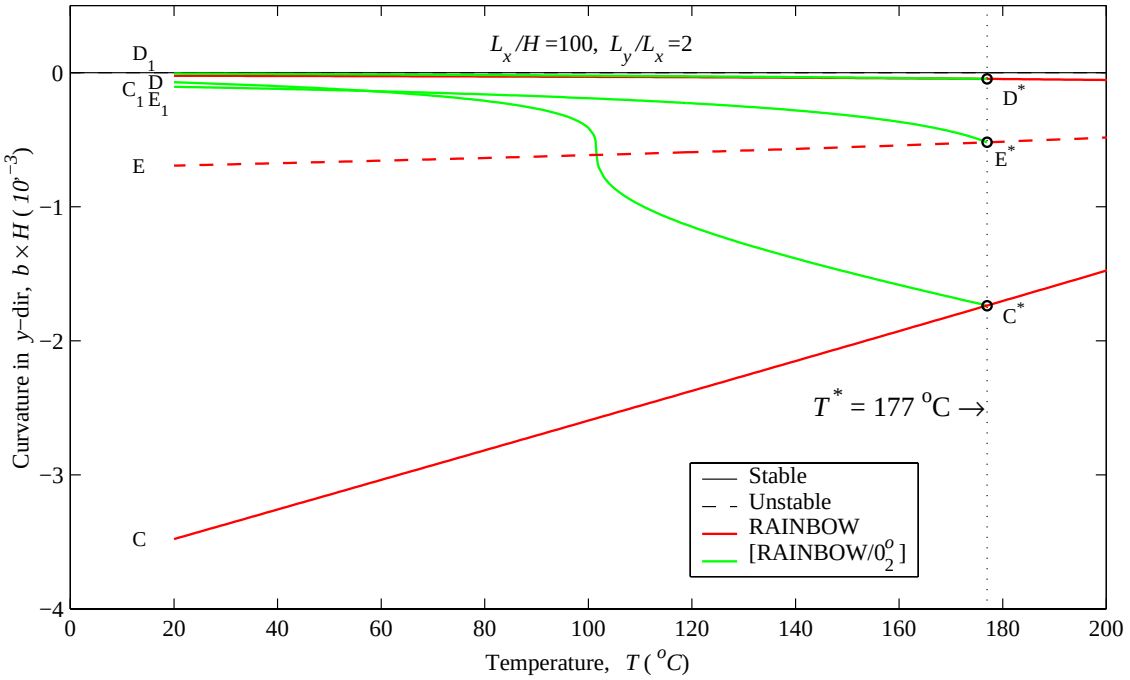


Figure 3.19: Temperature-curvature relation of rectangular [RAINBOW/$0_2^o$] ($L_y/L_x$=2, $L_x/H$=100, $H_r/H$=0.35).

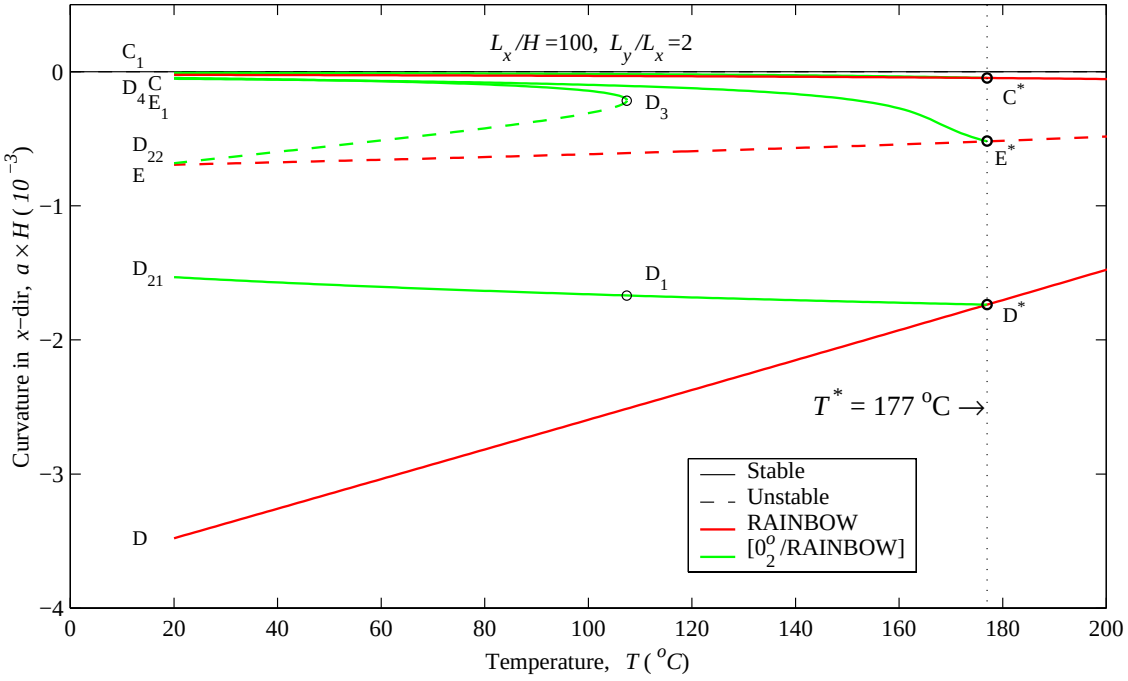


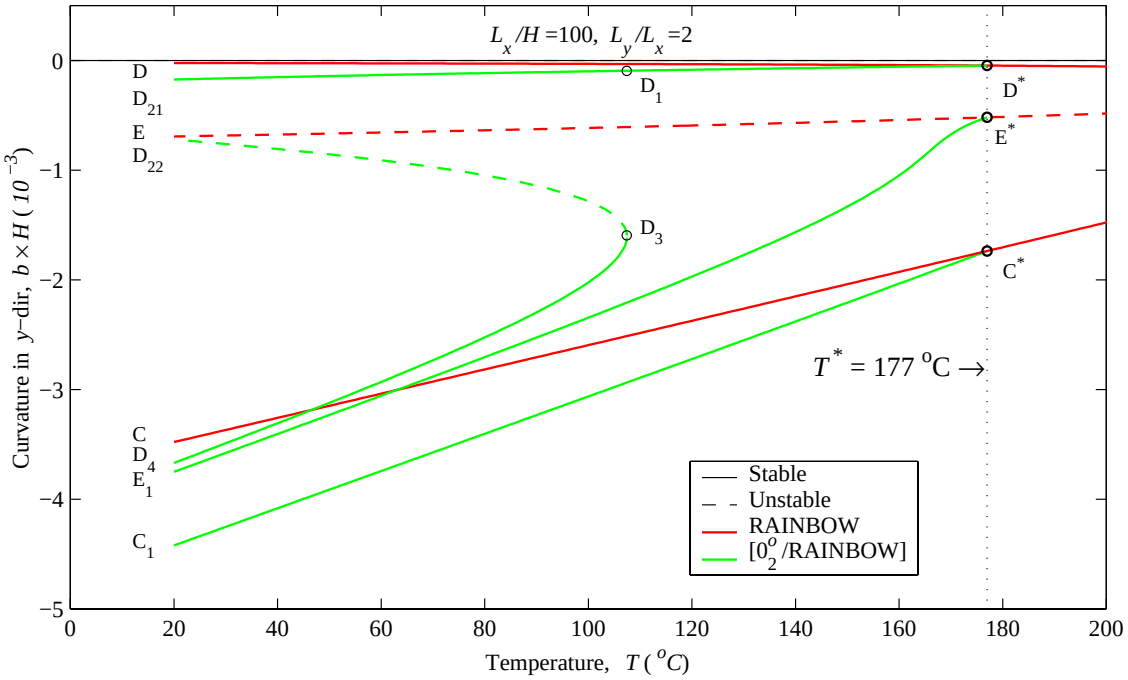


Figure 3.20: Temperature-curvature relation of rectangular $[0^o_2/\text{RAINBOW}]$ ($L_y/L_x$=2, $L_x/H$=100, $H_r/H$=0.35).

### 3.3.2 Application of an Electric Field

Figure 3.23 illustrates the relationship between the change in GRAPHBOW curvatures relative to their room-temperature values, $\Delta a$ and $\Delta b$, as a function of the electric field strength for the range $E$=$\pm$1.5 MV/m. It is assumed that the GRAPHBOW device is in a shape represented by a large negative curvature in the $y$ direction and a smaller curvature in the $x$ direction, point $C_1$ in Figure 3.3 ($L_x$=63.5 mm, $L_y$=38.1 mm, GRAPHBOW=[$0^o$/RAINBOW]). The polarity of the unreduced piezoceramic material is assumed to be as shown in Figure 2.5. Figure 3.23 shows that a reasonable change in the major curvature, $\Delta b$, can be achieved with a moderate field strength. For the case considered, a positive $E$ tends to flatten the [$0^o$/RAINBOW] actuator in the $y$ direction. As can be seen in Figure 3.23, the relationship between $\Delta b$, the major curvature, and $E$ is very close to being linear, and to first approximation, the relationship between $\Delta a$, the minor curvature, and $E$ is also linear. The slight nonlinearity in the relation between $\Delta a$ and $E$ may be unimportant since this curvature is smaller in magnitude than $b$. The linearity of the relation between $E$ and $\Delta a$ and $\Delta b$ could simplify an analysis of the dynamic behavior of GRAPHBOW actuators.

If GRAPHBOW is assumed to be in a shape corresponding to point $D_5$ in Figure 3.3, then the relationship between the change in its curvatures relative to their room-temperature values as a function of the electric field strength for the range $E$=$\pm$1.5 MV/m is illustrated in Figure 3.24. Again, as can be seen in Figure 3.24, a positive $E$ tends to flatten the [$0^o$/RAINBOW] actuator in the $y$ direction and that the relationship between $\Delta b$, the major curvature, and $E$ is very close to being linear. The change in the minor curvature, $\Delta a$, is somewhat higher than in the previous case, but nonetheless it is small in magnitude and is unimportant. However, it is important to note that for point $C_1$, Figure 3.23, $\Delta a$ is positive for positive $E$, while for point $D_5$, $\Delta a$ is negative for $E$. Although the GRAPHBOW equilibrium configuration corresponding to point $D_5$ in Figure 3.3 encountered a saddle node bifurcation at point $D_2$, the application of an electric up to +1.5 MV/m did not generate a sudden change in the shape, this due to the fact that the saddle node-bifurcation at point $D_3$ is away from room temperature. However, an electric field strength of +1.5 MV/m can push [$0^o$/RAINBOW] into the bistability zone ($D_4D_3$) and with the coupling of outside factors, such as change in temperature of service environment, can result in GRAPHBOW jumping to another shape with different features. Hence, proper care has to be taken when designing GRAPHBOW

actuators. Finally, GRAPHBOW is assumed to be in a shape corresponding to point $E_1$ in Figure 3.3, and the relationship between the change in curvatures, $\Delta a$ and $\Delta b$, and the electric field strength for the range $E$=±1.5 MV/m is illustrated in Figure 3.25. Figure 3.25 indicates that the relationship between $\Delta b$, the major curvature, and $E$ is very close to being linear; however, the change in the minor curvature, $\Delta a$ varies quadratically with $E$, but since it very small in magnitude it is negligible. This quadratic variation, however, is quite interesting; and provides a contrast with Figure 3.23 for point $C_1$, and Figure 3.24 for point $D_5$.

## 3.4 Chapter Summary

In this chapter, a multi-step thermoelastic analysis has been developed to model the addition of the composite layer. Numerical results were presented to illustrate the influence of the composite layer arrangements on the room-temperature shapes of GRAPHBOW. It was found that if the RAINBOW bifurcation temperature is lower than the composite cure temperature then, a unique stable GRAPHBOW shape is obtained for the case of $L_x/H$=100 and $L_y/L_x$=1/2. These shapes are near-cylindrical with larger curvature in the $x$ direction than in the $y$ direction for [RAINBOW/$0^o$], [RAINBOW/$0_2^o$], [$0^o$/$90^o$/RAINBOW], and with larger curvature in the $y$ curvature than in the $x$ direction for [$0^o$/RAINBOW] and [$0_2^o$/RAINBOW]. On the other hand, the shape of [RAINBOW/$0^o$/$90^o$] is more spherical. For larger GRAPHBOW ($L_x/H$=100, $L_y/L_x$=1), the RAINBOW bifurcation temperature is above the composite cure temperature, resulting in three stable room-temperature GRAPHBOW shapes. The unstable spherical RAINBOW configuration has been "converted" to a stable near-cylindrical configuration. The influence of the composite layer arrangements on room-temperature GRAPHBOW shapes seems to be similar to the case described above, except the fact that instead of having a unique room-temperature, three similar room-temperature configurations, which might be very hard to distinguish as being different, are obtained. For GRAPHBOW with $L_x/H$=100 and $L_y/L_x$=2, the bifurcation temperature of RAINBOW is much larger than the composite cure temperature, resulting in saddle-node bifurcations during the cooling to room temperature of [$0^o$/RAINBOW], [RAINBOW/$0^o$], and [$0_2^o$/RAINBOW]. From the results shown in this chapter, [RAINBOW/$0^o$/$90^o$] seems to be less likely to encounter saddle-node bifurcations. The presence of such bifurcations in the behavior of GRAPHBOW is

undesired if GRAPHBOW are to be used as actuators. Finally, it was shown that the relationship between the change in the major curvature and the electric field is very close to being linear for GRAPHBOW even in the presence of saddle-node bifurcations, if they are far away from room temperature. However, if the saddle-node bifurcation is close to room-temperature, the relationship will likely not be linear. In some cases, the change in the minor curvature can vary quadratically with the electric field, but since the variation is very small in magnitude it is not important.

In the next chapter, the model for predicting the manufactured shape and piezoelectric-induced deformations of disk-style RAINBOW will be presented. The methodology is similar to the one developed in Chapter 2 for rectangular RAINBOW, except the analysis is conducted in polar coordinates.

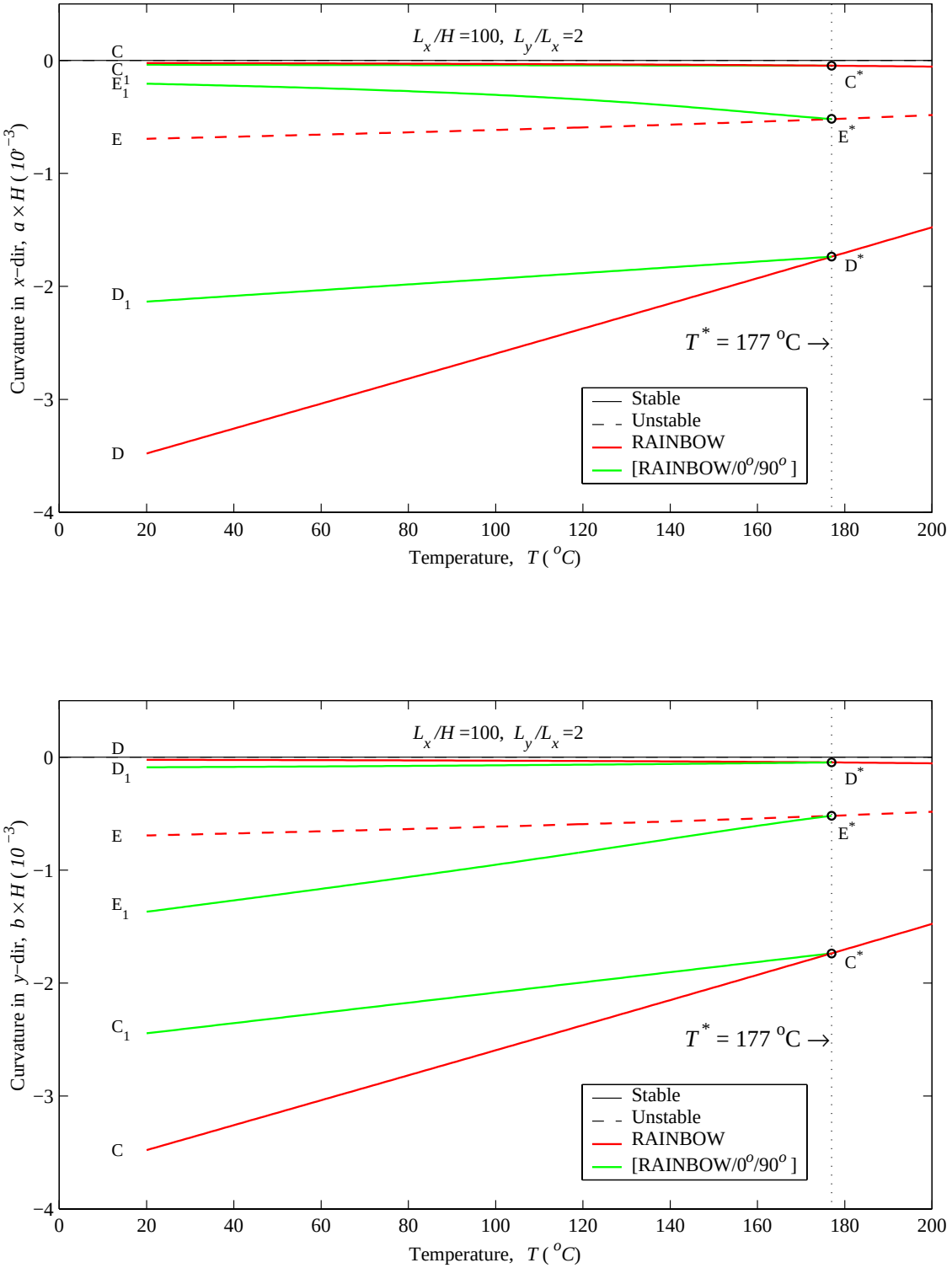


Figure 3.21: Temperature-curvature relation of rectangular [RAINBOW/$0^o$/$90^o$] ($L_y/L_x$=2, $L_x/H$=100, $H_r/H$=0.35).

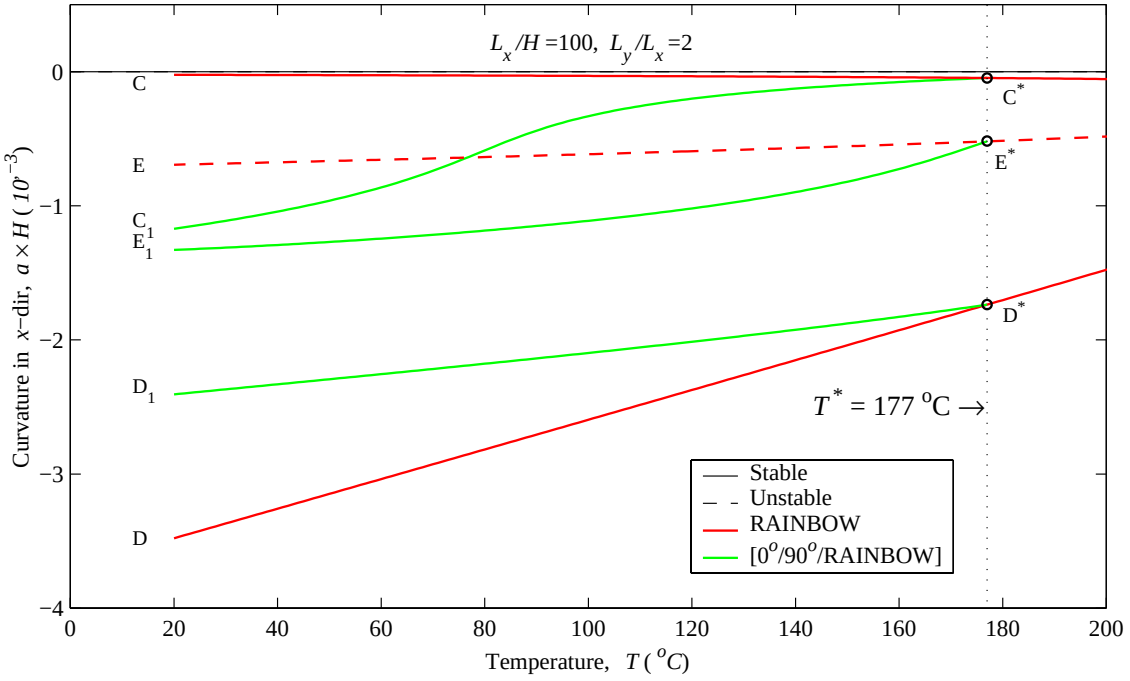


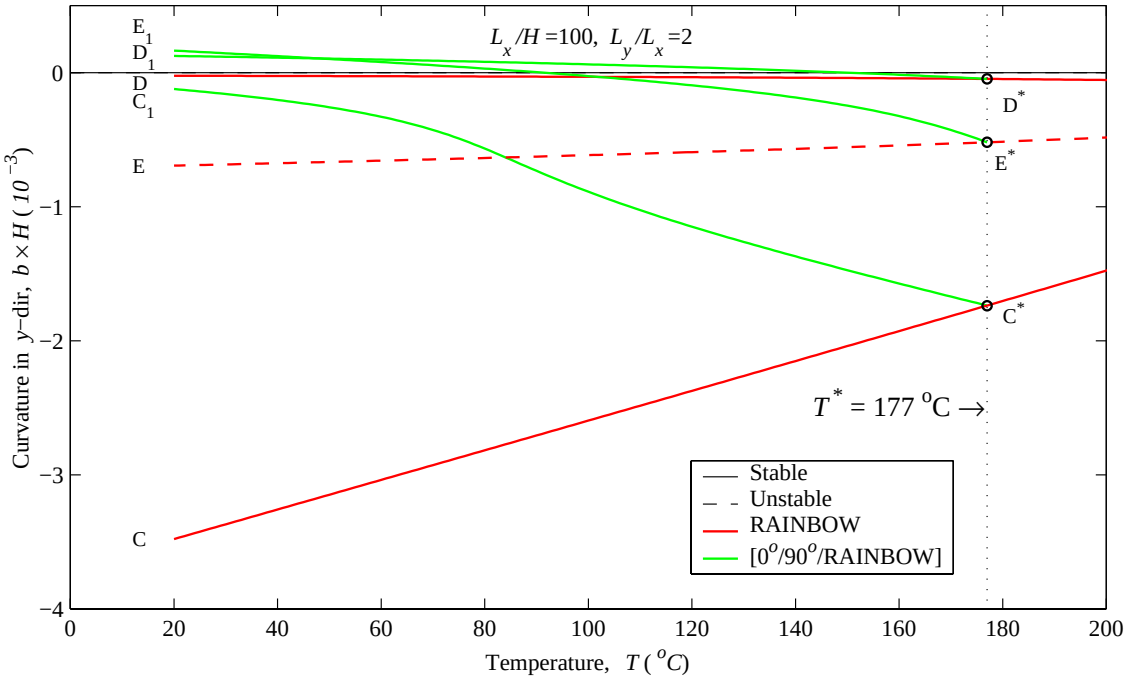


Figure 3.22: Temperature-curvature relation of rectangular [$0^o$/$90^o$/RAINBOW] ($L_y/L_x$=2, $L_x/H$=100, $H_r/H$=0.35).

Table 3.3: Room-temperature curvatures of various GRAPHBOW devices with $L_y/L_x$=2 (refer to Figures 3.17–3.22).

| Material | Solution originating from $C^*$ | | | Solution originating from $D^*$ | | | Solution originating from $E^*$ | | |
|---|---|---|---|---|---|---|---|---|---|
| | $a \times H$ ($10^{-3}$) | $b \times H$ ($10^{-3}$) | Stability state | $a \times H$ ($10^{-3}$) | $b \times H$ ($10^{-3}$) | Stability state | $a \times H$ ($10^{-3}$) | $b \times H$ ($10^{-3}$) | Stability state |
| RAINBOW | -0.0234 | -3.4790 | Stable | -3.4790 | -0.0234 | Stable | -0.6938 | -0.6938 | Unstable |
| [RAINBOW/$0^o$] | -1.5113 | -0.0664 | Stable† | -2.6955 | -0.0188 | Stable | -1.8108 | -0.0915 | Stable† |
| [$0^o$/RAINBOW] | -0.0083 | -4.3506 | Stable | -1.5612<br>-0.0318<br>-0.7453 | -0.1562<br>-3.9113<br>-0.5974 | Stable†<br>Stable<br>Unstable† | -0.0394 | -3.9594 | Stable† |
| [RAINBOW/$0_2^o$] | -0.9261 | -0.0716 | Stable | -2.2914 | -0.0069 | Stable | -1.2753 | -0.1057 | Stable |
| [$0_2^o$/RAINBOW] | -0.0088 | -4.4214 | Stable | -1.5320<br>-0.0468<br>-0.6827 | -0.1744<br>-3.6695<br>-0.7203 | Stable†<br>Stable<br>Unstable† | -0.0529 | -3.7504 | Stable |
| [RAINBOW/$0^o$/$90^o$] | -0.0385 | -2.4454 | Stable | -2.1349 | -0.0902 | Stable | -0.2063 | -1.3691 | Stable |
| [$0^o$/$90^o$/RAINBOW] | -1.1721 | -0.1221 | Stable | -2.4058 | +0.1245 | Stable | -1.3288 | +0.1645 | Stable |

† Saddle-node bifurcation encountered during cooling.

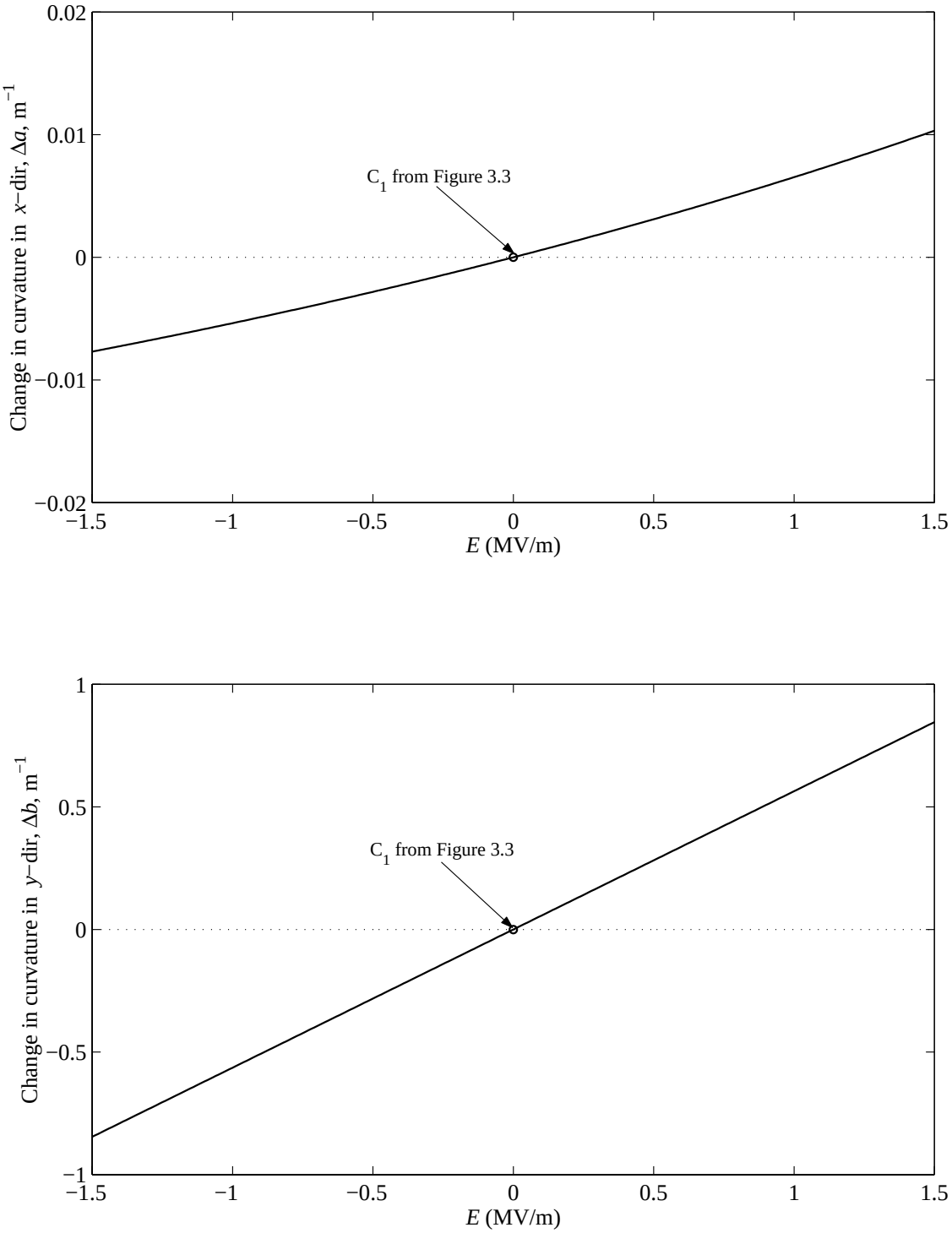


Figure 3.23: Variations of $a$ and $b$ as a function of $E$ for rectangular [$0^o$/RAINBOW] (refer to point $C_1$ in Figure 3.3).

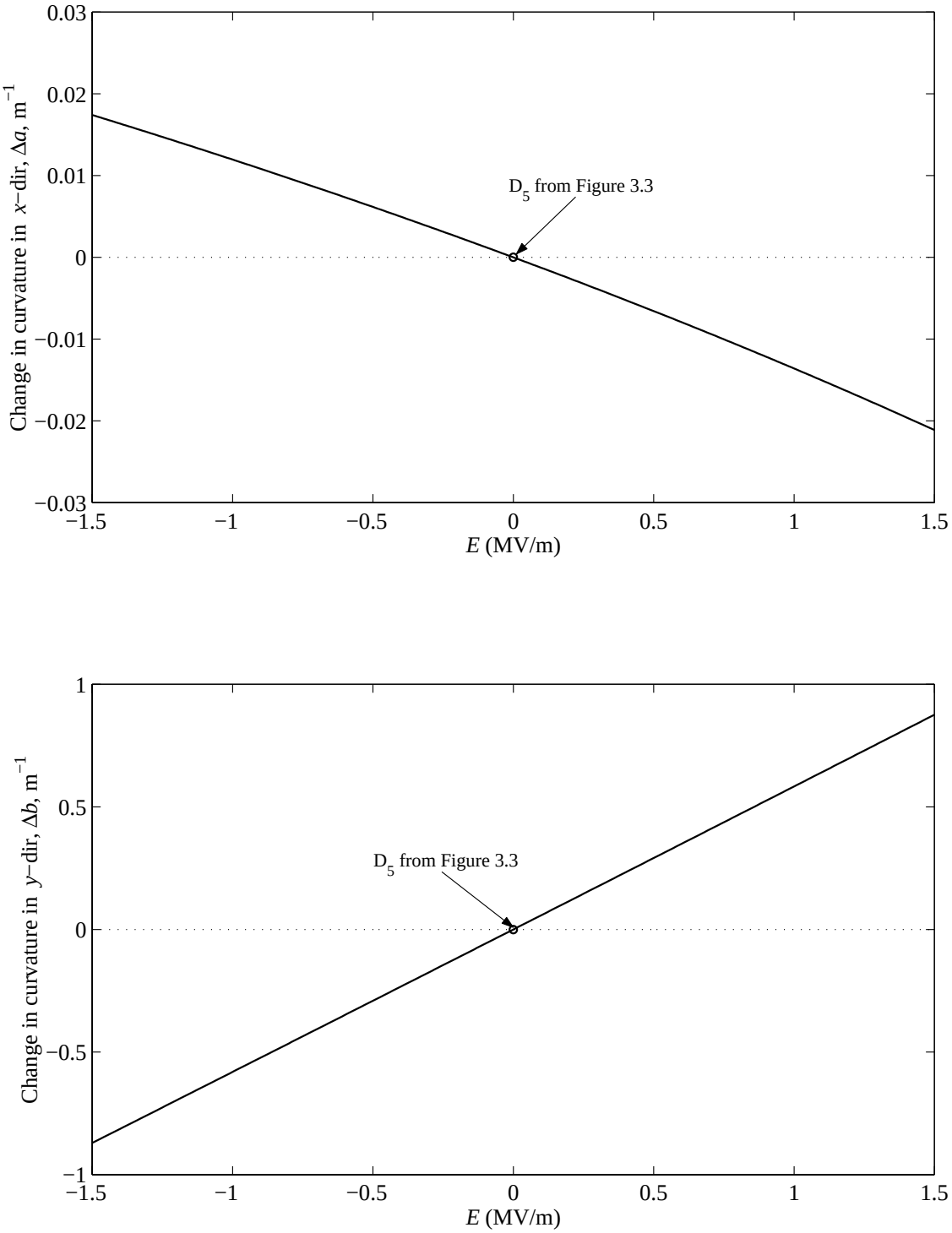


Figure 3.24: Variations of $a$ and $b$ as a function of $E$ for rectangular [$0^o$/RAINBOW] (refer to point $D_5$ in Figure 3.3).

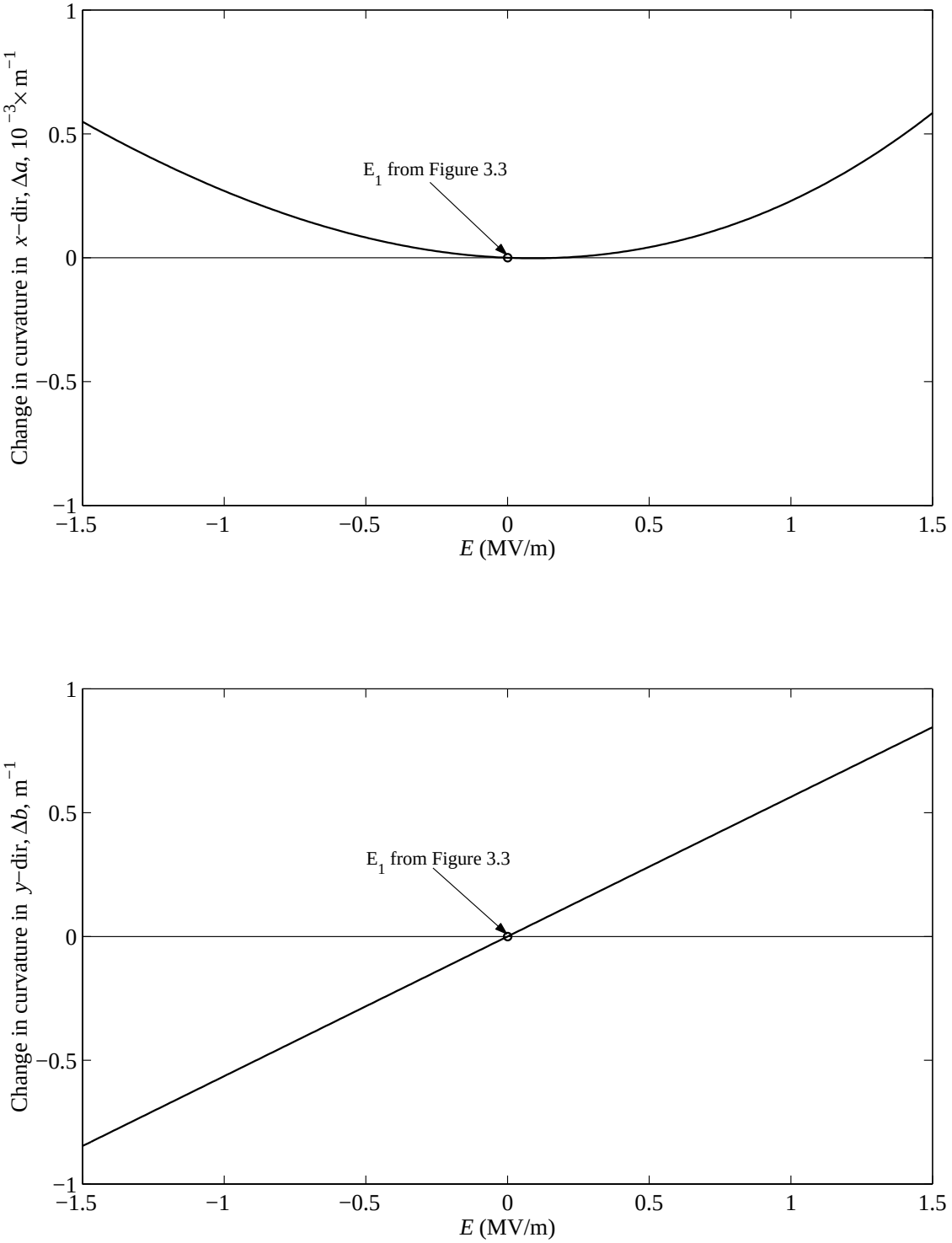


Figure 3.25: Variations of $a$ and $b$ as a function of $E$ for rectangular [$0^o$/RAINBOW] (refer to point $E_1$ in Figure 3.3).

# Chapter 4

# Disk-Style RAINBOW Actuators

## 4.1 Introduction

As has been shown in the last chapter, the geometry of rectangular RAINBOW and GRAPHBOW benders is quite important in determining the manufactured shape of the devices. As there are so-called critical length-to-thickness ratios, the geometry influences not only the manufactured shape, but also the actuation characteristics. This chapter examines disk-style benders, and since the disk provides a distinctively different geometry relative to the rectangle, differences in response might be expected. As with the last two chapters, this chapter discusses the theory developed to predict the manufacturing and piezoelectric-induced deformation characteristics of disk-style RAINBOW. Discussed are the key assumptions, the stress-strain relations, the strain-displacement relations, including geometric nonlinearities, total potential energy and variational methods. With the disk geometry, a possible deformation is one that is axisymmetric. Further, if geometric nonlinearities are assumed to be of negligible importance, then the conditions governing the axisymmetric problem are described by ordinary linear differential equations, which can be solved in closed form. In this chapter these axisymmetric solutions are developed and studied, in addition to the non-axisymmetric solutions. Qualitative and quantitative information regarding the deformation characteristics predicted by the developed theory is given.

## 4.2 Modeling Definitions and Assumptions

Figure 4.1 describes the geometry and nomenclature of the problem. RAINBOW is assumed to be made of $N$ thin layers of orthotropic materials, and each layer is assumed to be homogeneous. The disk device radius is $R$ and the total thickness, which is greatly exaggerated for clarity, is $H$. The layers can represent reduced and unreduced piezoceramic material. As seen in the figure, cylindrical coordinates are used, with $r$, $\theta$, and $z$ being the radial, circumferential, and through-thickness coordinates, respectively. The location $z = 0$ is the geometric midsurface, here taken to be the reference surface of the originally flat disk, and $\theta$ is measured from the $x$ axis of a rectangular coordinate system. The lower and upper boundaries of layer 1 are located at $z = z_o = -\frac{H}{2}$ and $z = z_1$ and the boundaries of layer 2 at $z_1$ and $z_2$, and in general, the boundaries of the $k^{th}$ layer at $z_{k-1}$ and $z_k$. The radial, circumferential, and out-of-plane displacements of the reference surface are denoted $u^o$, $v^o$, and $w^o$, respectively. Figure 4.2 illustrates the problem in question and defines the coordinate system in the study. Figure 4.2(a) illustrates RAINBOW flat at the Curie temperature. As RAINBOW cools from the Curie temperature, the through-the-thickness asymmetries in thermoelastic properties in the individual layers cause the actuator to deform into one of the shapes given by Figures 4.2(b), (c), and (d). The out-of-plane displacements are accompanied by inplane displacements (radial and tangential), but these are not evident to an observer. Figure 4.2(b) shows the cooled RAINBOW in an axisymmetric dome-like shape, and Figures 4.2(c) and 4.2(d) show RAINBOW in near-cylindrical shapes. All the assumptions in section 2.2 are considered to be valid for disk-style RAINBOW.

## 4.3 Axisymmetric Solution

If the individual layers in Figure 4.1 are assumed to be isotropic, the stress-strain relations and the final expression for the total potential energy simplify considerably. Additionally, it is possible to have axisymmetric response. Such a condition is characterized by having no circumferential displacement, $v^o$=0, and having all response variables independent of $\theta$. For this situation, the first variation of the total potential energy leads to ordinary differential equations. In this section, axisymmetric solutions of disk-style RAINBOW are considered. For the axisymmetric condition,

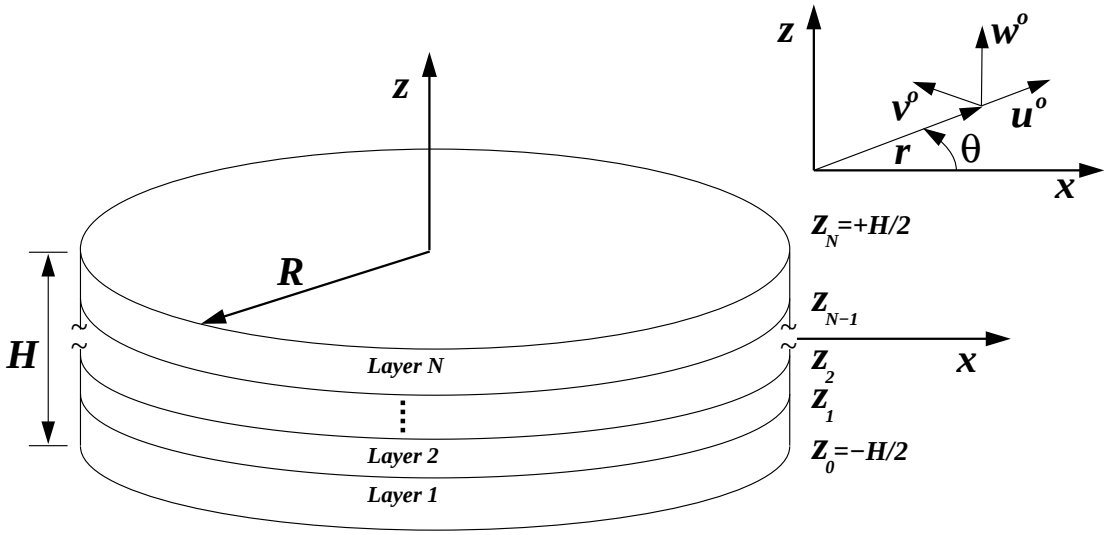


Figure 4.1: Geometry and nomenclature of disk-style RAINBOW considered.

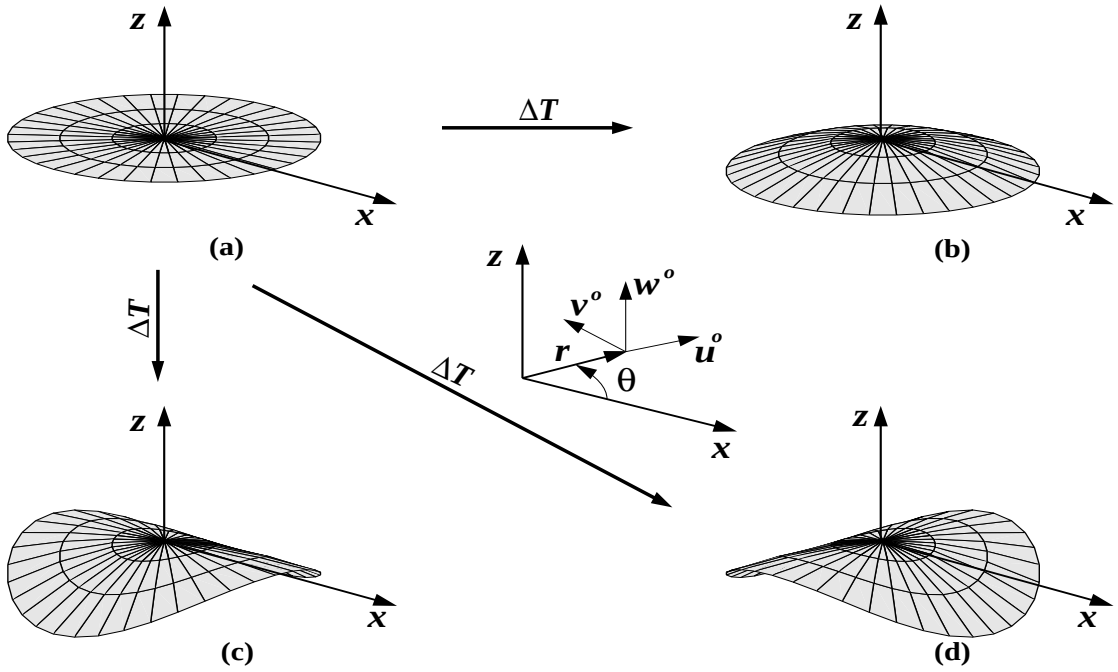


Figure 4.2: Disk-style RAINBOW shapes: (a) flat at the elevated reducing temperature, (b) axisymmetric dome-like shape at room temperature, (c) a near-cylindrical shape at room temperature, and (d) another near-cylindrical shape at room temperature.

the total potential energy for RAINBOW, which is assumed to be flat at the piezoceramic Curie temperature, and is then cooled, can be expressed as

$$\Pi = \frac{1}{2}\int_0^R \int_0^{2\pi} \int_{-H/2}^{+H/2} \left[(\sigma_r - \sigma^T)\epsilon_r + (\sigma_\theta - \sigma^T)\epsilon_\theta\right] r dr d\theta dz \tag{4.1}$$

where the integral is over the volume of the layered device and the stresses and strains have their usual notation. The stress-strain relation for a given isotropic layer is

$$\left\{ \begin{array}{c} \sigma_r \\ \sigma_\theta \end{array} \right\} = \left[ \begin{array}{cc} Q & \nu Q \\ \nu Q & Q \end{array} \right] \left\{ \begin{array}{c} \epsilon_r - \alpha\Delta T \\ \epsilon_\theta - \alpha\Delta T \end{array} \right\} \tag{4.2}$$

or

$$\begin{aligned} \sigma_r &= Q\epsilon_r + \nu Q\epsilon_\theta - \sigma^T \\ \sigma_\theta &= \nu Q\epsilon_r + Q\epsilon_\theta - \sigma^T \end{aligned} \tag{4.3}$$

In the above

$$Q = \frac{E}{1-\nu^2} \text{ and } \sigma^T = (1+\nu)Q\alpha\Delta T \tag{4.4}$$

where $E$ is the extensional modulus of the isotropic material and $\nu$ and $\alpha$ are the Poisson's ratio and the coefficient of thermal expansion, respectively. Due to the condition of axisymmetry and isotropy, there are no inplane shear effects. The inplane strains are given by

$$\epsilon_r = \frac{\partial u}{\partial r} + \frac{1}{2}\left(\frac{\partial w}{\partial r}\right)^2 \quad \epsilon_\theta = \frac{u}{r} \tag{4.5}$$

where the second term in $\epsilon_r$ reflects the nonlinear effects due to the rotations associated with out-of-plane displacements being greater than the disk thickness.

Because of the Kirchhoff hypothesis, the displacements are given as

$$\begin{aligned} u(r,z) &= u^o(r) + z\beta_r^o(r) \\ w(r,z) &= w^o(r) \end{aligned} \tag{4.6}$$

where the out-of-plane rotation of the reference surface, $\beta_r^o$, is defined by

$$\beta_r^o(r) = -\frac{dw^o(r)}{dr} \tag{4.7}$$

Substituting the displacements of Equation (4.6) into the strains of Equation (4.5) leads to

$$\begin{aligned} \epsilon_r(r,z) &= \epsilon_r^o(r) + z\kappa_r^o(r \\ \epsilon_\theta(r,z) &= \epsilon_\theta^o(r) + z\kappa_\theta^o(r) \end{aligned} \tag{4.8}$$

where

$$\begin{aligned} \epsilon_r^o &= \frac{du^o}{dr} + \underline{\frac{1}{2}\left(\frac{dw^o}{dr}\right)^2} \quad \kappa_r^o = \frac{d\beta_r^o}{dr} = -\frac{d^2w^o}{dr^2} \\ \epsilon_\theta^o &= \frac{u^o}{r} \qquad\qquad\qquad\quad \kappa_\theta^o = \frac{\beta_r^o}{r} = -\frac{1}{r}\frac{dw^o}{dr} \end{aligned} \tag{4.9}$$

where the underlined term represents the effect of geometric nonlinearities. Substituting the expressions of Equations (4.8) and (4.9), in turn, into the total potential energy expression, Equation (4.1), and integrating through the thickness, and with respect to $\theta$, results in

$$\Pi = \pi \int_0^R \left\{(N_r - N^T)\epsilon_r^o + (M_r - M^T)\kappa_r^o + (N_\theta - N^T)\epsilon_\theta^o + (M_\theta - M^T)\kappa_\theta^o\right\} r dr \tag{4.10}$$

In the above, the force and moment resultants are given by

$$\begin{aligned} N_r &\equiv \int_{-\frac{H}{2}}^{+\frac{H}{2}} \sigma_r dz = A\epsilon_r^o + A_\nu \epsilon_\theta^o + B\kappa_r^o + B_\nu \kappa_\theta^o - \hat{N}^T \Delta T \\ N_\theta &\equiv \int_{-\frac{H}{2}}^{+\frac{H}{2}} \sigma_\theta dz = A_\nu \epsilon_r^o + A\epsilon_\theta^o + B_\nu \kappa_r^o + B\kappa_\theta^o - \hat{N}^T \Delta T \\ M_r &\equiv \int_{-\frac{H}{2}}^{+\frac{H}{2}} z\sigma_r dz = B\epsilon_r^o + B_\nu \epsilon_\theta^o + D\kappa_r^o + D_\nu \kappa_\theta^o - \hat{M}^T \Delta T \\ M_\theta &\equiv \int_{-\frac{H}{2}}^{+\frac{H}{2}} z\sigma_\theta dz = B_\nu \epsilon_r^o + B\epsilon_\theta^o + D_\nu \kappa_r^o + D\kappa_\theta^o - \hat{M}^T \Delta T \end{aligned} \tag{4.11}$$

The $A$s, $B$s, $D$s, $\hat{N}^T$, and $\hat{M}^T$ are strictly functions of layer material properties and geometry and

are given by

$$\begin{aligned}
A &= \sum_{k=1}^{N} \frac{E_k}{1-\nu_k^2}(z_k - z_{k-1}) \\
A_\nu &= \sum_{k=1}^{N} \frac{\nu_k E_k}{1-\nu_k^2}(z_k - z_{k-1}) \\
B &= \frac{1}{2}\sum_{k=1}^{N} \frac{E_k}{1-\nu_k^2}(z_k^2 - z_{k-1}^2) \\
B_\nu &= \frac{1}{2}\sum_{k=1}^{N} \frac{\nu_k E_k}{1-\nu_k^2}(z_k^2 - z_{k-1}^2) \\
D &= \frac{1}{3}\sum_{k=1}^{N} \frac{E_k}{1-\nu_k^2}(z_k^3 - z_{k-1}^3) \\
D_\nu &= \frac{1}{3}\sum_{k=1}^{N} \frac{\nu_k E_k}{1-\nu_k^2}(z_k^3 - z_{k-1}^3) \\
\hat{N}^T &= \sum_{k=1}^{N} \frac{E_k \alpha_k}{1-\nu_k}(z_k - z_{k-1}) \\
\hat{M}^T &= \frac{1}{2}\sum_{k=1}^{N} \frac{E_k \alpha_k}{1-\nu_k}(z_k^2 - z_{k-1}^2)
\end{aligned} \tag{4.12}$$

where the subscripts on the material properties merely identify the material properties with a particular layer number.

Substituting the strains of Equation (4.9) into Equation (4.11), then Equation (4.10), and taking the first variation of Equation (4.10) with respect to $u^o$ and $w^o$ results in the following Euler-Lagrange equations and boundary conditions which govern equilibrium:

$$\begin{aligned}
&\frac{d(rN_r)}{dr} - N_\theta = 0 \\
&\frac{d}{dr}\left(\frac{d(rM_r)}{dr} + \underline{rN_r\frac{dw^o}{dr}} - M_\theta\right) = 0
\end{aligned} \tag{4.13}$$

and at $r = 0$ and $R$

$$\begin{aligned} &(rN_r)\,\delta u^o = 0 \\ &\left(\frac{d(rM_r)}{dr} + \underline{rN_r\frac{dw^o}{dr}} - M_\theta\right)\delta w^o = 0 \\ &(rM_r)\,\delta\left(\frac{dw^o}{dr}\right) = 0 \end{aligned} \tag{4.14}$$

The expression in parenthesis in the second equation of Equations (4.13) and (4.14) can be identified with the transverse shear force resultant. The underlined terms in the equations denote the contributions of the geometric nonlinearities. At $r = R$ the terms in parenthesis in the equations of Equation (4.14) should be set to zero, as that represents a traction-free outer boundary of the disk. From kinematic arguments, $u^o$, $w^o$, and $dw^o/dr$ ($=-\beta_r^o$) should be set to zero at $r = 0$. The problem is thus completely specified.

### 4.3.1 Linear Case

If the geometrically nonlinear terms in the reference surface strain in Equation (4.9), and hence in the equations of Equations (4.13) and (4.14) are eliminated, the equations governing equilibrium become

$$\begin{aligned} &A\left(u - r\frac{du}{dr} - r^2\frac{d^2u}{dr^2}\right) + B\left(r^2\frac{d^3w}{dr^3} + r\frac{d^2w}{dr^2} - \frac{dw}{dr}\right) = 0 \\ &B\left(-u + r\frac{du}{dr} - 2r^2\frac{d^2u}{dr^2}\right) + D\left(r^3\frac{d^4w}{dr^4} + 2r^2\frac{d^3w}{dr^3} - r\frac{d^2w}{dr^2} + \frac{dw}{dr}\right) = 0 \end{aligned} \tag{4.15}$$

where the superscript 'o' has been dropped for convenience of notation. The solution to these equations is

$$\begin{aligned} u^o(r) &= \frac{c_{-1}^l}{r} + c_1^l r \\ w^o(r) &= a_0^l + a_2^l r^2 + a_3^l \ln(r) \end{aligned} \tag{4.16}$$

where $c_{-1}^l$, $c_1^l$, $a_0^l$, $a_2^l$, and $a_3^l$ are constants and the superscript $l$ denotes the linear solution. The kinematic conditions at $r = 0$ require that

$$c_{-1}^l = a_0^l = a_3^l = 0 \tag{4.17}$$

and the traction-free conditions at $r = R$ lead to

$$\begin{aligned} c_1^l &= \frac{\left(B\,\hat{M}^T - D\,\hat{N}^T + \hat{M}^T\,B_\nu - \hat{N}^T\,D_\nu\right)\Delta T}{B^2 - A\,D + 2\,B\,B_\nu + {B_\nu}^2 - A\,D_\nu - A_\nu\,(D + D_\nu)} \\ a_2^l &= \frac{\left(A\,\hat{M}^T - B\,\hat{N}^T + \hat{M}^T\,A_\nu - \hat{N}^T\,B_\nu\right)\Delta T}{2\,\left(B^2 - A\,D + 2\,B\,B_\nu + {B_\nu}^2 - A\,D_\nu - A_\nu\,(D + D_\nu)\right)} \end{aligned} \tag{4.18}$$

The linear problem is thus solved in closed form.

### 4.3.2 Nonlinear Case

When the geometrically nonlinear term in the strain-displacement relation of Equation (4.9), and thus the underlined terms in Equations (4.13) and (4.14), are retained, the problem is more difficult to solve in closed form. However, approximate methods can be used. Two such methods are used here.

#### 4.3.2.1 Shooting Method

The first method used is strictly a numerical method and relies on formatting the governing equations as first-order differential equations. The particular approach is effective for solving a two-point boundary value problem ($r$=0, $r$=$R$) and is called the shooting method. If the transverse shear force resultant $Q_r$ is formally defined by

$$Q_r = \frac{1}{r}\left(\frac{d(rM_r)}{dr} - rN_r\beta_r^o - M_\theta\right) \tag{4.19}$$

then the definition can be rewritten as

$$\frac{d(rM_r)}{dr} = rQ_r + M_\theta + rN_r\beta_r^o \tag{4.20}$$

After substitution for the strains in Equation (4.11), and dropping the superscript 'o', the force and moments resultants can be rewritten as

$$\begin{aligned}
N_r &= A(\frac{du}{dr} + \frac{\beta_r^2}{2}) + A_\nu\frac{u}{r} + B\frac{d\beta_r}{dr} + B_\nu\frac{\beta_r}{r} - \hat{N}^T\Delta T \\
N_\theta &= A_\nu(\frac{du}{dr} + \frac{\beta_r^2}{2}) + A\frac{u}{r} + B_\nu\frac{d\beta_r}{dr} + B_\nu\frac{\beta_r}{r} - \hat{N}^T\Delta T \\
M_r &= B(\frac{du}{dr} + \frac{\beta_r^2}{2}) + B_\nu\frac{u}{r} + D\frac{d\beta_r}{dr} + D_\nu\frac{\beta_r}{r} - \hat{M}^T\Delta T \\
M_\theta &= B_\nu(\frac{du}{dr} + \frac{\beta_r^2}{2}) + B\frac{u}{r} + D_\nu\frac{d\beta_r}{dr} + D_\nu\frac{\beta_r}{r} - \hat{M}^T\Delta T
\end{aligned} \tag{4.21}$$

Solving Equation (4.21) for $du/dr$, $d\beta_r/dr$, $N_\theta$, and $M_\theta$ in terms of $N_r$, $M_r$, $u$, $\beta_r$, $\hat{N}^T\Delta T$, $\hat{M}^T\Delta T$ and substituting the expressions for $N_\theta$ and $M_\theta$ into Equations (4.13) and (4.20), respectively, yields a system of six nonlinear first-order equations:

$$\begin{aligned}
\frac{d\mathcal{N}_r}{dr} &= \frac{1}{(B^2-AD)\,r}\Big[(B^2-AD)(B\beta_r-\hat{N}^T\Delta Tr+Au)+DuA_\nu{}^2-B\beta_rB_\nu{}^2 \\
&+ A_\nu((B\hat{M}^T-D\hat{N}^T)\Delta Tr+B\mathcal{M}_r-D\mathcal{N}_r+(\beta_rD-2Bu)B_\nu-B\beta_rD_\nu) \\
&+ B_\nu(-A\hat{M}^T\Delta Tr+B\hat{N}^T\Delta Tr-A\mathcal{M}_r+B\mathcal{N}_r+A\beta_rD_\nu)+AuB_\nu{}^2\Big] \\
\frac{d\mathcal{Q}_r}{dr} &= 0 \\
\frac{d\mathcal{M}_r}{dr} &= \frac{1}{(B^2-AD)r}\Big[(B^2-AD)(\beta_r(D+r\mathcal{N}_r)+r(\mathcal{Q}_r-\hat{M}^T\Delta T)+Bu)+A\beta_rD_\nu^2 \\
&+ B_\nu((B\hat{M}^T-D\hat{N}^T)\Delta Tr+B\mathcal{M}_r+D(uA_\nu-\mathcal{N}_r)+D_\nu(Au-2B\beta_r)) \\
&- D_\nu((A\hat{M}^T-B\hat{N}^T)\Delta Tr+A\mathcal{M}_r-B\mathcal{N}_r+BuA_\nu)+(\beta_rD-Bu)B_\nu{}^2\Big]
\end{aligned} \tag{4.22}$$

$$\begin{aligned}
\frac{dw}{dr} &= -\beta_r \\
\frac{du}{dr} &= \frac{1}{2\,(B^2-AD)\,r}\Big[-(B^2-AD)\beta_r{}^2 r-2DuA_\nu-2\beta_r DB_\nu+2BuB_\nu \\
&+ \; 2D\mathcal{N}_r-2B\mathcal{M}_r-2B\hat{M}^T\Delta Tr+2D\hat{N}^T\Delta Tr+2B\beta_r D_\nu\Big]
\end{aligned}$$

$$\frac{d\beta_r}{dr} = \frac{(B\hat{N}^T-A\hat{M}^T)\Delta Tr-A\mathcal{M}_r+B(\mathcal{N}_r+uA_\nu)-(B\beta_r-Au)B_\nu+A\beta_r D_\nu}{(B^2-AD)\,r}$$

where

$$\begin{aligned}
\mathcal{N}_r &= rN_r \\
\mathcal{M}_r &= rM_r \\
\mathcal{Q}_r &= rQ_r
\end{aligned} \tag{4.23}$$

The boundary conditions are as with the linear case, namely,

$$\begin{aligned}
u=0, \quad w=0, \quad \text{and} \quad \beta_r=0 \quad \text{at} \quad r=0 \\
N_r=0, \quad M_r=0, \quad \text{and} \quad Q_r=0 \quad \text{at} \quad r=R
\end{aligned} \tag{4.24}$$

Approximate solutions to the above system of differential equations and boundary conditions are obtained using an IMSL multiple shooting method subroutine (DBVPMS) [40] which avoids the serious ill-conditioning problems encountered when having to compute a Jacobian.

#### 4.3.2.2 Rayleigh-Ritz Method

The second method used is the Rayleigh-Ritz approach used in the previous chapters. Since there is no *a priori* reason to expect the solution to the linear problem to approximate the solution to the geometrically nonlinear problem, extending the functional form of the approximate solution is in order. In that context, then, the solution could be assumed to be of the following form:

$$u^\circ(r) = c_1 r + c_2 r^2 \quad \text{and} \quad w^\circ(r) = a_2 r^2 + a_3 r^3 \tag{4.25}$$

where the superscript 'o' has been reintroduced. The coefficients $c_1$, $c_2$, $a_2$, and $a_3$ are solved for from the four algebraic equations that result from setting the derivatives of the total potential energy with respect to $c_1$, $c_2$, $a_2$, and $a_3$ to zero. The issue to be considered when adding more terms to the expressions for $u^\circ(r)$ and $w^\circ(r)$ is whether the addition of one more term to each expression changes the behavior of the predicted variation of $u^\circ(r)$ and $w^\circ(r)$ with $r$, or whether the addition of one more term changes the value of $w^\circ(r)$ at, for example, $r = R$. If additional terms make little difference, then the problem can, in some sense, be considered converged. Convergence of the solution and the influence of geometric nonlinearities on the axisymmetric response will be discussed in the next section.

## 4.4 General Solutions

In this section, the approximate theory for predicting the non-axisymmetric room-temperature shapes of disk-style RAINBOW, as depicted in Figure 4.2(c) and (d), is presented. The axisymmetric case of the previous section is included as a subset of possible solutions for the non-axisymmetric case. Again, approximate displacement fields and the Rayleigh-Ritz approach along with variational methods are used to minimize the total potential energy. The axisymmetric solution is included because it may well represent a maximum energy state, an unstable condition. Thus combining non-axisymmetric and axisymmetric solutions provides a new view of the axisymmetric solutions. This view was not possible with the model developed in the last section, since the axisymmetric solution was the only one considered.

### 4.4.1 Total Potential Energy

Assuming the Kirchhoff hypothesis is valid, the radial, tangential, and out-of-plane displacements are given, respectively, as

$$\begin{aligned} u(r,\theta,z) &= u^o(r,\theta) + z\beta_r^o \\ v(r,\theta,z) &= v^o(r,\theta) + z\beta_\theta^o \\ w(r,\theta,z) &= w^o(r,\theta) \end{aligned} \tag{4.26}$$

where

$$\beta_r^o = -\frac{\partial w^o}{\partial r} \text{ and } \beta_\theta^o = -\frac{1}{r}\frac{\partial w^o}{\partial \theta} \tag{4.27}$$

are identified with the the out-of-plane rotations of the reference surface. Furthermore, assuming that the the out-of-plane deflections develop only because of the asymmetries in the material properties relative to the geometric midplane of RAINBOW, the total potential energy can be written as

$$\Pi = \frac{1}{2}\int_0^R \int_0^{2\pi} \int_{-H/2}^{H/2} \left\{(\sigma_r - \sigma_r^T)\epsilon_r + (\sigma_\theta - \sigma_\theta^T)\epsilon_\theta + (\tau_{r\theta} - \tau_{r\theta}^T)\gamma_{r\theta}\right\} dr\, d\theta\, dz \tag{4.28}$$

The strains in the energy expression are given by the Kirchhoff hypothesis as

$$\begin{aligned} \epsilon_r &= \epsilon_r^o + z\kappa_\theta^o \\ \epsilon_\theta &= \epsilon_\theta^o + z\kappa_\theta^o \\ \gamma_{r\theta} &= \gamma_{r\theta}^o + z\kappa_{r\theta}^o \end{aligned} \tag{4.29}$$

The quantities $\epsilon_r^o$, $\epsilon_\theta^o$, $\gamma_{r\theta}^o$, and $\kappa_r^o$, $\kappa_\theta^o$, $\kappa_{r\theta}^o$ are the total reference surface strains and curvatures, respectively. The reference surface quantities are functions of $r$ and $\theta$. Including the effects of moderate rotations, the reference surface strains are

$$\begin{aligned} \epsilon_r^o &= \frac{\partial u^o}{\partial r} + \underline{\frac{1}{2}(\beta_r^o)^2} \\ \epsilon_\theta^o &= \frac{1}{r}\frac{\partial v^o}{\partial \theta} + \frac{u^o}{r} + \underline{\frac{1}{2}(\beta_\theta^o)^2} \\ \gamma_{r\theta}^o &= \frac{1}{r}\frac{\partial u^o}{\partial \theta} + \frac{\partial v^o}{\partial r} - \frac{v^o}{r} + \underline{\beta_r^o \beta_\theta^o} \end{aligned} \tag{4.30}$$

where the underlined terms are the von Karman terms reflecting the nonlinear effects due to the rotations associated with out-of-plane displacements being greater than the disk thickness. These approximations assume the elongation and shearing strains and the squares of the rotations are the same order of magnitude, and this order is small compared to unity. The reference surface

curvatures are given by

$$\begin{aligned}
\kappa_r^o &= \frac{\partial \beta_r^o}{\partial r} = -\frac{\partial^2 w^o}{\partial r^2} \\
\kappa_\theta^o &= \frac{1}{r}\beta_r^o + \frac{1}{r}\frac{\partial \beta_\theta^o}{\partial \theta} = -\frac{1}{r}\frac{\partial w^o}{\partial r} - \frac{1}{r^2}\frac{\partial^2 w^o}{\partial \theta^2} \\
\kappa_{r\theta}^o &= -\frac{1}{r}\beta_\theta^o + \frac{1}{r}\frac{\partial \beta_r^o}{\partial \theta} + \frac{\partial \beta_r^o}{\partial r} = \frac{2}{r^2}\frac{\partial w^o}{\partial \theta} - \frac{2}{r}\frac{\partial^2 w^o}{\partial r \partial \theta}
\end{aligned} \tag{4.31}$$

Expanding the stresses in Equation (2.3) in the $r$-$\theta$ coordinate system, and enforcing the plane-stress assumption, the following relations are obtained:

$$\begin{aligned}
\sigma_r &= \bar{Q}_{11}(\epsilon_r - \epsilon_r^T) + \bar{Q}_{12}(\epsilon_\theta - \epsilon_\theta^T) + \bar{Q}_{16}(\gamma_{r\theta} - \gamma_{r\theta}^T) \\
\sigma_\theta &= \bar{Q}_{12}(\epsilon_r - \epsilon_r^T) + \bar{Q}_{22}(\epsilon_\theta - \epsilon_\theta^T) + \bar{Q}_{26}(\gamma_{r\theta} - \gamma_{r\theta}^T) \\
\tau_{ry}^T &= \bar{Q}_{16}(\epsilon_r - \epsilon_r^T) + \bar{Q}_{26}(\epsilon_\theta - \epsilon_\theta^T) + \bar{Q}_{66}(\gamma_{r\theta} - \gamma_{r\theta}^T)
\end{aligned} \tag{4.32}$$

or

$$\begin{aligned}
\sigma_r &= \bar{Q}_{11}\epsilon_r + \bar{Q}_{12}\epsilon_\theta + \bar{Q}_{16}\gamma_{r\theta} - \sigma_r^T \\
\sigma_\theta &= \bar{Q}_{12}\epsilon_r + \bar{Q}_{22}\epsilon_\theta + \bar{Q}_{26}\gamma_{r\theta} - \sigma_\theta^T \\
\tau_{r\theta} &= \bar{Q}_{16}\epsilon_r + \bar{Q}_{26}\epsilon_\theta + \bar{Q}_{66}\gamma_{r\theta} - \tau_{r\theta}^T
\end{aligned} \tag{4.33}$$

where

$$\begin{aligned}
\sigma_r^T &= \bar{Q}_{11}\epsilon_r^T + \bar{Q}_{12}\epsilon_\theta^T + \bar{Q}_{16}\gamma_{r\theta}^T \\
\sigma_\theta^T &= \bar{Q}_{12}\epsilon_r^T + \bar{Q}_{22}\epsilon_\theta^T + \bar{Q}_{26}\gamma_{r\theta}^T \\
\tau_{r\theta}^T &= \bar{Q}_{66}\epsilon_r^T + \bar{Q}_{26}\epsilon_\theta^T + \bar{Q}_{66}\gamma_{r\theta}^T
\end{aligned} \tag{4.34}$$

The $\bar{Q}_{ij}$ terms are the transformed reduced stiffnesses, where the values 1 and 2 are associated with the $r$ and $\theta$ directions of RAINBOW, respectively. The thermally-induced strains are defined by

$$\begin{aligned} \epsilon_r^T &= \alpha_r \Delta T \\ \epsilon_\theta^T &= \alpha_\theta \Delta T \\ \gamma_{r\theta}^T &= \alpha_{r\theta} \Delta T \end{aligned} \tag{4.35}$$

where $\alpha_r$, $\alpha_\theta$, and $\alpha_{r\theta}$ are the thermal expansion coefficients in the $r$-$\theta$ coordinate system. Substituting for the strains from Equation (4.29) into the energy expression given by Equation (4.28) and integrating with respect to $z$, through the thickness, leads to

$$\begin{aligned} \Pi &= \frac{1}{2}\int_0^R \int_0^{2\pi} \Big\{ (N_r - \hat{N}_r^T \Delta T)\epsilon_r^o + (N_\theta - \hat{N}_\theta^T \Delta T)\epsilon_\theta^o \\ &+ (N_{r\theta} - \hat{N}_{r\theta}^T \Delta T)\gamma_{r\theta}^o + (M_r - \hat{M}_r^T \Delta T)\epsilon_r^o \\ &+ +(M_\theta - \hat{M}_\theta^T \Delta T)\kappa_\theta^o + (M_{r\theta} - \hat{M}_{r\theta}^T \Delta T)\kappa_{r\theta}^o \Big\} \, dr d\theta \end{aligned} \tag{4.36}$$

The quantities $N_r$, $N_\theta$, $N_{r\theta}$, $M_r$, $M_\theta$, and $M_{r\theta}$ are the force and moment resultants respectively, and $\hat{N}_r^T$, $\hat{N}_\theta^T$, $\hat{N}_{r\theta}^T$, $\hat{M}_r^T$, $\hat{M}_\theta^T$, and $\hat{M}_{r\theta}^T$ are the effective inplane thermal loads and the effective thermal moments, respectively. The force and moment resultants are given by

$$\begin{Bmatrix} N_r \equiv \int_{-\frac{H}{2}}^{+\frac{H}{2}} \sigma_r dz \\ N_\theta \equiv \int_{-\frac{H}{2}}^{+\frac{H}{2}} \sigma_\theta dz \\ N_{r\theta} \equiv \int_{-\frac{H}{2}}^{+\frac{H}{2}} \tau_{r\theta} dz \\ M_r \equiv \int_{-\frac{H}{2}}^{+\frac{H}{2}} z\sigma_r dz \\ M_\theta \equiv \int_{-\frac{H}{2}}^{+\frac{H}{2}} z\sigma_\theta dz \\ M_{r\theta} \equiv \int_{-\frac{H}{2}}^{+\frac{H}{2}} z\tau_{r\theta} dz \end{Bmatrix} = \begin{bmatrix} [A] & [B] \\ [B] & [D] \end{bmatrix} \begin{Bmatrix} \epsilon_r^o \\ \epsilon_\theta^o \\ \gamma_{r\theta}^o \\ \kappa_r^o \\ \kappa_\theta^o \\ \kappa_{r\theta}^o \end{Bmatrix} - \begin{Bmatrix} \hat{N}_r^T \\ \hat{N}_\theta^T \\ \hat{N}_{r\theta}^T \\ \hat{M}_r^T \\ \hat{M}_\theta^T \\ \hat{M}_{r\theta}^T \end{Bmatrix} \Delta T \tag{4.37}$$

where

$$[A] = \begin{bmatrix} A_{11} & A_{12} & A_{16} \\ A_{12} & A_{22} & A_{26} \\ A_{16} & A_{26} & A_{66} \end{bmatrix} \tag{4.38}$$

$$[B] = \begin{bmatrix} B_{11} & B_{12} & B_{16} \\ B_{12} & B_{22} & B_{26} \\ B_{16} & B_{26} & B_{66} \end{bmatrix} \tag{4.39}$$

$$[D] = \begin{bmatrix} D_{11} & D_{12} & D_{16} \\ D_{12} & D_{22} & D_{26} \\ D_{16} & D_{26} & D_{66} \end{bmatrix} \tag{4.40}$$

Also, the effective thermal force and moment resultants are defined as

$$\hat{N}_r^T \equiv \int_{-\frac{H}{2}}^{+\frac{H}{2}} \left(\bar{Q}_{11}\alpha_r + \bar{Q}_{12}\alpha_\theta + \bar{Q}_{16}\alpha_{r\theta}\right) dz \tag{4.41}$$

$$\hat{N}_\theta^T \equiv \int_{-\frac{H}{2}}^{+\frac{H}{2}} \left(\bar{Q}_{12}\alpha_r + \bar{Q}_{22}\alpha_\theta + \bar{Q}_{26}\alpha_{r\theta}\right) dz \tag{4.42}$$

$$\hat{N}_{r\theta}^T \equiv \int_{-\frac{H}{2}}^{+\frac{H}{2}} \left(\bar{Q}_{16}\alpha_r + \bar{Q}_{26}\alpha_\theta + \bar{Q}_{66}\alpha_{r\theta}\right) dz \tag{4.43}$$

$$\hat{M}_r^T \equiv \int_{-\frac{H}{2}}^{+\frac{H}{2}} \left(\bar{Q}_{11}\alpha_r + \bar{Q}_{12}\alpha_\theta + \bar{Q}_{16}\alpha_{r\theta}\right) z dz \tag{4.44}$$

$$\hat{M}_\theta^T \equiv \int_{-\frac{H}{2}}^{+\frac{H}{2}} \left(\bar{Q}_{12}\alpha_r + \bar{Q}_{22}\alpha_\theta + \bar{Q}_{26}\alpha_{r\theta}\right) z dz \tag{4.45}$$

$$\hat{M}_{r\theta}^T \equiv \int_{-\frac{H}{2}}^{+\frac{H}{2}} \left(\bar{Q}_{16}\alpha_r + \bar{Q}_{26}\alpha_\theta + \bar{Q}_{66}\alpha_{r\theta}\right) z dz \tag{4.46}$$

In the above, the $A$'s, $B$'s and $D$'s have the usual definitions associated with laminates [28].

### 4.4.2 The Rayleigh-Ritz Approach

As in past sections, the three components of displacement are approximated for use in the Rayleigh-Ritz approach. Here functional forms in the cylindrical coordinates system are required. The three reference surface displacements components $u^o$, $v^o$, and $w^o$ are approximated by a functions of the form

$$u^o(r,\theta) = \sum_{i=1}^{K}\sum_{j=0,2}^{2L} c_{ij} r^i \cos(j\theta) \tag{4.47}$$

$$v^o(r,\theta) = \sum_{i=1}^{K}\sum_{j=2,2}^{2L} d_{ij} r^i \sin(j\theta) \tag{4.48}$$

$$w^o(r,\theta) = \sum_{i=2}^{K+1}\sum_{j=0,2}^{L} a_{ij} r^i \cos(j\theta) \tag{4.49}$$

where $K$ and $L$ are positive integers and $a_{ij}$, $c_{ij}$, and $d_{ij}$ are to-be-determined constants. These displacement fields are constructed based on physical grounds. Indeed, they account for both axisymmetric (power series of $r$, when $j$=0, see Equation (4.25)) and the near-cylindrical (power series of $r$ + $\sum$power series of $r$ $\times$ $\cos(j\theta)$, $j = 0, 2, ..., L$) equilibrium shapes observed in Figure 4.2. Furthermore, it was reasoned that since the inplane strains contain the squares of the the derivative of the out-of-displacement $w^o$, the $u^o$, $v^o$ displacements must have twice the order of $\theta$ terms as in $w^o$. Finally, based on kinematic arguments, it was concluded that $u^o$, $v^o$, $w^o$, and $\partial w^o/\partial r$ should be zero at $r = 0$.

The expressions for the approximate displacement fields are substituted into the strain-displacement and curvature displacement relations, and these, in turn, are substituted into the expressions for the force and moment resultants, and into the expression for the total potential energy. The total potential energy expression is then a function of material properties and geometry, $K(5L/2 + 2)$ constants ($K(L/2 + 1)$ $a$'s, $K(L + 1)$ $c$'s, and $KL$ $d$'s), and $r$ and $\theta$. The energy expression is integrated with respect to $r$ and $\theta$ over the dimensions of RAINBOW, resulting in a purely algebraic expression for the total potential energy involving material properties, geometry, and the $K(5L/2+2)$ constants. The first and second variations of the total potential energy are then taken with respect to $a_{ij}$, $b_{ij}$, and $d_{ij}$. As the first variation must be zero for equilibrium, the result is

$K(5L/2+2)$ nonlinear algebraic equations for $a_{ij}$, $b_{ij}$, and $d_{ij}$. These are given by the following expression

$$\delta\Pi = \sum_{i=2}^{K+1}\sum_{j=0,2}^{L}\frac{\partial\Pi}{\partial a_{ij}}\delta a_{ij} + \sum_{i=1}^{K}\sum_{j=0,2}^{2L}\frac{\partial\Pi}{\partial c_{ij}}\delta c_{ij} + \sum_{i=1}^{K}\sum_{j=2,2}^{2L}\frac{\partial\Pi}{\partial d_{ij}}\delta d_{ij} = 0 \tag{4.50}$$

The above equations can be solved and numerical results obtained for specific values of material and geometric parameters. Stability is evaluated by checking the positive definiteness of the second variation. The second variation can be written in the form

$$\delta^2\Pi = \left[\begin{array}{cccccc} \delta a_{20} & \cdots & \delta a_{K+1\ L} & \delta c_{10} & \cdots & \delta c_{K\ 2L}\ \ \delta d_{12}\cdots\delta d_{K\ 2L} \end{array}\right]\left[\begin{array}{c} C \end{array}\right]\left[\begin{array}{c} \delta a_{20} \\ \vdots \\ \delta a_{K+1\ L} \\ \delta c_{10} \\ \vdots \\ \delta c_{K\ 2L} \\ \delta d_{12} \\ \vdots \\ \delta d_{K\ 2L} \end{array}\right] \tag{4.51}$$

The study of stability reduces to examining the eigenvalues of the matrix $[C]$. If all eigenvalues are positive, the equilibrium solution is stable, otherwise the equilibrium solution is unstable. These calculations, which were done with the aid of the symbolic algebra package *Mathematica*® [32], are much more complicated than the rectangular case.

### 4.4.3 Piezoelectric Effects

To study the deformations due to an applied electric field through the unreduced piezoceramic, the total energy expression of Equation (4.36) is modified to include the effective force and moment resultants produced by the electric-field-induced dilatational strains. Hence, the following terms

are appended to the total potential energy expression:

$$\hat{N}_r^E E_z \equiv \int_{-\frac{H}{2}}^{+\frac{H}{2}} \left(\bar{Q}_{11} d_{31} + \bar{Q}_{12} d_{32}\right) E_z dz \tag{4.52}$$

$$\hat{N}_\theta^E E_z \equiv \int_{-\frac{H}{2}}^{+\frac{H}{2}} \left(\bar{Q}_{12} d_{31} + \bar{Q}_{22} d_{32}\right) E_z dz \tag{4.53}$$

$$\hat{M}_r^E E_z \equiv \int_{-\frac{H}{2}}^{+\frac{H}{2}} \left(\bar{Q}_{11} d_{31} + \bar{Q}_{12} d_{32}\right) E_z z dz \tag{4.54}$$

$$\hat{M}_\theta^E E_z \equiv \int_{-\frac{H}{2}}^{+\frac{H}{2}} \left(\bar{Q}_{12} d_{31} + \bar{Q}_{22} d_{32}\right) E_z z dz \tag{4.55}$$

It should be noted that only the unreduced piezoceramic layer contributes to the integrals of Equations (4.52)–(4.55), as $d_{31}$ and $d_{32}$ are considered to be zero for the reduced layer. Again, it is assumed that the displacements resulting from the temperature change plus the application of the electric field are approximated by Equations (4.47)-(4.49). The computation of the first variation, and the resulting governing equations, and the second variation, and the resulting $[C]$ matrix, follow the steps outlined in the previous section.

## 4.5 Numerical Results

### 4.5.1 Axisymmetric Solution

In this section numerical results from the exact linear and approximate nonlinear axisymmetric analyses will be presented to demonstrate the influence of geometry and geometric nonlinearities on the manufactured shape of disk-style RAINBOW. This, of course, assumes only the dome-like shapes result from the manufacturing process. It is also assumed the two piezoceramic layers are stress-free at the piezoceramic Curie temperature ($T_C$ =340 $^o$C) and that internal stresses do not develop above that temperature. The material properties and thicknesses are given in Table 2.1 and a schematic of cooling the disk-style RAINBOW is shown in Figure 4.3. Two specific disk-style RAINBOW actuators will be discussed for the purpose of determining the sensitivity of the room-temperature shape to the geometric parameters. The two actuators have a radius $R$ of 25.4 mm (1.0 in.) and 12.7 mm (0.5 in.), respectively, and a reduced layer thickness to total thickness

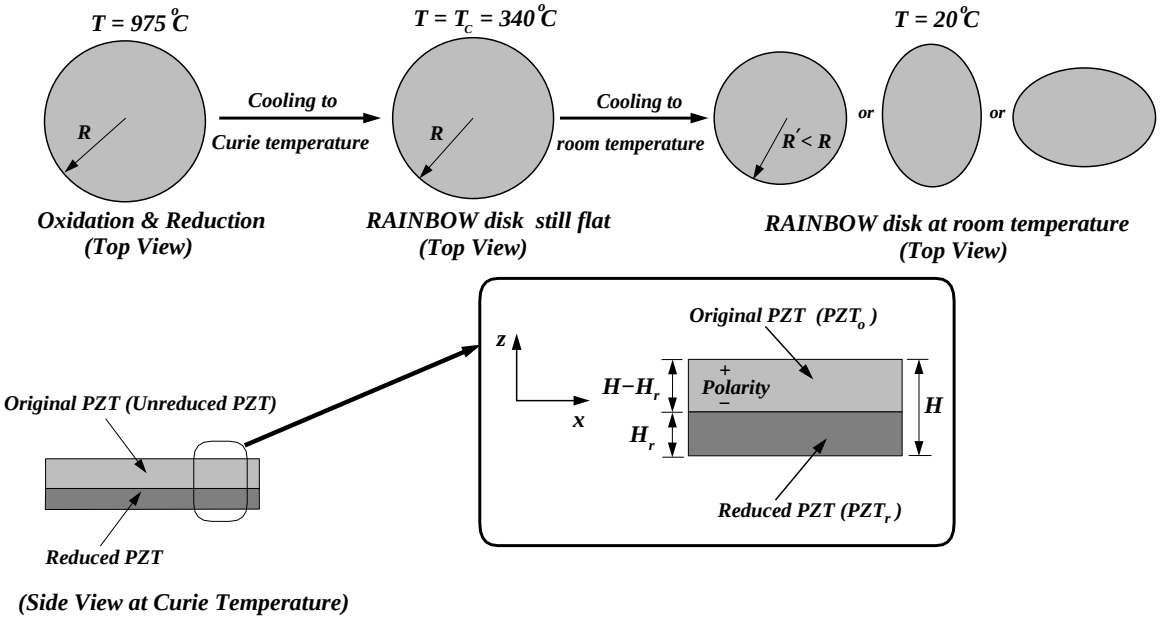


Figure 4.3: Schematic of disk-style RAINBOW considered.

ratio of $H_r/H$=0.35.

Any functions that satisfy the kinematic boundary conditions of the problem can be used as approximations in the Rayleigh-Ritz method for the nonlinear analysis. As the sophistication of these functions increase, the accuracy should also increase, hopefully converging to the correct solution. To study convergence for the nonlinear problem considered, a series of functions with an increasing number of to-be-determined coefficients is used. Each coefficient is multiplied by a power of the radial coordinate $r$. The five pairs of solutions considered are as follows:

$$u_1^o = c_{10}r \quad \text{and} \quad w_1^o = a_{20}r^2 \tag{4.56}$$

$$u_2^o = c_{10}r + c_{20}r^2 \quad \text{and} \quad w_2^o = a_{20}r^2 + a_{30}r^3 \tag{4.57}$$

$$u_3^o = c_{10}r + c_{20}r^2 + c_{30}r^3 \quad \text{and} \quad w_3^o = a_{20}r^2 + a_{30}r^3 + a_{40}r^4 \tag{4.58}$$

$$u_4^o = c_{10}r + c_{20}r^2 + c_{30}r^3 + c_{40}r^4 \quad \text{and} \quad w_4^o = a_{20}r^2 + a_{30}r^3 + a_{40}r^4 + a_{50}r^5 \tag{4.59}$$

$$u_5^o = c_{10}r + c_{20}r^2 + c_{30}r^3 + c_{40}r^4 + c_{50}r^5 \text{ and } w_5^o = a_{20}r^2 + a_{30}r^3 + a_{40}r^4 + a_{50}r^5 + a_{60}r^6 \tag{4.60}$$

The above five pairs of functions will be used to study the axisymmetric room-temperature shape of RAINBOW with radius $R$=25.4 mm. Figure 4.4 illustrates the convergence characteristics of the

five pairs of functions. In Figure 4.4, the out-of-plane and radial components of displacement relative to the flat configuration at Curie temperature, $w^o(r)$ and $u^o(r)$, are plotted as a function of radial position, $r$. Shown for comparison is the exact linear solution for the same device. From Figure 4.4 it can be seen that one-term approximation, Equation (4.56), is not quite sufficient. However, it should be pointed out that since the one-term nonlinear approximation and the exact linear solution are quite different, the one-term approximation to the nonlinear problem does reflect the influence of the geometric nonlinearities. However, it is not a particularly accurate approximation. Adding another term, as in Equation (4.57), changes the results. The three-, four-, and five-term approximations are in close agreement, and it is clear that five coefficients in each functional approximation are sufficient. Needless to say, using a one-term approximate solution in the Rayleigh-Ritz method with geometric nonlinearities deleted will give the exact linear solution. The five-term approximation, Equation (4.60), will be considered converged and will be used herein.

To examine the influence of radius on the room-temperature shape of disk-style RAINBOW, another device with a radius R=12.7 mm is considered in Figure 4.5. By taking note of the coordinate system in Figures 4.1 and 4.2, it is seen when looking at Figure 4.5 that the out-of-plane component of displacement is negative and thus represents a device that has deformed into a dome shape at room temperature where the center of the device is upward relative to the edges. The predictions of the exact linear analysis, Equations (4.16)–(4.18), and the nonlinear analysis computed using the shooting method and the Rayleigh-Ritz method using the expressions in Equation (4.60) are shown in the figure. Also, for purpose of comparison, the predictions from the commercially available finite-element code ABAQUS programmed to include geometric nonlinearities are also shown. As can be seen, all three nonlinear predictions agree very well with each other, and they differ from the predictions of the linear theory. For the device with $R$=25.4 mm, relative to the nonlinear analyses, the linear analysis predicts about 142% greater out-of-plane displacement at the outer edge of the device. On the other hand, for the outer edge the linear analysis predicts 38% less radial displacement than the nonlinear analyses. Because of the smaller value of out-of-plane displacement, the nonlinear analyses predict a flattening of the dome shape relative to the linear analysis. In addition to the smaller value of displacement, the distribution of the out-of-plane displacement with radial position $r$ is different with the nonlinear prediction. The format of Figure 4.5 allows for direct comparison of displacement components of both devices, and it is seen that decreasing

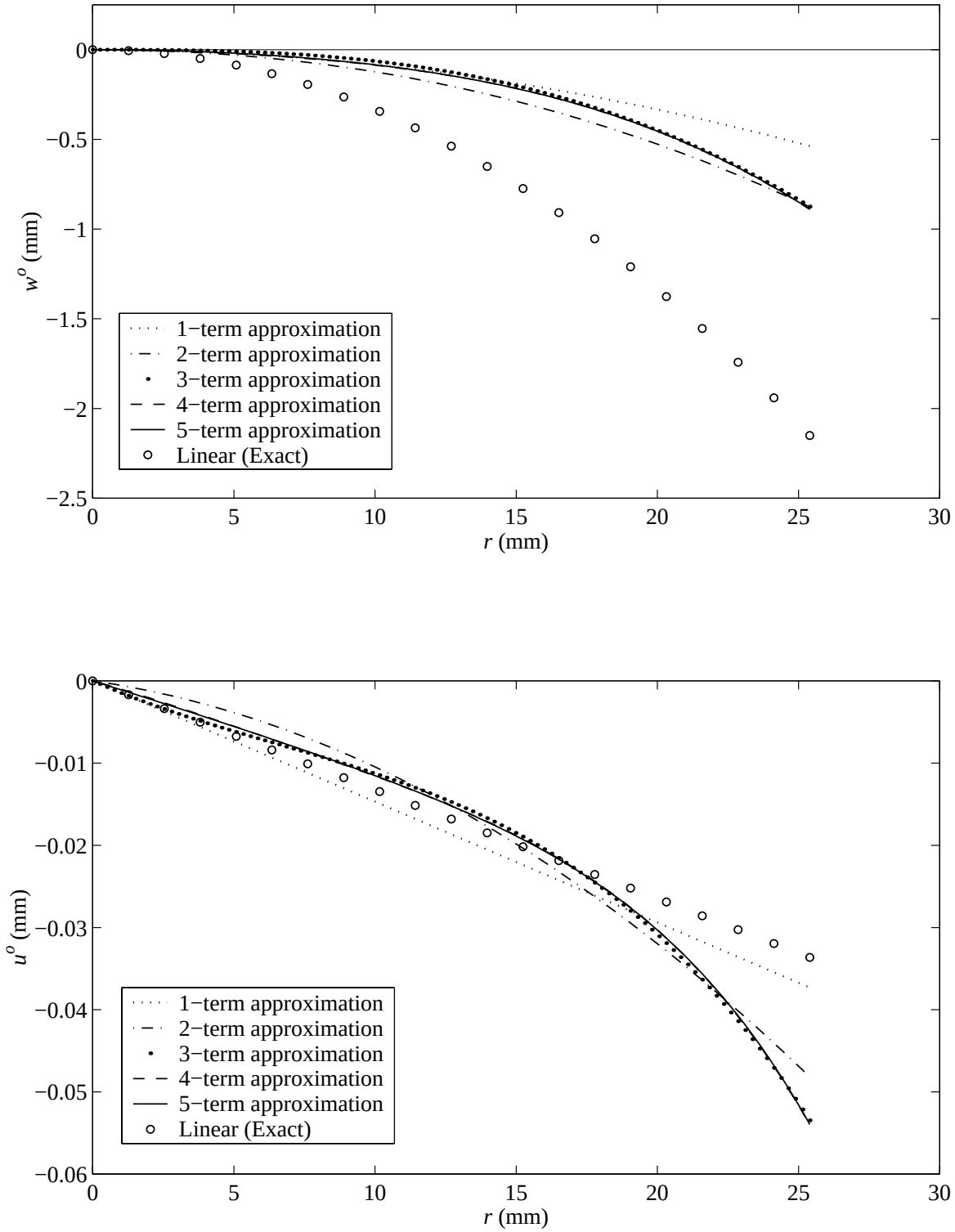


Figure 4.4: Convergence of the Rayleigh-Ritz method for axisymmetric room-temperature displacements of disk-style RAINBOW ($R$=25.4 mm, $H$=0.381 mm, $H_r/H$=0.35).

the radius of the device results in decreased displacements. Furthermore, for the smaller device ($R$=12.7 mm) there is a closer agreement between linear and nonlinear analyses. Specifically, the linear analysis over-predicts the out-of-plane displacements by just 30% and not as much flattening is predicted as for the 25.4 mm radius device. It is is felt that the disagreement between linear and nonlinear analysis is roughly proportional to the ratio of radius to total thickness, $R/H$. Materials being the same, the smaller this ratio is, the more closely linear analysis will predict the out-of-plane displacement. It should be noted that the Rayleigh-Ritz method was programmed with *Mathematica*® [32] and was rather straightforward and executed quite quickly.

Note that the nonlinear effects for the 25.4 mm radius device are strong and stability can be an issue. Generally, the loss of stability for a static equilibrium configuration means there could be another static equilibrium configuration for the problem for the same conditions, here the given temperature change, that is stable. In the case of disk-like devices, the alternate stable static equilibrium configuration could be a non-axisymmetric one. As shown in Figure 4.2, it has been observed that for some conditions disk-like RAINBOW deform into configurations other than domes when they are cooled from the Curie temperature. Hence, the predictions of the 25.4 mm radius RAINBOW must be viewed with caution, as the axisymmetric dome shape is unstable, as will be shown in the next section, and would never be observed. Thus, an axisymmetric analysis would be irrelevant and, in fact, misleading. In the next section, numerical results of the non-axisymmetric analysis are presented.

### 4.5.2 General Solutions

To illustrate the convergence characteristics and results predicted by the general nonlinear analysis using Rayleigh-Ritz method, consider again the 25.4 mm radius RAINBOW of Figure 4.4. To study convergence for the problem considered, a series of functions with an increasing number of to-be-determined coefficients is used (refer to Equations (4.47)–(4.49)). The three sets of functions considered here are as follows

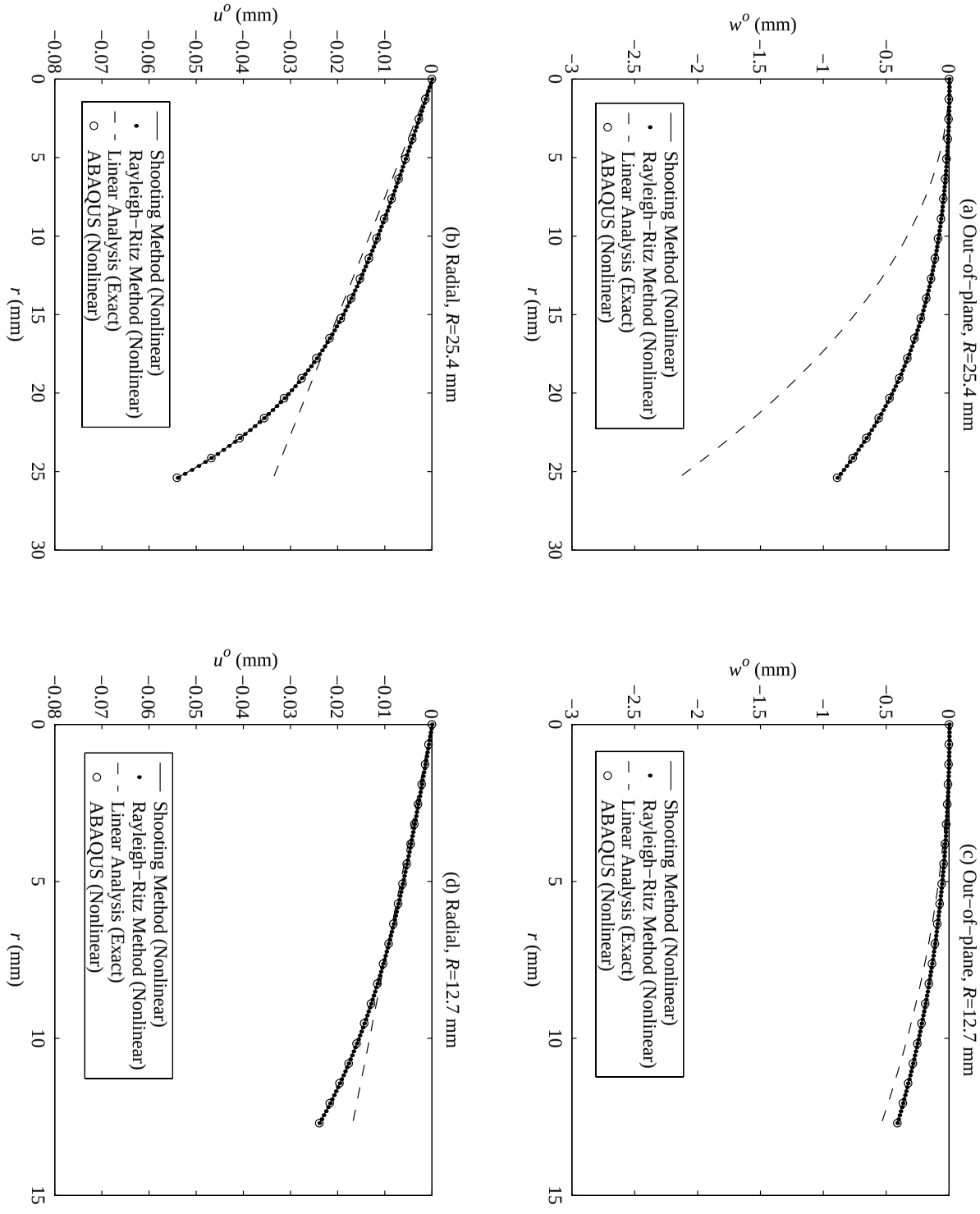


Figure 4.5: Displacements of disk-style RAINBOW ($R$=25.4 mm and $R$=12.7 mm, $H$=0.381 mm, $H_r/H$=0.35).

**14 term-approximation (K=2, L=2)**

$$w_{14}^{o}(r,\theta) = a_{20}r^2 + a_{30}r^3 + (a_{22}r^2 + a_{32}r^3)\cos(2\theta) \tag{4.61}$$

$$u_{14}^{o}(r,\theta) = c_{10}r + c_{20}r^2 + (c_{12}r + c_{22}r^2)\cos(2\theta) + (c_{14}r + c_{24}r^2)\cos(4\theta) \tag{4.62}$$

$$v_{14}^{o}(r,\theta) = (d_{12}r + d_{22}r^2)\sin(2\theta) + (d_{14}r + d_{24}r^2)\sin(4\theta) \tag{4.63}$$

**35 term-approximation (K=5, L=2)**

$$\begin{aligned} w_{35}^{o}(r,\theta) &= a_{20}r^2 + a_{30}r^3 + a_{40}r^4 + a_{50}r^5 + a_{60}r^6 \\ &\quad +(a_{22}r^2 + a_{32}r^3 + a_{42}r^4 + a_{52}r^5 + a_{62}r^6)\cos(2\theta) \end{aligned} \tag{4.64}$$

$$\begin{aligned} u_{35}^{o}(r,\theta) &= c_{10}r + c_{20}r^2 + c_{30}r^3 + c_{40}r^4 + c_{50}r^5 \\ &\quad +(c_{12}r + c_{22}r^2 + c_{32}r^3 + c_{42}r^4 + c_{52}r^5)\cos(2\theta) \\ &\quad +(c_{14}r + c_{24}r^2 + c_{34}r^3 + c_{44}r^4 + c_{54}r^5)\cos(4\theta) \end{aligned} \tag{4.65}$$

$$\begin{aligned} v_{35}^{o}(r,\theta) &= (d_{12}r + d_{22}r^2 + d_{32}r^3 + d_{42}r^4 + d_{52}r^5)\sin(2\theta) \\ &\quad +(d_{14}r + d_{24}r^2 + d_{34}r^3 + d_{44}r^4 + d_{54}r^5)\sin(4\theta) \end{aligned} \tag{4.66}$$

**85 term-approximation (K=5, L=6)**

$$\begin{aligned} w_{85}^{o}(r,\theta) &= a_{20}r^2 + a_{30}r^3 + a_{40}r^4 + a_{50}r^5 + a_{60}r^6 \\ &\quad +(a_{22}r^2 + a_{32}r^3 + a_{42}r^4 + a_{52}r^5 + a_{62}r^6)\cos(2\theta) \\ &\quad +(a_{24}r^2 + a_{34}r^3 + a_{44}r^4 + a_{54}r^5 + a_{64}r^6)\cos(4\theta) \\ &\quad +(a_{26}r^2 + a_{36}r^3 + a_{46}r^4 + a_{56}r^5 + a_{66}r^6)\cos(6\theta) \end{aligned} \tag{4.67}$$

$$
\begin{aligned}
u^o_{85}(r,\theta) &= c_{10}r + c_{20}r^2 + c_{30}r^3 + c_{40}r^4 + c_{50}r^5 \\
&\quad +(c_{12}r + c_{22}r^2 + c_{32}r^3 + c_{42}r^4 + c_{52}r^5)\cos(2\theta) \\
&\quad +(c_{14}r + c_{24}r^2 + c_{34}r^3 + c_{44}r^4 + c_{54}r^5)\cos(4\theta) \\
&\quad +(c_{16}r + c_{26}r^2 + c_{36}r^3 + c_{46}r^4 + c_{56}r^5)\cos(6\theta) \\
&\quad +(c_{18}r + c_{28}r^2 + c_{38}r^3 + c_{48}r^4 + c_{58}r^5)\cos(8\theta) \\
&\quad +(c_{110}r + c_{210}r^2 + c_{310}r^3 + c_{410}r^4 + c_{510}r^5)\cos(10\theta) \\
&\quad +(c_{112}r + c_{212}r^2 + c_{312}r^3 + c_{412}r^4 + c_{512}r^5)\cos(12\theta) \qquad (4.68) \\
v^o_{85}(r,\theta) &= (d_{12}r + d_{22}r^2 + d_{32}r^3 + d_{42}r^4 + d_{52}r^5)\sin(2\theta) \\
&\quad +(d_{14}r + d_{24}r^2 + d_{34}r^3 + d_{44}r^4 + d_{54}r^5)\sin(4\theta) \\
&\quad +(d_{16}r + c_{26}r^2 + d_{36}r^3 + d_{46}r^4 + d_{56}r^5)\sin(6\theta) \\
&\quad +(d_{18}r + c_{28}r^2 + d_{38}r^3 + d_{48}r^4 + d_{58}r^5)\sin(8\theta) \\
&\quad +(d_{110}r + d_{210}r^2 + d_{310}r^3 + d_{410}r^4 + d_{510}r^5)\sin(10\theta) \\
&\quad +(d_{112}r + d_{212}r^2 + d_{312}r^3 + d_{412}r^4 + d_{512}r^5)\sin(12\theta) \qquad (4.69)
\end{aligned}
$$

Note that the axisymmetric portions of the 35- and 85-term solutions are identical to Equation 4.60, the approximate solutions which are considered fully converged. To dramatize the convergence characteristics of the Rayleigh-Ritz method, the above three sets of functions will be used to predict the room-temperature displacements at the outer edge, i.e., at $r = R$. Figures 4.6–4.8 illustrate these displacements. Shown for comparison is the solution from the commercially available finite-element code ABAQUS programmed to include geometric nonlinearities. The displacements evaluated by finite element analysis at the nodes located at the outer edge ($r = R$) are indicated by the label ABAQUS. Figures 4.6–4.8 show that there are three equilibrium configurations at room temperature. In these figures, the horizontal line solution corresponds to the dome-like axisymmetric configuration and the other two solutions correspond to the near-cylindrical configurations. The cooling scenario of disk-style RAINBOW will be discussed in the following paragraphs. Because there are multiple equilibrium configurations, once the bifurcation temperature occurs, ABAQUS must be coaxed to continue on a particular path to obtain the different configurations at room temperature. To force ABAQUS to follow a particular path, a slight imperfection in the initial shape of

RAINBOW was introduced. With slight imperfection, ABAQUS would converge to one of the two stable solutions. To get ABAQUS to converge to the axisymmetric solution below the bifurcation temperature, the nodes at the edge were forced to have the same out-of-plane displacement. Thus, to obtain the room-temperature shapes of RAINBOW considered, three series of finite element calculations were conducted. For each finite element analysis a mesh of 36 6-node triangular (STRI65) and 360 8-node doubly curved thin shell (S8R5) elements [35] was used. Both types of shell elements allow transverse shear in the element. RAINBOW was free on the edges, but clamped at the node at its geometric center. A constant temperature change was applied at the nodes. From Figures 4.6–4.8, it can be seen that the 14-term approximation, Equations (4.61)–(4.63), is not sufficient enough to achieve accurate approximations. Adding 21 more terms, as in Equations (4.64)–(4.66), greatly improves the results. The 85-term approximation is in excellent agreement with finite-element results, and it is clear that using $K = 5$ and $L = 6$ in Equations (4.67)–(4.69) leads to very accurate results. As can be seen in the three figures, the out-of-plane displacement converges the most quickly, and the two inplane components of displacement converge less quickly. It should be noted that the ABAQUS results were computed using shear-deformable theory, whereas the Rayleigh-Ritz-based theory is a non-shear deformable theory. The excellent agreement between ABAQUS and and the 35- and 85-term solutions strongly suggests shear deformations are not an issue in this problem.

Figures 4.9–4.13 illustrate the behavior of a 25.4 mm radius disk-style RAINBOW as it cooled from the Curie temperature of the piezoceramic to room temperature. Specifically, in Figures 4.9–4.13 the parameters $a_{ij}$ of Equation (4.49) are shown as a function of the temperature. For convenience, the coefficients $a_{ij}$ have been nondimensionalized by using RAINBOW thickness, $H$, as a scaling parameter. These parameters are considered because they describe the out-of-plane shape of RAINBOW, the most visible aspect of the deformation. Specifically, these parameters define the curvatures. For simplicity and ease of interpretation of the results, the 35-term Rayleigh-Ritz approximation was used to obtain numerical values of the $a_{ij}$ coefficients of Equation (4.64). These

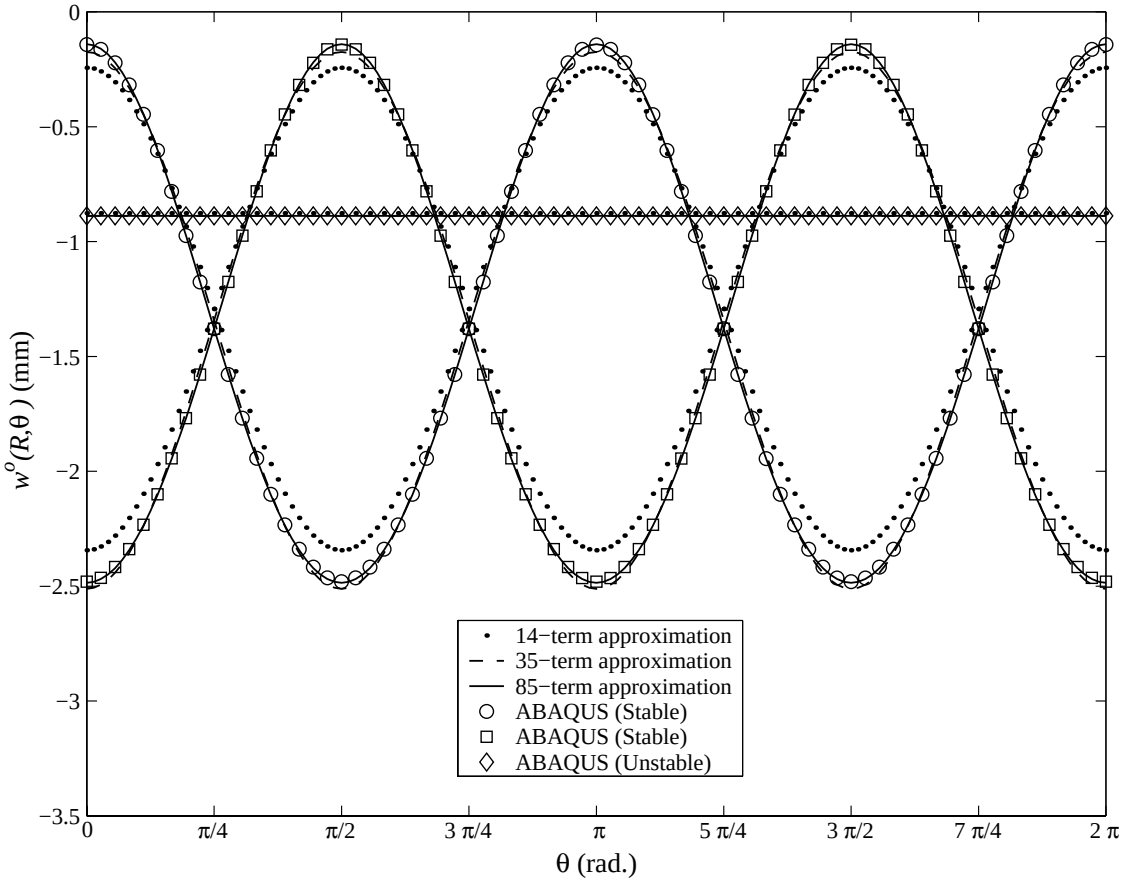


Figure 4.6: Convergence of the Rayleigh-Ritz method for the room-temperature outer edge out-of-plane displacement $w^o$ of disk-style RAINBOW ($R$=25.4 mm, $H$=0.381 mm, $H_r/H$=0.35).

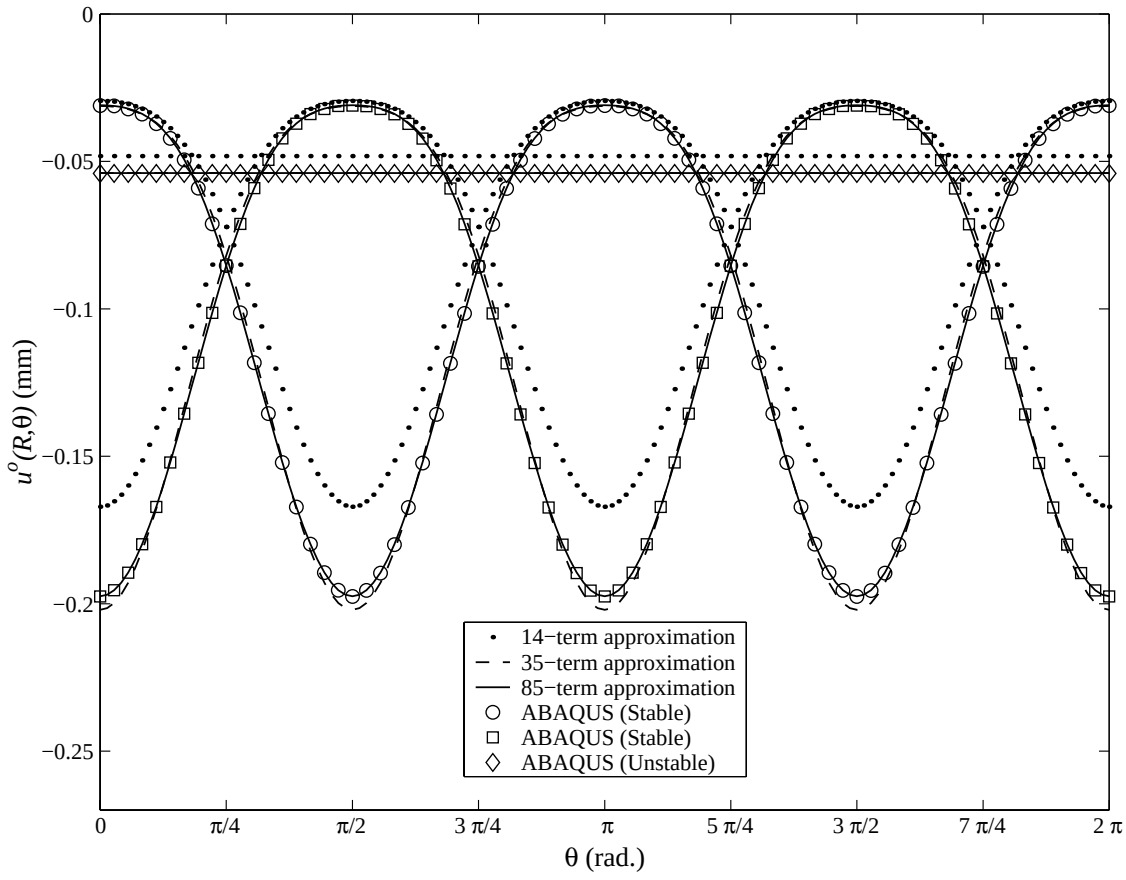


Figure 4.7: Convergence of the Rayleigh-Ritz method for the room-temperature outer edge radial displacement $u^o$ of disk-style RAINBOW ($R$=25.4 mm, $H$=0.381 mm, $H_r/H$=0.35).

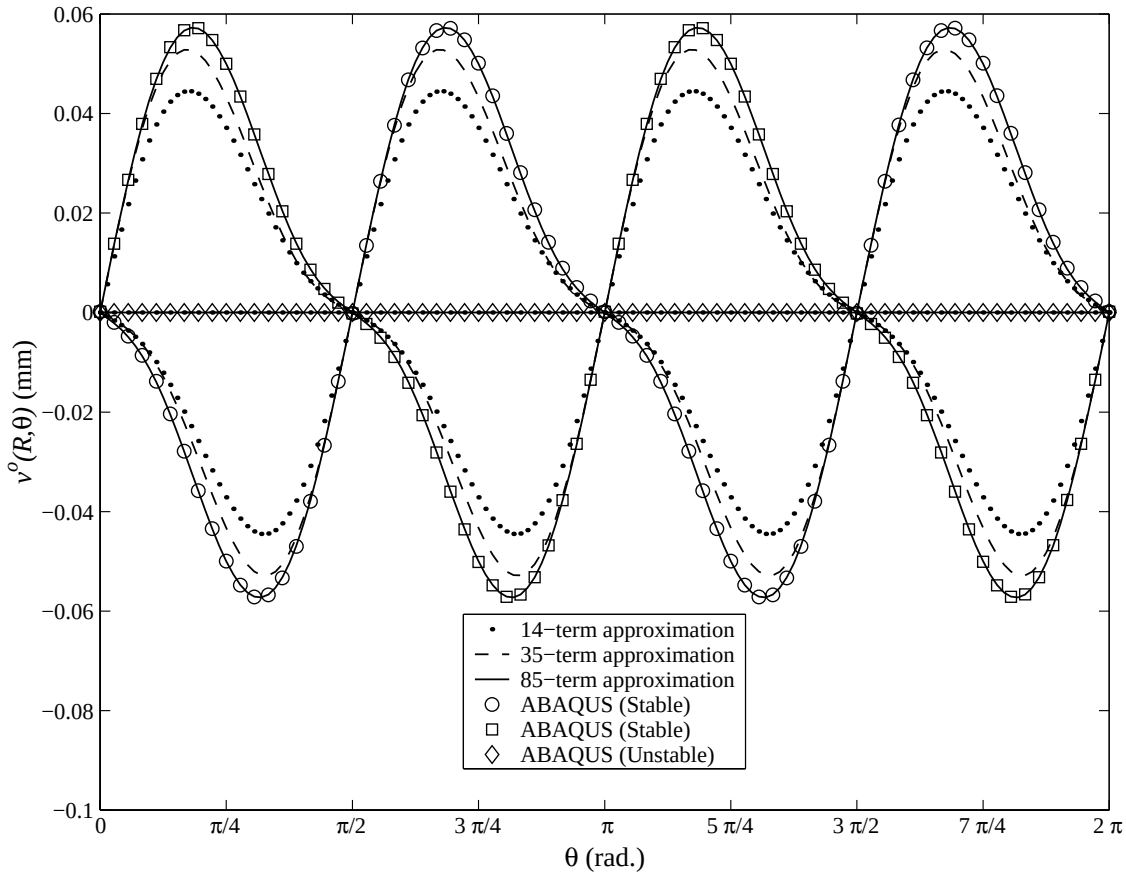


Figure 4.8: Convergence of the Rayleigh-Ritz method for the room-temperature outer edge circumferential displacement $v^o$ of disk-style RAINBOW ($R$=25.4 mm, $H$=0.381 mm, $H_r/H$=0.35).

coefficients can be substituted in the following curvature equations

$$\begin{aligned}
\kappa_r^o &= -(2a_{20} + 6a_{30}r + 12a_{40}r^2 + 20a_{50}r^3 + 30a_{60}r^4) \\
&\quad -(2a_{22} + 6a_{32}r + 12a_{42}r^2 + 20a_{52}r^3 + 30a_{62}r^4)\cos(2\theta) \qquad (4.70) \\
\kappa_\theta^o &= -(2a_{20} + 3a_{30}r + 4a_{40}r^2 + 5a_{50}r^3 + 6a_{60}r^4) \\
&\quad +(2a_{22} + a_{32}r - a_{52}r^3 - 2a_{62}r^4)\cos(2\theta) \qquad (4.71) \\
\kappa_{r\theta}^o &= 4(a_{22} + 2a_{32}r + 3a_{42}r^2 + 4a_{52}r^3 + 5a_{62}r^4)\sin(2\theta) \qquad (4.72)
\end{aligned}$$

to obtain quantitative predictions of the curvatures $\kappa_r^o$, $\kappa_\theta^o$, and $\kappa_{r\theta}^o$. Figure 4.14 illustrates the actual room-temperature shapes of disk-style RAINBOW obtained using the Rayleigh-Ritz 35-term approximation.

Referring to Figures 4.9–4.13, point A represents RAINBOW flat at its Curie temperature ($a_{ij}$=0, i=2,6, j=0,2). As the temperature is reduced, the 35-term Rayleigh-Ritz approximation develops single-valued nonzero coefficients $a_{20}$, $a_{30}$, $a_{40}$, $a_{50}$, and $a_{60}$ with the other coefficients ($a_{22}$, $a_{32}$, $a_{42}$, $a_{52}$, $a_{62}$) being zero. These nonzero coefficients represent curvatures which are independent of $\theta$ and the equilibrium solution is thus a dome-like axisymmetric shape. As the temperature is reduced further below the Curie temperature, the axisymmetric shape deepens. At a temperature corresponding to points B and B′, the coefficients $a_{20}$, $a_{30}$, $a_{40}$, $a_{50}$, and $a_{60}$ bifurcate into branches BC and BE, while the coefficients $a_{22}$, $a_{32}$, $a_{42}$, $a_{52}$, $a_{62}$ trifurcate into branches B′C′, B′E′, and B′C″. For this specific device the bifurcation temperature is 198 $^o$C. The bifurcation occurring at point B is referred to as a *symmetry-breaking static bifurcation* in the temperature-$a_{i0}$ coefficients domain because it leads to the creation of asymmetric solutions (the non-axisymmetric solutions in this case). The bifurcation occurring at point B' is referred to as a *supercritical pitchfork static bifurcation* in the temperature–$a_{i2}$ coefficients domain because the branches AB′, B′C′, B′E′, and B′C″ have the geometry of a pitchfork at point B′. Reducing the temperature below the 198 $^o$C level, solution paths BC and B′C′ represent a change from the dome-like axisymmetric shape to a non-axisymmetric shape, with the largest out-of-plane displacements occurring at $\theta = 0$ and $\theta = \pi$ and the smallest occurring at $\theta = \pi/2$ and $\theta = 3\pi/2$ (Figure 4.14(a)). If instead of following paths BC and B′C′, paths BC and B′C″ are followed, the solution represents another non-axisymmetric shape with smallest out-of-plane displacements occurring at $\theta = 0$ and $\theta = \pi$ and the largest

occurring at $\theta = \pi/2$ and $\theta = 3\pi/2$ (Figure 4.14(b)). At room-temperature the solution is similar to the solution represented by paths BC and B′C′ but with roles of curvatures $\kappa_r^o$, $\kappa_\theta^o$, and $\kappa_{r\theta}^o$ out of phase by a $\pi/2$ angle. Finally, if paths BE and B′E′ are followed through the bifurcations points B and B′, respectively, the dome-like axisymmetric shape deepens further (Figure 4.14(c)). It is important to note the magnitudes of coefficients $a_{30}$, $a_{32}$, $a-40$, $a_{42}$, $a_{50}$, $a_{52}$, $a_{60}$, $a_{62}$ relative to coefficients $a_{20}$ and $a_{22}$. The coefficients $a_{20}$ and $a_{22}$ are the dominant terms in the approximation for $w^o(r,\theta)$.

A stability analysis reveals the important details of these three pairs of paths. Specifically, paths BC, B′C′, and B′C″ represent stable equilibrium shapes and paths BE and B′E′ represent unstable equilibrium shapes. Therefore, the shapes represented by paths BE and B′E′ will never be observed. The shapes represented by paths BC, B′C′, and B′C″ will be what is observed when RAINBOW actuators are actually manufactured. Furthermore, paths B′C′ and B′C″ represent shapes with the same total potential energy and neither one is more likely to occur than the other. In practice, imperfections in the device will cause one path to be favored relative to the other. A RAINBOW with a shape represented by paths BC and B′C′ can be changed to the shape represented by paths BC and B′C″ by a snap-through action.

Figure 4.14(a) depicts disk-style RAINBOW at the room-temperature condition corresponding to points C and C′. As can be seen, RAINBOW device has a near-cylindrical shape with the maximum out-of-plane displacements occurring at $\theta = 0$ and $\theta = \pi$. Likewise, Figure 4.14(b) depicts RAINBOW at the room-temperature condition corresponding to point C and C″. This is another near-cylindrical shape with the maximum out-of-plane displacements occurring at $\theta = \pi/2$ and $\theta = 3\pi/2$. Finally, Figure 4.11(c) shows the unstable dome-like axisymmetric shape at room temperature corresponding to point E and E' in Figures 4.9–4.10.

Figures 4.15–4.19 illustrate the convergence characteristics of the $a_{ij}$ coefficients for the three sets of functions. Again, from these figures, it can be seen that the 14-term approximation is not sufficient enough to obtain accurate answers; however, it is able to predict the bifurcation point to within 12 $^o$C (8.5% of $\Delta T_{critical}$=−142 $^o$C). These figures also indicate that the 35-term approximation is enough to predict an accurate calculation for the bifurcation temperature. For $T > 150$ $^o$C ($\Delta T > -190$ $^o$C), all the branches in Figures 4.15–4.19 corresponding to the 35-

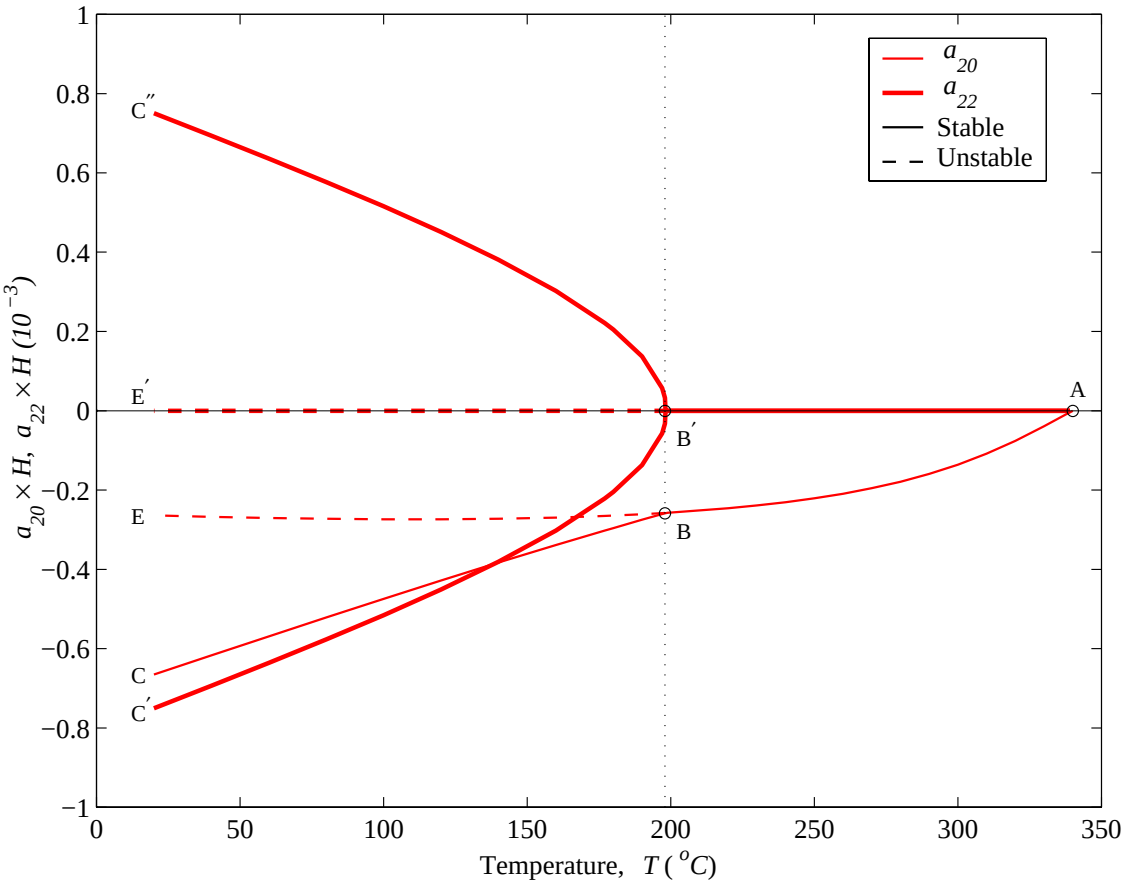


Figure 4.9: Temperature-curvature ($a_{20}$ and $a_{22}$) relation of disk-style RAINBOW ($R$=25.4 mm, $H$=0.381 mm, $H_r/H$=0.35).

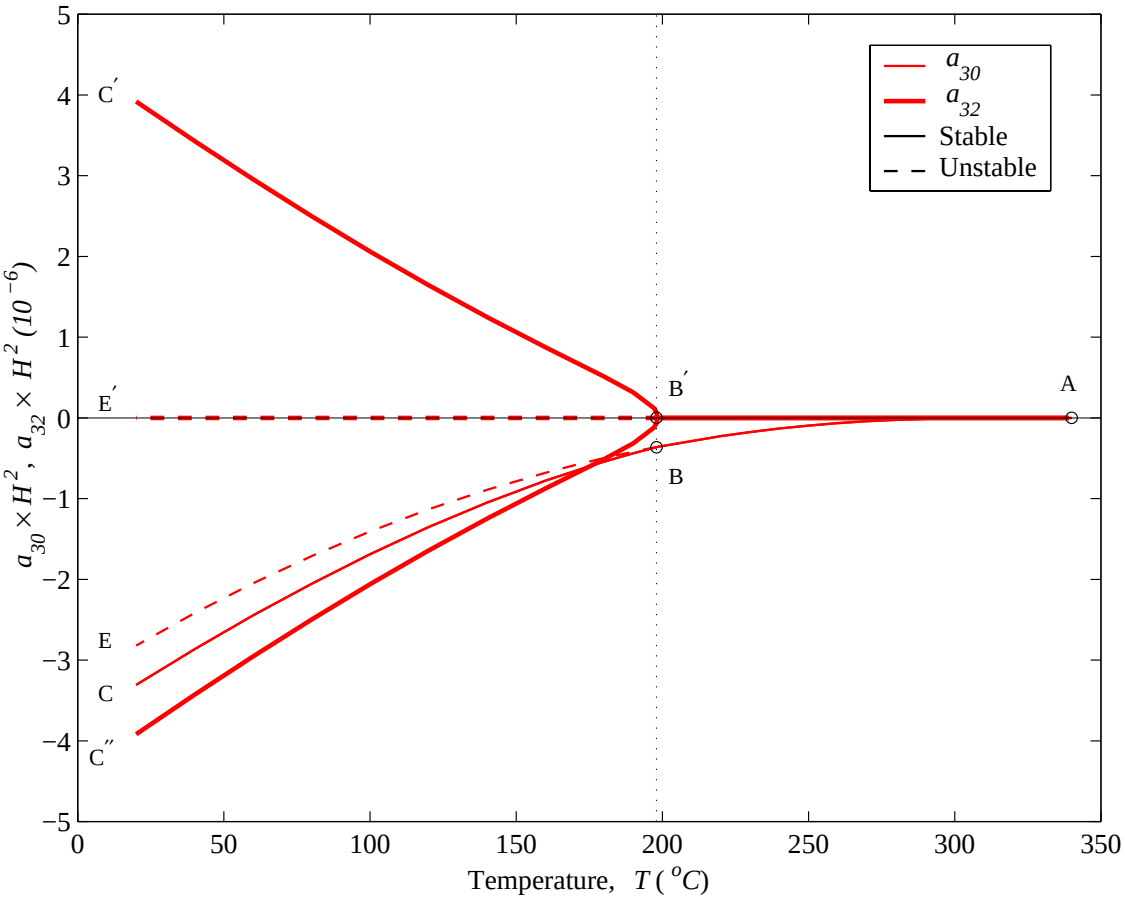


Figure 4.10: Temperature-curvature ($a_{30}$ and $a_{32}$) relation of disk-style RAINBOW ($R$=25.4 mm, $H$=0.381 mm, $H_r/H$=0.35).

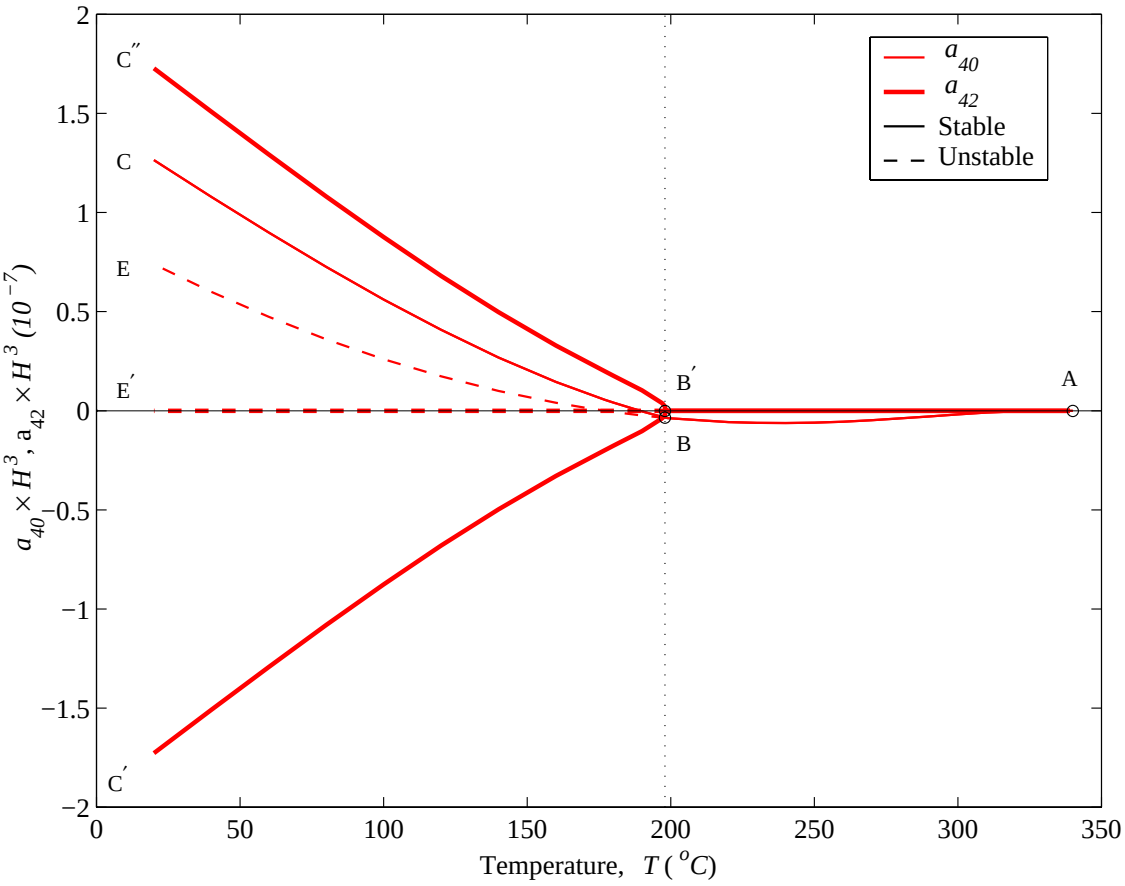


Figure 4.11: Temperature-curvature ($a_{40}$ and $a_{42}$) relation of disk-style RAINBOW ($R$=25.4 mm, $H$=0.381 mm, $H_r/H$=0.35).

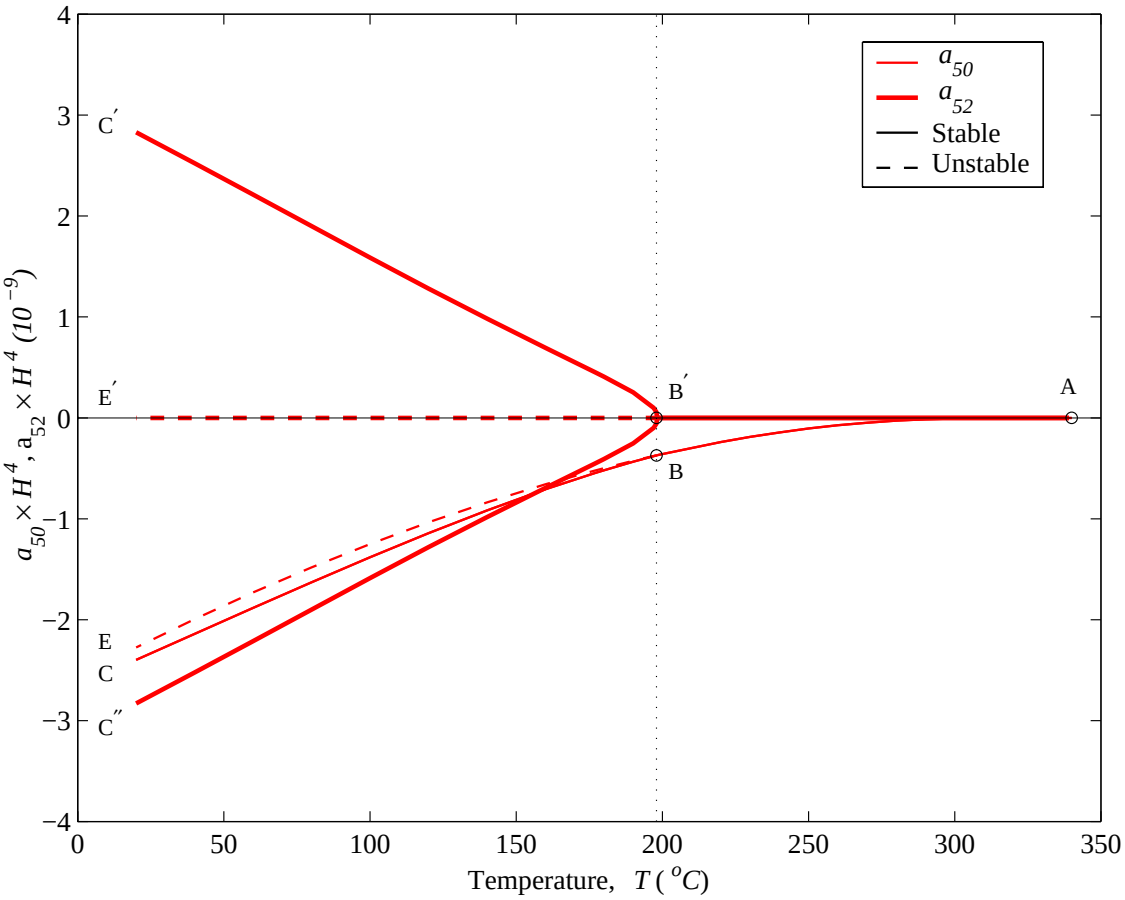


Figure 4.12: Temperature-curvature ($a_{50}$ and $a_{52}$) relation of disk-style RAINBOW ($R$=25.4 mm, $H$=0.381 mm, $H_r/H$=0.35).

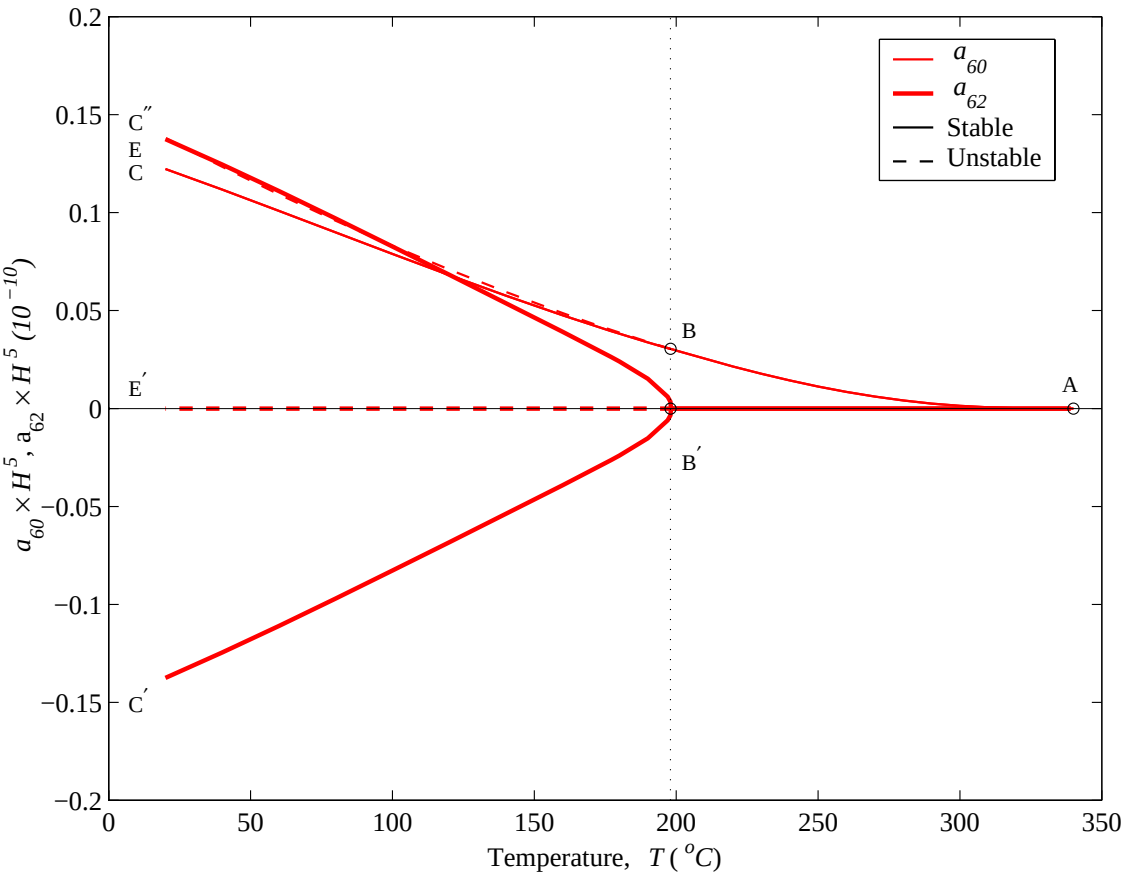


Figure 4.13: Temperature-curvature ($a_{60}$ and $a_{62}$) relation of disk-style RAINBOW ($R$=25.4 mm, $H$=0.381 mm, $H_r/H$=0.35).

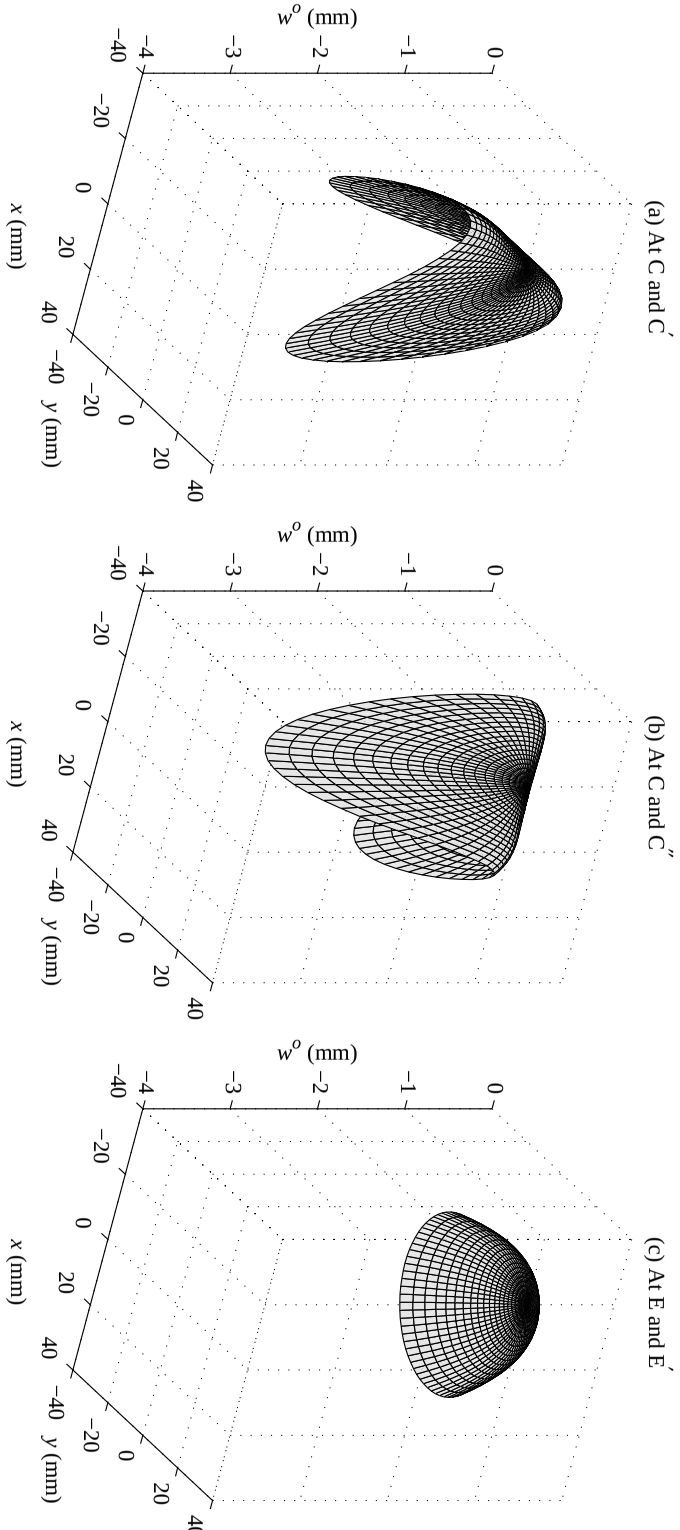


Figure 4.14: Equilibrium shapes of disk-style RAINBOW ($R$=25.4 mm, $H$=0.381 mm, $H_r/H$=0.35) (refer to Figures 4.9–4.13).

and 85-term approximations coincide. The results obtained using the 35-term approximation for $T < 150\ ^oC$ are less accurate than those for $T > 150\ ^oC$, because of the overly-stiff characteristics inherent in the Rayleigh-Ritz method. Moreover, in Figure 4.15 the calculations of $a_{20}$ and $a_{22}$, the dominant terms in the curvature expressions, are almost the same for both the 35- and 85-term approximations. Since the 35-term approximation takes much less computational effort than the 85-term approximation, it is more efficient and is used to carry out the numerical calculations in the sections to follow.

### 4.5.3 Effect of Geometry on Room-Temperature Shape

It is of interest to determine the influence of disk-style RAINBOW geometry on the characteristics of the shapes at room temperature. In particular, it is of interest to know how the radius influences the shapes. Figures 4.20-4.24 illustrate one of the most important features of the dependence of the room-temperature shape on geometry. In these figures the parameters $a_{ij}$, defining the curvatures, are plotted as a function of RAINBOW radius. For convenience, the axes in Figures 4.20-4.24 have been nondimensionalized by using RAINBOW thickness, $H$, as a scaling parameter. The reduced layer thickness to total thickness ratio, $H_r/H$, is fixed at 0.35. Referring to any of these figures, moving from small (small $R/H$) to large RAINBOW, it is seen that the relationship between room-temperature curvature and radius changes from being single-valued to being multiple-valued. For small radii, denoted by branches AB and A′B′ in Figures 4.20–4.24, the 35-term Rayleigh-Ritz approximation predicts single-valued nonzero coefficients $a_{20}$, $a_{30}$, $a_{40}$, $a_{50}$, and $a_{60}$, with the other coefficients ($a_{22}$, $a_{32}$, $a_{42}$, $a_{52}$, $a_{62}$) being zero. The nonzero coefficients represent curvatures which are independent of $\theta$ and the equilibrium configuration is thus a dome-like axisymmetric shape, and it is stable. At a radius corresponding to points B and B′, the coefficients $a_{20}$, $a_{30}$, $a_{40}$, $a_{50}$, and $a_{60}$ bifurcate into branches BC and BE, while the coefficients $a_{22}$, $a_{32}$, $a_{42}$, $a_{52}$, and $a_{62}$ trifurcate into branches B′C′, B′E′, and B′C″. This is interpreted to mean that for radii greater than the value corresponding to points B and B′, RAINBOW exhibits multiple room-temperature shapes. For radii considerably larger than that corresponding to points B and B′, one of these shapes is near-cylindrical, with a large curvature $\kappa_r^o$ occurring in the $\theta$=0 direction and practically no curvature $\kappa_r^o$ in the $\theta$=$\pi/2$ direction (Figure 4.14(a)). The other shape is also near-cylindrical

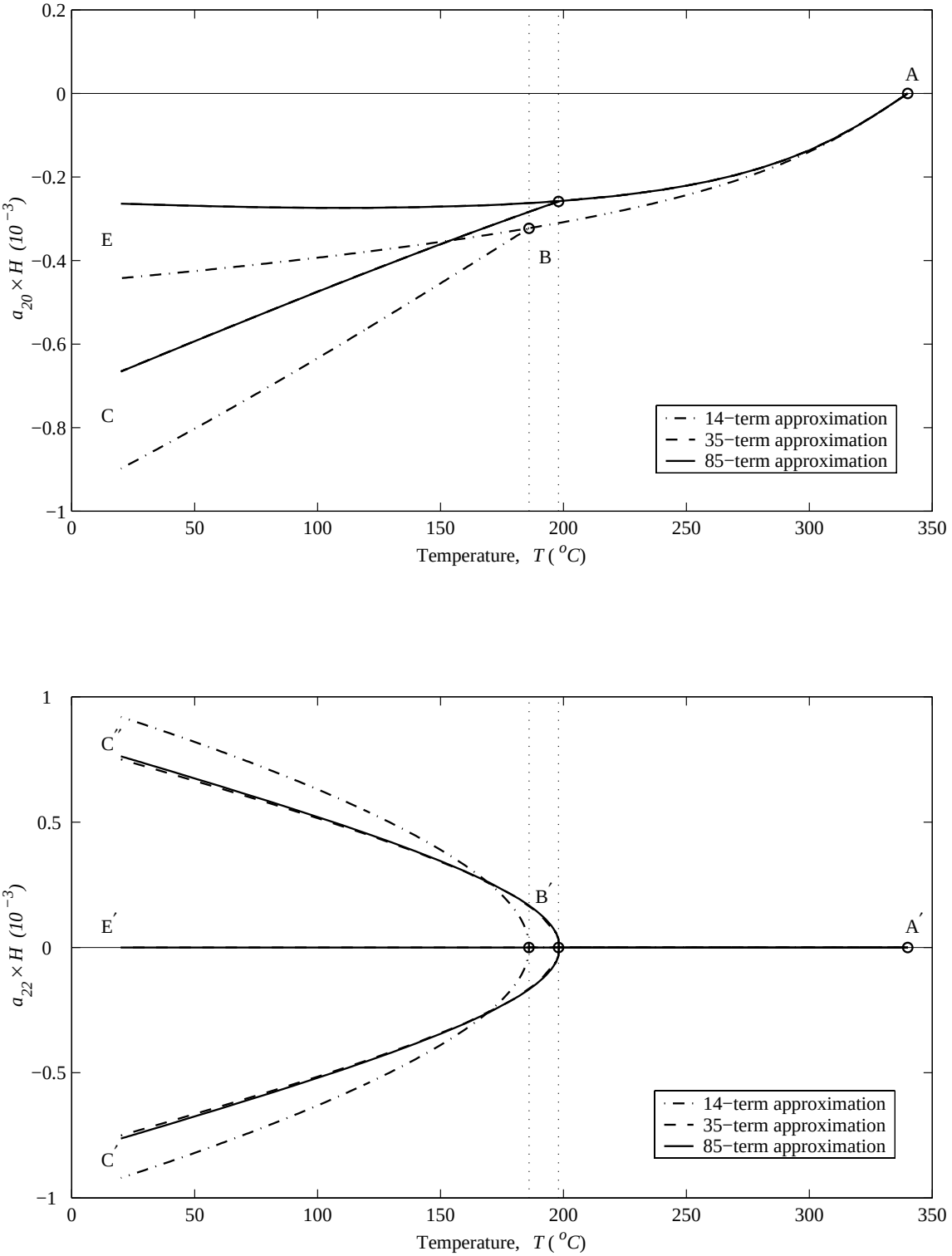


Figure 4.15: Convergence of the Rayleigh-Ritz method for the curvatures ($a_{20}$ and $a_{22}$) of disk-style RAINBOW ($R$=25.4 mm, $H$=0.381 mm, $H_r/H$=0.35).

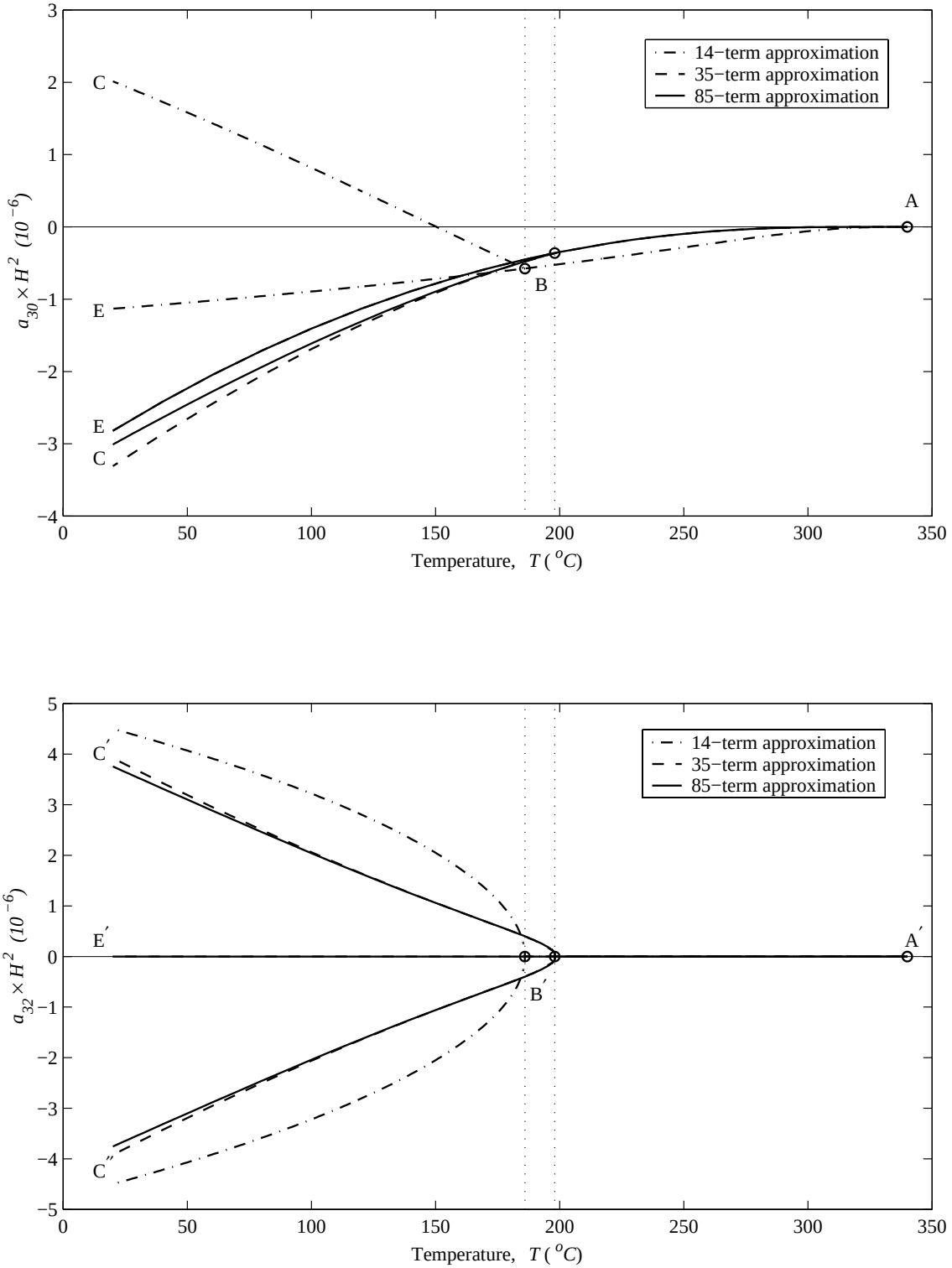


Figure 4.16: Convergence of the Rayleigh-Ritz method for the curvatures ($a_{30}$ and $a_{32}$) of disk-style RAINBOW ($R$=25.4 mm, $H$=0.381 mm, $H_r/H$=0.35).

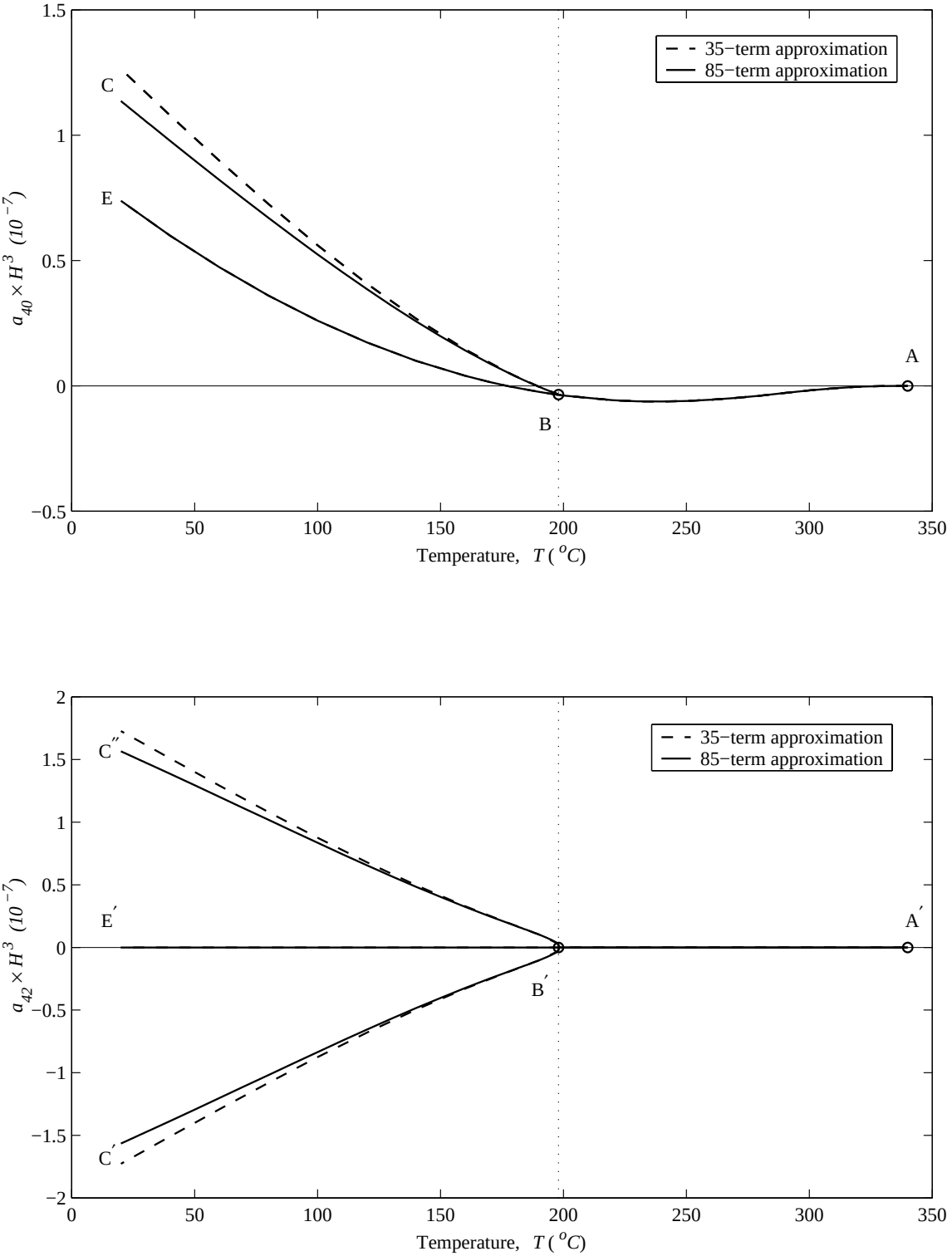


Figure 4.17: Convergence of the Rayleigh-Ritz method for the curvatures ($a_{40}$ and $a_{42}$) of disk-style RAINBOW ($R$=25.4 mm, $H$=0.381 mm, $H_r/H$=0.35).

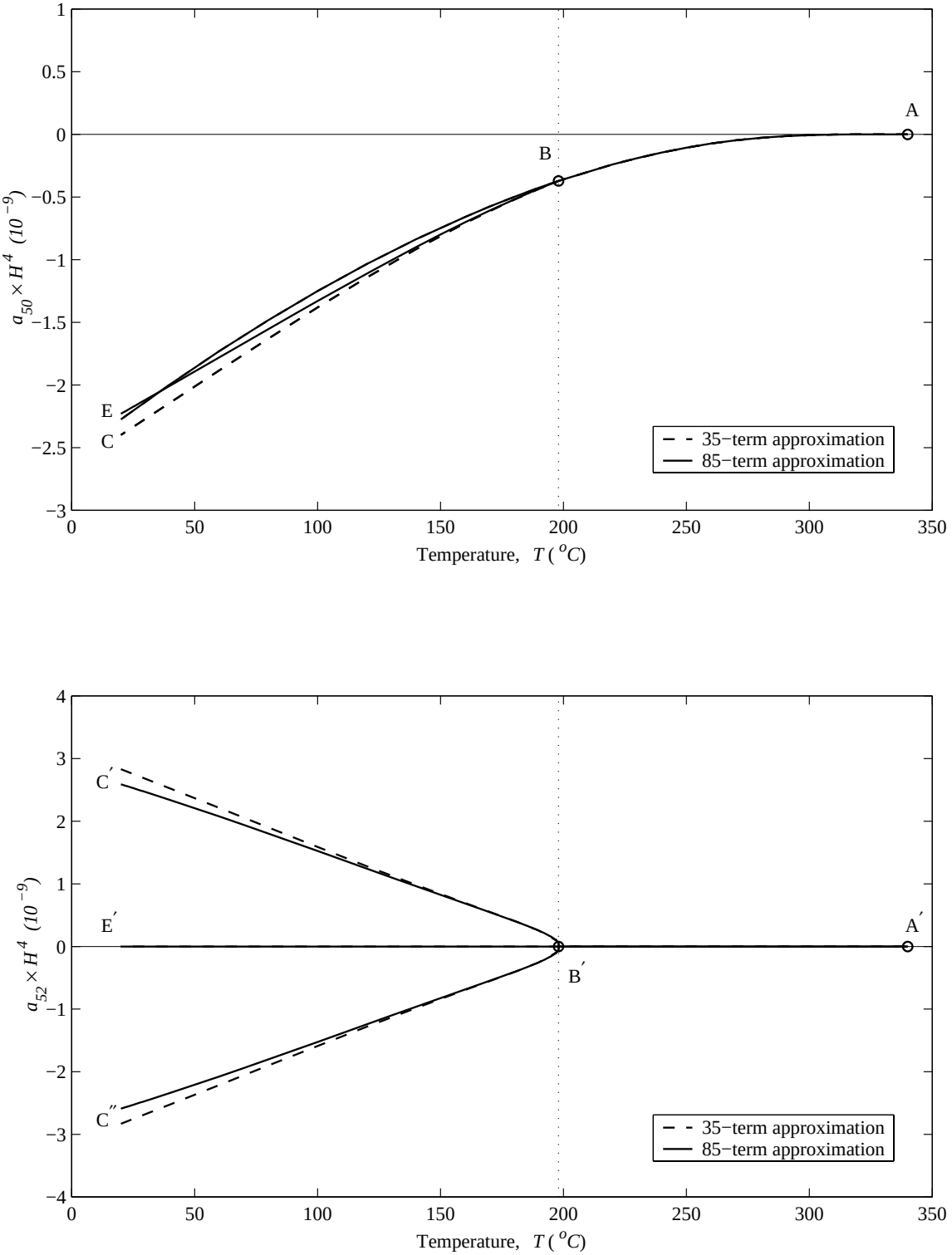


Figure 4.18: Convergence of the Rayleigh-Ritz method for the curvatures ($a_{50}$ and $a_{52}$) of disk-style RAINBOW ($R$=25.4 mm, $H$=0.381 mm, $H_r/H$=0.35).

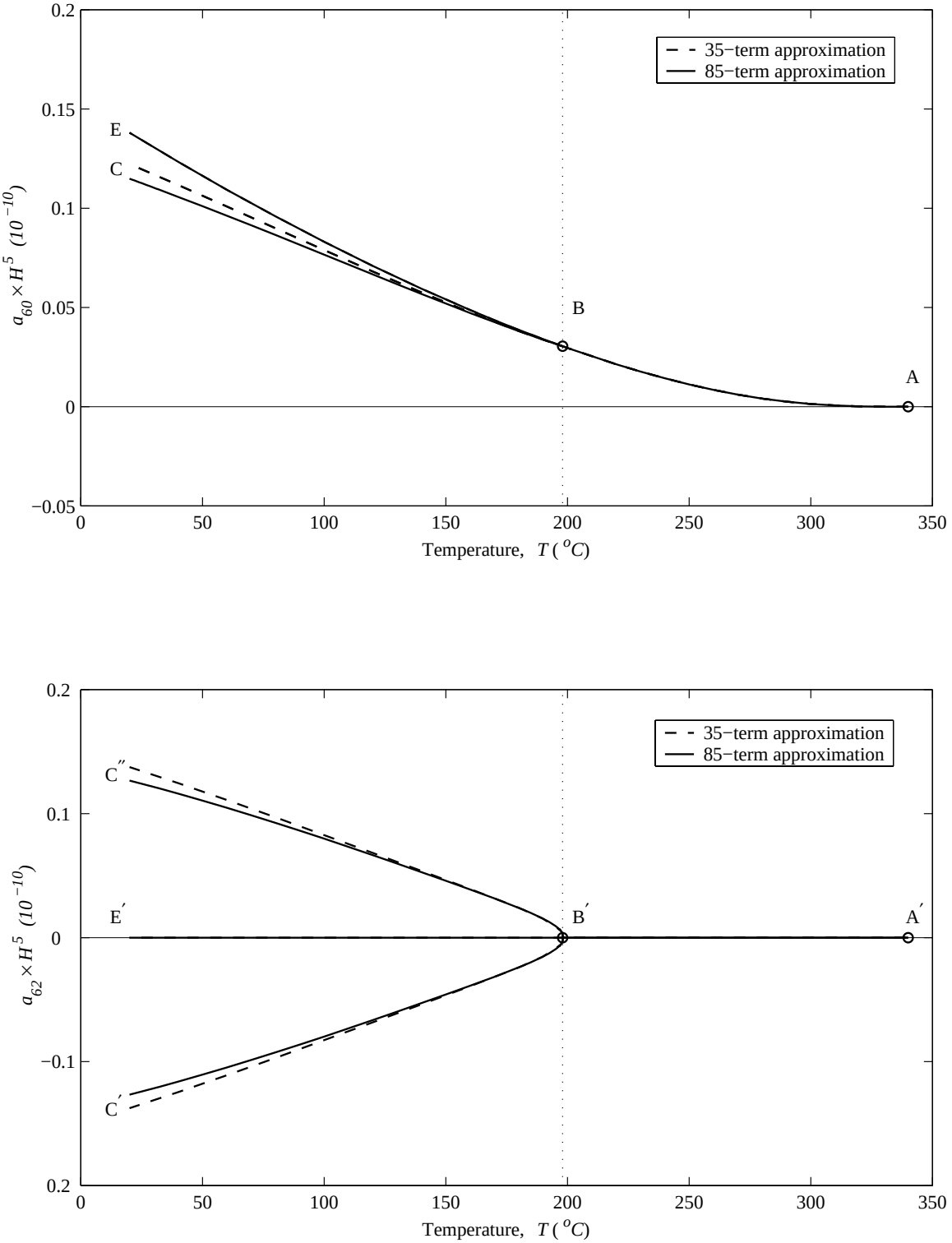


Figure 4.19: Convergence of the Rayleigh-Ritz method for the curvatures ($a_{60}$ and $a_{62}$) of disk-style RAINBOW ($R$=25.4 mm, $H$=0.381 mm, $H_r/H$=0.35).

but with practically no curvature $\kappa_r^o$ in the $\theta$=0 direction and a large curvature $\kappa_r^o$ in the $\theta$=$\pi/2$ direction (Figure 4.14(b)). Both of these shapes are stable. These two shapes are similar, but with the roles of curvatures $k_r^o$, $k_\theta^o$, and $k_{r\theta}^o$ differing in phase by a $\pi/2$ angle. The third shape is dome-like and it is unstable. Thus there is a critical radius to thickness ratio. For the case considered in Figures 4.20–4.24 the critical value is 44.3. For RAINBOW with a radius to thickness ratio just slightly larger than the critical value, it would not require much force to transform one shape to the other. In fact, the shape may change by simple handling of RAINBOW. For reference purposes, the value of $R/H$ for RAINBOW in Figures 4.9–4.13 is 67 ($R$=24.4 mm, $H$=0.381 mm), a value grater than the critical value. The existence of a critical value of $R/H$ could lead to unusual behavior. Unknowingly, RAINBOW may be manufactured that has a value of $R/H$ very close to the critical value. If two disk-style RAINBOW are manufactured with this geometry, they may behave quite differently because of small variations in material properties or thicknesses, nonuniform cooling, and other such defects in manufacturing.

For the record, Figures 4.25–4.29 illustrate the convergence characteristics of the $a_{ij}$ coefficients vs. $R/H$ for the three sets of functions in Equations (4.61), (4.66), and (4.69). Again, from these figures, it can be seen that the 14-term approximation is not in complete agreement with the 35- and 85-term approximations; however, it is able to predict the critical value of $R/H$ to within 4.3% of the converged value $R/H$=44.3. As the number of terms in approximation is increased, the critical value of $R/H$ converges to the 'exact' value from above. This verifies the general trend that the Rayleigh-Ritz method provides an upper bound on solutions when the potential energy is being minimized. These figures also indicate that the 35-term approximation is enough to predict an accurate approximation for the critical value of $R/H$. For $R/H < 50$, all the branches corresponding to the 35- and 85-term approximations are coincident. The results obtained using the 35-term approximation corresponding to higher values of $R/H$ ($R/H > 50$) are less accurate than those corresponding to $R/H < 50$, because of the overly-stiff characteristics inherent in the Rayleigh-Ritz method. The error may be made as small as desired by increasing the number of terms in the approximation, which is reflected in the 85-term approximation.

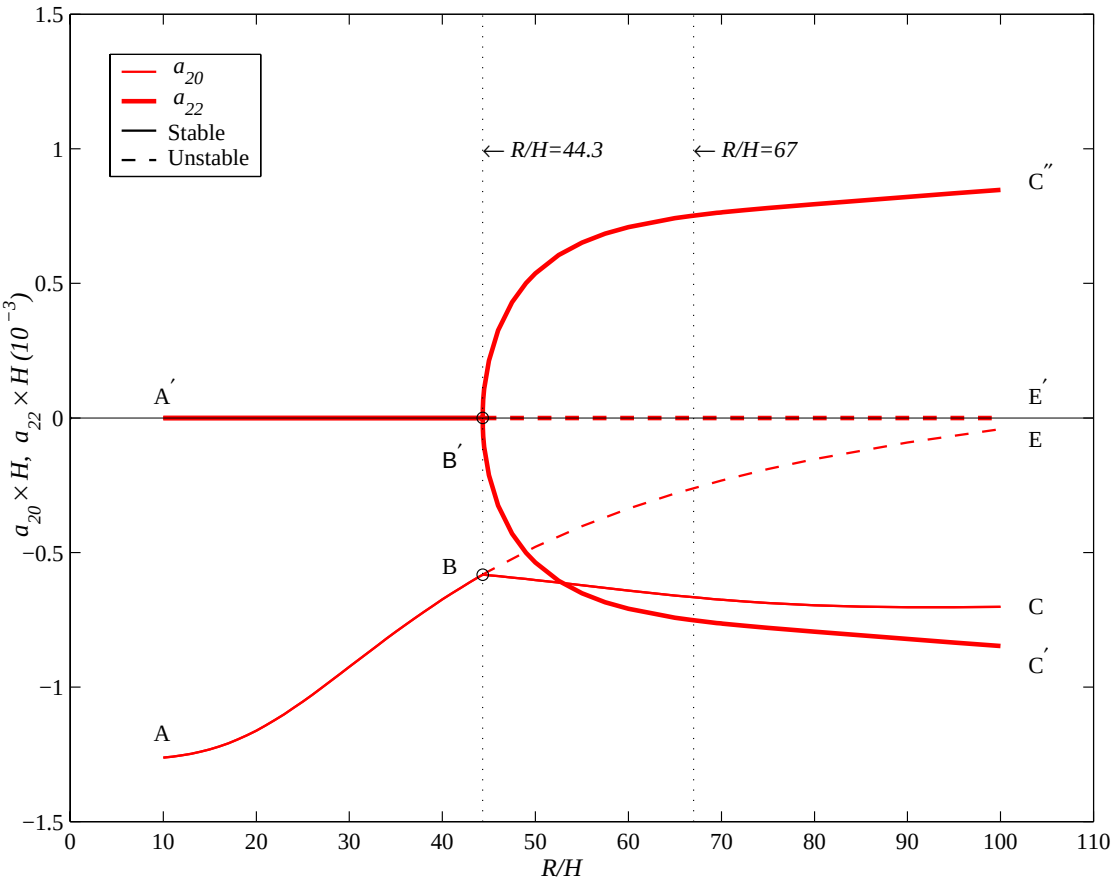


Figure 4.20: Room-temperature shapes ($a_{20}$ and $a_{22}$) of disk-style RAINBOW as a function of geometry ($H_r/H$=0.35).

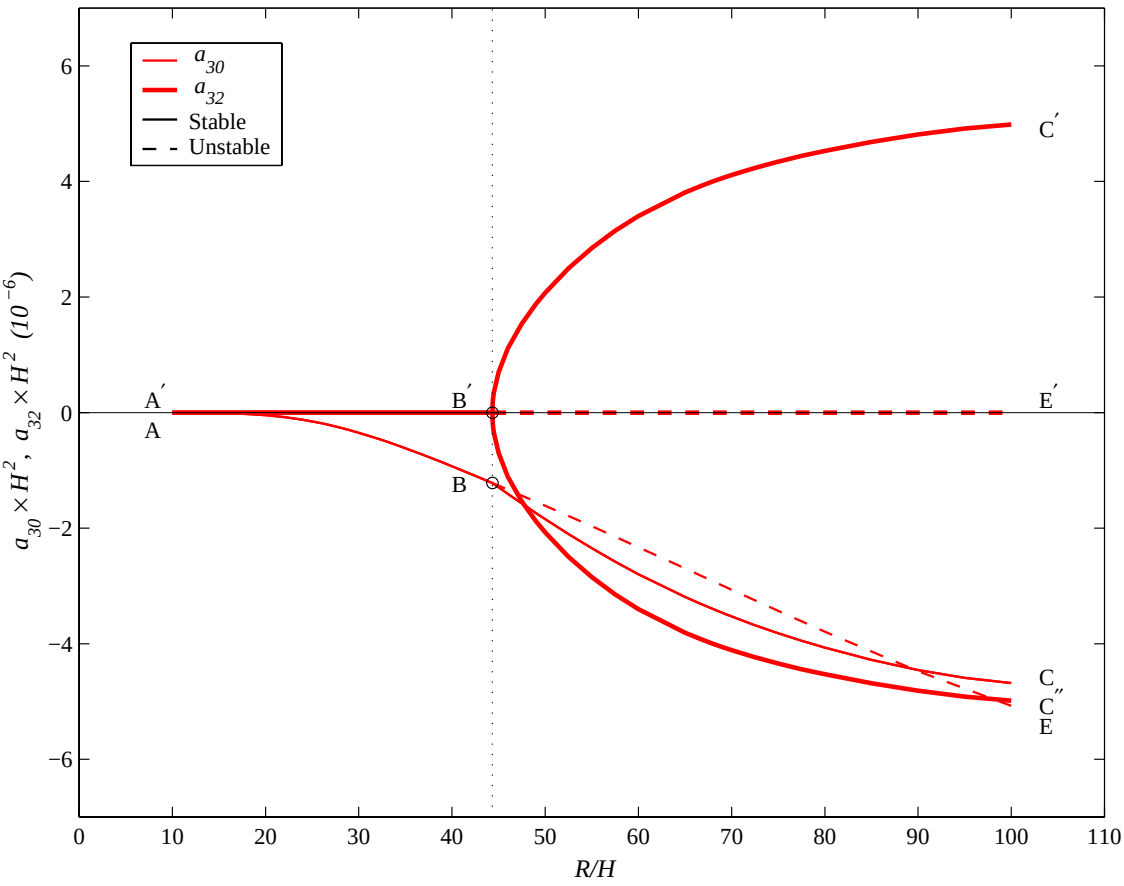


Figure 4.21: Room-temperature shapes ($a_{30}$ and $a_{32}$) of disk-style RAINBOW as a function of geometry ($H_r/H$=0.35).

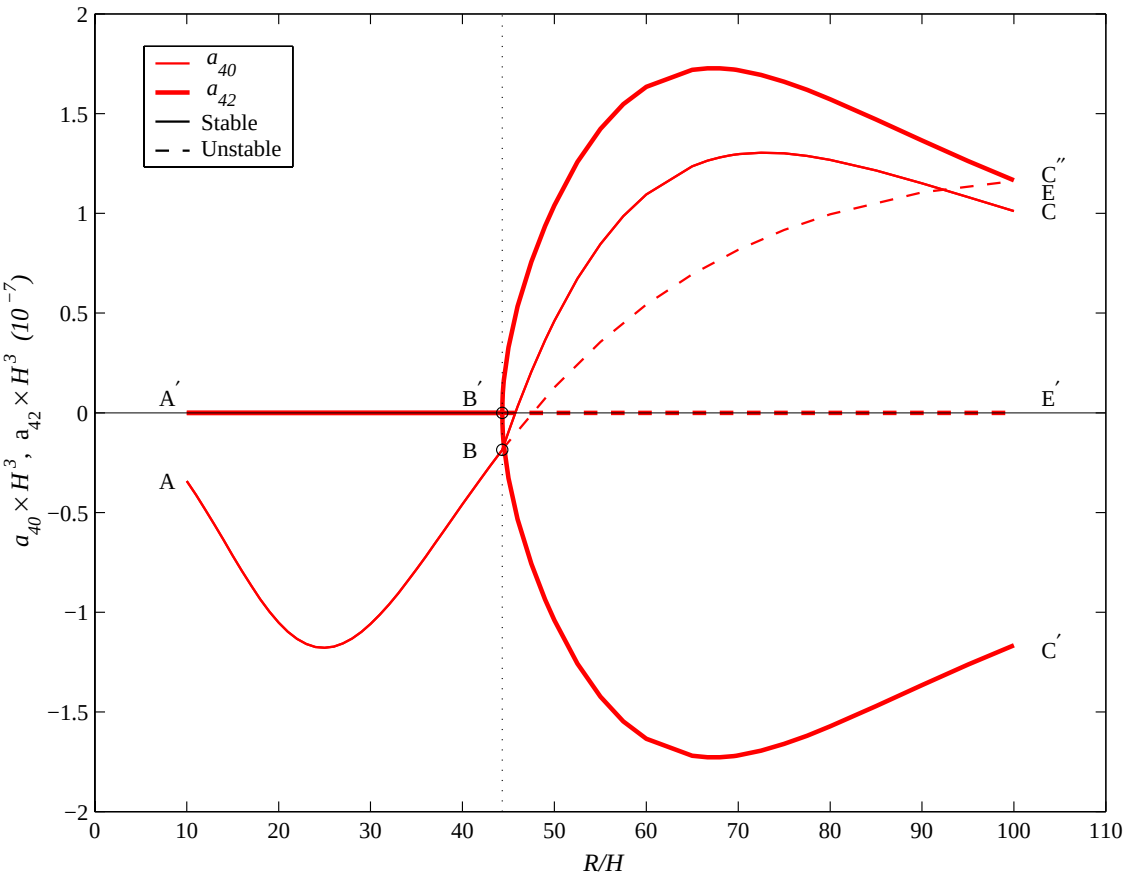


Figure 4.22: Room-temperature shapes ($a_{40}$ and $a_{42}$) of disk-style RAINBOW as a function of geometry ($H_r/H$=0.35).

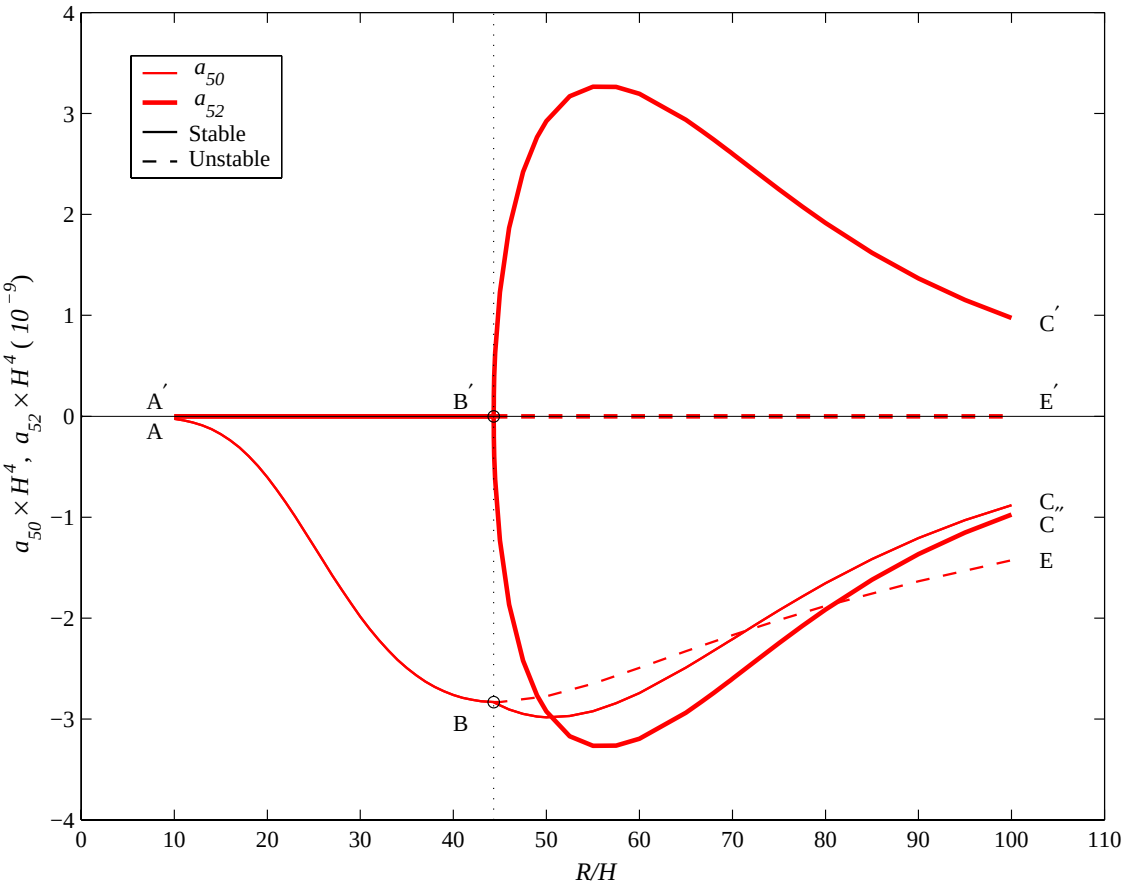


Figure 4.23: Room-temperature shapes ($a_{50}$ and $a_{52}$) of disk-style RAINBOW as a function of geometry ($H_r/H$=0.35).

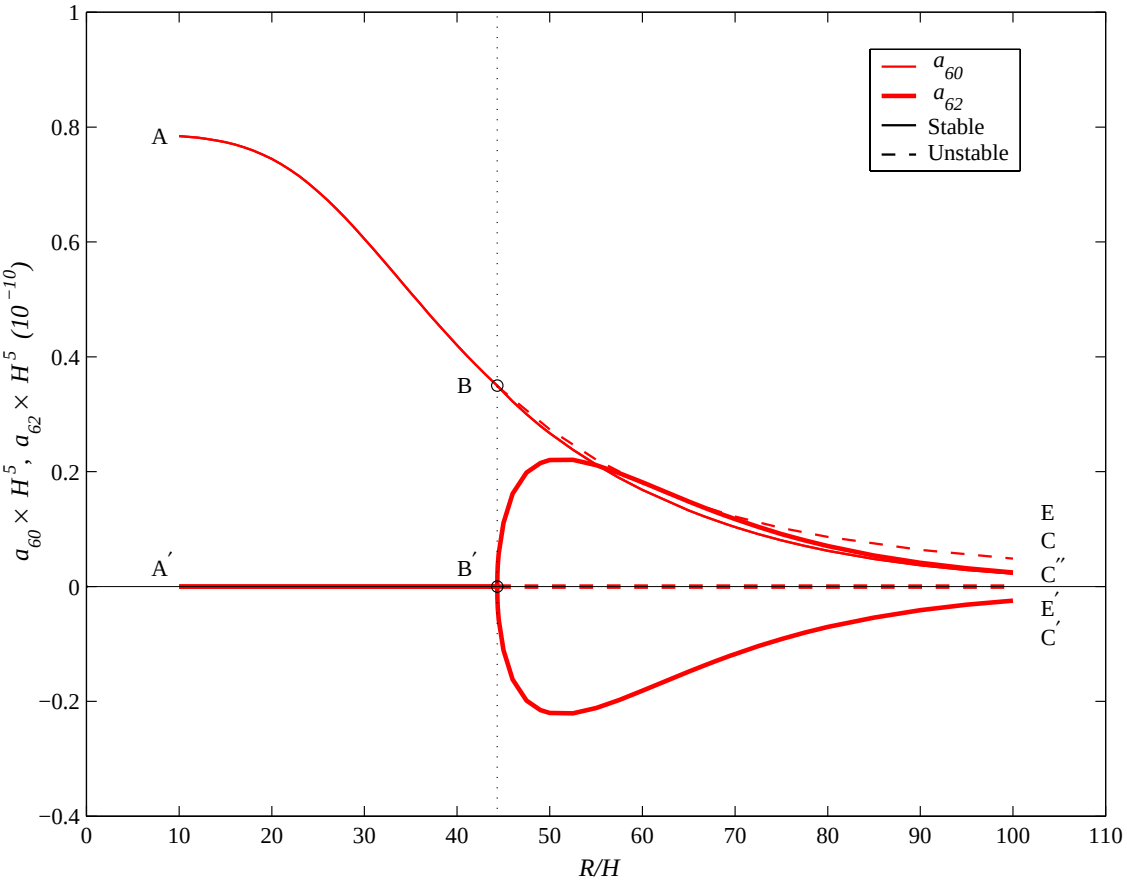


Figure 4.24: Room-temperature shapes ($a_{60}$ and $a_{62}$) of disk-style RAINBOW as a function of geometry ($H_r/H$=0.35).

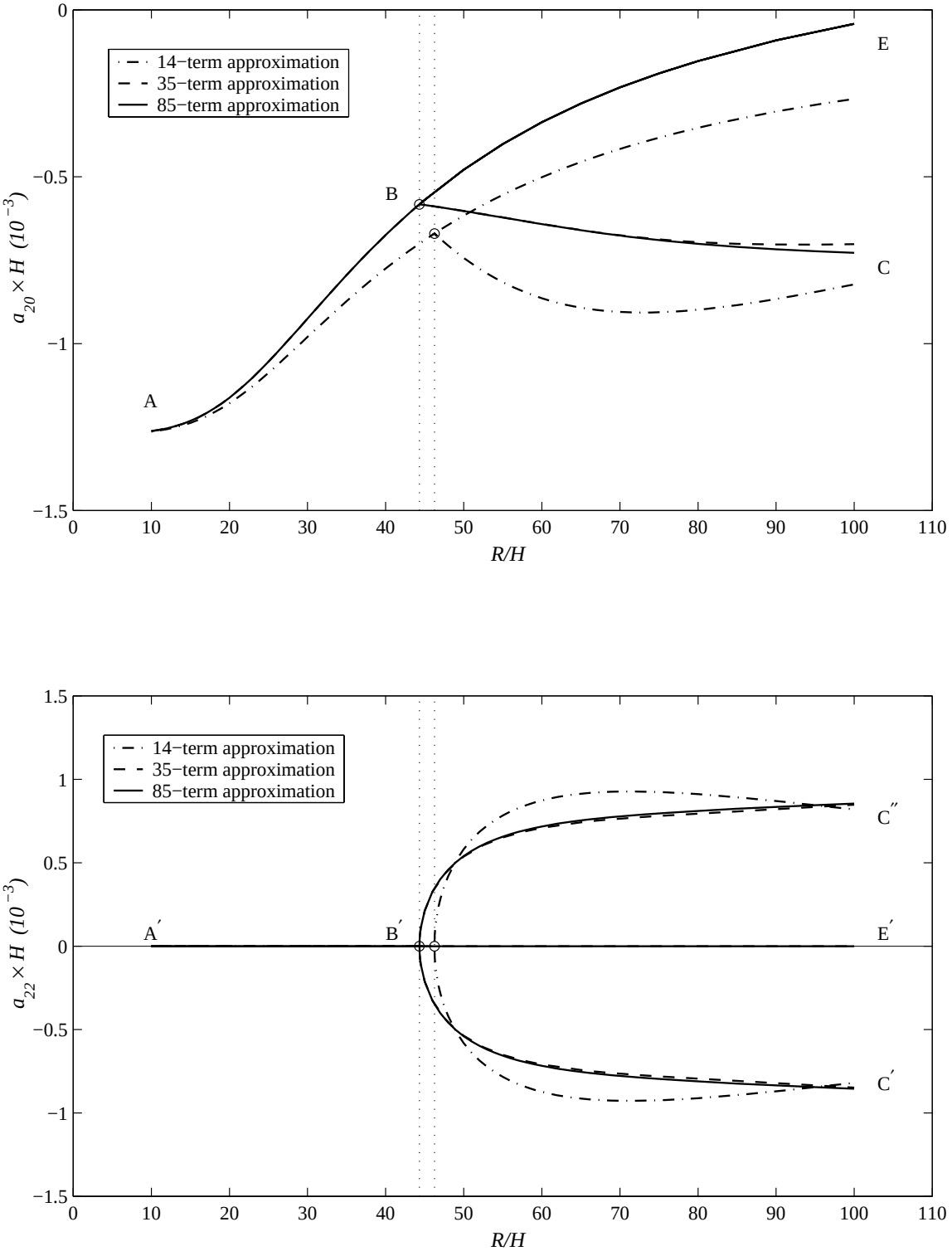


Figure 4.25: Convergence of the Rayleigh-Ritz method for the room-temperature curvatures ($a_{20}$ and $a_{22}$) of disk-style RAINBOW as a function of geometry ($H_r/H$=0.35).

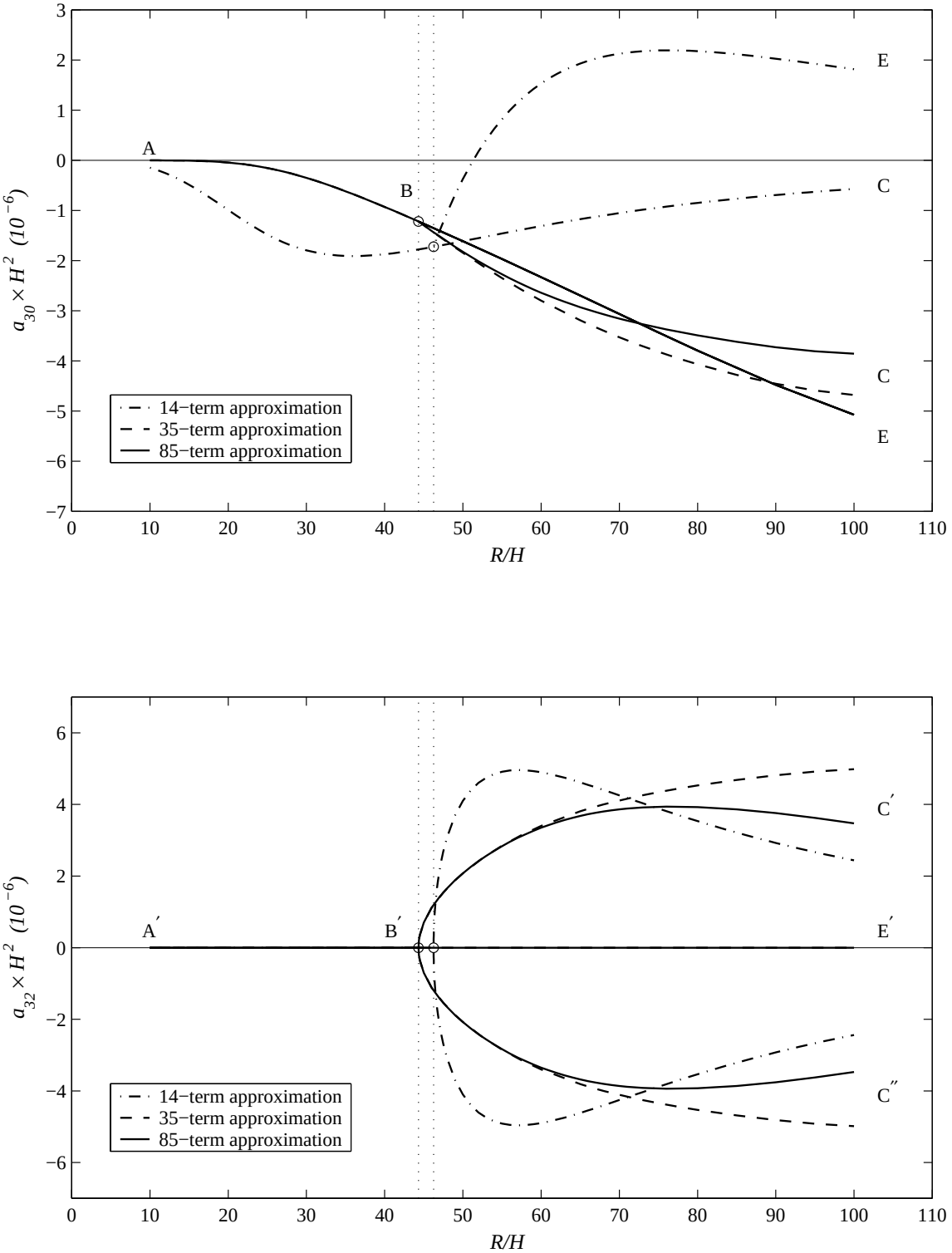


Figure 4.26: Convergence of the Rayleigh-Ritz method for the room-temperature curvatures ($a_{30}$ and $a_{32}$) of disk-style RAINBOW as a function of geometry ($H_r/H$=0.35).

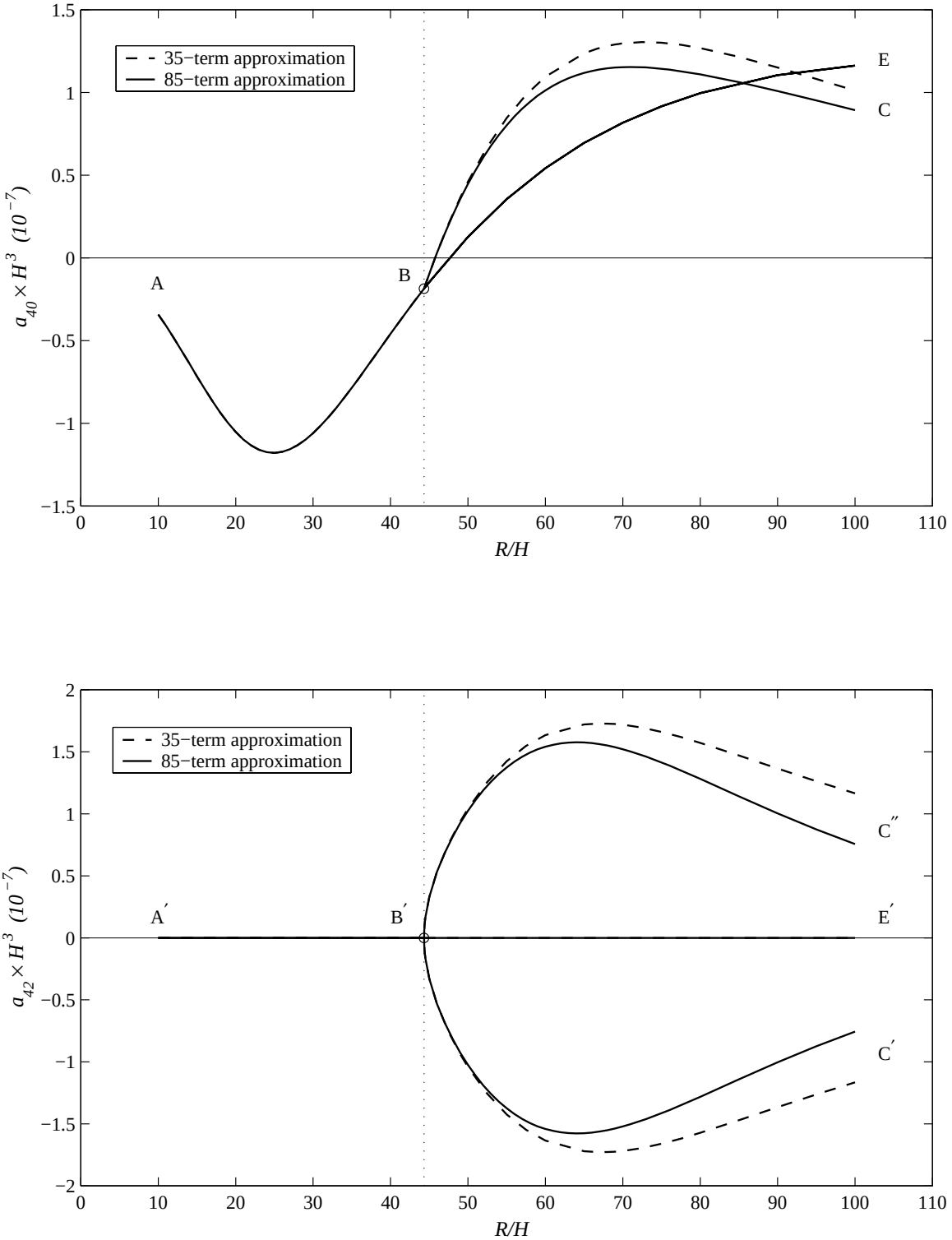


Figure 4.27: Convergence of the Rayleigh-Ritz method for the room-temperature curvatures ($a_{40}$ and $a_{42}$) of disk-style RAINBOW as a function of geometry ($H_r/H$=0.35).

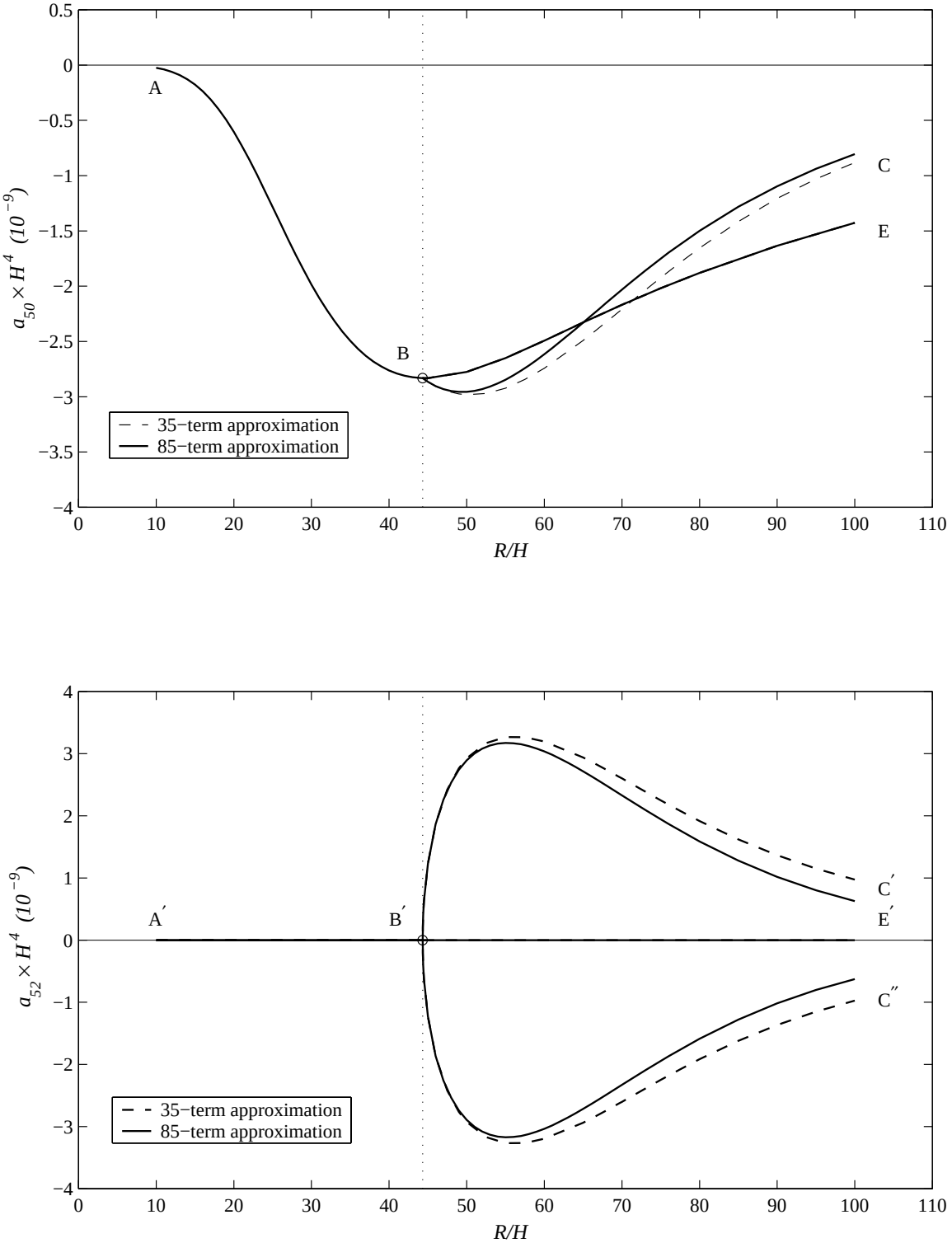


Figure 4.28: Convergence of the Rayleigh-Ritz method for the room-temperature curvatures ($a_{50}$ and $a_{52}$) of disk-style RAINBOW as a function of geometry ($H_r/H$=0.35).

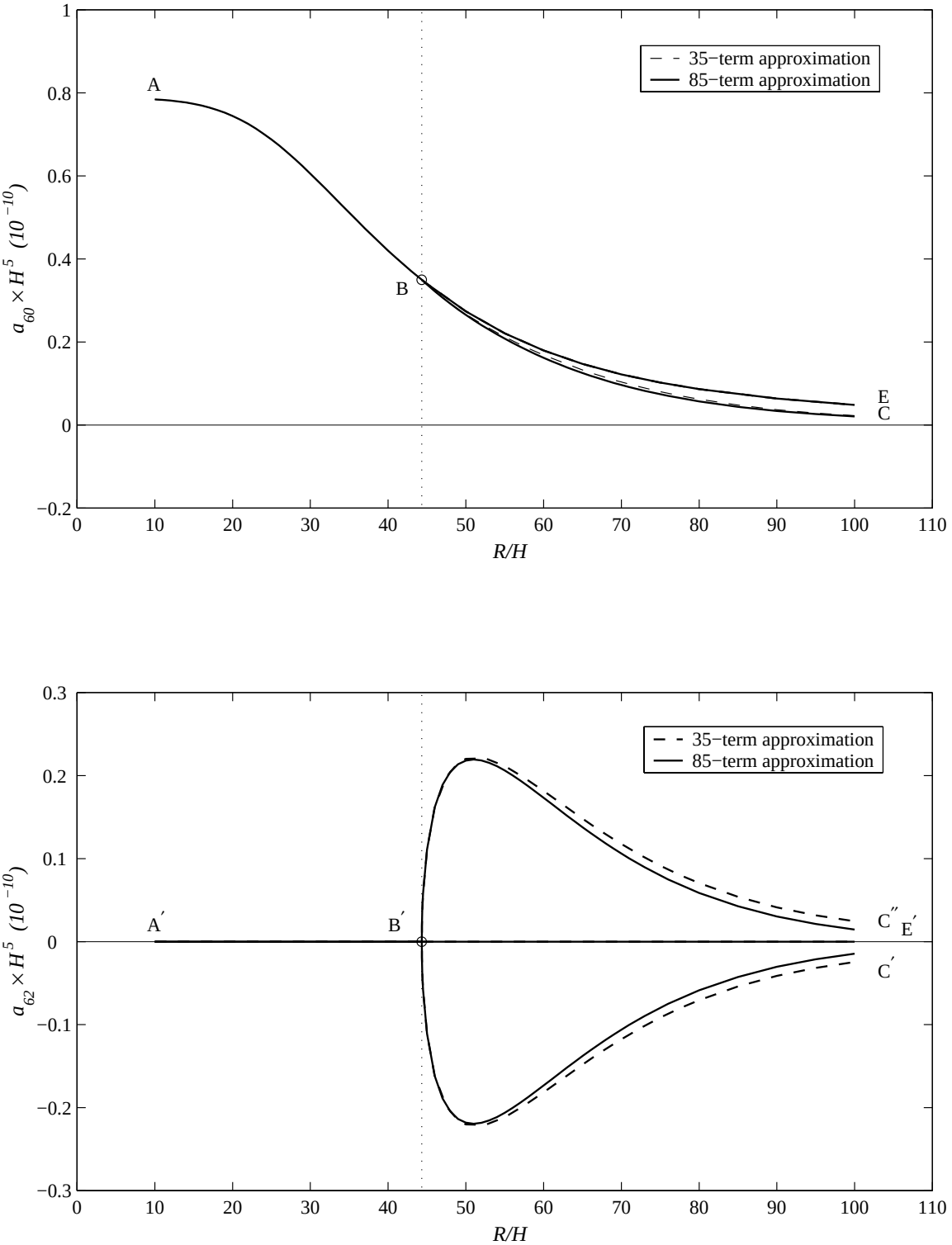


Figure 4.29: Convergence of the Rayleigh-Ritz method for the room-temperature curvatures ($a_{60}$ and $a_{62}$) of disk-style RAINBOW as a function of geometry ($H_r/H$=0.35).

### 4.5.4 Effect of Reduced Layer Thickness on Room-Temperature Shape

In addition to the effect of geometry on room-temperature shapes, it is of interest to determine the influence of the reduced layer thickness on the characteristics of the shapes of disk-style RAINBOW at room temperature. Figures 4.30–4.34 illustrate the most important features of the dependence of the room-temperature shape on reduced layer thickness. In these figures the parameters $a_{ij}$ are plotted as a function of reduced layer thickness. Again, for convenience the axes have been nondimensionalized by using RAINBOW thickness, $H$, as a scaling parameter. The radius-to-thickness ratio in Figures 4.30-4.34 is fixed at 67. In these figures, it is shown that the relationship between reduced layer thickness and room-temperature curvatures changes from being single valued to multiple valued and again to single valued as the reduced layer thickness is increased from 0 to 100% of total thickness. For small reduced layer thickness, denoted by branches $\mathrm{A_1B_1}$ and $\mathrm{A'_1B'_1}$ in Figures 4.30–4.34, RAINBOW is predicted to have but one room-temperature shape. That shape is an axisymmetric dome shape and it is stable. At a reduced layer thickness corresponding to points $B_1$ and $B'_1$, the coefficients $a_{20}$, $a_{30}$, $a_{40}$, $a_{50}$, and $a_{60}$ bifurcate into branches $\mathrm{B_1C_1}$ and and $\mathrm{B_1E_1}$, while the coefficients $a_{22}$, $a_{32}$, $a_{42}$, $a_{52}$, and $a_{62}$ trifurcate into branches $\mathrm{B'_1C'_1}$, $\mathrm{B'_1C''_1}$, and $\mathrm{B'_1E'_1}$. On the other hand, at a reduced layer thickness corresponding to points $B_2$ and $\mathrm{B'_2}$, the relationship changes from being multiple valued to being single values, as depicted by branches $\mathrm{B_2A_2}$ and $\mathrm{B'_2A'_2}$. This is interpreted to mean that for reduced layer thickness between the two values corresponding to points $\mathrm{B_1}$ and $\mathrm{B'_1}$ and points $\mathrm{B_2}$ and $\mathrm{B'_2}$, RAINBOW exhibits multiple room-temperature shapes. One of these shapes is near-cylindrical, with a larger curvature $\kappa_r^o$ in the $\theta$=0 direction than in the $\theta$=$\pi/2$ direction. The other is also near-cylindrical, but with the roles of curvatures $k_r^o$, $k_\theta^o$, and $k_{r\theta}^o$ different in phase by $\pi/2$. The third shape is axisymmetric and it is unstable. For reduced layer thickness smaller than the value corresponding to points $\mathrm{B_1}$ and $\mathrm{B'_1}$ or greater than the value corresponding to points $\mathrm{B_2}$ and $\mathrm{B'_2}$, RAINBOW exhibits one stable axisymmetric room-temperature shape. For the case considered in Figures 4.30–4.34 the critical values corresponding to points $\mathrm{B_1}$ and $\mathrm{B'_1}$ and points $\mathrm{B_2}$ and $\mathrm{B'_2}$ are 14% and 92%, respectively. Figures 4.30–4.34 indicate that at a reduced layer thickness of 55%, the maximum values (major curvature) and the minimum values (minor curvature) of $a_{ij}$ are achieved. For the sake of comparison of the characteristics of the shapes of disk-style RAINBOW at room temperature, the results shown in Figures 4.9–4.13 and 4.20–4.24

of sections 4.3.2 and 4.3.3, respectively, are reproduced using a reduced layer thickness of 55%. These results are depicted in Figures 4.35–4.44. Figures 4.35–4.39 indicate that the trifurcation temperature corresponding to points B and B′ is 217 $^o$C, 19 $^o$C higher than the one in Figures 4.9–4.13. In Figures 4.40–4.44, the critical radius to thickness ratio $R/H$ corresponding to points B and B′ is 41.3. This value is lower than the one corresponding to 35% reduced layer thickness, which results in a critical radius to thickness value of 44.3.

The results discussed above show that the existence of critical values of reduced layer thickness could add more complexity to the unusual behavior of disk-style RAINBOW. A nonuniform reduction process during the manufacturing of RAINBOW will no doubt influence the room-temperature shapes. If two RAINBOW with the same geometry are manufactured with reduced layer thickness close to a critical value, they may perform differently due to small inconsistencies between the two.

### 4.5.5 Application of an Electric Field

Figures 4.45–4.49 illustrate the relationship between the change in the coefficients $a_{ij}$ relative to their room-temperature values, $\Delta a_{ij}$, as a function of the electric field strength for the range $E$=1.5 MV/m. It is assumed that RAINBOW is in a shape represented by a large curvature $\kappa_r^o$ in the $\theta = 0$ direction, point C′ in Figures 4.9–4.13. The polarity of the unreduced piezoceramic material is assumed to be as shown in Figure 4.3 and, as in Chapters 2 and 3, the sign of $E$ is such so as to produce contraction strains in the unreduced piezoceramic in the $r$ and $\theta$ directions. The piezoelectric coefficients of the unreduced piezoceramic are given in Table 2.1. As can be seen in Figure 4.45, a reasonable change in the major coefficients, $\Delta a_{20}$ and $\Delta a_{22}$, can be achieved with a moderate field strength. For the case considered, a positive $E$ tends to flatten RAINBOW in the $\theta = 0$ and $\theta = \pi$ directions. Figures 4.46–4.49 indicate that the coefficients $\Delta a_{32}$, $\Delta a_{40}$, $\Delta a_{52}$, and $\Delta a_{60}$ behave in an opposite way to $\Delta a_{20}$ and $\Delta a_{22}$, i.e., they decrease with a positive $E$ and increase with a negative $E$. However, since the variations $\Delta a_{32}$, $\Delta a_{40}$, $\Delta a_{52}$, and $\Delta a_{60}$, are small compared to variations $\Delta a_{20}$ and $\Delta a_{22}$, the behavior of RAINBOW is, to a large extent, governed by the variations in $a_{20}$ and $a_{22}$. It should be noted that the relationship between $\Delta a_{ij}$ and $E$ is very close to being linear, which makes the task of analyzing the dynamical actuation of disk-style RAINBOW much simpler.

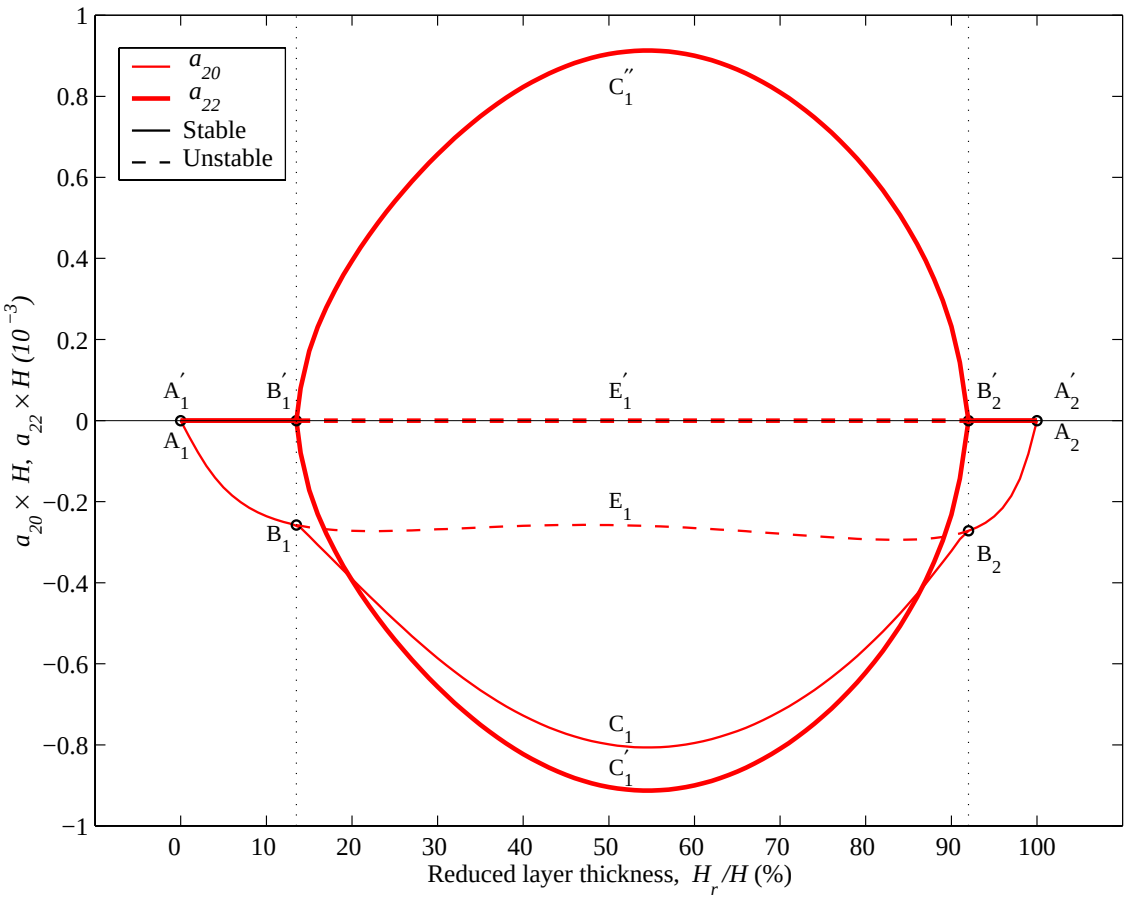


Figure 4.30: Room-temperature shapes ($a_{20}$ and $a_{22}$) of disk-style RAINBOW as a function of reduced layer thickness ($R$=25.4 mm, $H$=0.381 mm).

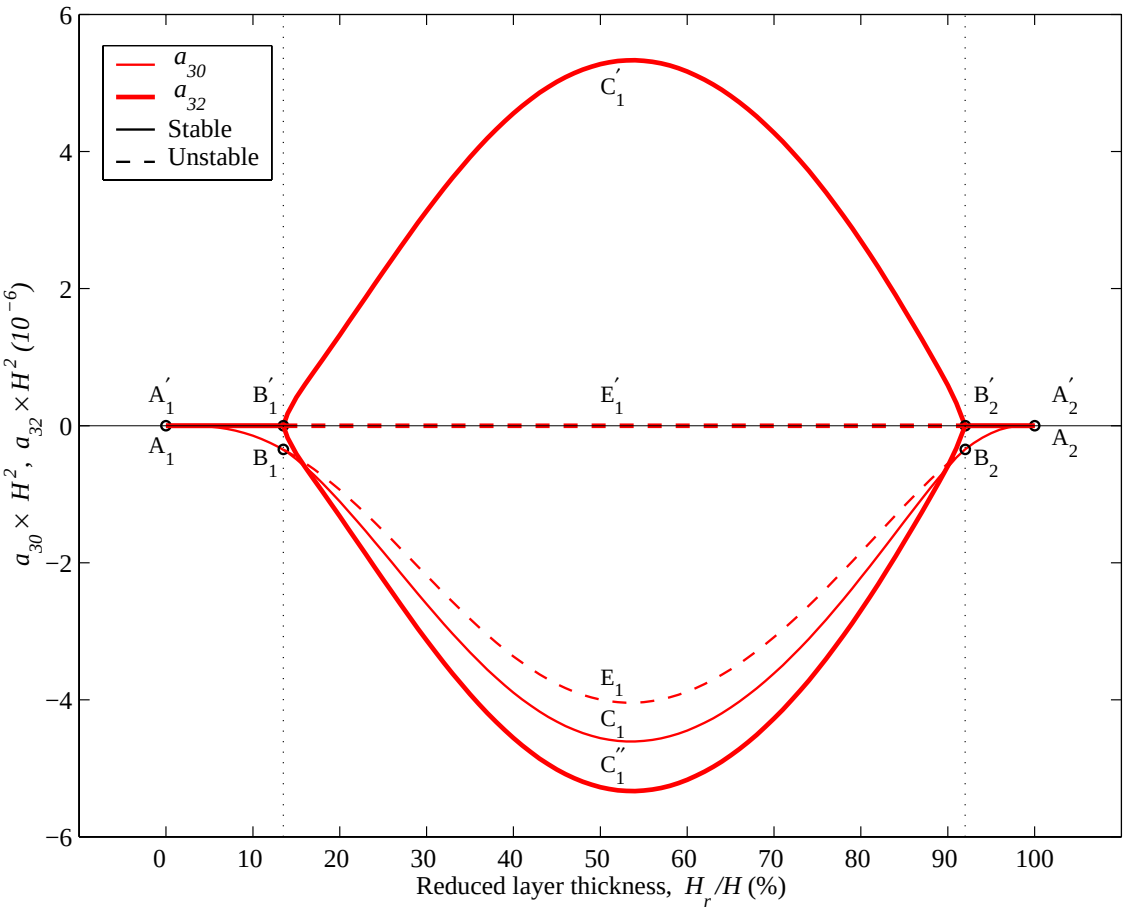


Figure 4.31: Room-temperature shapes ($a_{30}$ and $a_{32}$) of disk-style RAINBOW as a function of reduced layer thickness ($R$=25.4 mm, $H$=0.381 mm).

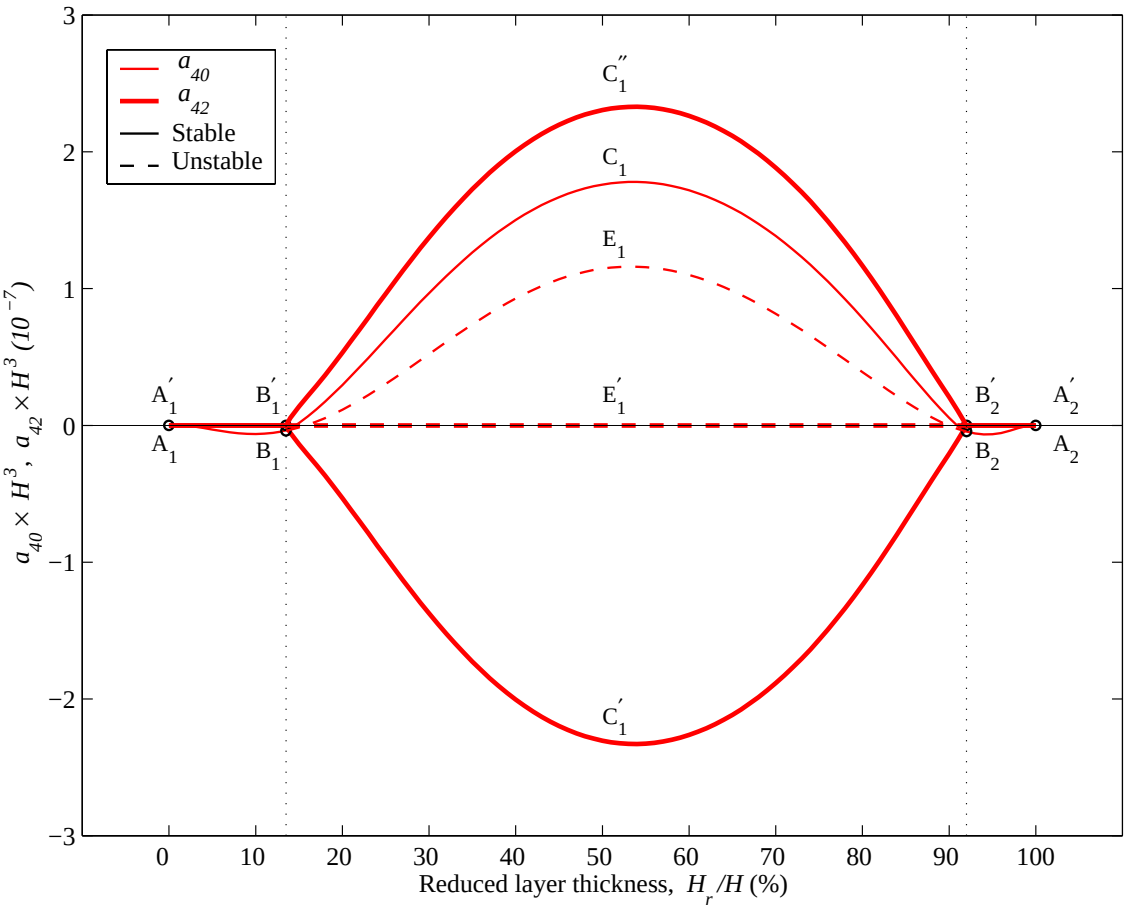


Figure 4.32: Room-temperature shapes ($a_{40}$ and $a_{42}$) of disk-style RAINBOW as a function of reduced layer thickness ($R$=25.4 mm, $H$=0.381 mm).

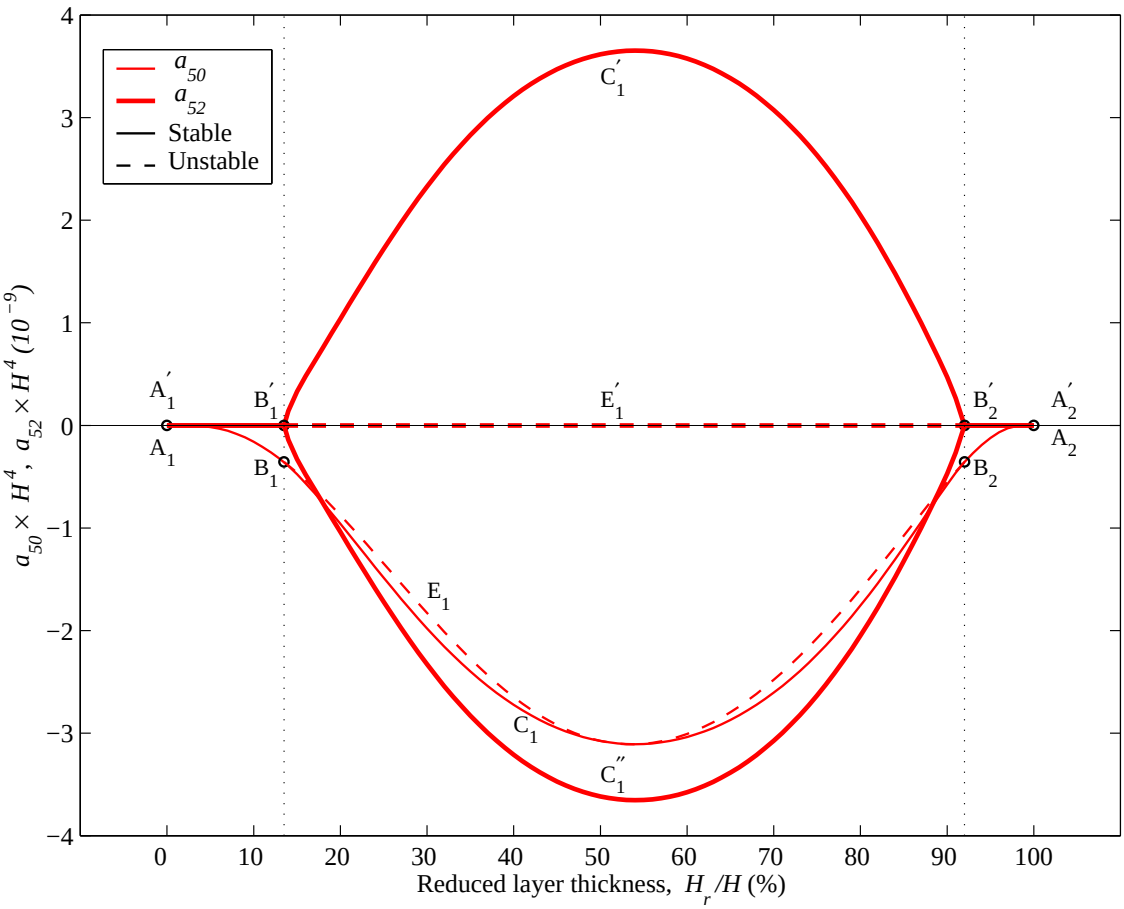


Figure 4.33: Room-temperature shapes ($a_{50}$ and $a_{52}$) of disk-style RAINBOW as a function of reduced layer thickness ($R$=25.4 mm, $H$=0.381 mm).

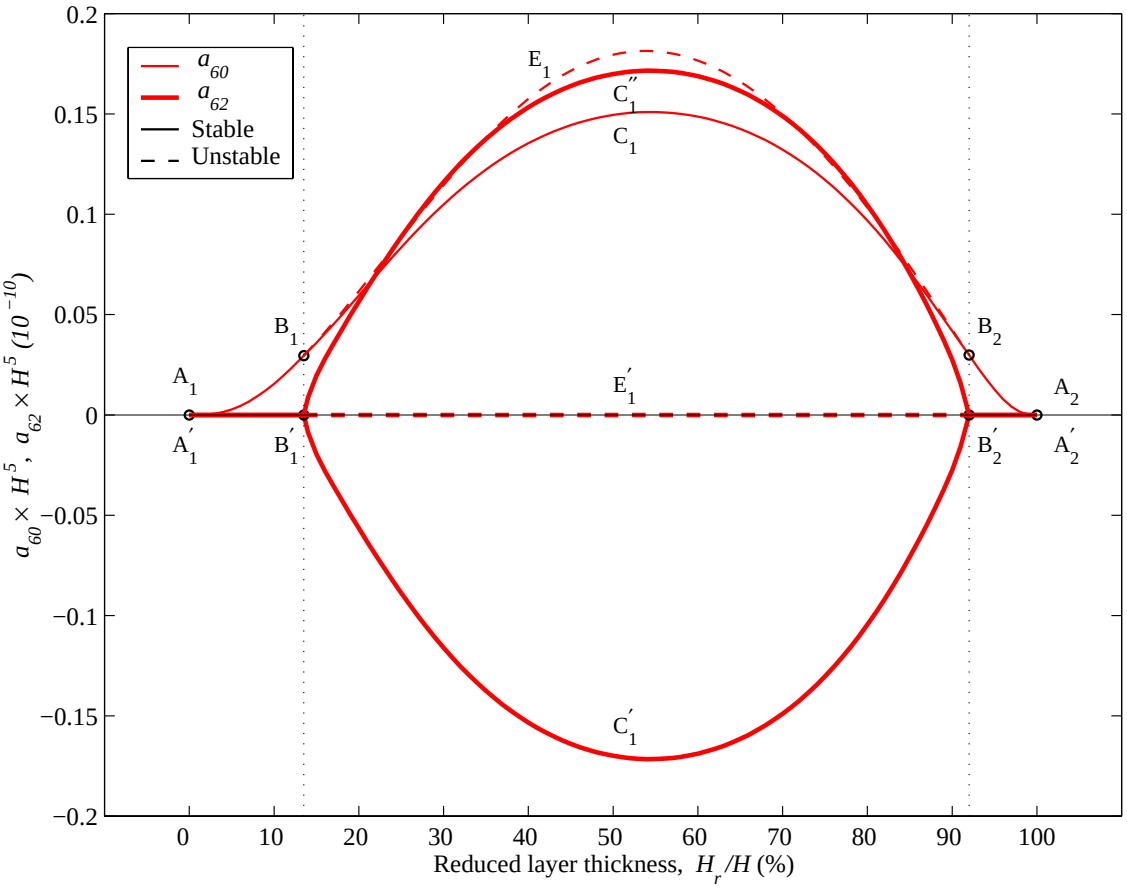


Figure 4.34: Room-temperature shapes ($a_{60}$ and $a_{62}$) of disk-style RAINBOW as a function of reduced layer thickness ($R$=25.4 mm, $H$=0.381 mm).

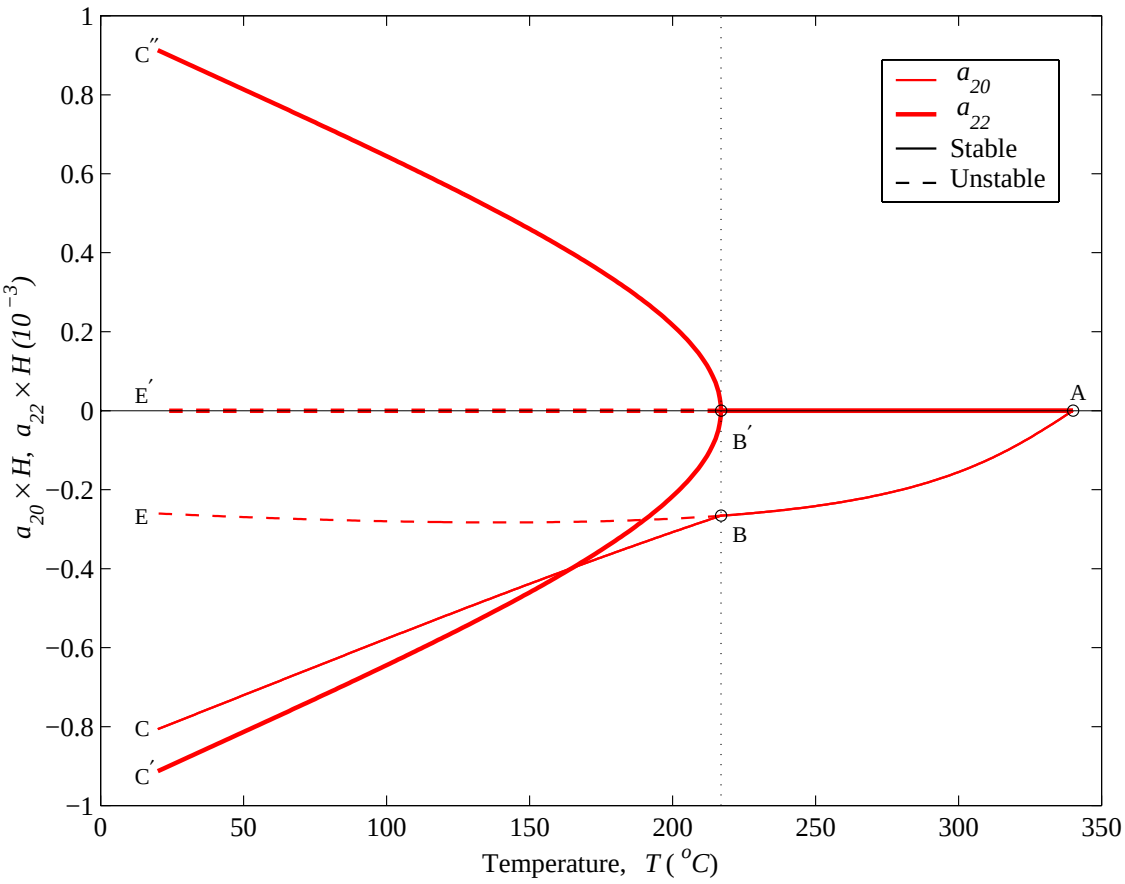


Figure 4.35: Temperature-curvature ($a_{20}$ and $a_{22}$) relation of disk-style RAINBOW ($R$=25.4 mm, $H$=0.381 mm, $H_r/H$=0.55).

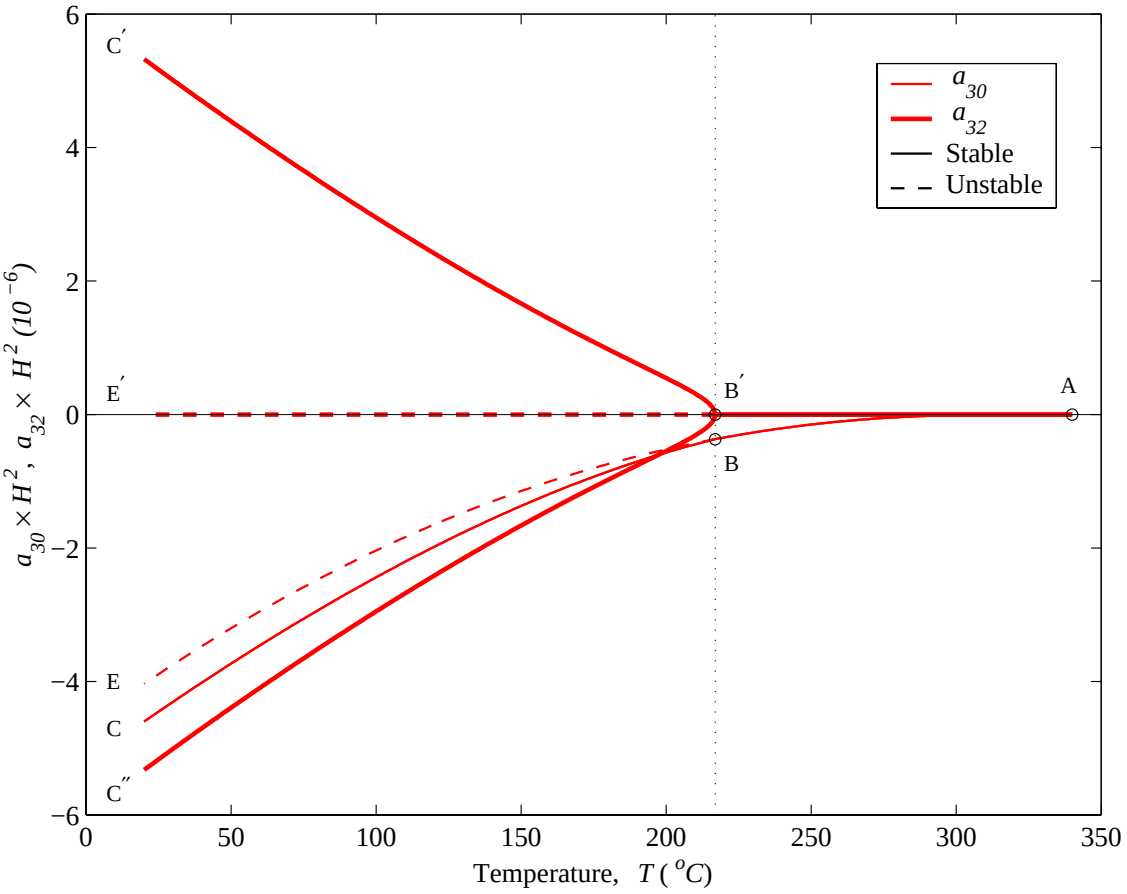


Figure 4.36: Temperature-curvature ($a_{30}$ and $a_{32}$) relation of disk-style RAINBOW ($R$=25.4 mm, $H$=0.381 mm, $H_r/H$=0.55).

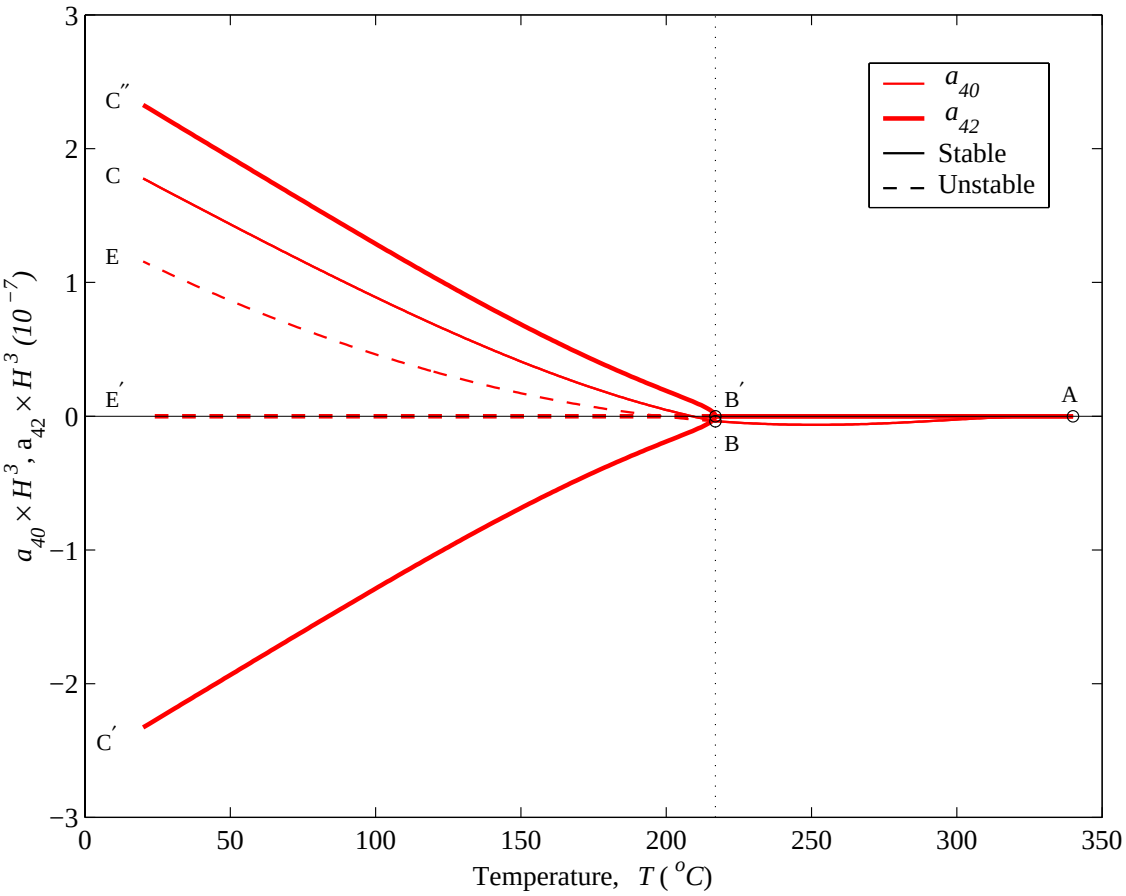


Figure 4.37: Temperature-curvature ($a_{40}$ and $a_{42}$) relation of disk-style RAINBOW ($R$=25.4 mm, $H$=0.381 mm, $H_r/H$=0.55).

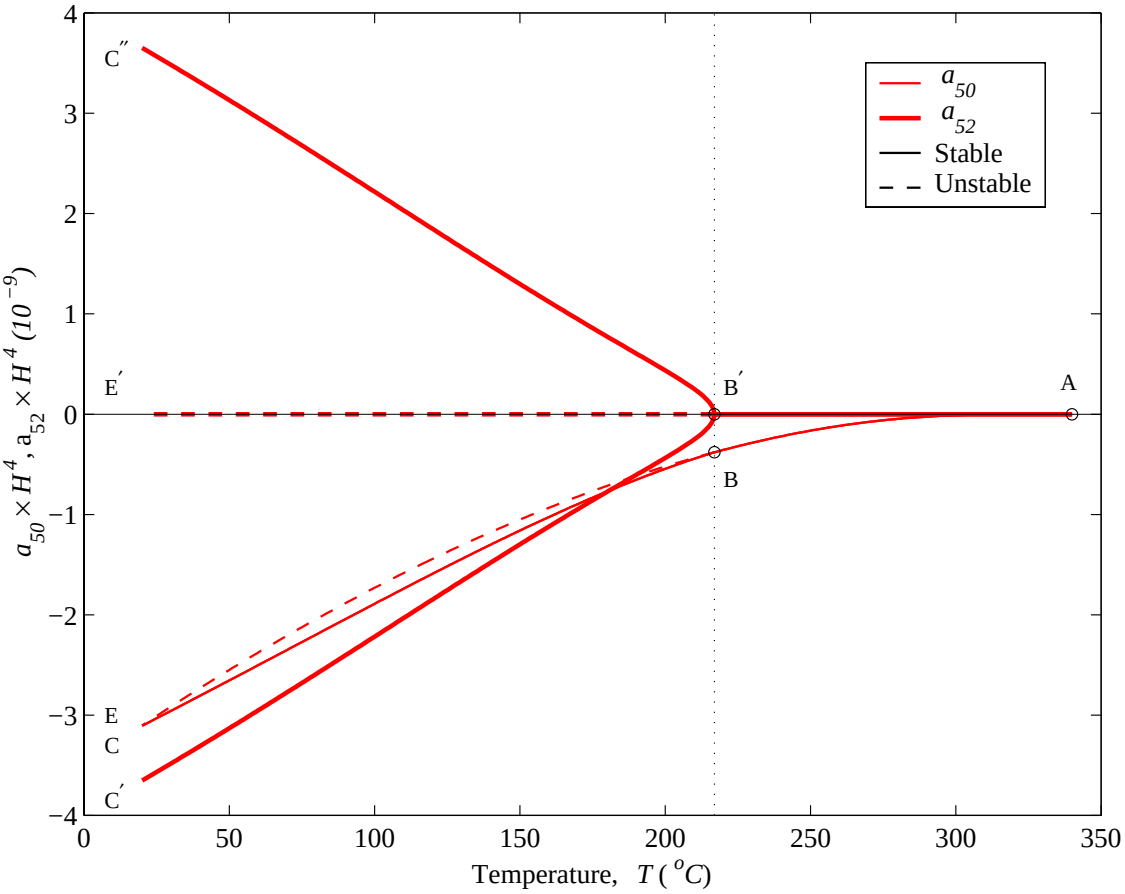


Figure 4.38: Temperature-curvature ($a_{50}$ and $a_{52}$) relation of disk-style RAINBOW ($R$=25.4 mm, $H$=0.381 mm, $H_r/H$=0.55).

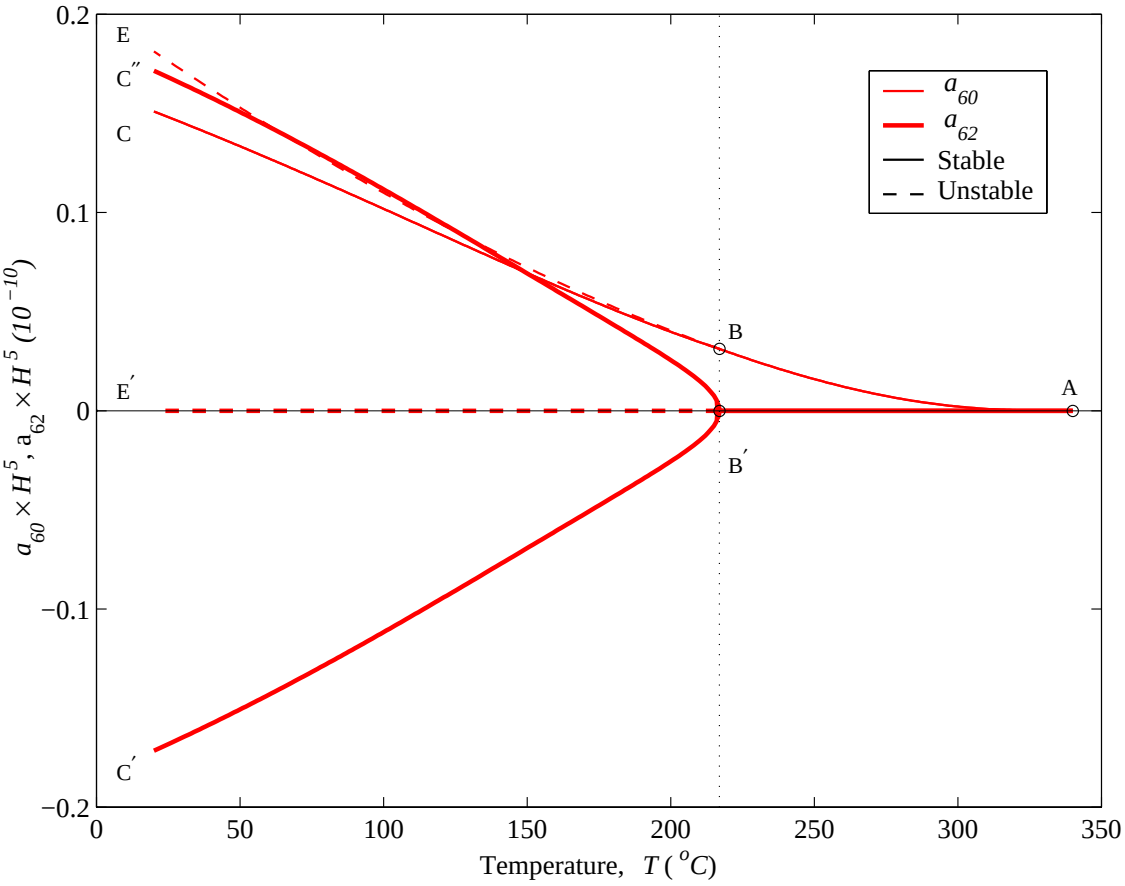


Figure 4.39: Temperature-curvature ($a_{60}$ and $a_{62}$) relation of disk-style RAINBOW ($R$=25.4 mm, $H$=0.381 mm, $H_r/H$=0.55).

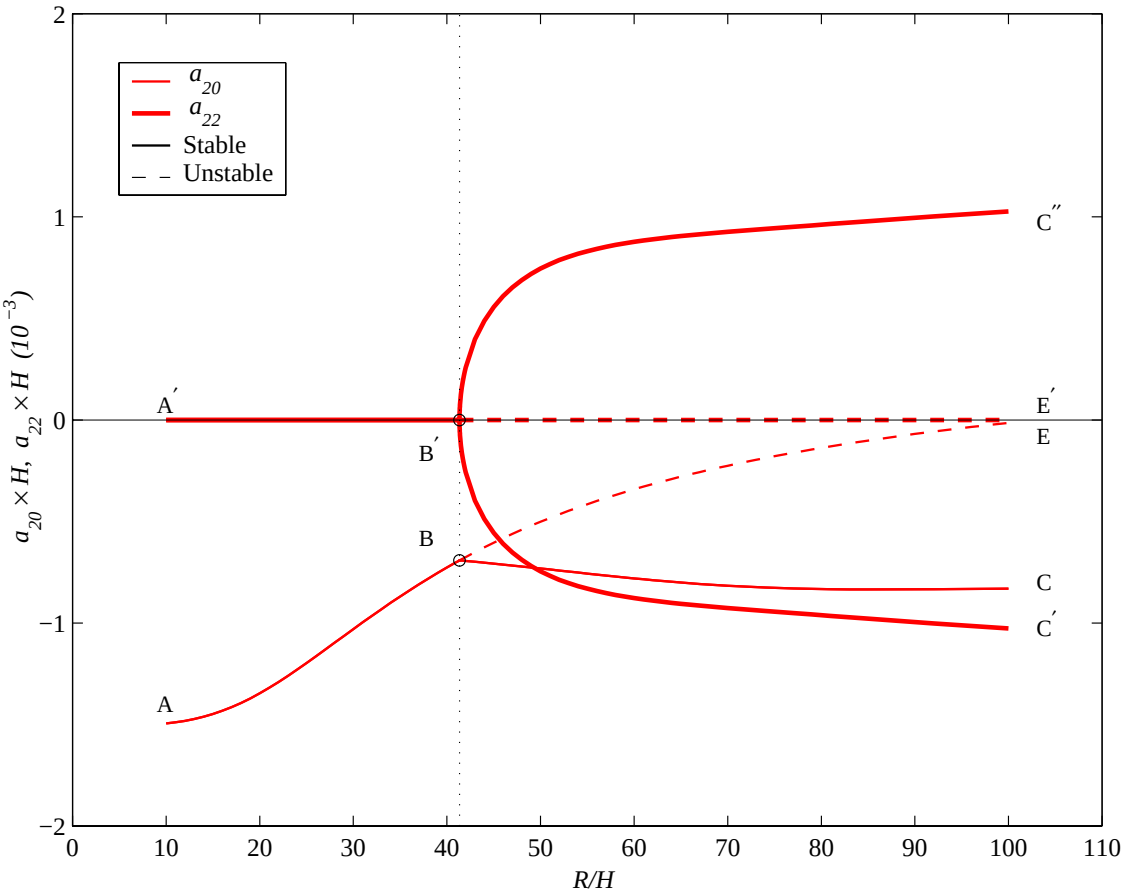


Figure 4.40: Room-temperature shapes ($a_{20}$ and $a_{22}$) of disk-style RAINBOW as a function of geometry ($H_r/H$=0.55).

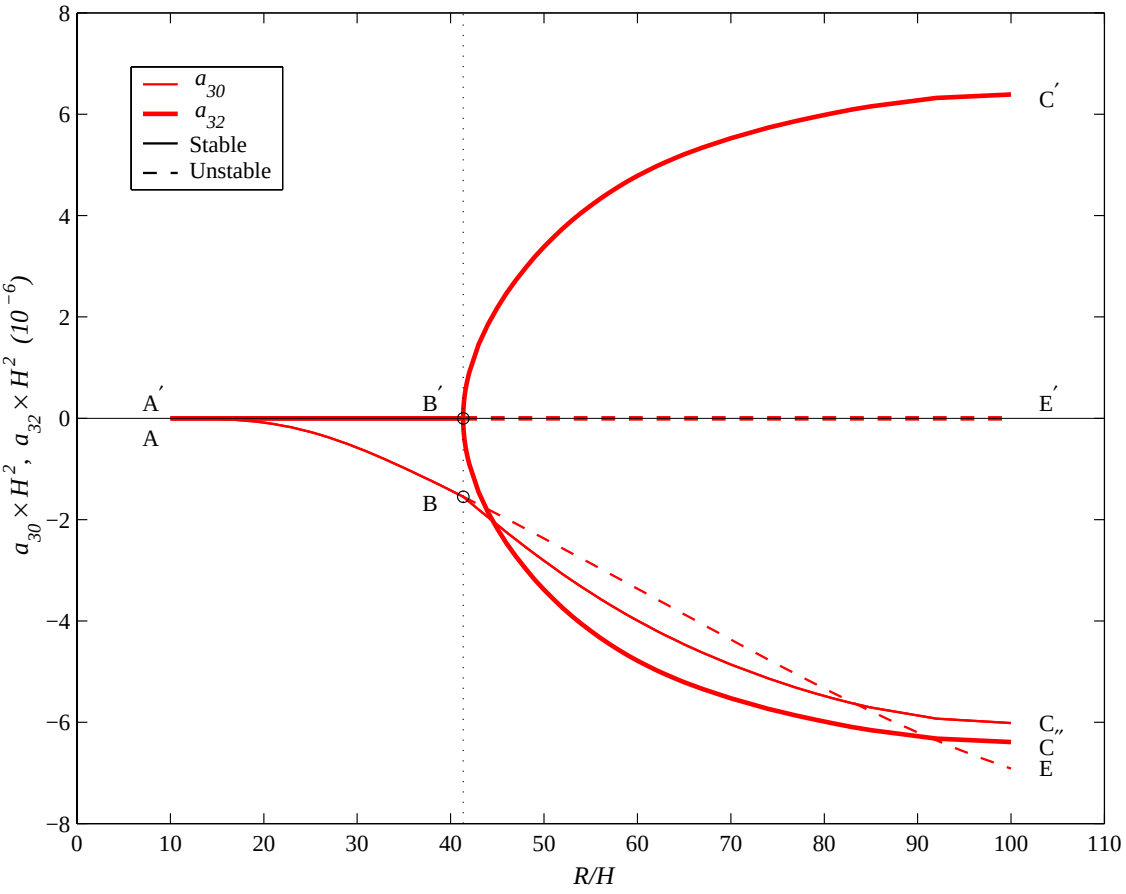


Figure 4.41: Room-temperature shapes ($a_{30}$ and $a_{32}$) of disk-style RAINBOW as a function of geometry ($H_r/H$=0.55).

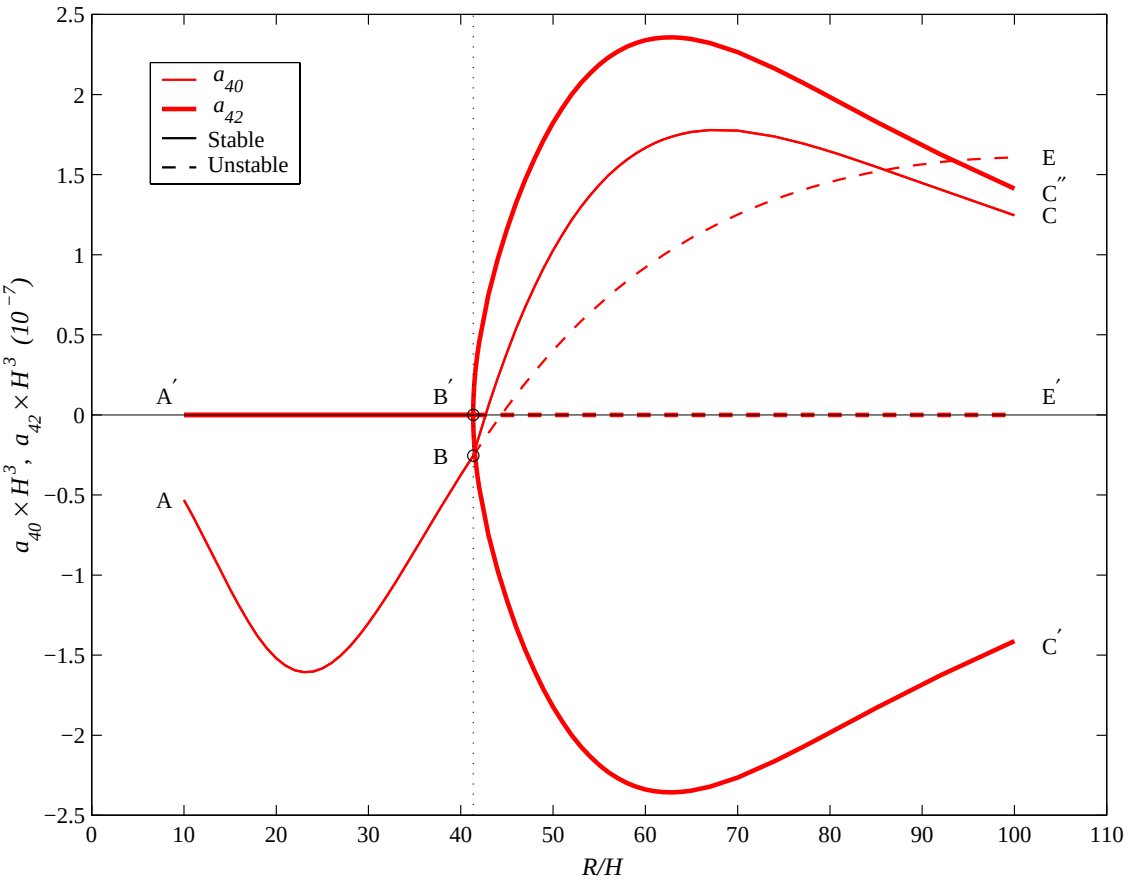


Figure 4.42: Room-temperature shapes ($a_{40}$ and $a_{42}$) of disk-style RAINBOW as a function of geometry ($H_r/H$=0.55).

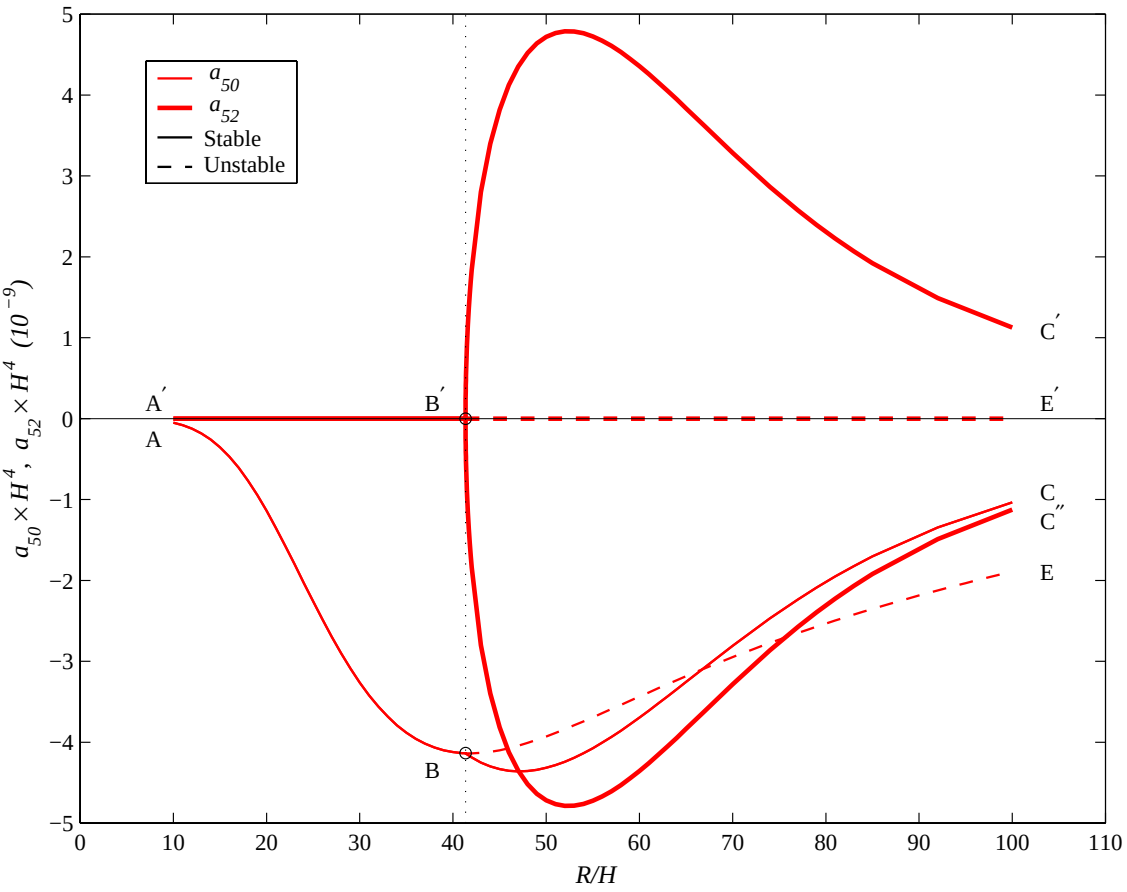


Figure 4.43: Room-temperature shapes ($a_{50}$ and $a_{52}$) of disk-style RAINBOW as a function of geometry ($H_r/H$=0.55).

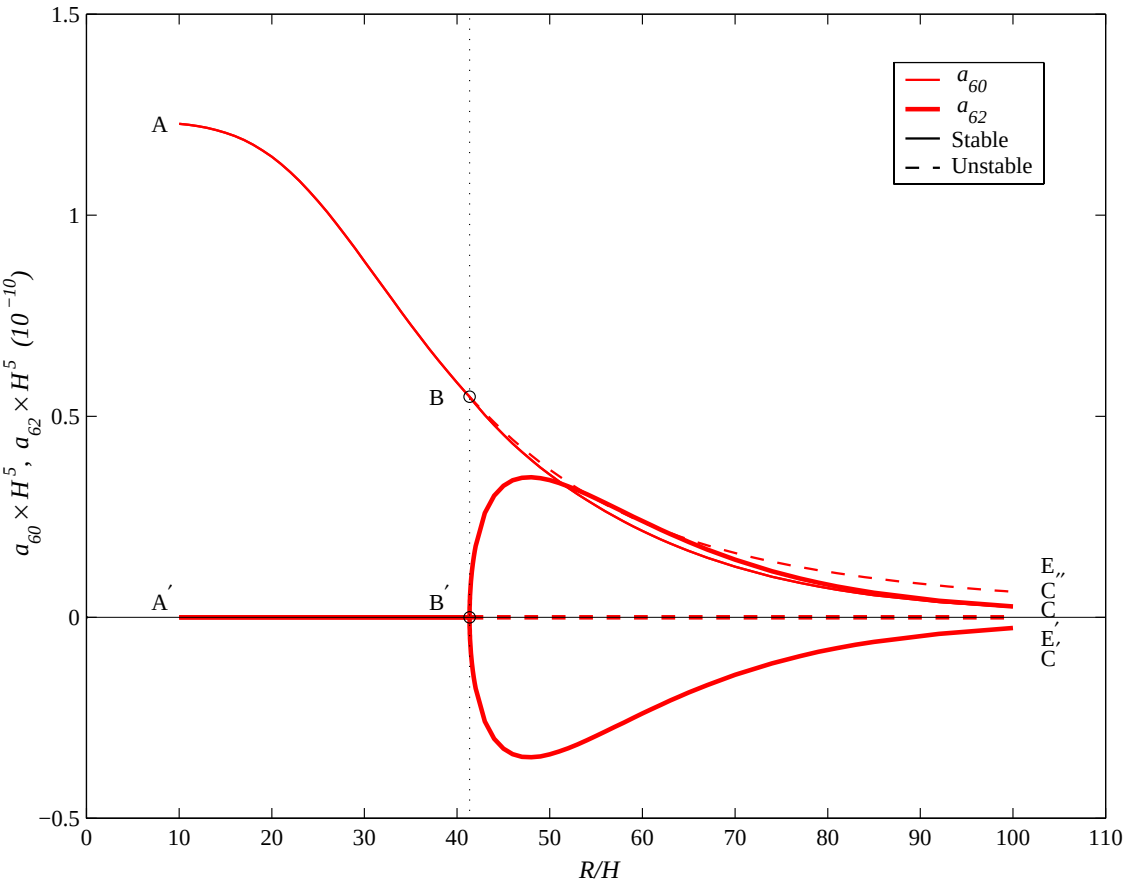


Figure 4.44: Room-temperature shapes ($a_{60}$ and $a_{62}$) of disk-style RAINBOW as a function of geometry ($H_r/H$=0.55).

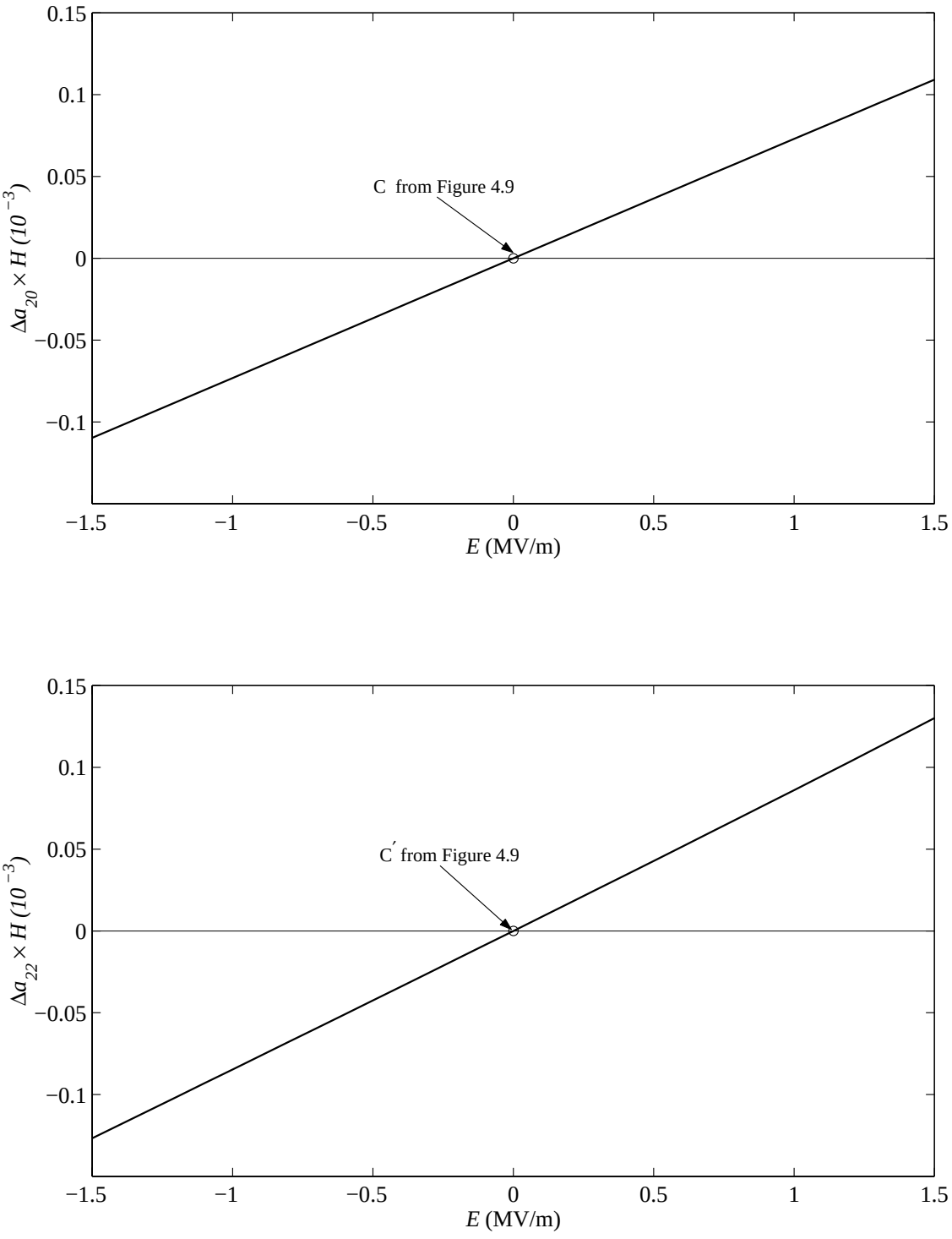


Figure 4.45: Variations of $a_{20}$ and $a_{22}$ as a function of $E$ ($R$=25.4 mm, $H$=0.381 mm, $H_r/H$=0.35).

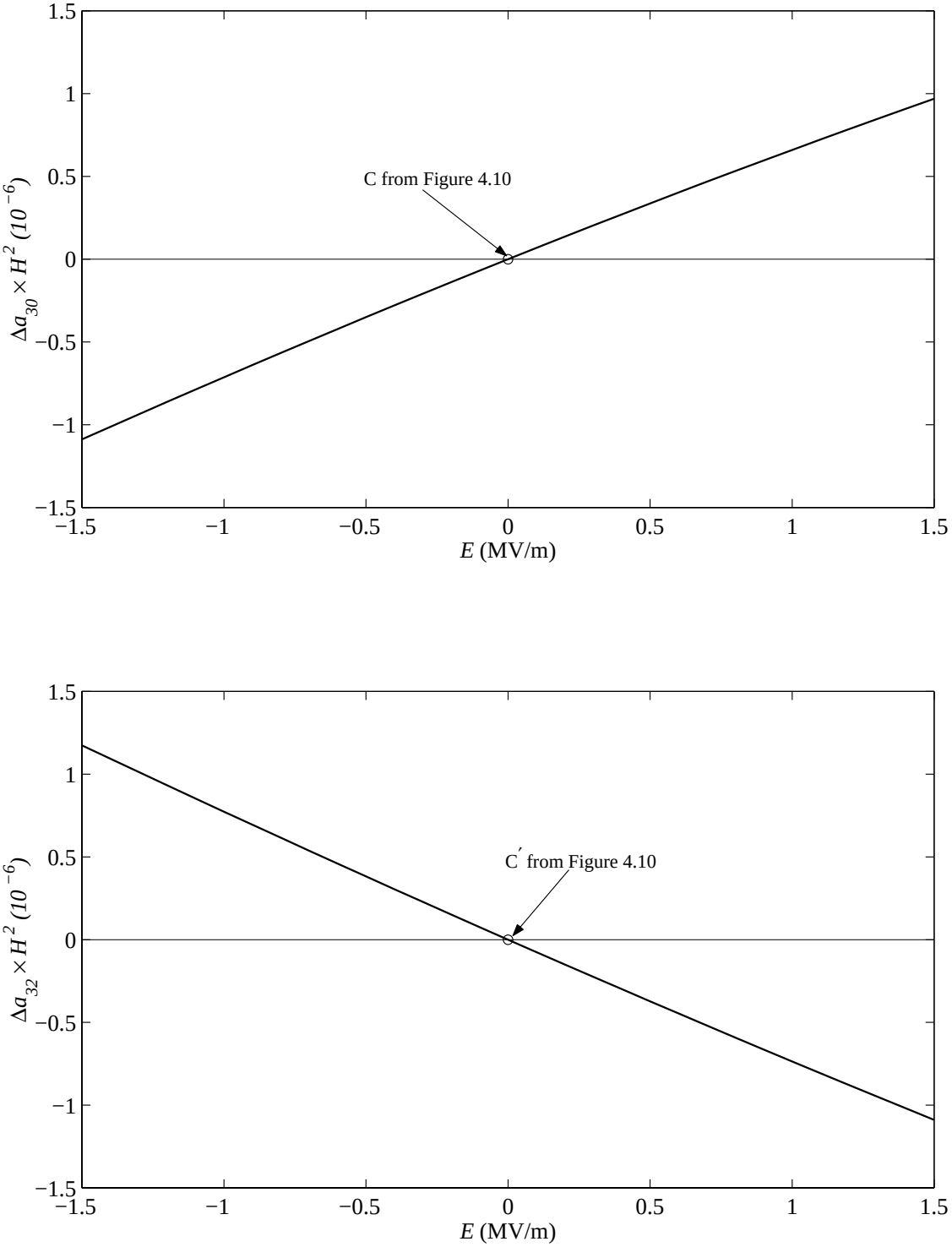


Figure 4.46: Variations of $a_{30}$ and $a_{32}$ as a function of $E$ ($R$=25.4 mm, $H$=0.381 mm, $H_r/H$=0.35).

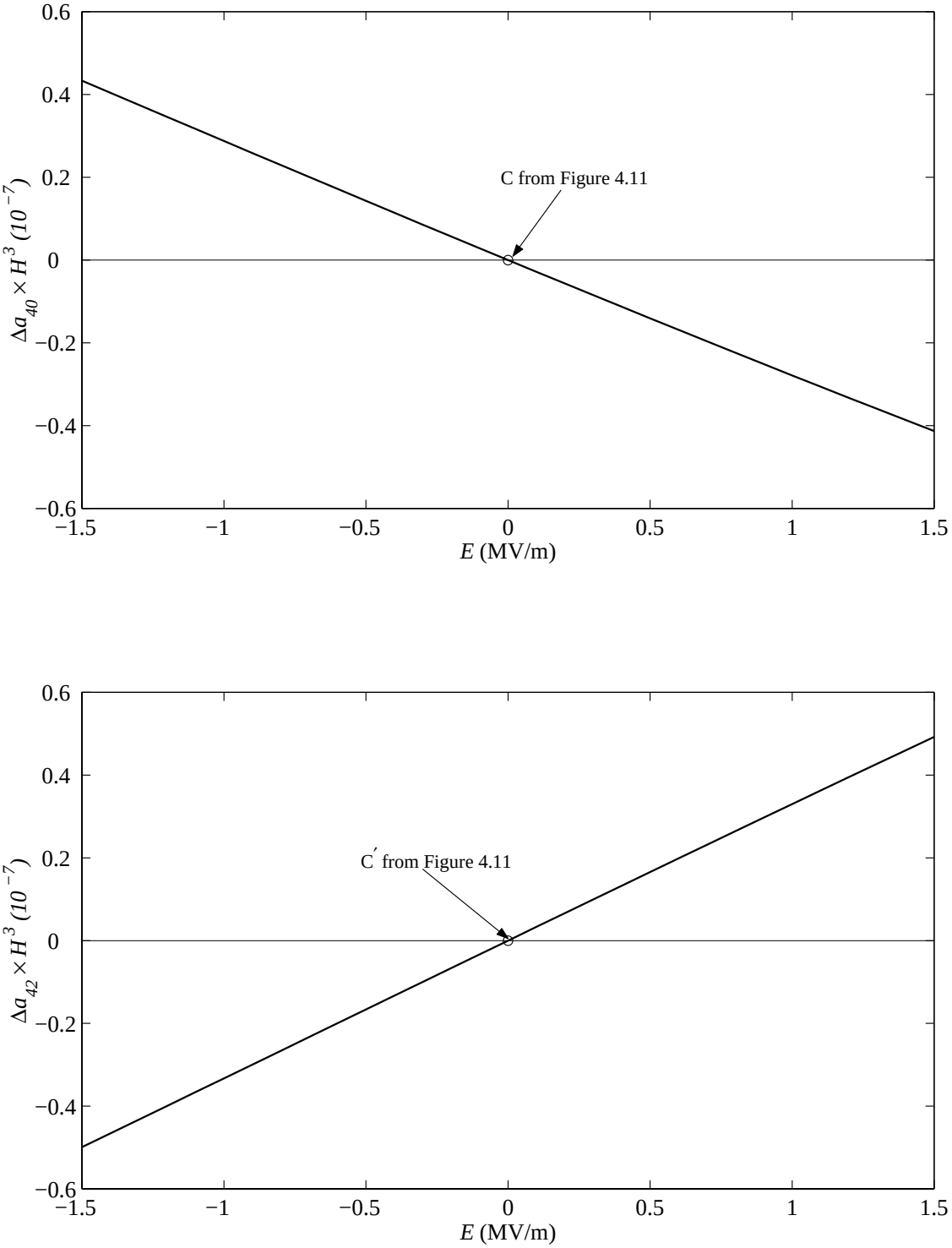


Figure 4.47: Variations of $a_{40}$ and $a_{42}$ as a function of $E$ ($R$=25.4 mm, $H$=0.381 mm, $H_r/H$=0.35).

### 4.5.6 Effect of Geometry on the Piezoelectric-Induced Deformations

The results shown in Figures 4.45–4.49 for the case of Figures 4.9–4.13, RAINBOW with $R/H = 67$ and $H_r/H$=0.35, can change dramatically if a disk-style RAINBOW is considered which has a value of $R/H$=47.5, a value closer to the critical value of 44.3. The value of $R/H = 67$ is sufficiently removed from the critical value of $R/H$=44.3 that the effect of applying a $E$=± 1.5 MV/m results in the linear relations shown in Figures 4.45-4.49. If an electric field of $E$± 1.5 MV/m is applied to RAINBOW with $R/H$=47.5, the results shown in Figures 4.50–4.54 are predicted. These figures are more complicated than Figure 4.45-4.49 because of the potential for a change in shape due to applied electric field, and because coefficients $a_{ij}$ rather than $\Delta a_{ij}$ are plotted. If disk-style RAINBOW has a room temperature shape represented by points $C_3$ and $C_3'$ in Figures 4.50–4.54, then a negative $E$ results in an increase in the magnitude of $a_{ij}$. That is, RAINBOW becomes more cylindrical, with increased $\kappa_r^o$ curvature in the $\theta = 0$ and $\theta = \pi$ directions. On the other hand, if $E$ is positive, a change in the overall shape of RAINBOW is possible. Again referring to Figures 4.50–4.54, as $E$ increases from zero at points $C_3$ and $C_3'$, the values of $a_{20}$, $a_{30}$, $a_{40}$, $a_{50}$, and $a_{60}$ decrease in magnitude, and the values of $a_{22}$, $a_{32}$, $a_{42}$, $a_{52}$, and $a_{62}$ tend to go to zero. When the electric field strength reaches a value represented by $B_3$ and $B_3'$, the shape of rainbow becomes axisymmetric dome. A further increase in electric field strength beyond points $B_3$ and $B_3'$ results in an axisymmetric dome shape, but one that is less deep. If the electric field strength is decreased, the axisymmetric shape begins to deepen again. At points $B_3$ and $B_3'$, RAINBOW can follow paths $B_3C_3$ and $B_3'C_3'$ or $B_3C_3$ and $B_3'C_3''$. If RAINBOW follows paths $B_3C_3$ and $B_3'C_3'$, it will return to the original shape as $E$ approaches zero. If it follows paths $B_3'C_3''$, RAINBOW will assume the 'snapped through' room-temperature shape when $E$ approaches zero. Thus, the application of the electric field has the potential for changing the overall character of the shape.

### 4.5.7 Effect of Reduced-Layer Thickness on the Piezoelectric-Induced Deformations

It is of interest to determine the influence of the reduced layer thickness on the characteristics of the piezoelectric deformations of RAINBOW at room temperature. Figures 4.55–4.59 illustrate the important features of the dependence of the piezoelectric-induced deformations on reduced

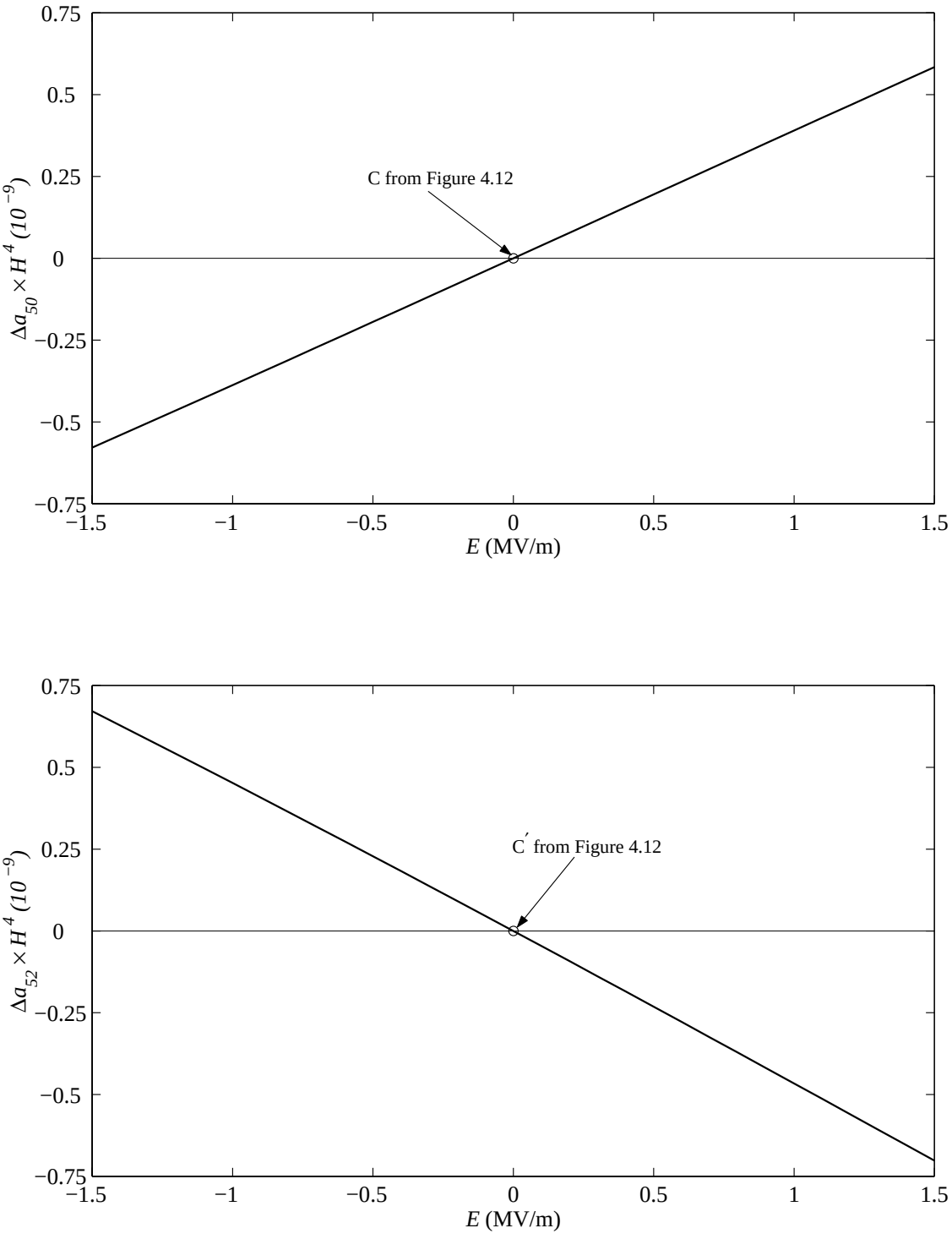


Figure 4.48: Variations of $a_{50}$ and $a_{52}$ as a function of $E$ ($R$=25.4 mm, $H$=0.381 mm, $H_r/H$=0.35).

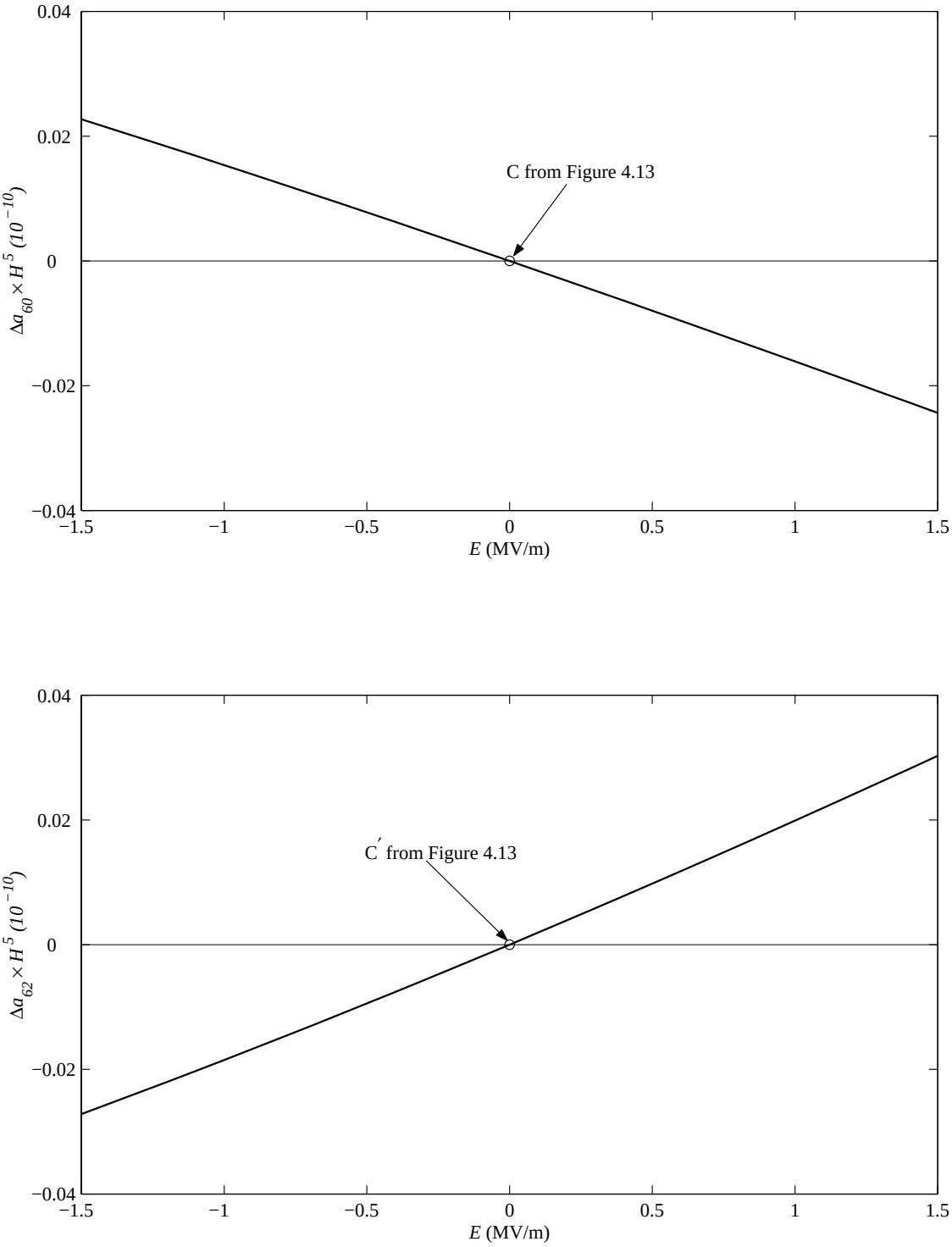


Figure 4.49: Variations of $a_{60}$ and $a_{62}$ as a function of $E$ ($R$=25.4 mm, $H$=0.381 mm, $H_r/H$=0.35).

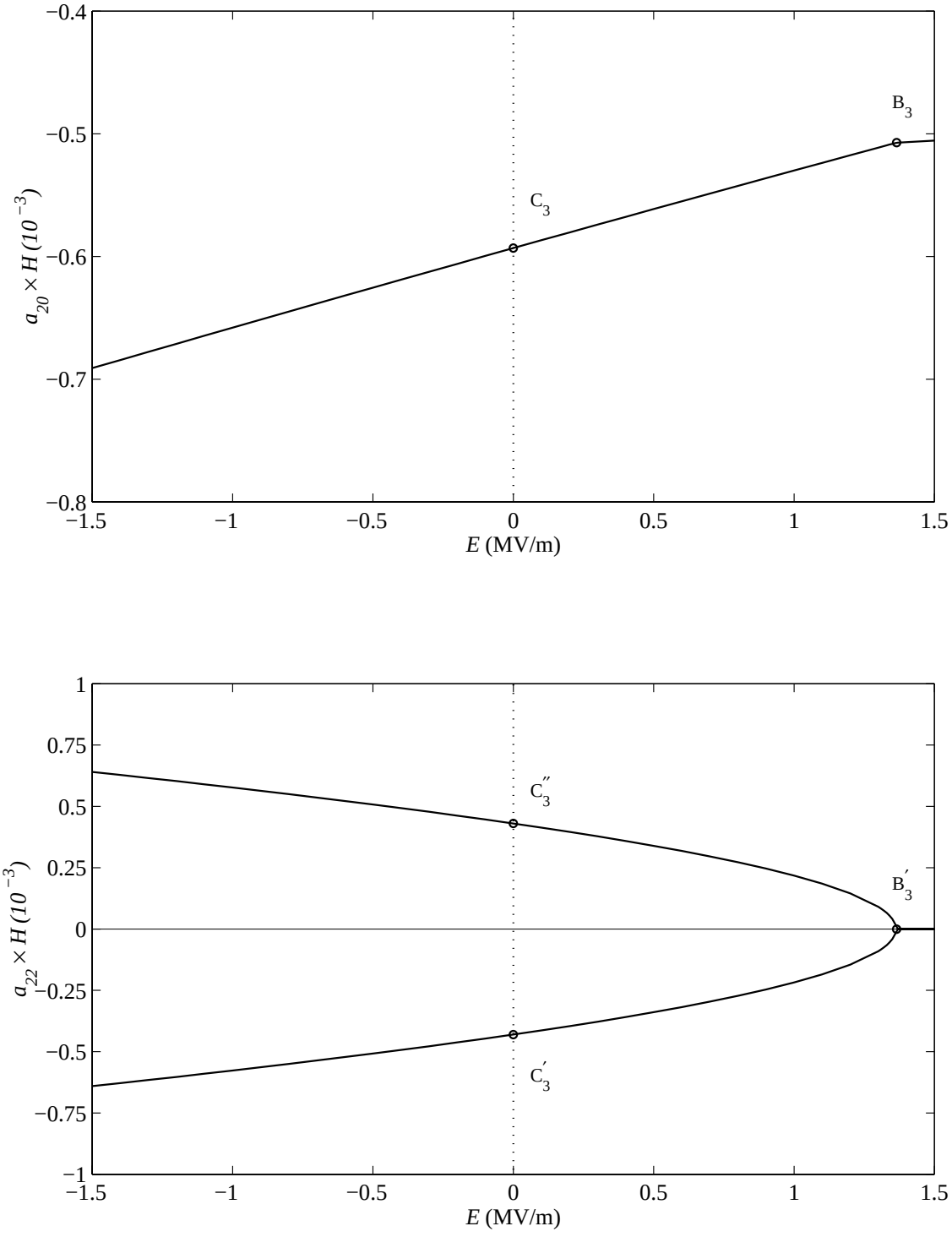


Figure 4.50: Variations of $a_{20}$ and $a_{22}$ as a function of $E$ ($R/H$=47.5, $H_r/H$=0.35).

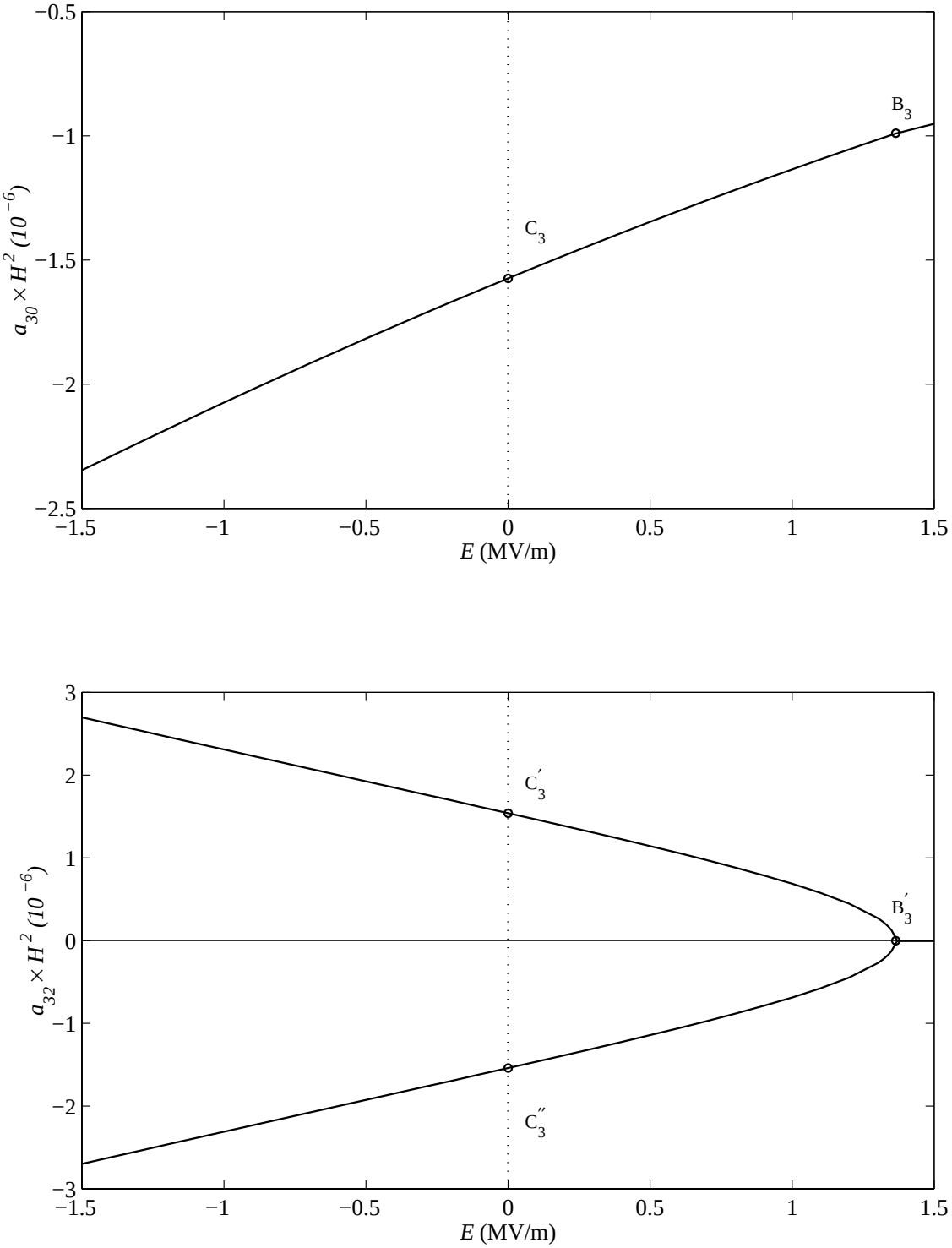


Figure 4.51: Variations of $a_{30}$ and $a_{32}$ as a function of $E$ ($R/H$=47.5, $H_r/H$=0.35).

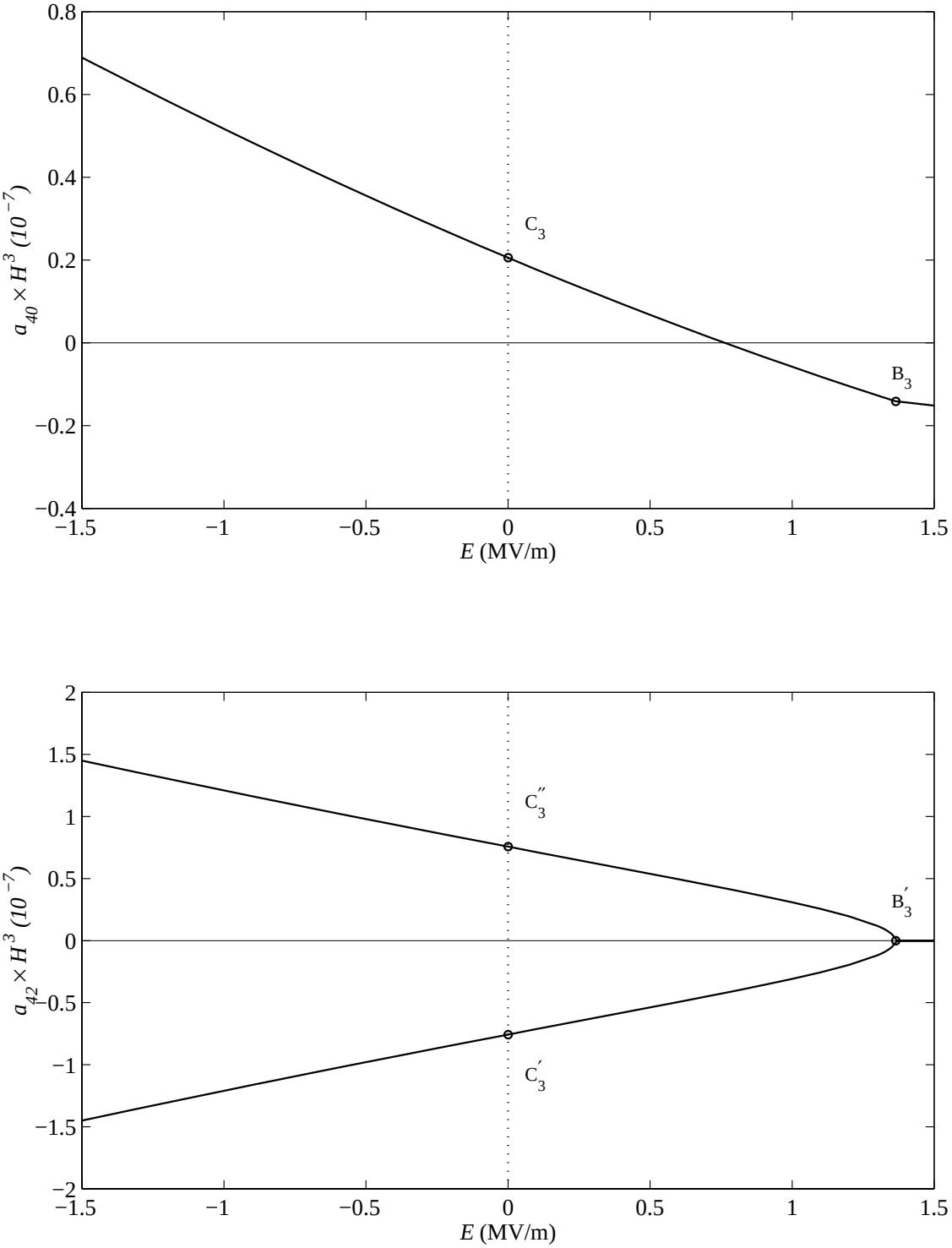


Figure 4.52: Variations of $a_{40}$ and $a_{42}$ as a function of $E$ ($R/H$=47.5, $H_r/H$=0.35).

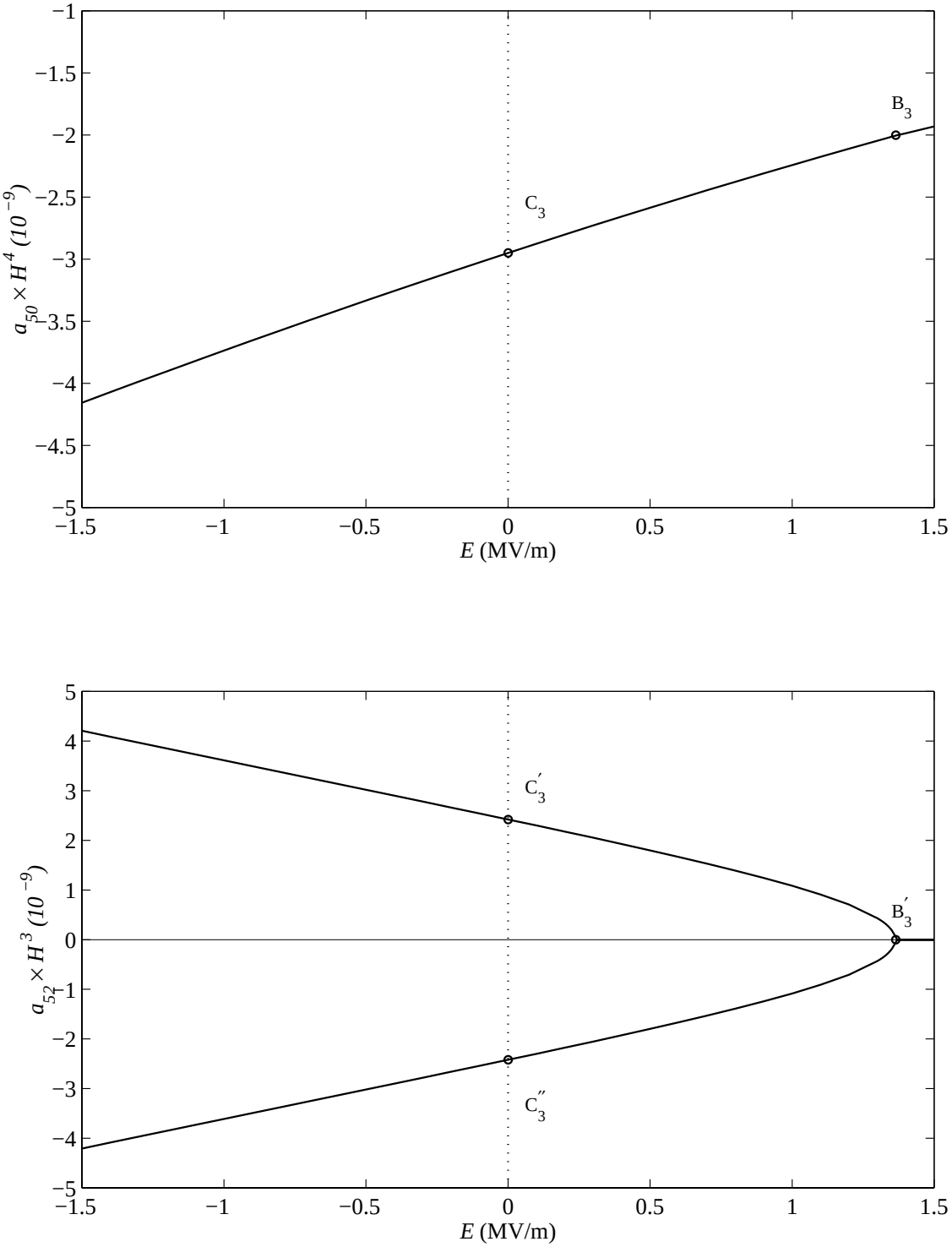


Figure 4.53: Variations of $a_{50}$ and $a_{52}$ as a function of $E$ ($R/H$=47.5, $H_r/H$=0.35).

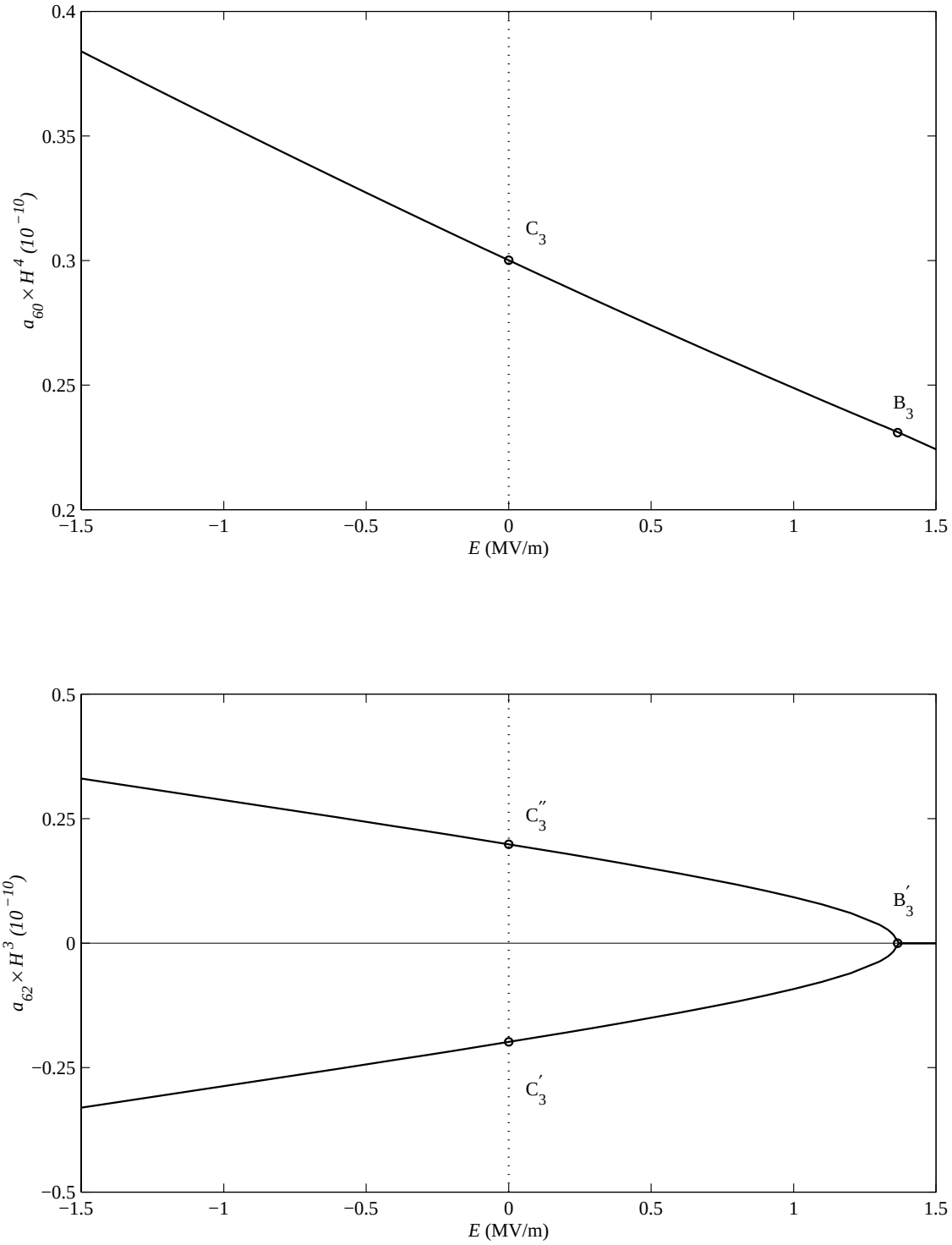


Figure 4.54: Variations of $a_{60}$ and $a_{62}$ as a function of $E$ ($R/H$=47.5, $H_r/H$=0.35).

layer thickness. In these figures the change in $a_{ij}$ at room temperature are plotted as a function of reduced layer thickness under applied electric fields of 0.25, 0.5, 1.0, and 1.5 MV/m. Again, for convenience, the axes in Figures 4.55–4.59 have been nondimensionalized by using the total thickness of RAINBOW, $H$, as a scaling parameter. The radius to thickness ratio of RAINBOW in these figures is fixed at 67. As seen in Figure 4.55, for coefficient $a_{22}$ the maximum change occurs in the range of 14% to 17% or 89% to 92%. However, the maximum change in $a_{22}$ the leading coefficient in the curvature expressions, is very sensitive to the exact value of $H_r/H$ in the ranges, due to the steepness of the slope of the relation. Furthermore, the changes in coefficients $a_{32}$, $a_{42}$, $a_{52}$, and $a_{62}$ are also very sensitive to the exact value of $H_r/H$. This sensitivity is due to the fact that in the neighborhood of the two ranges, a bifurcation in the room-temperature shape occurs, as shown in Figures 4.30-4.34. The existence of bifurcation points in these ranges can lead to unexpected behavior of RAINBOW, such as sudden changes in curvatures, when an electric field is applied. It is, therefore, best to stay away from these two ranges of $H_r/H$. On the other hand, as seen in Figures 4.55-4.59, the maximum absolute change in the coefficient $a_{ij}$, with the exception of $a_{22}$, can be achieved when the reduced layer thickness is 55%. A local maximum for the change in $a_{22}$ occurs at 55%. In view of this, the optimal reduced layer thickness would be at 55%, a value far removed from the critical values.

## 4.6 Chapter Summary

In this chapter, a model for predicting the room-temperature shape of disk-style RAINBOW has been developed. A discussion of the assumptions adopted to develop the model was presented. The methodology was similar to the one developed for rectangular RAINBOW except the analysis was developed in polar coordinates. The model for disk-style RAINBOW was shown to have an excellent agreement with the finite element results of ABAQUS. Again, the present analysis is shown to have formulative and computational advantages over finite element analysis in terms of the ease of extending the model to account for piezoelectric-induced deformations and the computational effort. The results shown in this chapter indicate that the predicted room-temperature shape of disk-style RAINBOW can be either near-cylindrical or axisymmetric. As was the case for rectangular RAINBOW, for a given set of material properties of RAINBOW, there exists a critical value

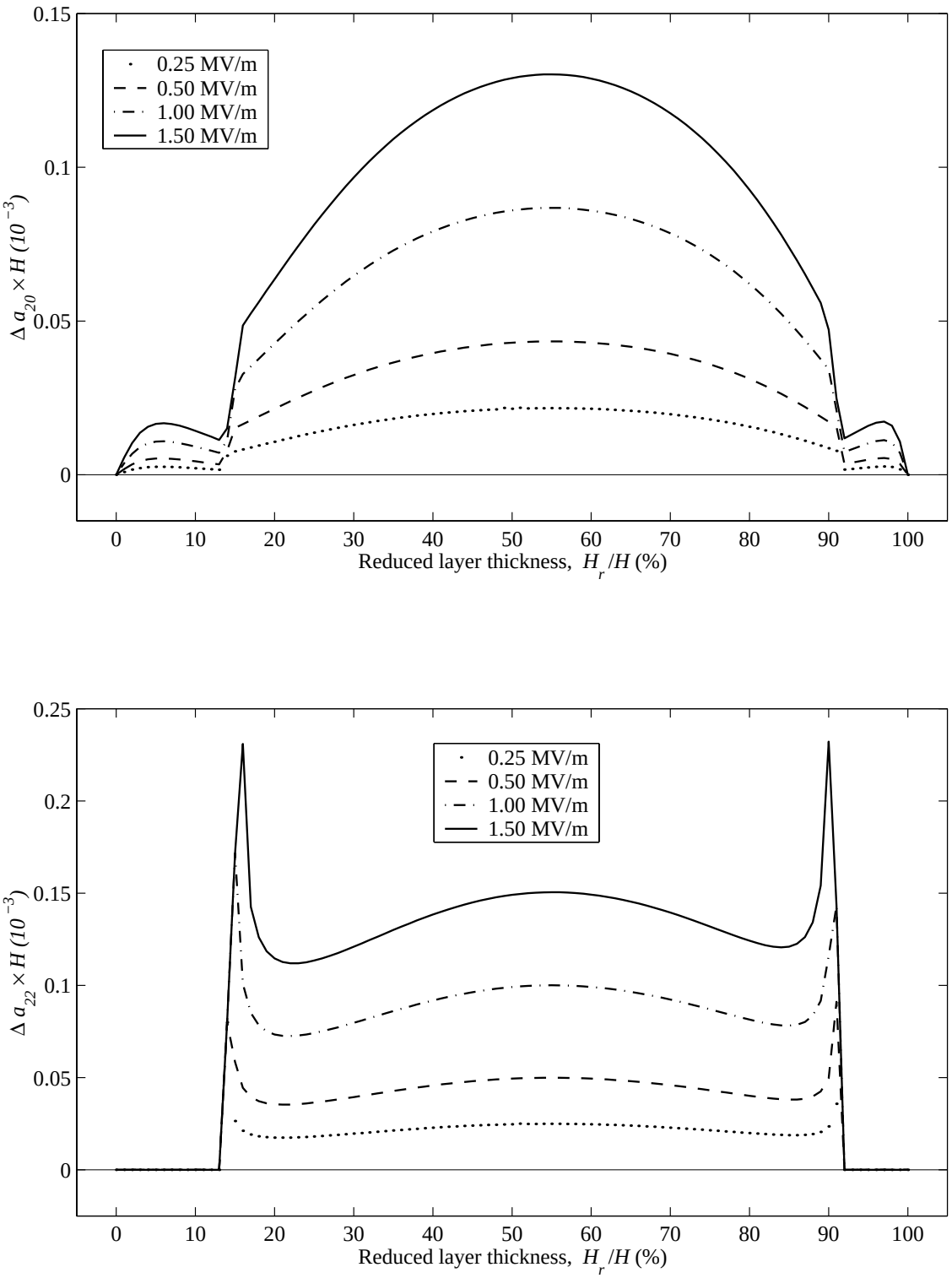


Figure 4.55: Variations of $a_{20}$ and $a_{22}$ as a function of reduced layer thickness under selected applied electric fields $E$ ($R$=25.4 mm, $H$=0.381 mm).

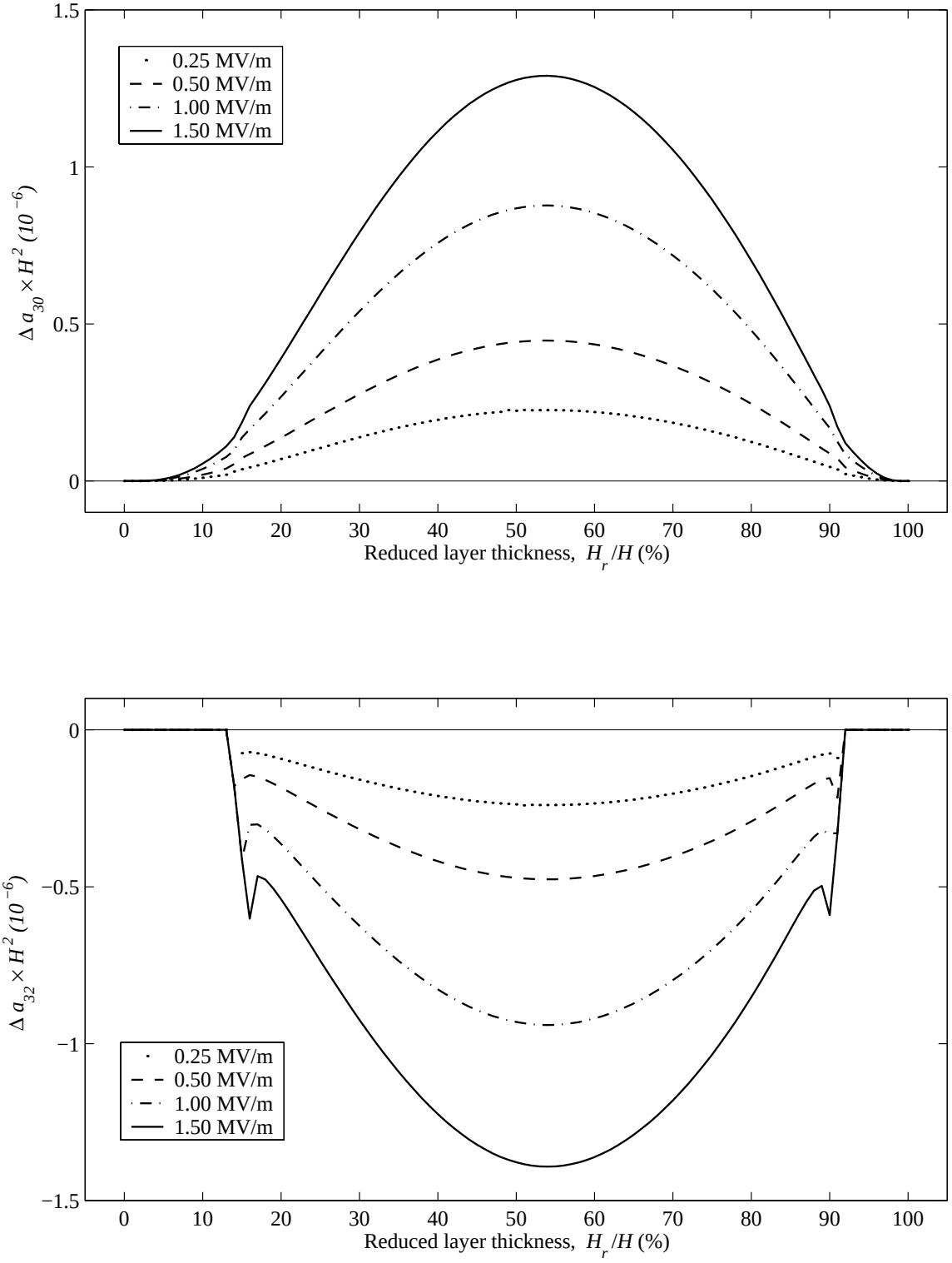


Figure 4.56: Variations of $a_{30}$ and $a_{32}$ as a function of reduced layer thickness under selected applied electric fields $E$ ($R$=25.4 mm, $H$=0.381 mm).

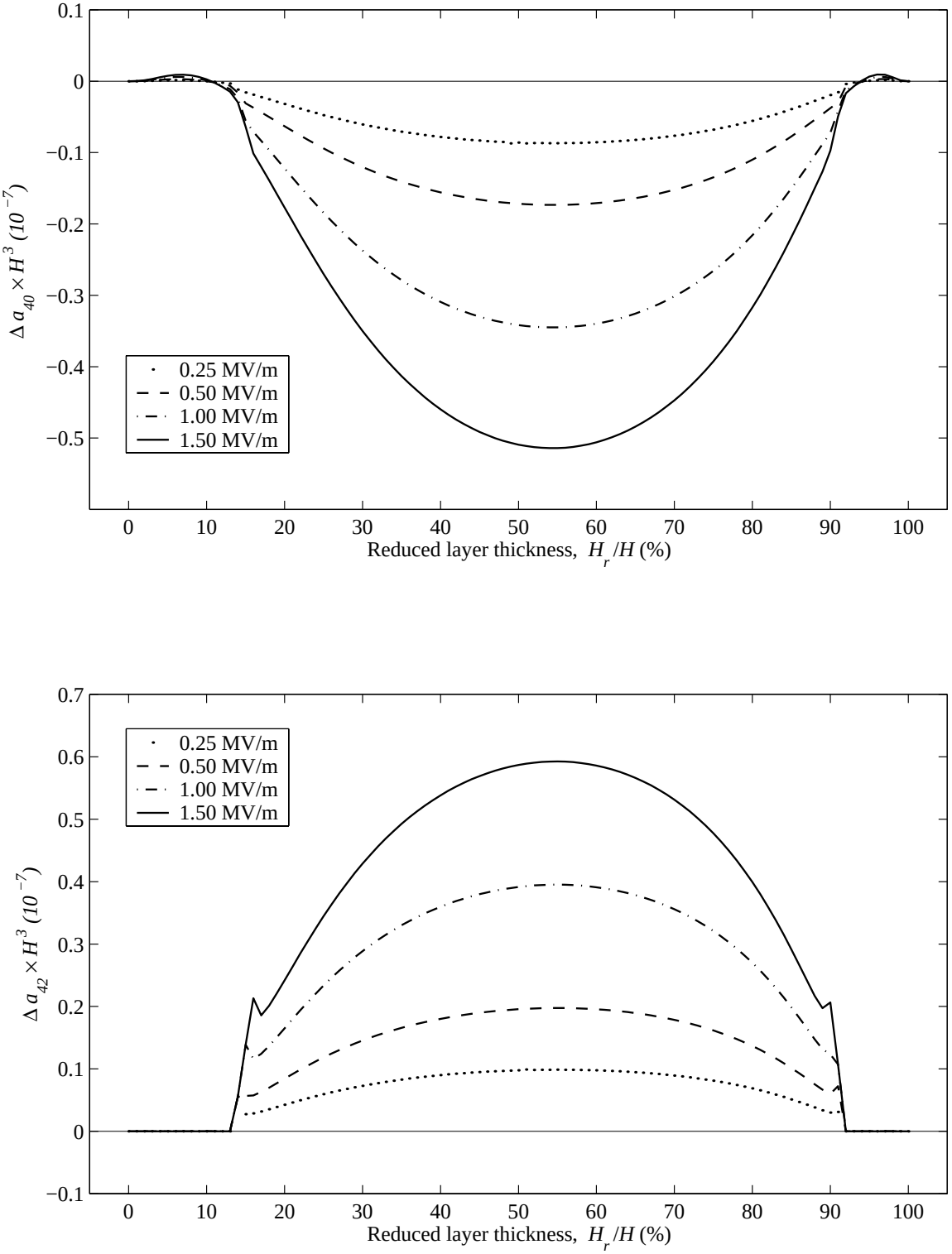


Figure 4.57: Variations of $a_{40}$ and $a_{42}$ as a function of reduced layer thickness under selected applied electric fields $E$ ($R$=25.4 mm, $H$=0.381 mm).

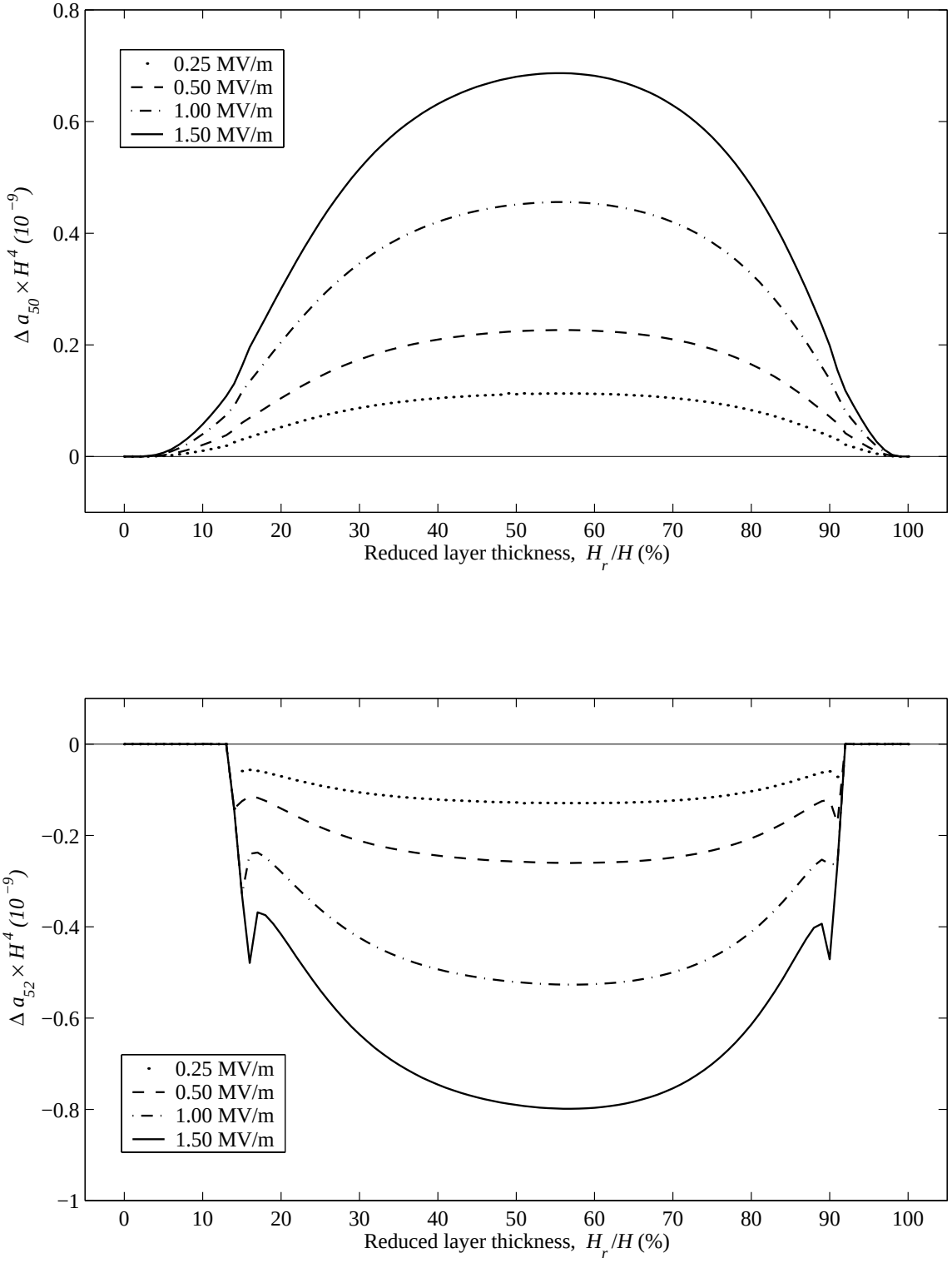


Figure 4.58: Variations of $a_{50}$ and $a_{52}$ as a function of reduced layer thickness under selected applied electric fields $E$ ($R$=25.4 mm, $H$=0.381 mm).

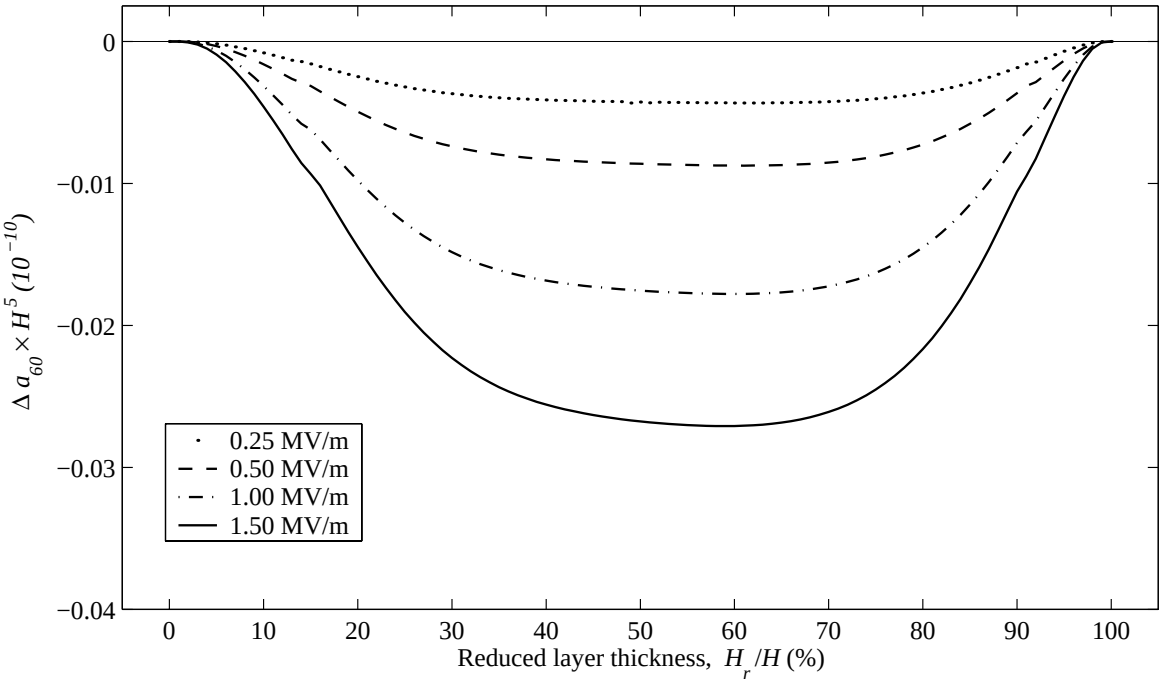


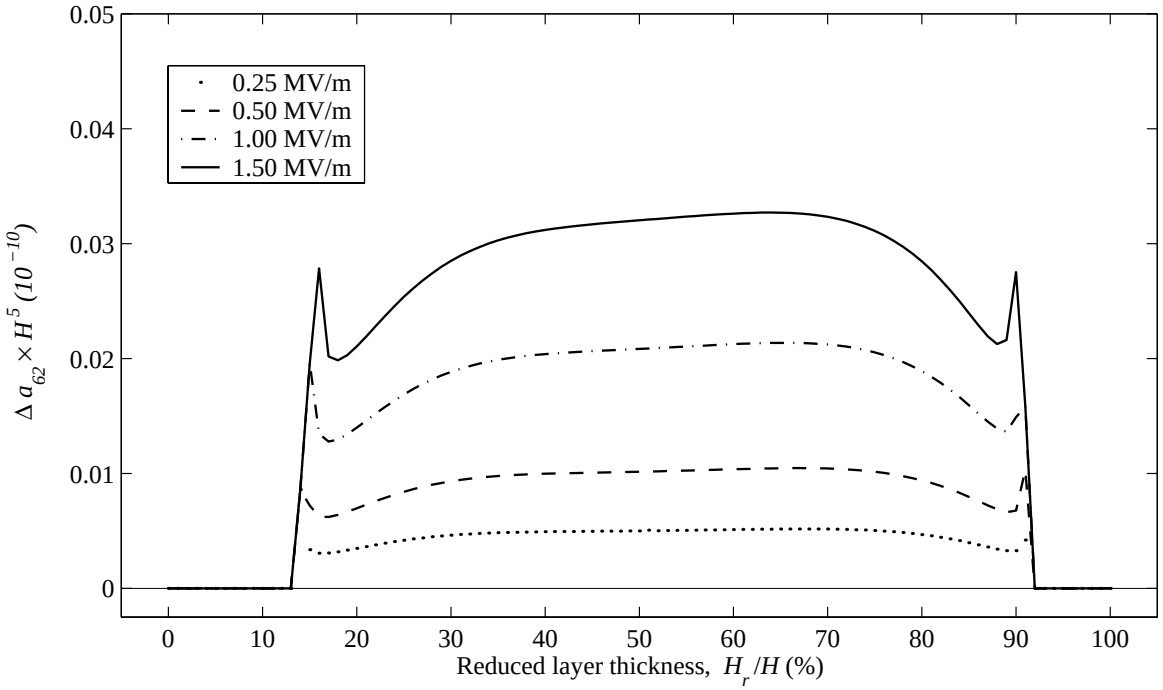


Figure 4.59: Variations of $a_{60}$ and $a_{62}$ as a function of reduced layer thickness under selected applied electric fields $E$ ($R$=25.4 mm, $H$=0.381 mm).

of radius-to-thickness ratio $R/H$ below which RAINBOW exhibits a unique axisymmetric stable room-temperature shape. For values of $R/H$ greater than the critical value, RAINBOW exhibits multiple room-temperature shapes, two of which are in near-cylindrical and the third shape is axisymmetric and is unstable. Comparison between the results of the present model and the results of the linear analysis indicates that the nonlinear geometric effects are important and should be included in the strain-displacement relations. The results presented in this chapter also reveal the existence of two critical values of reduced layer thickness. For a reduced layer thickness bounded by these two critical values, RAINBOW exhibits two stable near-cylindrical shapes and one unstable axisymmetric shape. On the other hand, if the reduced layer thickness is outside the interval bounded by the critical values, RAINBOW exhibits a unique and stable axisymmetric shape. Hence, for RAINBOW with a value of $R/H$ or a reduced layer thickness that is close to the critical value, irregularities in manufacturing will no doubt influence the room-temperature shapes. The extension of the model to include piezoelectric-induced deformations indicates that the relationship between the change in the dominant terms defining the curvatures ($\Delta a_{20}$ and $\Delta a_{22}$) is very close to being linear with electric field strength. As was the case for rectangular RAINBOW, it is found that the optimal reduced layer thickness would be at 55%, since the maximum change in the dominant coefficients is achieved while maintaining the linear relationship between the dominant coefficients, $a_{20}$ and $a_{22}$, and the electric field. This value seems to be dependent on the material properties of RAINBOW rather than its geometry.

Comparison between the predicted and the manufactured shapes of disk-style RAINBOW is provided in section B.2.2 of Appendix B. In the next chapter, the present model is modified to predict the room-temperature shapes of disk-style GRAPHBOW and their piezoelectric-induced deformation characteristics under application of electric field.

# Chapter 5

# Disk-Style GRAPHBOW Actuators

## 5.1 Introduction

The main objective in this chapter is the extension of the model described in Chapter 4 for predicting the manufacturing and piezoelectric deformation characteristics of disk-style GRAPHBOW. The discussion of the extension of the model of disk-style GRAPHBOW is condensed because of its analogy to its counterpart for rectangular GRAPHBOW described in Chapter 3. Numerical results corresponding to the formulations in this chapter are presented. The primary qualitative and quantitative characteristics of interest are the room-temperature shapes and the piezoelectric-induced deformations of disk-style GRAPHBOW.

## 5.2 Modeling Definitions and Assumptions

Figure 3.1 describes the process used to incorporate one or more thin layers of fiber-reinforced composite onto RAINBOW. As in Chapter 3, a multi-step thermoelastic analysis is developed to model the addition of the composite layers. Again, the analysis is based on the total potential energy approach along with the Rayleigh-Ritz method. Figure 5.1 describes the geometry and nomenclature of the problem considered. The first $N$ layers are assumed to be made of thin layers of orthotropic materials (reduced and unreduced piezoceramic) with thickness, $H$, and the next $M$

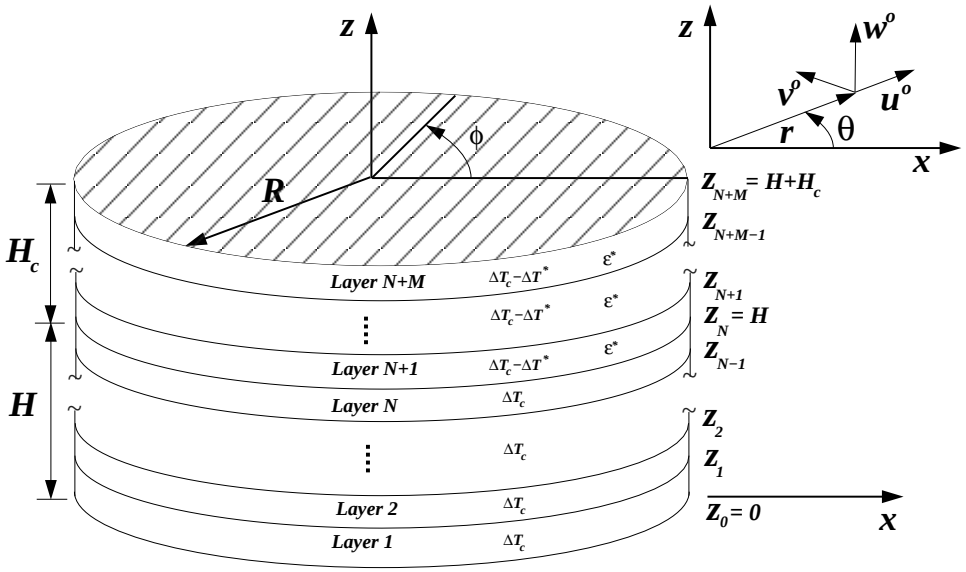


Figure 5.1: Geometry and nomenclature of a disk-style GRAPHBOW device considered.

layers represent additional layers of fiber-reinforced composite material with thickness $H_c$. The $\phi$ angle shown in Figure 5.1 is the angle that the composite fibers make with the $x$ direction. Layer positions, locations of the upper and lower boundaries of the $k^{th}$ layer, i.e., $z_k$ and $z_{k-1}$, radius $R$, and analysis coordinate system are the same as for the disk-style RAINBOW analysis.

### 5.2.1 Total Potential Energy

Using the same logic adopted to obtain Equation (3.1), but using polar coordinates, the total potential energy is given by

$$\Pi = \frac{1}{2}\int_0^R \int_0^{2\pi} \int_{z_o}^{z_{N+M}} \big\{(\sigma_r - \sigma_r^T)(\epsilon_r^o + z\kappa_r^o) + (\sigma_\theta - \sigma_\theta^T)(\epsilon_\theta^o + z\kappa_\theta^o) + (\tau_{r\theta} - \tau_{r\theta}^T)(\gamma_{r\theta}^o + z\kappa_{r\theta}^o)\big\}\, r dr\, d\theta\, dz \qquad (5.1)$$

Again, the stress components superscripted with a "$T$" denote the equivalent stresses due to thermal effects. The strains and curvatures in the energy expression are given by Equations (4.30) and (4.31). Since not all layers are present at all temperatures, the integration of $\Pi$ through the thickness should be carried out with care. The location $z = z_o = 0$ is taken here to be the reference surface for the original two-layer flat RAINBOW device, and the quantities $u^o$, $v^o$, and $w^o$ are the

total displacements in the $r$, $\theta$, and $z$ directions, respectively, of the reference surface. Expanding the stresses in Equation (5-1), we obtain the following relations

$$\begin{aligned}
\sigma_r &= \bar{Q}_{11}(\epsilon_r - \epsilon_r^T) + \bar{Q}_{12}(\epsilon_\theta - \epsilon_\theta^T) + \bar{Q}_{16}(\gamma_{r\theta} - \gamma_{r\theta}^T) \\
\sigma_\theta &= \bar{Q}_{12}(\epsilon_r - \epsilon_r^T) + \bar{Q}_{22}(\epsilon_\theta - \epsilon_\theta^T) + \bar{Q}_{26}(\gamma_{r\theta} - \gamma_{r\theta}^T) \\
\tau_{r\theta} &= \bar{Q}_{16}(\epsilon_r - \epsilon_r^T) + \bar{Q}_{26}(\epsilon_\theta - \epsilon_\theta^T) + \bar{Q}_{66}(\gamma_{r\theta} - \gamma_{r\theta}^T)
\end{aligned} \tag{5.2}$$

where $\epsilon_r^T$, $\epsilon_\theta^T$ and $\gamma_{r\theta}^T$ are the equivalent strains due to thermal effects and the the fact that strains in the composite are important only below the cure temperature. Equation (5.2) can be rewritten as

$$\begin{aligned}
\sigma_r &= \bar{Q}_{11}\epsilon_r + \bar{Q}_{12}\epsilon_\theta + \bar{Q}_{16}\gamma_{r\theta} - \sigma_r^T \\
\sigma_\theta &= \bar{Q}_{12}\epsilon_r + \bar{Q}_{22}\epsilon_\theta + \bar{Q}_{26}\gamma_{r\theta} - \sigma_\theta^T \\
\tau_{r\theta} &= \bar{Q}_{16}\epsilon_r + \bar{Q}_{26}\epsilon_\theta + \bar{Q}_{66}\gamma_{r\theta} - \tau_{r\theta}^T
\end{aligned} \tag{5.3}$$

where

$$\begin{aligned}
\sigma_r^T &= \bar{Q}_{11}\epsilon_r^T + \bar{Q}_{12}\epsilon_\theta^T + \bar{Q}_{16}\gamma_{r\theta}^T \\
\sigma_\theta^T &= \bar{Q}_{12}\epsilon_r^T + \bar{Q}_{22}\epsilon_\theta^T + \bar{Q}_{26}\gamma_{r\theta}^T \\
\tau_{r\theta}^T &= \bar{Q}_{16}\epsilon_r^T + \bar{Q}_{26}\epsilon_\theta^T + \bar{Q}_{66}\gamma_{r\theta}^T
\end{aligned} \tag{5.4}$$

Since the temperature in the piezoceramic layers is changed by $\Delta T_C$, the equivalent strains in the two layers of RAINBOW are given by

$$\begin{aligned}
\epsilon_{r(PZT)}^P &= \alpha_r \Delta T_C \\
\epsilon_{\theta(PZT)}^P &= \alpha_\theta \Delta T_C \\
\gamma_{r\theta(PZT)}^P &= \alpha_{r\theta} \Delta T_C
\end{aligned} \tag{5.5}$$

In similar fashion to equation (3.6), the equivalent strains in the composite layer, assumed to be graphite-epoxy, are defined by

$$\begin{aligned} \epsilon^T_{r(Composite)} &= \alpha_r(\Delta T_C - \Delta T^*) + \epsilon^*_r \\ \epsilon^T_{\theta(Composite)} &= \alpha_\theta(\Delta T_C - \Delta T^*) + \epsilon^*_\theta \\ \gamma^T_{r\theta(Composite)} &= \alpha_{r\theta}(\Delta T_C - \Delta T^*) + \gamma^*_{r\theta} \end{aligned} \tag{5.6}$$

where $\epsilon^*_r$, $\epsilon^*_\theta$, and $\gamma^*_{r\theta}$ are the strains computed at temperature $T^*$. Integrating with respect to $z$ through the thickness of GRAPHBOW results in

$$\begin{aligned} \Pi &= \frac{1}{2}\int_0^R \int_0^{2\pi} \Big\{(N_r - \hat{N}_r^T \Delta T_C - N_r^*)\epsilon_r^o + (N_\theta - \hat{N}_\theta^T \Delta T_C - N_\theta^*)\epsilon_\theta^o \\ &+ (N_{r\theta} - \hat{N}_{r\theta}^T \Delta T_C - N_{r\theta}^*)\gamma_{r\theta}^o + (M_r - \hat{M}_r^T \Delta T_C - M_r^*)\kappa_r^o \\ &+ +(M_\theta - \hat{M}_\theta^T \Delta T_C - M_\theta^*)\kappa_\theta^o + (M_{r\theta} - \hat{M}_{r\theta}^T \Delta T_C - M_{r\theta}^*)\kappa_{r\theta}^o \Big\} r dr d\theta \end{aligned} \tag{5.7}$$

where

$$\begin{Bmatrix} N_r \equiv \int_0^{H+H_c} \sigma_r dz \\ N_\theta \equiv \int_0^{H+H_c} \sigma_\theta dz \\ N_{r\theta} \equiv \int_0^{H+H_c} \tau_{r\theta} dz \\ M_r \equiv \int_0^{H+H_c} z\sigma_r dz \\ M_\theta \equiv \int_0^{H+H_c} z\sigma_\theta dz \\ M_{r\theta} \equiv \int_0^{H+H_c} z\tau_{r\theta} dz \end{Bmatrix} = \begin{bmatrix} [A] & [B] \\ [B] & [D] \end{bmatrix} \begin{Bmatrix} \epsilon_r^o \\ \epsilon_\theta^o \\ \gamma_{r\theta}^o \\ \kappa_r^o \\ \kappa_\theta^o \\ \kappa_{r\theta}^o \end{Bmatrix} - \begin{Bmatrix} \hat{N}_r^T \\ \hat{N}_\theta^T \\ \hat{N}_{r\theta}^T \\ \hat{M}_r^T \\ \hat{M}_\theta^T \\ \hat{M}_{r\theta}^T \end{Bmatrix} \Delta T_C - \begin{Bmatrix} N_r^* \\ N_\theta^* \\ N_{r\theta}^* \\ M_r^* \\ M_\theta^* \\ M_{r\theta}^* \end{Bmatrix} \tag{5.8}$$

$$\left\{\begin{array}{rl} N_r^* \equiv & \int_H^{H+H_c} \sigma_r dz \\ N_\theta^* \equiv & \int_H^{H+H_c} \sigma_\theta dz \\ N_{r\theta}^* \equiv & \int_H^{H+H_c} \tau_{r\theta} dz \\ M_r^* \equiv & \int_H^{H+H_c} z\sigma_r dz \\ M_\theta^* \equiv & \int_H^{H+H_c} z\sigma_\theta dz \\ M_{r\theta}^* \equiv & \int_H^{H+H_c} z\tau_{r\theta} dz \end{array}\right\} = \left[\begin{array}{cc} [A^*] & [B^*] \\ [B^*] & [D^*] \end{array}\right] \left\{\begin{array}{c} \epsilon_r^{o*} \\ \epsilon_\theta^{o*} \\ \gamma_{r\theta}^{o*} \\ \kappa_r^{o*} \\ \kappa_\theta^{o*} \\ \kappa_{r\theta}^{o*} \end{array}\right\} - \left\{\begin{array}{c} \hat{N}_r^{T*} \\ \hat{N}_\theta^{T*} \\ \hat{N}_{r\theta}^{T*} \\ \hat{M}_r^{T*} \\ \hat{M}_\theta^{T*} \\ \hat{M}_{r\theta}^{T*} \end{array}\right\} \Delta T^* \tag{5.9}$$

$$[A^*] = \left[\begin{array}{ccc} A_{11}^* & A_{12}^* & A_{16}^* \\ A_{12}^* & A_{22}^* & A_{26}^* \\ A_{16}^* & A_{26}^* & A_{66}^* \end{array}\right] \tag{5.10}$$

$$[B^*] = \left[\begin{array}{ccc} B_{11}^* & B_{12}^* & B_{16}^* \\ B_{12}^* & B_{22}^* & B_{26}^* \\ B_{16}^* & B_{26}^* & B_{66}^* \end{array}\right] \tag{5.11}$$

$$[D^*] = \left[\begin{array}{ccc} D_{11}^* & D_{12}^* & D_{16}^* \\ D_{12}^* & D_{22}^* & D_{26}^* \\ D_{16}^* & D_{26}^* & D_{66}^* \end{array}\right] \tag{5.12}$$

Also the effective thermal force and moment resultants are defined as

$$\hat{N}_r^T \equiv \int_0^{H+H_c} \left(\bar{Q}_{11}\alpha_r + \bar{Q}_{12}\alpha_\theta + \bar{Q}_{16}\alpha_{r\theta}\right) dz \tag{5.13}$$

$$\hat{N}_\theta^T \equiv \int_0^{H+H_c} \left(\bar{Q}_{12}\alpha_r + \bar{Q}_{22}\alpha_\theta + \bar{Q}_{26}\alpha_{r\theta}\right) dz \tag{5.14}$$

$$\hat{N}_{r\theta}^T \equiv \int_0^{H+H_c} \left(\bar{Q}_{16}\alpha_r + \bar{Q}_{26}\alpha_\theta + \bar{Q}_{66}\alpha_{r\theta}\right) dz \tag{5.15}$$

$$\hat{M}_r^T \equiv \int_0^{H+H_c} \left(\bar{Q}_{11}\alpha_r + \bar{Q}_{12}\alpha_\theta + \bar{Q}_{16}\alpha_{r\theta}\right) z dz \tag{5.16}$$

$$\hat{M}_\theta^T \equiv \int_0^{H+H_c} \left(\bar{Q}_{12}\alpha_r + \bar{Q}_{22}\alpha_\theta + \bar{Q}_{26}\alpha_{r\theta}\right) z dz \tag{5.17}$$

$$\hat{M}_{r\theta}^T \equiv \int_0^{H+H_c} \left(\bar{Q}_{16}\alpha_r + \bar{Q}_{26}\alpha_\theta + \bar{Q}_{66}\alpha_{r\theta}\right) z dz \tag{5.18}$$

$$\hat{N}_r^{T*} \equiv \int_H^{H+H_c} \left(\bar{Q}_{11}\alpha_r + \bar{Q}_{12}\alpha_\theta + \bar{Q}_{16}\alpha_{r\theta}\right) dz \tag{5.19}$$

$$\hat{N}_\theta^{T*} \equiv \int_H^{H+H_c} \left(\bar{Q}_{12}\alpha_r + \bar{Q}_{22}\alpha_\theta + \bar{Q}_{26}\alpha_{r\theta}\right) dz \tag{5.20}$$

$$\hat{N}_{r\theta}^{T*} \equiv \int_H^{H+H_c} \left(\bar{Q}_{16}\alpha_r + \bar{Q}_{26}\alpha_\theta + \bar{Q}_{66}\alpha_{r\theta}\right) dz \tag{5.21}$$

$$\hat{M}_r^{T*} \equiv \int_H^{H+H_c} \left(\bar{Q}_{11}\alpha_r + \bar{Q}_{12}\alpha_\theta + \bar{Q}_{16}\alpha_{r\theta}\right) z dz \tag{5.22}$$

$$\hat{M}_\theta^{T*} \equiv \int_H^{H+H_c} \left(\bar{Q}_{12}\alpha_r + \bar{Q}_{22}\alpha_\theta + \bar{Q}_{26}\alpha_{r\theta}\right) z dz \tag{5.23}$$

$$\hat{M}_{r\theta}^{T*} \equiv \int_H^{H+H_c} \left(\bar{Q}_{16}\alpha_r + \bar{Q}_{26}\alpha_\theta + \bar{Q}_{66}\alpha_{r\theta}\right) z dz \tag{5.24}$$

In the above, the matrices $[A]$, $[B]$, and $[D]$ and the $A$'s, $B$'s, $D$'s, $A^*$'s, $B^*$'s and $D^*$'s are defined in Equations (4.38)–(4.40) and (3.32)–(3.37), respectively.

### 5.2.2 The Rayleigh-Ritz Approach

The displacement fields for GRAPHBOW are assumed to have the same functional form as for disk-style RAINBOW, i.e., Equations (4.47)–(4.49). Again the values of $a_{ij}$, $c_{ij}$, and $d_{ij}$ are sought by using the first variation of the total potential energy, and stability is evaluated using the second variation. The procedures are identical to those discussed in Chapter 4 with Equations (4.50) and (4.51).

### 5.2.3 Piezoelectric Effects

To investigate to deformation characteristics due to applying an electric field through the unreduced piezoceramic, the total potential energy expression of Equation (5.7) is modified to account for the effective force and moment resultants produced by the electric-field-induced dilatational strains. Thus, the following terms are appended to the total potential energy expression:

$$\hat{N}_r^E E_z \equiv \int_0^{H+H_c} \left(\bar{Q}_{11} d_{31} + \bar{Q}_{12} d_{32}\right) E_z dz \tag{5.25}$$

$$\hat{N}_\theta^E E_z \equiv \int_0^{H+H_c} \left(\bar{Q}_{12} d_{31} + \bar{Q}_{22} d_{32}\right) E_z dz \tag{5.26}$$

$$\hat{M}_r^E E_z \equiv \int_0^{H+H_c} \left(\bar{Q}_{11} d_{31} + \bar{Q}_{12} d_{32}\right) E_z z dz \tag{5.27}$$

$$\hat{M}_\theta^E E_z \equiv \int_0^{H+H_c} \left(\bar{Q}_{12} d_{31} + \bar{Q}_{22} d_{32}\right) E_z z dz \tag{5.28}$$

Attention should be brought to the fact that only the unreduced piezoceramic layer contributes to the integrals of Equations (5.25)–(5.28), as $d_{31}$ and $d_{32}$ are considered to be zero for the reduced layer and the composite, and that the assumed displacements resulting from the temperature change plus the application of the electric field are approximated by Equations (4.47)–(4.49).

## 5.3 Numerical Results

### 5.3.1 Effect of Composite Layer Arrangements on GRAPHBOW Room-Temperature Shape

To illustrate the results predicted by the present model and to study convergence of the Rayleigh-Ritz method, consider the disk-style RAINBOW discussed in Chapter 4 with $R$=25.4 mm, $H$=0.381 mm, and $H_r/H$=0.35. The relationships between temperature and the coefficients $a_{20}$, $a_{22}$, $a_{30}$, $a_{32}$, $a_{40}$, $a_{42}$, $a_{50}$, $a_{52}$, and $a_{60}$ and $a_{62}$ are shown in Figures 4.9–4.13. Recall, from Equations (4.70)–(4.72) that these coefficients describe the curvatures. Assume a single layer of graphite-epoxy is applied to the reduced side of RAINBOW. With this arrangement, layer no. 1 is the composite, layer no. 2 is the reduced layer, and layer no. 3 is the unreduced layer. The fibers

are aligned with the $x$ direction (refer to Figure 5.1), i.e., the composite layer is considered a $0^o$ layer. The material properties of the composite are given in section 3.3. A convergence study of the Rayleigh-Ritz method is made by assuming the layer of composite is present from the onset of cooling of GRAPHBOW, as opposed to adding the layer of composite partway through the cooling cycle and then continuing to cool. This approach is taken because of the difficulty with developing an ABAQUS model whereby elements are added after cooling partway through the cooling cycle. This essentially means the case is considered where $T_C = T^*$, i.e., in Figure 3.1 $\Delta T^* = 0$. The $\Delta T_C$ considered was $\Delta T_C$=-157 $^o$C and the out-of-plane, radial, and circumferential displacements of the outer radius are compared for three sets of approximations, Equations (4.61)–(4.69). Figures 5.2–5.4 illustrate the convergence characteristics of the three sets of functions. For the finite-element analysis, the mesh, type of elements, type of loading, and boundary conditions used are the same as those described in Chapter 4. As it can be seen, increasing the number of terms in the approximation greatly improves the results. Since the 35-term approximation takes much less computational effort than the 85-term approximation, and compares very well with the ABAQUS results, it is used to obtain numerical values of the $a_{ij}$ coefficients which can be substituted in Equations (4.70)–(4.72) to compute the curvatures of GRAPHBOW for given $r$ and $\theta$ coordinates.

Considering a more realistic case, a multiple-step temperature change case, Figures 5.5–5.9 illustrate the behavior of the disk-style [$0^o$/RAINBOW] described above, and by Figures 3.1 and 5.1, as it is cooled from the composite cure temperature $T^*$=177 $^o$C to room temperature. For temperatures greater than $T^*$, the results of Figures 4.9–4.13 apply. Specifically, in Figures 5.5–5.9 the parameters $a_{ij}$ of Equations (4.70)-(4.72) are shown as a function of the temperature. Figure 5.10 illustrates GRAPHBOW room-temperature shapes. For comparison, the room-temperature shapes of their counterpart RAINBOW from Figure 4.14 are included.

Referring to Figures 5.5–5.9, the solid lines and dashed lines correspond to the stable and unstable equilibrium solutions, respectively. At a temperature lower than $T^*$, the temperature-$a_{ij}$ relationship of GRAPHBOW is depicted by curves with rectangular (Solution I), triangular (Solution II), and circular (Solution III) symbols. The solution paths of branches BC, BE, B′C′, B′C″, and B′E′ in Figures 4.9–4.13 are included for direct comparison. From Figures 5.5–5.9, it is observed that the coefficients $a_{ij}$ along the three solution paths, Solution I, Solution II, and Solution III, are single-

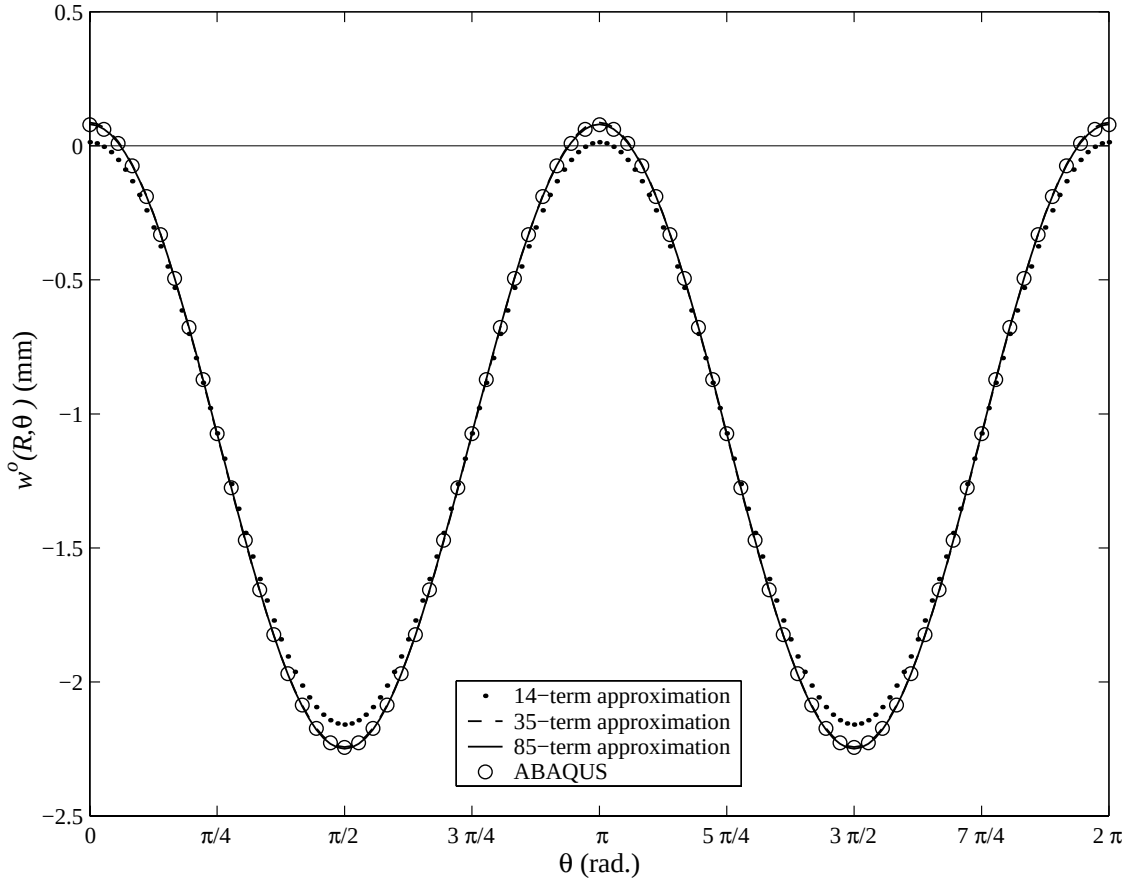


Figure 5.2: Convergence of the Rayleigh-Ritz method for the out-of-plane displacement $w^o$ of disk-style [$0^o$/RAINBOW] ($R$=25.4 mm, $H$=0.381 mm, $H_r/H$=0.35, $\Delta T_C$=-157 $^o$C, $\Delta T^*$=0 $^o$C).

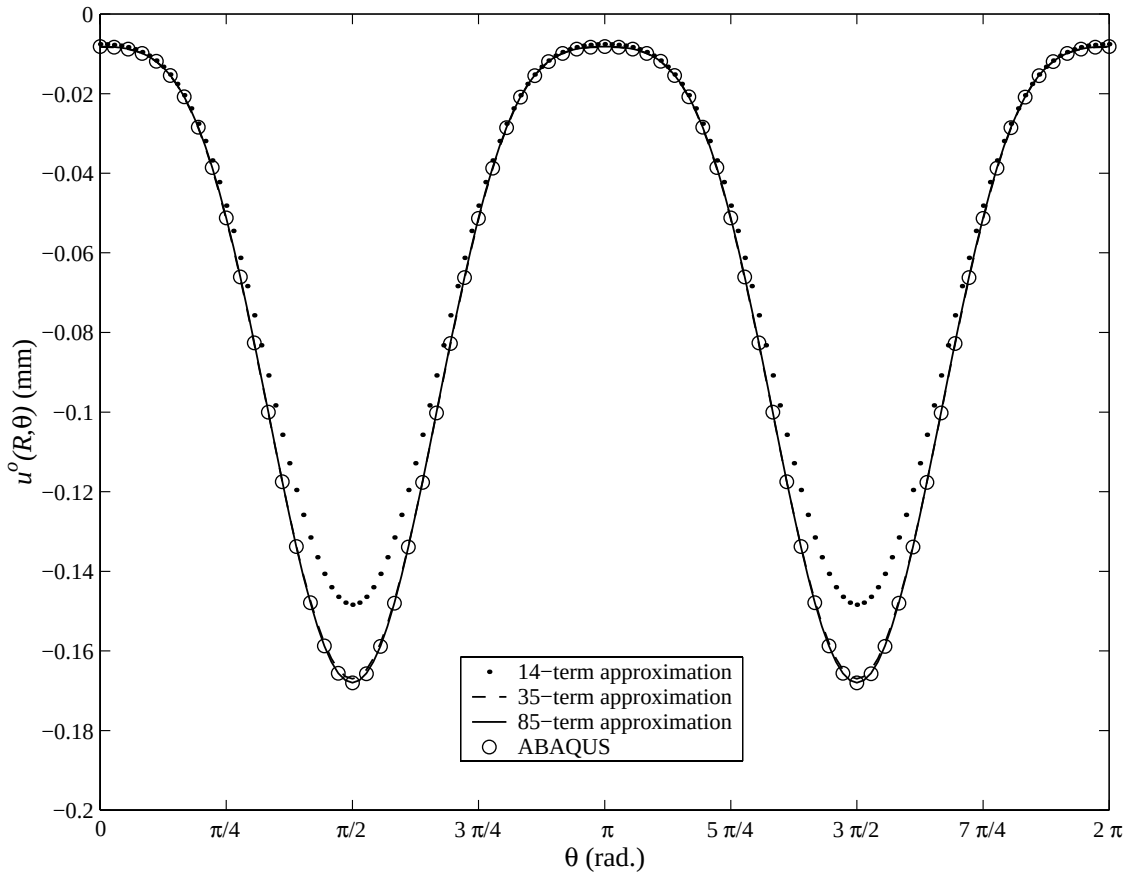


Figure 5.3: Convergence of the Rayleigh-Ritz method for the radial displacement $u^o$ of disk-style [$0^o$/RAINBOW] ($R$=25.4 mm, $H$=0.381 mm, $H_r/H$=0.35, $\Delta T_C$=-157 $^o$C, $\Delta T^*$=0 $^o$C).

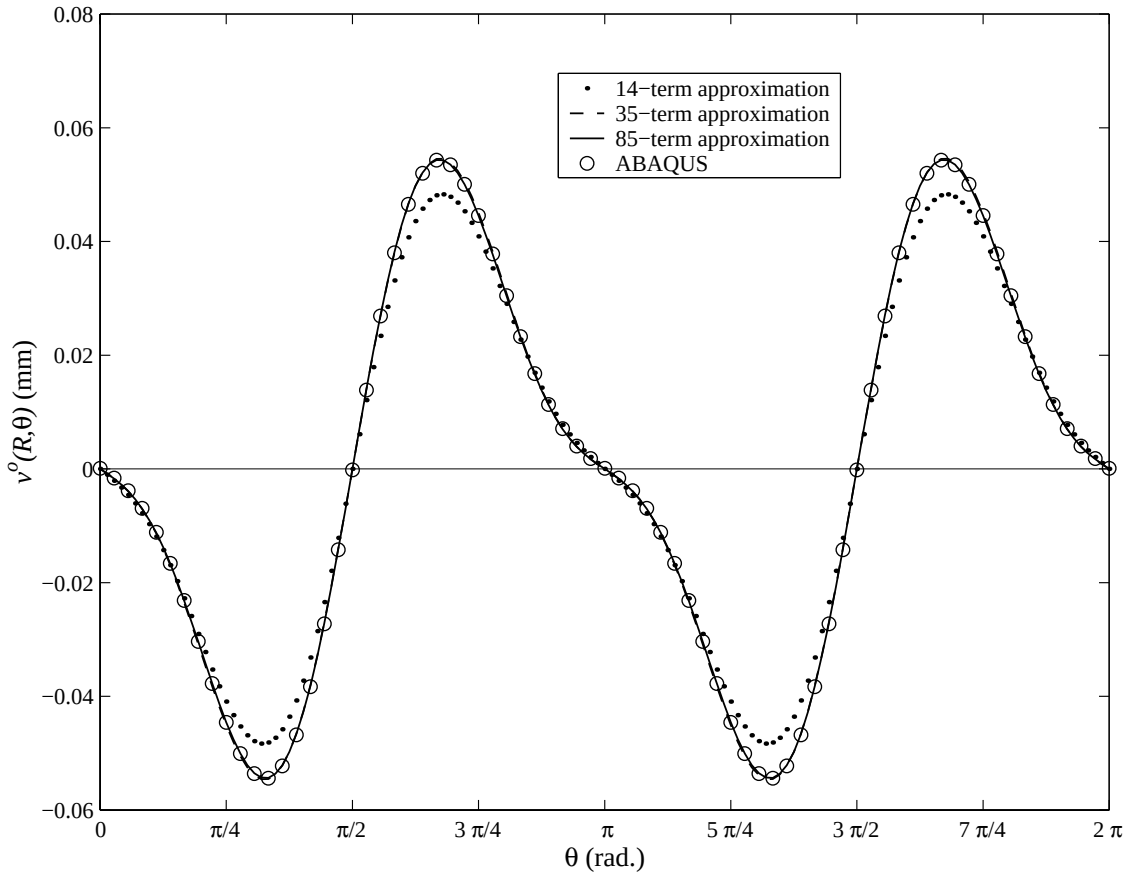


Figure 5.4: Convergence of the Rayleigh-Ritz method for the circumferential displacement $v^o$ of disk-style [$0^o$/RAINBOW] ($R$=25.4 mm, $H$=0.381 mm, $H_r/H$=0.35, $\Delta T_C$=-157 $^o$C, $\Delta T^*$=0 $^o$C).

valued. A stability study shows that the three GRAPHBOW room-temperature shapes shown in Figure 5.10 are stable. Hence, the unstable branches BE and B′E′ are stabilized and the 'converted' stable branches are given by Solution III. Figure 5.10 indicates that bonding a $0^o$ composite layer to the reduced layer of RAINBOW results in three similar room-temperature configurations, i.e., larger $\kappa_r$ along the $\theta$=$\pi/2$ and $\theta$=$3\pi/2$ directions than along the $\theta$=0 and $\theta$=$\pi$ directions. These three configurations are all near-cylindrical and exhibit larger out-of plane displacements than their RAINBOW counterparts. It is quite interesting that the unstable dome configuration is eliminated by the addition of the $0^o$ layer. This behavior was seen with rectangular RAINBOW. Again, it is important to note the relative magnitude of the coefficients $a_{20}$, $a_{22}$, $a_{30}$, $a_{32}$, etc.

In Figures 5.11–5.15 a single $0^o$ layer of fiber reinforced composite material is bonded to the unreduced side of RAINBOW. With this arrangement, layer no. 1 is the reduced layer, layer no. 2 is the unreduced layer, and layer no. 3 is the composite. The room-temperature shapes of [RAINBOW/$0^o$], as shown in Figure 5.16, are three stable near-cylindrical shapes with larger $\kappa_r$ along the $\theta$=0 and $\theta$=$\pi$ directions than along the $\theta$=$\pi/2$ and $\theta$=$3\pi/2$ directions. These larger curvature directions are different than for the case when the composite is bonded to the opposite side of RAINBOW, Figure 5.10. This is somewhat surprising in light of the increased stiffness in the $0^o$ direction in both cases. The two configurations corresponding to Solution I and Solution II exhibit smaller out-of-plane displacements than their RAINBOW counterparts. This is also different than the case of Figure 5.10, where the addition of the composite layer led to larger out-of-plane displacements for all three solutions.

The behavior of [$0^o_2$/RAINBOW], shown in Figures 5.17–5.21, is not much different than [$0^o$/RAINBOW], shown in Figures 5.5–5.10. The three stable near-cylindrical shapes are shown in Figure 5.22. Moreover, the behavior of [RAINBOW/$0^o_2$] shown in Figures 5.23–5.28 is similar to the behavior of [RAINBOW/$0^o$], shown in Figures 5.11–5.16.

Referring to Figures 5.29–5.33 and 5.35–5.39, bonding [$0^o$/$90^o$] composite layers either to the reduced layer or to the unreduced layer seems to produce similar behavior. In both cases the room-temperature shape of Solution I is dome-like and the room-temperature shapes corresponding to Solution II and Solution III are near-cylindrical with a larger $\kappa_r$ along the $\theta$=$\pi/2$ and $\theta$=$3\pi/2$ directions than along $\theta$=0 and $\theta$=$\pi$ directions. All of the room-temperature shapes of

[$0^o/90^o$/RAINBOW] and [RAINBOW/$0^o/90^o$] are stable and are shown in Figures 5.34 and 5.40, respectively. The behavior in both cases of [$0^o/90^o$] composite layers being added to RAINBOW appears to favor the dome-like behavior. In Figures 5.34 and 5.40, comparing the solution of C and C$'$ with Solution I, it is seen that the dome-like behavior is induced by the addition of the [$0^o/90^o$] composite layers. Comparing the solution at C and C$''$ with Solution II, it is seen that the cylindrical shape of C and C$''$ is less pronounced when the [$0^o/90^o$] composite layers are added. And Solution III returns to a large degree the dome-like behavior of E and E$'$.

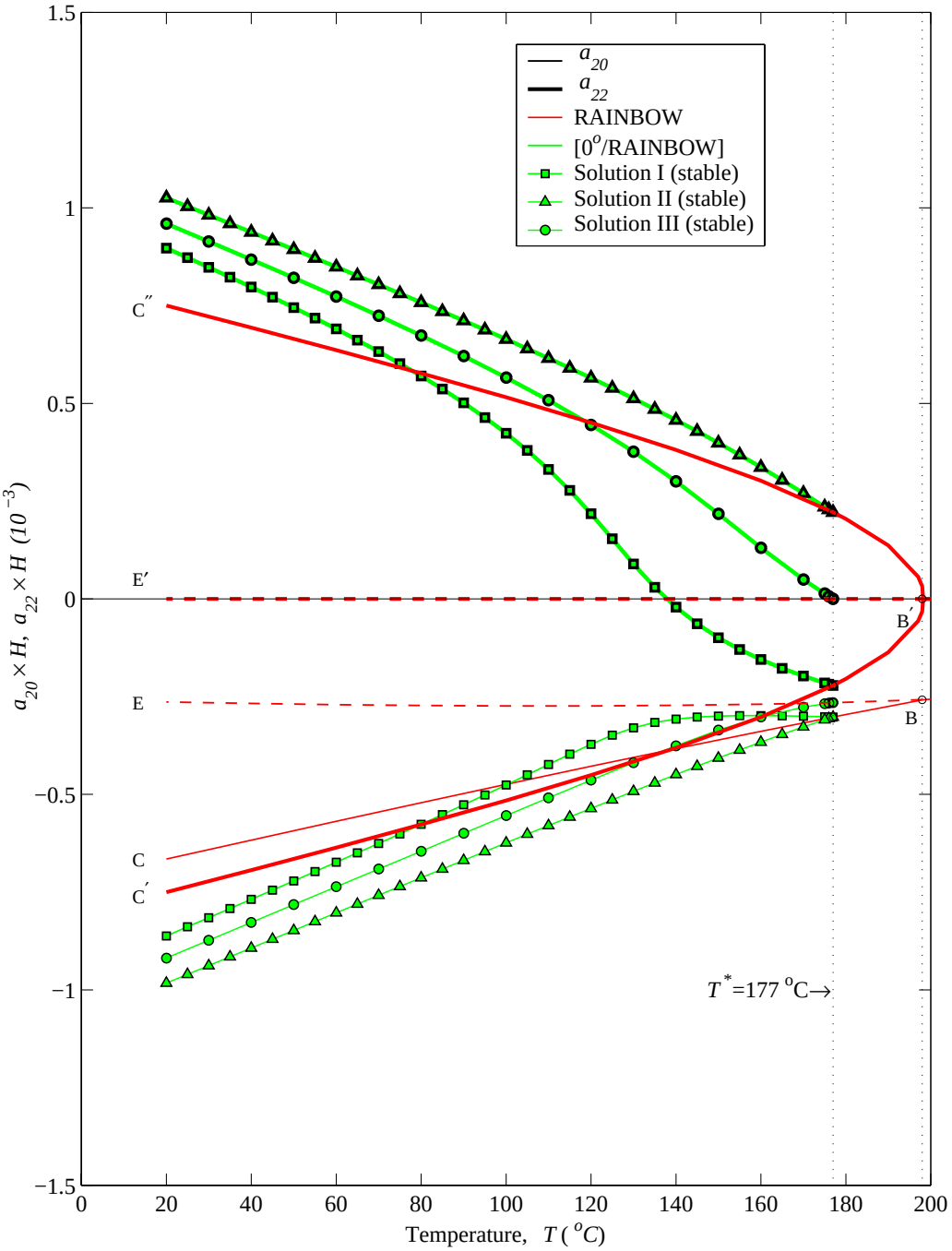


Figure 5.5: Temperature-curvature ($a_{20}$ and $a_{22}$) relation of disk-style [$0^o$/RAINBOW] ($R$=25.4 mm, $H$=0.381 mm, $H_r/H$=0.35).

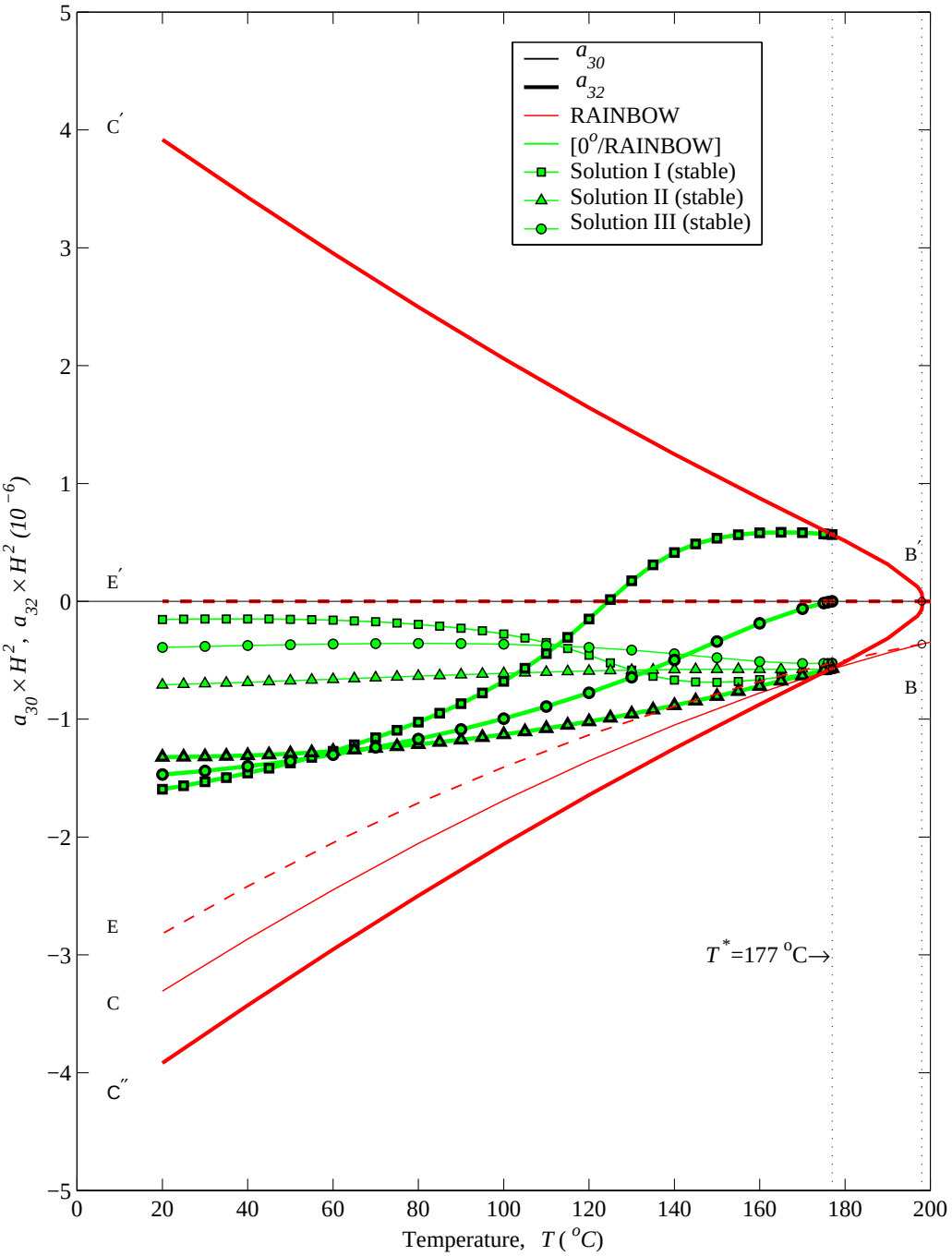


Figure 5.6: Temperature-curvature ($a_{30}$ and $a_{32}$) relation of disk-style [$0^o$/RAINBOW] ($R$=25.4 mm, $H$=0.381 mm, $H_r/H$=0.35).

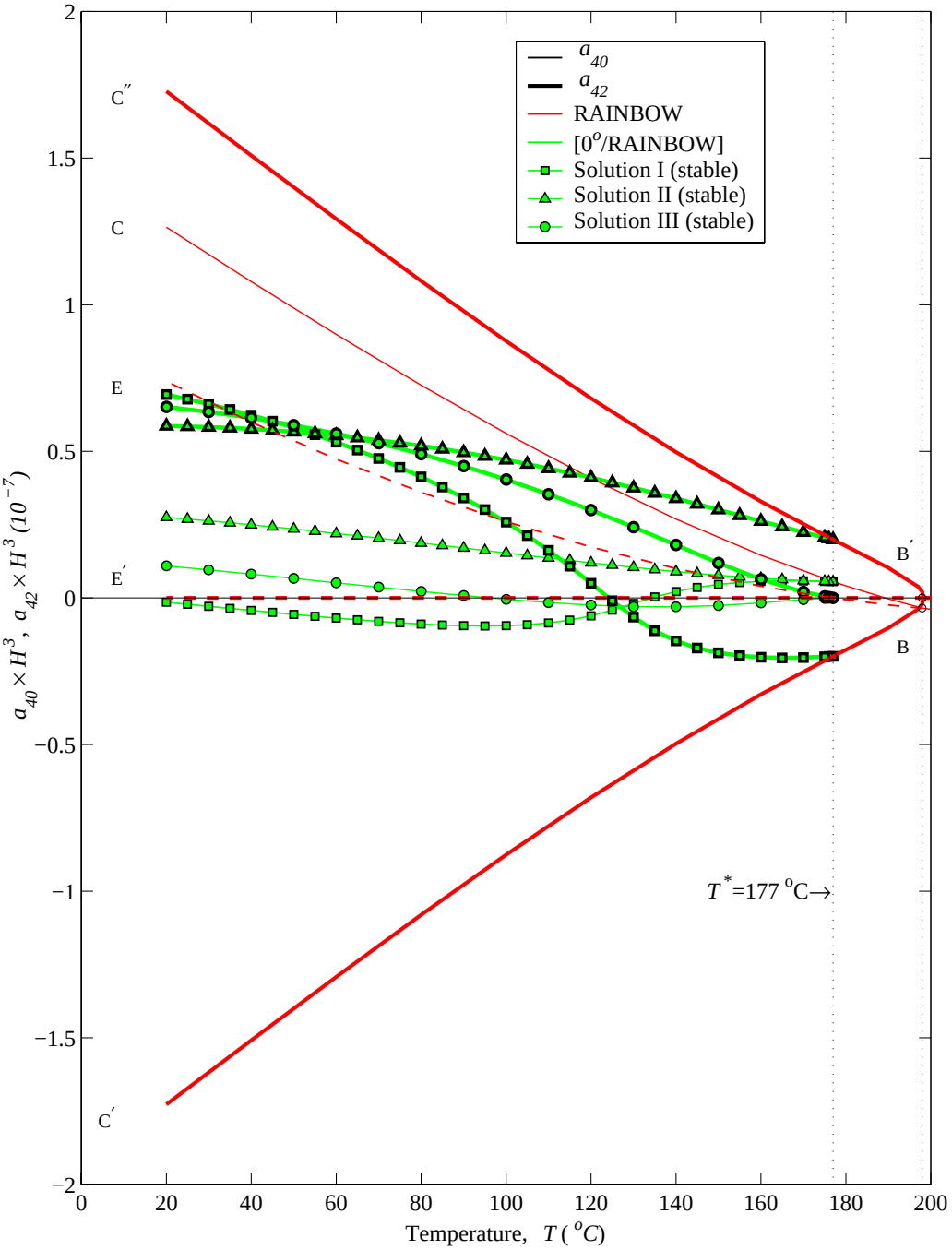


Figure 5.7: Temperature-curvature ($a_{40}$ and $a_{42}$) relation of disk-style [$0^o$/RAINBOW] ($R$=25.4 mm, $H$=0.381 mm, $H_r/H$=0.35).

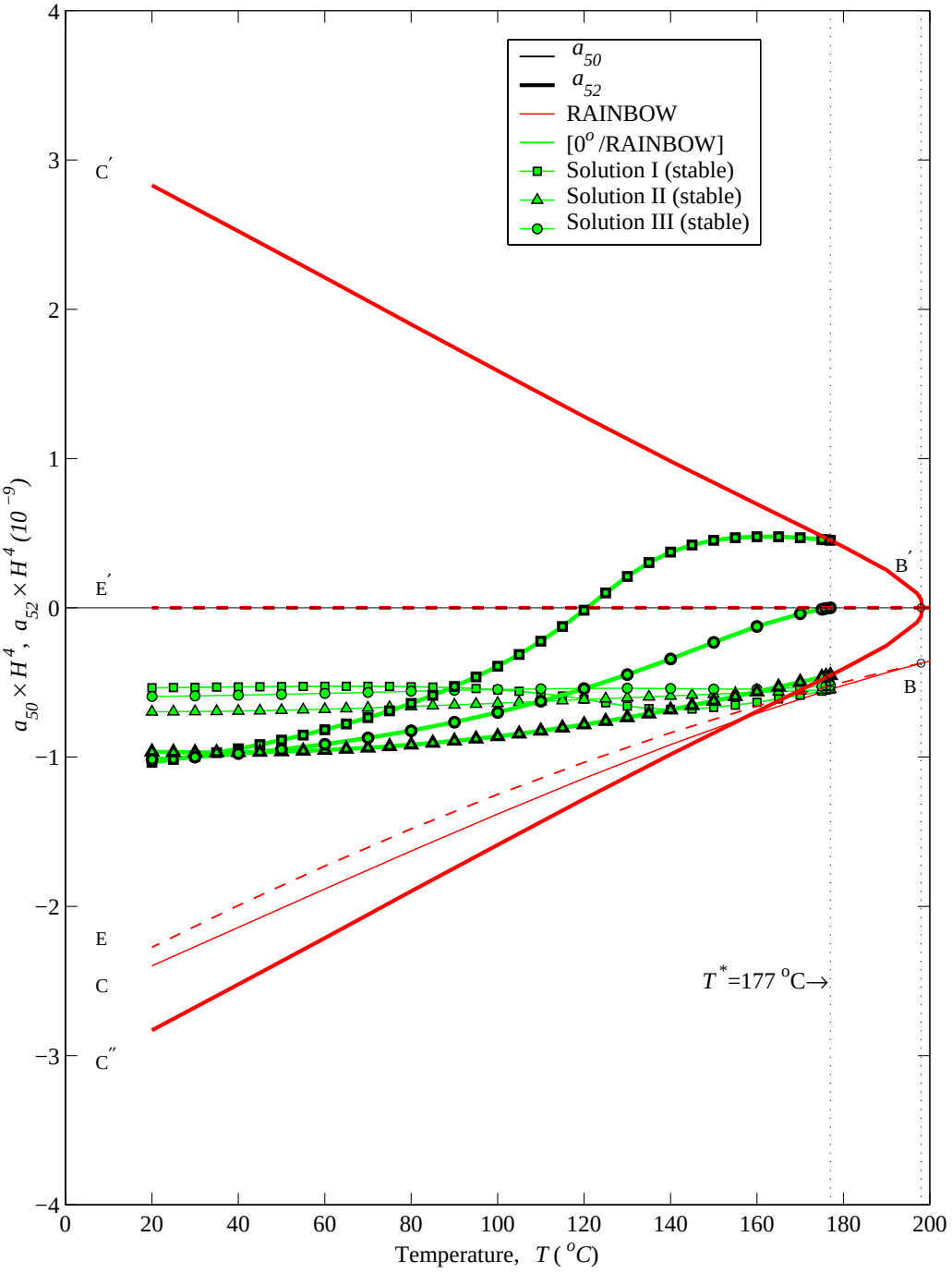


Figure 5.8: Temperature-curvature ($a_{50}$ and $a_{52}$) relation of disk-style [$0^o$/RAINBOW] ($R$=25.4 mm, $H$=0.381 mm, $H_r/H$=0.35).

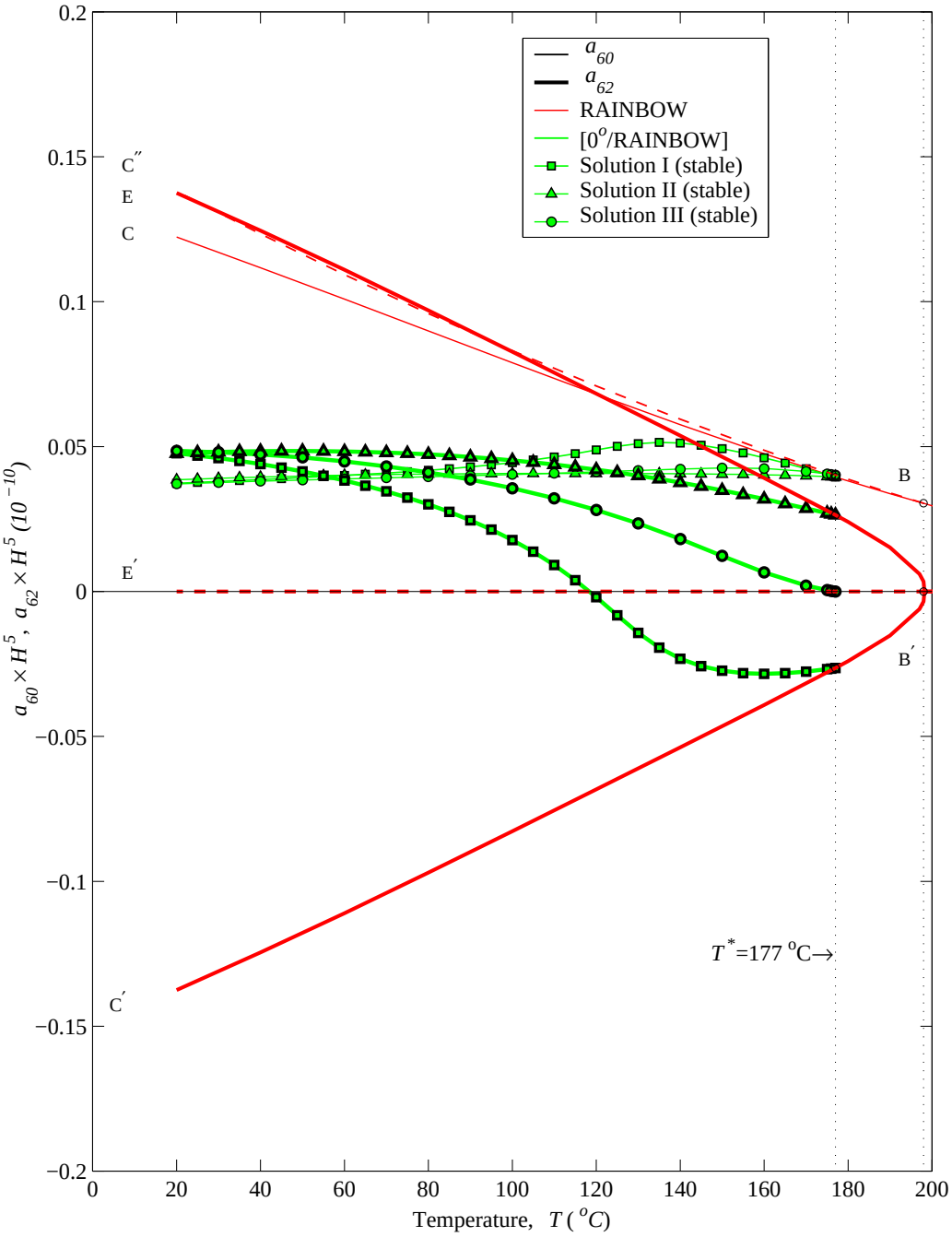


Figure 5.9: Temperature-curvature ($a_{60}$ and $a_{62}$) relation of disk-style [$0^o$/RAINBOW] ($R$=25.4 mm, $H$=0.381 mm, $H_r/H$=0.35).

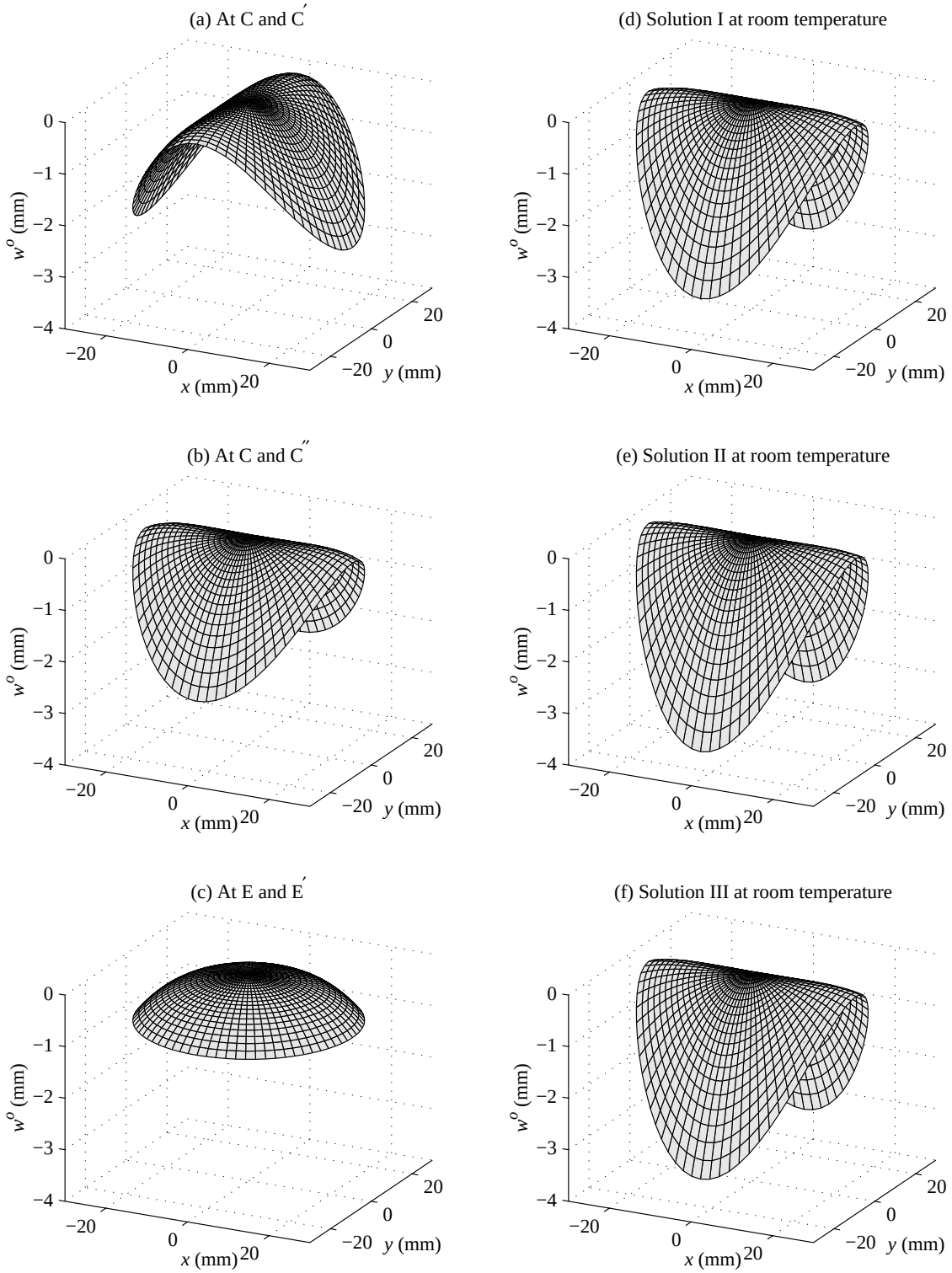


Figure 5.10: Comparison of room-temperature shapes of disk-style RAINBOW and [$0^o$/RAINBOW] (R=25.4 mm, $H$=0.381 mm, $H_r/H$=0.35) (refer to Figures 5.5–5.9).

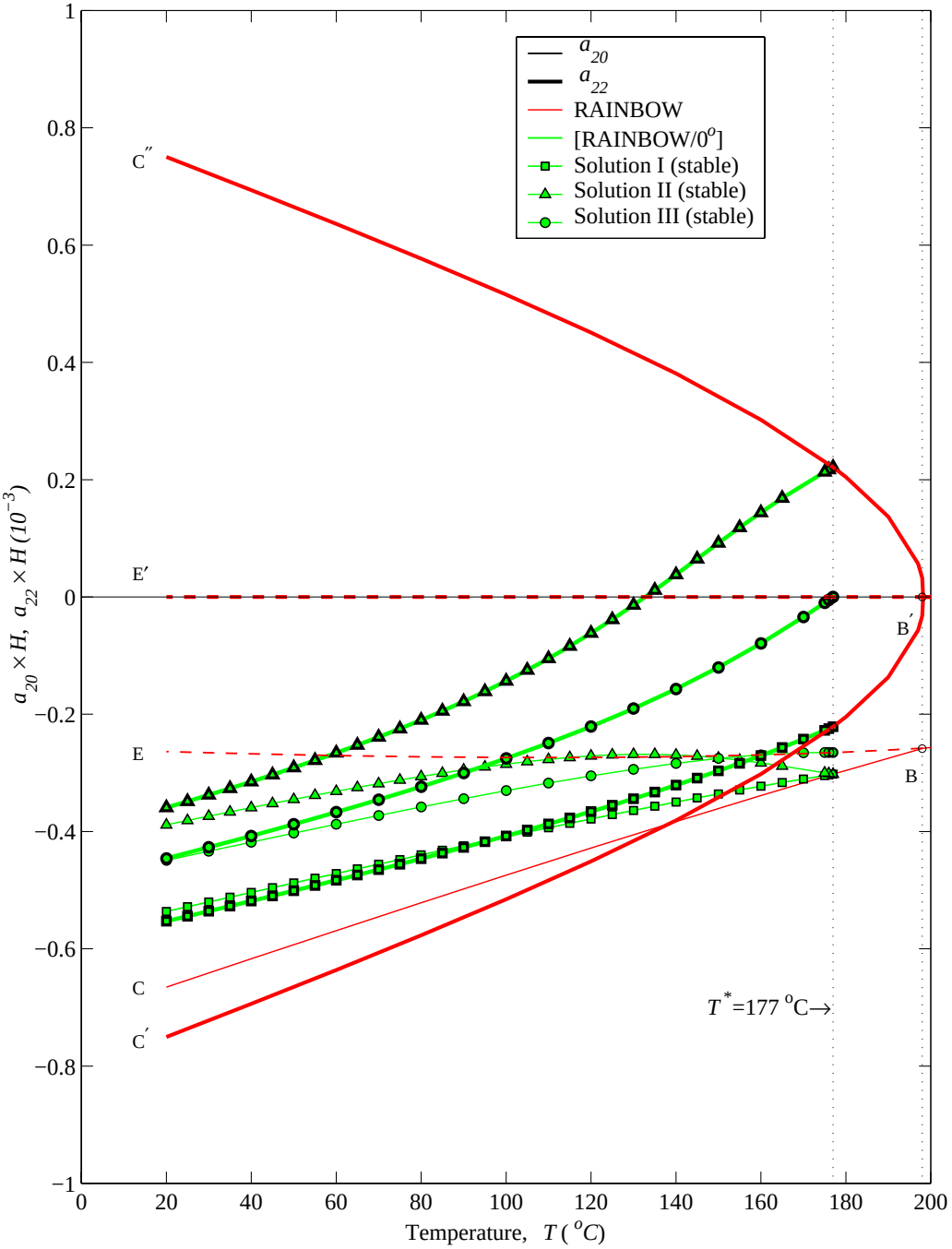


Figure 5.11: Temperature-curvature ($a_{20}$ and $a_{22}$) relation of disk-style [RAINBOW/$0^o$] ($R$=25.4 mm, $H$=0.381 mm, $H_r/H$=0.35).

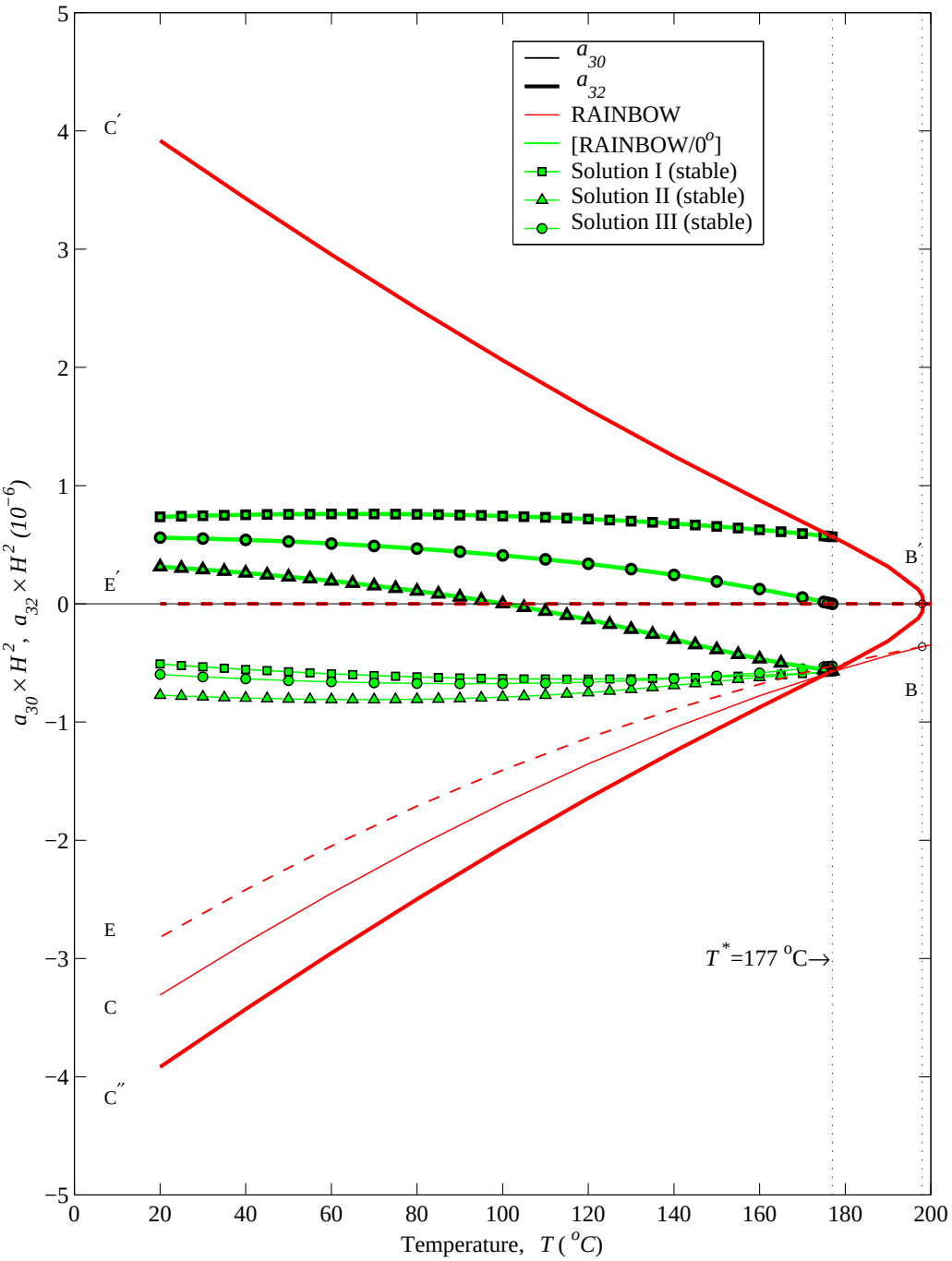


Figure 5.12: Temperature-curvature ($a_{30}$ and $a_{32}$) relation of disk-style [RAINBOW/$0^o$] ($R$=25.4 mm, $H$=0.381 mm, $H_r/H$=0.35).

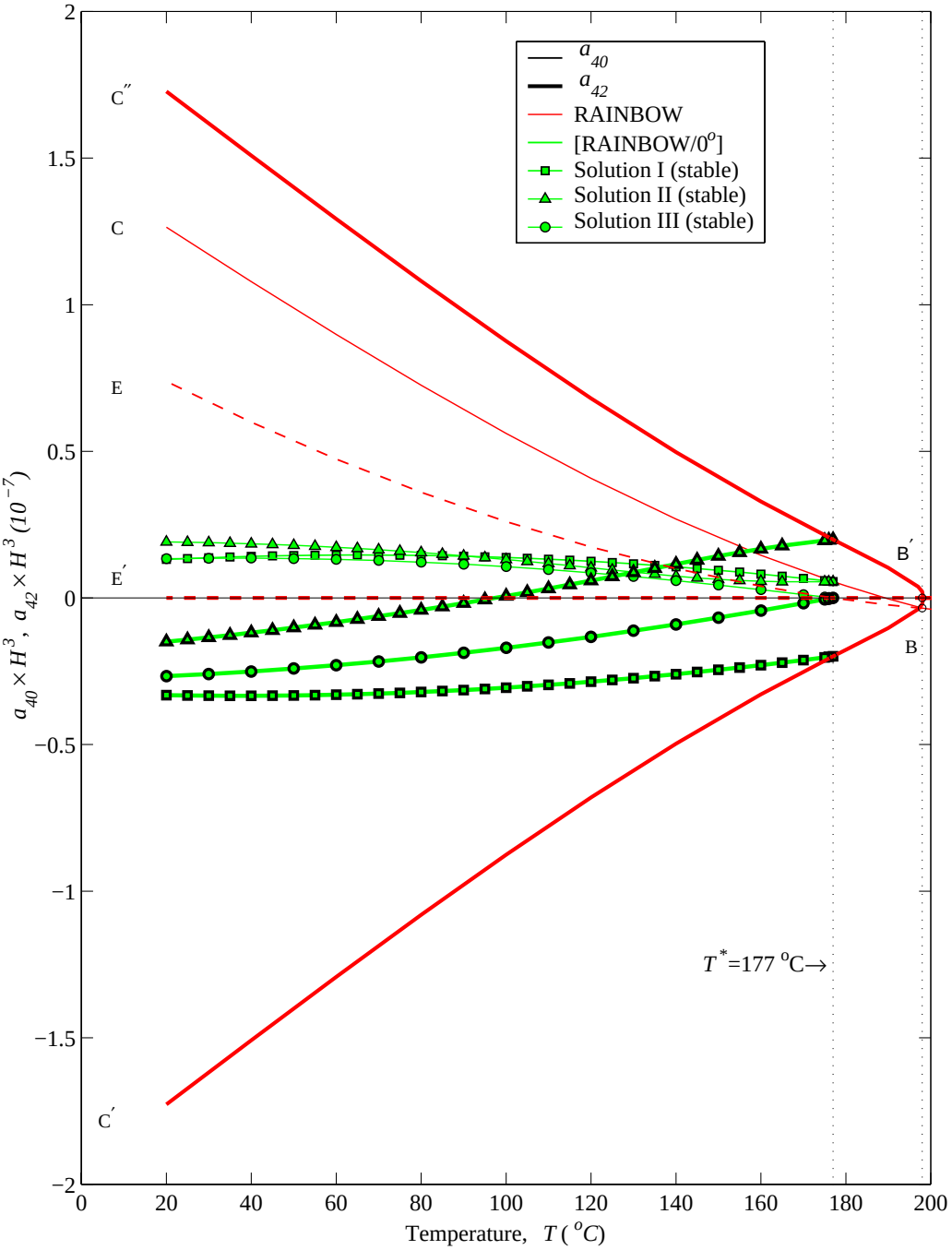


Figure 5.13: Temperature-curvature ($a_{40}$ and $a_{42}$) relation of disk-style [RAINBOW/$0^o$] ($R$=25.4 mm, $H$=0.381 mm, $H_r/H$=0.35).

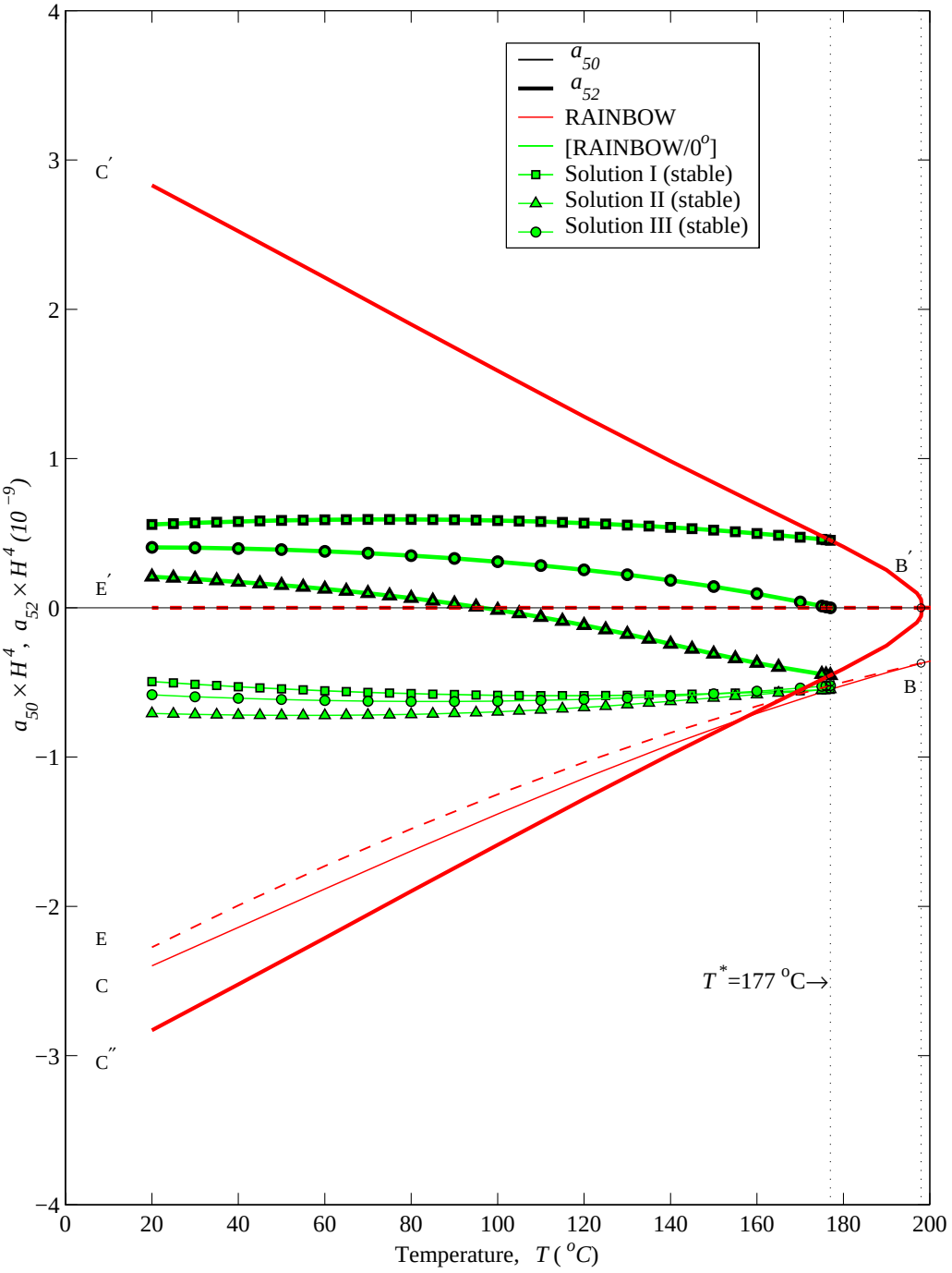


Figure 5.14: Temperature-curvature ($a_{50}$ and $a_{52}$) relation of disk-style [RAINBOW/$0^o$] ($R$=25.4 mm, $H$=0.381 mm, $H_r/H$=0.35).

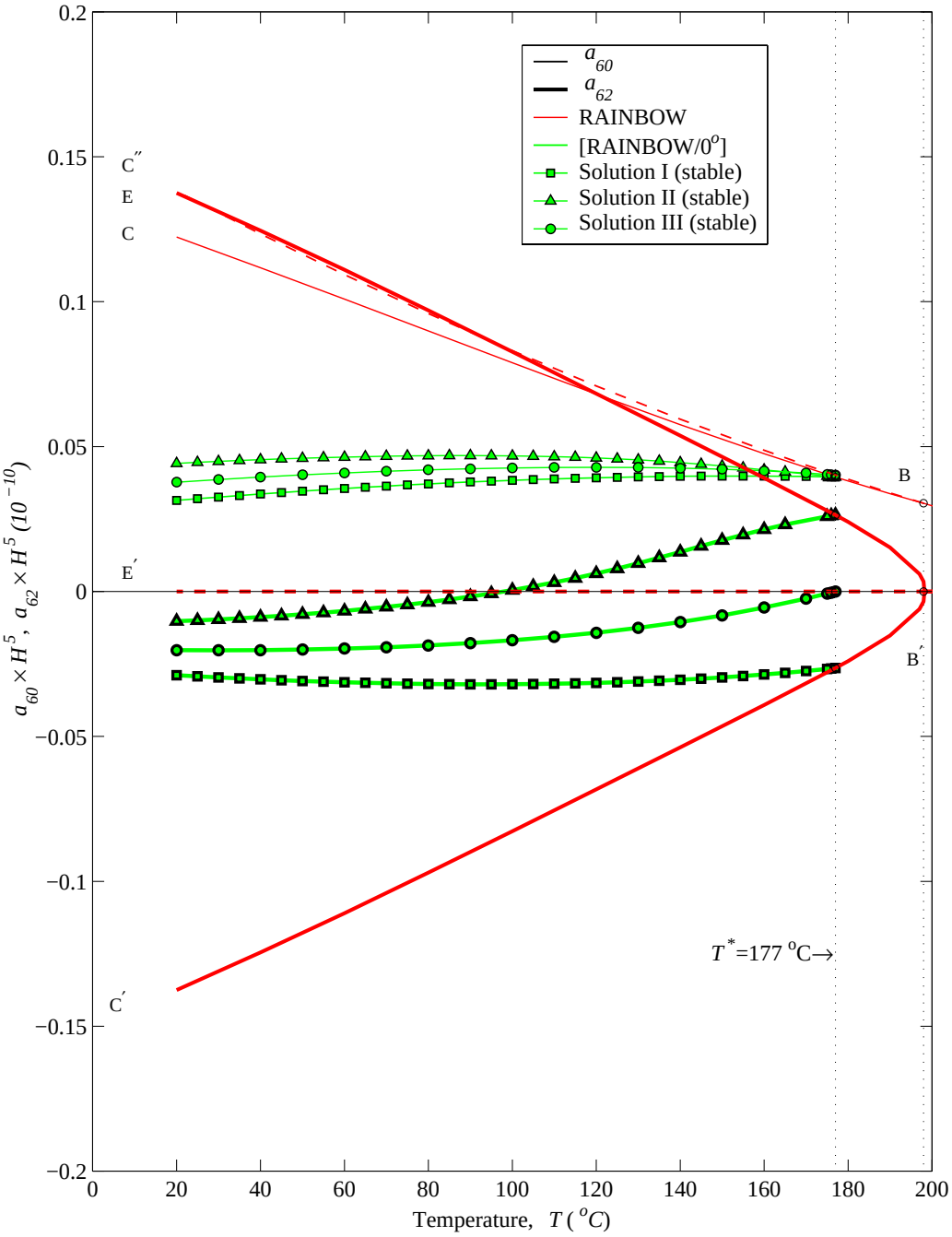


Figure 5.15: Temperature-curvature ($a_{60}$ and $a_{62}$) relation of disk-style [RAINBOW/$0^o$] ($R$=25.4 mm, $H$=0.381 mm, $H_r/H$=0.35).

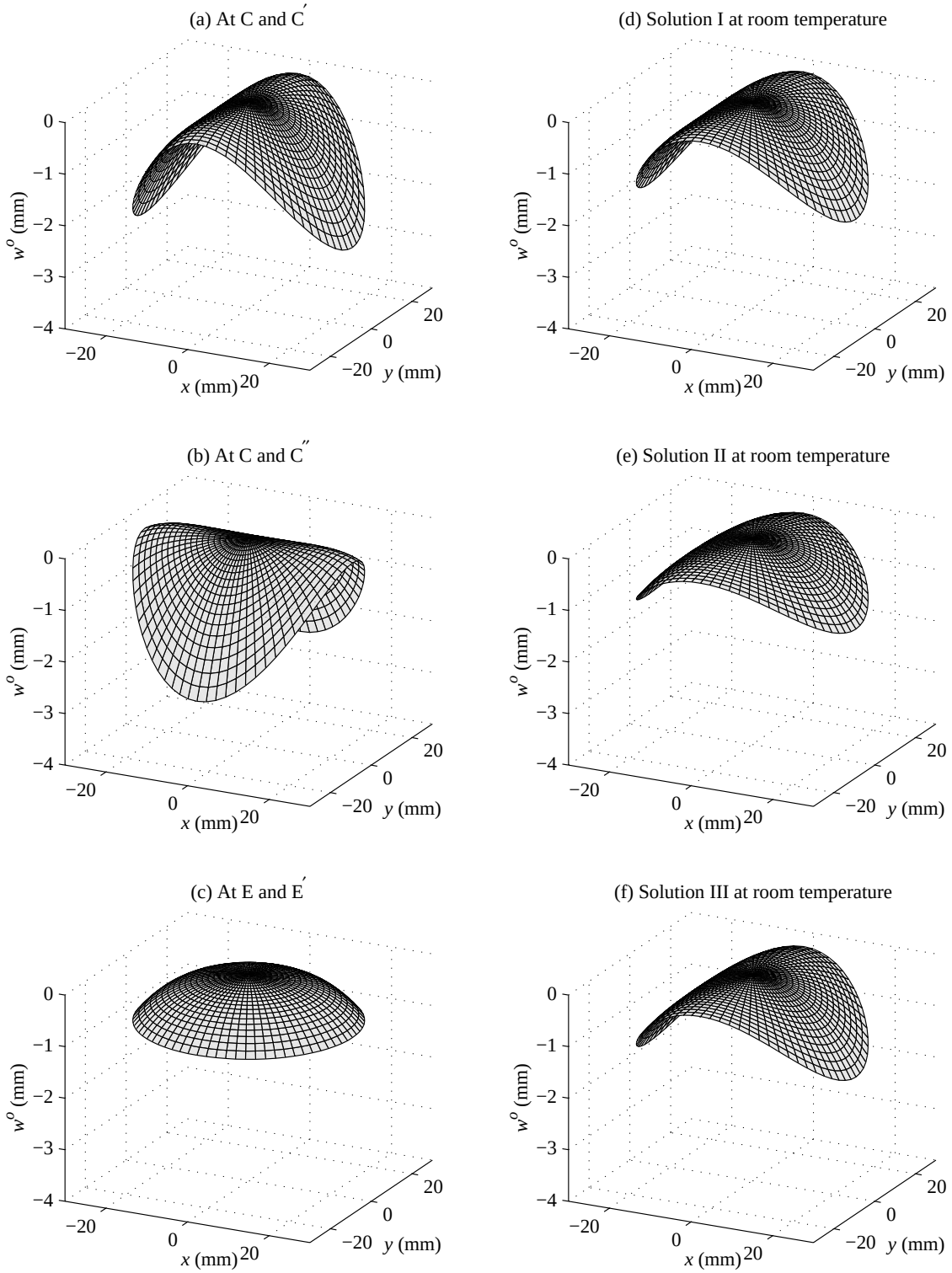


Figure 5.16: Comparison of room-temperature shapes of disk-style RAINBOW and [RAINBOW/$0^o$] (R=25.4 mm, $H$=0.381 mm, $H_r/H$=0.35) (refer to Figures 5.11–5.15).

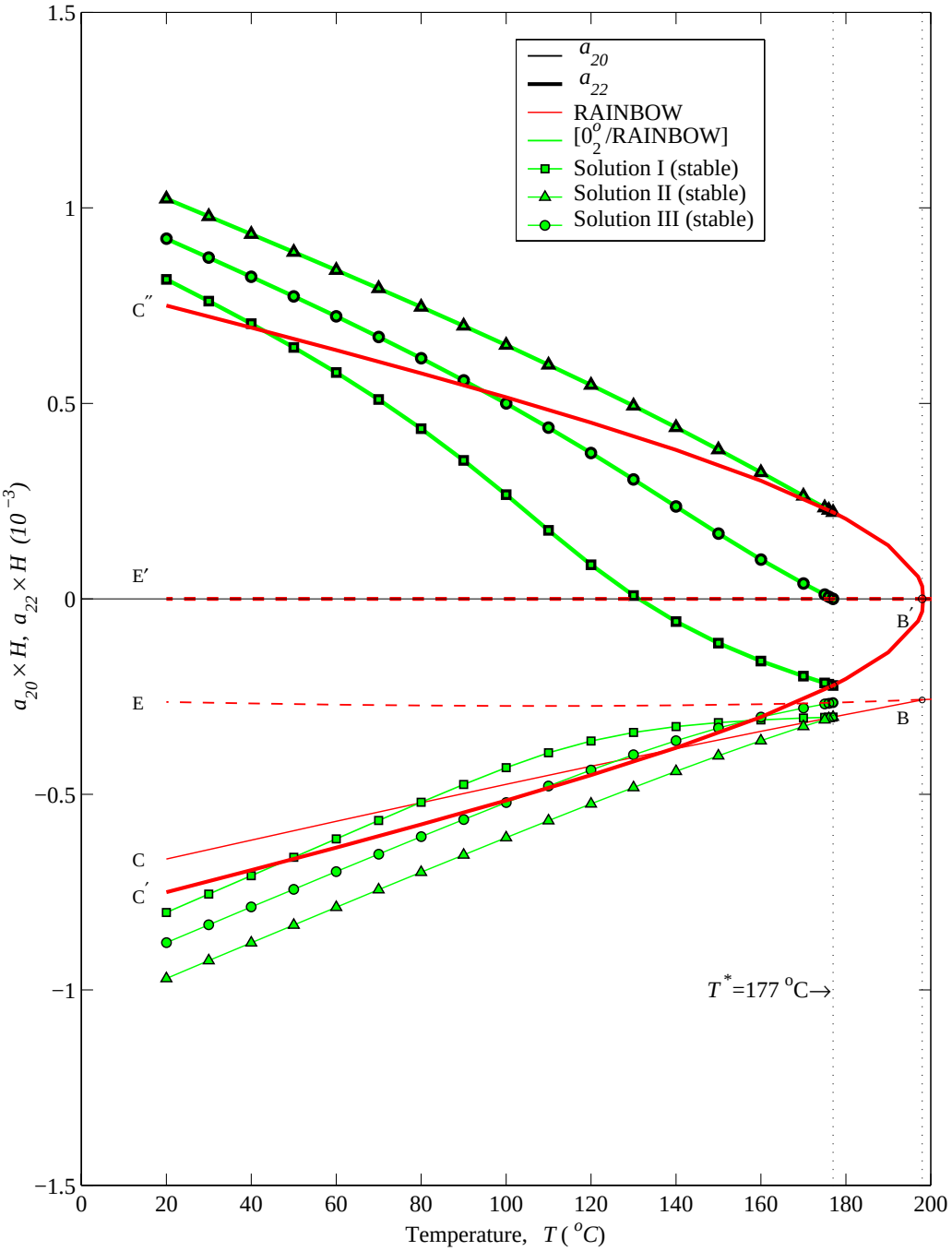


Figure 5.17: Temperature-curvature ($a_{20}$ and $a_{22}$) relation of disk-style [$0_2^o$/RAINBOW] ($R$=25.4 mm, $H$=0.381 mm, $H_r/H$=0.35).

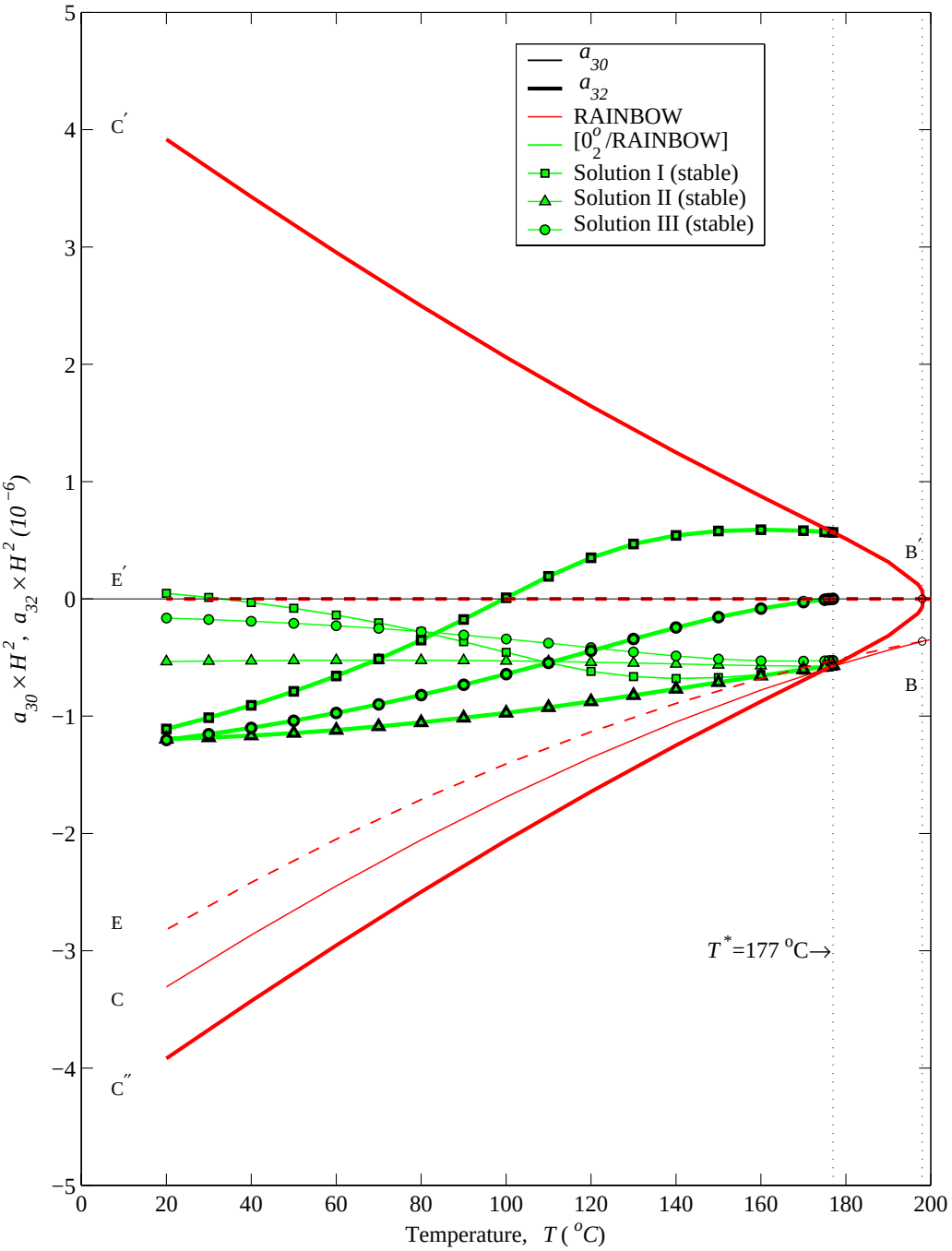


Figure 5.18: Temperature-curvature ($a_{30}$ and $a_{32}$) relation of disk-style $[0^o_2$/RAINBOW] ($R$=25.4 mm, $H$=0.381 mm, $H_r/H$=0.35).

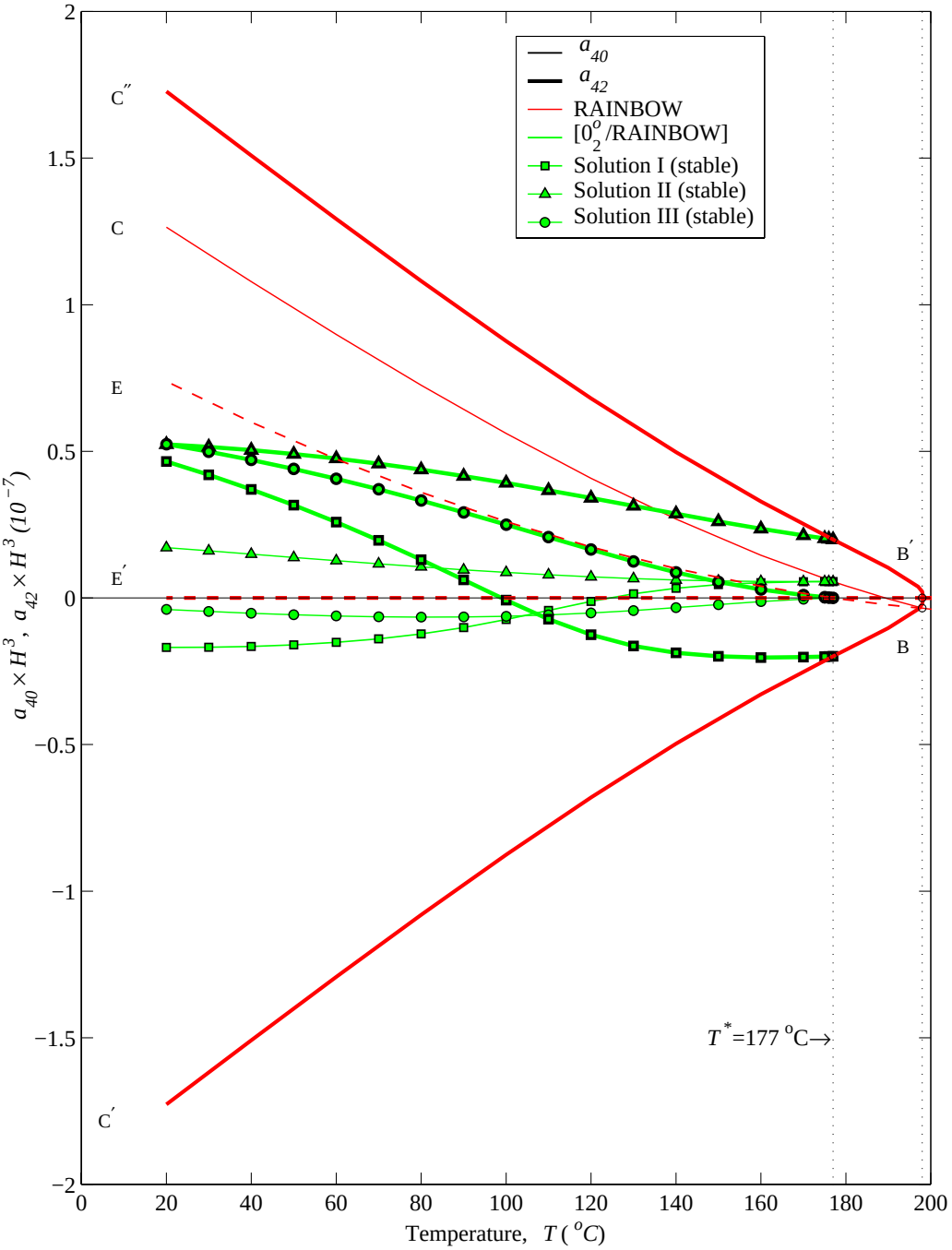


Figure 5.19: Temperature-curvature ($a_{40}$ and $a_{42}$) relation of disk-style $[0_2^o$/RAINBOW] ($R$=25.4 mm, $H$=0.381 mm, $H_r/H$=0.35).

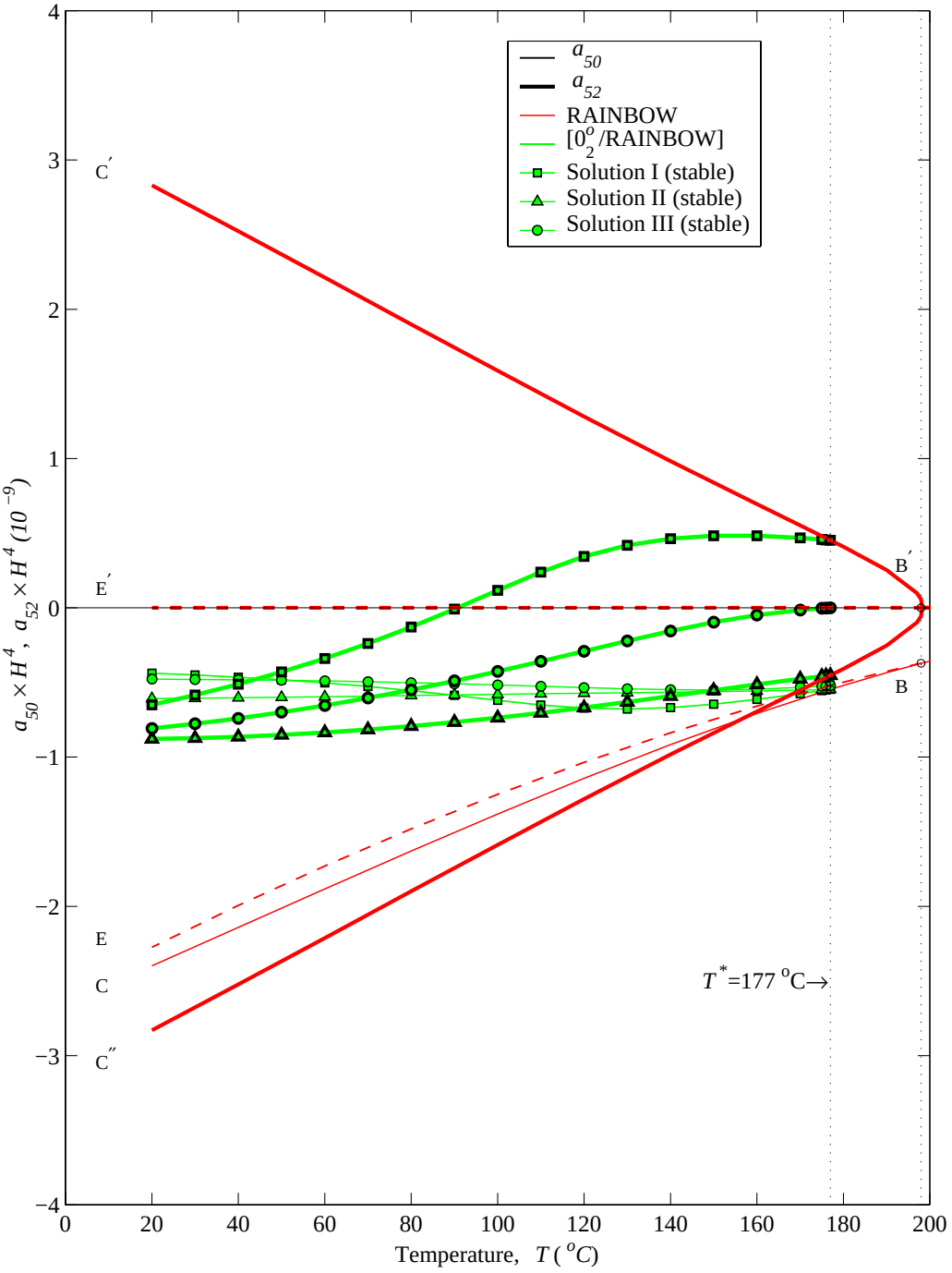


Figure 5.20: Temperature-curvature ($a_{50}$ and $a_{52}$) relation of disk-style [$0^o_2$/RAINBOW] ($R$=25.4 mm, $H$=0.381 mm, $H_r/H$=0.35).

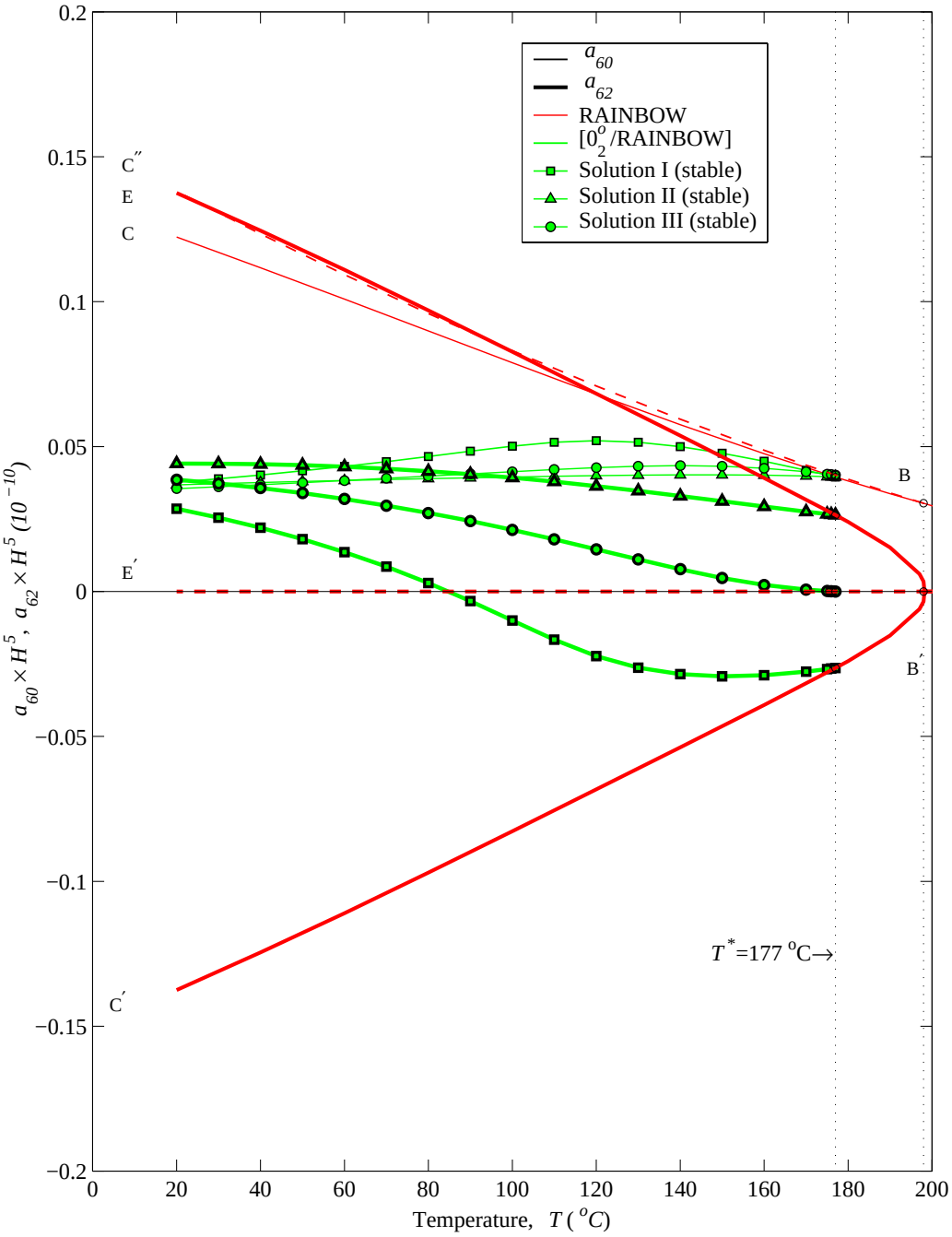


Figure 5.21: Temperature-curvature ($a_{60}$ and $a_{62}$) relation of disk-style [$0_2^o$/RAINBOW] ($R$=25.4 mm, $H$=0.381 mm, $H_r/H$=0.35).

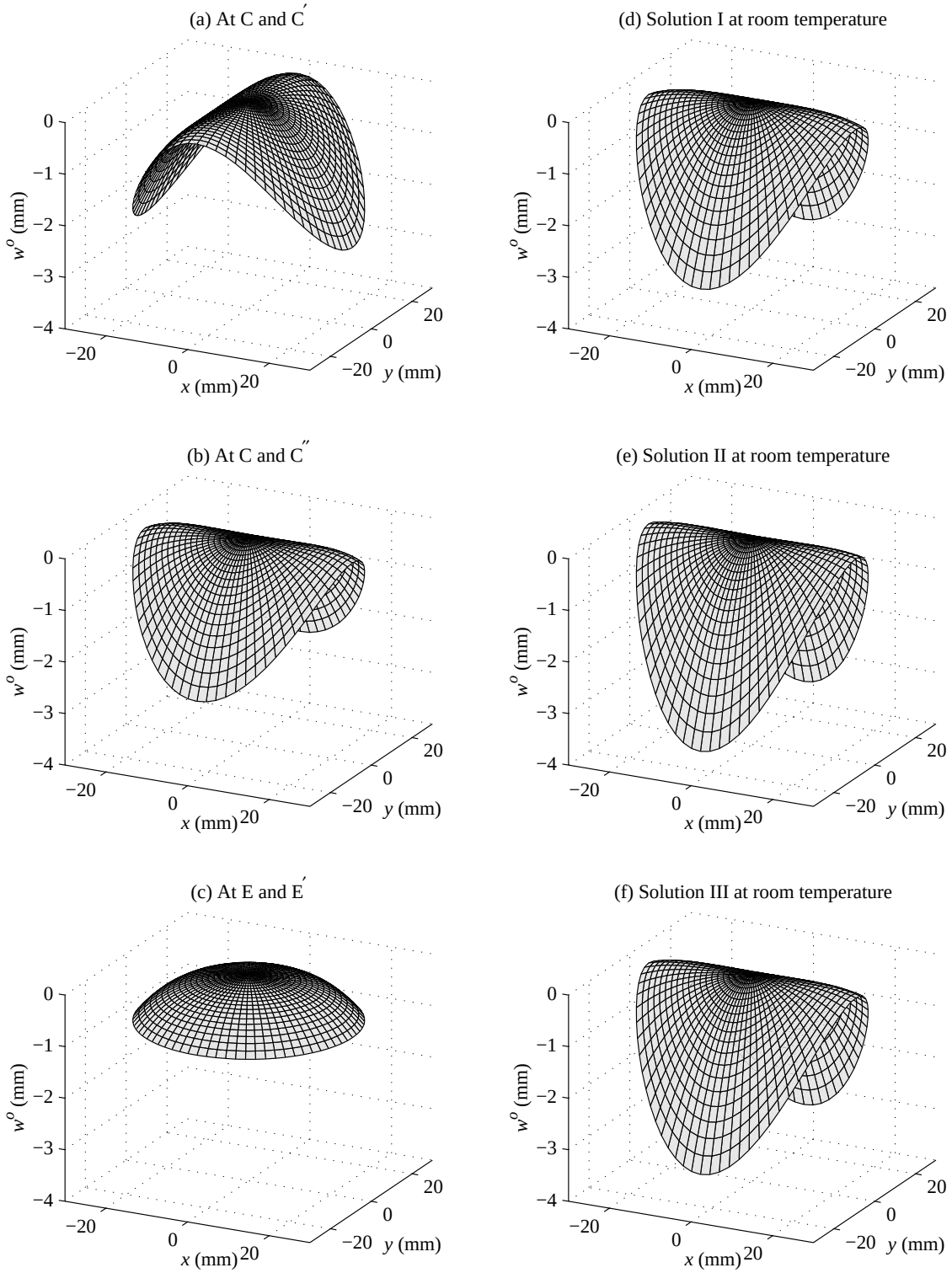


Figure 5.22: Comparison of room-temperature shapes of disk-style RAINBOW and $[0_2^o/\text{RAINBOW}]$ (R=25.4 mm, $H$=0.381 mm, $H_r/H$=0.35) (refer to Figures 5.17–5.21).

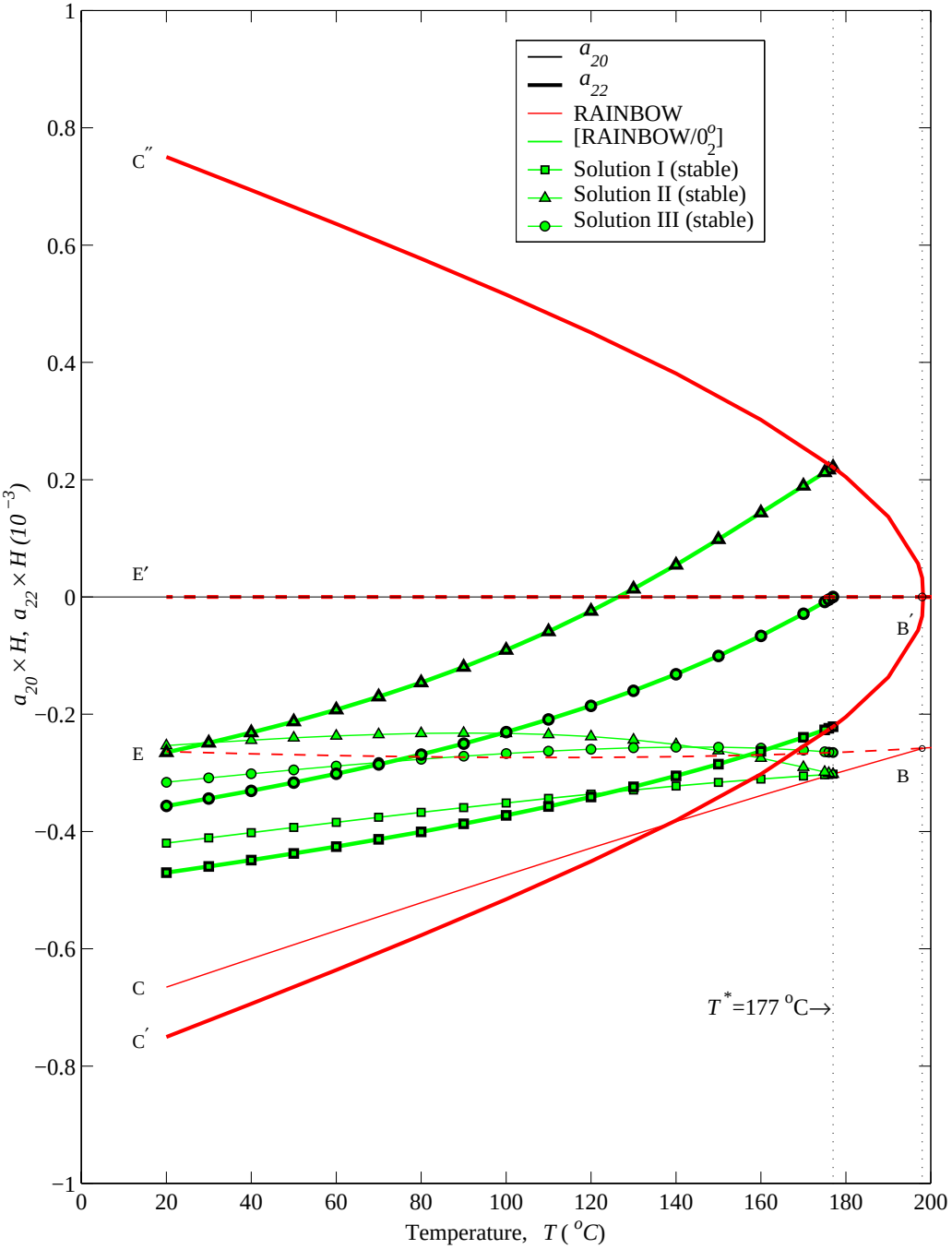


Figure 5.23: Temperature-curvature ($a_{20}$ and $a_{22}$) relation of disk-style [RAINBOW/$0^o$] ($R$=25.4 mm, $H$=0.381 mm, $H_r/H$=0.35).

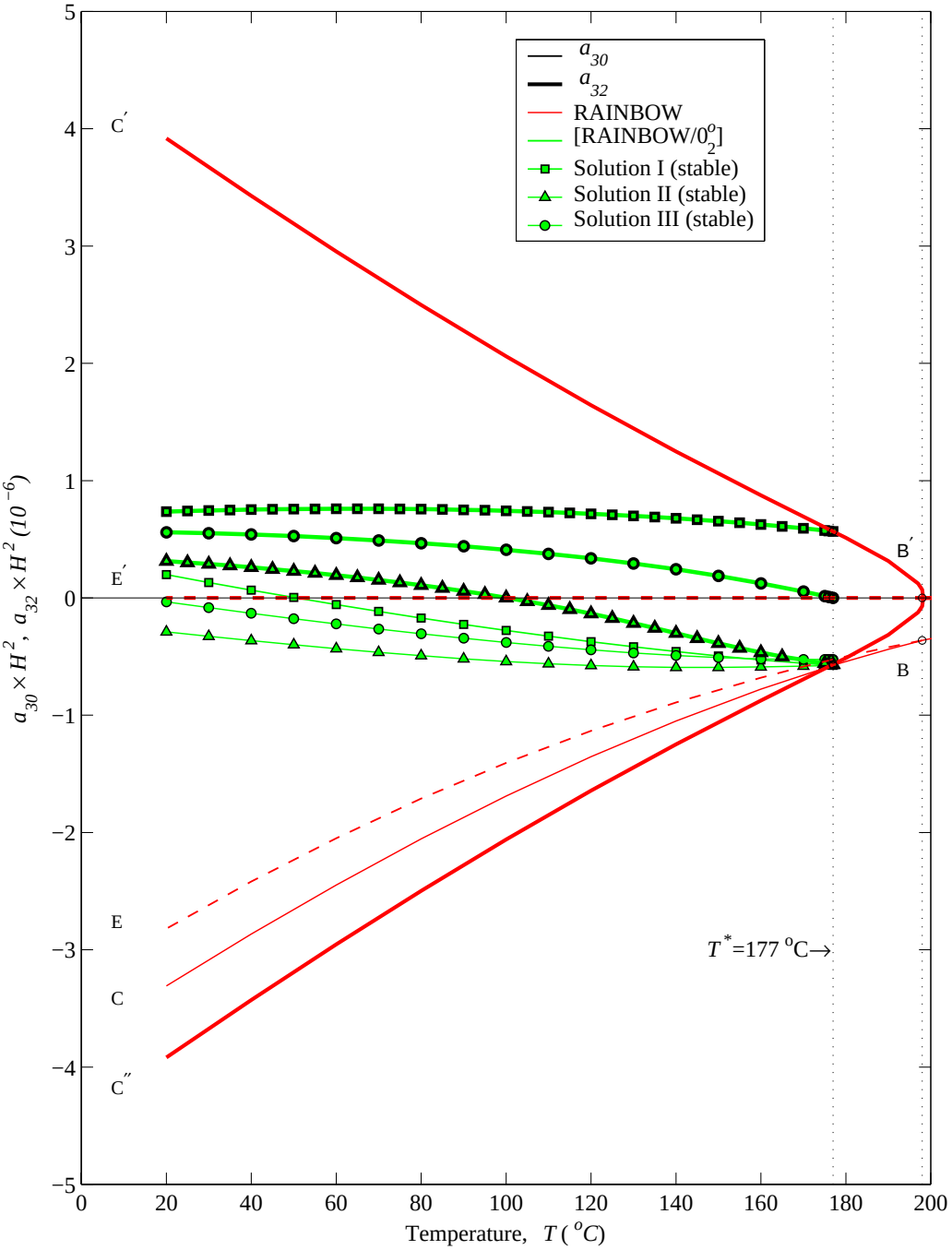


Figure 5.24: Temperature-curvature ($a_{30}$ and $a_{32}$) relation of disk-style [RAINBOW/$0_2^o$] ($R$=25.4 mm, $H$=0.381 mm, $H_r/H$=0.35).

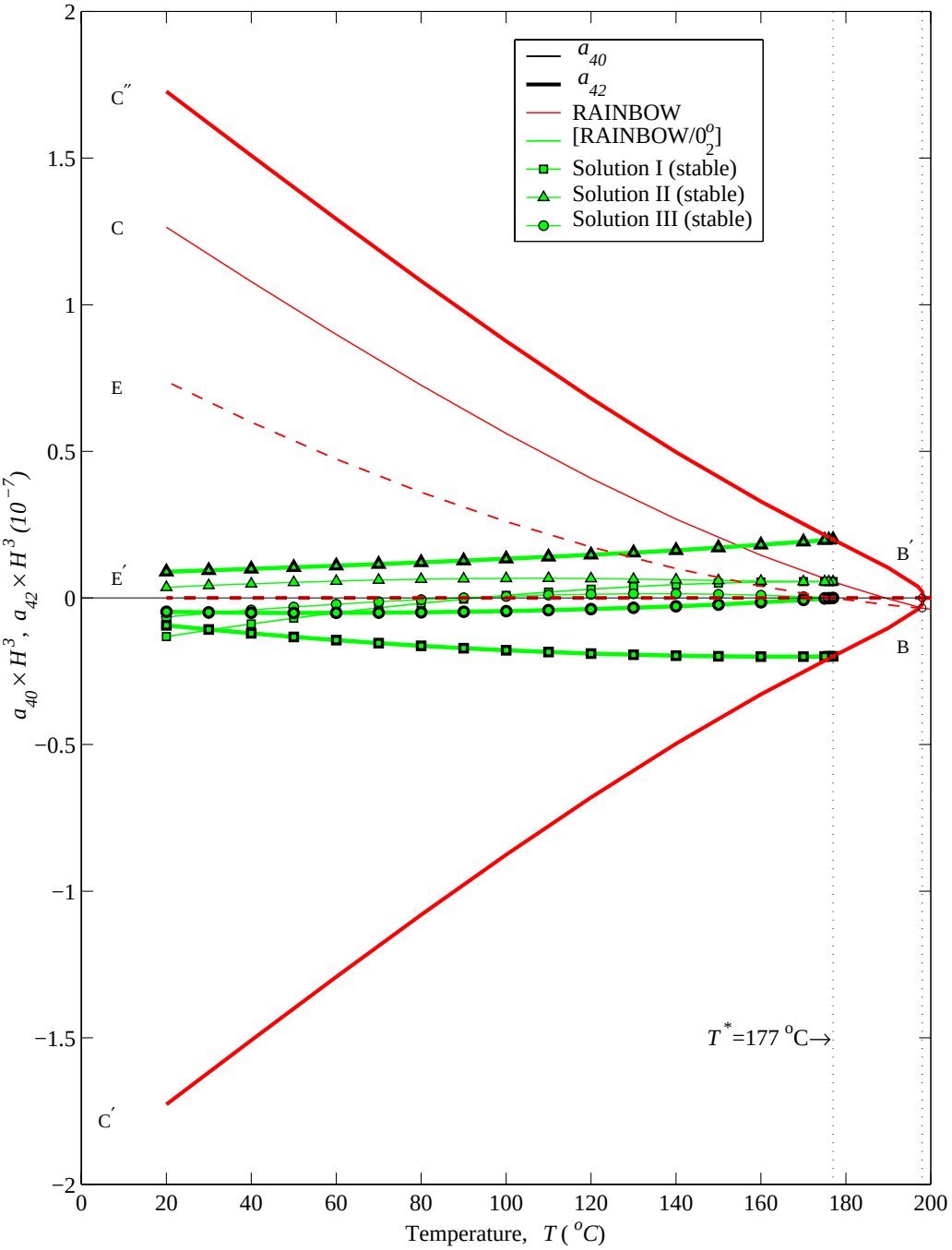


Figure 5.25: Temperature-curvature ($a_{40}$ and $a_{42}$) relation of disk-style [RAINBOW/$0^o_2$] ($R$=25.4 mm, $H$=0.381 mm, $H_r/H$=0.35).

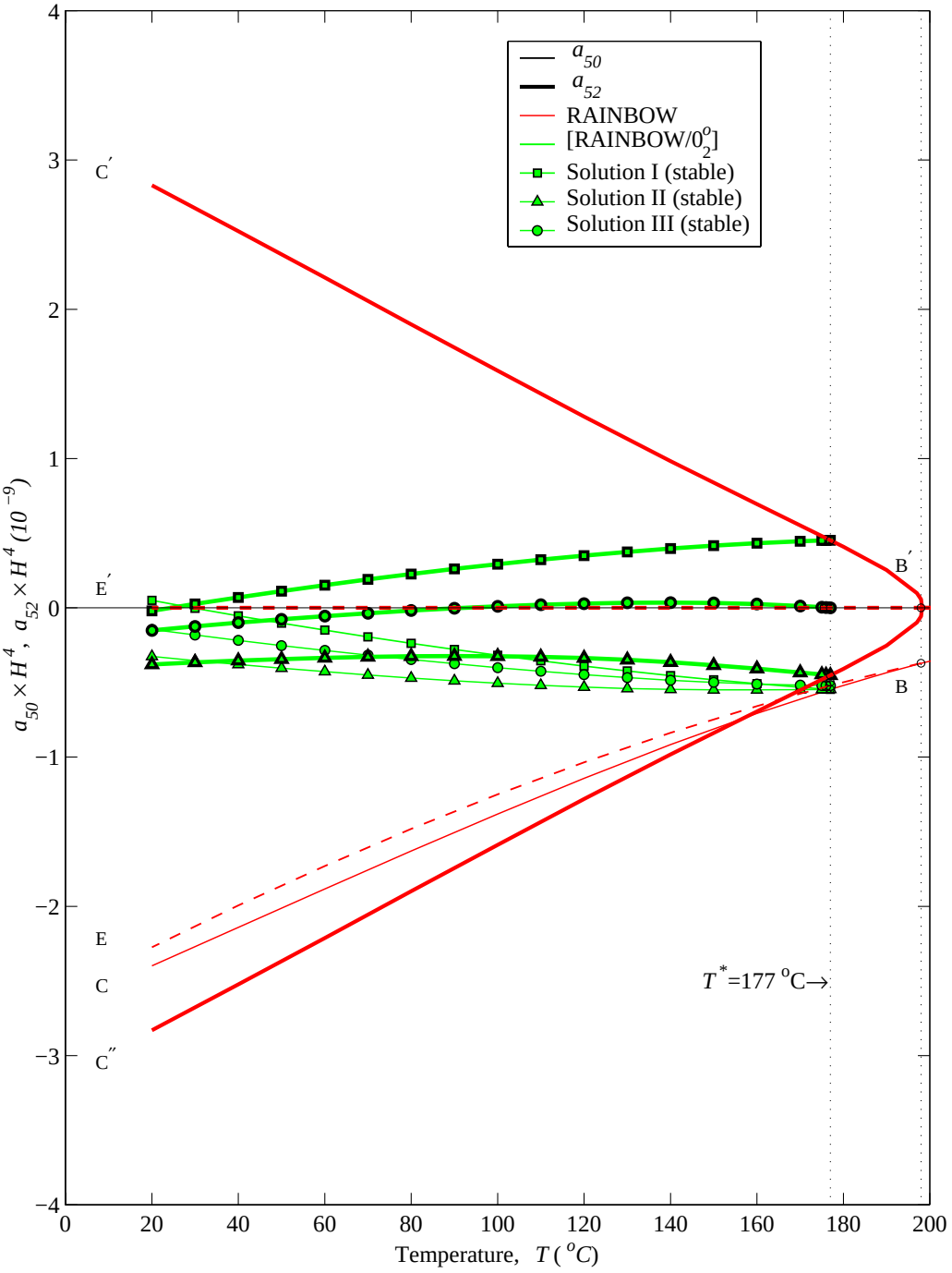


Figure 5.26: Temperature-curvature ($a_{50}$ and $a_{52}$) relation of disk-style [RAINBOW/$0_2^o$] ($R$=25.4 mm, $H$=0.381 mm, $H_r/H$=0.35).

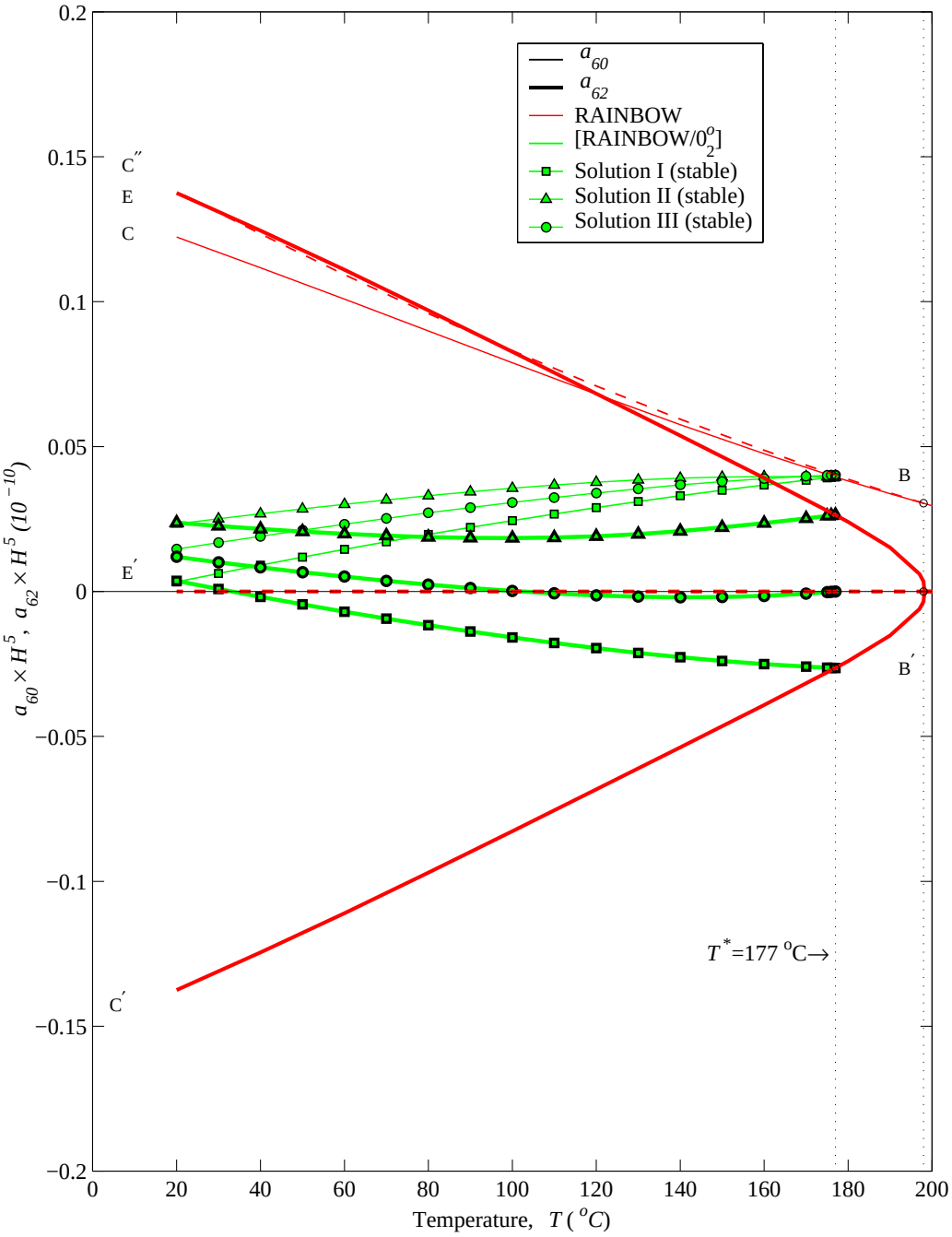


Figure 5.27: Temperature-curvature ($a_{60}$ and $a_{62}$) relation of disk-style [RAINBOW/$0_2^o$] ($R$=25.4 mm, $H$=0.381 mm, $H_r/H$=0.35).

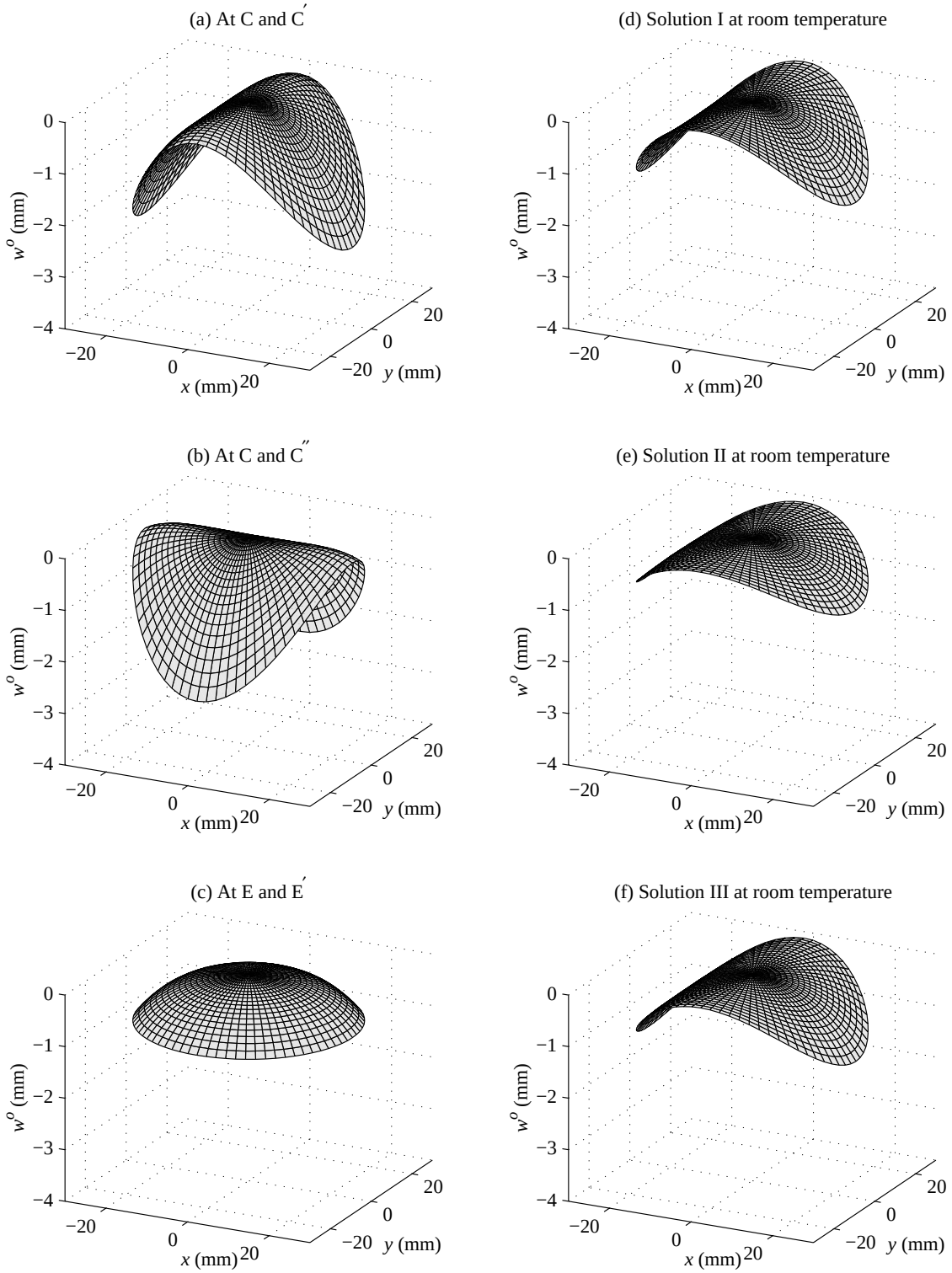


Figure 5.28: Comparison of room-temperature shapes of disk-style RAINBOW and [RAINBOW/$0_2^o$] (R=25.4 mm, $H$=0.381 mm, $H_r/H$=0.35) (refer to Figures 5.23–5.27).

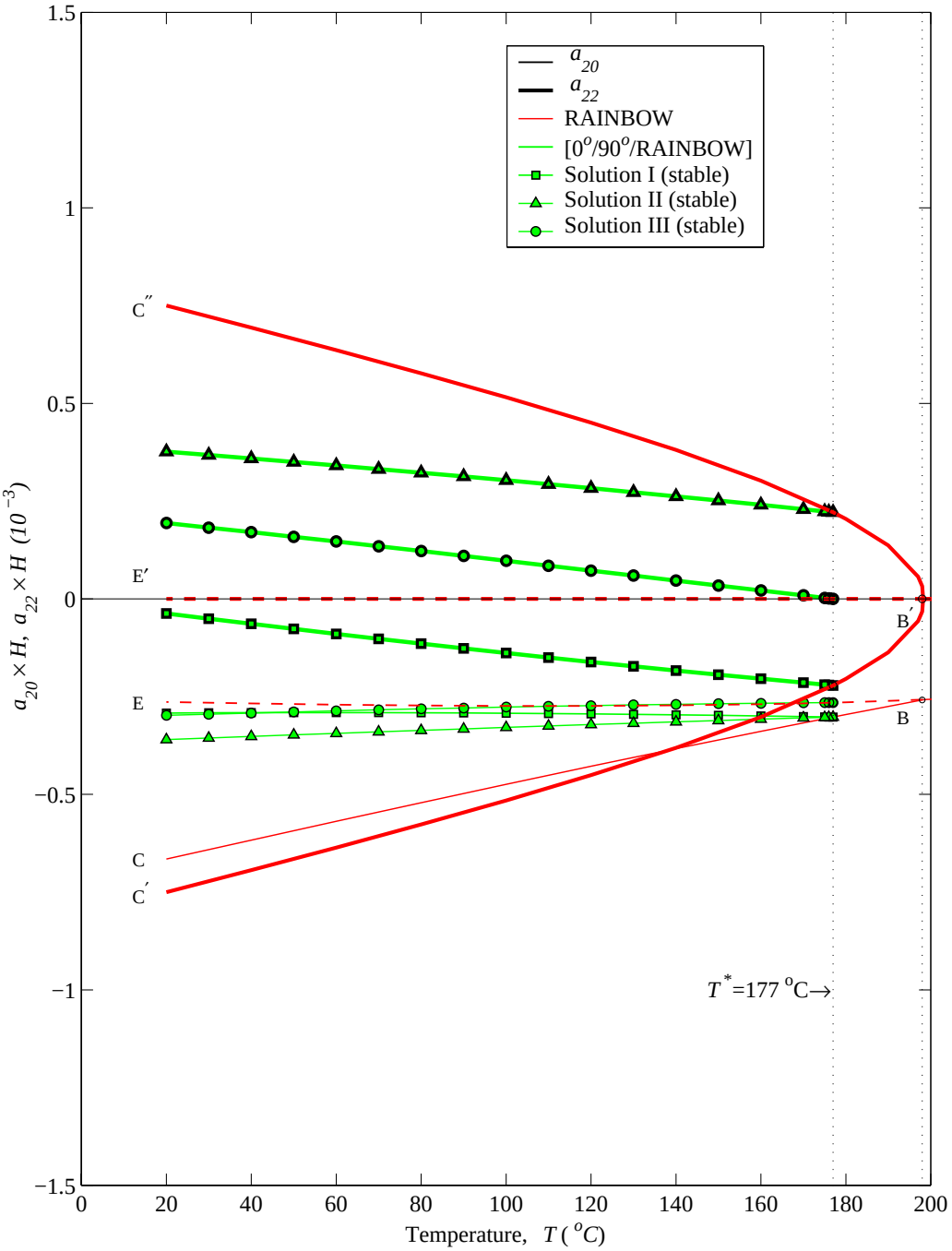


Figure 5.29: Temperature-curvature ($a_{20}$ and $a_{22}$) relation of disk-style [$0^o$/$90^o$/RAINBOW] ($R$=25.4 mm, $H$=0.381 mm, $H_r/H$=0.35).

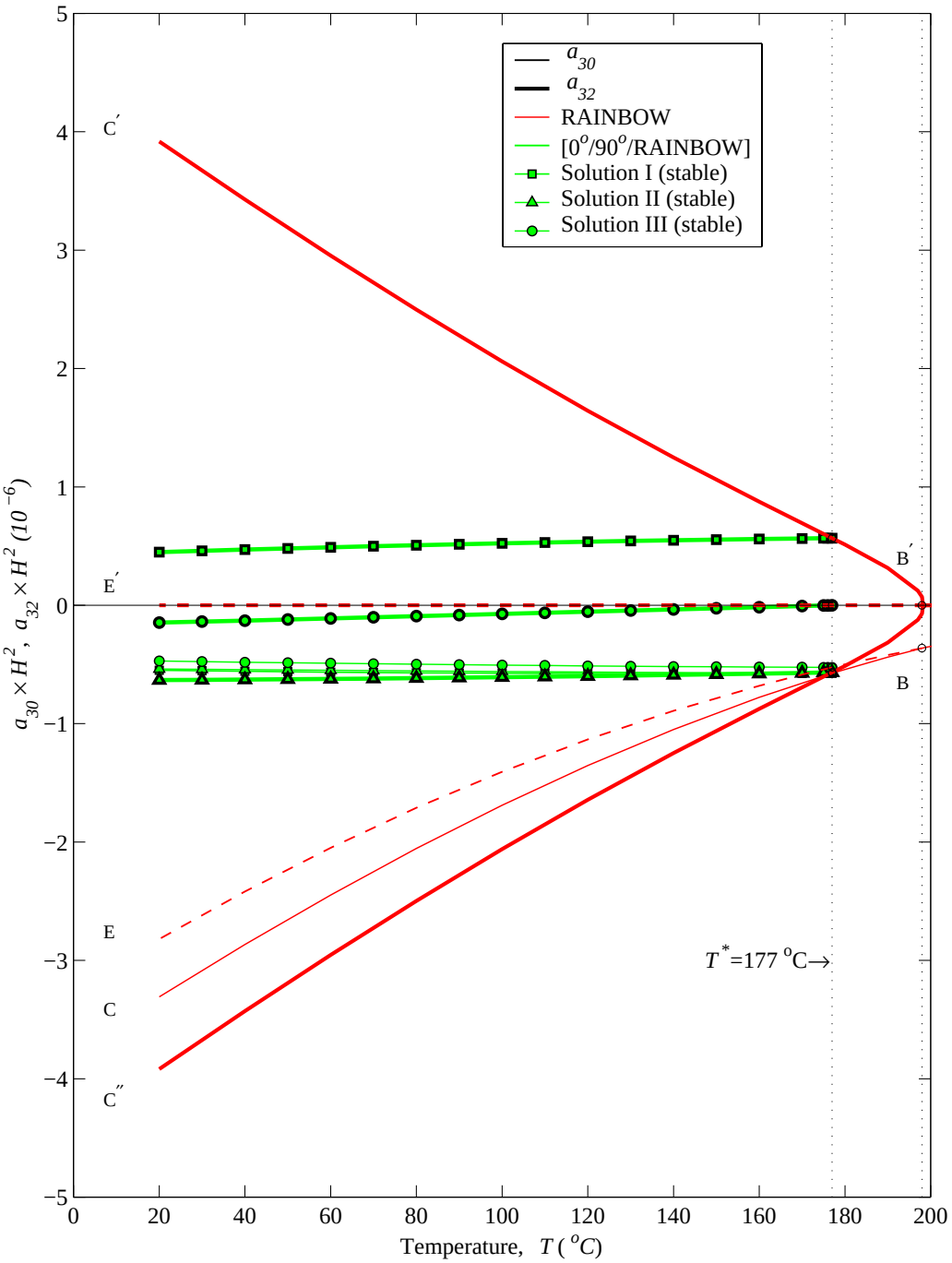


Figure 5.30: Temperature-curvature ($a_{30}$ and $a_{32}$) relation of disk-style [$0^o$/$90^o$/RAINBOW] ($R$=25.4 mm, $H$=0.381 mm, $H_r/H$=0.35).

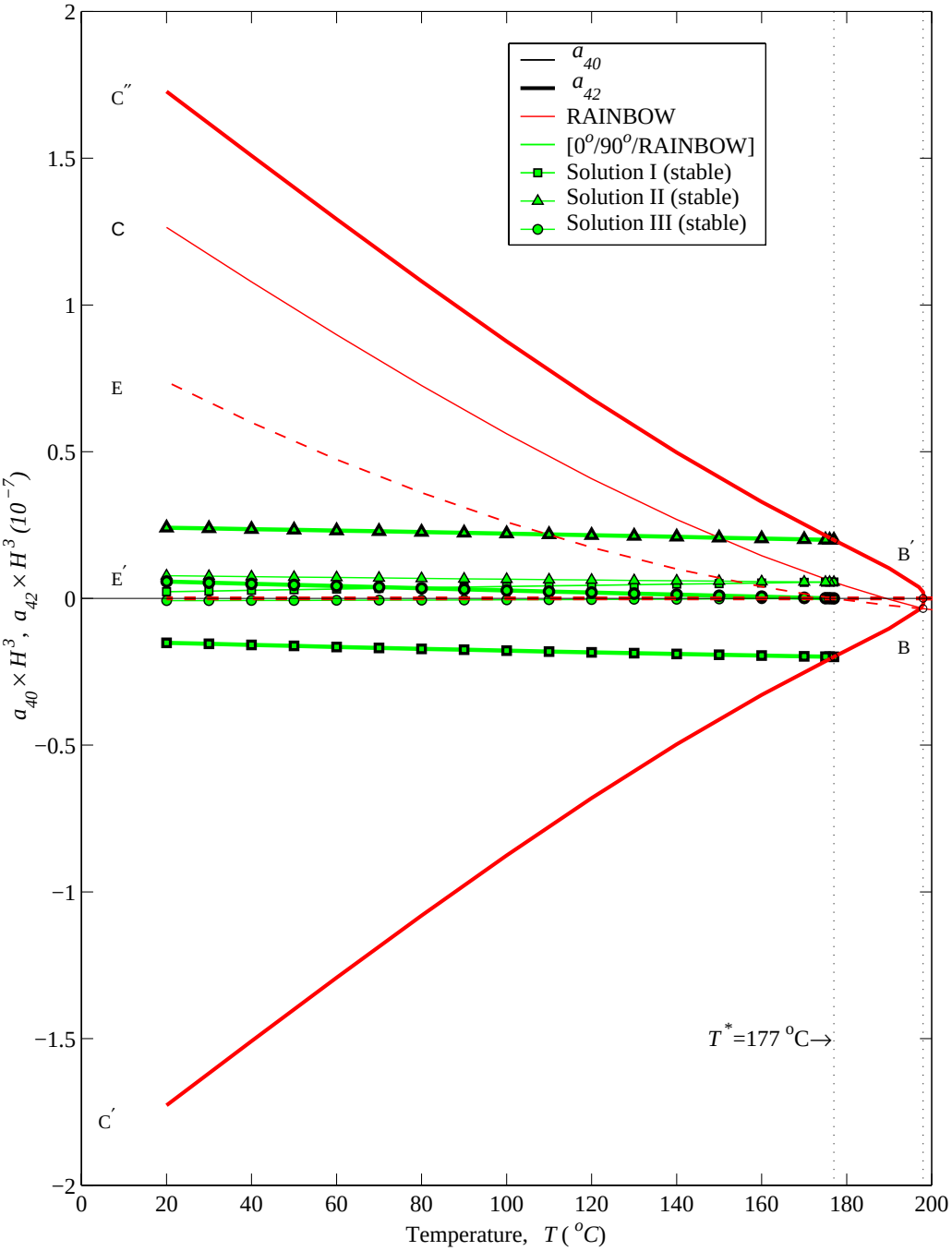


Figure 5.31: Temperature-curvature ($a_{40}$ and $a_{42}$) relation of disk-style [$0^o$/$90^o$/RAINBOW] ($R$=25.4 mm, $H$=0.381 mm, $H_r/H$=0.35).

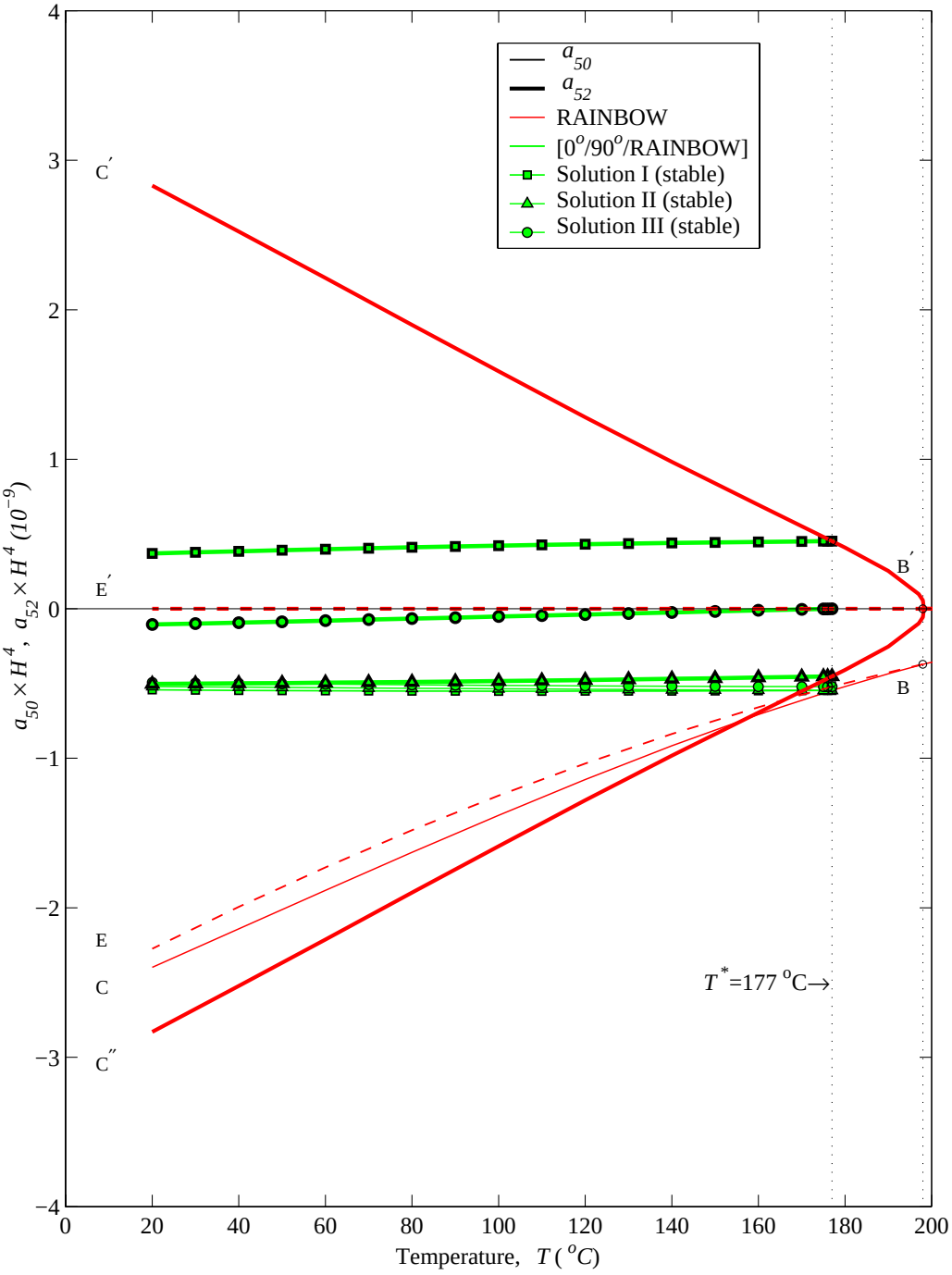


Figure 5.32: Temperature-curvature ($a_{50}$ and $a_{52}$) relation of disk-style [$0^o$/$90^o$/RAINBOW] ($R$=25.4 mm, $H$=0.381 mm, $H_r/H$=0.35).

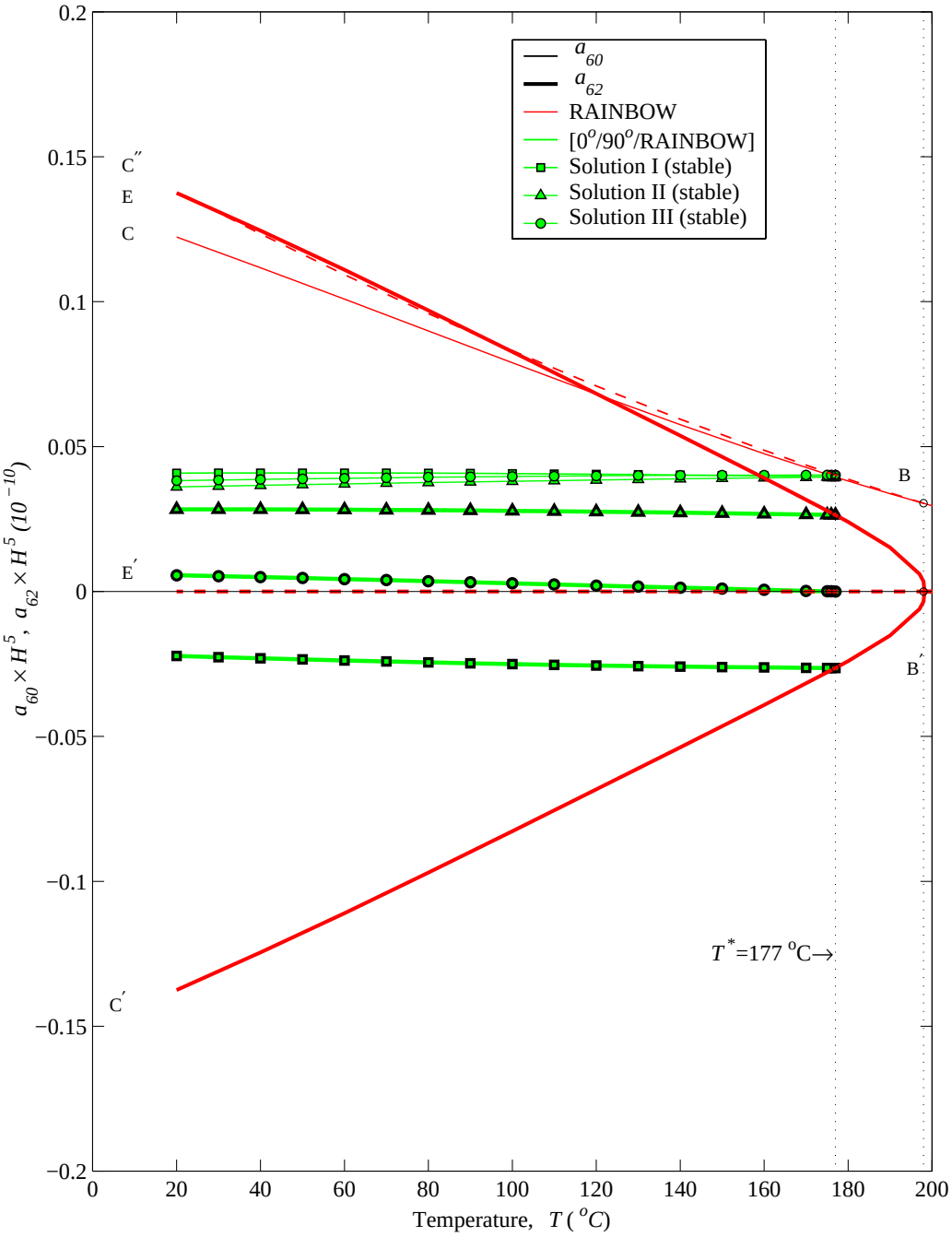


Figure 5.33: Temperature-curvature ($a_{60}$ and $a_{62}$) relation of disk-style [$0^o$/$90^o$/RAINBOW] ($R$=25.4 mm, $H$=0.381 mm, $H_r/H$=0.35).

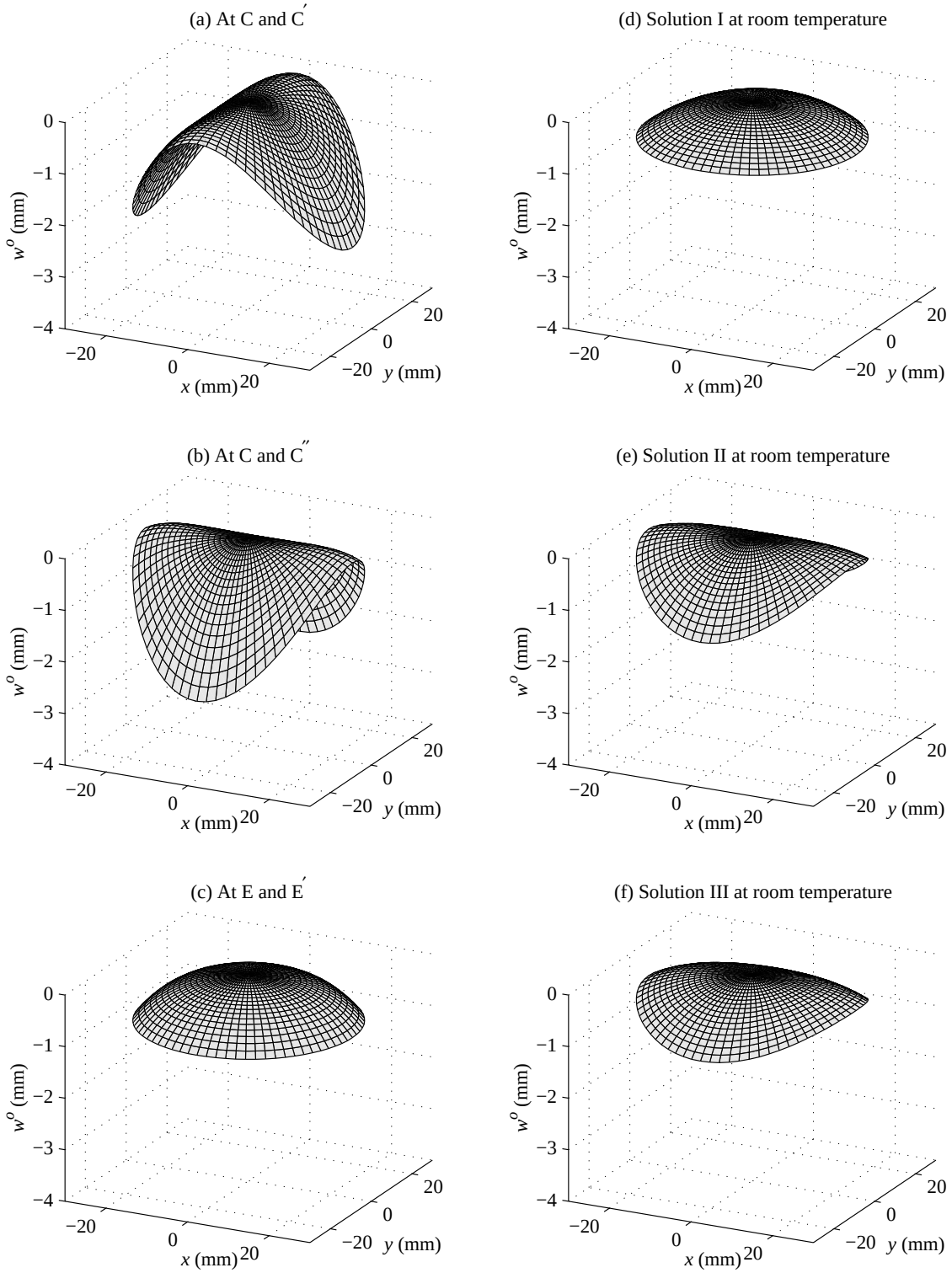


Figure 5.34: Comparison of room-temperature shapes of disk-style RAINBOW and [$0^o$/$90^o$/RAINBOW] (R=25.4 mm, $H$=0.381 mm, $H_r/H$=0.35) (refer to Figures 5.29–5.33).

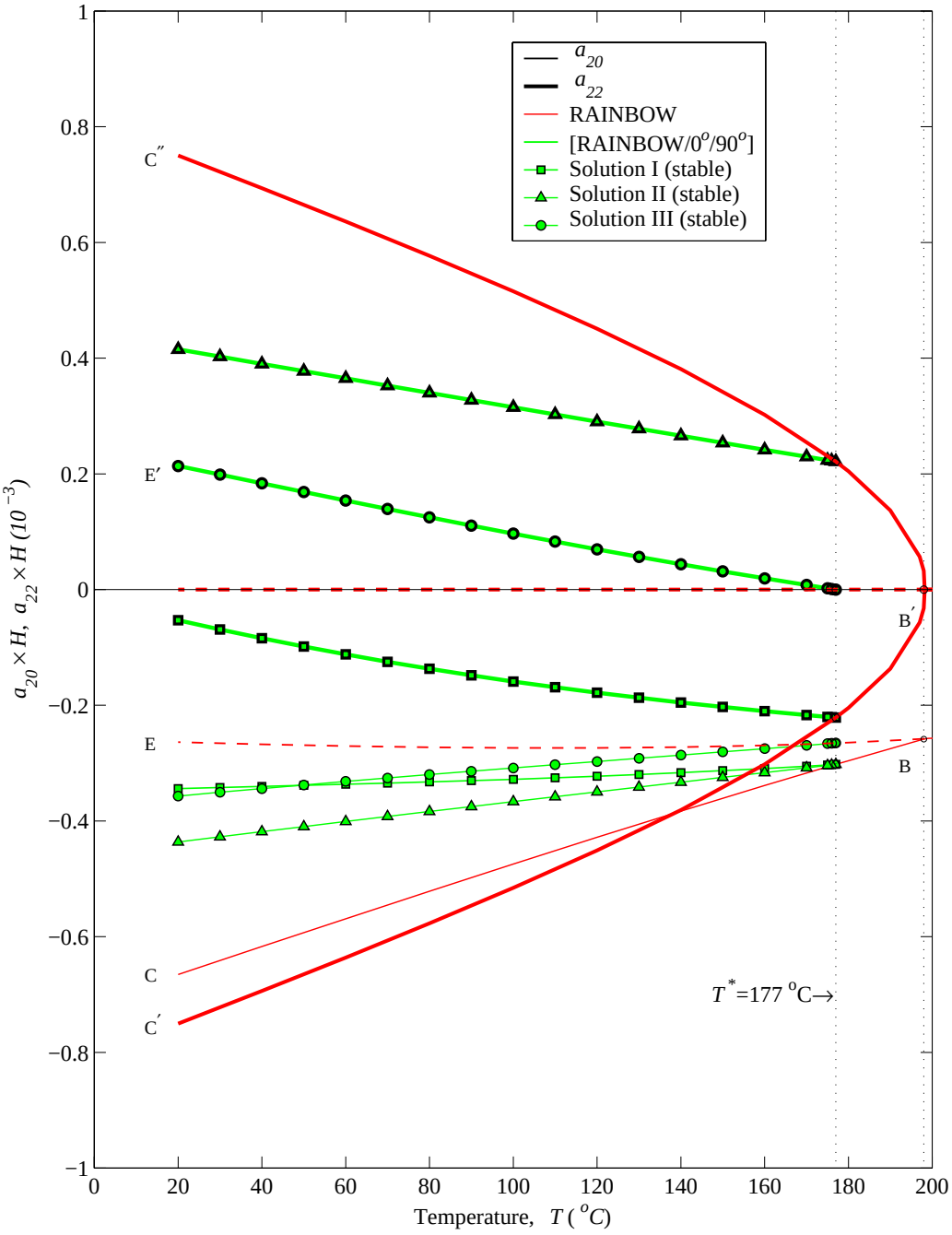


Figure 5.35: Temperature-curvature ($a_{20}$ and $a_{22}$) relation of disk-style [RAINBOW/0$^o$] ($R$=25.4 mm, $H$=0.381 mm, $H_r/H$=0.35).

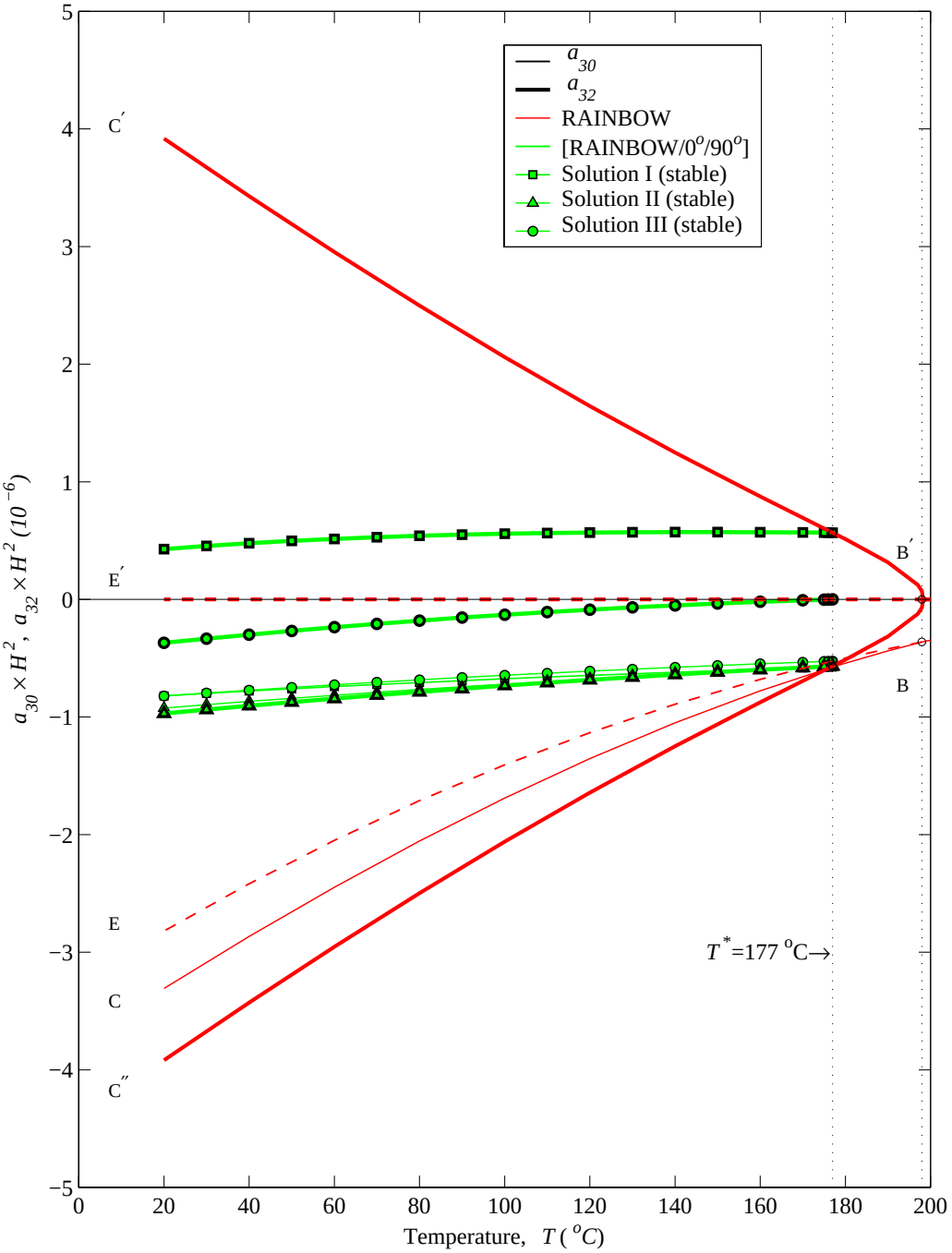


Figure 5.36: Temperature-curvature ($a_{30}$ and $a_{32}$) relation of disk-style [RAINBOW/$0^o$/$90^o$] ($R$=25.4 mm, $H$=0.381 mm, $H_r/H$=0.35).

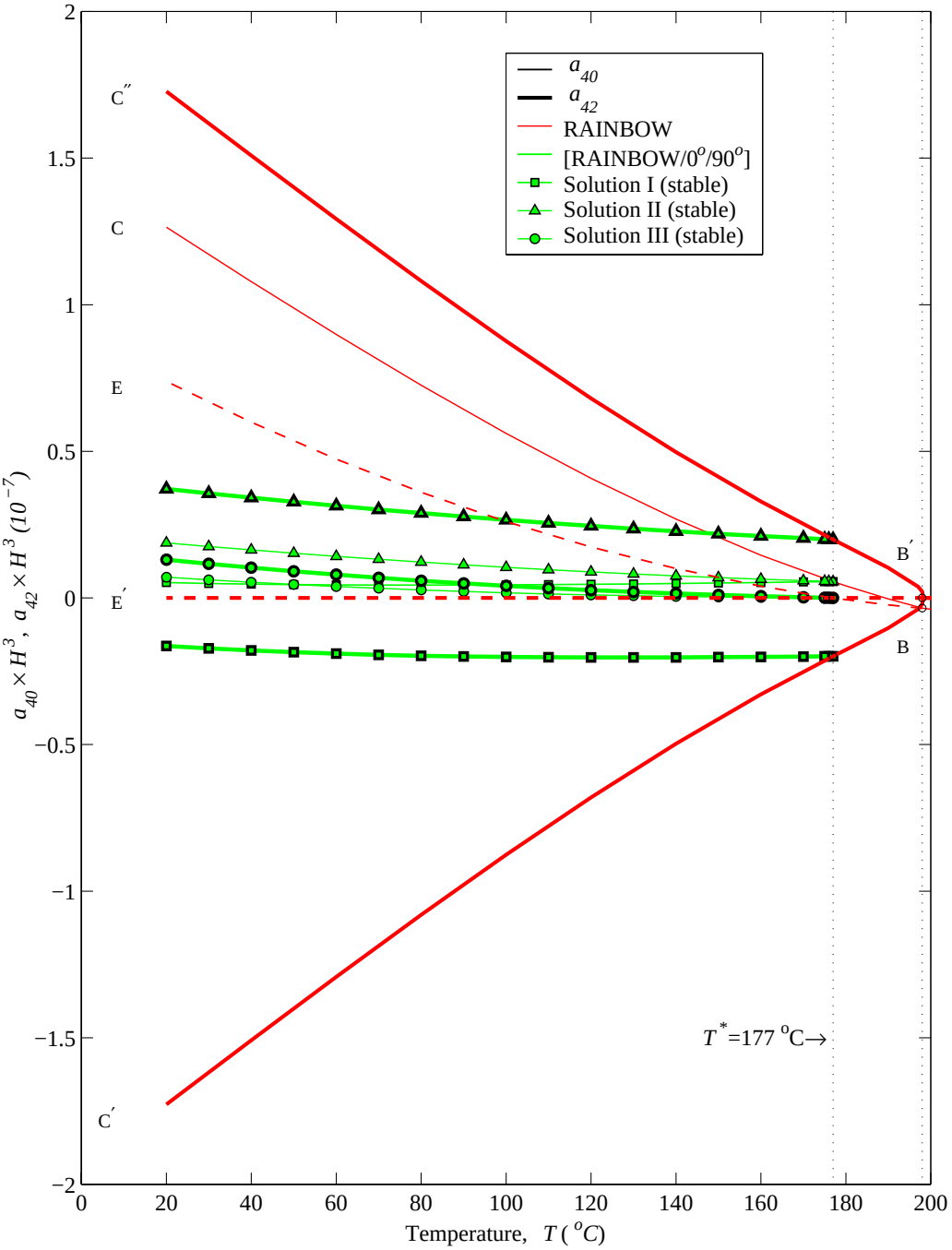


Figure 5.37: Temperature-curvature ($a_{40}$ and $a_{42}$) relation of disk-style [RAINBOW/$0^o$/$90^o$] ($R$=25.4 mm, $H$=0.381 mm, $H_r/H$=0.35).

### 5.3.2 Application of an Electric Field

Figures 5.41–5.45 illustrate the relationship between the change in the coefficients $a_{ij}$ relative to their room-temperature values, $\Delta a_{ij}$, as a function of the electric field strength for the range $E$=± 1.5 MV/m. It is assumed that the GRAPHBOW device is in a shape represented in Figure 5.10(d) ($R$=25.4 mm, $H$=0.381 mm, $H_r/H$=0.35, [$0^o$/RAINBOW]). The polarity of the unreduced piezoceramic material is assumed to be as shown in Figure 4.3. Figure 5.46 depicts the room-temperature shapes of [$0^o$/RAINBOW] under electric field strength of ± 1.5 MV/m. For comparison, the room-temperature shape of [$0^o$/RAINBOW] from Figure 5.10(d) is included. Figure 5.46 shows that a reasonable change in the major curvature can be achieved with the application of electric field of ± 1.5 MV/m . For the GRAPHBOW considered, a positive $E$ tends to flatten the GRAPHBOW actuator along the $\theta$=$\pi/2$ and $\theta$=$3\pi/2$ directions. However, a negative $E$ tends to increase the curvature $\kappa_r$ along these directions. As can be seen in Figures 5.41–5.45, the relationships between $a_{20}$ and $a_{22}$, the major terms in the curvatures, and $E$ are very close to being linear. To first approximation, the relationships between the $a_{30}$, $a_{32}$, $a_{40}$, $a_{42}$, $a_{50}$, $a_{52}$, $a_{60}$, and $a_{62}$, the minor terms in the curvatures, and $E$ are also close to being linear. The slight nonlinearity in the relation between $a_{30}$, $a_{32}$, $a_{40}$, $a_{42}$, $a_{50}$, $a_{52}$, $a_{60}$, $a_{62}$ and $E$ may be unimportant since these terms are much smaller than $a_{20}$ and $a_{22}$. Again, the linearity of the relation between $E$ and $\Delta a_{ij}$ simplifies the extension of the present model to study the dynamic behavior of GRAPHBOW actuators.

## 5.4 Chapter Summary

In this chapter, a multi-step thermoelastic analysis has been developed to model the incorporation of the composite layer onto disk-style RAINBOW. A special case was considered for which $T = T^*$ to make it possible to compare results with results obtained using ABAQUS. The results presented indicate that there is an excellent agreement between the results obtained using the present model and those obtained using ABAQUS. Moreover, the numerical results presented in this chapter reveal that 25.4 mm radius [$0^o$/RAINBOW] and [$0^o_2$/RAINBOW] exhibit three similar stable room-temperature configurations that are near-cylindrical (larger $k_r$ along the $\theta = \pi/2$ and $\theta = 3\pi/2$ directions than along the $\theta = 0$ and $\theta = \pi$ directions) that have larger out-of-plane dis-

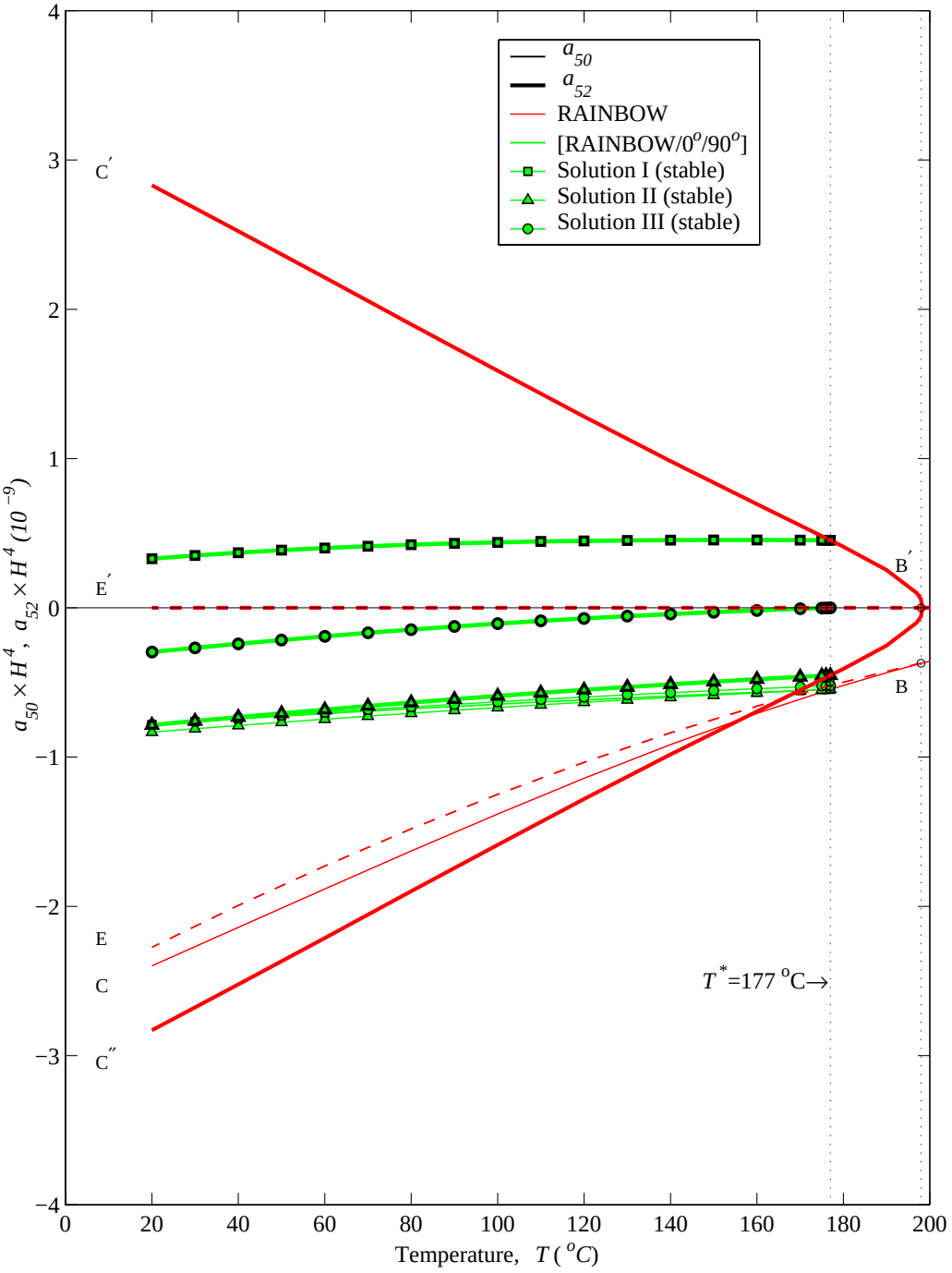


Figure 5.38: Temperature-curvature ($a_{50}$ and $a_{52}$) relation of disk-style [RAINBOW/$0^o$/$90^o$] ($R$=25.4 mm, $H$=0.381 mm, $H_r/H$=0.35).

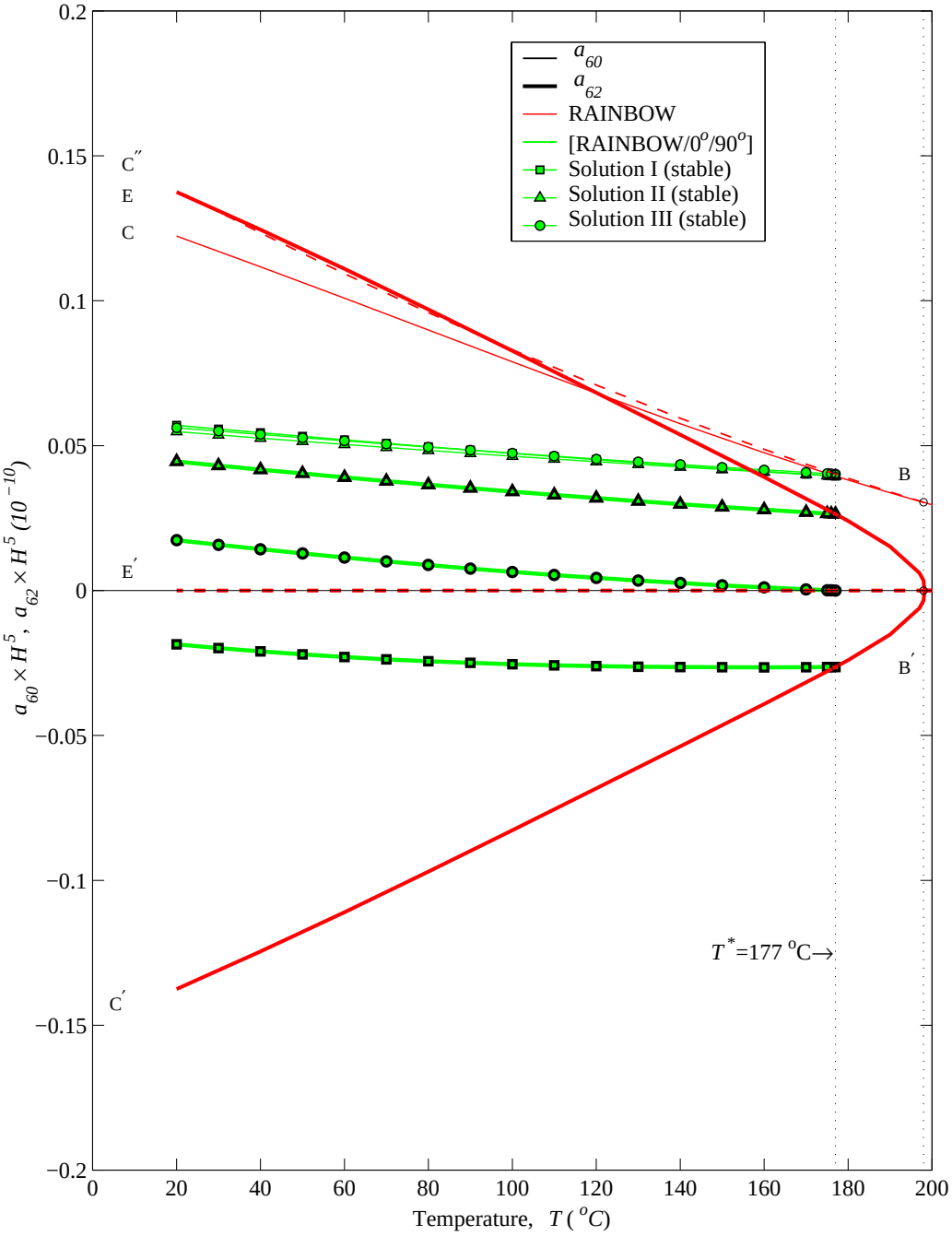


Figure 5.39: Temperature-curvature ($a_{60}$ and $a_{62}$) relation of disk-style [RAINBOW/$0^o$/$90^o$] ($R$=25.4 mm, $H$=0.381 mm, $H_r/H$=0.35).

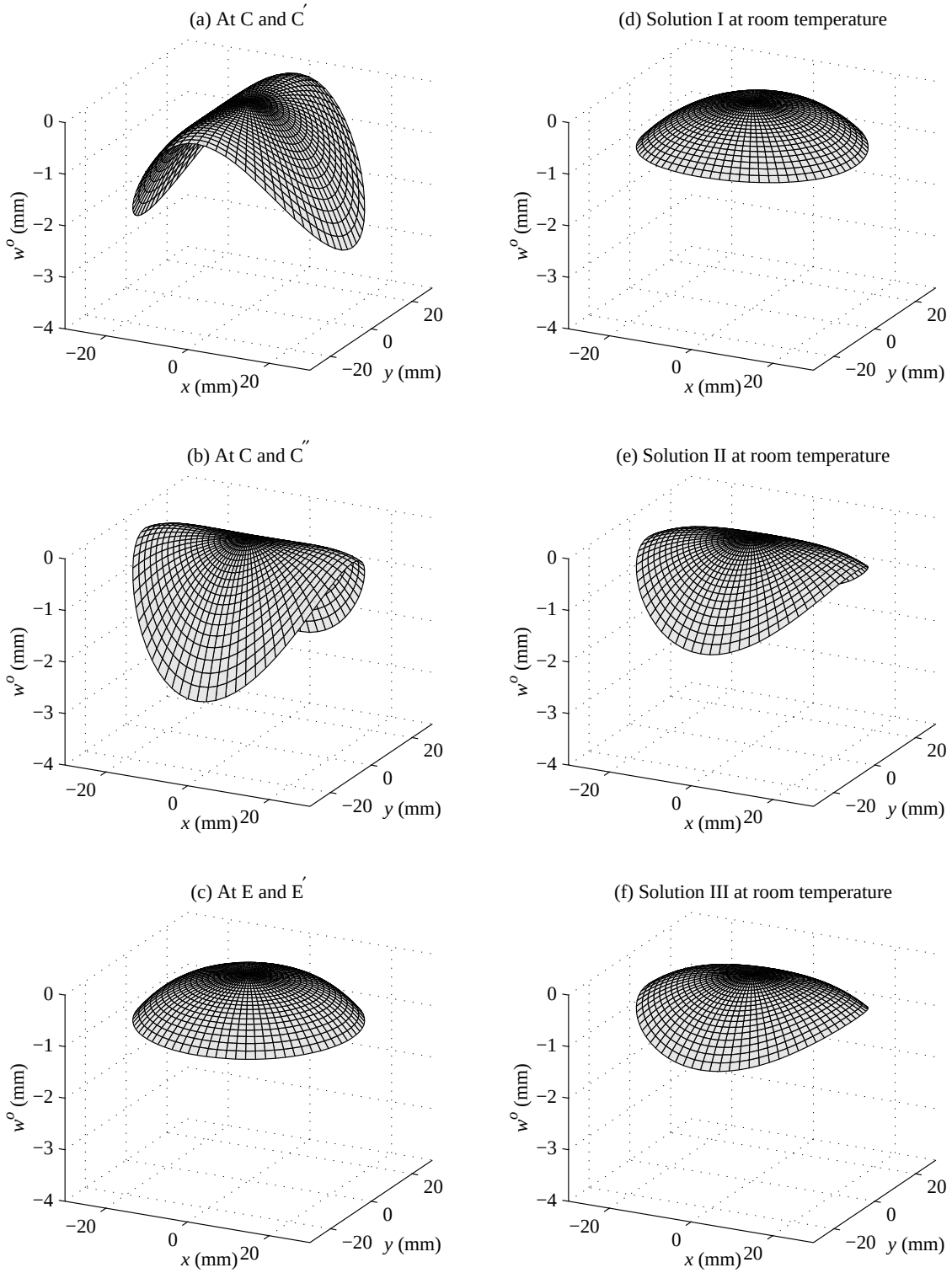


Figure 5.40: Comparison of room-temperature shapes of disk-style RAINBOW and [RAINBOW/$0^o$/$90^o$] (R=25.4 mm, $H$=0.381 mm, $H_r/H$=0.35) (refer to Figures 5.35–5.39).

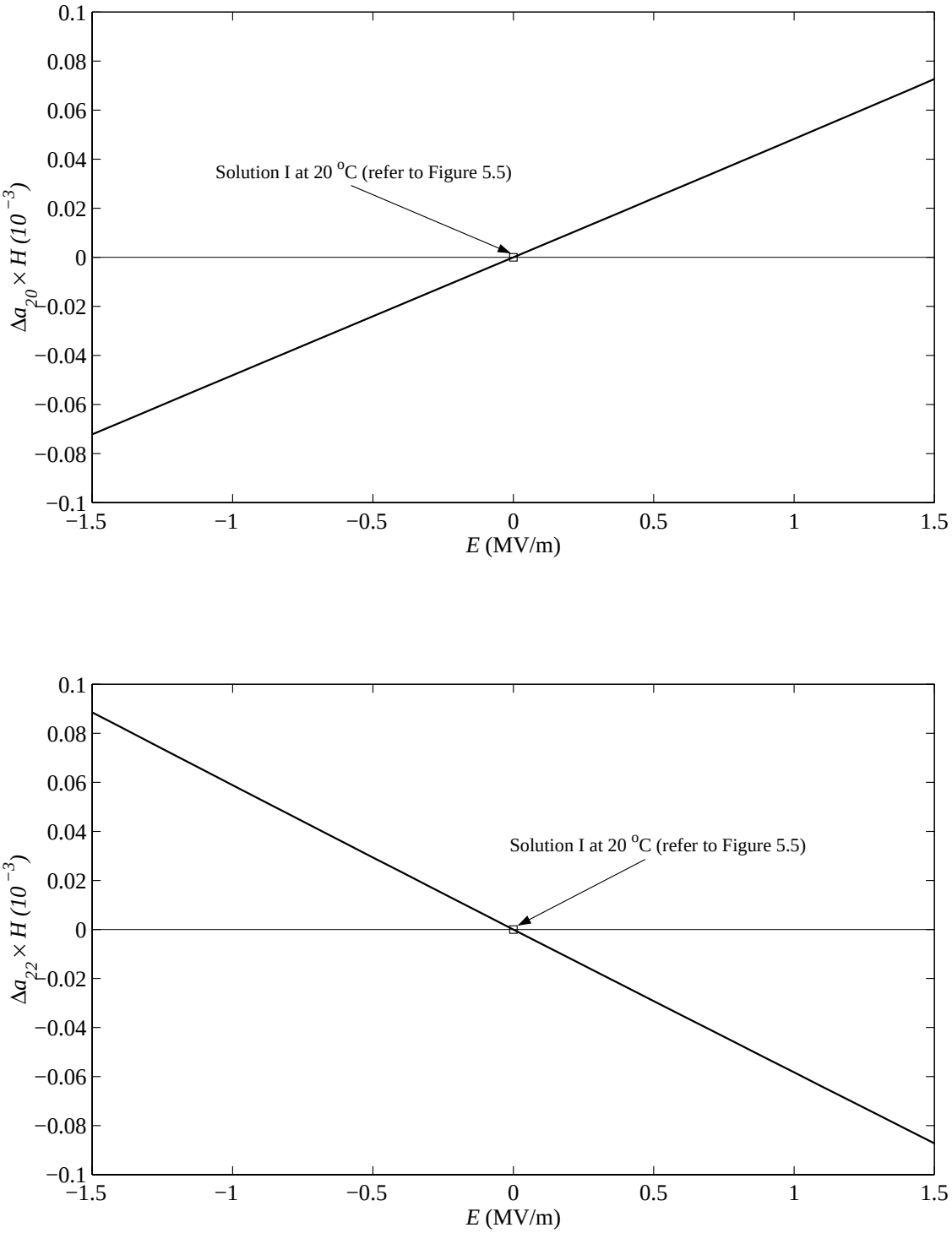


Figure 5.41: Variations of $a_{20}$ and $a_{22}$ as a function of $E$ for [$0^o$/RAINBOW] ($R$=25.4 mm, $H$=0.381 mm, $H_r/H$=0.35).

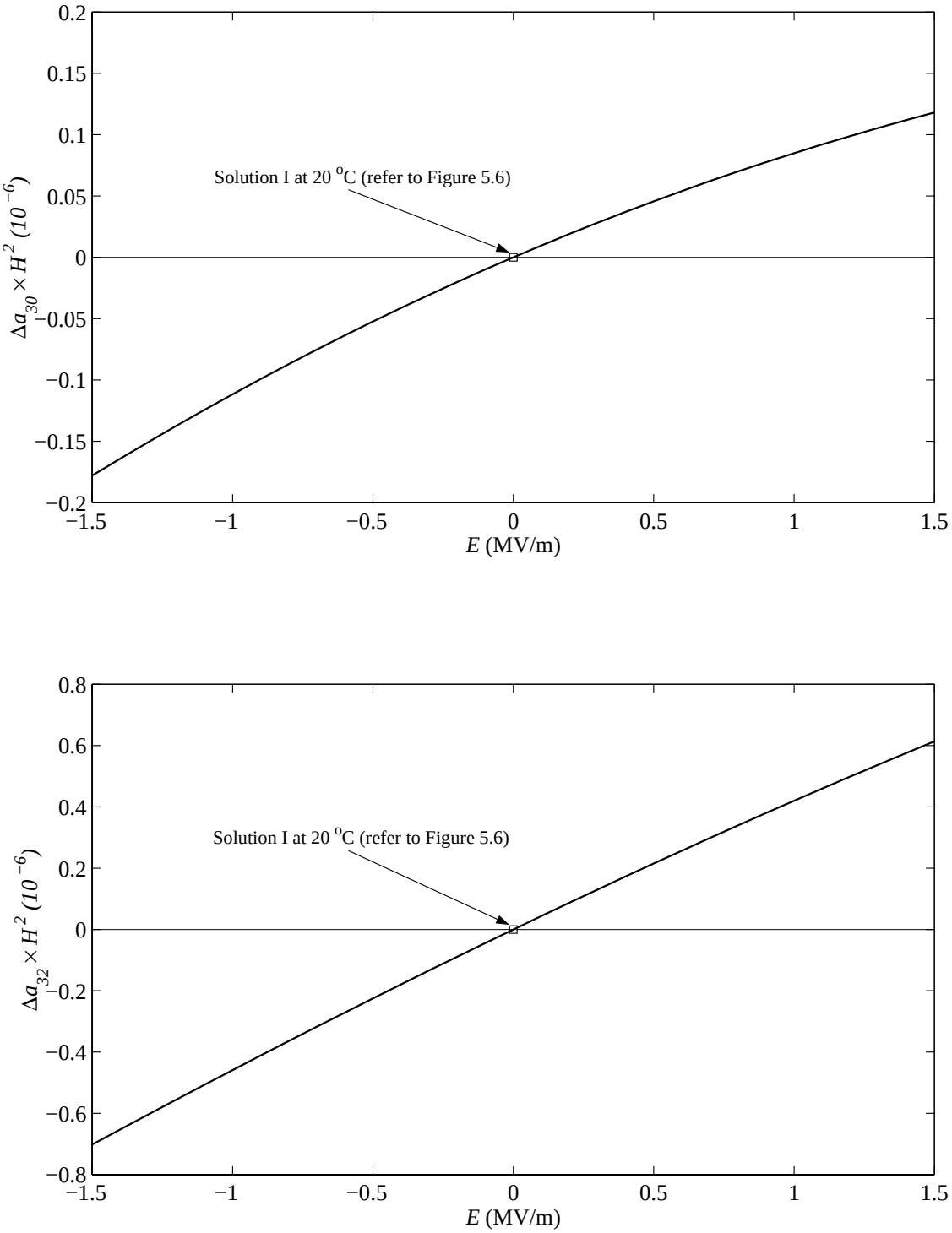


Figure 5.42: Variations of $a_{30}$ and $a_{32}$ as a function of $E$ for [$0^o$/RAINBOW] ($R$=25.4 mm, $H$=0.381 mm, $H_r/H$=0.35).

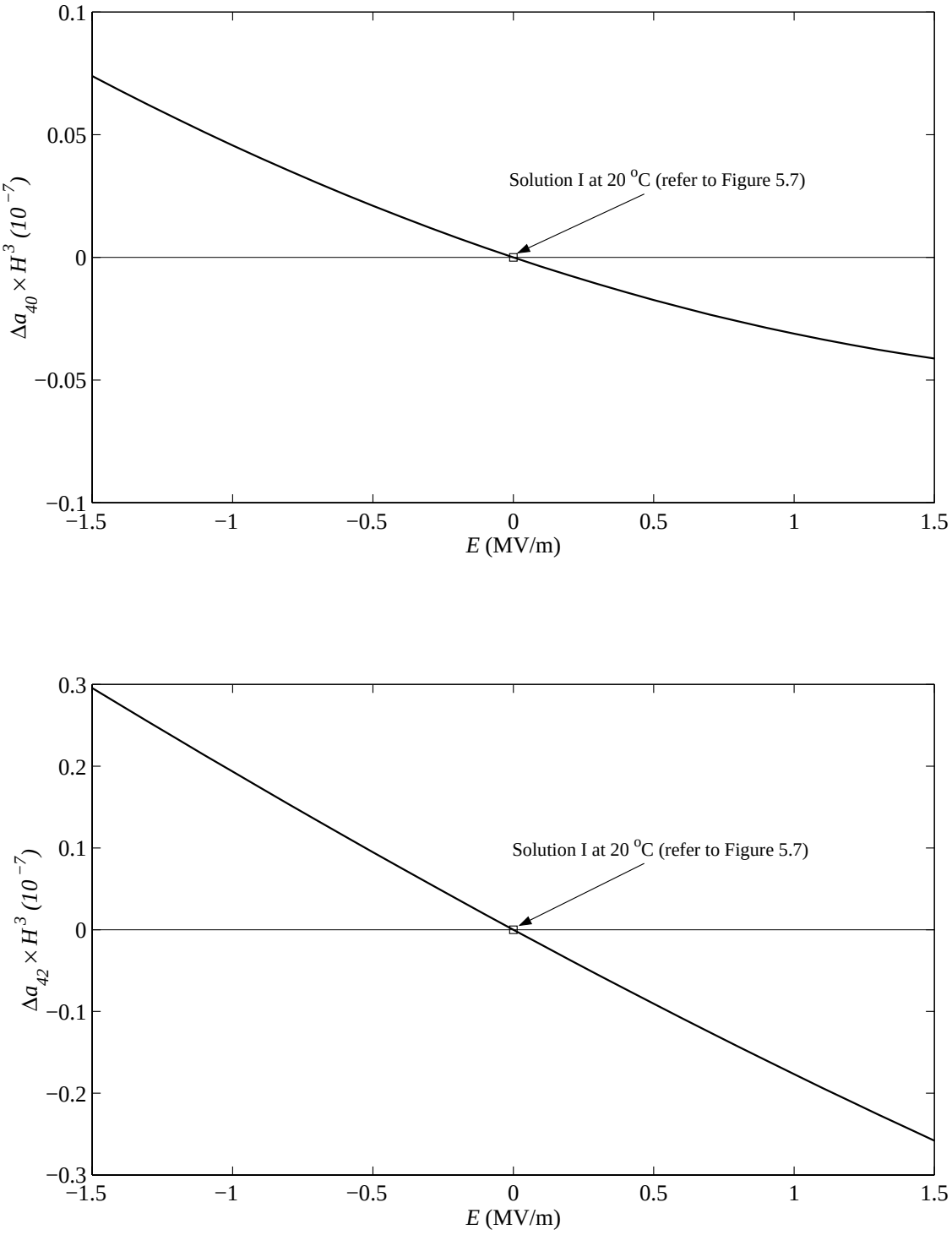


Figure 5.43: Variations of $a_{40}$ and $a_{42}$ as a function of $E$ for [$0^o$/RAINBOW] ($R$=25.4 mm, $H$=0.381 mm, $H_r/H$=0.35).

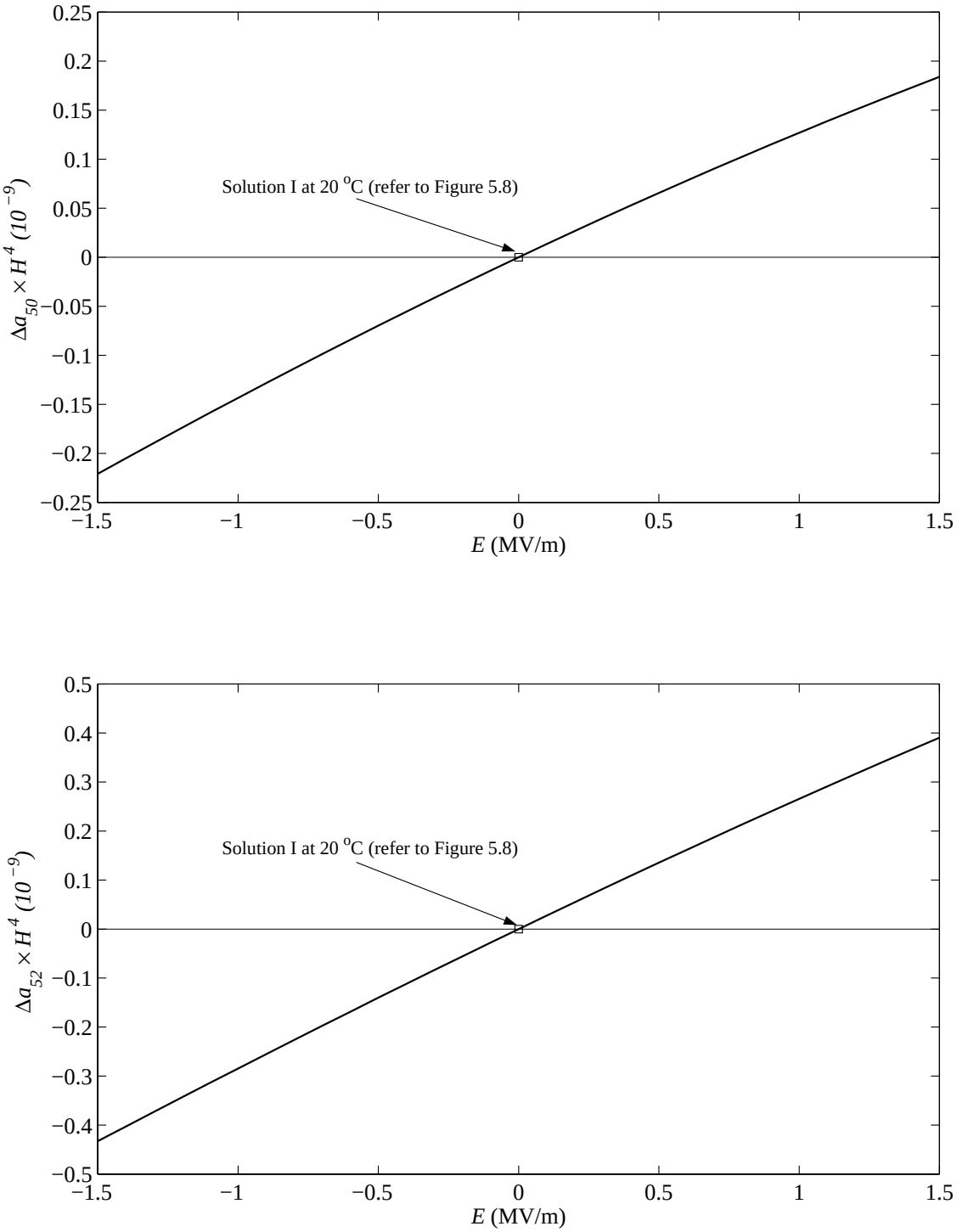


Figure 5.44: Variations of $a_{50}$ and $a_{52}$ as a function of $E$ for [$0^o$/RAINBOW] ($R$=25.4 mm, $H$=0.381 mm, $H_r/H$=0.35).

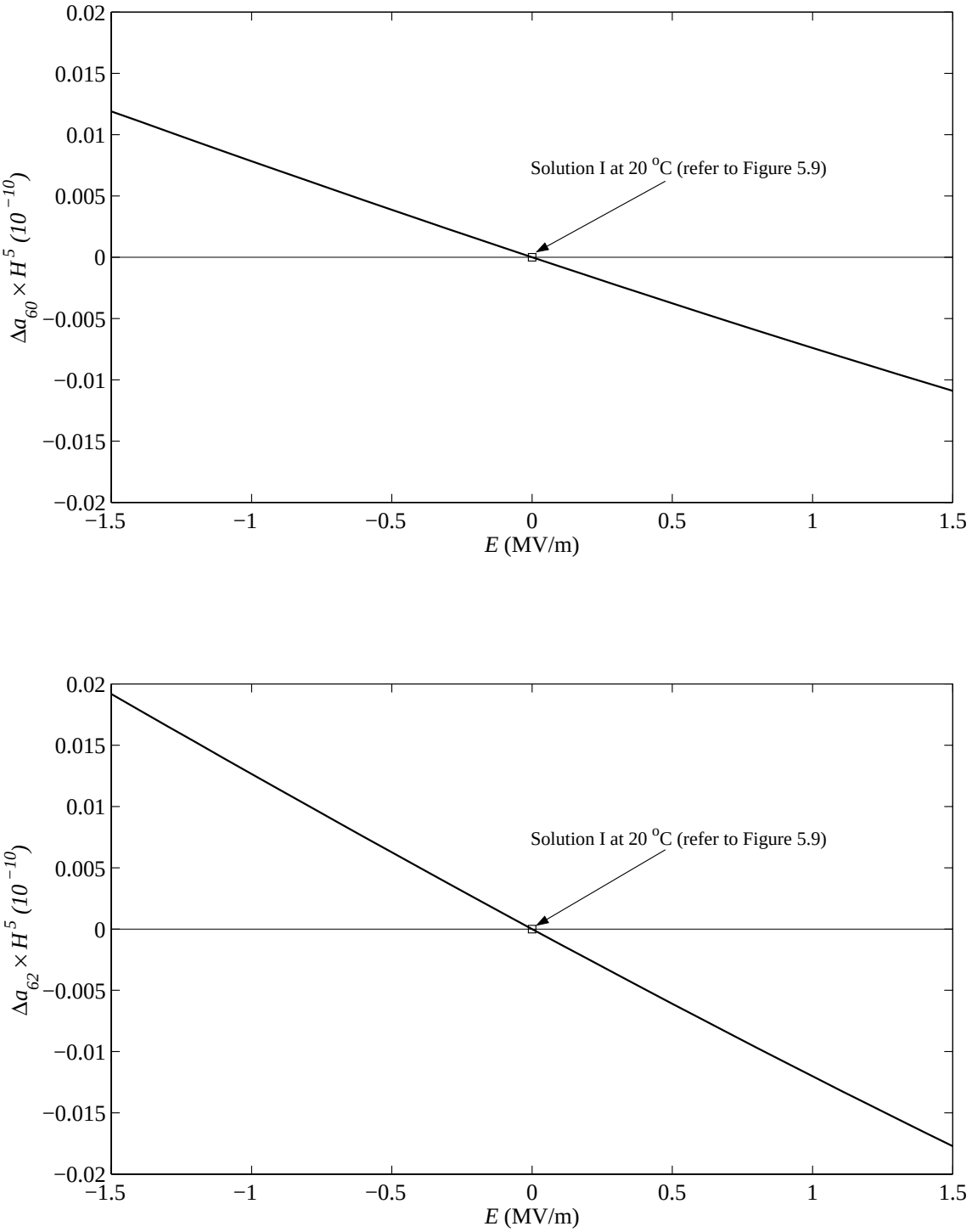


Figure 5.45: Variations of $a_{60}$ and $a_{62}$ as a function of $E$ for [$0^o$/RAINBOW] ($R$=25.4 mm, $H$=0.381 mm, $H_r/H$=0.35).

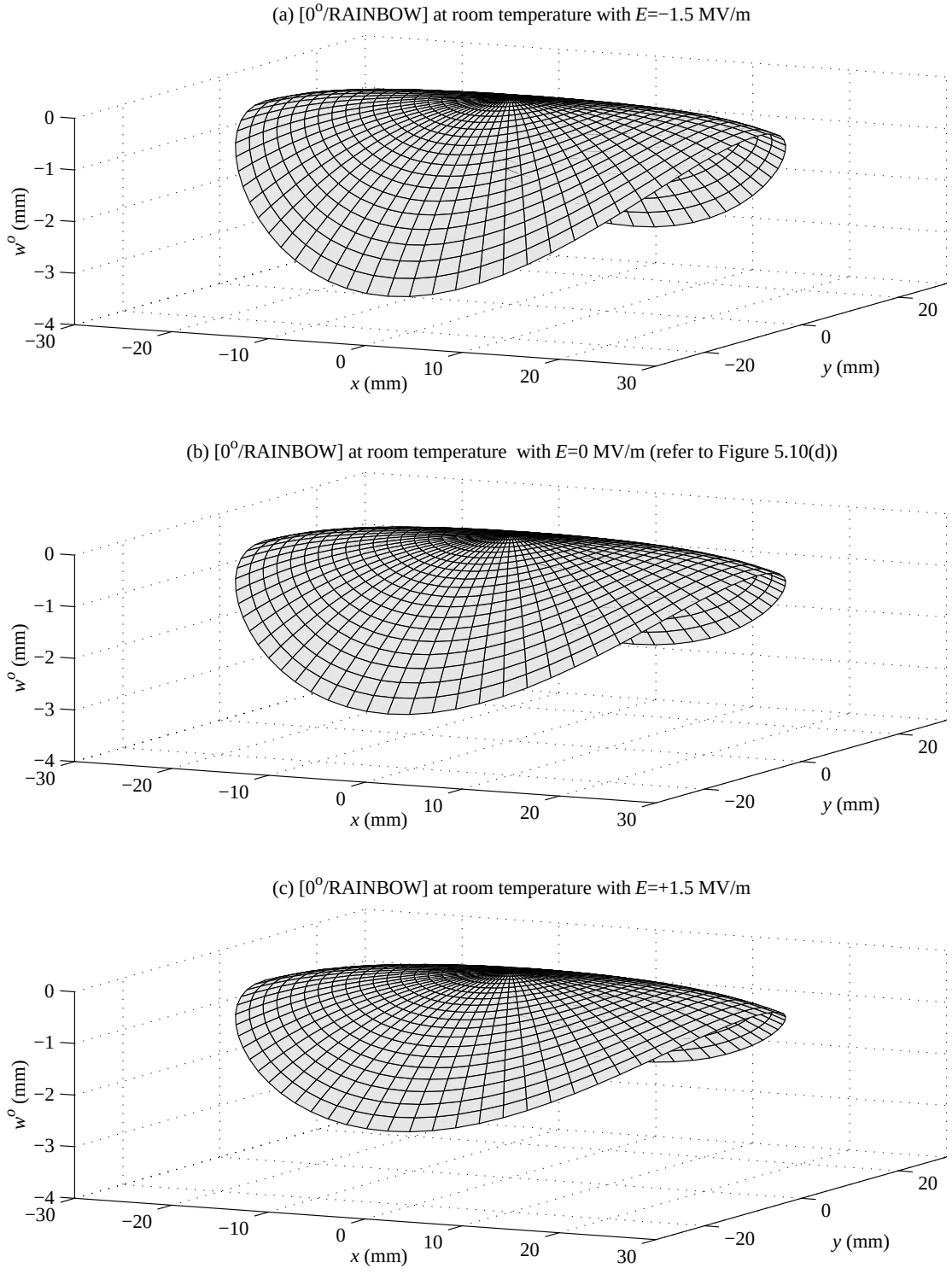


Figure 5.46: Room-temperature shapes of [$0^o$/RAINBOW] at (a) -1.5 MV/m, (b) 0 MV/M, and (c) +1.5 MV/m ($R$=25.4 mm, $H$=0.381 mm, $H_r/H$=0.35).

placements than their RAINBOW counterparts. On the other hand, the room-temperature shapes of [RAINBOW/$0^o$] and [RAINBOW/$0_2^o$] are near-cylindrical but with larger $k_r$ along the $\theta = 0$ and $\theta = \pi$ directions than along the $\theta = \pi/2$ and $\theta = 3\pi/2$ directions and with the smaller out-of-plane displacements than their RAINBOW counterparts. It is interesting to note that bonding [$0^o/90^o$] composite layers either to the reduced layer or unreduced layer of RAINBOW results in one stable dome-like shape and two stable cylinder-like shapes with larger $k_r$ along the $\theta = \pi/2$ and $\theta = 3\pi/2$ directions than along the $\theta = 0$ and $\theta = \pi$ directions. The relationship between the dominant coefficients in the curvature expressions ($a_{20}$ and $a_{22}$) and the electric field was shown to be very close to being linear.

In the next chapter, conclusions regarding the present study are made and recommendations for future work are specified.

# Chapter 6

# Conclusions

In this work, a number of predictive analyses were developed to determine the deformation characteristics of the manufactured shape of rectangular and disk-style RAINBOW piezoceramic actuators. These analyses were based on developing approximate displacement responses that minimize the total potential energy of these layered actuators. This was accomplished through the use of variational methods along with a Rayleigh-Ritz approximation to the displacement fields. All analyses were based on classical layered plate theory and assumed the various layers exhibited linear elastic, temperature-independent behavior. Since the out-of-plane deformations of these actuators when cooled from the processing temperature to room temperature are several times the thickness of the actuator, geometric nonlinearities were important and were included in the strain-displacement relations. The Rayleigh-Ritz procedure was aided by the fact that the cooled shape of the devices can be either near-cylindrical or domed. Based on physical observations, these shapes were represented accordingly by reasonably well-behaved functions of the spatial coordinates. The presence of geometric nonlinearities implies the possibility of having more than one room-temperature shape predicted for a given set of parameters. For that purpose, an examination of the stability of the predicted shapes was considered. This was achieved by examining the second variation of the total potential energy. Although, the methodology for predicting the room-temperature shapes of rectangular RAINBOW was similar to the methodology used for the disk-style RAINBOW, the predictive tool for the rectangular devices was based on analyses in a Cartesian coordinate system, while the predictive tool for the disk-style devices was based on a polar coordinate system. These

models were then easily modified to account for piezoelectric-induced deformations.

Both models presented in Chapters 2 and 4 are shown to have good agreement with the finite element results obtained using ABAQUS. The present models are shown to have several formulative and computational advantages over finite element analysis. These advantages include simplicity of formulation and the relative ease of extending the model to include piezoelectric-induced deformations. This is in contrast to ABAQUS, which requires a three-dimensional analysis to model the piezoelectric-induced deformations. In addition, the formulation of the present analysis is quite straightforward, and the bulk of the computational effort can be completed in much less time than the finite element analysis.

The numerical results presented in Chapters 2 indicate that for a given set of material properties, rectangular RAINBOW can have critical values of sidelength-to-thickness ratio ($L_x/H$ or $L_y/H$) below which RAINBOW exhibits unique, or single-valued, spherical, or domed, shapes when cooled from the processing temperature to room temperature. For values of sidelength-to-thickness ratio greater than the critical value, RAINBOW exhibits multiple room-temperature shapes. Two of the shapes are stable and are, in general, near-cylindrical. The third shape is spherical and is unstable. Similarly, results in Chapter 4 show that disk-style RAINBOW can have critical values of radius-to-thickness ratios ($R/H$) below which RAINBOW exhibits axisymmetric room-temperature shapes. For values of $R/H$ greater than the critical value, disk-style RAINBOW exhibits two stable near-cylindrical shapes and one unstable axisymmetric shape. The existence of these critical values suggests that care should be taken when designing RAINBOW actuators. Indeed, if two RAINBOW actuators are manufactured with a geometry that is very close to the critical value, they may behave quite differently. Specifically, manufacturing irregularities such as small variations in material properties, variation in layer thickness, or nonuniform cooling may result in different effective sidelength-to-thickness ratio or radius-to-thickness ratio. Hence, two 'identical' RAINBOW will not behave the same way. Moreover, the present study reveals the existence of two critical values of reduced layer thickness. This adds more complexity to the unusual behavior of RAINBOW. Indeed, it shown that for a reduced layer thickness bounded by these two critical values, disk-style RAINBOW exhibit two stable near-cylindrical shapes and one unstable axisymmetric spherical shape. However, if the reduced layer thickness is outside the interval bounded by the critical values,

RAINBOW exhibit a unique and stable axisymmetric spherical shape. Thus, the variation in the reduced layer thickness due to nonuniform reduction will no doubt influence the room-temperature shapes. The extension of the model to account for piezoelectric-induced deformations shows that the relationship between the change in curvatures of rectangular and disk-style RAINBOW and the electric field strength is very close to be linear. This is an important character, as it makes the analysis of the dynamic behavior of RAINBOW much simpler. Moreover, it is found that for the set of material properties used in this study, the optimal reduced layer thickness would be 55%, since then the maximum change in curvature is achieved under the application of an electric field, while the relationship between the change in curvatures and the electric field is kept very close to being linear. Considering the defects in the manufacturing of both rectangular and disk-style RAINBOW, the predicted results shown in Appendix B agree qualitatively with the experimental results.

In Chapters 3 and 5 a multi-step thermoelastic analysis was developed to model the addition of the fiber-reinforced composite layer. Numerical results were presented to illustrate the influence of the composite layer arrangements on the room-temperature shapes of GRAPHBOW. It was found for rectangular RAINBOW that if the bifurcation temperature is lower than the composite cure temperature, as is the case, for example, with $L_x/H$=100 and $L_y/L_x$=1/2, then a unique stable GRAPHBOW shape is obtained. This shape is near-cylindrical with larger curvature in the $x$ direction than in the $y$ direction for [RAINBOW/$0^o$], [RAINBOW/$0_2^o$], [$0^o$/$90^o$/RAINBOW], and with larger curvature in the $y$ direction than in the $x$ direction for [$0^o$/RAINBOW] and [$0_2^o$/RAINBOW]. The shape of [RAINBOW/$0^o$/$90^o$] is more spherical.

On the other hand, for different geometry, for example, $L_x/H$=100, $L_x/L_y$=1, the RAINBOW bifurcation temperature is above the composite cure temperature, resulting in three stable room-temperature GRAPHBOW shapes. The unstable spherical RAINBOW configuration has been "converted" to a stable near-cylindrical configuration. Thus the influence of the composite layer arrangements on the room-temperature shapes of GRAPHBOW with $L_x/H$=100, $L_y/L_x$=1 seems to be similar to the case with $L_x/H$=100, $L_y/L_x$=1/2, except the fact that instead of having a unique room-temperature, three similar room-temperature configurations, which might be very hard to distinguish as being different, are obtained.

For GRAPHBOW with $L_x/H$=100 and $L_y/L_x$=2, the bifurcation temperature of RAINBOW is much larger than the composite cure temperature, resulting in saddle-node bifurcations during the cooling to room temperature of [$0^o$/RAINBOW], [RAINBOW/$0^o$], and [$0^o_2$/RAINBOW]. It is interesting to note that rectangular [RAINBOW/$0^o$/$90^o$] seems to be less likely to encounter saddle-node bifurcations. The presence of such bifurcations in the behavior of GRAPHBOW is undesired if GRAPHBOW are to be used as actuators. Finally, it was shown that the relationship between the change in the major curvature and the electric field is very close to linear for GRAPHBOW with saddle-node bifurcations which, if they do exist, are far away from room temperature. However, the change in the minor curvature can vary quadratically with the electric field, but since the variation is very small in magnitude, it is negligible.

The results presented in Chapter 5, which focused specifically on disk-style actuators 25.4 mm (1.0 in.) in radius, revealed that [$0^o$/RAINBOW] and [$0^o_2$/RAINBOW] exhibit three similar stable room-temperature configurations and are near-cylindrical, with larger $k_r$ along the $\theta = \pi/2$ and $\theta = 3\pi/2$ directions than along the $\theta = 0$ and $\theta = \pi$ directions, and that have larger out-of-plane displacements than their RAINBOW counterparts. On the other hand, the room-temperature shapes of [RAINBOW/$0^o$] and [RAINBOW/$0^o_2$] are near-cylindrical, but with larger $k_r$ along the $\theta = 0$ and $\theta = \pi$ directions than along the $\theta = \pi/2$ and $\theta = 3\pi/2$ directions and with smaller out-of-plane displacements than their RAINBOW counterparts. It is interesting to note that bonding [$0^o$/$90^o$] composite layers either to the reduced layer or unreduced layer of RAINBOW results in one stable dome-like shape and two stable near-cylindrical shapes with larger $k_r$ along the $\theta = \pi/2$ and $\theta = 3\pi/2$ directions than along the $\theta = 0$ and $\theta = \pi$ directions. The relationship between the dominant coefficients in the curvature expressions ($a_{20}$ and $a_{22}$) and the electric field was shown to be very close to being linear.

The development of these predictive analyses is expected to greatly aid many current research efforts in the area of piezoelectric actuators. The high promise of these analyses suggests the following future activities:

- fabricate RAINBOW with reduced layer thickness ratio $H_r/H$ of 55%,
- investigate the experimental piezoelectric-induced deformation response of RAINBOW with

$H_r/H$=14%,

- fabricate GRAPHBOW and verify if the unstable dome configuration disappears and becomes stable near-cylindrical,
- investigate the experimental piezoelectric-induced deformation response of GRAPHBOW with saddle-node bifurcations that are close to room temperature,
- explore the deformation response of RAINBOW and GRAPHBOW devices when the thermal strains are function of temperature, such as in Figure B.3.

# Bibliography


[1] B. Jaffe, W. R. Cook, and H. Jaffe. *Piezoelectric Ceramics*. Academic Press, New York, 1971.

[2] G. H. Haertling. *Piezoelectric and Electrooptic Ceramics*. Ceramic Materials for Electronics. Marcel Dekker, Inc., New York, edited by R. C. Buchanan, 1986.

[3] E. C. Guyer. *Handbook of Applied Thermal Design*. McGraw-Hill, New York, New York, 1989.

[4] How Thermometers Work. *How Stuff Works* (http://www.howstuffworks.com), by Marshall Brain. BYG Publishing, Inc., 1998.

[5] E. F. Crawley. "Intelligent Structures for Aerospace: A Technology Overview and Assessment". *AIAA Journal*, 32(8):1689–1699, 1994.

[6] S. S. Rao and M. Sunar. "Piezoelectricity and Its Use in Disturbance Sensing and Control of Flexible Structures: A Survey". *Applied Mechanics Reviews*, 47(4):113–123, 1994.

[7] R. G. Loewry. "Recent Developments in Smart Structures with Aeronautical Applications". *Smart Materials and Structures*, 6:R11–R42, 1997.

[8] K. B. Lazarus, E. F. Crawley, and J. D. Bohlmann. "Static Aeroelastic Control Using Strain Actuated Adaptive Structures". *Journal of Intelligent Material Systems and Structures*, 2(3):386–410, 1991.

[9] D. L. Palumbo, S. L. Sadula, K. H. Lyle, J. H. Cline, and R. H. Cabell. Performance of optimized actuator and sensor arrays in an active noise control system. Technical Report TM 110281, NASA, 1996.

[10] J. Heeg. Analytical and experimental investgation of flutter supression by piezoelectric actuation. Technical Report TP 3241, NASA, 1993.

[11] R. W. Moses. Vertical tail buffeting alleviation using piezoelectric actuators - some results of the actively controlled response of buffet-affected tails (acrobat) program. Technical Report TM 110336, NASA, 1997.

[12] P. P. Friedman and T. A. Millott. "Vibration Reduction in Rotorcraft Using Active Control: A Comparison of Various Approaches". *Journal of Guidance, Control, and Dynamics*, 18:664–673, 1994.

[13] S. R. Hall and E. F. Prechtl. "Development of a Piezoelectric Servoflap for Helicopter Rotor Control". *Smart Materials and Structures*, 5:26–34, 1996.

[14] J. Shaw and N. Albion. "Active Control of the Helicopter Rotor for Vibration Reduction". *Journal of the American Helicopter Society*, 30:3–20, 1981.

[15] H. Honmou, R. Ishikawa, and S. Takahashi. "Automatic Optical Fiber Polarization Control System Using Multilayer Piezoelectric Actuators". *Japanese Journal of Applied Physics*, 24:187–189, 1985.

[16] K. Uchino. "Electrostrictive Actuators: Materials and Applications". *American Ceramic Society Bulletin*, 65(4):647–652, 1986.

[17] K. Uchino, M. Yoshisaki, K. Kasai, H. Yamamura, N. Sakai, and H. Asakura. "Monomorph Actuators Using Semiconductive Ferroelectrics". *Japanese Journal of Applied Physics*, 26(7):1046–1049, 1987.

[18] M. A. Ealey and P. A. Davis. "Standard Select Electrostrictive Lead Magnesium Niobate Actuators for Active and Adaptive Optical Components". *Optical Engineering*, 29(11):1373–1382, 1990.

[19] W. P. Robbins, D. L. Polla, and D. E. Glumac. "High-Displacement Piezoelectric Actuator Utilizing a Meander-Line Geometry-Part I: Experimental Characterization". *IEEE Transactions on Ultrasonics, Ferroelectrics, Frequency Control*, 38(5):454–467, 1991.

[20] Q. C. Xu, S. Yoshikawa, J. R. Belsick, and R. E. Newnham. "Piezoelectric Composites with High Sensitivity and High Capacitance for Use at High Pressures". *IEEE Transactions on Ultrasonics, Ferroelectrics, Frequency Control*, 38(6):634–639, 1991.

[21] Y. Sugawara, K. Onitsuka, Q. C. Yoshikawa, Q. C. Xu, and R. E. Newnham. "Metal-Ceramic Composite Actuators". *Journal of American Ceramic Society*, 75(4):996–998, 1992.

[22] G. H. Haertling. "Rainbow Ceramics–A New Type of Ultra-High-Displacement Actuator". *American Ceramic Society Bulletin*, 73(1):93–96, 1994.

[23] S. A. Wise. "Research and Technology Highlights 1994". Technical Report TM-4708, NASA Langley Research Center, 1994.

[24] S. A. Wise. "Displacement Properties of Rainbow and Thunder Piezoelectric Actuators". *Sensors and Actuators A Physical*, 69:33–38, 1998.

[25] Y.C. Fung. *Foundations of Solid Mechanics.* Prentice-Hall, Inc., Englewood Cliffs, New Jersey, 1965.

[26] C.-Y. Chia. *Nonlinear Analysis of Plates.* McGraw-Hill, Inc., New York, 1980. Ch. 1.

[27] V. V. Novoshilov. *Foundations of the Nonlinear Theory of Elasticity.* Graylock Press, Rochester, New York, 1953.

[28] M. W. Hyer. *Stress Analysis of Fiber-Reinforced Composite Materials.* WCB/McGraw-Hill, Inc., New York, 1998.

[29] M. W. Hyer. "Calculations of the Room-Temperature Shapes of Unsymmetric Laminates". *Journal of Composite Materials*, 15:296–310, 1981.

[30] M. W. Hyer. "The Room-Temperature Shapes of Four-Layer Unsymmetric Cross-Ply Laminates". *Journal of Composite Materials*, 16:318–340, 1981.

[31] A. Hamamoto and M. W. Hyer. "Nonlinear Temperature-Curvature Relationships for Unsymmetric Graphite Epoxy Laminates". *International Journal of Solids and Structures*, 23:919–935, 1987.

[32] S. Wolfram. *Mathematica: A System for doing Mathematics by Computer.* Addison-Wesley, Redwood City, California, 1998.

[33] W. P. Mason. *Piezoelectric Crystals and their Applications to Ultrasonics.* D. Van Nostrand Co., Inc., Princeton, New Jersey, 1950.

[34] Personnel communication.

[35] ABAQUS/STANDARD. *Theory Manual.* Hibbitt, Karlsson, & Sorensen, Inc., Pawtucket, Rhode Island, 1998.

[36] G. H. Haertling. "Chemically Reduced PLZT Actuators". *Ferroelectrics*, 154:101–106, 1994.

[37] M. Kubicek and M. Marek. *Computational Methods in Bifurcation Theory and Dissipative Structures.* Springer-Verlag, New York, 1983.

[38] H. B. Keller. *Lectures on Numerical Methods in Bifurcation Problems.* Springer-Verlag, New York, 1987.

[39] A. H. Nayfeh and B. Balachandran. *Applied Nonlinear Dynamics: Analytical, Computational, and Experimental Methods.* John Wiley & Sons, Inc., New York, New York, 1995.

[40] IMSL MATH/LIBRARY. *Fortran Subroutines for Mathematical Applications.* IMSL, Inc., Houston, Texas, 1987.

# Appendix A

# Equilibrium Equations and Stability Matrix for Rectangular RAINBOW Actuators

**Equilibrium equations**

**Coefficient of $\delta a$**

$$\begin{aligned} & \frac{b^2\,B_{22}\,{L_x}^2}{48} - \frac{A_{12}\,b\,c\,{L_x}^2}{48} - \frac{A_{22}\,b\,d\,{L_x}^2}{48} + \frac{a\,A_{22}\,b^2\,{L_x}^4}{1280} - \frac{A_{11}\,b\,c\,{L_y}^2}{48} - \frac{A_{12}\,b\,d\,{L_y}^2}{48} \\ + & \frac{a\,A_{12}\,b^2\,{L_x}^2\,{L_y}^2}{1152} + \frac{a\,A_{11}\,b^2\,{L_y}^4}{1280} + + \frac{a\,b\,{L_y}^2}{24} + \frac{B_{12}\,\left(-48\,d + 2\,a\,b\,{L_x}^2 + b^2\,{L_y}^2\right)}{48} \\ + & a\,D_{11} + b\,D_{12} - c + \hat{M}_x^T\,\Delta T + \frac{b\,{L_y}^2\,\hat{N}_x^T\,\Delta T}{48} + \frac{b\,{L_x}^2\,\hat{N}_y^T\,\Delta T}{48} = 0 \end{aligned} \tag{A.1}$$

**Coefficient of $\delta b$**

$$\begin{aligned} & \frac{a\,b\,B_{22}\,{L_x}^2}{24} - \frac{a\,A_{12}\,c\,{L_x}^2}{48} - \frac{a\,A_{22}\,d\,{L_x}^2}{48} + \frac{a^2\,A_{22}\,b\,{L_x}^4}{1280} + \frac{a^2\,B_{11}\,{L_y}^2}{48} - \frac{a\,A_{11}\,c\,{L_y}^2}{48} \\ - & \frac{a\,A_{12}\,d\,{L_y}^2}{48} + \frac{a^2\,A_{12}\,b\,{L_x}^2\,{L_y}^2}{1152} + \frac{a^2\,A_{11}\,b\,{L_y}^4}{1280} + \frac{B_{12}\,\left(-48\,c + a\,\left(a\,{L_x}^2 + 2\,b\,{L_y}^2\right)\right)}{48} \\ & -B_{22}\,d + a\,D_{12} + b\,D_{22} + \hat{M}_y^T\,\Delta T + \frac{a\,{L_y}^2\,\hat{N}_x^T\,\Delta T}{48} + \frac{a\,{L_x}^2\,\hat{N}_y^T\,\Delta T}{48} = 0 \end{aligned} \tag{A.2}$$

**Coefficient of $\delta c$**

$$A_{11}\,c + A_{12}\,d - b\,B_{12} - \frac{a\,\left(48\,B_{11} + A_{12}\,b\,{L_x}^2 + A_{11}\,b\,{L_y}^2\right)}{48} - \hat{N}_x^T\,\Delta T = 0 \tag{A.3}$$

**Coefficient of $\delta d$**

$$A_{12}\,c + A_{22}\,d - b\,B_{22} - \frac{a\,\left(48\,B_{12} + A_{22}\,b\,{L_x}^2 + A_{12}\,b\,{L_y}^2\right)}{48} - \hat{N}_y^T\,\Delta T = 0 \tag{A.4}$$

**Stability matrix**

$$\left[\ C\ \right] = \begin{bmatrix} C_{11} & C_{12} & C_{13} & C_{14} \\ C_{12} & C_{22} & C_{23} & C_{24} \\ C_{13} & C_{23} & C_{33} & C_{34} \\ C_{14} & C_{24} & C_{34} & C_{44} \end{bmatrix} \tag{A.5}$$

where

$$C_{11} = D_{11} + \frac{bB_{12}L_x^2}{24} + \frac{A_{22}b^2L_x^4}{1280} + \frac{bB_{11}L_y^2}{24} + \frac{A_{12}b^2L_x^2L_y^2}{1152} + \frac{A_{11}b^2L_y^4}{1280} \tag{A.6}$$

$$\begin{aligned} C_{12} &= D_{12} + \frac{bB_{22}L_x^2}{24} - \frac{A_{12}cL_x^2}{48} - \frac{A_{22}dL_x^2}{48} + \frac{aA_{22}bL_x^4}{640} + \frac{aB_{11}L_y^2}{24} - \frac{A_{11}cL_y^2}{48} \\ &- \frac{A_{12}dL_y^2}{48} + \frac{aA_{12}bL_x^2L_y^2}{576} + \frac{aA_{11}bL_y^4}{640} + \frac{B_{12}(2aL_x^2 + 2bL_y^2)}{48} \\ &+ \frac{(L_y^2\hat{N}_x^T + L_x^2\hat{N}_y^T)\Delta T}{48} \end{aligned} \tag{A.7}$$

$$C_{13} = -B_{11} - \frac{A_{12}bL_x^2}{48} - \frac{A_{11}bL_y^2}{48} \tag{A.8}$$

$$C_{14} = B_{12} - \frac{A_{22}bL_x^2}{48} - \frac{A_{12}bL_y^2}{48} \tag{A.9}$$

$$C_{22} = D_{22} + \frac{aB_{22}L_x^2}{24} + \frac{a^2A_{22}L_x^4}{1280} + \frac{aB_{12}L_y^2}{24} + \frac{a^2A_{12}L_x^2L_y^2}{1152} + \frac{a^2A_{11}L_y^4}{1280} \tag{A.10}$$

$$C_{23} = -B_{12} - \frac{aA_{12}L_x^2}{48} - \frac{aA_{11}L_y^2}{48} \quad \text{(A.11)}$$

$$C_{24} = -B_{22} - \frac{aA_{22}L_x^2}{48} - \frac{aA_{12}L_y^2}{48} \quad \text{(A.12)}$$

$$C_{33} = A_{11} \quad \text{(A.13)}$$

$$C_{34} = A_{12} \quad \text{(A.14)}$$

$$C_{44} = A_{22} \quad \text{(A.15)}$$

# Appendix B

# RAINBOW Devices: Experimental Results

## B.1 Measurement of Material Properties

Rectangular and disk-style RAINBOW were manufactured by Dr. W. L. Vaughn at NASA Langley Research Center. The size, thickness, and reducing time for the RAINBOW actuators are given in the next sections. The RAINBOW actuators were made of PZT-5A piezoceramic material. The moduli of elasticity of the reduced and unreduced piezoceramic were obtained by performing compression tests on reduced and unreduced piezoceramic bars (see Figure B.1). The load-strain curves of unreduced and reduced bars are shown in Figure B.2. The geometry, mass, density, slope of the load-strain curves, and compression modulus of each bar is tabulated in Table B.1. In the table, the 5A- bars are unreduced and the R- bars are reduced. The computed moduli are based on the load-stain curves in the range of 5 to 40 lbs of load. (In this appendix the units cited are the units that were used in the actual measurements). The bars were loaded lengthwise as shown in Figure B.1 and a one-inch clip gage was used to measure strain. From Table B.1, the average Young's modulus and its standard of deviation for the unreduced and reduced bars are 6.44 Msi and 1.37 Msi, and 4.34 Msi and 0.57 Msi, respectively. Although measurements of strain were taken for loads up to 100 lbs, one unreduced bar was loaded up to 750 lbs without failure. The R- bars

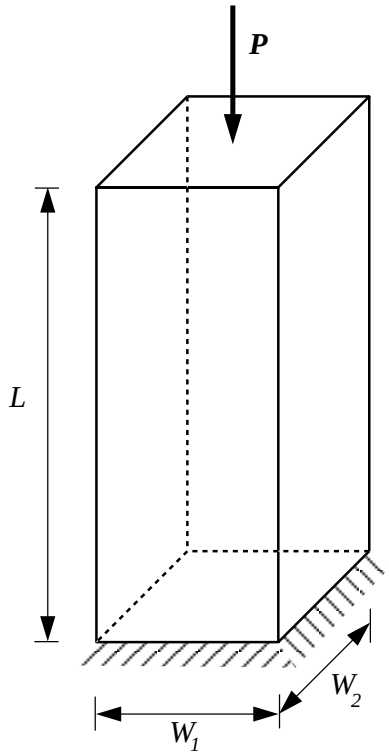


Figure B.1: Compressive loading of piezoceramic bars.

were reduced for 36 hours at 975 $^o$C using a carbon block in an air furnace. A witness bar was used to track the reduction.

To obtain measurements of the coefficients of thermal expansion of the reduced and unreduced piezoceramic, a LINSEIS dilatometer was used to measure the change in length in three piezoceramic bars ($L \times W \times W$, $L/W$=6): PZT5A-1 (unreduced, $L$=24.73 mm), PZT5A-3 (unreduced, $L$=21.12 mm), and PZT5AR-1 (reduced, $L$=22.42 mm). The temperature ranged from 20 $^o$C to 600 $^o$C. The rates of change of temperature for PZT5A-1, PZT5A-3, and PZT5AR-1 were 2 $^o$C/min, 3 $^o$C/min, and 3 $^o$C/min, respectively. Figure B.3 shows the relative change in length as a function of temperature for the three specimens. Since the experimental data of $\Delta L/L$ for PZT5A-3 and PZT5AR-1 were obtained using the temperature rate 3 $^o$C/min, they were used to evaluate the thermal expansion coefficients for the unreduced and reduced piezoceramic. It is seen from Figure B.3 that at a temperature greater than the Curie temperature, $T_C$=340 $^o$C, the relationship between $\Delta L/L$ and temperature is very close to being linear. The experimental results of $\Delta L/L$ were thus extrapolated for temperatures above 600 $^o$C to 970 $^o$C. It is obvious from Figure B.3

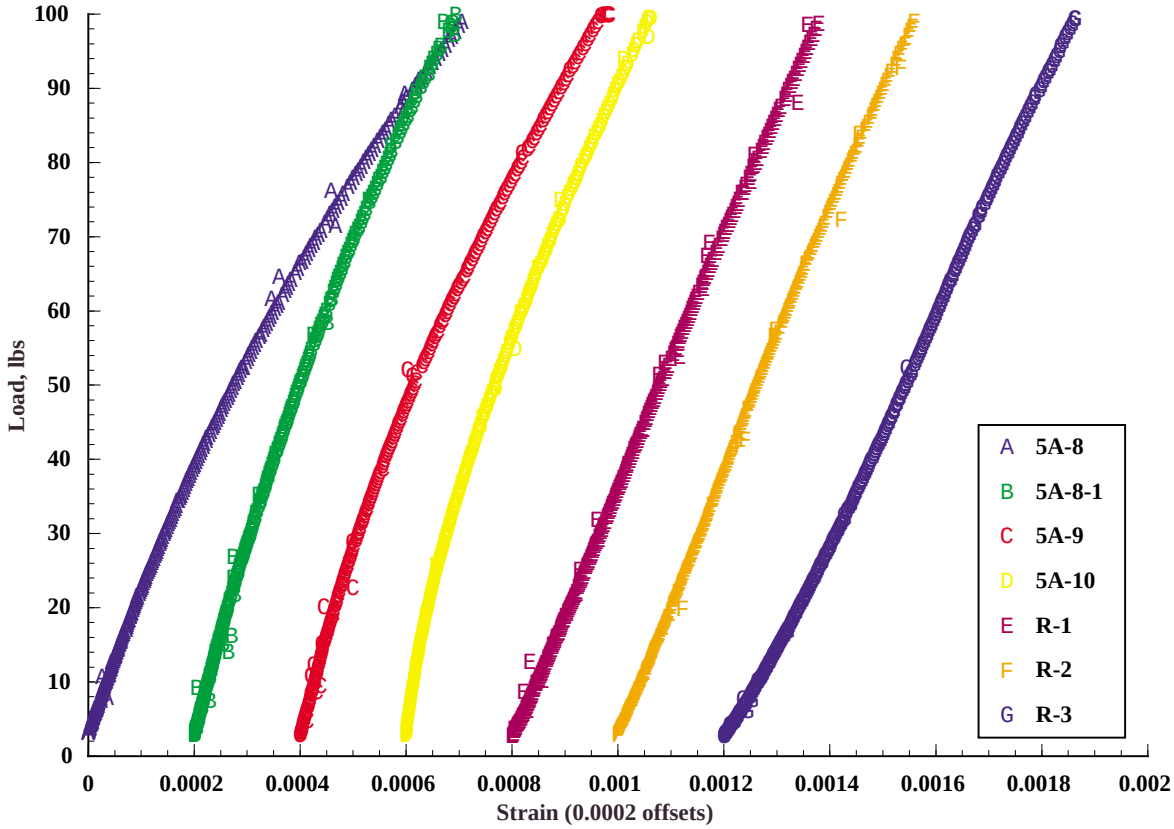


Figure B.2: Load-strain curves for the unreduced and reduced PZT5-A bars.

Table B.1: Geometric and material properties of unreduced and reduced PZT-5A bars.

| Specimen | Length, $L$ (in.) | Average $W_1$ (in.) | Average $W_2$ (in.) | Area (in.$^2$) | Mass (g) | Density (g/cm$^3$) | $\Delta P/\Delta\epsilon$ $10^5\times$(lbs) | Modulus (Msi) |
|---|---|---|---|---|---|---|---|---|
| 5A-8 | 1.501 | 0.2497 | 0.1504 | 0.0375 | 7.0786 | 7.67 | 2.48 | 6.61 |
| 5A-8-1 | 1.501 | 0.2497 | 0.1504 | 0.0375 | 7.0786 | 7.67 | 1.80 | 4.80 |
| 5A-9 | 1.502 | 0.2498 | 0.1501 | 0.0375 | 7.0684 | 7.66 | 2.33 | 6.21 |
| 5A-10 | 1.501 | 0.2496 | 1.493 | 0.0373 | 7.0348 | 7.68 | 3.03 | 8.13 |
| R-1 | 1.492 | 0.2482 | 0.1493 | 0.0370 | 5.4546 | 6.02 | 1.69 | 4.56 |
| R-2 | 1.490 | 0.2481 | 0.1494 | 0.0370 | 5.4546 | 6.02 | 1.77 | 4.78 |
| R-3 | 1.490 | 0.2477 | 0.1498 | 0.0371 | 5.3476 | 5.90 | 1.37 | 3.69 |

that for temperatures greater than 340 $^o$C, the thermal expansion coefficients, slopes of $\Delta L/L$ vs. temperature, for the unreduced piezoceramic (PZT5A-3) and the reduced piezoceramic (PZT5AR-3) did not differ that much. However, at temperatures lower than the Curie temperature, the difference in thermal expansion coefficients was significant. It is thus expected that the majority of the manufactured shape develops as RAINBOW is cooled below 340 $^o$C. Therefore, instead of using a temperature change from 975 $^o$C to room temperature to predict the room-temperature shape, a temperature change from 340 $^o$C to room temperature is used. Additionally, the theory developed to predict the room-temperature shape of RAINBOW and GRAPHBOW depends only on the difference in free thermal strains from one temperature to the next, not on the exact cooling path. Therefore, the thermal expansion data are interpreted as providing an effective thermal expansion coefficient between 340 $^o$C and room temperature. Thus, $\alpha_o$, the thermal expansion coefficient of the unreduced piezoceramic, and $\alpha_r$, the thermal expansion coefficient of the reduced piezoceramic, are taken to be $2.13\times10^{-6}$ $^o$C$^{-1}$ and $8.41\times10^{-6}$ $^o$C$^{-1}$, respectively.

## B.2 Comparison with Experimental Results

### B.2.1 Rectangular RAINBOW Devices

The reduced layer thickness, $H_r$, was determined using the experimental data reported by Haertling [36]. For a given reducing time, the reduced layer thickness was obtained from Figure B.4, which is reproduced from [36]. Figure B.4 shows that the reduced layer thickness increases at a near linear rate with reduction time.

To measure the room-temperature out-of-plane displacements of each of the manufactured RAINBOW, a simple dial-gage, mounted in a vertical milling machine was used (see Figure B.5). The milling machine table normally used to hold the material being milled was used to hold the RAINBOW specimen with double-sided adhesive tape. The table could be moved horizontally known amounts in the $x$- and $y$- directions, and thus the out-of-plane dial measurements as a function of known $x$ and $y$ location could be recorded (see Figure B.6). In Figure B.5 the out-of-plane displacements, being the vertical displacements, are seen being measured at every 0.125 in. in the $x$ and $y$ directions to within 0.0005 in. of accuracy. For RAINBOW devices for which $L_y$ is equal to

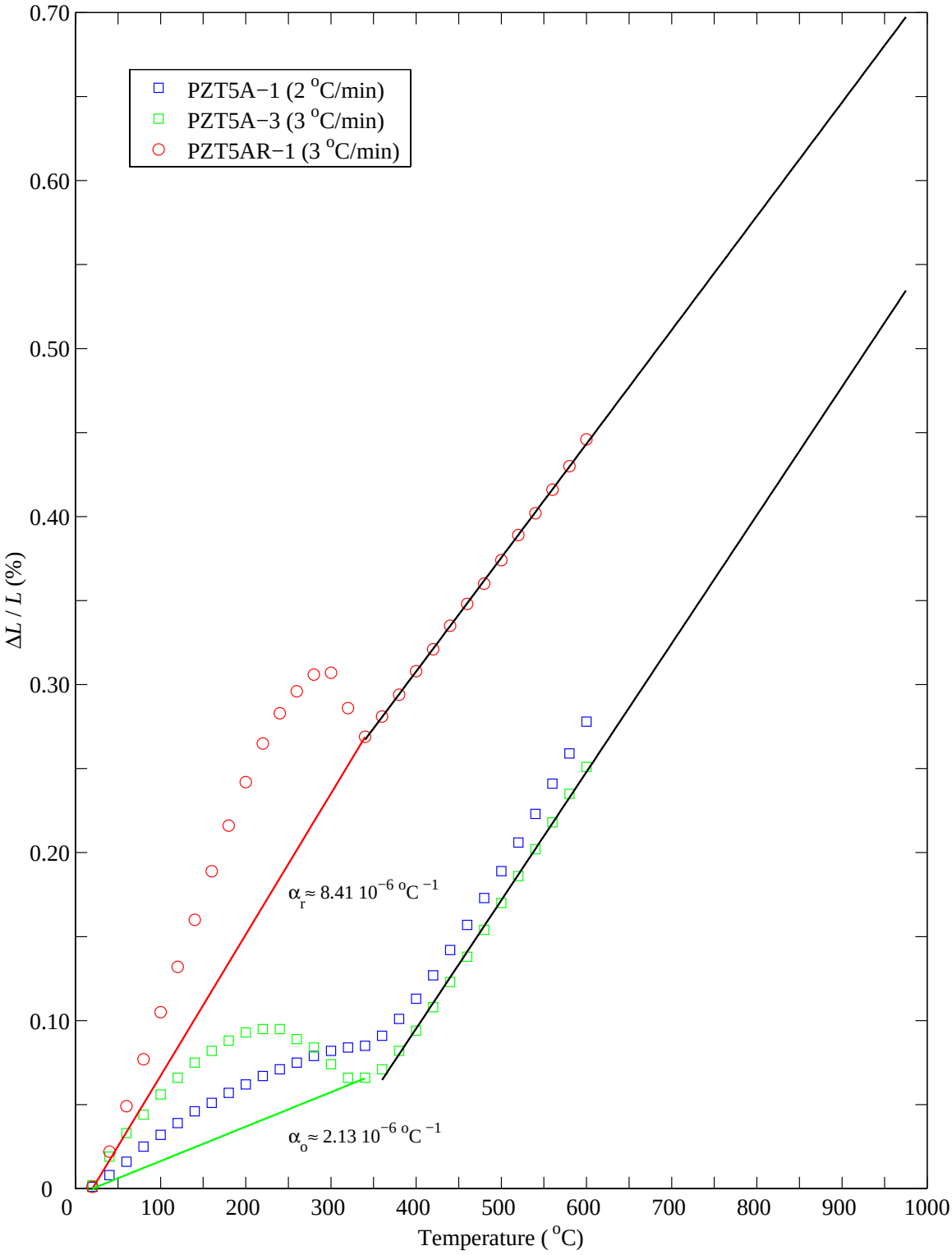


Figure B.3: Experimental evaluation of thermal expansion coefficients.

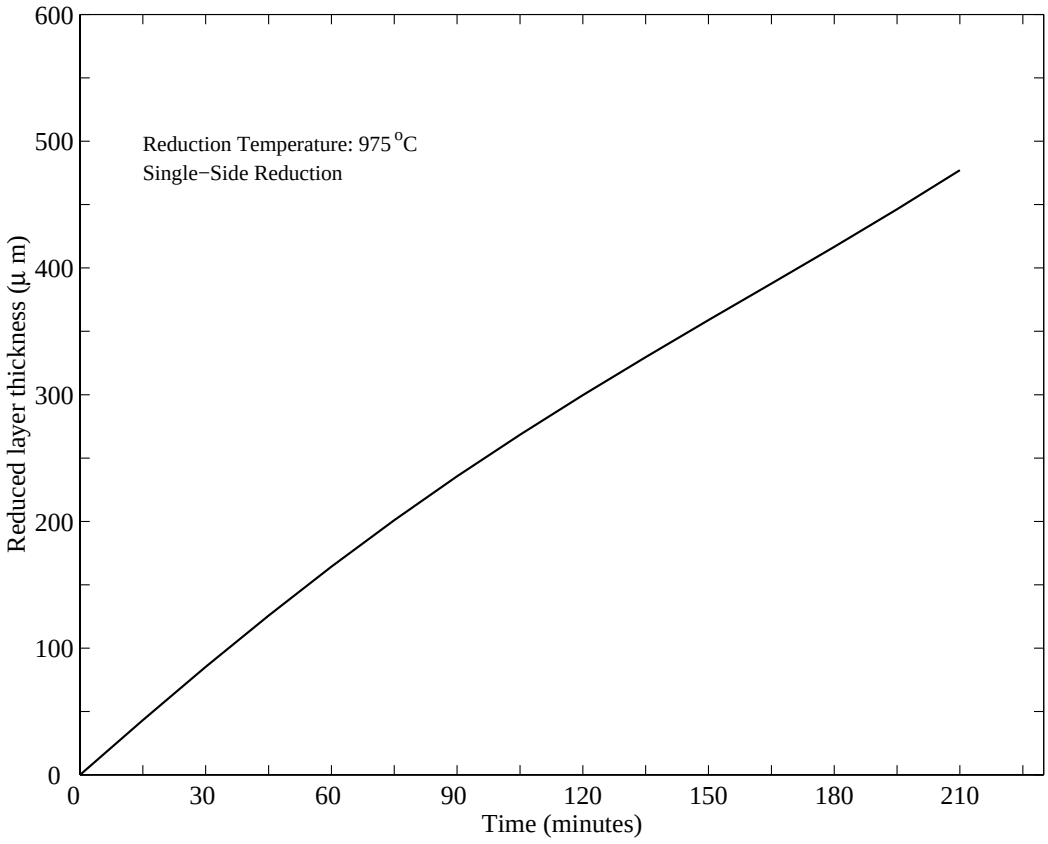


Figure B.4: Effect of reduction time on the reduced layer thickness (reproduced from [36]).

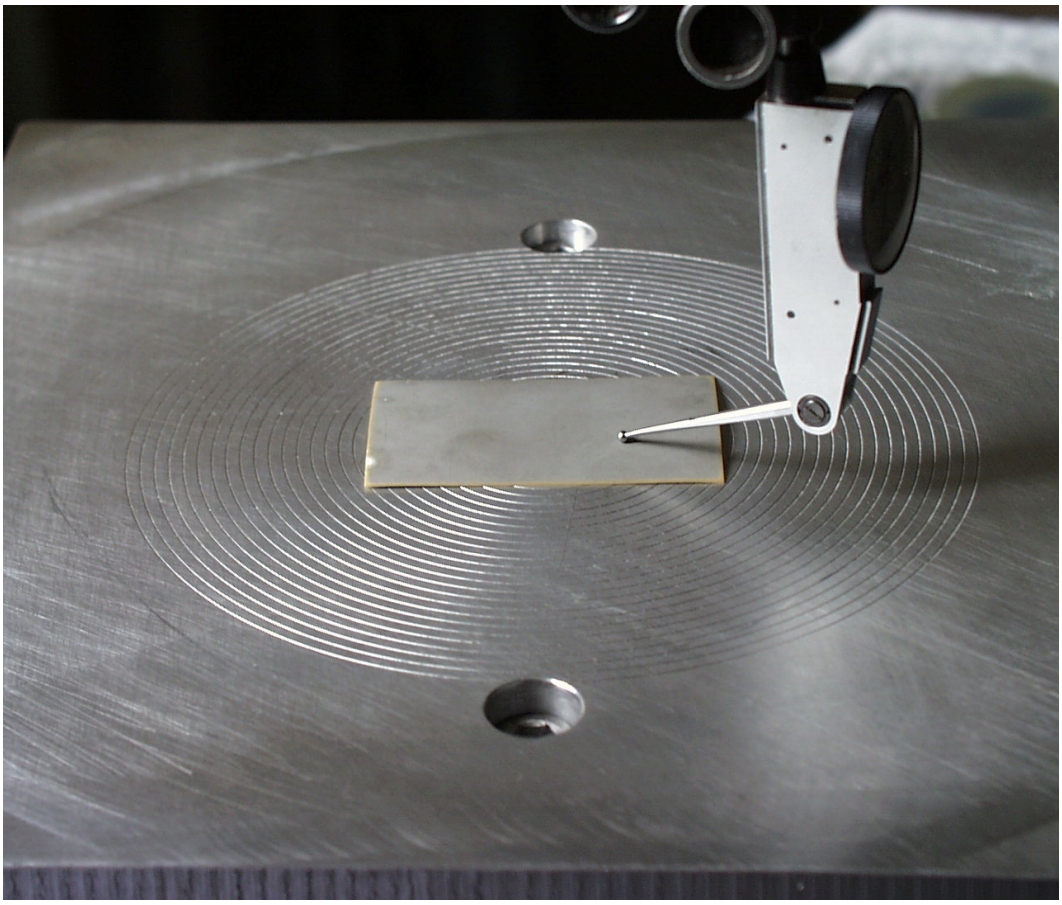

Figure B.5: Measurement of out-of-plane displacements for a 2.5 in.×1.5 in. rectangular RAINBOW).

0.25 in., measurements of the out-of-plane displacements were taken in the $x$ direction only along $y = 0$ axis. As can be seen in Figure B.5, the measurements were made on the convex side of the specimens. Once the out-of-plane displacements were measured, they were fit to a polynomial equation of the form

$$w^o(x, y) = \bar{c}_1 x^2 + \bar{c}_2 y^2 + \bar{c}_3 xy + \bar{c}_4 x + \bar{c}_5 y + \bar{c}_6. \tag{B.1}$$

A least-square fit of the measured out-of-plane displacements was used to determine the six coefficients of the above polynomial. The coefficients $\bar{c}_1$, $\bar{c}_2$ and $\bar{c}_3$ represented the curvatures $\kappa_x^o$, $\kappa_y^o$, and $\kappa_{xy}^o$, respectively, and the coefficients $\bar{c}_4$–$\bar{c}_6$ accounted for rigid body rotations and out-of-plane displacement of RAINBOW relative to the measurement fixture. These coefficients could be used to account for any arbitrary tilt of the specimen relative to the milling machine axes due to misalignment in mounting the specimen on the milling machine table.

In Table B.2 the measured curvatures are compared with predictions obtained using the model developed in Chapter 2. Table B.2 also includes geometric data regarding the specimen, including the computed critical length-to-thickness ratio. The estimated thickness of the reduced layer, based on the reducing time, is also shown. Although Table B.2 shows some discrepancies between the values of measured and predicted curvatures, in general there is a qualitative agreement between the results, i.e., if a spherical shape was predicted, a spherical shape was observed, if a near-cylindrical shape was predicted, a near-cylindrical shape was observed. The measured $\kappa_{xy}^o$ is very close to zero for all cases, indicating that the shear strain $\gamma_{xy}^o$ is negligible, which supports the assumption adopted in the development of the model in Chapter 2. The two RAINBOW devices for which there is a qualitative disagreement, samples 6-3 and 6-4, happen to have values of $L_x/H$ somewhat close to the critical values. Thus, unexpected behavior might occur. Samples 6-1 and 6-2 also happen to have $L_x/H$ close to the critical values, but it was not possible to confirm discrepancies between the measured and predicted curvatures, as no measured curvatures in $y$ direction were made due to the narrowness of the specimens. A whole-field optical technique might be better suited for measuring the shape of narrow specimens, or all specimens for that matter.

As an example of the sensitivity of the predicted results to material properties, Table B.2 is reproduced using $\alpha_r$=$10.5 \times 10^{-6}$ $^o\mathrm{C}^{-1}$, a value 25% higher than the one used in Table B.2. This case is

considered since the quantity $(\alpha_r - \alpha_o)$ is expected to be the most influential term in controlling the governing equations for the curvatures $a$ and $b$ (refer to Equations 2.42 and 2.43). For that reason, a hypothetical variation of 25% in $\alpha_r$ is made to test its influence on the qualitative character of the room-temperature shapes of the RAINBOW samples. Indeed, Table B.3 indicates the increase in $\alpha_r$ by 25% changes the character of the room-temperature shape of sample 6-4 to qualitatively match the experimental one, though it did not favorably influence sample 6-3. The increase in $\alpha_r$ seemed to make the predicted values of curvatures closer to the experimental ones for samples 5-3, 5-4, 7-3, 7-4, 8-3, 8-4, and 9-4.

To further understand the discrepancies between predictions and measurements, sample 5-3 was sectioned along $x = 0$ and $x = 1$ in. and a microscope was used to obtain micro-graphs of polished cross-sections in the neighborhood of the center ($y$=0) and the edges ($y = \pm 0.75$ in. of the specimen). Figure B.6 shows these cross-section coordinates. Specimen 5-3 was selected for sectioning because it was one of the larger specimens and perhaps provided a more typical cross-section region. The six micro-graphs obtained are shown in Figures B.7–B12. These figures show a visible and abrupt interface between the reduced (dark) and unreduced (light) piezoceramic and reveal that this boundary is not smooth. Furthermore, Figures B.8, B.9, B.11, B.12 reveal that at the edges of the specimen the piezoceramic may not be reduced, indicating that the diffusion of oxygen does not reach these areas, and hence preventing the occurrence of the reduction process. This means around the outer edges of the specimens there is no layering effect with the material properties, i.e., the material properties are the same through the entire thickness. To investigate the effects of unreduced edges shown in the micro-graphs, the models described in the main text were modified to account for these manufacturing characteristics. The logic adopted to obtain the total potential energy of the modified rectangular RAINBOW is described in Figure B.13. Essentially, as shown in the upper portion of the figure, RAINBOW with an irregular interface between the reduced and unreduced layers, and an edge effect, shown on the left, is idealized as shown on the right. The lighter and darker shaded materials actually represent volumes of material, as the model has depth into the page and there is an edge effect on all four edges. This idealized model is then analyzed using superposition of three simple parts. Part 1 is the smaller volume consisting of just two layers of material, reduced piezoceramic ($\mathrm{PZT}_r$) and unreduced piezoceramic ($\mathrm{PZT}_o$). Part 2 is the the entire volume and consists of only unreduced material. Part 3 is a smaller volume and

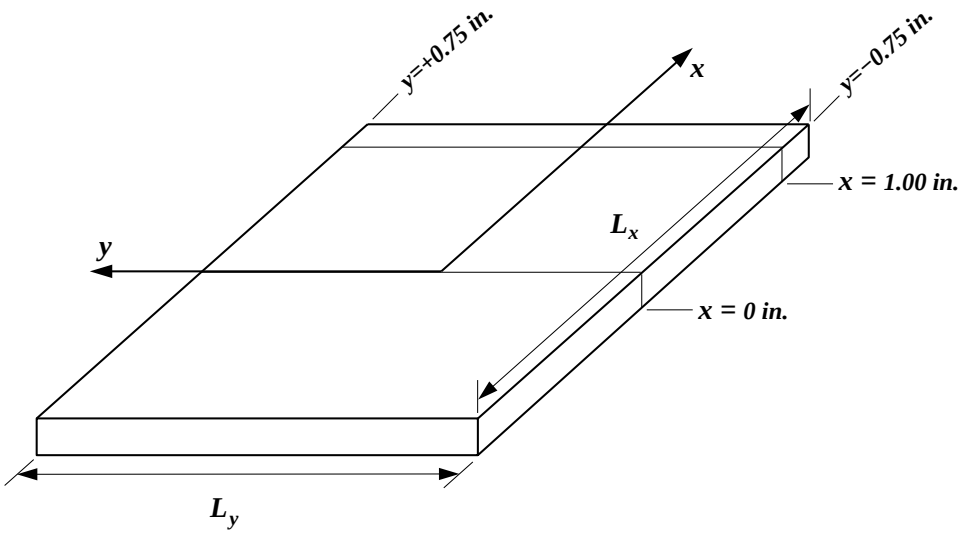


Figure B.6: Cross-section coordinates of RAINBOW sample 5-3.

contains only unreduced material. The total potential energy, Π, for every part of the modified RAINBOW is as defined in Equation 2.15, except the limits of the integral vary accordingly to the part considered, and the A's, B's, and D's in Equations 2.16-2.27 should match the material shown as a subscript of Π. The subscript abbreviation 'RB' is used for RAINBOW. To illustrate results of the modified model, the curvatures in the $x$ and $y$ directions of sample 5-3 and 5-4 were recomputed using $L'_x/L_x$=95%, $L'_y/L_y$=95%, and $\alpha_r = 10.51 \times 10^{-6}\ ^o\text{C}^{-1}$. The result is $\kappa_x^o$ and $\kappa_y^o$ are +0.00165 in.$^{-1}$ and -0.26840 in.$^{-1}$, respectively for sample 5-3, and +0.00359 in.$^{-1}$ and -0.32167 in.$^{-1}$ for sample 5-4. Hence, it can be seen from Table B.3 that the presence of the edge effect makes RAINBOW flatter.

### B.2.2 Disk-style RAINBOW Devices

Twenty disk-style RAINBOW were made at NASA Langley Research Center. The geometric properties of these specimens such as radius, thickness, and reduced layer thickness are tabulated in Table B.4. If the $ZO_2$ number in Table B.4 is 1, it indicates that a zirconate block was placed on the top of the unreduced piezoceramic during reducing process. However, if the number is 0, it indicates no zirconate block was used. The critical value of the radius to thickness ratio, based on these properties and the analysis of Chapter 4, is also reported on Table B.4.

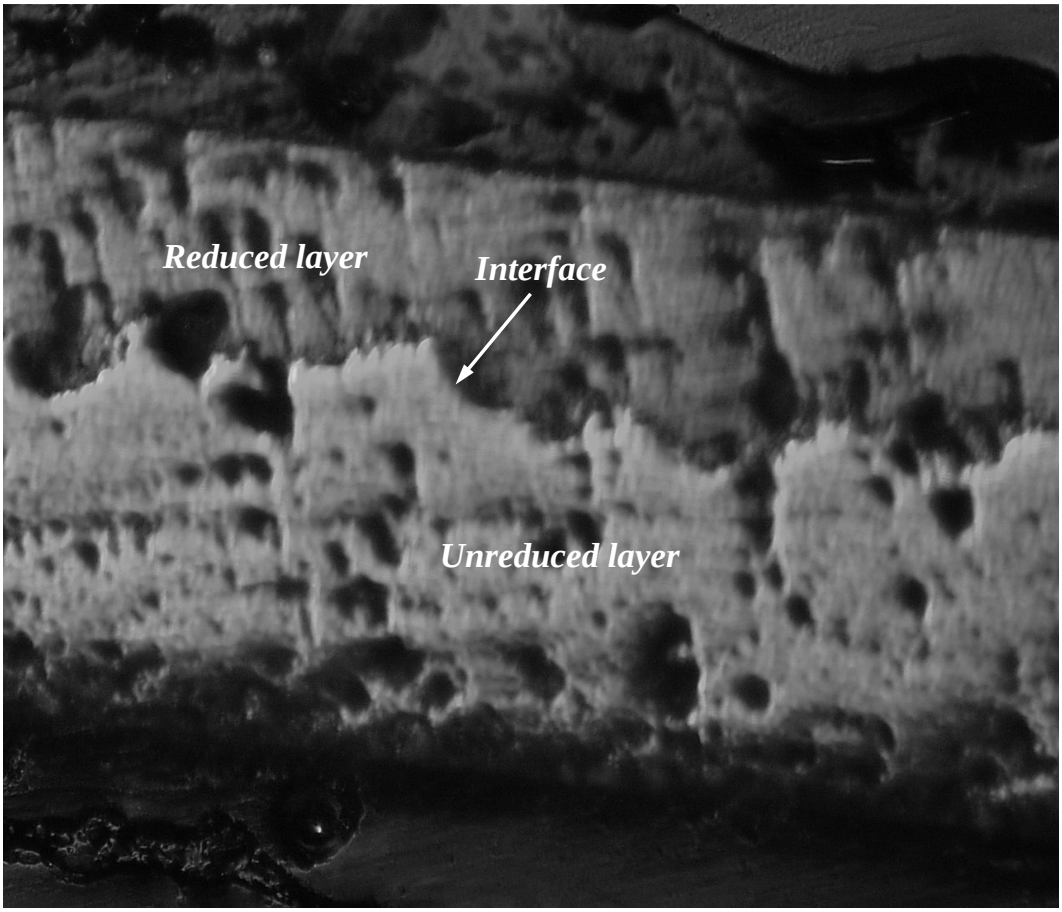


Figure B.7: A polished cross section of RAINBOW sample 5-3 in the neighborhood of $x$ =0 and $y$=0 (magnification factor=100).

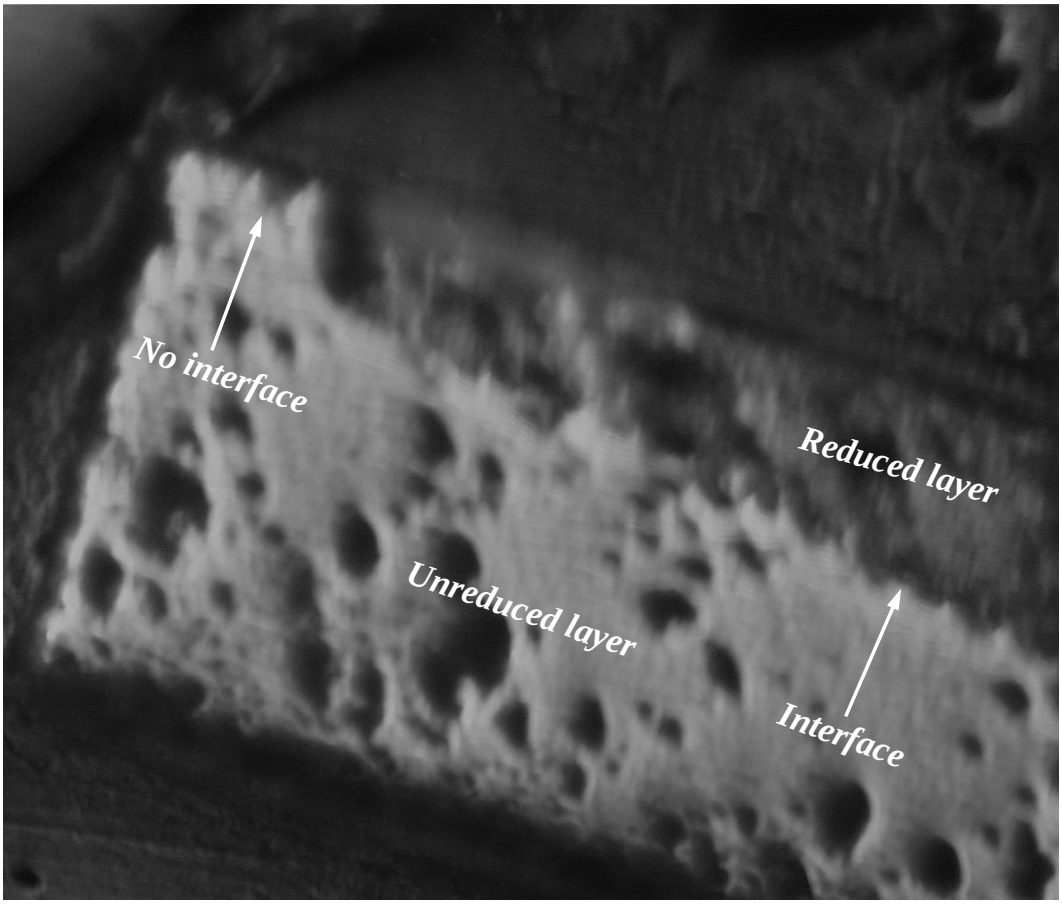


Figure B.8: A polished cross section of RAINBOW sample 5-3 in the neighborhood of $x$ =0 and $y$=+0.75 in. (magnification factor=100).

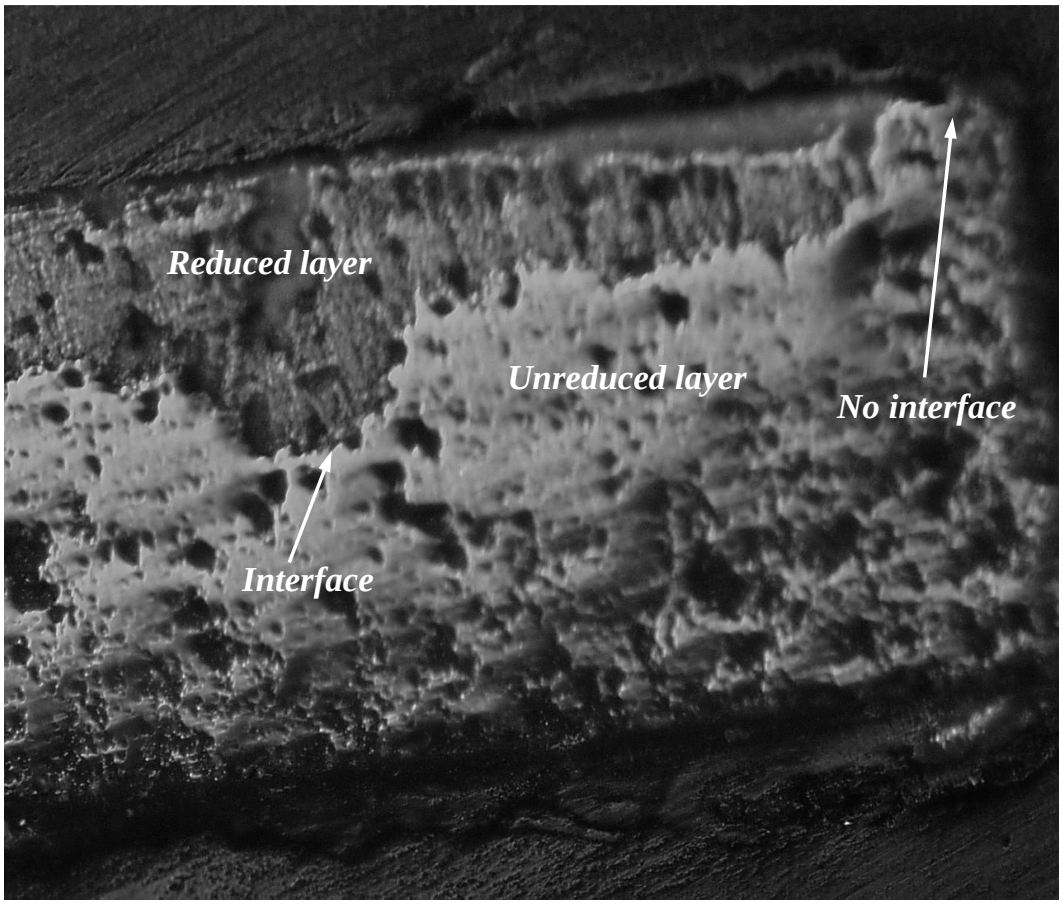


Figure B.9: A polished cross section of RAINBOW sample 5-3 in the neighborhood of $x$ =0 and $y$=-0.75 in. (magnification factor=100).

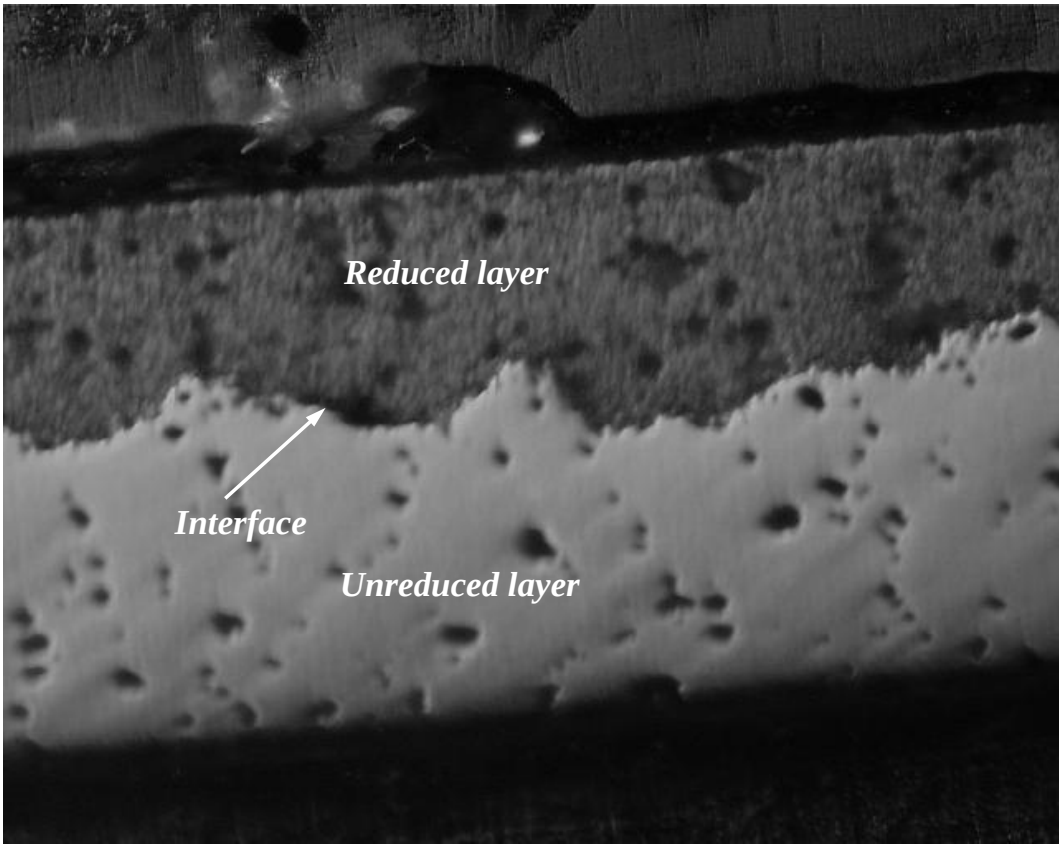


Figure B.10: A polished cross section of RAINBOW sample 5-3 in the neighborhood of $x$ =1.00 in. and $y$=0 (magnification factor=100).

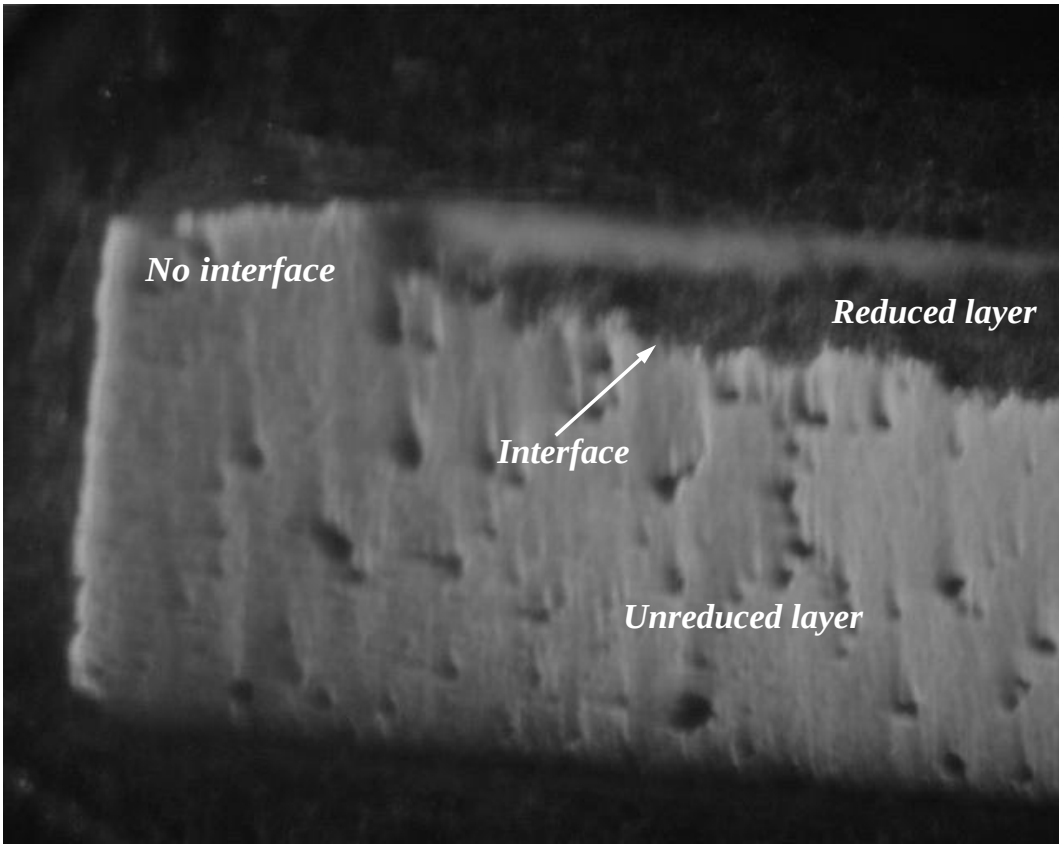


Figure B.11: A polished cross section of RAINBOW sample 5-3 in the neighborhood of $x$ =1.00 in. and $y$=+0.75 in. (magnification factor=100).

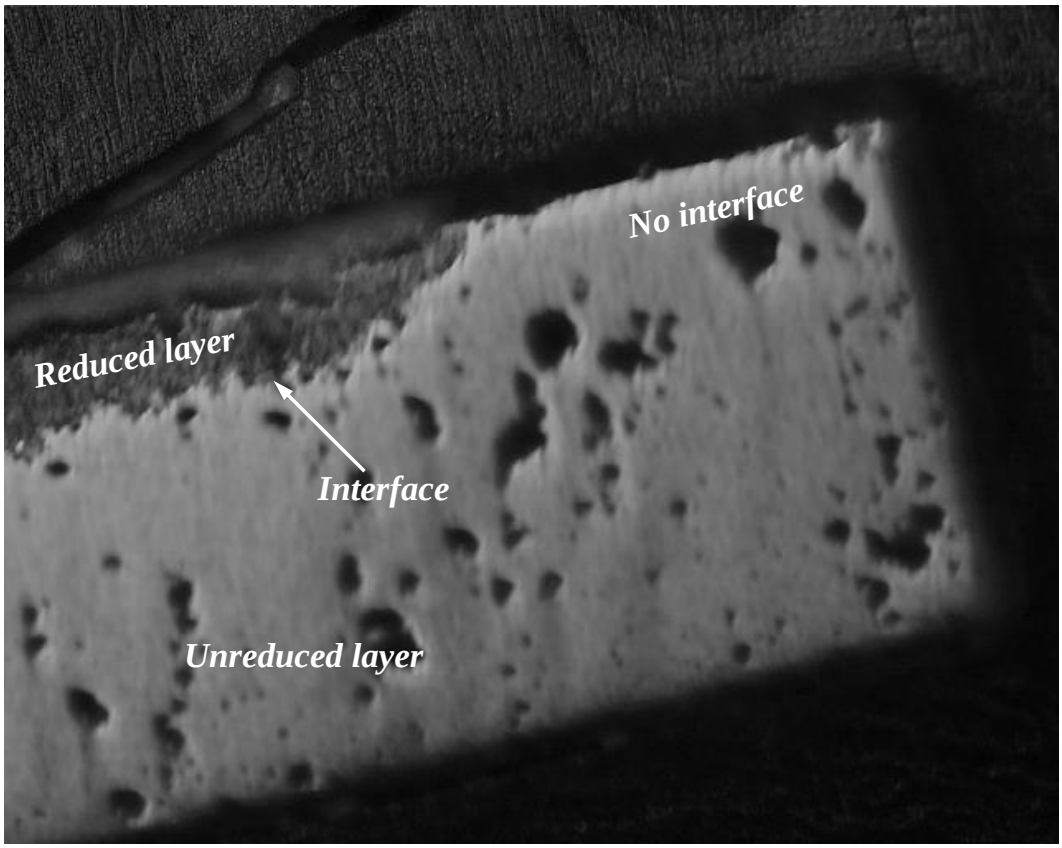


Figure B.12: A polished cross section of RAINBOW sample 5-3 in the neighborhood of $x$ =1.00 in. and $y$=-0.75 in. (magnification factor=100).

Table B.2: Comparison of predicted room-temperature curvatures of various RAINBOW devices with experimental results.

| Specimen | Size $L_x \times L_y$ (in.×in.) | Thickness $H$ (mils) | $L_y/L_x$ | $L_x/H$ | $(L_x/H)_{critical}$ | Reducing Time (minutes) | $H_r/H$ (%) | Measured | | | Computed | |
|---|---|---|---|---|---|---|---|---|---|---|---|---|
| | | | | | | | | $\kappa_x^o$ (in.$^{-1}$) | $\kappa_y^o$ (in.$^{-1}$) | $\kappa_{xy}^o$ (in.$^{-1}$) | $\kappa_x^o$ (in.$^{-1}$) | $\kappa_y^o$ (in.$^{-1}$) |
| 5-3 | 2.5×1.5 | 15 | 1.67 | 167 | $< 81$ | 45 | 34 | -0.01053 | -0.30711 | -0.01211 | -0.00312 | -0.22594 |
| 5-4 | 2.5×1.5 | 15 | 1.67 | 167 | $< 75$ | 68 | 51 | -0.01009 | -0.31519 | -0.00488 | -0.00271 | -0.27279 |
| 6-1 | 1×0.25 | 15 | 4 | 67 | 82 | 45 | 34 | -0.12963 | - | - | -0.13239 | -0.13239 |
| 6-2 | 1×0.25 | 15 | 4 | 67 | 76 | 68 | 51 | -0.19519 | - | - | -0.15161 | -0.15161 |
| 6-3 | 1×0.5 | 15 | 2 | 67 | 81 | 45 | 34 | -0.12645 | -0.34622 | -0.01182 | -0.13130 | -0.13130 |
| 6-4 | 1×0.5 | 15 | 2 | 67 | 75 | 68 | 51 | -0.27165 | -0.33596 | +0.00067 | -0.15021 | -0.15021 |
| 7-1 | 2.5×0.25 | 15 | 10 | 167 | 82 | 45 | 34 | -0.07561 | - | - | -0.22553 | -0.00353 |
| 7-2 | 2.5×0.25 | 15 | 10 | 167 | 76.5 | 68 | 51 | -0.12897 | - | - | -0.27243 | -0.00307 |
| 7-3 | 0.5×0.5 | 15 | 1 | 33 | 69 | 45 | 34 | -0.26589 | -0.25327 | +0.01053 | -0.15886 | -0.15886 |
| 7-4 | 0.5×0.5 | 15 | 1 | 33 | 64 | 68 | 51 | -0.34014 | -0.33002 | -0.00110 | -0.18828 | -0.18828 |
| 8-1 | 1×0.25 | 10 | 4 | 100 | 82 | 30 | 34 | -0.11707 | - | - | -0.29727 | -0.04633 |
| 8-2 | 1×0.25 | 10 | 4 | 100 | 76 | 45 | 51 | -0.19551 | - | - | -0.37461 | -0.03865 |
| 8-3 | 1×0.5 | 10 | 2 | 100 | 81 | 30 | 34 | -0.06367 | -0.41677 | -0.00385 | -0.04334 | -0.30026 |
| 8-4 | 1×0.5 | 10 | 2 | 100 | 75 | 45 | 51 | -0.09365 | -0.40927 | +0.02048 | -0.03629 | -0.37697 |
| 9-3 | 0.5×0.5 | 10 | 1 | 50 | 69 | 30 | 34 | -0.24200 | -0.24103 | -0.00088 | -0.21095 | -0.21095 |
| 9-4 | 0.5×0.5 | 10 | 1 | 50 | 64 | 45 | 51 | -0.22839 | -0.22772 | -0.00934 | -0.24365 | -0.24365 |

Table B.3: Effect of increasing $\alpha_r$ by 25% on the predicted room-temperature curvatures of various RAINBOW devices.

| Specimen | Size $L_x \times L_y$ (in.×in.) | Thickness $H$ (mils) | $L_y/L_x$ | $L_x/H$ | $H_r/H$ (%) | Measured | | | Computed $\alpha_r = 8.41 \times 10^{-6}\ ^o\text{C}^{-1}$ | | Computed $\alpha_r = 10.51 \times 10^{-6}\ ^o\text{C}^{-1}$ | |
|---|---|---|---|---|---|---|---|---|---|---|---|---|
| | | | | | | $\kappa_x^o$ (in.$^{-1}$) | $\kappa_y^o$ (in.$^{-1}$) | $\kappa_{xy}^o$ (in.$^{-1}$) | $\kappa_x^o$ (in.$^{-1}$) | $\kappa_y^o$ (in.$^{-1}$) | $\kappa_x^o$ (in.$^{-1}$) | $\kappa_y^o$ (in.$^{-1}$) |
| 5-3 | 2.5×1.5 | 15 | 1.67 | 167 | 34 | -0.01053 | -0.30711 | -0.01211 | -0.00312 | -0.22594 | -0.00232 | -0.30343 |
| 5-4 | 2.5×1.5 | 15 | 1.67 | 167 | 51 | -0.01009 | -0.31519 | -0.00488 | -0.00271 | -0.27279 | -0.00203 | -0.36572 |
| 6-1 | 1×0.25 | 15 | 4 | 67 | 34 | -0.12963 | - | - | -0.13239 | -0.13239 | -0.16103 | -0.16103 |
| 6-2 | 1×0.25 | 15 | 4 | 67 | 51 | -0.19519 | - | - | -0.15161 | -0.15161 | -0.21895 | -0.14880 |
| 6-3 | 1×0.5 | 15 | 2 | 67 | 34 | -0.12645 | -0.34622 | -0.01182 | -0.13130 | -0.13130 | -0.15942 | -0.15942 |
| 6-4 | 1×0.5 | 15 | 2 | 67 | 51 | -0.27165 | -0.33596 | +0.00067 | -0.15021 | -0.15021 | -0.12886 | -0.23889 |
| 7-1 | 2.5×0.25 | 15 | 10 | 167 | 34 | -0.07561 | - | - | -0.22553 | -0.00353 | -0.30313 | -0.00263 |
| 7-2 | 2.5×0.25 | 15 | 10 | 167 | 51 | -0.12897 | - | - | -0.27243 | -0.00307 | -0.36545 | -0.00229 |
| 7-3 | 0.5×0.5 | 15 | 1 | 33 | 34 | -0.26589 | -0.25327 | +0.01053 | -0.15886 | -0.15886 | -0.20592 | -0.20592 |
| 7-4 | 0.5×0.5 | 15 | 1 | 33 | 51 | -0.34014 | -0.33002 | -0.00110 | -0.18828 | -0.18828 | -0.242197 | -0.242197 |
| 8-1 | 1×0.25 | 10 | 4 | 100 | 34 | -0.11707 | - | - | -0.29727 | -0.04633 | -0.31021 | -0.03714 |
| 8-2 | 1×0.25 | 10 | 4 | 100 | 51 | -0.19551 | - | - | -0.37461 | -0.03865 | -0.39014 | -0.02919 |
| 8-3 | 1×0.5 | 10 | 2 | 100 | 34 | -0.06367 | -0.41677 | -0.00385 | -0.04334 | -0.30026 | -0.03242 | -0.31493 |
| 8-4 | 1×0.5 | 10 | 2 | 100 | 51 | -0.09365 | -0.40927 | +0.02048 | -0.03629 | -0.37697 | -0.02474 | -0.39460 |
| 9-3 | 0.5×0.5 | 10 | 1 | 50 | 34 | -0.24200 | -0.24103 | -0.00088 | -0.21095 | -0.21095 | -0.20487 | -0.20487 |
| 9-4 | 0.5×0.5 | 10 | 1 | 50 | 51 | -0.22839 | -0.22772 | -0.00934 | -0.24365 | -0.24365 | -0.23541 | -0.23541 |

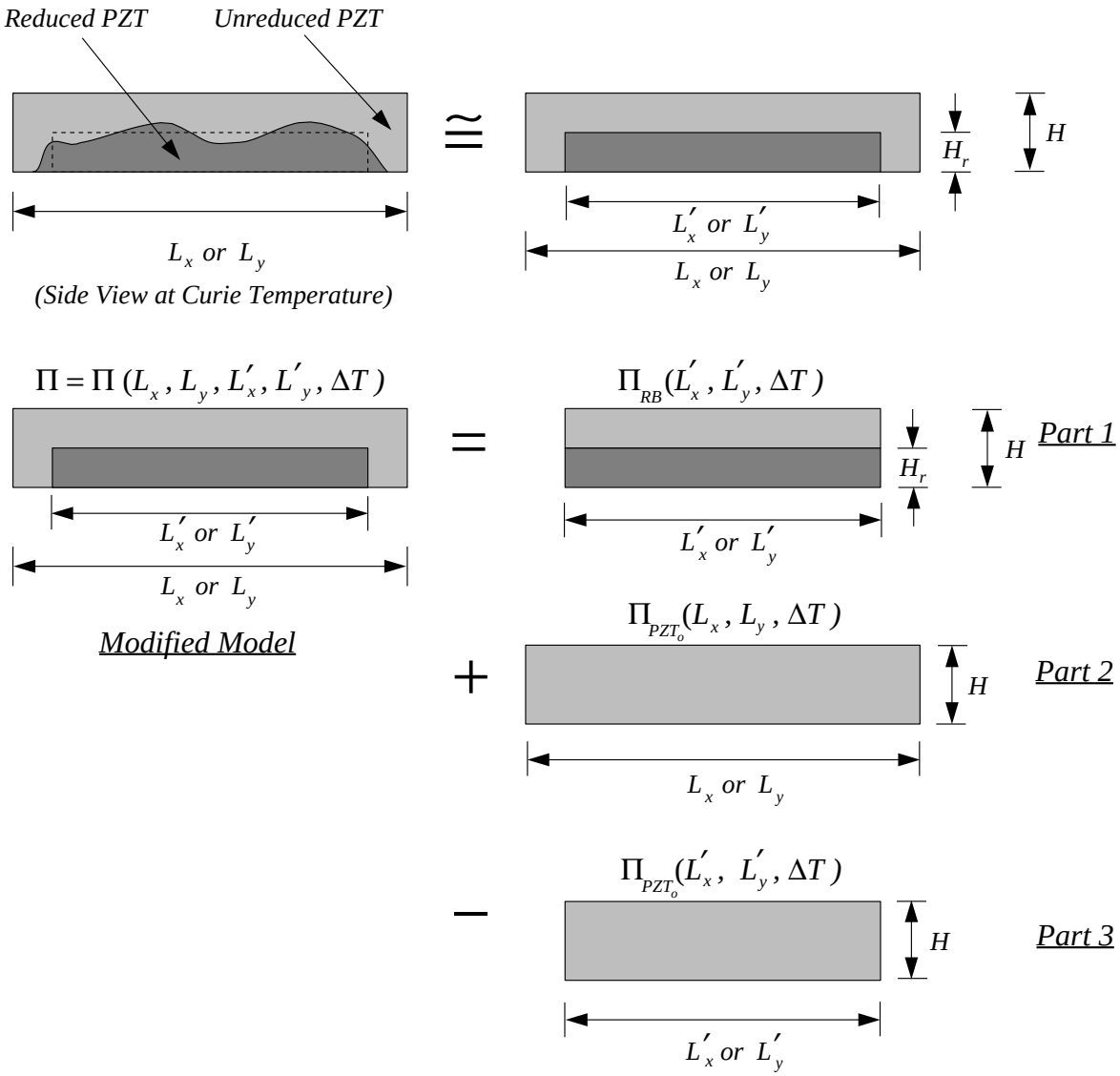


Figure B.13: Description of the modified model to account for manufacturing defects of rectangular RAINBOW.

Table B.4: Geometric properties of various disk-style RAINBOW devices.

| Specimen | Radius $R$ (in.) | Thickness $H$ (mils) | $R/H$ | $(R/H)_{critical}$ | Reducing Time (minutes) | $H_r/H$ (%) | $ZO_2$ Used | Graphite Block Diameter (in.) |
|---|---|---|---|---|---|---|---|---|
| 1-1 | 0.5 | 10 | 50 | 44.3 | 30 | 34 | 1 | 2 |
| 1-2 | 0.5 | 10 | 50 | 41.4 | 45 | 51 | 1 | 2 |
| 1-3 | 0.5 | 10 | 50 | 44.3 | 30 | 34 | 0 | 2 |
| 1-4 | 0.5 | 10 | 50 | 41.4 | 45 | 51 | 0 | 2 |
| 2-1 | 0.5 | 15 | 33.3 | 44.3 | 45 | 34 | 0 | 2 |
| 2-2 | 0.5 | 15 | 33.3 | 41.4 | 68 | 51 | 0 | 2 |
| 2-3 | 0.5 | 15 | 33.3 | 44.3 | 45 | 34 | 1 | 2 |
| 2-4 | 0.5 | 15 | 33.3 | 41.4 | 68 | 51 | 1 | 2 |
| 3-1 | 0.5 | 20 | 25 | 44.3 | 60 | 34 | 1 | 2 |
| 3-2 | 0.5 | 20 | 25 | 41.4 | 90 | 51 | 1 | 2 |
| 3-3 | 0.75 | 15 | 50 | 44.3 | 45 | 34 | 1 | 4 |
| 3-4 | 0.75 | 15 | 50 | 41.4 | 68 | 51 | 1 | 4 |
| 4-1 | 0.75 | 20 | 37.5 | 44.3 | 60 | 34 | 1 | 4 |
| 4-2 | 0.75 | 20 | 37.5 | 41.4 | 90 | 51 | 1 | 4 |
| 4-3 | 1.0 | 15 | 66.7 | 44.3 | 45 | 34 | 1 | 4 |
| 4-4 | 1.0 | 15 | 66.7 | 41.4 | 68 | 51 | 1 | 4 |
| 5-1 | 1.0 | 20 | 50 | 44.3 | 60 | 34 | 1 | 4 |
| 5-2 | 1.0 | 20 | 50 | 41.4 | 90 | 51 | 1 | 4 |
| 10-1 | 0.25 | 15 | 16.7 | 44.3 | 45 | 34 | 1 | 2 |
| 10-2 | 0.25 | 15 | 16.7 | 41.4 | 68 | 51 | 1 | 2 |

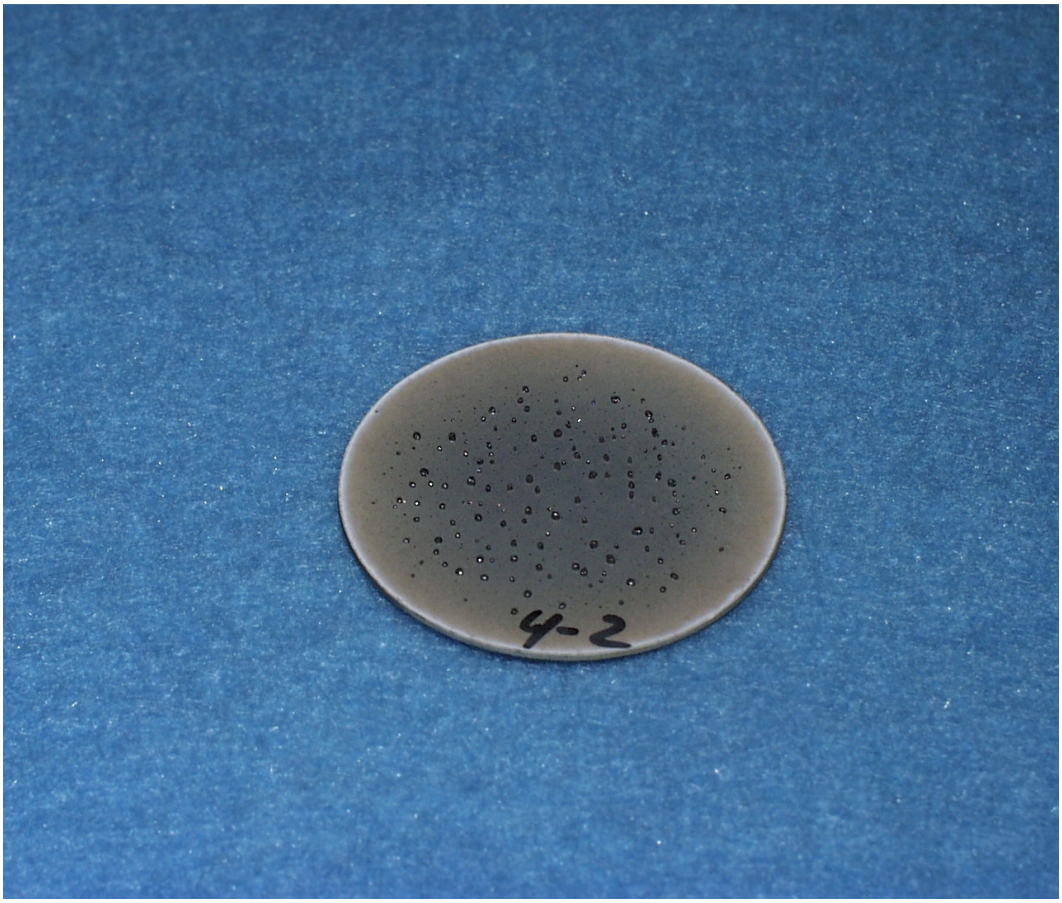


Figure B.14: Photo of RAINBOW sample 4-2 (lead beads visible).

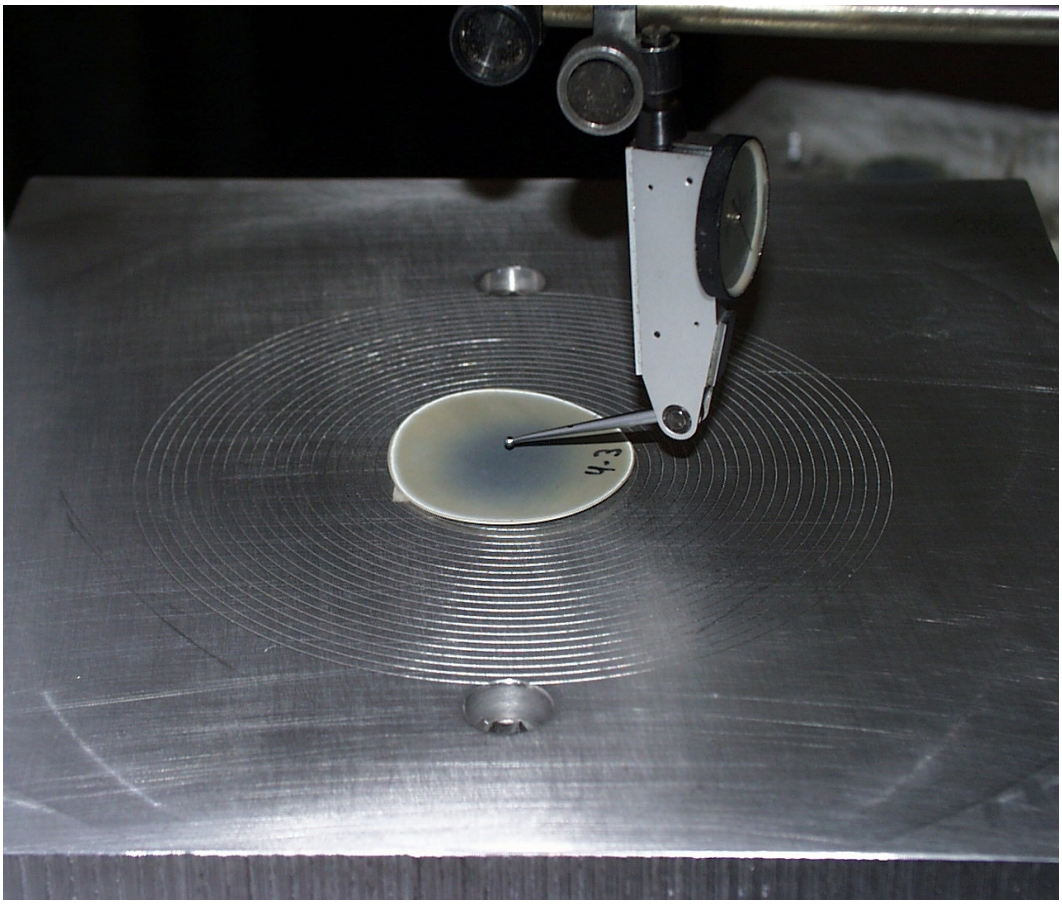


Figure B.15: Measurement of out-of-plane displacements for a 1 in. disk-style RAINBOW (sample 4-3).

To measure the room-temperature out-of-plane displacements of each of the manufactured disk-style RAINBOW, the device was sanded lightly on the reduced side to remove the deposit of lead beads. Again, the vertical milling machine set-up was used to measure values of the out-of-plane displacements in the $r$-$\theta$ coordinate system on the concave side of the specimens. Figure B.14 shows the concave side of a disk-style RAINBOW device. The lead beads, which were a result of the reducing process, are visible. These also occurred on the rectangular specimens, but since the convex side of those specimens was measured, the presence of the beads did not hinder displacement measurements. As shown In Figure B.15, the disk-style RAINBOW was centered with respect to the concentric circles of the measurement fixture. The out-of-plane displacements were measured at every $30^o$ for $r$=0.125 in. and $r$=0.25 in., $15^o$ for $r$=0.375 in. and $r$=0.5 in., and $7.5^o$ for $r$=0.625 in., $r$=0.75 in., $r$=0.875 in. and $r$=1.0 in. Once, the out-of-plane displacements were measured, they were fit to a Fourier series of the form

$$\begin{aligned} w^o(r,\theta) &= \bar{a}_{00} + \bar{a}_{11} r\cos(\theta) + \bar{b}_{11} r\sin(\theta) \\ &\quad + \bar{a}_{20} r^2 + \bar{a}_{30} r^3 + \bar{a}_{40} r^4 + \bar{a}_{50} r^5 + \bar{a}_{60} r^6 \\ &\quad + (\bar{a}_{21} r^2 + \bar{a}_{32} r^3 + \bar{a}_{41} r^4 + \bar{a}_{51} r^5 + \bar{a}_{61} r^6)\cos(\theta) \\ &\quad + (\bar{b}_{21} r^2 + \bar{b}_{32} r^3 + \bar{b}_{41} r^4 + \bar{b}_{51} r^5 + \bar{b}_{61} r^6)\sin(\theta) \\ &\quad + (\bar{a}_{22} r^2 + \bar{a}_{32} r^3 + \bar{a}_{42} r^4 + \bar{a}_{52} r^5 + \bar{a}_{62} r^6)\cos(2\theta) \\ &\quad + (\bar{b}_{22} r^2 + \bar{b}_{32} r^3 + \bar{b}_{42} r^4 + \bar{b}_{52} r^5 + \bar{b}_{62} r^6)\sin(2\theta) \\ &\quad + (\bar{a}_{23} r^2 + \bar{a}_{32} r^3 + \bar{a}_{43} r^4 + \bar{a}_{53} r^5 + \bar{a}_{63} r^6)\cos(3\theta) \\ &\quad + (\bar{b}_{23} r^2 + \bar{b}_{32} r^3 + \bar{b}_{43} r^4 + \bar{b}_{53} r^5 + \bar{b}_{63} r^6)\sin(3\theta) \\ &\quad + (\bar{a}_{24} r^2 + \bar{a}_{34} r^3 + \bar{a}_{44} r^4 + \bar{a}_{54} r^5 + \bar{a}_{64} r^6)\cos(4\theta) \\ &\quad + (\bar{b}_{24} r^2 + \bar{b}_{34} r^3 + \bar{b}_{44} r^4 + \bar{b}_{54} r^5 + \bar{b}_{64} r^6)\sin(4\theta) \end{aligned} \tag{B.2}$$

A least-square fit of the measured out-of-plane displacements was used to determine the $\bar{a}_{ij}$ and $\bar{b}_{ij}$ coefficients of the above approximation. This approximation contains general Fourier series terms (sines and cosines) up to order 4 to account for any irregularities in the room-temperature shapes of RAINBOW due to manufacturing defects not accountable by using just a cosine series. The approximation also accounts for rigid body rotation and displacement of the specimen relative to

the measurement fixture. For comparison, Figures B.16–B.34 illustrate the predicted and measured room-temperature shapes of disk-style RAINBOW samples listed in Table B.4. Illustrating the deformed shape, as opposed to just comparing curvature numbers as was done for the rectangular RAINBOW, is done because of the more complicated expressions for curvature for the disk-style RAINBOW devices. No experimental results are available for sample 3-2, as cracks developed in the device and caused it to break.

With the exception of Figures B.16, B.21, and B.23 (samples 1-1, 2-2, and 2-4, respectively), the figures indicate that there is a qualitative agreement between the room-temperature shapes predicted using the model of Chapter 4 and the manufactured ones. To study the cross-sectional characteristics, sample 4-2 was cut along the diameter aligned with the $x$ direction ($\theta = 0,\ \pi$) and micro-graphs of polished cross-sections at the rim (outer edge) of RAINBOW and at the center were taken. The three micro-graphs are shown in Figures B.35-B.37. Figure B.37 reveals that at the edge ($r \approx R$) the piezoceramic is not layered. Furthermore, Figures B.35 and B.36 show that the reduced layer thickness is irregular, which is in contrast with the assumption adopted in the model developed in Chapter 4. It is interesting to note both RAINBOW samples 1-1 and 1-3 have the same size, thickness, and reducing time, but the $ZO_2$ number is different, indicating that the reducing process was different. Surprisingly, the manufactured room-temperature shape of sample 1-1 is a domed-shape but the shape of sample 1-3 is a near-cylindrical shape, as shown in Figures B.16 and B.18. More surprisingly, Table B.4 indicates that samples 1-1 and 1-3 happen to have a radius to thickness ratio of $R/H$=50, which is close to the critical value 44.3. Any irregularities in the manufacturing, such as inconsistencies in the reduced layer thickness, can change the character of the room-temperature shape for RAINBOW with $R/H$ close to the critical value. Indeed, the room-temperature shape of sample 1-1 is re-predicted using a reduced layer thickness to total thickness ratio of $H_r/H$=24% to represent the influence of the irregularities in reduced layer thickness, and is depicted in Figure B.38. Figure B.38 indicates that the new predicted room-temperature shape is a domed-shape. This matches the character of the manufactured room-temperature shape. This leads credibility to the idea that the irregularities in reduced layer thickness have the effect of an overall smaller reduced layer. Since the reducing time of samples 1-2 and 1-4 is longer than for 1-1 and 1-3, their radius to thickness ratio $R/H$=50 is somewhat further from the critical value of 41.4. Therefore, thickness irregularities would not have as much influence. Figures B.16, B.17, and

B.20–B.23 suggest that an increase in the reduced layer thickness, can change the character of the manufactured room-temperature shape from a domed-shape to a non-axisymmetric shape.

The qualitative discrepancies between the predicted shape and the manufactured shape was originally thought to be due to the fact that the value of $\alpha_r$ used in the model was lower than the actual one. To investigate the influence of $\alpha_r$ on the disk-style RAINBOW, the value of $\alpha_r$ used in the model is increased by 25%, and the new predicted room-temperature shape was compared with the manufactured shapes of samples 2-2 and 2-4 in Figures B.39 and B.40, respectively. Comparing these figures with with Figures B.21 and B.23, respectively, it was concluded that an increase of 25% in the thermal expansion coefficient of the reduced piezoceramic, $\alpha_r$, does not cause the predicted room-temperature shape of samples 2.2 and 2.4 to change character. The configuration remains domed-shape. This is due to the fact that the radius to thickness ratio for samples 2-2 and 2-4 is 33.3, a value lower than the critical value of 41.3. By further examining samples 2.2 and 2.4, it was found that the reduced layer was not axisymmetric with respect to the geometric center of the devices, resulting in an effective orthotropy of the RAINBOW material. Since the model developed in Chapter 4 accounts for orthotropic materials, an effective orthotropy of 20% in the reduced layer was introduced by increasing the extensional modulus and coefficient of thermal expansion by 20% in the $x$ direction relative to their values in the $y$ direction. The resulting new predicted room-temperature shapes of samples 2.2 and 2.4 are shown in Figures B.41 and B.42, respectively. These figures indicate that the qualitative agreement between the new predicted room-temperature shapes and the manufactured ones is, in general, good.

Finally, to model the unreduced edge effects, the present model was modified using the logic shown in Figure B.43. To illustrate results of the modified model, the room-temperature shape of sample 4.2 is re-predicted using $R'/R$=90% and it is depicted in Figure B.44. A comparison of Figures B.28 and B.44 indicates that the presence of unreduced edges causes a flattening in RAINBOW sample, as it did in the rectangular RAINBOW case.

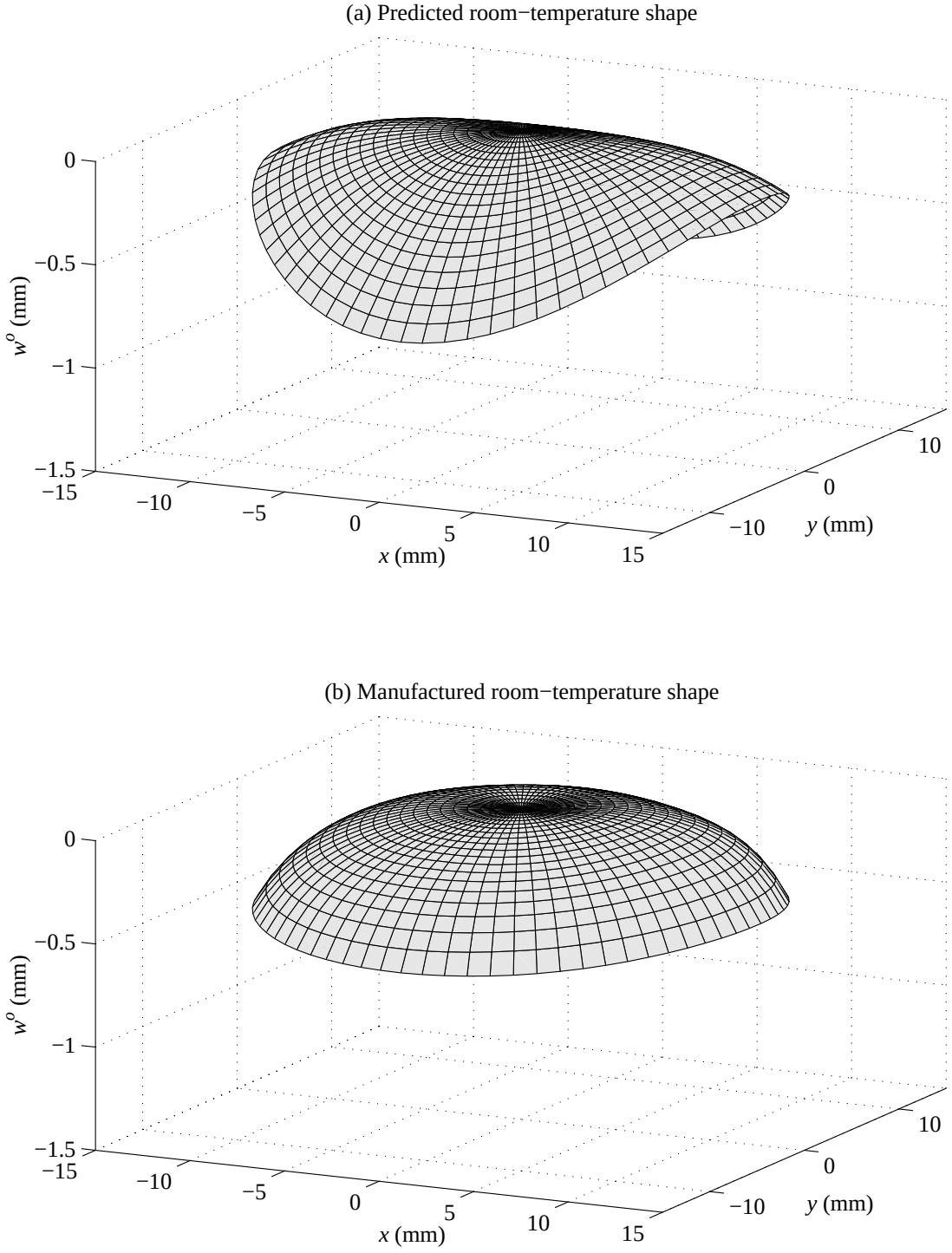


Figure B.16: Comparison of predicted and manufactured room-temperature shapes of RAINBOW sample 1-1.

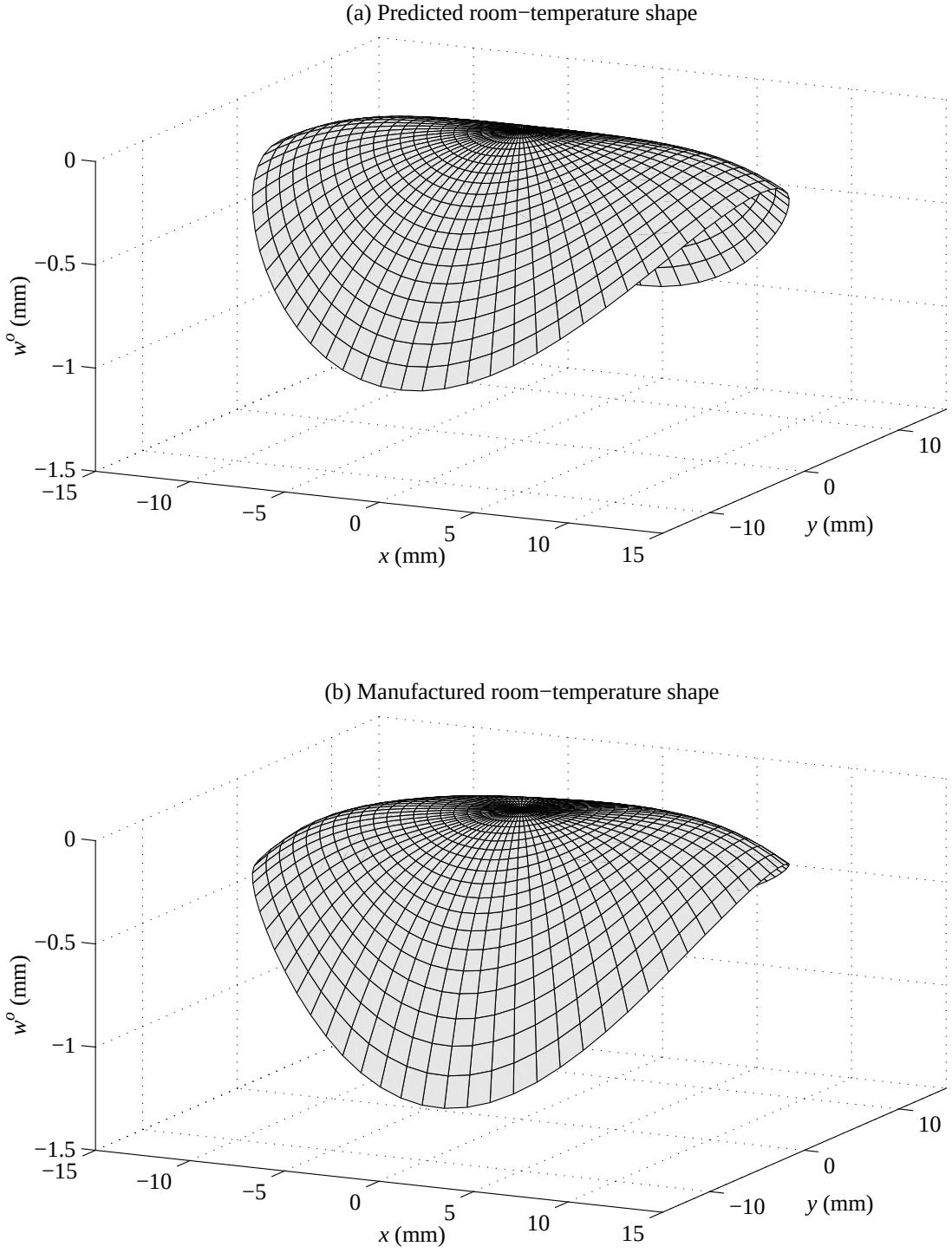


Figure B.17: Comparison of predicted and manufactured room-temperature shapes of RAINBOW sample 1-2.

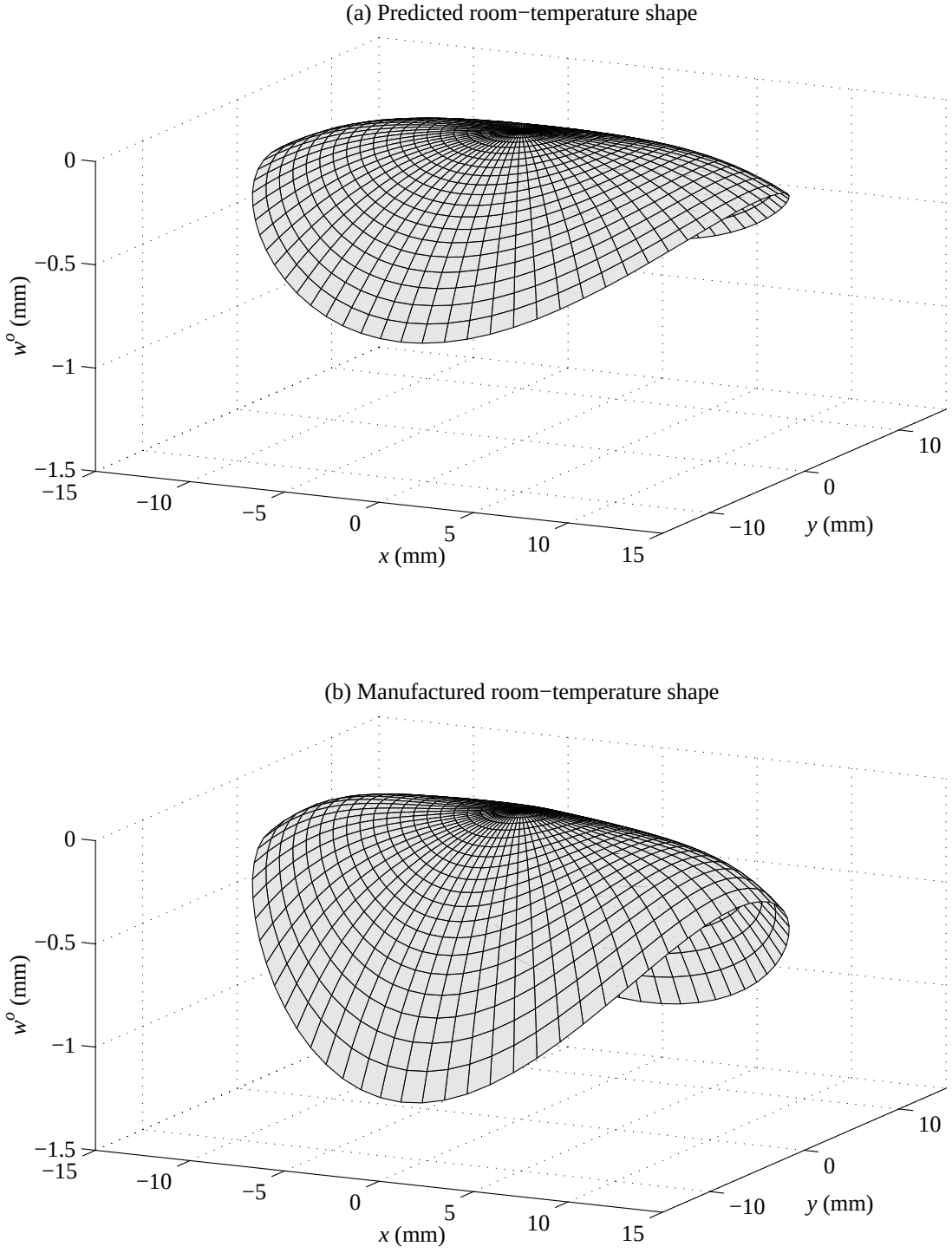


Figure B.18: Comparison of predicted and manufactured room-temperature shapes of RAINBOW sample 1-3.

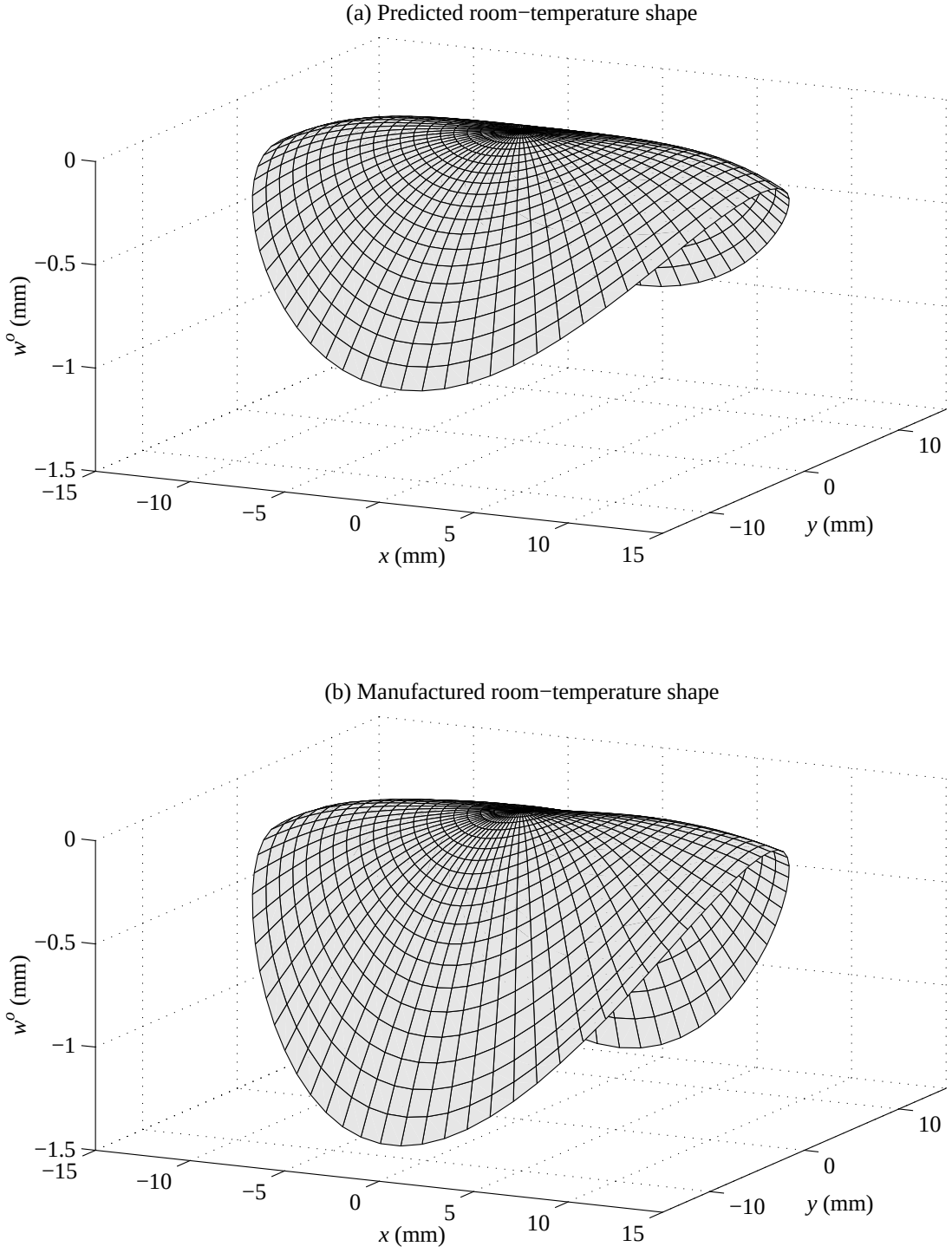


Figure B.19: Comparison of predicted and manufactured room-temperature shapes of RAINBOW sample 1-4.

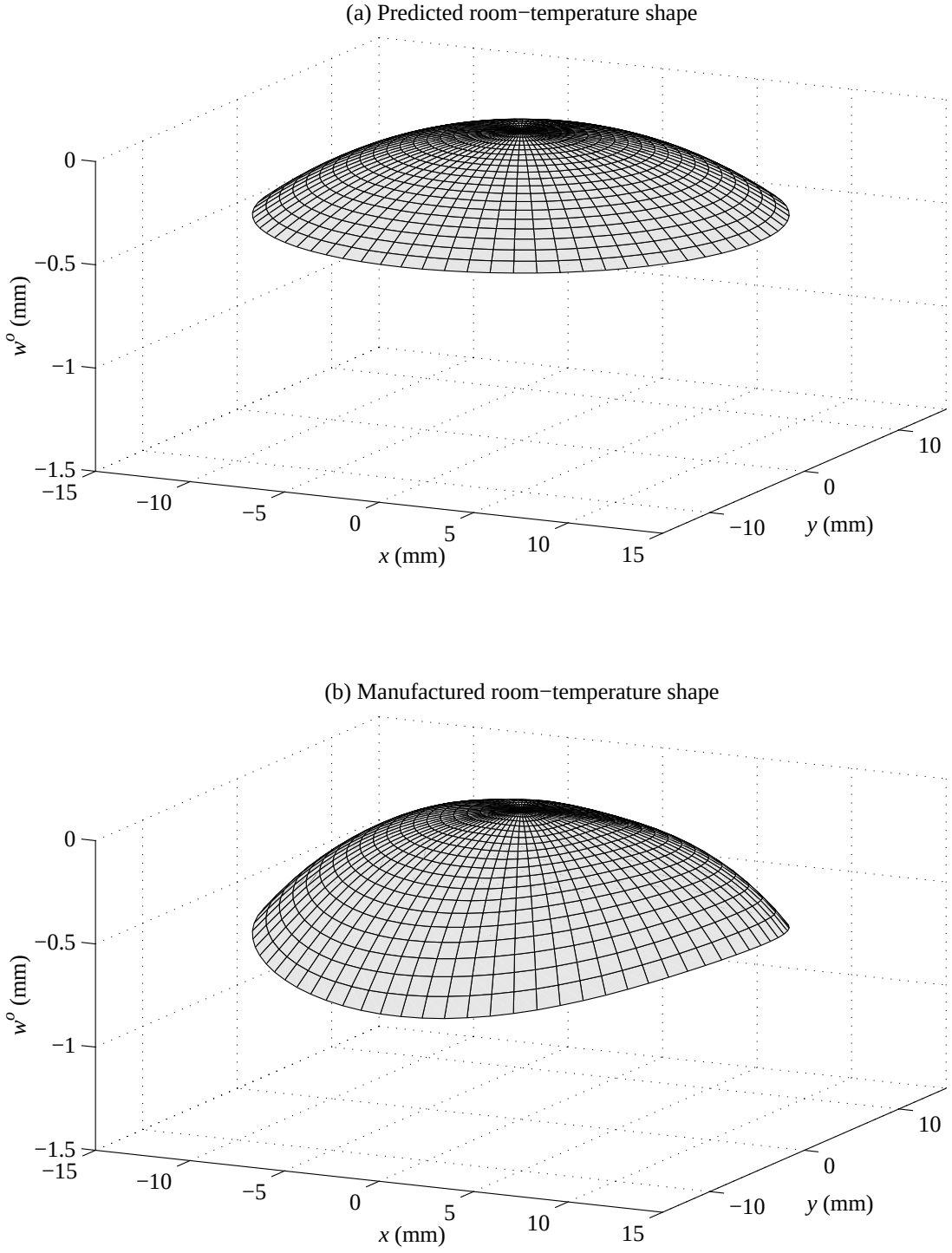


Figure B.20: Comparison of predicted and manufactured room-temperature shapes of RAINBOW sample 2-1.

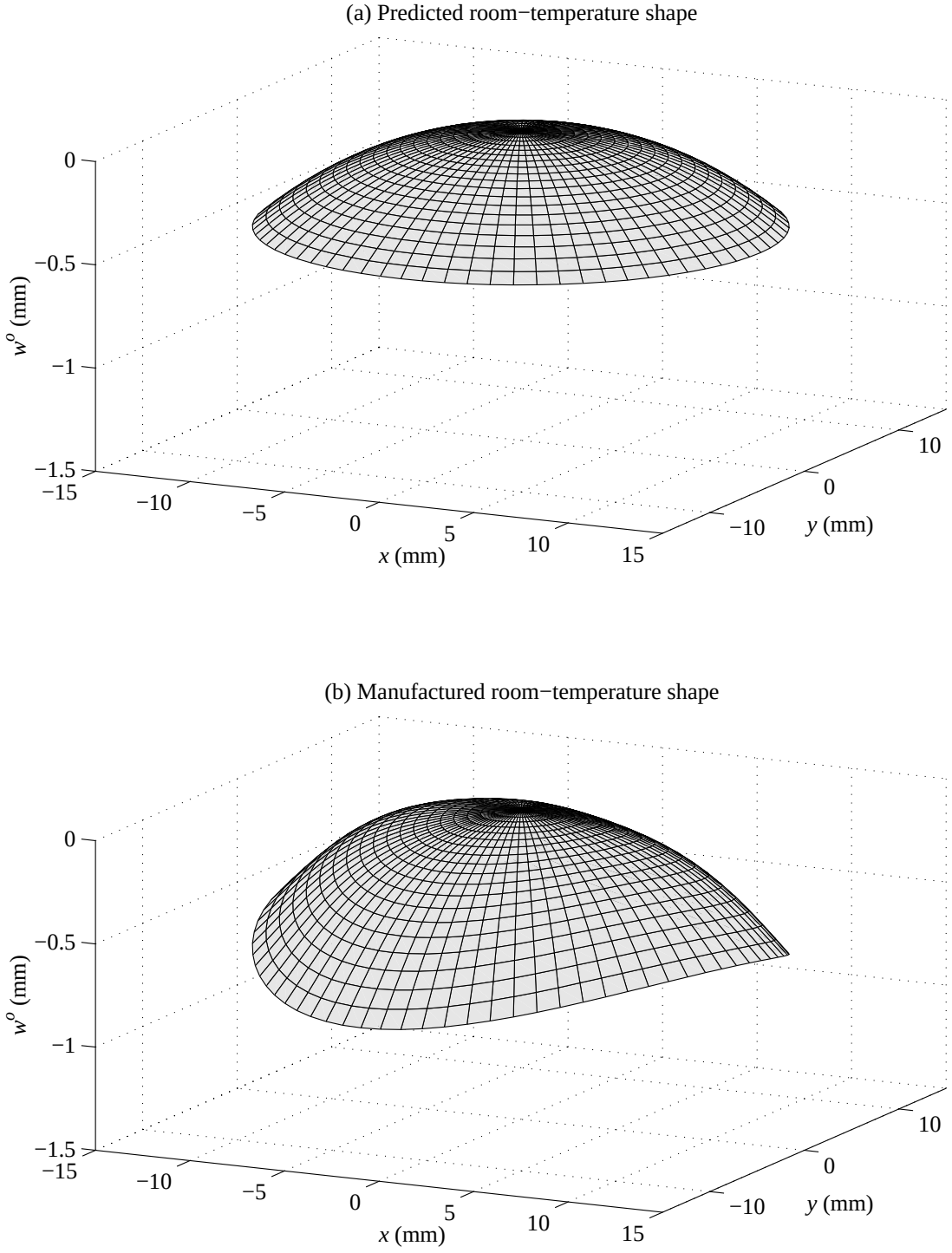


Figure B.21: Comparison of predicted and manufactured room-temperature shapes of RAINBOW sample 2-2.

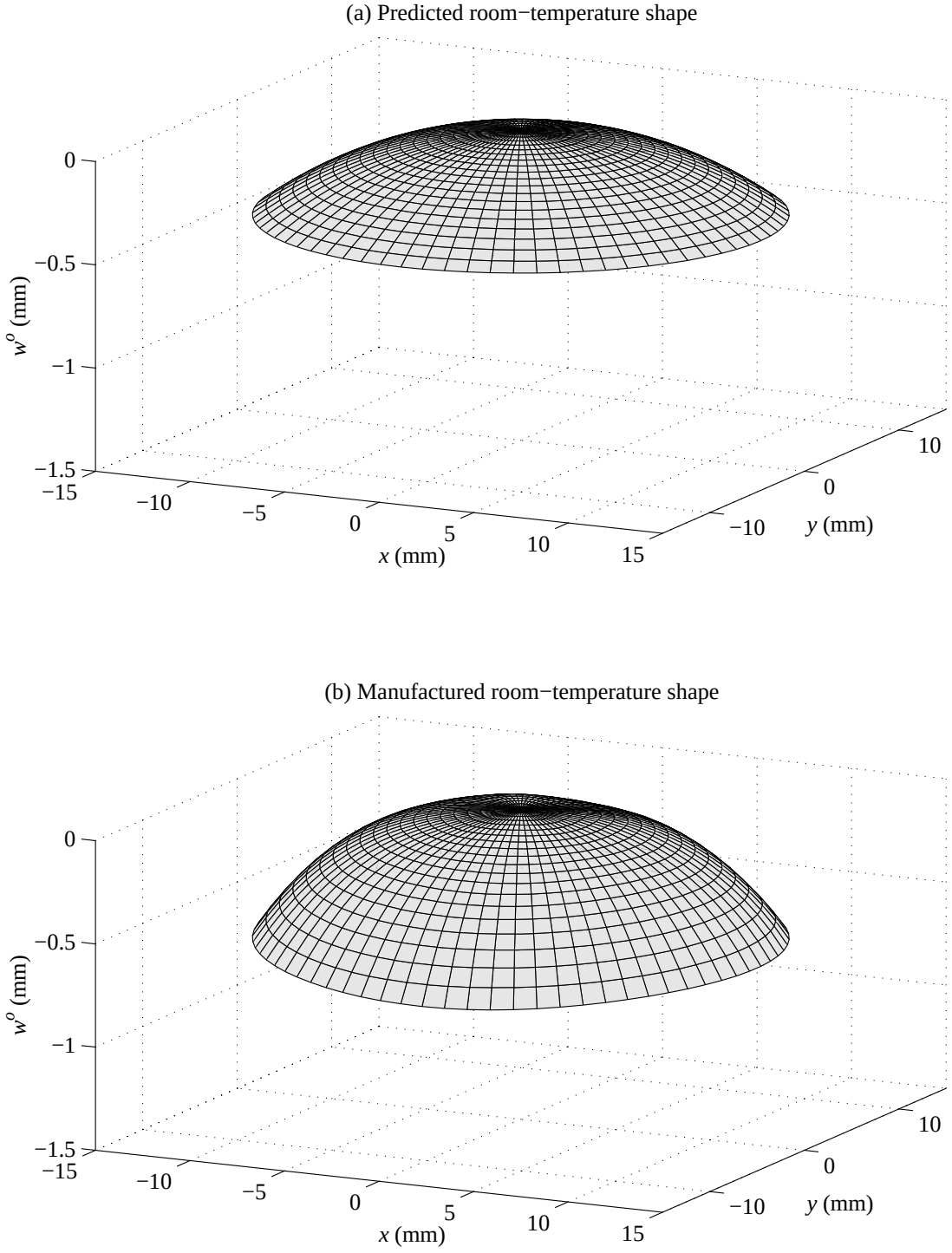


Figure B.22: Comparison of predicted and manufactured room-temperature shapes of RAINBOW sample 2-3.

(a) Predicted room−temperature shape

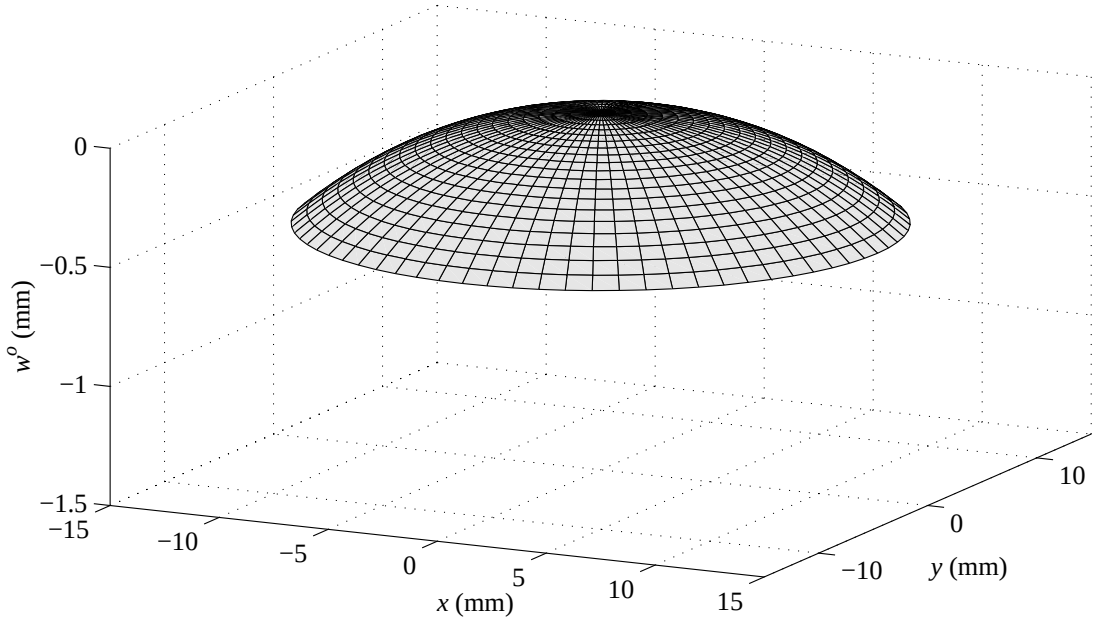


(b) Manufactured room−temperature shape

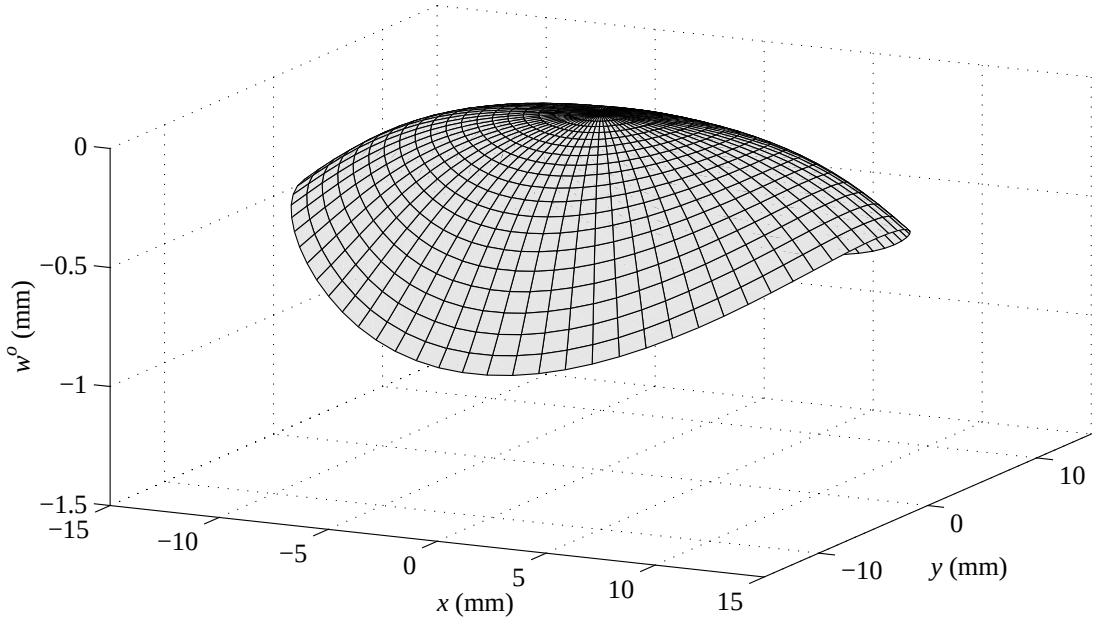


Figure B.23: Comparison of predicted and manufactured room-temperature shapes of RAINBOW sample 2-4.

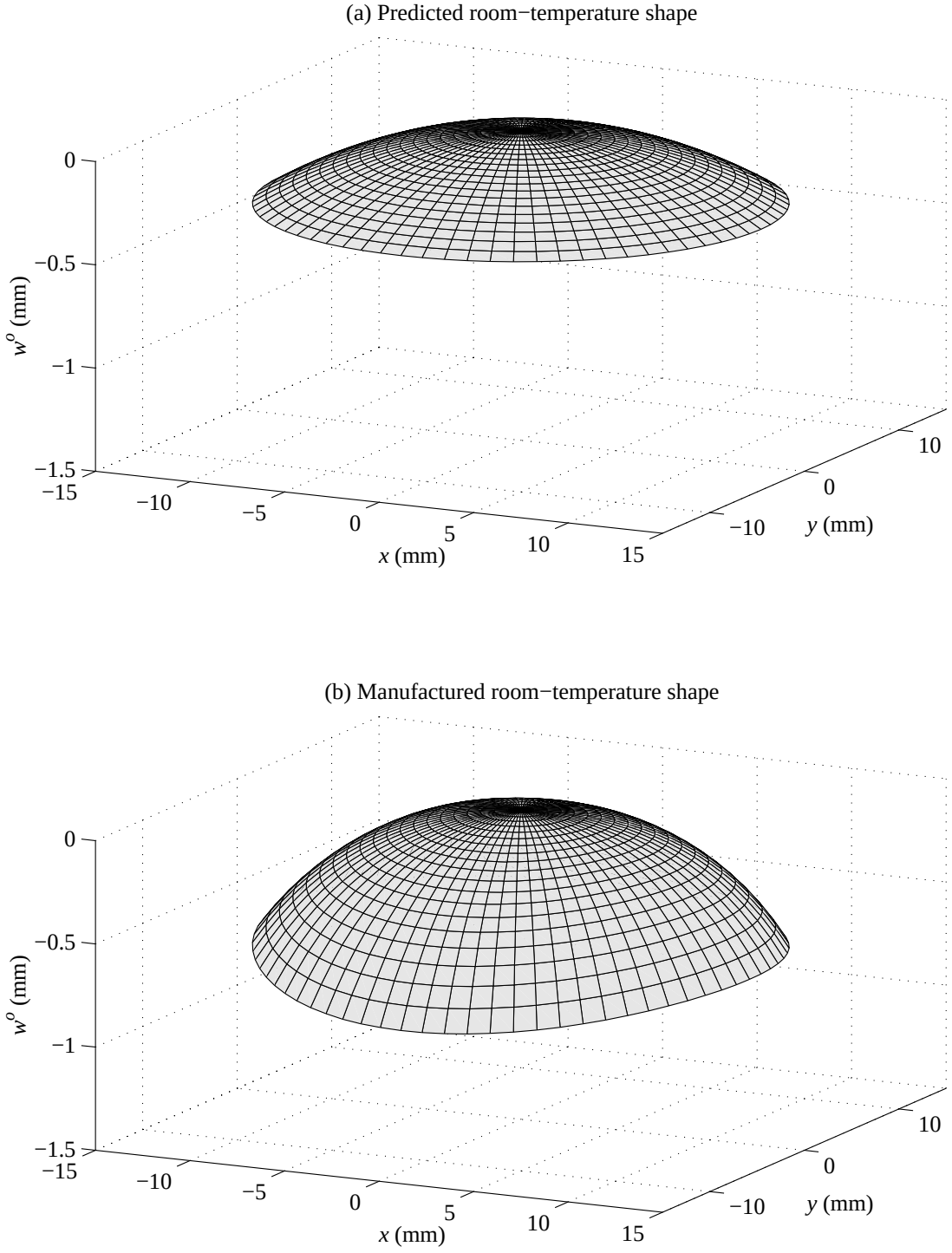


Figure B.24: Comparison of predicted and manufactured room-temperature shapes of RAINBOW sample 3-1.

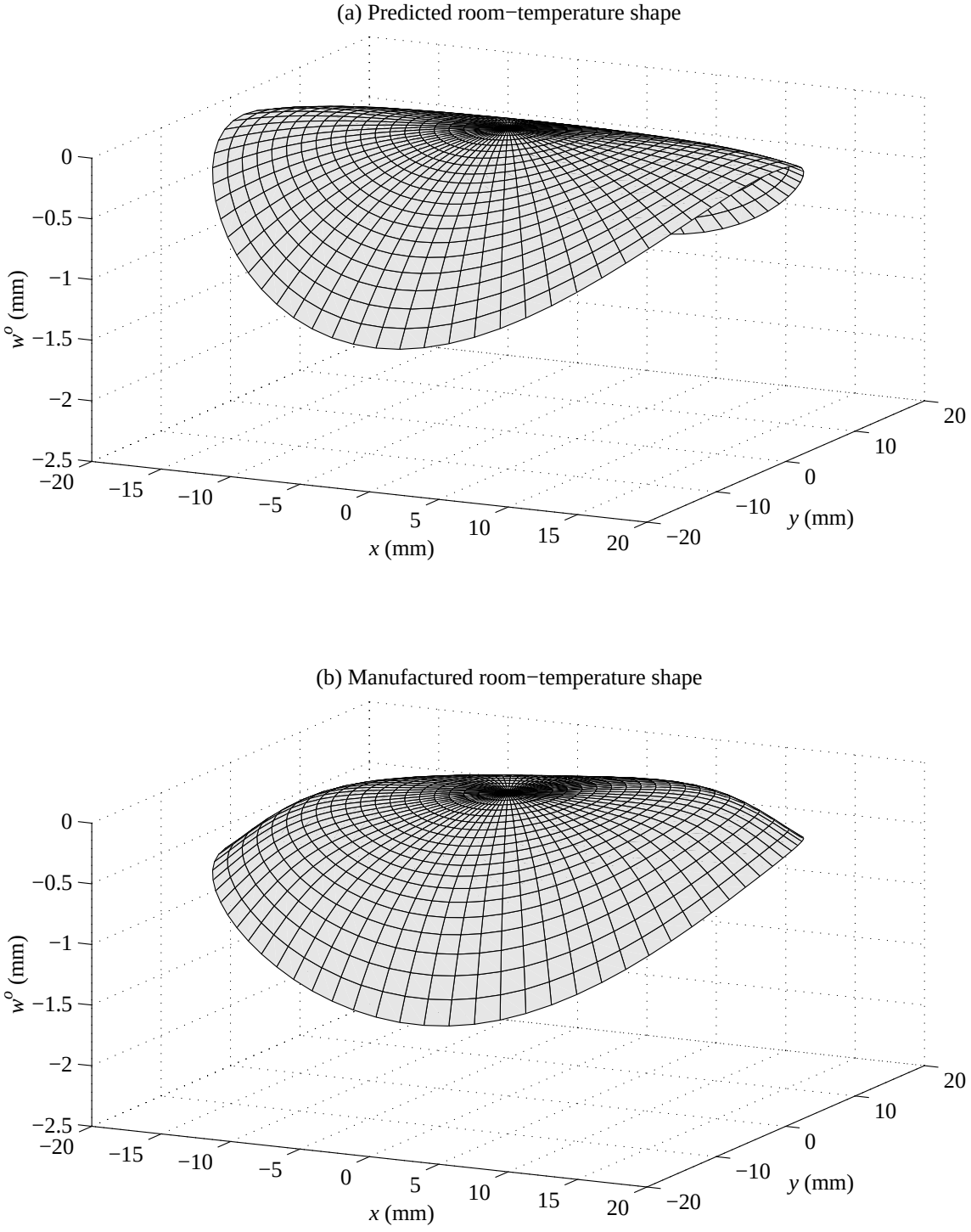


Figure B.25: Comparison of predicted and manufactured room-temperature shapes of RAINBOW sample 3-3.

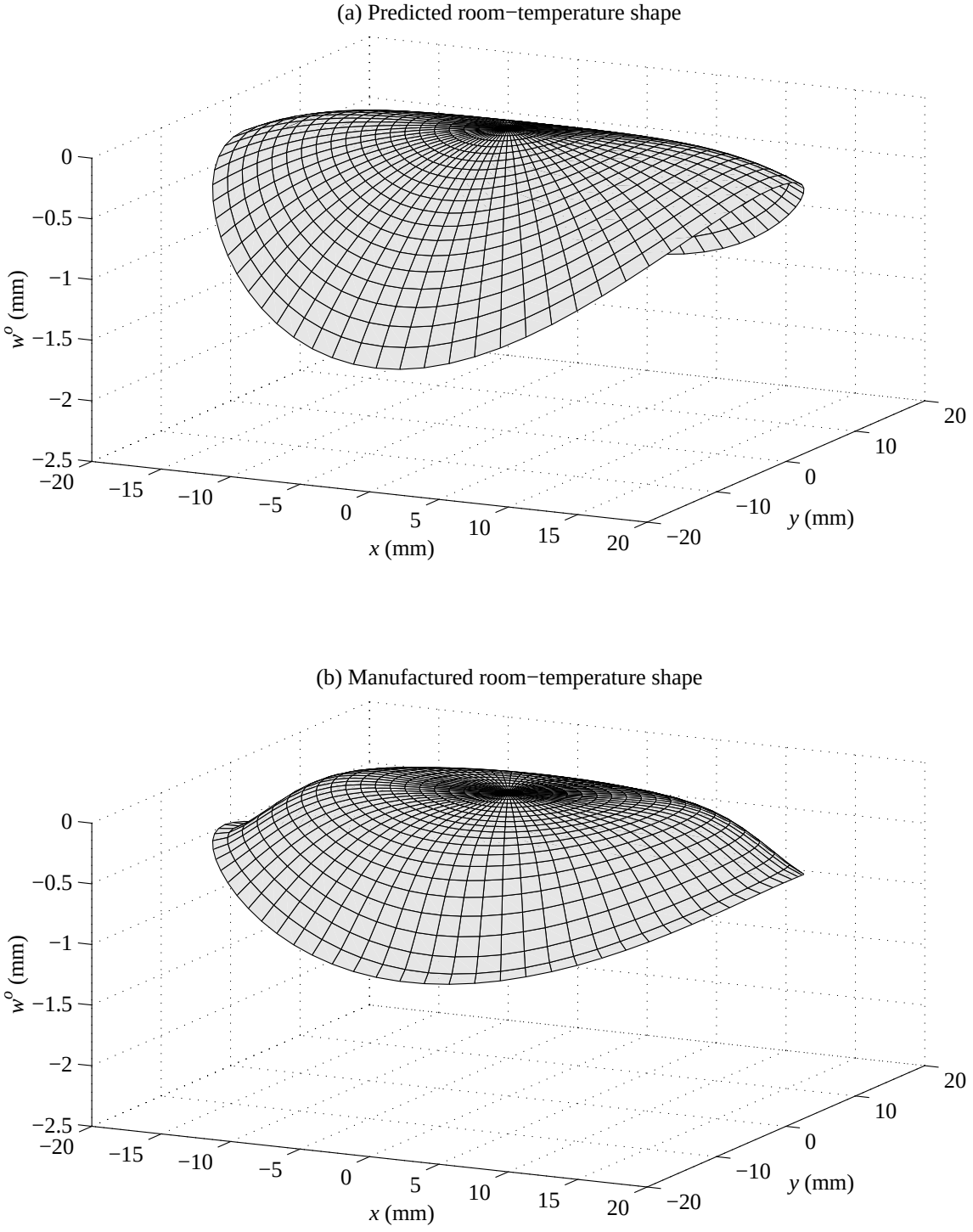


Figure B.26: Comparison of predicted and manufactured room-temperature shapes of RAINBOW sample 3-4.

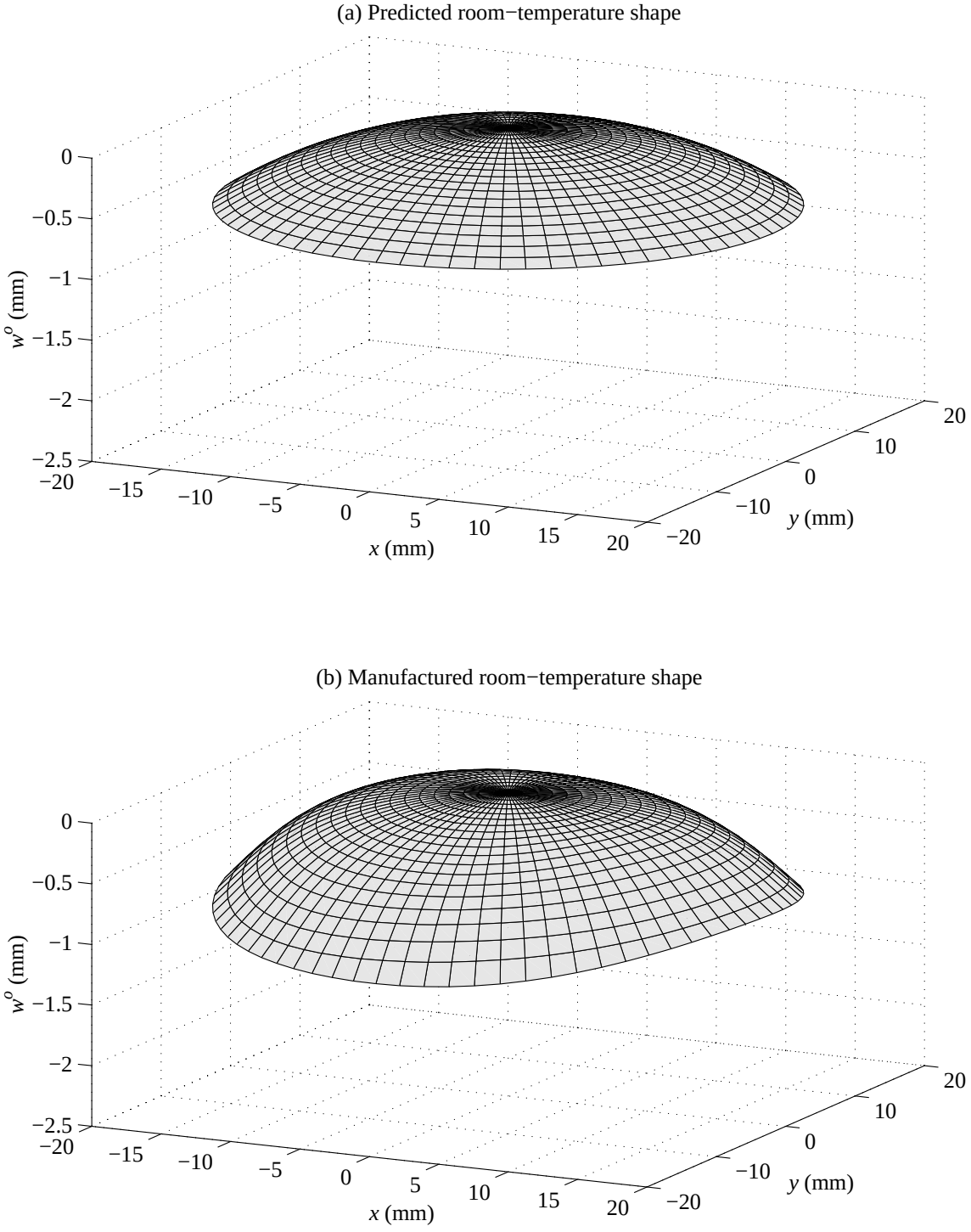


Figure B.27: Comparison of predicted and manufactured room-temperature shapes of RAINBOW sample 4-1.

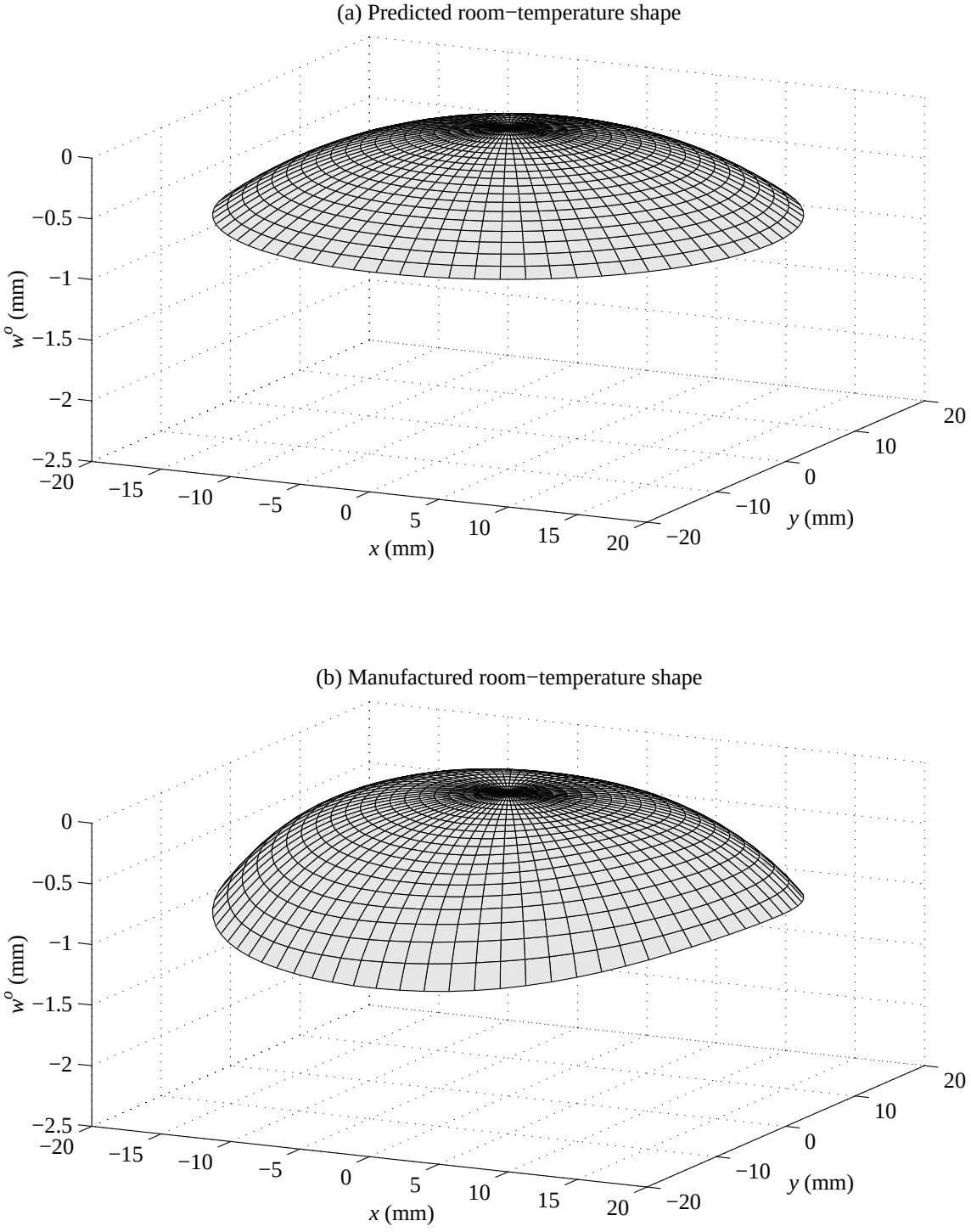


Figure B.28: Comparison of predicted and manufactured room-temperature shapes of RAINBOW sample 4-2.

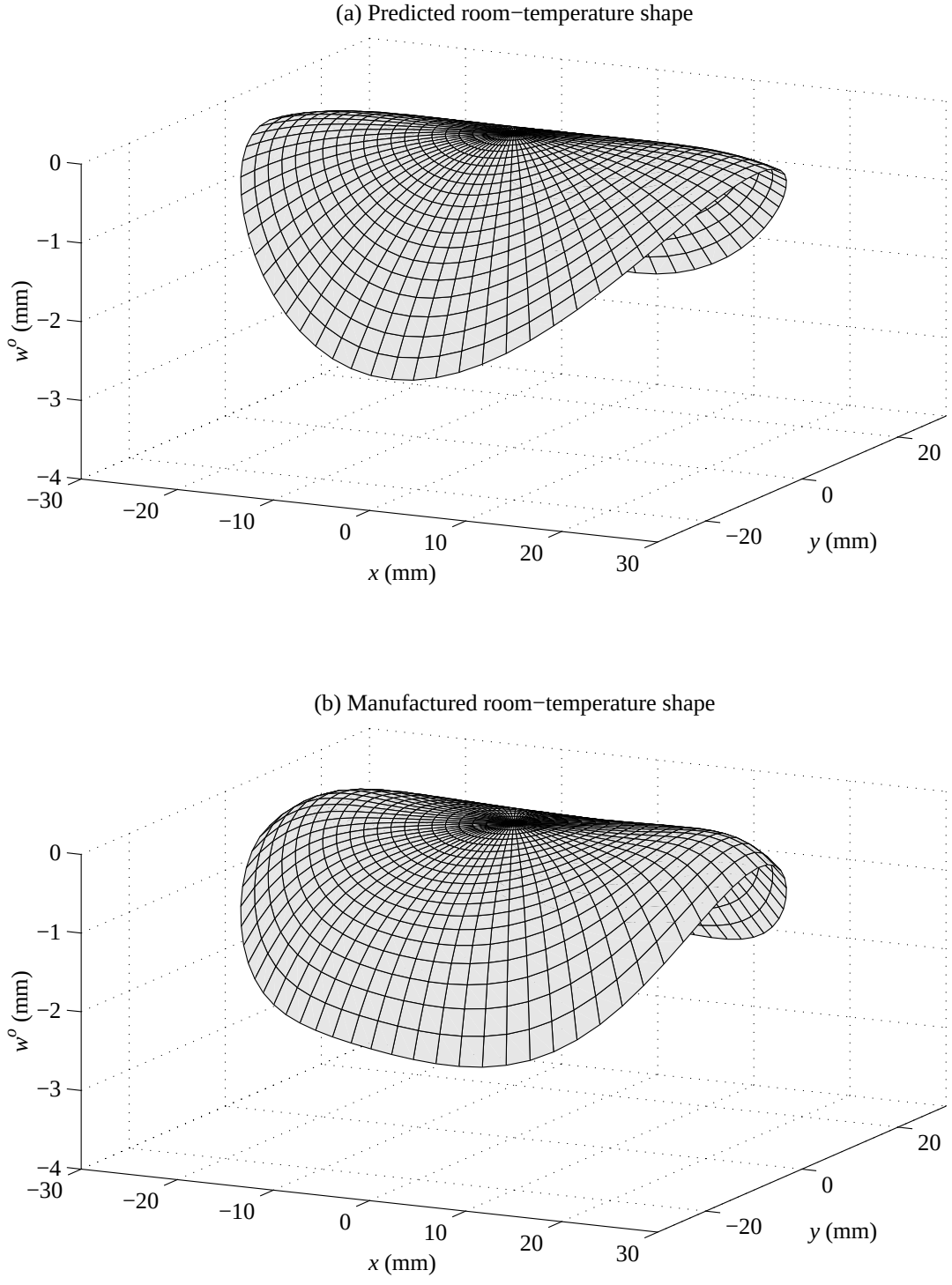


Figure B.29: Comparison of predicted and manufactured room-temperature shapes of RAINBOW sample 4-3.

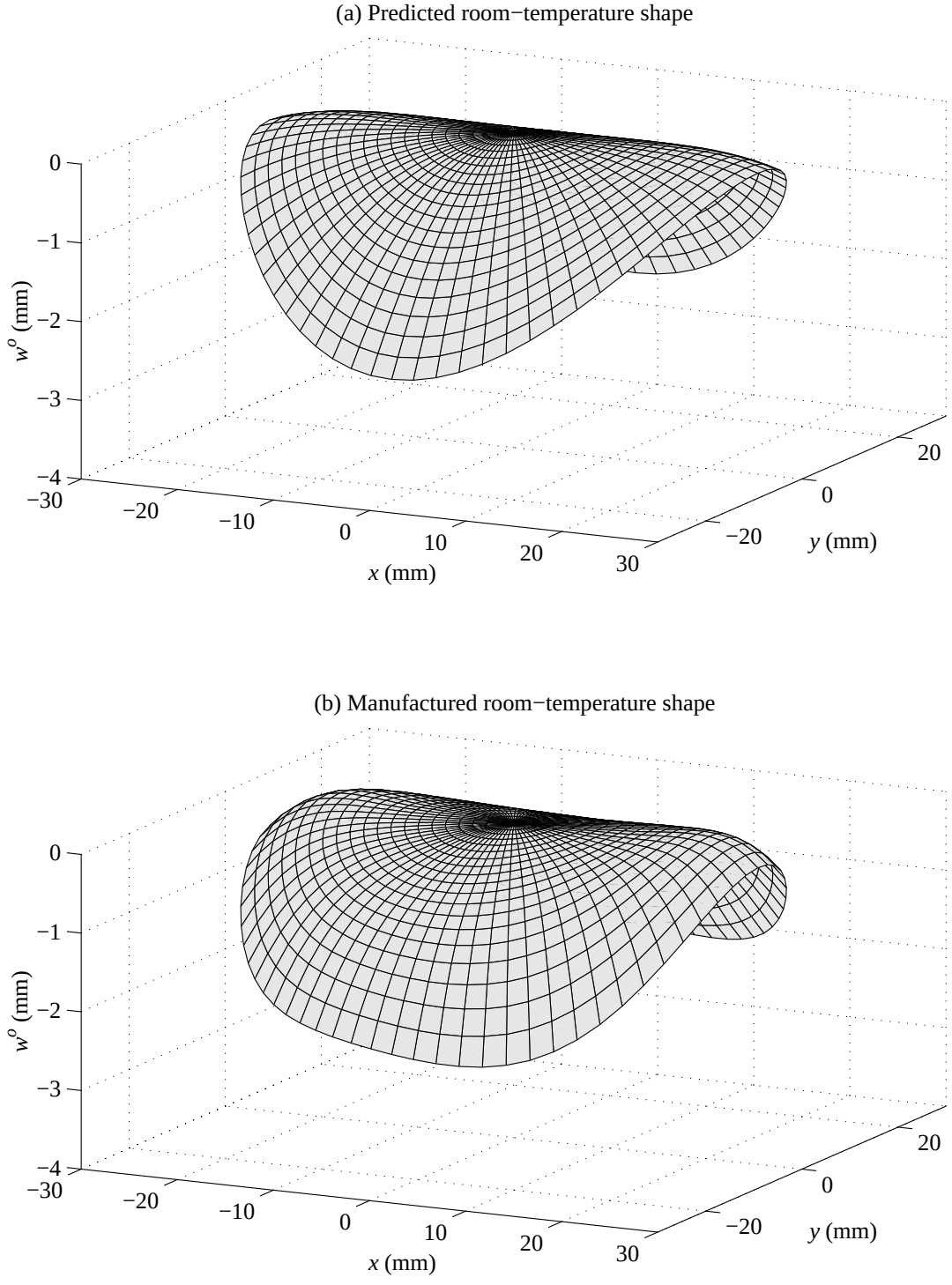


Figure B.30: Comparison of predicted and manufactured room-temperature shapes of RAINBOW sample 4-4.

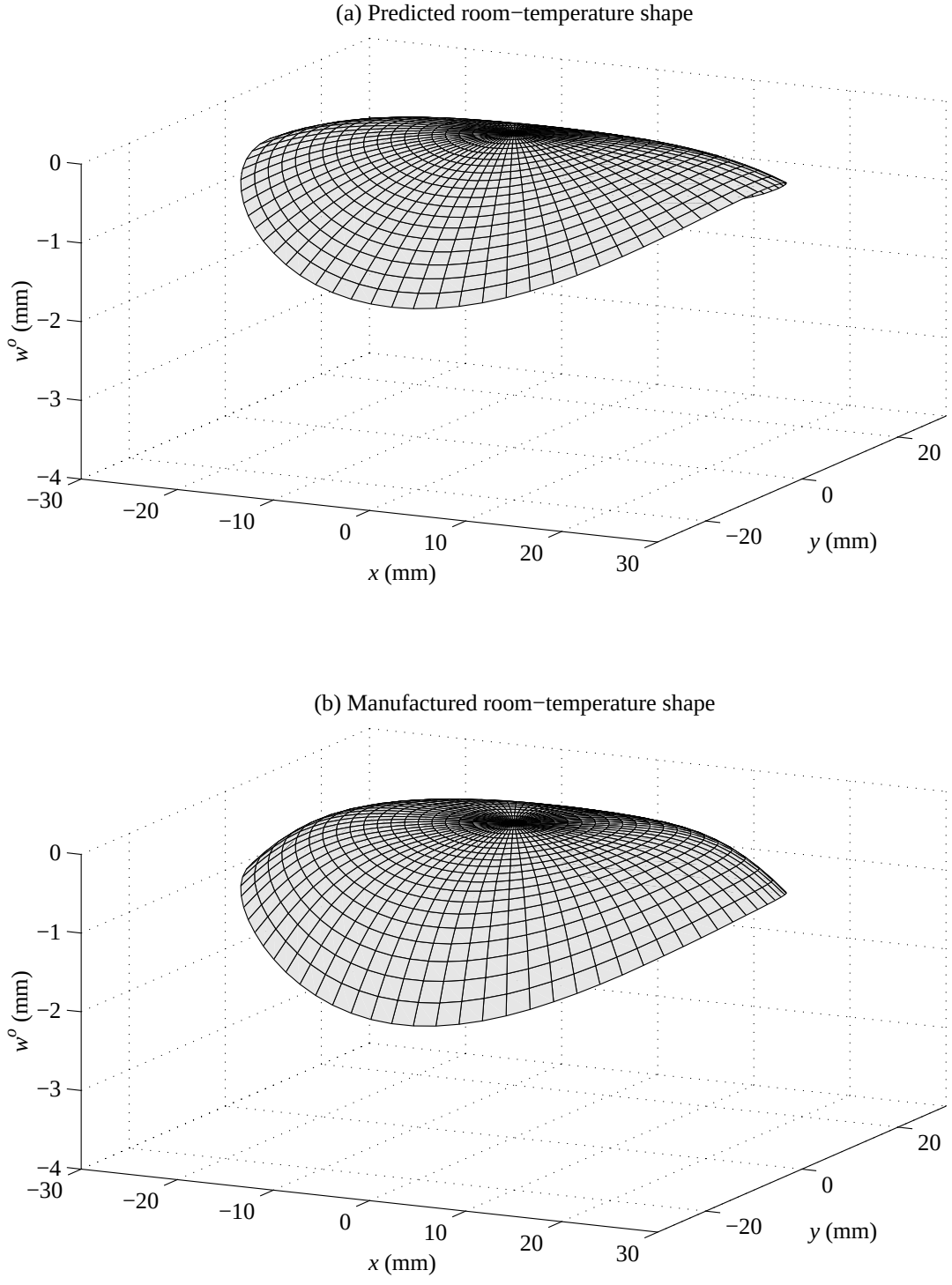


Figure B.31: Comparison of predicted and manufactured room-temperature shapes of RAINBOW sample 5-1.

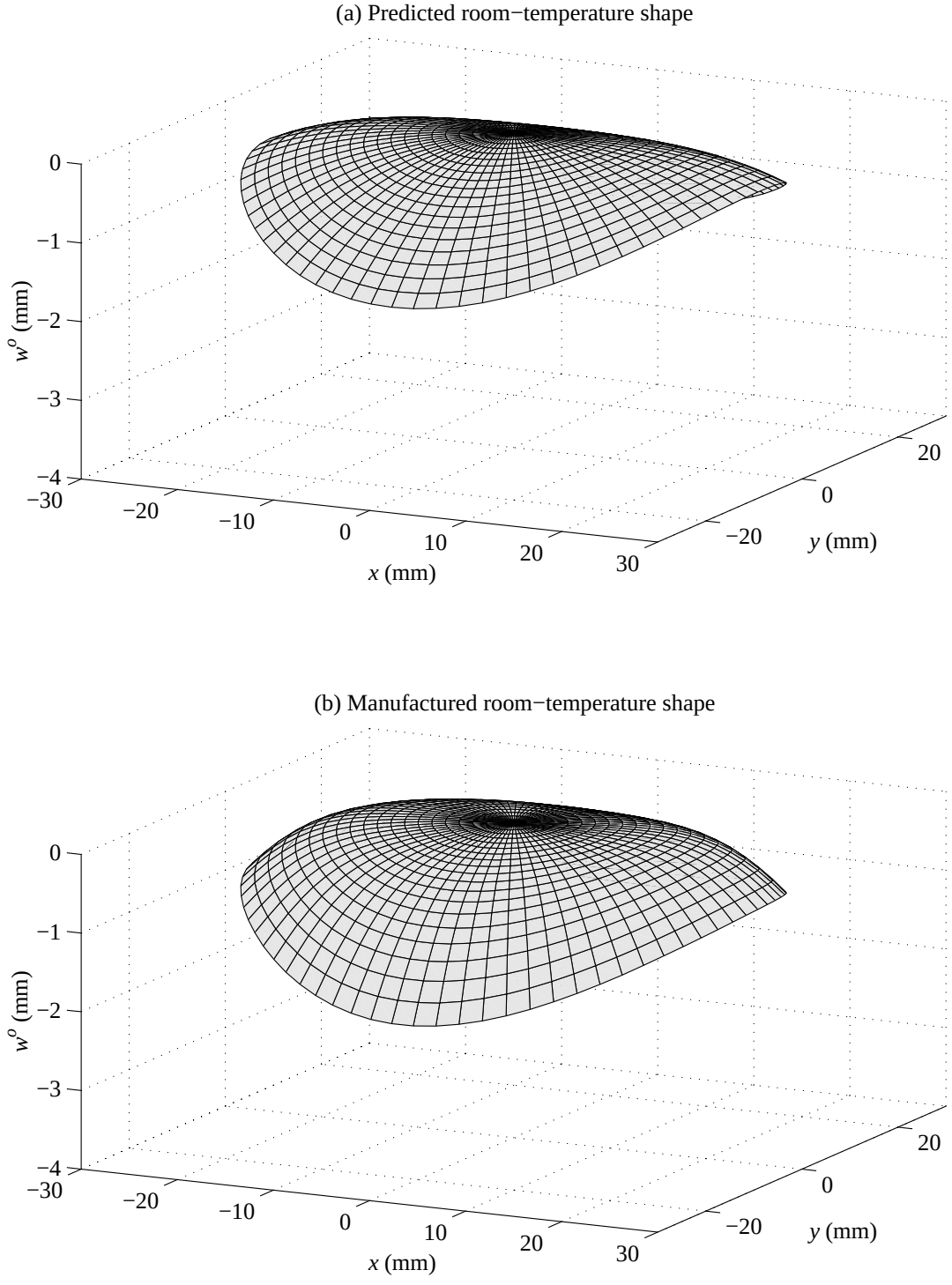


Figure B.32: Comparison of predicted and manufactured room-temperature shapes of RAINBOW sample 5-2.

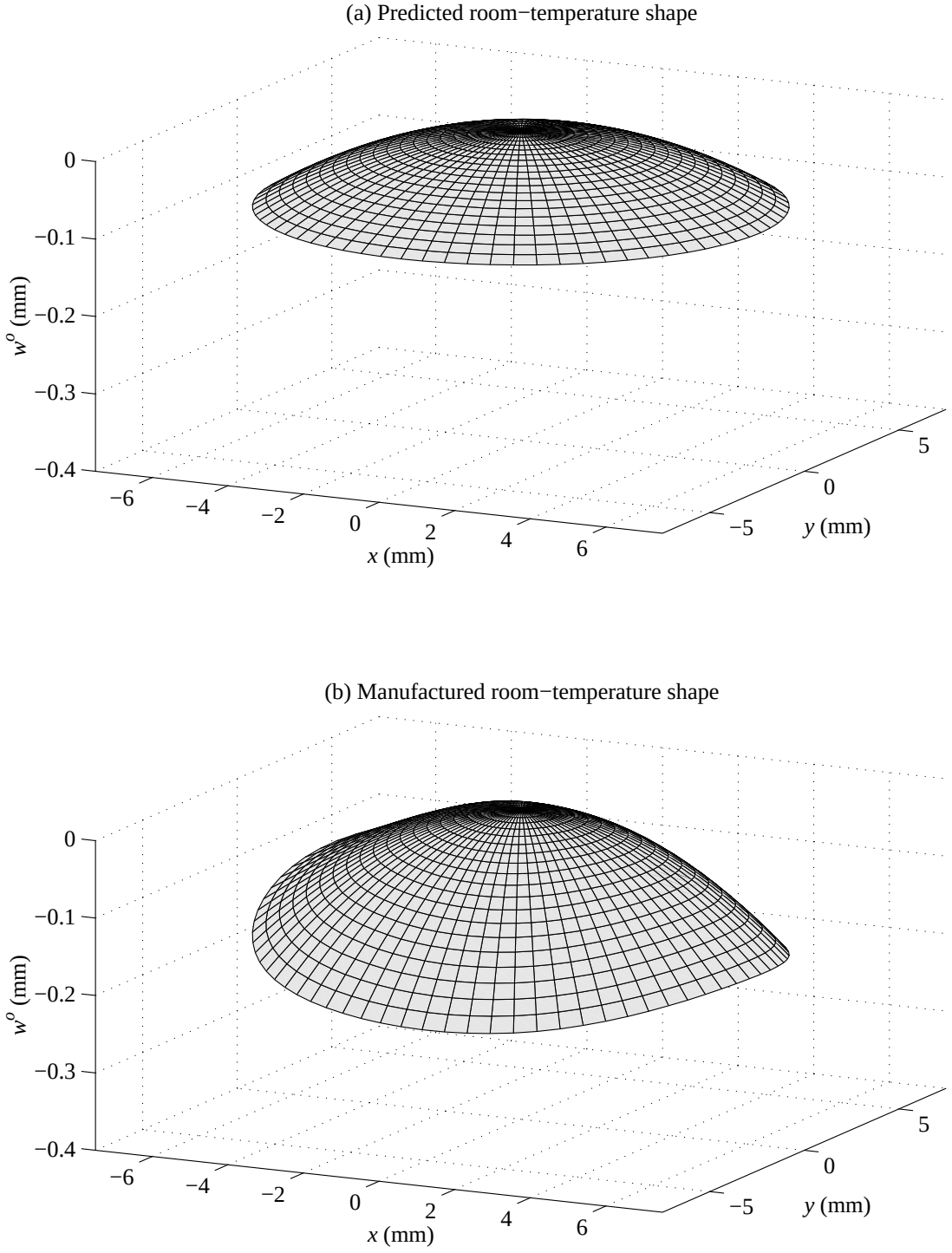


Figure B.33: Comparison of predicted and manufactured room-temperature shapes of RAINBOW sample 10-1.

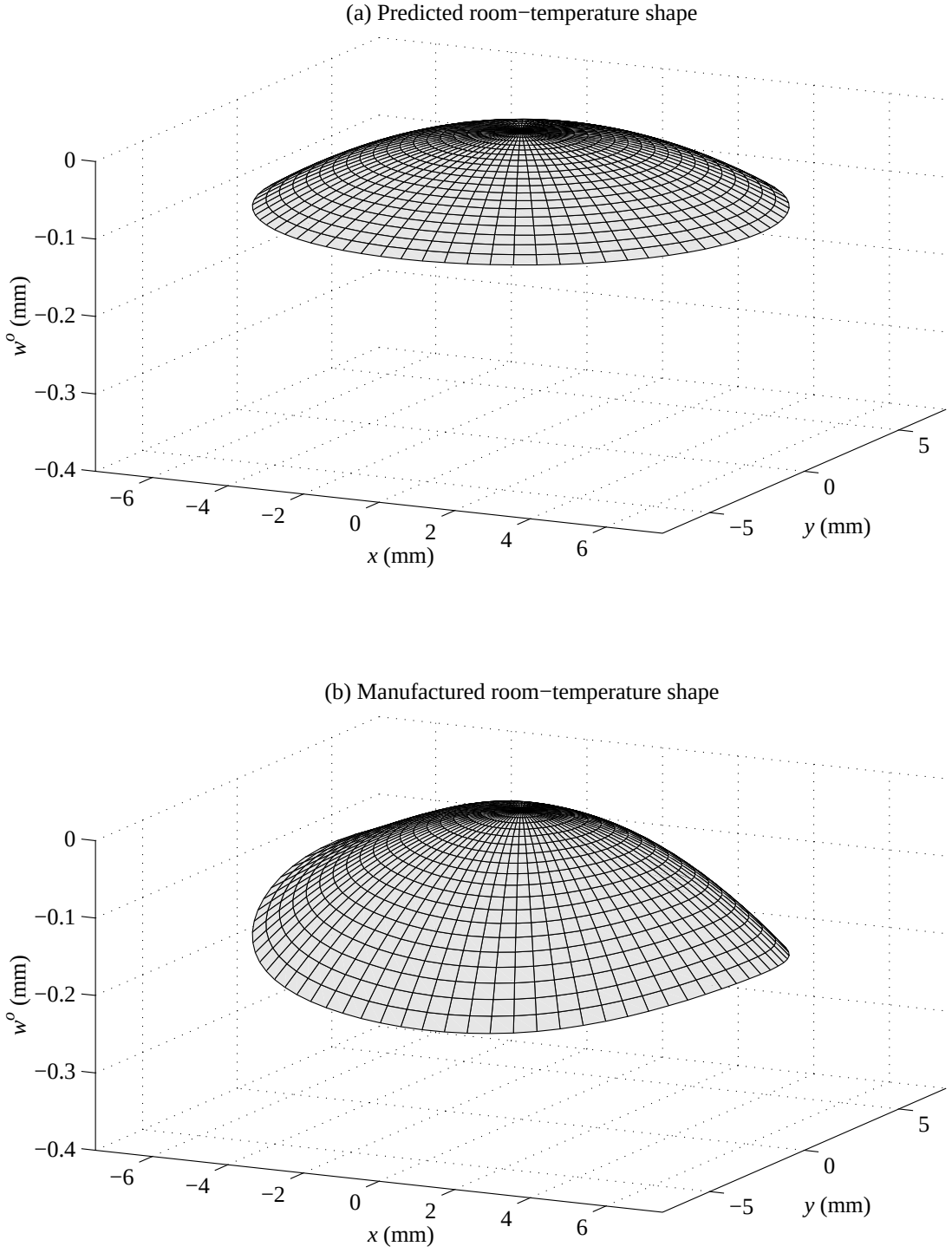


Figure B.34: Comparison of predicted and manufactured room-temperature shapes of RAINBOW sample 10-2.

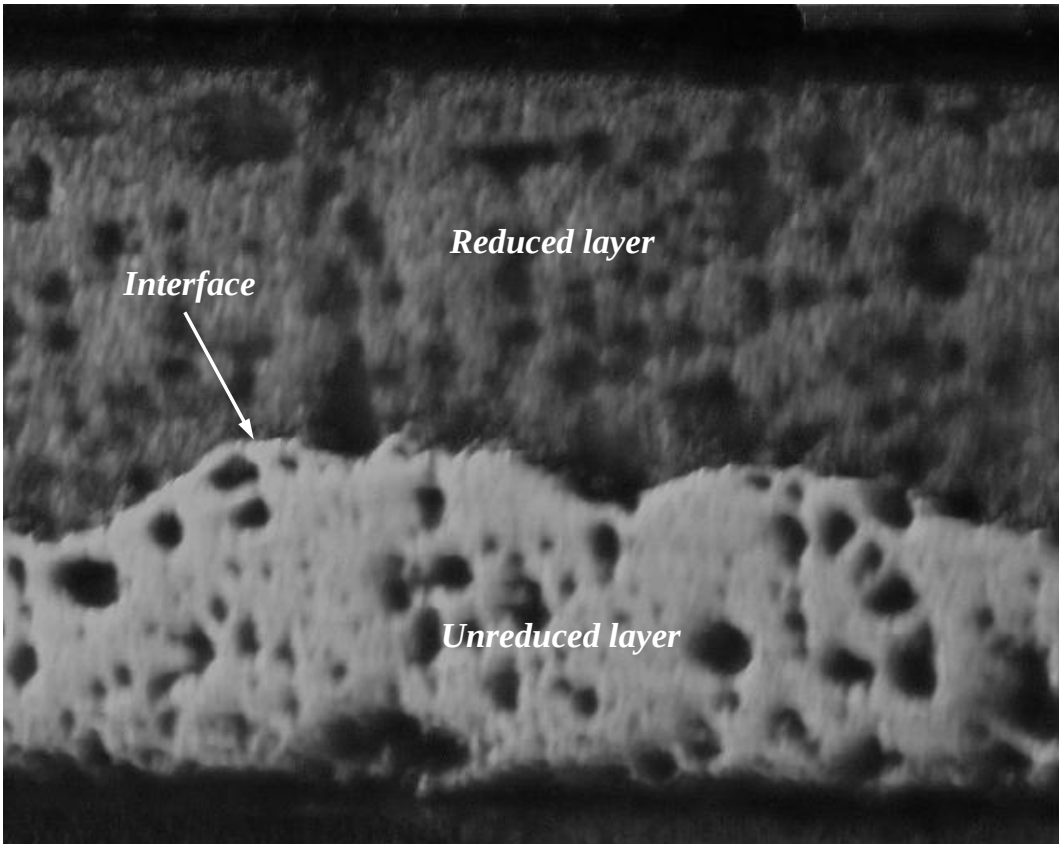


Figure B.35: A polished cross section of RAINBOW sample 4-2 in the neighborhood of $r = 0$ and $\theta = 0$ (magnification factor= 100).

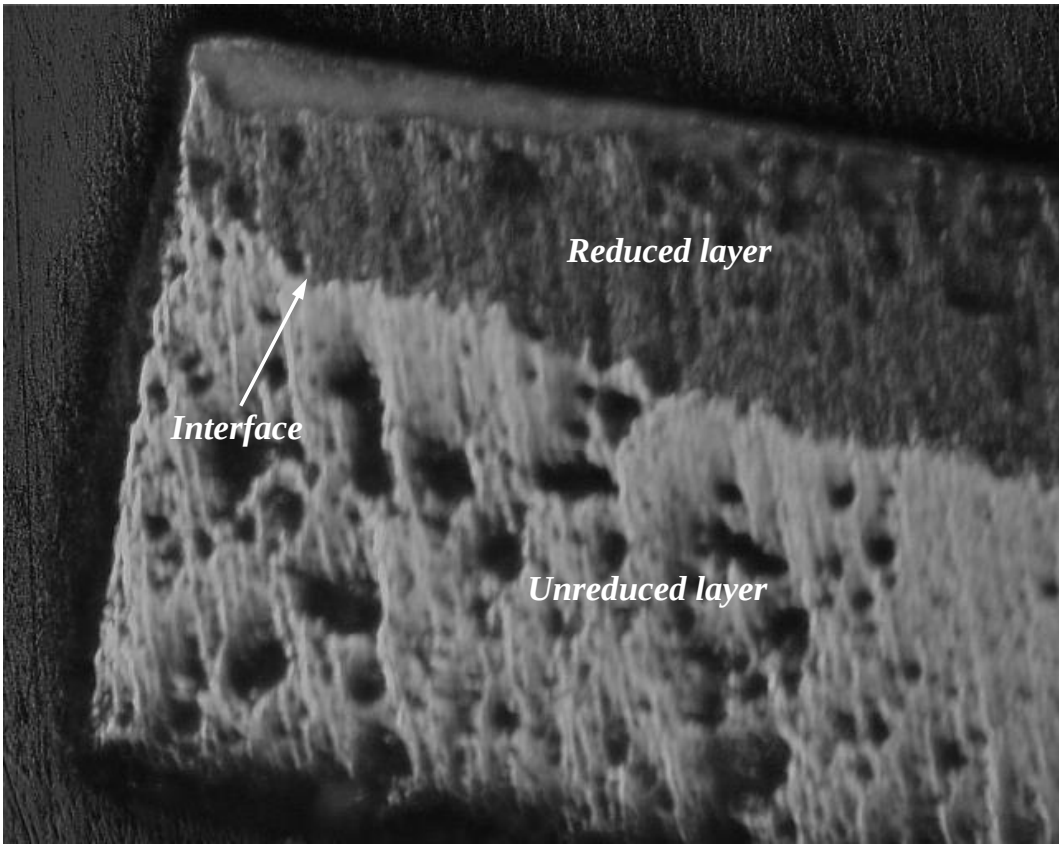


Figure B.36: A polished cross section of RAINBOW sample 4-2 in the neighborhood of $r = R$ and $\theta = 0$ (magnification factor= 100).

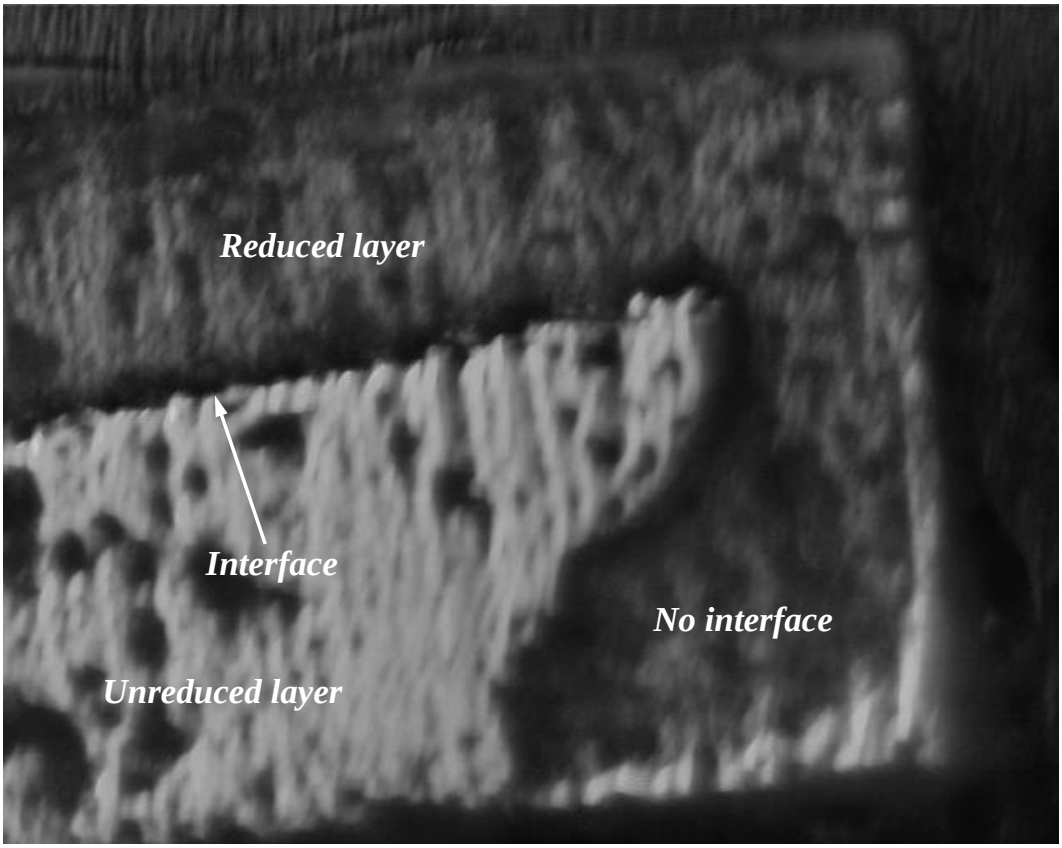


Figure B.37: A polished cross section of RAINBOW sample 4-2 in the neighborhood of $r = R$ and $\theta = \pi$ (magnification factor= 100).

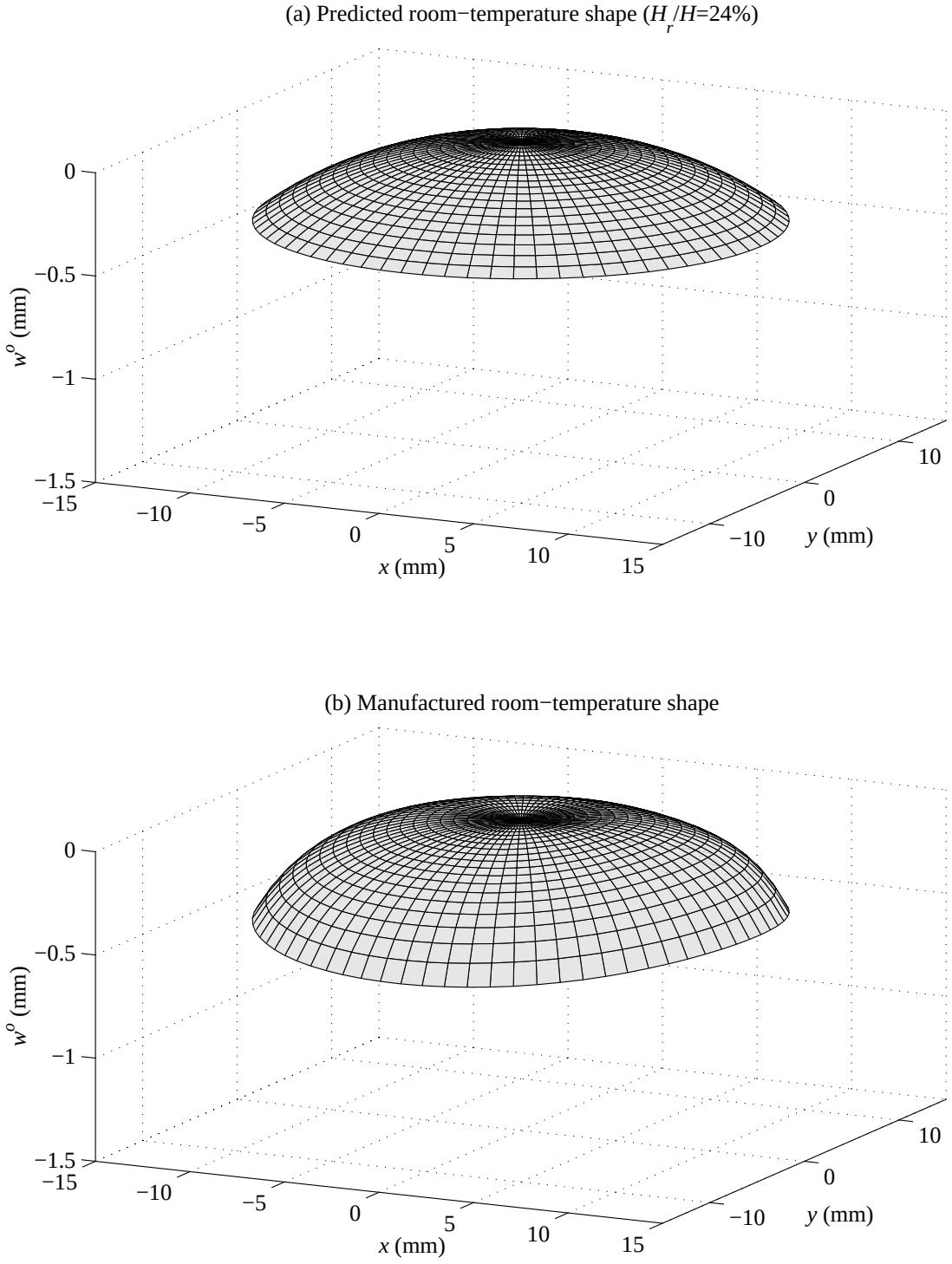


Figure B.38: Comparison of predicted ($H_r/H$=24%) and manufactured room-temperature shapes of RAINBOW sample 1-1.

(a) Predicted room−temperature shape ($\alpha_r$=10.51 × 10 $^{-6}$ $^{o}$C$^{-1}$)

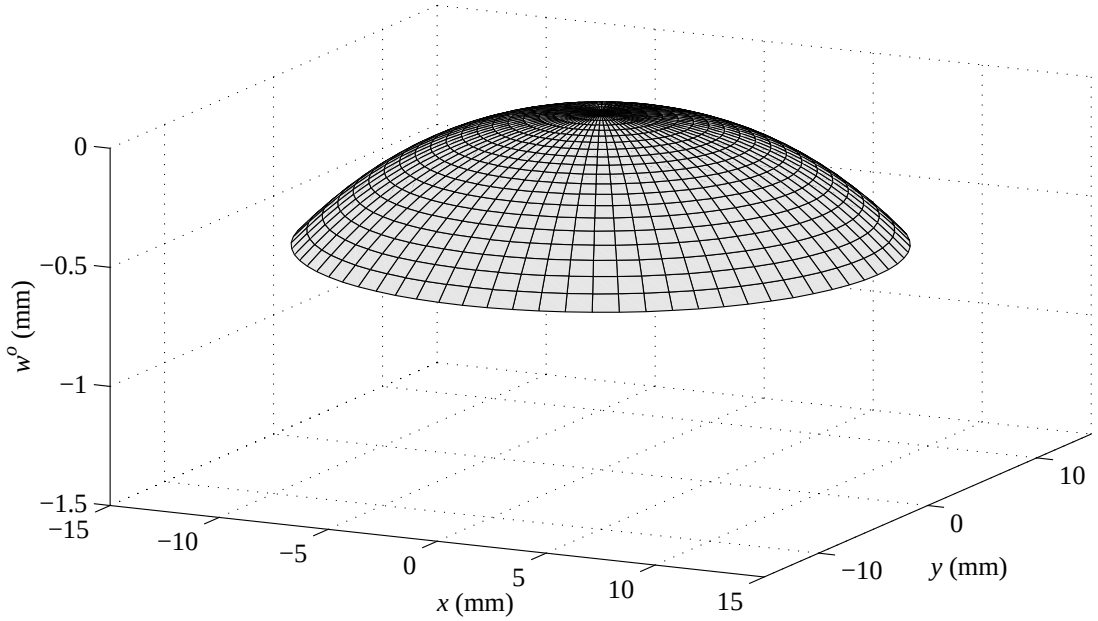


(b) Manufactured room−temperature shape

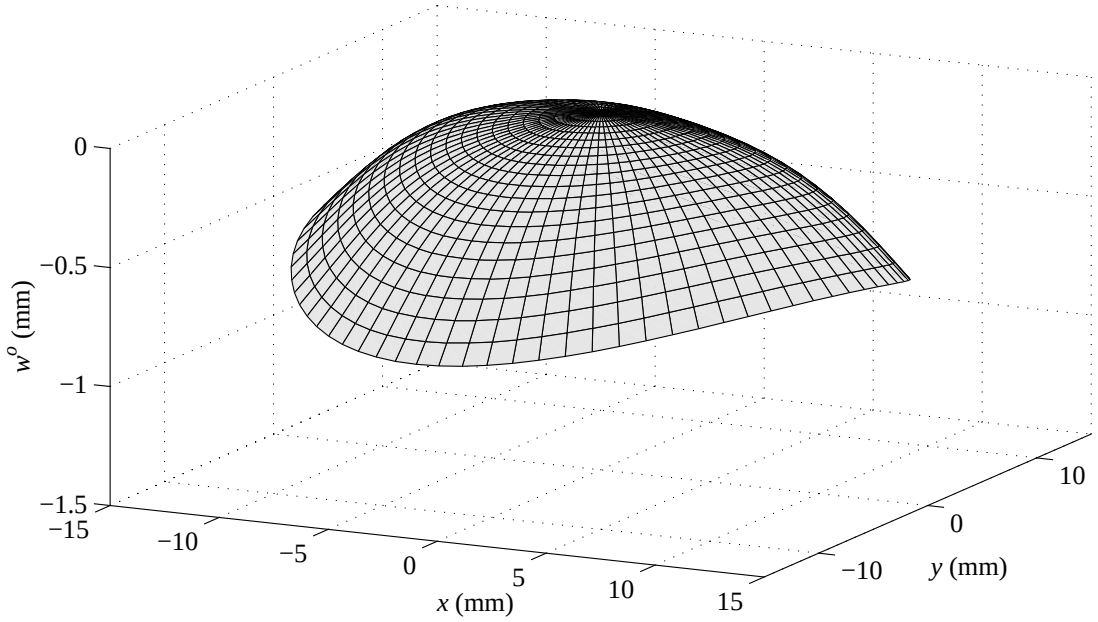


Figure B.39: Comparison of predicted ($\alpha_r = 10.51 \times 10^{-6}$ $^{o}$C$^{-1}$) and manufactured room-temperature shapes of RAINBOW sample 2-4.

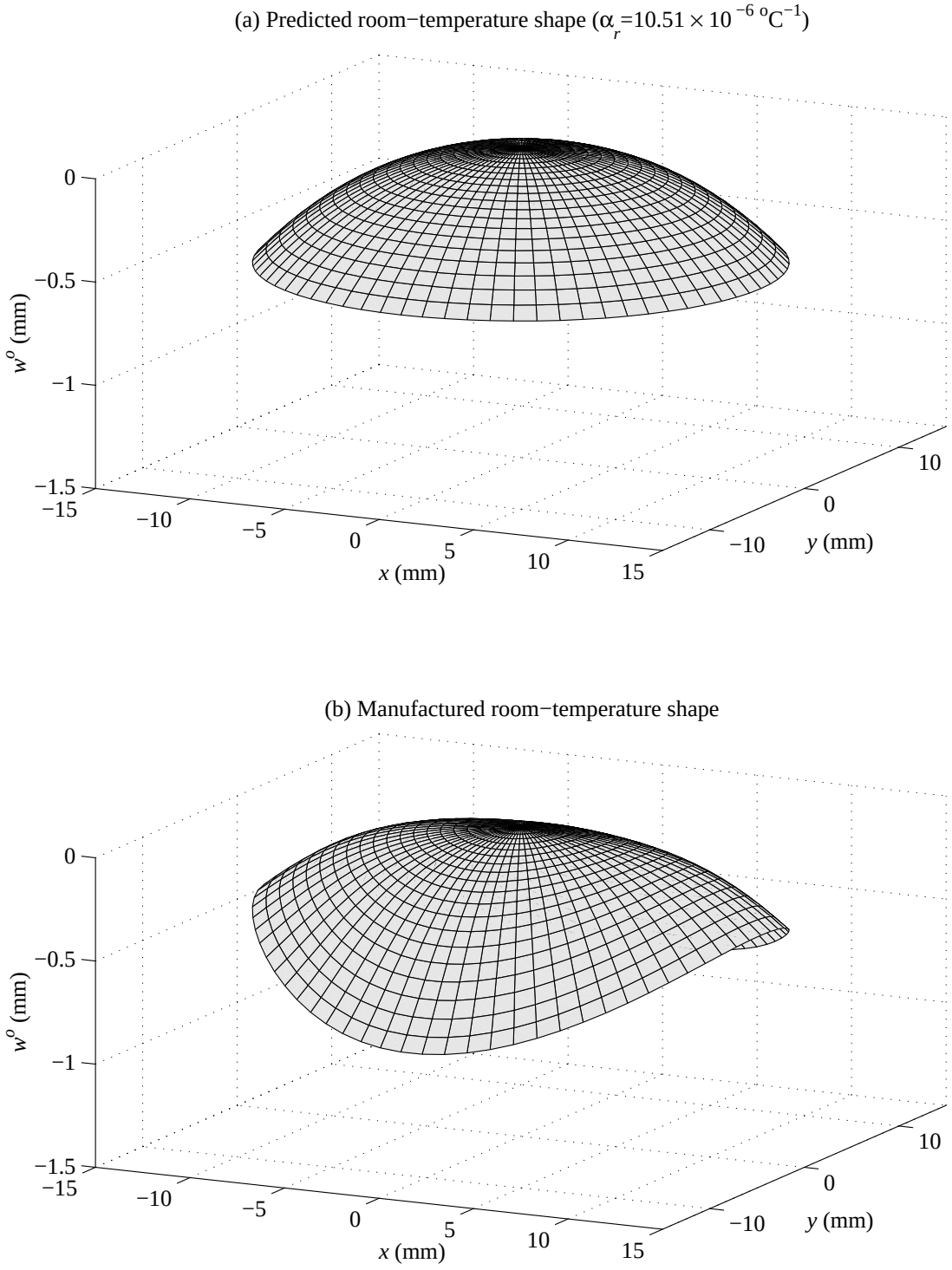


Figure B.40: Comparison of predicted ($\alpha_r = 10.51 \times 10^{-6}$ $^{o}$C$^{-1}$) and manufactured room-temperature shapes of RAINBOW sample 2-2.

(a) Predicted room−temperature shape (20% orthotropy in the reduced layer)

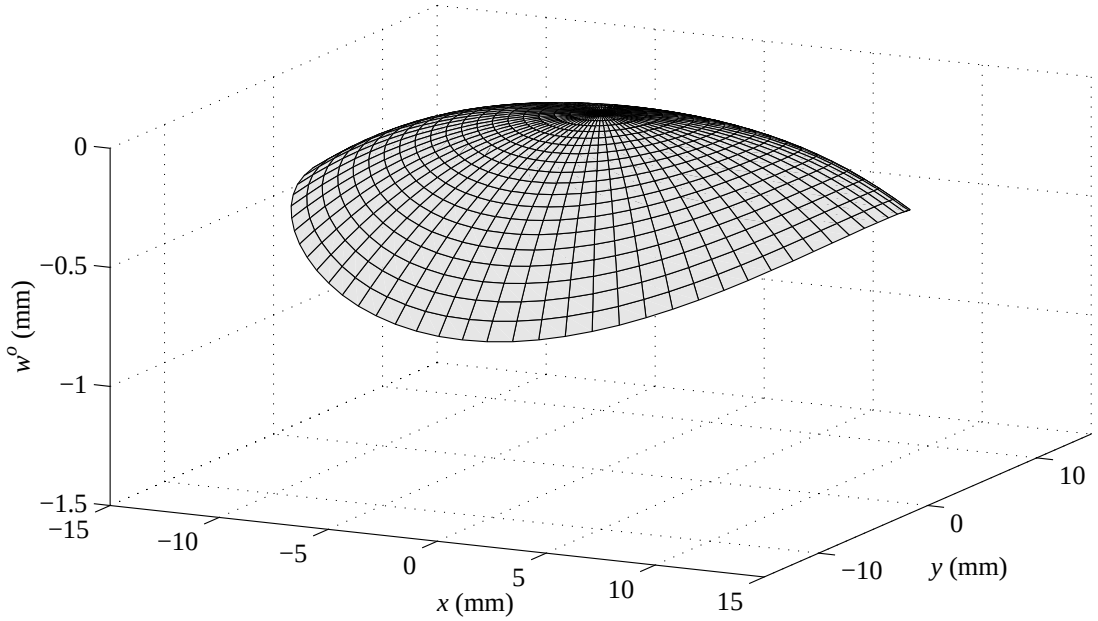


(b) Manufactured room−temperature shape

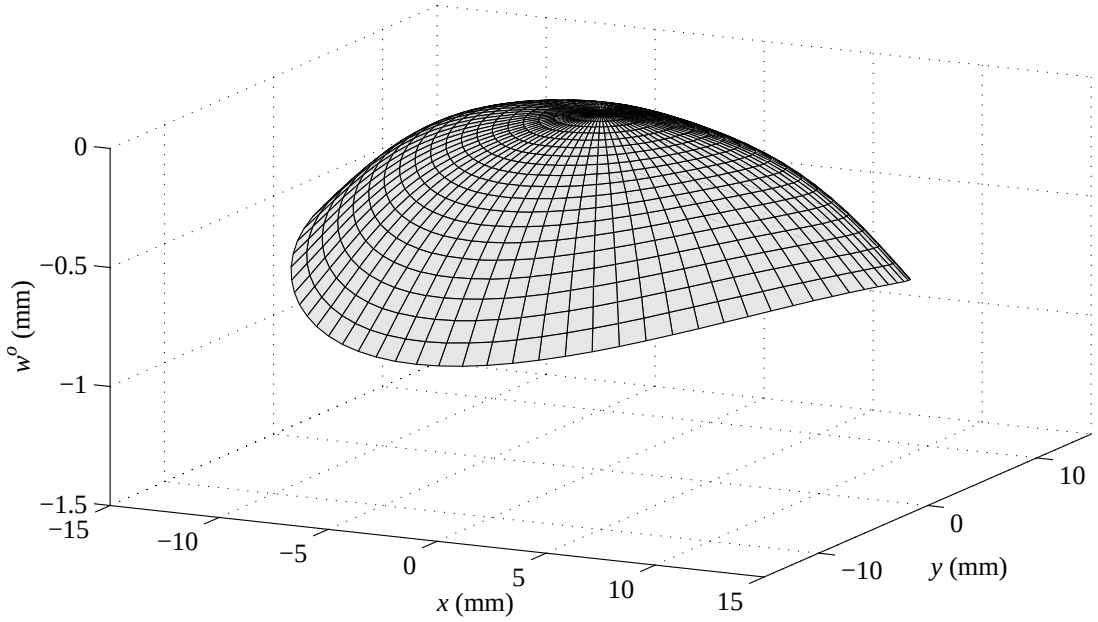


Figure B.41: Comparison of predicted (20% orthotropy in the reduced layer) and manufactured room-temperature shapes of RAINBOW sample 2-2.

(a) Predicted room−temperature shape (20% orthotropy in the reduced layer)

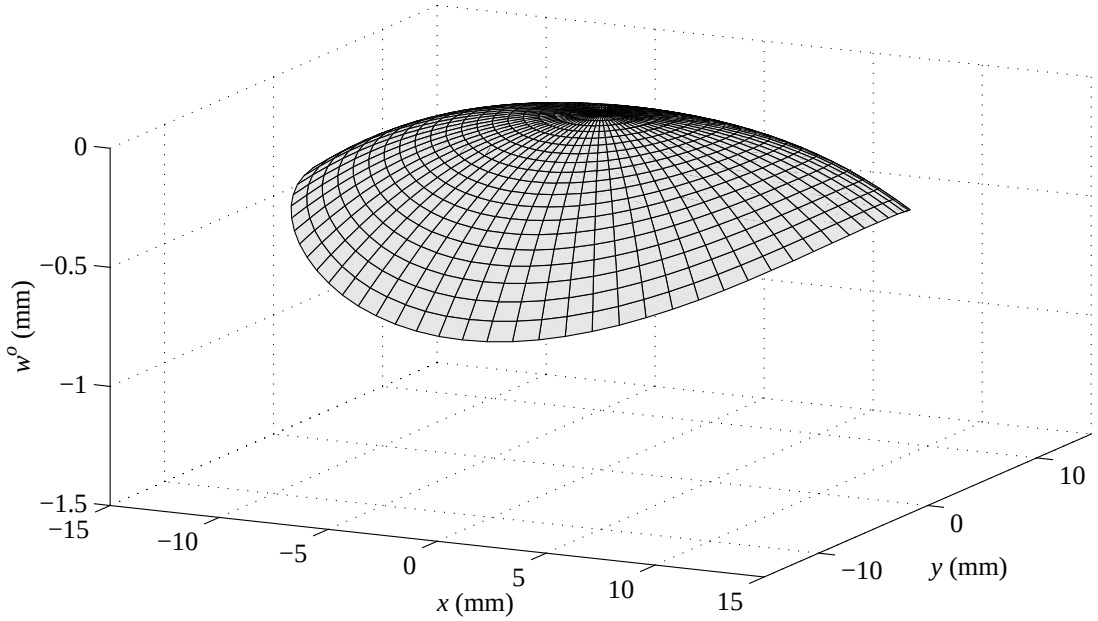


(b) Manufactured room−temperature shape

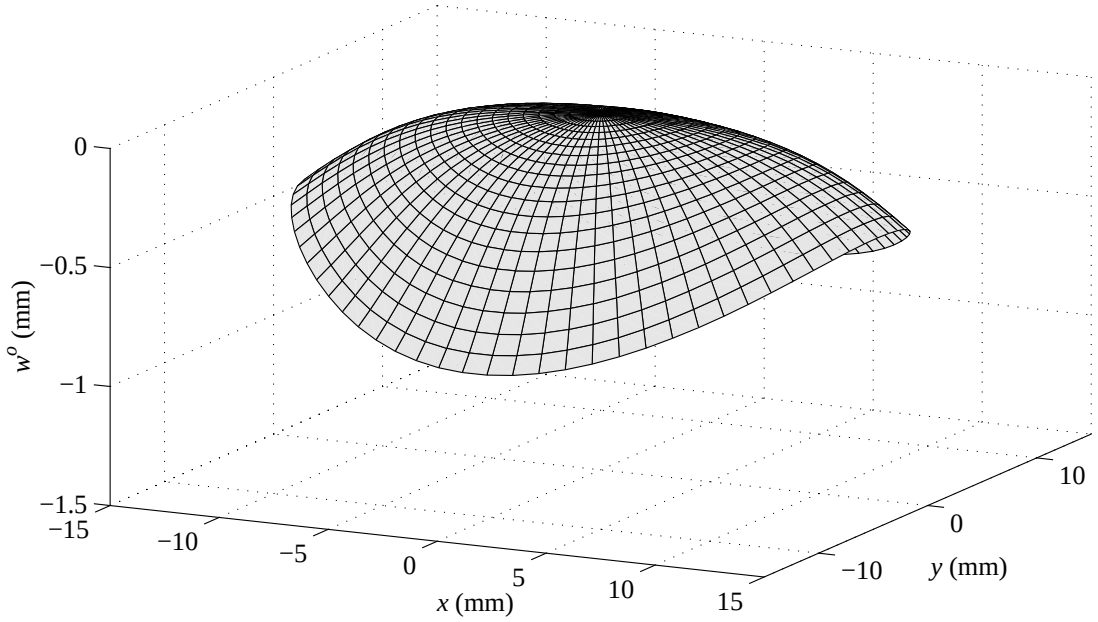


Figure B.42: Comparison of predicted (20% orthotropy in the reduced layer) and manufactured room-temperature shapes of RAINBOW sample 2-4.

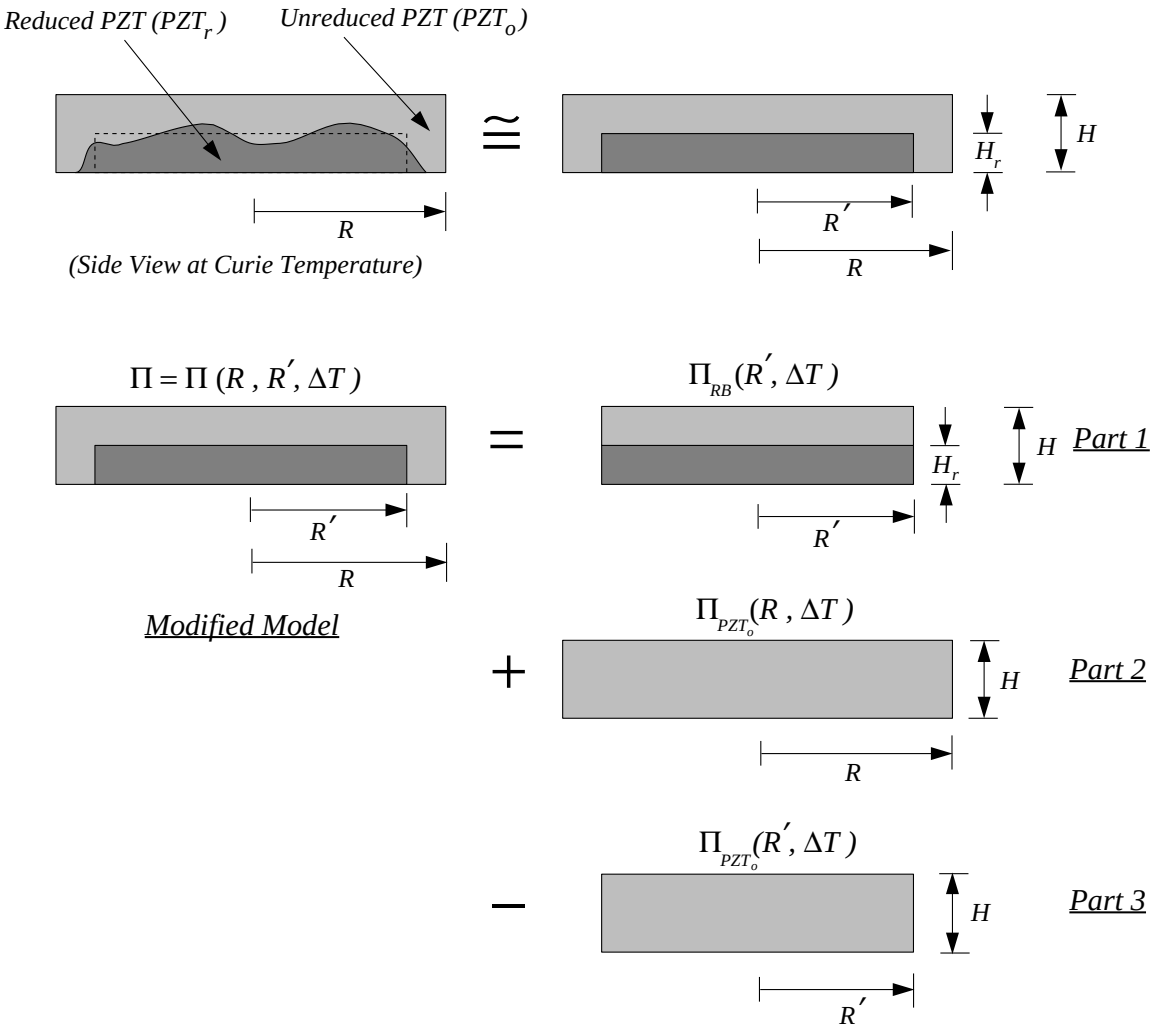


Figure B.43: Description of the modified model to account for manufacturing defects in disk-style RAINBOW.

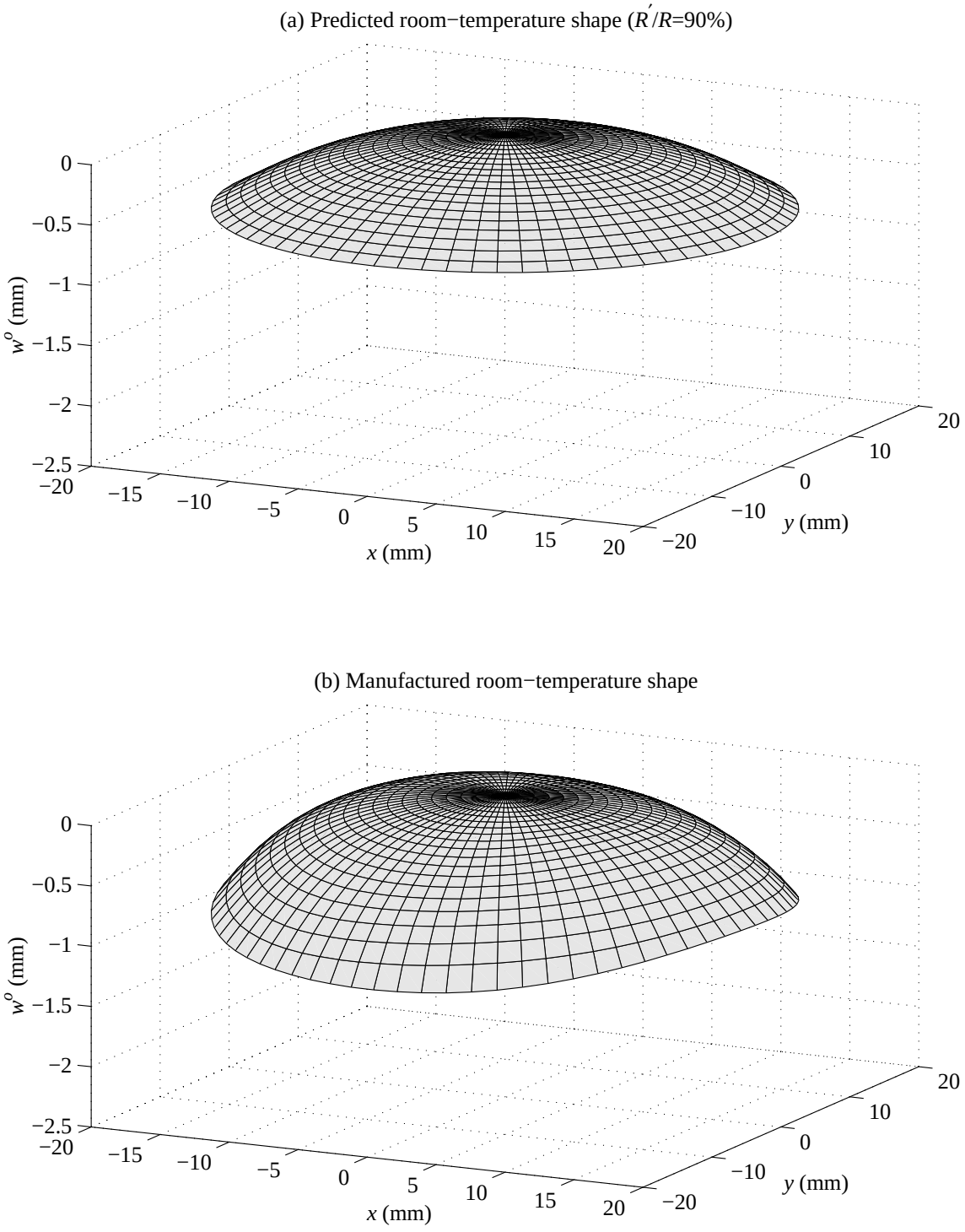


Figure B.44: Comparison of predicted (including unreduced edges) and manufactured room-temperature shapes of RAINBOW sample 4-2.

# Vita

Adel Benhaj Jilani

Adel Benhaj Jilani was born on December 1, 1966 in Sousse, Tunisia. He was awarded a Bachelor of Science degree with distinction in Civil Engineering from *Colorado State University* in May of 1989. At the same university he carried out graduate research work in the field of solid mechanics under the supervision of Prof. Paul R. Heyliger and he received a Master of Science in Civil Engineering in May 1992. After working at the *Groupe de Recherche en Biomécanique et Biomatériaux* of *École Polytechnique de Montréal* as a research associate, under the supervision of Prof. Shirazi-Adl, and receiving another Master of Science degree in Mechanical Engineering in December 1995, he enrolled at *Virginia Polytechnic Institute and State University* as a doctoral student of Engineering Mechanics in January 1996. He received the degree of Doctor of Philosophy of Engineering Mechanics in December 1999. He began work as a hardware design engineer for *Hewlett-Packard* in Corvallis, Oregon in November 1999.